Franco Tassi
Orlando Vaselli
Alberto Tomas Caselli   *Editors*

Copahue Volcano

Springer

Editors
Franco Tassi
Department of Earth Sciences
University of Florence
Florence
Italy

Orlando Vaselli
Department of Earth Sciences
University of Florence
Florence
Italy

Alberto Tomas Caselli
National University of Rio Negro
General Roca, Rio Negro
Argentina

Contents

Preface

As Editors and researchers we are flattered to present this monograph dedicated to the Copahue volcano ("The smoking mountain between Argentina and Chile") that is located in a remote site of Patagonia, right at the border between Chile and Argentina. The three recent volcanic eruptions (2000, 2012, and 2013) and the present unrest state have had a global echo. The acidic crater lake on the top of the mountain is suffering strikingly modifications and after the eruptive event of 2012, it completely disappeared and then, after a few months the pre-existing conditions almost recovered, although a balance between the inner (e.g., deep fluids) and outer (e.g., meteoric precipitation and ice melting) forces has not yet been established. These repeatedly changing volcanic situations have seen the involvement of several scientists from different part of the world who have contributed with their efforts to a better understanding of the volcanic plumbing and the hydrothermal/magmatic systems. Attempts to build a seismic monitoring array and periodic geochemical and ground deformation surveys are presently underway. Difficulties in retrieving appropriate financial supports, logistic problems, long distances from the main cities of Argentina, instrumental supplies, and trained personnel are some of the many challenges to be solved. The final target would be that to create a volcanological and seismological observatory in this area of Patagonia, able to monitor Copahue and the other volcanic edifices nearby located, such as Peteroa, Lanin, Tromen, and Domuyo.

This monograph, belonging to the Volcanoes of the World Book Series published by Springer-Verlag, is intended to represent a sort of a benchmark for those researchers who want to know more about Copahue.

The volume is divided into five parts: (1) Geology; (2) Eruptive History; (3) Petrology and Geochemistry; (4) Volcanic Monitoring and (5) Volcano and Society.

The volume opens with two interesting reviews by Folguera et al. and Groppelli et al. on the geological and geodynamical settings of this part of the Andes, whose interpretations indicate the need to acquire more data to achieve a common view on the development of the volcanism affecting the area. These aspects are basic and fundamental tools to explain the volcanic events of Copahue. The two contributions by Caselli et al. on the prehistoric to the recent volcanic activity and the December 2012 event summarize what is known about the eruptive style of this volcano. Varekamp et al. provides a

nice review of published and original data of trace and radiogenic elements, highlighting the petrological features of the Copahue volcanic products. This section precedes that of Tassi et al. where a geochemical conceptual model based on chemical and isotope composition of hydrothermal/volcanic gas discharges is presented and gives important hints on a possible gas geo-chemistry monitoring activity at Copahue. The volcanic monitoring session includes two contributions devoted to ground deformation (Vélez et al.) and water geochemistry (Agusto and Varekamp), where innovative views about the possible volcanic surveillance activities are considered. Caselli et al. provide a comprehensive overview of the risk assessment, focusing on the main hazards related to the activity of this volcano, whereas Rodríguez et al. describe the chemistry of the acid rivers and lakes characterizing this system, interpreted as a good terrestrial analogue for the aqueous paleo-environments on Mars. The fifth part of the volume includes three chapters concerning the geothermal energy and its historical development in the Copahue area by Mas et al., the use of the numerous thermal waters mainly discharging in the village of Caviahue where several spas and resorts are operating (Monasterio et al.), and the religion and popular believes inspired to Mapuche by the presence of the smoking mountain (Castaño et al.).

It is the hope of the Editors that this volume may keep interested the scientific community about the volcanic system of Copahue, which, for different reasons, in the past has somehow not been considered a serious threat for the local population. The recent reactivation of Copahue has unfortunately demonstrated that a lot of work has to be done. To avoid that new and more dangerous eruptions are going to hit unprepared the popula-tion, a tighter collaboration between the local and regional authorities and the scientists is a must.

A Review of the Geology, Structural Controls, and Tectonic Setting of Copahue Volcano, Southern Volcanic Zone, Andes, Argentina

1

A. Folguera, E. Rojas Vera, L. Vélez, J. Tobal, D. Orts,
M. Agusto, A. Caselli and V.A. Ramos

Abstract

Copahue Volcano lies in the Southern Volcanic Zone of the Andes Mountains, although its geology and local structural controls differ from nearby active volcanic centers. Most of its geology is substantially older than active volcanoes at these latitudes, as the postglacial component is relatively minor. The basement of Copahue Volcano, represented by the Agrio Caldera products and its basal sections, accumulated in extensional depocenters when the arc narrowed from a broad geometry on both sides of the Andes to its present configuration. Initial stages comprise early Pliocene basaltic-andesitic eruptions associated with extensional (transtensional?) processes that ended with the formation of a series of rhombohedral calderas that emitted important amounts of ignimbrites in latest Pliocene-early Pleistocene time. Copahue Volcano concentrates the Pleistocene activity of one of these calderas, the Agrio Caldera, before the emplacement and development of the Present arc front to the west. Volcano morphology reflects this particular evolution, looking more degraded than Antuco, Callaqui and Lonquimay volcanoes located immediately to the west in the arc front. Most of Copahue's volume is early Pleistocene in age, showing a thin resurfacing cover in synglacial (>27 ka) and postglacial times. A synglacial stage occurred mainly to the east of Copahue Volcano toward the caldera interior in a series of independent, mostly monogenetic centers. Postglacial eruptions occurred

A. Folguera (✉) · E. Rojas Vera · L. Vélez · J. Tobal
D. Orts · M. Agusto · V.A. Ramos
Facultad de Ciencias Exactas y Naturales, Instituto
de Estudios Andinos (IDEAN), Universidad de
Buenos Aires-CONICET, Buenos Aires, Argentina
e-mail: folguera@gl.fcen.uba.ar

A. Caselli
Facultad de Ciencias Exactas y Naturales,
Universidad de Río Negro e Instituto de Estudios
Andinos (IDEAN), Universidad de Buenos Aires,
Buenos Aires, Argentina

as both central and fissural emissions reactivating the old Pleistocene conduits. Its particular geological record and eastern longitudinal position indicate that Copahue was probably part of the late Pliocene-Pleistocene arc mostly developed in the axial and eastern Andes. Narrowing and westward retraction of the arc front, proposed in previous works for the last 5 Ma at 38°S, could have been the result of the eastward migration of the asthenospheric wedge during slab steepening. Reasons for this long-lived eruptive history at Copahue volcano could be related to the particular geometry of the active Liquiñe-Ofqui dextral strike-slip fault system that runs through the arc front from south to north when penetrates the retroarc area at the latitude of Copahue volcano. This behavior could be due to the collision of the oceanic Mocha plateau at these latitudes, as recently proposed. This jump and related deflection would have produced local transtensional deformation associated with abundant emissions of syn- and post-glacial products that could have partially resurfaced this long-lived center.

1.1 Introduction

Copahue volcano has been studied due to its frequent eruptions since the 1990s (see Delpino and Bermúdez 1993, 1995; González Ferrán 1994; Naranjo and Polanco 2004). Structural and tectonic models associated with this center proposed since then are summarized in this review, although it still lacks a robust stratigraphic framework over which these hypotheses are supported. The few available isotopic ages are K-Ar (Linares et al. 1999) and have significant errors (see Melnick et al. 2006a). Available geological maps are based on these ages and proposed lateral correlations that could be inappropriate for volcanic environments. Dellapé and Pando (1975) and Pesce (1989) were the first attempts to represent the different units of the Agrio Caldera, where the Copahue Volcano is hosted. Latter representations were more focused on studying the associated structural controls than the volcanic stratigraphy itself (Folguera and Ramos 2000; Melnick et al. 2006a; Rojas Vera et al. 2009a).

The most outstanding feature associated with Copahue volcano is the Agrio Caldera (Pesce 1989), also denominated in other works as the Caviahue Caldera. This 15 × 20 km depression was initially interpreted as the product of strong glacial erosion (Groeber 1921) based on the finding of presumably related diamictites. However, these were recently reinterpreted as large mass wasting deposits emplaced from the perimeters of the caldera towards its interior (Hermanns et al. 2011). The identification of this depression during the 1920s constituted an important discovery since no remote images existed at that time. Its linkage with volcanic processes waited until the late 1980s when Pesce (1989) identified the perimeter of the caldera and the location of Copahue volcano in one of the main collapse scars. Other resurgent centers,

partially coeval to Copahue volcano, have been identified along the caldera perimeters that have been erupted in the last 1 Ma (Linares et al. 1999).

A description of the state of knowledge of the tectonic setting associated with Copahue volcano and the Agrio Caldera is presented, including a discussion about the peculiarities of this center, which is morphologically distinctive and not aligned with the arc front at these latitudes.

1.2 Tectonic Framework at 37–39°S and Sublithospheric Structure

Recently released seismic tomography developed after the Maule earthquake has shed light on the sublithospheric structure of the Southern Volcanic Zone where Copahue volcano is located (Fig. 1.1) (Pesicek et al. 2012). The Nazca plate is illuminated as a zone of fast P-wave velocities, with some complexity previously not noted. Between
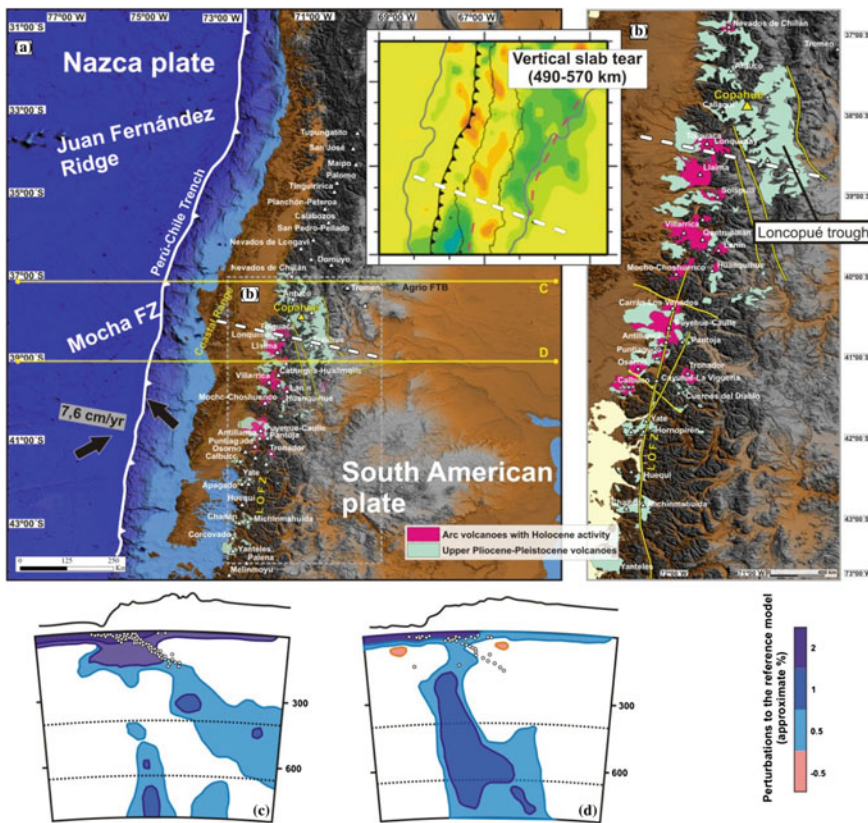
Fig. 1.1 a b Pliocene-Early Pleistocene and Pleistocene-Holocene arc activity in the Main Andes between 37–39°S (Lara et al. 2001; Lara and Folguera 2006), and seismic tomography of the retroarc zone modified from Pesicek et al. (2012). **c d** Pale blue and blue colors indicate P-wave velocity contours that are interpreted as subducted oceanic lithosphere while white dots indicate the Benioff zone (Pesicek et al. 2012). Note that along 39°S a steeper configuration of the subducted Nazca plate is not coincident with the present seismogenic zone. The thick dashed line in **a** and **b** indicates the tearing in the subducted Nazca plate interpreted by Pesicek et al. (2012). The Copahue Volcano is indicated with a triangle in yellow. Note that, as depicted in B, arc volcanoes with Holocene activity between 37° and 41°S are mainly emplaced on the western Andean slope, in comparison with late Pliocene to early Pleistocene centers developed on both sides of the Andes (see text for further details)

37° and 39°S, a tear zone appears to have developed in the subducting Nazca plate, leaving a steeper subduction angle to the south (Fig. 1.1). This tearing likely developed prior to 5–3 Ma, since the interplate seismogenic zone at 39°S, indicating the present fate of the subducted slab, is not coincident with the steeper zone of fast P-wave velocities (Fig. 1.1). Then, the present geometry of the subducting Nazca plate is considerably shallower than that steeper configuration, showing a physical continuation to the north (Pesicek et al. 2012). Thus a change in subduction geometry would have been achieved in the last 5–3 Ma between 37º and 39°S from a steeper configuration to a shallower one.

This important change has a correlation with the pattern of arc activity between 36º and 40ºS. Lara et al. (2001) demonstrated that, over the last 2 Ma the arc passed from a broad and diffuse morphology, covering a wide area from the current active arc to the retroarc zone to the east, to become contracted to a narrow band in the west at the axial Andean zone (Fig. 1.1).

This westward retraction was accompanied by within-plate volcanism in the Loncopué extensional trough in the last 2 Ma (Rojas Vera et al. 2010, 2013). Eruptions at the eastern retroarc zone during Quaternary time cover an area that is coincident at surface with the Nazca slab tearing described by Pesicek et al. (2012).

Shallow structure through this segment is characterized by two distinctive systems: (i) Along the arc front, the Liquiñe-Ofqui fault system accommodates lateral displacements imposed by the oblique convergence between the Nazca and South American plates (Lavenu and Cembrano 1999) from the triple junction among the South American, Nazca and Antarctica plates (~46°S) to the Mandolegüe volcanic lineament (~38°S) (Radic 2010). From this point to the north, strike-slip displacements are absorbed at the western retroarc zone over the Argentinian territory by the Antiñir-Copahue fault system (Fig. 1.2; Folguera et al. 2004). Copahue volcano is located at the transition zone between these two neotectonic systems. (ii) To the east, over the eastern retroarc area, Pliocene to Quaternary within-plate volcanic rocks have been related to extensional deformation (Fig. 1.3) (Kay et al. 2006; Folguera et al. 2006). Normal faults affect postglacial volcanic products, indicating young deformation of the upper crust more than 300 km east of the arc front (Fig. 1.3; Folguera et al. 2006; Rojas Vera et al. 2010). Crustal attenuation is identified beneath the arc and retroarc in coincidence with the area of Pliocene to Quaternary volcanic eruptions at 39°S and extensional deformation using receiver function techniques (Yuan et al. 2006). Density models derived from gravity data predict this area is elongate through the whole retroarc area parallel to the arc (Fig. 1.3; Folguera et al. 2012).

This crustal attenuation and associated retroarc magmatism have been explained by steepening of the Nazca plate during westward arc retraction about 5–2 Ma and consequent injection of hot asthenospheric material, after a period (13–5 Ma) of shallow subduction in the area (Kay et al. 2006; Folguera et al. 2007). This injection of hot asthenosphere material has been recently illuminated through magnetotelluric analysis (Burd et al. 2013).

1.2.1 The Mandolegüe Volcanic Lineament

This 60–70-km-long volcanic lineament is formed by the partial amalgamation of seven main volcanic centers, which from west to east, are the Callaqui Volcano, Copahue Volcano, Las Mellizas volcanic center, Trolón Volcano, Bayo Dome, and Huecú and Mandolegüe monogenetic basaltic fields (Figs. 1.4 and 1.5). This volcanic lineament is interposed between the northern termination of the Liquiñe-Ofqui and the Antiñir-Copahue fault systems along a NE direction (Fig. 1.4).

Mechanisms and ages of the different volcanic vents are highly variable along the strike of the Mandolegüe volcanic lineament (Fig. 1.5). The youngest products are dominant in the eastern sector where the Huecú and Mandolegüe volcanic fields were emplaced. There, monogenetic fields with fissural vents and, more locally,
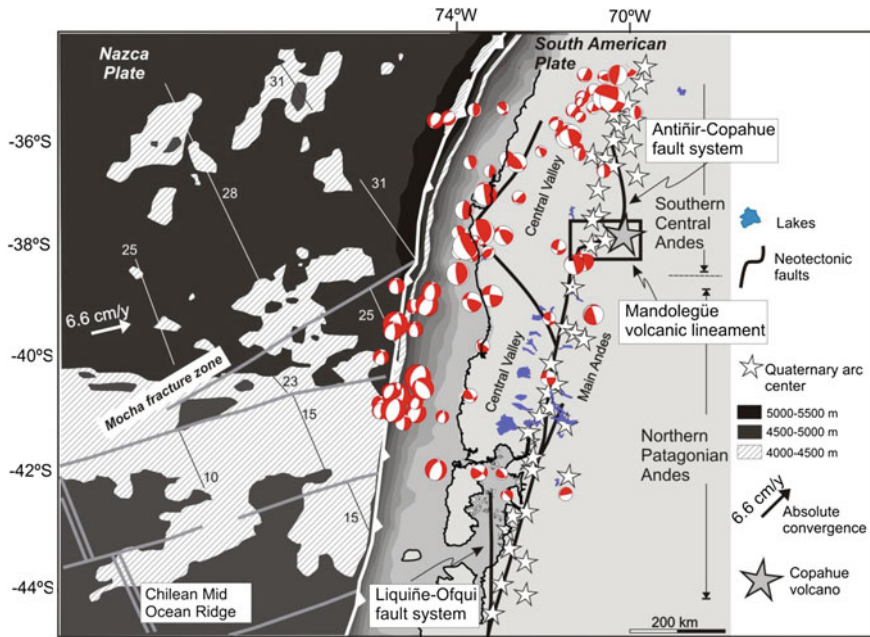
Fig. 1.2 Tectonic framework of the Southern Volcanic Zone (modified from Hervé 1976; Cembrano et al. 1996, 2002; Hervé 1994; López Escobar et al. 1995; Lavenu and Cembrano 1999; Folguera et al. 2004). Note the location of the Mandolegüe volcanic lineament in the site where the Copahue Volcano is hosted at the northern termination of the strike-slip Liquiñe-Ofqui fault zone and the transition to the Antiñir-Copahue fault system. Note also that the Mandolegüe volcanic lineament coincides with the site of inception of the oceanic Mocha transform zone and associated plateau into the Chilean trench

basaltic calderas are associated with broad basaltic fields that are circumscribed by the present drainage network (Fig. 1.5). This fluvial morphology has been flooded in postglacial times and probably also in historical times by reduced lacustrine basins as a response of the youngest eruptions hosted in the southern flank of the Mandolegüe volcanic lineament (Fig. 1.5) (Groeber 1928; Rojas Vera et al. 2009b).

West of the 70º40′W meridian, the average age of the different units becomes older, with pre-glacial volcanic products associated with mostly central polygenetic volcanic vents. Polygenetic stratovolcanoes are represented by the Trolón, Callaqui and Copahue volcanoes. The three centers have postglacial lava flows associated with fissural and central mechanisms, although most of its structure is pre-glacial in age (Pesce 1989; Linares et al. 1999).

In particular, the active Callaqui volcano (Fig. 1.4) is a stratovolcano elongated in a N60°E direction (Moreno and Lahsen 1986). Here, post-glacial eruptions concentrated along a 700-m-long fissure formed by 22 connected individual vents, producing an elliptical 15-km-long and 8 km-wide stratocone, as can be seen in the digital elevation model (Fig. 1.4).

Copahue volcano to the east occupies the southwestern corner of the 15×20 km Agrio Caldera (Pesce 1989). This has been formed over a volcanic plateau of 5–4 Ma andesitic flows associated with the Cola de Zorro-Hualcupén Formations that constitute gently sloped to flat sections up to 1,500 m thick (Fig. 1.5) (Vergara and Muñoz 1982; Niemeyer and Muñoz 1982; Muñoz Bravo et al. 1989; Suárez and Emparán 1997). The thickest sections of these packages have been described as controlled by normal
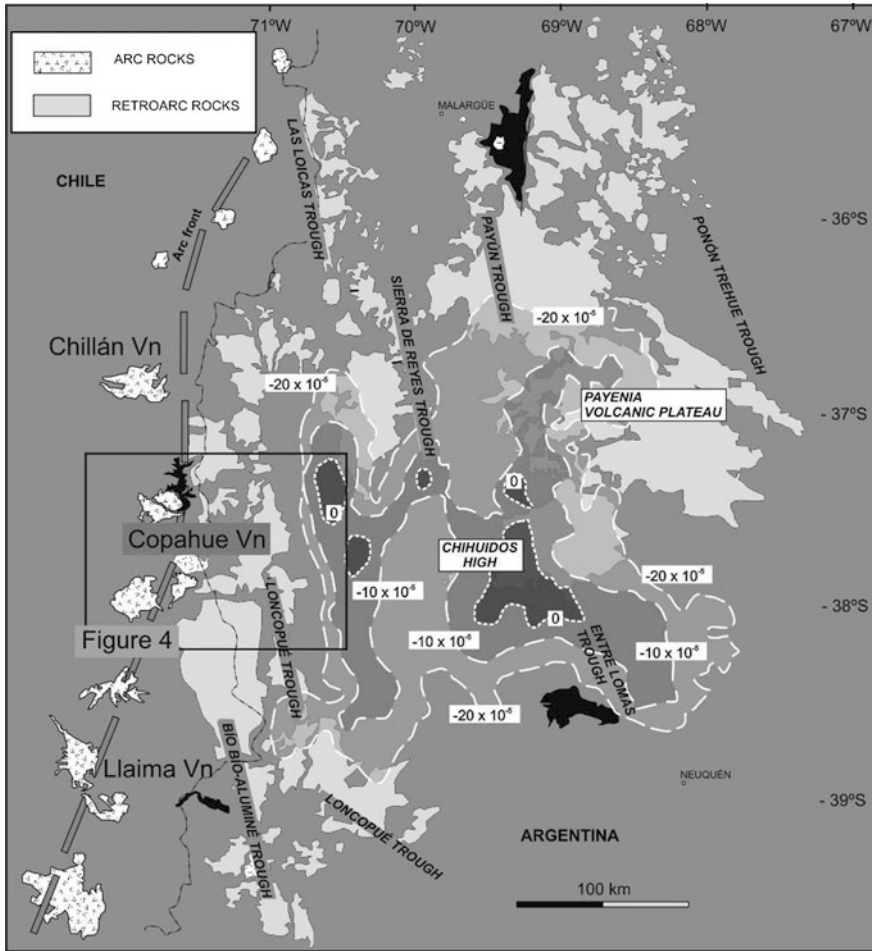
Fig. 1.3 Attenuated crust at the retroarc zone determined from a receiver function profile at 39°S (Yuan et al. 2006) where a plume-like feature is impacting against the base of the lithosphere (Burd et al. 2013) and gravimetric expression. Note that most of the volcanic plateaux at the arc-retroarc zone are coincident with the area of high gravimetric anomalies interpreted from 3D density models as caused by crustal attenuation (Folguera et al. 2012). Gravimetric values are in mGals

faults in a broad region from 36 to 39°S, defining half-graben geometries (Folguera et al. 2006; Melnick et al. 2006b).

Locally, these sections around Copahue volcano determine a broad volcanic morphology that is dipping outward from a central point situated at the 71ºW–37°50′S intersection in the center of the Agrio Caldera (Fig. 1.5). A thin cover of pyroclastic deposits of the Riscos Bayos Formation dated at 1.98 Ma (Pesce 1989; Linares et al. 1999; Mazzoni and Licitra 2000) is irregularly distributed through the external slopes of this feature, being interpreted as the outflow ignimbrites associated with the caldera collapse (Fig. 1.6). Ignimbritic sheets of the Las Mellizas Formation occupy the inner sector of the caldera and were dated at 2.5 Ma (Pesce 1989; Melnick et al. 2006a). The northern rim of the Agrio Caldera is occupied by lava fields associated with monogenetic vents aligned along fissures and have been gathered in an informal category denominated "*Basaltos de Fondo de Valle*" (Pesce 1989) (Fig. 1.6). These lava flows, dated at 1.6–0.8 Ma (Linares et al. 1999), are controlled by the glacial morphology and project through glacial tributaries beyond the rims of the
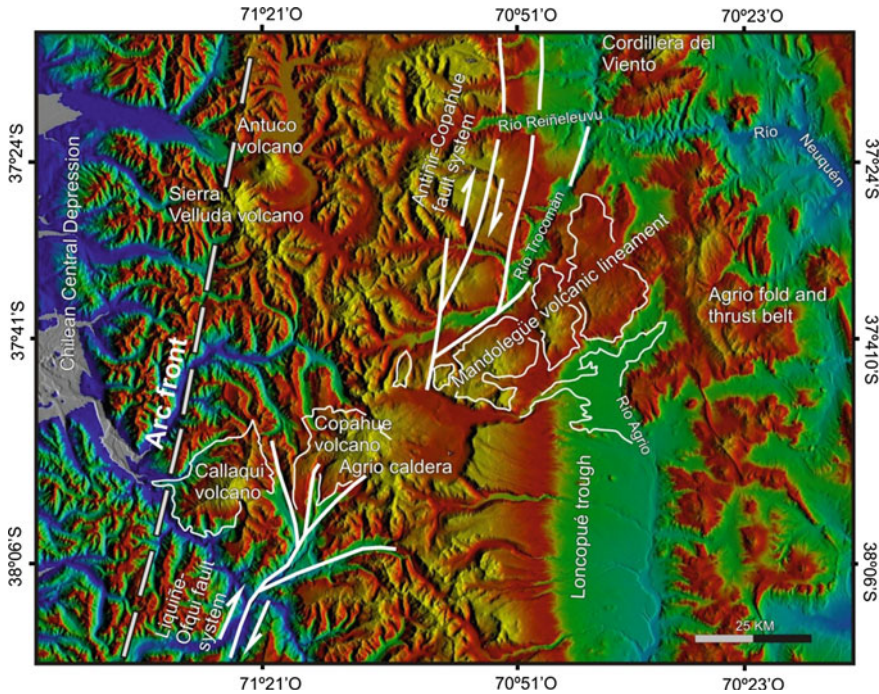
Fig. 1.4 Digital Elevation Model that shows the surficial expression of the Callaqui-Copahue-Mandolegüe volcanic lineament interposed between the Liquiñe-Ofqui and the Callaqui-Mandolegüe fault systems

Agrio Caldera, feeding lava fields corresponding to the El Huecú volcanic field (Fig. 1.5).

Activity less than 1 Ma at Copahue volcano occurred within the Agrio Caldera (Fig. 1.5). The volcano is formed by the amalgamation of several centers along a NE fissure, having 8–9 well preserved craters, similarly the neighboring Callaqui Volcano (Moreno and Lahsen 1986) (Fig. 1.4). The easternmost crater along the Copahue Volcano fissure has concentrated part of the postglacial eruptions as well as the 1990s and the 2000s eruptions. This center has an older section intruded by the 0.9 Ma dacitic Pucón Mahuida dome, which is in turn covered in an erosional unconformity by a younger section that can be divided in two parts, a lower pre-glacial section (Copahue Stage 1; Fig. 1.6) and an upper synglacial and postglacial section (Copahue Stage 2; Fig. 1.6). The upper synglacial section is eastwardly displaced with respect to the central Copahue vents, constituting small centers

over the southern flank of the volcano and smaller accumulations of hundred of meters of pillow lavas as independent centers. Even smaller volumes can be tracked up to the eastern rim of the caldera following a W–NW track (Fig. 1.5).

Postglacial vents are related to the volcano edifice itself along fissural systems hosted in its northern slope and central vents associated with the easternmost apical crater of the stratocone (Copahue Stage 3; Melnick et al. 2006a) (Figs. 1.5 and 1.6). Additionally, postglacial explosive products have been identified in the caldera perimeter east of the active crater (Polanco et al. 2000). The age of these products is less than 30–27 ka based on the determination of the final retreat of the ice sheet in the area. The last glacial retreat at these latitudes has been addressed from five different lines of evidence: (i) in 25.6 ± 1.2 and 23.3 ± 0.6 ka by whole-rock $^{40}Ar/^{39}Ar$, dating postglacial lava flows in the
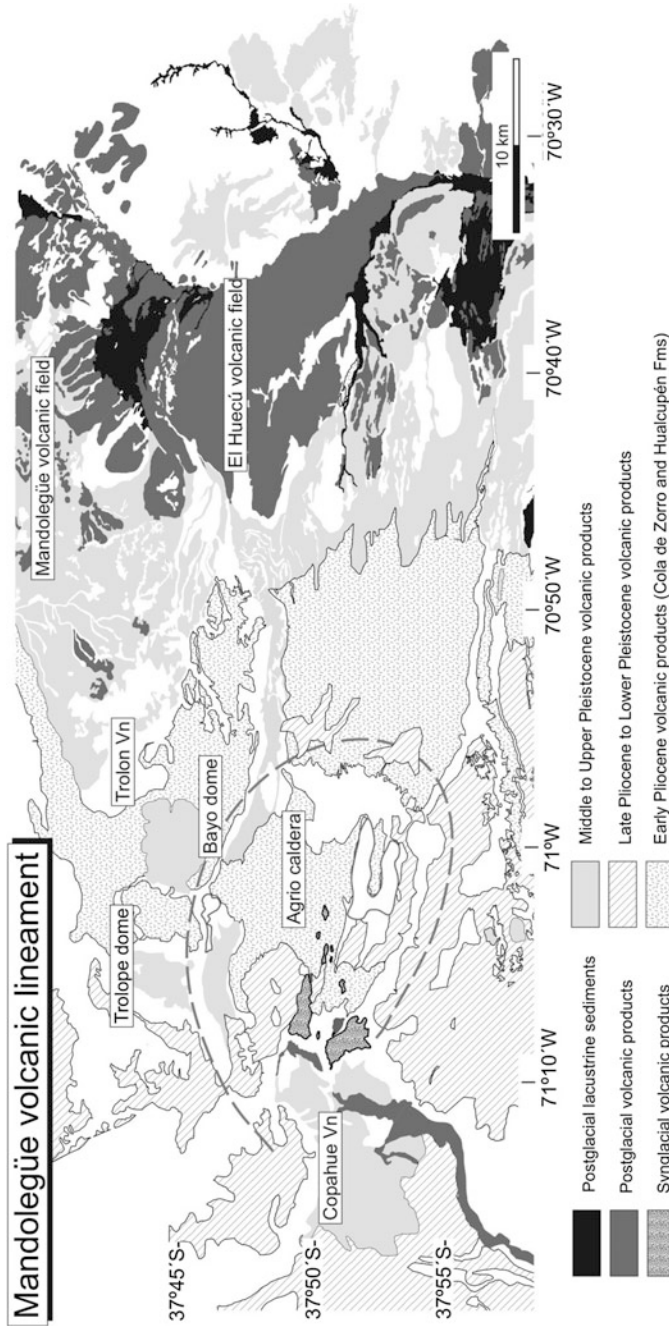
Fig. 1.5 Geology of the Callaqui-Copahue-Mandolegüe volcanic lineament, from the Agrio Caldera to the El Huecú volcanic field. Geology of the Copahue Volcano is based on Pesce (1989), JICA (1992), Folguera and Ramos (2000), Melnick et al. (2006a) and Rojas Vera et al. (2009b). Note that most of the postglacial volcanic eruptions have been emplaced over the retroarc area in the El Huecú volcanic field, while the Copahue Volcano and Agrio Caldera have minimum resurfacing during this stage
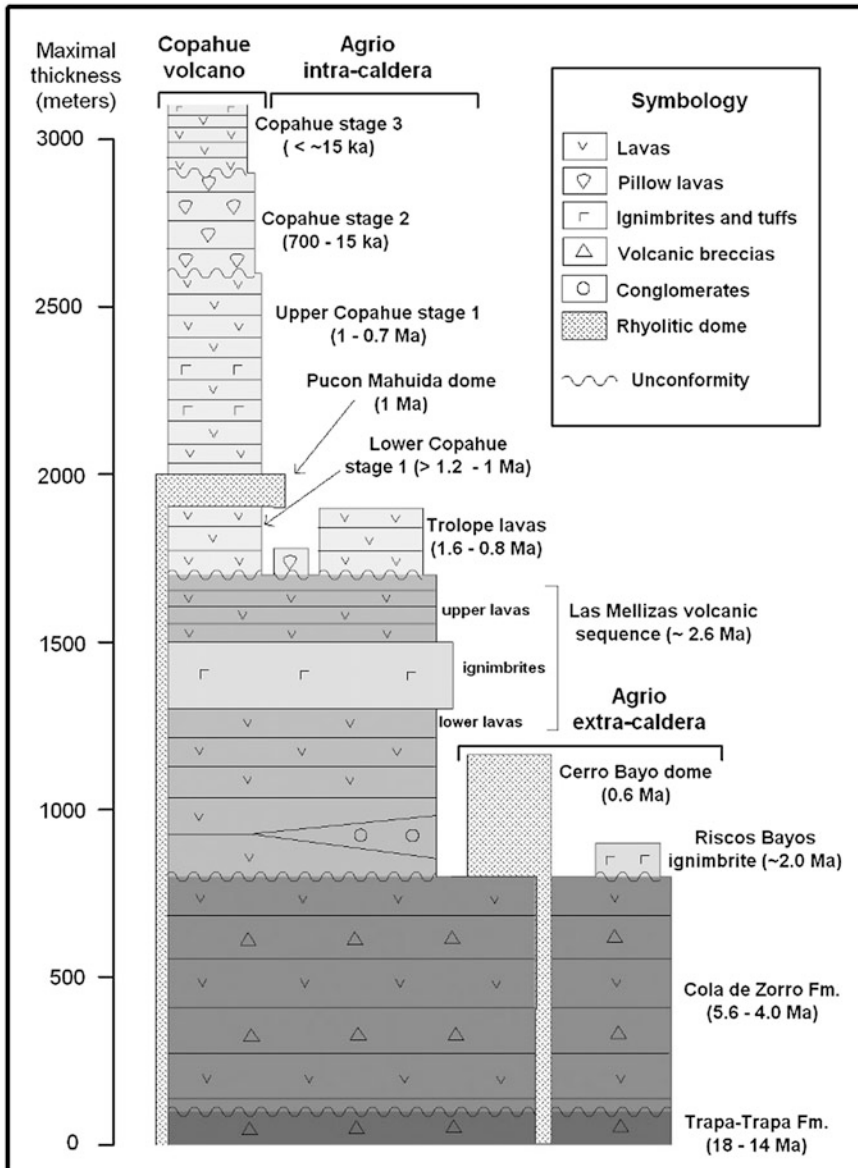
Fig. 1.6 Stratigraphic chart of the Agrio Caldera and Copahue Volcano (after Melnick et al. 2006a; based on Pesce 1989 and Linares et al. 1999)

Laguna del Maule area immediately to the north (36°S, 70°30′W) (Singer et al. 2000); in 30 ka by dating by cosmogenic ^{36}Cl the postglacial Varvarco rock avalanche deposit (36°26′S, 70°36′W) (Costa and González Díaz 2007); in 25–30 ka by whole-rock $^{40}Ar/^{39}Ar$, dating postglacial lava flows from the Chillán Volcano (37°S) (Dixon et al. 1999); in 30–35 ka by ^{10}Be, dating moraine deposits in the Rucachoroi valley (39°S) (Zech et al. 2008); and finally and more locally in 30 ka by ^{14}C, dating glaciofluvial deposits from Copahue volcano circumscribed to a glacial morphology (37°50′S, 71°03′W) (Bermúdez and Delpino 1999).

1.3 Structure of Copahue Volcano and Agrio Caldera

Copahue volcano is situated at the intersection point between two nearly perpendicular structural systems, the two WNW parallel Caviahue grabens and the NE contractional Chancho-Co hill (Fig. 1.7). The Caviahue grabens run through the southern section of the Agrio Caldera from the eastern inner wall to the northern Liquiñe-Ofqui fault system. These constitute symmetrical structures that broaden to the east where they are clearly separated by a small horst, whose deepest part is occupied by the Agrio lake. This extensional depression affects 2.5 Ma ignimbrites and lava flows of the Las Mellizas Formation and controls the emplacement of most of the synglacial volcanic rocks in the region (Fig. 1.7) (Melnick et al. 2006a).

The Caviahue grabens parallel the southern wall of the Agrio Caldera and are formed by a broken structural lineament composed of WNW and NW north-facing scarps affecting early Pliocene sections of the Cola de Zorro-Hualcupén Formations (Fig. 1.7). The northern flank of the caldera is formed by similarly oriented fault systems that, together with a degraded north-facing scarp north of Copahue town, delimits the Trolope graben where 1.6–0.8 Ma lava flows of the "*Basaltos de Fondo de Valle*" were emplaced (Fig. 1.7). North and south inner walls of the Agrio Caldera are tied by NNE and NW normal fault systems constituting the eastern west-facing wall of the Agrio Caldera (Fig. 1.7). The western caldera wall is not well defined south of its intersection with the Caviahue grabens. Pesce (1989) had proposed that this fault section would have been erased by later caldera-forming processes. This caldera perimeter, composed of kilometer-long fault segments, has a rhombhoedral shape with a maximum axis of 20 km in the NW direction and 15 km in the
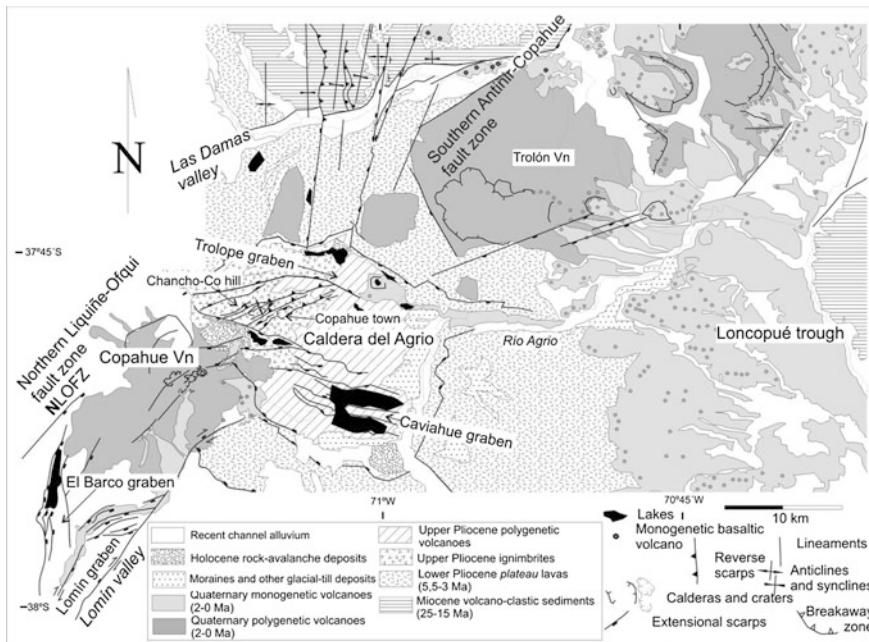
Fig. 1.7 Structural map of the Mandolegüe volcanic lineament between Copahue Volcano and northern Loncopué trough (modified from Folguera et al. 2004). Two main structural trends interact in the Agrio Caldera, a NE trend across the Copahue Volcano composed of reverse and strike slip structures of the Lomín and Chancho-Co structural systems and a WNW pattern of normal faults that define the two western Caviahue grabens

NE direction that suggests a tectonic origin (Folguera and Ramos 2000).

The Chancho-Co hill is north of Copahue Volcano and corresponds to a SW vergent structure that folded and uplifted Las Mellizas Formation in a broad structure in the NW extreme of the Agrio Caldera (Fig. 1.7). This anticline is affected at its southern part by the Caviahue grabens, which displace the Pliocene to Pleistocene sections beneath the basal lavas of Copahue Volcano. This relation suggests a chronology of events that starts with the uplift of the Chancho-Co hill followed by extension that led to the Caviahue grabens formation. However, SW-vergent reverse faults that uplift the Chancho-Co hill affect and displace a Pleistocene glacial pavement defining very fresh scarps, which is indicative of young deformation (Fig. 1.8). Additionally, part of these structures propagates toward Copahue town, where late Pliocene rocks are thrust over Pleistocene till deposits (Rojas Vera et al. 2009a).

Extinct and active hot springs of the Agrio Caldera are associated with the Chancho-Co structural system (see Varekamp et al. 2001, for a recent synthesis). Las Máquinas, Maquinitas, Copahue, Anfiteatro and Chancho-Co hot springs are aligned through the Chancho-Co hill frontal structures. In particular, the last lies in the upper Trapa Trapa river on the Chilean side at the intersection point between the Chancho-Co and the Caviahue structural systems.

South of the Chancho-Co hill, associated reverse faults propagate as southeast-facing scarps into the <1 Ma volcanic rocks and post-glacial products of Copahue volcano (Figs. 1.9 and 1.10). These structures act as conducts of fissural postglacial lavas flowing through the northern slope of the volcano towards the Trapa Trapa river in Chile (Figs. 1.7 and 1.10).

These two structural systems are spatially associated with indicators of ongoing deep activity in the caldera interior revealed using geophysical tools. In particular, Ibáñez et al. (2008) have measured shallow seismic activity since 2004 along the broadest and axial section of the Caviahue grabens (Fig. 1.11). This area does not show surficial evidence of young deformation, being fault scarps strongly affected by glacial abrasion, indicating that the structure formed at least in Pleistocene time since it is affecting latest Pliocene products. Additionally, radar interferometry data have shown deflation processes previously to 2011, at the intersection point between the Caviahue grabens and the Chancho-Co hill, where fissural postglacial products are emplaced in the Trapa Trapa upper valley, (Fig. 1.11) (Vélez et al. 2011). This anomaly is shifted with respect to the axial part of Copahue volcano and coincident with an area of normal faults affecting the youngest products at its northern slope. This deflation could indicate that collapse of the Chancho-Co structural system through WNW normal structures remains active. Mass-wasting phenomena associated with the northern slope of the volcano (Figs. 1.7 and 1.10) occurred prior to the postglacial fissural eruptions and coincide with the area of noted deformation, indicating slope instability.

After 2011 a new inflationary process started with an anomaly fairly coincident with the previous slope deflation (Fig. 1.12; Vélez et al., this book). However, in a closer view, it is noted that the area that accumulated nearly 5 cm of vertical displacements in half a year shows an elliptical shape (Fig. 1.12) aligned with the scarp that is affecting and controlling the emission of postglacial lava products (Fig. 1.10). The interferogram also shows displacements through the structures that are associated with the Chancho-Co hill suggesting its reactivation (Fig. 1.12).

1.4   Tectonic Evolution of Copahue Volcano and Agrio Caldera

Copahue volcano, as part of the Southern Volcanic Zone, has evolved through two distinctive southern Andean deformational stages. The description of these processes can explain
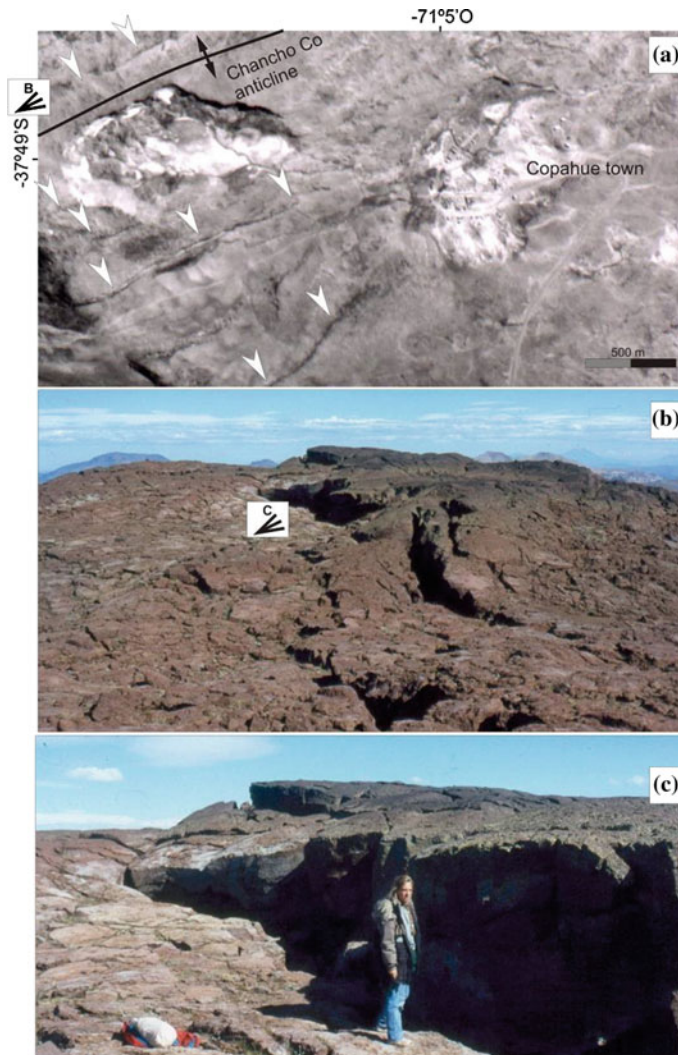
Fig. 1.8 Neotectonics in the basement rocks of the Copahue Volcano flanking the Chancho-Co hill. **a** Aerial picture where spatial relation between fault scarps associated with the Chancho Co hill and Copahue town are displayed (arrows indicate the scarp traces). **b** Axial zone of the Chancho-Co hill where a glacial pavement is folded and broken by a reverse fault. **c** Detail of **b**

variable mechanics through time and distribution of the structures that were developed previously to the emplacement of Copahue volcano, particularly during the Agrio Caldera formation, and synchronously. This center is located in the drainage divide area to the east of the present arc front and its basal section is older than these neighbor active volcanoes. Additionally, the basal section of Copahue volcano, particularly when considering the Agrio Caldera as part of its evolution, is more similar in age to the extinct Pliocene to Pleistocene centers emplaced on both sides of the Andes at these latitudes. Then, Copahue volcano could be considered as part of this old configuration with the exception that it has undergone a thin and restricted resurfacing in
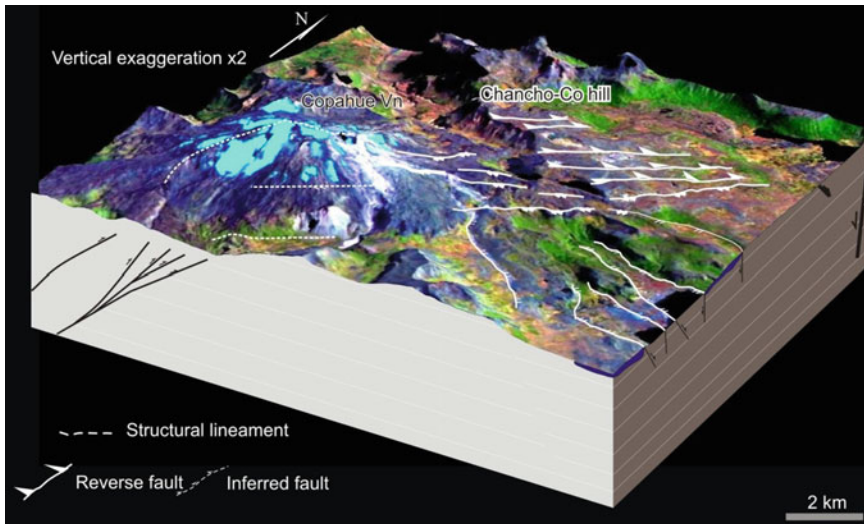
Fig. 1.9 Block diagram constructed with Aster image draped on DEM (modified from Rojas Vera et al. 2009a), where neotectonic contractional structure of the Chancho-Co hill is represented in the basement of

Copahue Volcano. Compare these with ground deformation contours determined from InSar studies shown in Vélez et al. (2011)

syn- and post-glacial times. During this stage, early Pleistocene to postglacial sections have been uplifted as a contractional structure in the caldera interior. This uplift constitutes the northern continuation of the Liquiñe-Ofqui fault system, denoting a profound change in deformational mechanisms in the last 1 Ma.

1.4.1 The Pliocene to Pleistocene Evolution

The basement of Copahue Volcano and the Agrio Caldera is formed by the Cola de Zorro and Las Mellizas Formations volcanic sections. These are hosted in quadrangular-rhombhoedral depocenters delimited by normal faults that contain sections up to 1,500 m (Folguera et al. 2006; Melnick et al. 2006b; Rojas Vera et al. 2009c). Younger products in the region are also associated with extensional/transtensional mechanisms in the lasts 2–1 Ma time period, both in the Andean and extra-Andean domains. These

processes were contemporaneous to the retraction and narrowing of the volcanic arc in the last 1 Ma from the eastern to the western Andean slope (Fig. 1.1). Even though this process was initially defined as a simple westward migration of the arc front (Stern 1989; Muñoz and Stern 1988, 1989), in the last decade it was redefined on the light of new isotopic ages as an arc narrowing, from a broad geometry through both Andean slopes in Pliocene to Pleistocene times to a narrower configuration in Pleistocene to Holocene times (Fig. 1.1) (Lara et al. 2001).

This arc narrowing coincides with the area of Pliocene to early Quaternary extensional deformation between 36 and 39°S that affected the arc and retroarc areas. In particular, the Loncopué trough, considered the major extensional depocenter in the area with more than 1,500 meters accumulated in the lasts 5 Ma (Rojas Vera et al. 2010), is partially superimposed on the crustal attenuation processes identified in the retroarc zone from receiver function analyses by Yuan
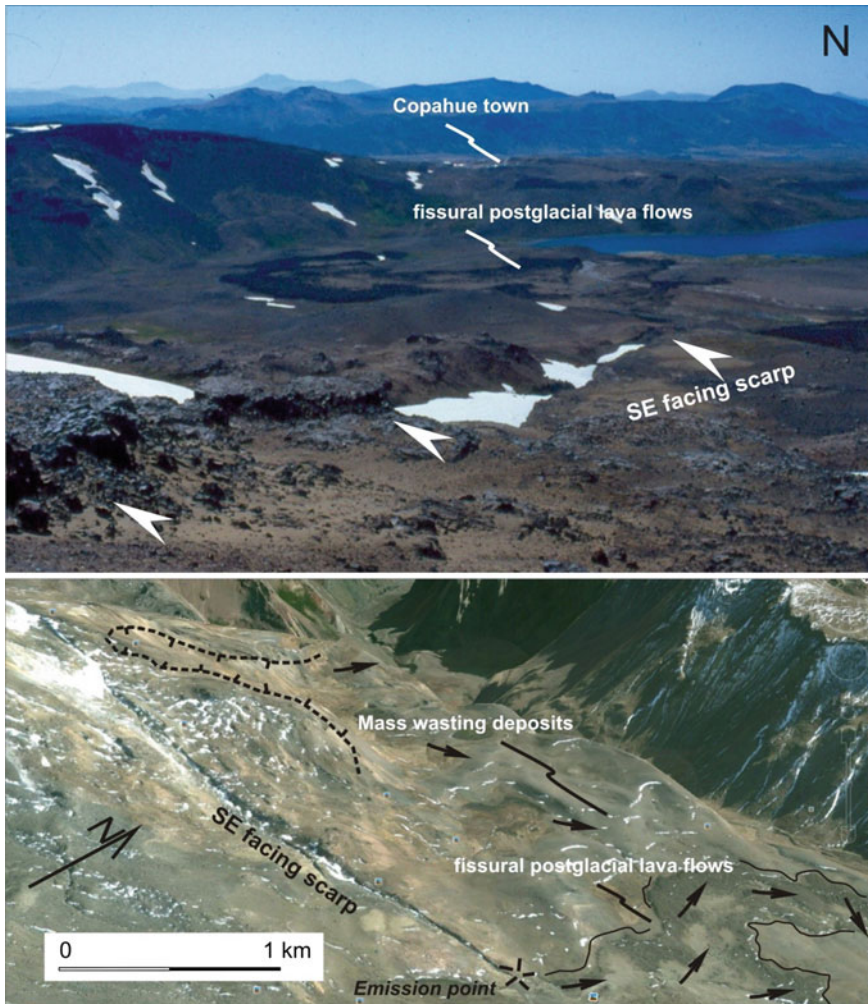
Fig. 1.10 *Above* Picture of the SE facing scarp affecting the northern slope of Copahue Volcano as part of the structures that are flanking the Chancho-Co hill (*below*).

Below Oblique view (ikonos image taken from Google Earth) and morphological expression of the fault associated with postglacial lava flows and mass wasting deposits

et al. (2006) (Fig. 1.13). This crustal attenuation zone has produced a broad positive gravity anomaly associated with the emplacement of mantle rocks in shallower levels beneath the retroarc zone that has a latitudinal extent similar to the arc narrowing registered in the last 1 Ma and to the extensional deformed zone and related within-plate volcanic series. Asthenospheric upwelling beneath the steepening subduction zone proposed from gravity models coincides

with the anomalies in ^{13}C and ^{3}He detected by Agusto et al. (2013) in the hot springs located north of the Copahue Volcano that are indicative of a relatively near mantle source.

The steeper configuration of the subducted Nazca plate at these latitudes (Fig. 1.1) revealed by seismic tomographies (Pesicek et al. 2012) is considered to have developed prior to 2 Ma, and could indicate the broadening of the asthenospheric wedge coeval to crustal attenuation and
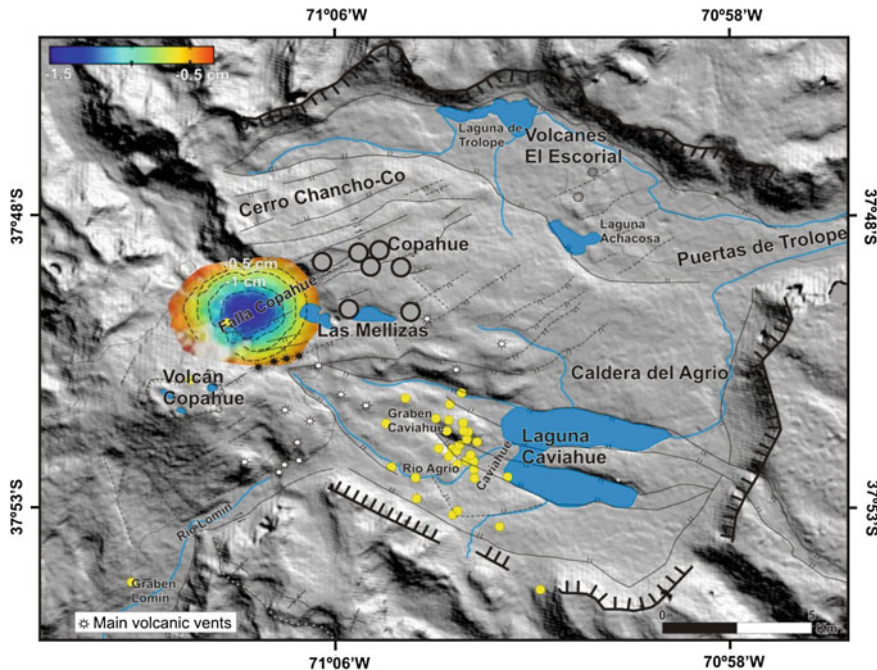
Fig. 1.11 Structural map of the Agrio Caldera and Copahue Volcano (modified from Rojas Vera et al. 2009a), with 2004s superimposed seismic events (small yellow dots; Ibáñez et al. 2008), ground deformation contours determined from satellite interferometry previous to 2011 (2002–2007) when a new inflationary process started (see next figure) (Vélez et al. 2011) and ^{3}He and ^{13}C anomalies determined in hot springs by Agusto et al. (2013). White stars indicate main eruptive synglacial vents. Note that synglacial activity is not coincident with the volcanic axial zone but slightly displaced to the northeast where neotectonic features have been described. Note also that seismic events are aligned with the axial zone of the Caviahue grabens

extensional processes registered in the area (Fig. 1.13). Agrio Caldera and lower sections of Copahue volcano were coeval to these processes and were circumscribed to extensional depocenters.

1.4.2   Processes Younger Than 1 Ma

WNW contractional structures involve glacial deposits and postglacial products of Copahue volcano (Fig. 1.8). Additionally, these control the emplacement of postglacial products. These structures are aligned with the Liquiñe-Ofqui fault system to the south, which abandons the arc front and penetrates at these latitudes to the Argentinian Andean slope (Figs. 1.7 and 1.14).

Reverse structures that affected postglacial products have subordinate right-lateral components displacing Quaternary deposits and landforms and producing small pull-apart depocenters (Folguera et al. 2004; Rojas Vera et al. 2009c). These structures determine the ENE Mandolegüe fault system, where the Chancho-Co hill occupies the western edge. To the north, these structural trends bend to the NW Antiñir-Copahue fault system trending through the eastern Andean front (Fig. 1.14). This system has accommodated maximum shortening in the 1.4–0.8 Ma time period, showing minor reactivations in postglacial times (Folguera et al. 2004). Its development is spatially coincident with the area of the inception of the Mocha transfer zone in the
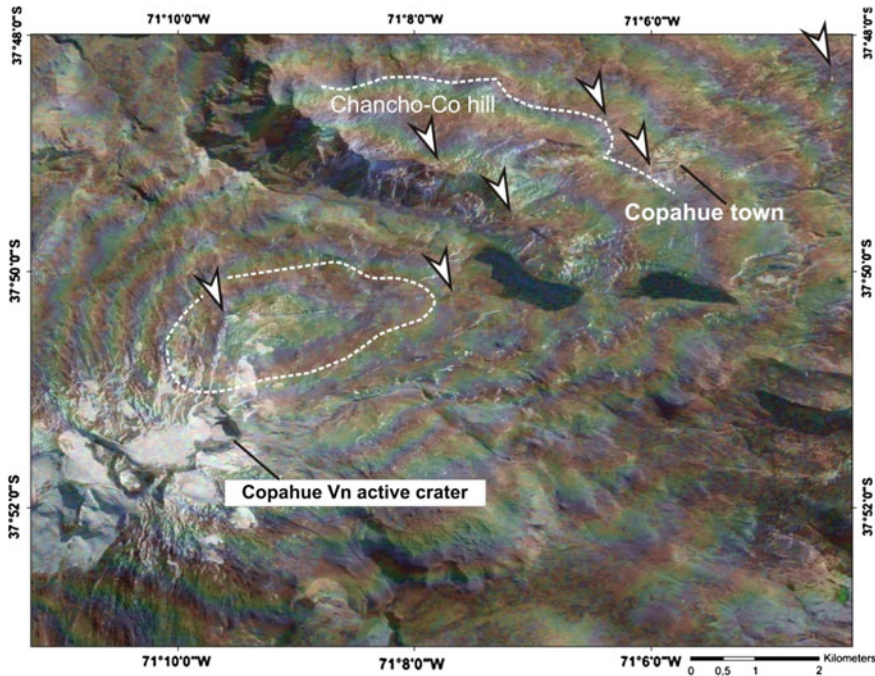
Fig. 1.12 Inflacionary processes detected by Insar over the NE slope of Copahue Volcano since 2011 (Vélez et al. this issue). This inflation accelerated since August-October 2011 and continues after 2012–13 eruptive cycle, accumulating nearly 5 cm in 6 months. Arrows indicate fault traces of the neotectonic structure affecting the northern slope of the volcano (see Fig. 1.10). Note that the area of higher displacements describes an ellipse with a major axis in the W–E direction surrounding the normal fault affecting postglacial products. Note also that curves of iso-displacement seem to be deflected in the north when crossing active faults in the Chancho-Co hill

Chilean trench in the lasts 3 Ma that could have produced an eastward wave of out-of-sequence contractional deformation through the forearc and western retroarc zones. The area of collision of the Mocha transfer zone coincides with a segment where the subducted slab penetrates with an angle 8° shallower in comparison to neighboring areas (Krawczyk et al. 2006; Tašárová 2004). Seismic tomography illuminates this shallow segment that would have been produced in the last 2–3 Ma and replaced a steeper previous configuration (Pesicek et al. 2012), showing a strong change in the subduction regime.

In this context, the Mandolegüe fault system could have officiated as a transfer zone between the Liquiñe-Ofqui and the Antiñir-Copahue fault systems that would have operated accommodating shortening and lateral displacements on opposite sides of the Andean drainage divide (Fig. 1.14) (Folguera and Ramos 2009). This transfer zone forms a 70–80-km-long volcanic lineament that can be explained by the collision of the southern part of an oceanic plateau whose size would be similar to the Mocha plateau presently subducted south of 38°S. Insar data show that this structure near Copahue volcano concentrates present deformation. Seismic tomography may show a steeper subduction configuration concomitant with older products and a shallower one contemporaneous to late contraction and transpressional deformation at the arc and retroarc areas.
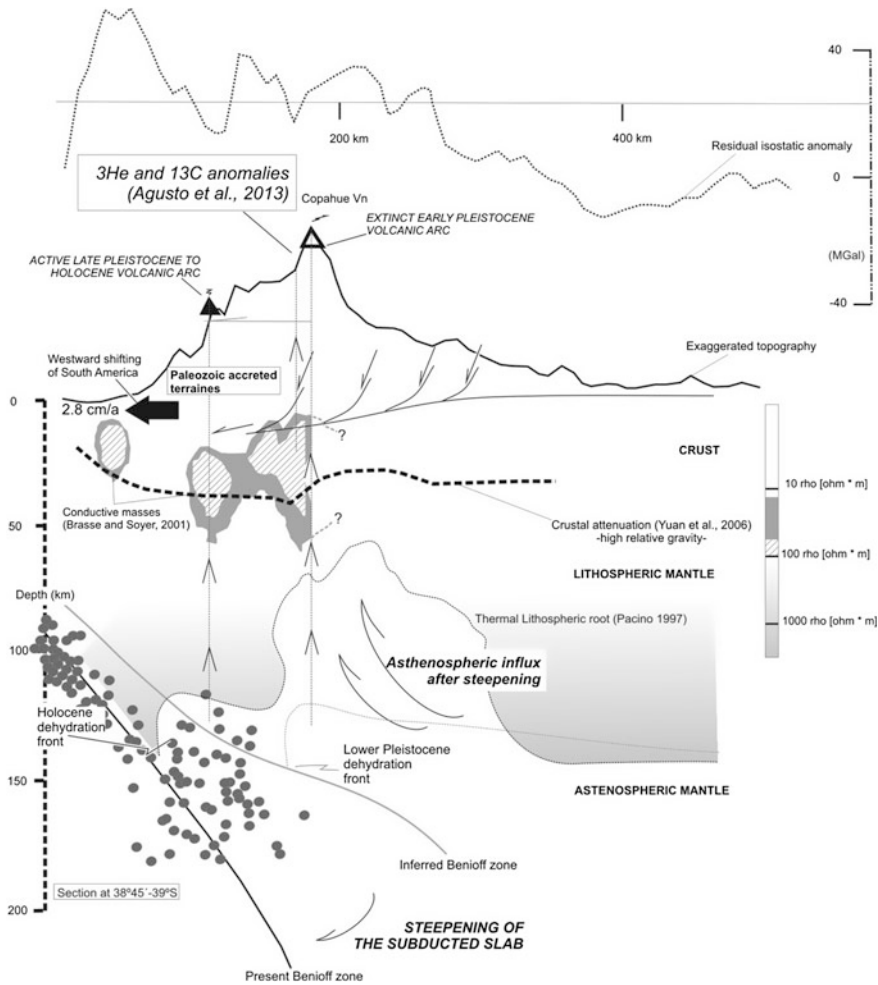
Fig. 1.13 Retraction of the arc front during the Pliocene and Quaternary time as a function of the steepening of the Nazca plate following Stern (1989)s hypotheses (modified from Folguera et al. 2007). Attenuated crust is determined from the receiver function analyses of Yuan et al. (2006). Note that highly conductive crustal masses from magnetotelluric studies of Brasse and Soyer (2001) are associated with the retroarc area immediately south of the Copahue Volcano area
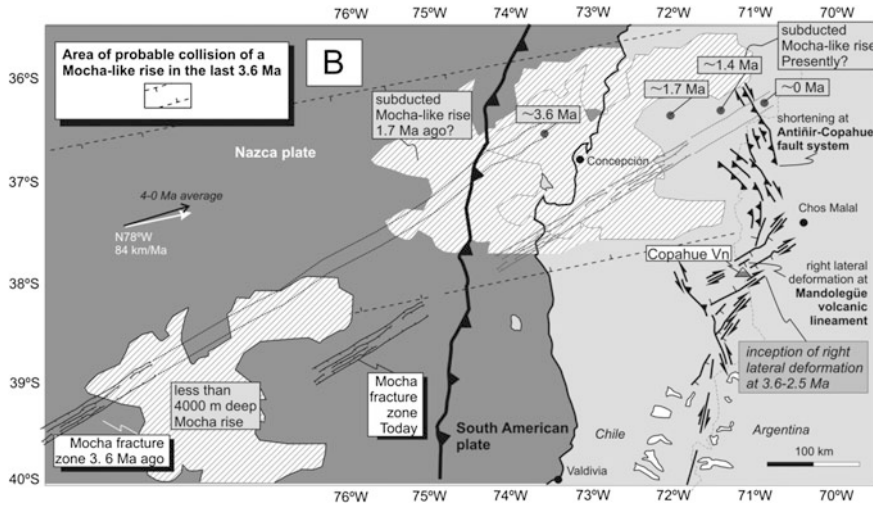
Fig. 1.14 Hypothesis related to the latest Pliocene to Quaternary collision of the Mocha plateau and inception of contractional and transtensional deformation in the arc zone (modified from Folguera et al. 2009)

References

Agusto M, Tassi F, Caselli A, Vaselli O, Rouwet D, Capaccioni B, Caliro S, Chiodini G, Darrah T (2013) Gas geochemistry of the magmatic-hydrothermal fluid reservoir in the Copahue-Caviahue volcanic complex (Argentina). J Volcanol Geoth Res 257:44–56

Bermúdez A, Delpino D (1999) Erupciones subglaciales y en contacto con hielo en la región volcánica de Copahue, Neuquén: Salta, Argentina. XIV Congreso Geológico Argentino, Còrdoba, Argentina 2:250–253

Brasse H, Soyer W (2001) A magnetoteluric study in the Southern Chilean Andes. Geophys Res Lett 28 (19):3757–3760

Burd A, Booker J, Mackie R, Favetto A, Pomposiello M (2013) Three-dimensional electrical conductivity in the mantle beneath the Payún Matrú Volcanic Field in the Andean back-arc of Argentina near 36.5°S: decapitation of a mantle plume by resurgent upper mantle shear during slab steepening? Geophys J Internat (in press)

Cembrano J, Hervé F, Lavenu A (1996) The Liquiñe Ofqui fault zone: a long-lived intra-arc fault system in southern Chile. Tectonophysics 259:55–66

Cembrano J, Lavenu A, Reynolds P, Arancibia G, López G, Sanhueza A (2002) Late Cenozoic transpressional ductile deformation north of the Nazca-South America-Antarctica triple junction. Tectonophysics 354:289–314

Costa CH, González Díaz EF (2007) Age constraints and paleoseismic implication of rock-avalanches in the Northern Patagonian Andes Argentina. J S Am Earth Sci 24(1):48–57. doi:10.1016/j.jsames.2007.03.001

Dellapé D, Pando G (1975) Relevamiento geológico de la cuenca geotérmica de Copahue. Yacimientos Petrolíferos Fiscales Unpublished Report 524. Buenos Aires

Delpino D, Bermúdez A (1993) La actividad volcánica del volcán Copahue durante 1992. Erupción con emisión de azufre piroclástico. Provincia de Neuquén. XII Congreso Geológico Argentino, Mendoza, Argentina 4:292–301

Delpino D, Bermúdez A (1995) Eruptions of pyroclastic sulphur at crater lake of Copahue volcano, Argentina. XXI International union of geodesy and geophysics. Boulder, USA, B410

Dixon HJ, Murphy MD, Sparks SJ, Chávez R, Naranjo JA, Dunkley PN, Young SR, Gilbert JS, Pringue MR (1999) The geology of Nevados de Chillán volcano Chile. Rev Geol Chile 26(2):227–253

Folguera A, Ramos VA (2000) Control estructural del volcán Copahue (38°S–71°O): implicancias tectónicas para el arco volcánico cuaternario (36–39°S). Rev Asoc Geol Arg 55:229–244

Folguera A, Ramos VA (2009) Collision of the Mocha fracture zone and a less than 4 Ma old wave of orogenic uplift in the Andes (36°–38°S). Lithosphere 1(6):364–369

Folguera A, Ramos V, Hermanns R, Naranjo J (2004) Neotectonics in the foothills of the Southernmost Central Andes (37°–38°S). Evidence of the strike-slip displacement along the Antiñir-Copahue fault zone. Tectonics 23 TC 5008

Folguera A, Zapata T, Ramos VA (2006) Late Cenozoic Extension and the evolution of the Neuquén Andes.

In: Kay SM, Ramos VA (eds) Late Cretaceous to Recent magmatism and tectonism of the Southern Andean margin at the latitude of the Neuquen basin (36–39°S). Geol S Am S 407:267–285

Folguera A, Introcaso A, Giménez M, Ruiz F, Martínez P, Tunstall C, García Morabito E, Ramos VA (2007) Crustal attenuation in the Southern Andean retroarc determined from gravimetric studies (38°–39°30′S): the Lonco-Luán asthenospheric anomaly. Tectonophysics 439:129–147. doi:10.1016/j.tecto.2007.04.001

Folguera A, Alasonati Tašárová Z, Götze H-J, Rojas Vera E, Giménez M, Ramos VA (2012) Retroarc extension in the last 6 Ma in the South-Central Andes (36°S–40°S) evaluated through a 3-D gravity modeling. J S Am Earth Sci 40:23–37

González-Ferrán O (1994) Volcanes de Chile. Instituto Geográfico Militar, Santiago, pp 640

Groeber P (1921) La región de Copahue y su glaciación diluvial. Rev Soc Arg Estud Geogr 1:92–110

Groeber P (1928) Traslado del vulcanismo de la falda oriental de la cordillera hacia la ladera occidental. An Soc Arg Estud Geogr 3(1):210–218

Hermanns RL, Folguera A, Penna I, González Díaz E, Fauque L, Niedermann S (2011) Landslide dams in the Central Andes of Argentina (northern Patagonia and the Argentine northwest). In: Evans SG, Hermanns RL, Strom A, Scarascia Mugnozza G (eds) Lecture notes in the earth sciences V 133: Natural and artificial rockslide dams. Springer, Berlin, pp 147–177

Hervé M (1976) Estudio geológico de la falla Liquiñe-Reloncaví an el área de Liquiñe: antecedentes de un movimiento transcurrente (Provincia de Vadivia). I Congreso Geológico Chileno, Actas B:39–56

Hervé F (1994) The southern Andes between 39° and 44° S latitude: the geological signature of a transpressive tectonic regime related to a magmatic arc. In: Reutter KJ, Scheuber E, Wigger PJ (eds) Tectonics of the Southern Central Andes. Springer, Berlin, pp 243–248

Ibáñez J, Del Pezzo E, Bengoa C, Caselli A, Badi G, Almendros J (2008) Volcanic tremor and local earthquakes at Copahue volcanic complex, southern Andes, Argentina. J Volcanol Geoth Res 174:284–294

JICA (Japan International Cooperation Agency) (1992) The feasibility study on the Northern Neuquén geothermal development project. Unpublished Ente Provincial de Energia de la Provincial del Neuquén, pp 89

Kay SM, Burns WM, Copeland PC, Mancilla O (2006) Upper Cretaceous to Holocene magmatism and evidence for transient Miocene shallowing of the Andean subduction zone under the northern Neuquén Basin. In: Kay S, Ramos VA (eds) Late Cretaceous to Recent magmatism and tectonism of the Southern Andean margin at the latitude of the Neuquen basin (36–39°S). Geol S Am S 407:19–60

Krawczyk C, Mechie J, Tašárová Z, Lüth S, Stiller M, Brasse H, Echtler HP, Bataille K, Wigger P, Araneda M (2006) Geophysical signatures and active tectonics at the southern central Chilean margin. In:

Oncken G et al (eds) The andes—active subduction orogeny: frontiers in earth sciences 1. Springer, Berlin Heidelberg New York, pp 171–192

Lara L, Rodríguez C, Moreno H, Pérez de Arce C (2001) Geocronología K-Ar y geoquímica del volcanismo plioceno superior-pleistoceno en los Andes del sur (39°–42°S). Rev Geol Chile 28:67–91

Lara L, Folguera A (2006) Plio-Quaternary narrowing of the volcanic arc at Southern Andes (37°–41°S), southwestern margin of Neuquén Basin: geochronologic and field tectonic data evaluated. In: Kay S, Ramos VA (eds) Late Cretaceous to Recent magmatism and tectonism of the Southern Andean margin at the latitude of the Neuquen basin (36–39°S). Geol S Am S 407:299–315

Lavenu A, Cembrano J (1999) Compressional and transpressional stress pattern for Pliocene and Quaternary brittle deformation in fore-arc and intra-arc zones (Andes of Central and Southern Chile). J Struct Geol 21:1669–1691

Linares E, Ostera HA, Mas L (1999) Cronología Potasio-Argón del conplejo efusivo Copahue-Caviahue, Provincia de Neuquén. Rev Asoc Geol Arg 54(3):240–247

López-Escobar L, Cembrano J, Moreno H (1995) Geochemistry and tectonics of the Chilean Southern Andes Quaternary volcanism (37°–46°S). Rev Geol Chile 22(2):219–234

Mazzoni MM, Licitra D (2000) Significado estratigráfico y volcanológico de ignimbritas neógenas con composición intermedia en la zona del lago Caviahue, Neuquén. Rev Asoc Geol Arg 55(3):188–200

Melnick D, Folguera A, Ramos V (2006a) Structural control on arc volcanism: the Caviahue-Copahue complex, Central to Patagonian Andes transition (38°S). J S Am Earth Sci 22:66–88

Melnick D, Rosenau M, Folguera A, Echtler H (2006b) Neogene Tectonics of the Western flank of the Neuquén Andes, 37°–39°30′S. In: Kay S, Ramos VA (eds) Late Cretaceous to Recent magmatism and tectonism of the Southern Andean margin at the latitude of the Neuquen basin (36–39°S). Geol S Am S 407:73–95

Moreno H, Lahsen A (1986) El volcán Callaqui: ejemplo de volcanismo fisural en los Andes del Sur. Rev Asoc Geol Arg 42:1–8

Muñoz J, Stern C (1988) The Quaternary volcanic belt of the southern continental margin of South America: transverse structural and petrochemical variations across the segment between 38° and 39°S. J S Am Earth Sci 1(2):147–161

Muñoz J, Stern C (1989) Alkaline magmatism within the segment 38°–39°S of the Plio-Quaternary volcanic belt of the Southern South American continental margin. J Geophys Res 94:4545–4560

Muñoz Bravo J, Stern C, Bermúdez A, Delpino D, Dobbs MF, Frey FA (1989) El volcanismo plio–cuaternario a través de los 38° y 39°S de los Andes. Rev Asoc Geol Arg 44(1–4):270–286

Naranjo JA, Polanco E (2004) The 2000 AD eruption of Copahue Volcano, Southern Andes. Rev Geol Chile 31:279–292

Niemeyer H, Muñoz J (1982) Hoja Laguna de La Laja, Región del Bío-Bío, scale 1:250.000, Servicio Nacional de Geología y Minería

Pesce A (1989) Evolución volcano-tectónica del complejo efusivo Copahue-Caviahue y su modelo geotérmico preliminar. Rev Asoc Geol Arg 44:307–327

Pesicek J, Engdahl E, Thurber C, DeShon H, Lange D (2012) Mantle subducting slab structure in the region of the 2010 M8.8 Maule earthquake (30–40°S), Chile. Geophys J Int 191:317–324

Polanco E, Naranjo JA, Young S, Moreno H (2000) Volcanismo Explosivo Holoceno en la cuenca del alto Bío-Bío, Andes del Sur (37°45′–38°30′S). IX Congreso Geológico Chileno, Puerto Varas, Chile 2:59–61

Radic J (2010) Las cuencas cenozoicas y su control en el volcanismo de los complejos Nevados de Chillán y Copahue-Callaqui (36°–39°S). Andean Geol 37 (1):220–246

Rojas Vera E, Folguera A, Spagnuolo M, Ramos VA (2009a) La neotectónica del arco volcánico a la latitud del volcán Copahue (38°S). In: Geología de los Andes del Sur. Rev Asoc Geol Arg 65(1):204–214

Rojas Vera E, Folguera A, Ramos VA (2009b) Estratigrafía del sector central de la cuenca de Loncopué: El depocentro cuaternario del Huecú (sector occidental de la cuenca neuquina). En: Geología de la Cuenca Neuquina. Rev Asoc Geol Arg 65(2):400–412

Rojas Vera E, Folguera A, Gímenez M, Martínez P, Ruiz F, Ramos VA (2009c) Evolución tectónica de la fosa de Loncopué: Estructura del depocentro cuaternario del Huecú y su relación con la sedimentación y el volcanismo. Rev Asoc Geol Arg 64(2):213–229

Rojas Vera E, Folguera A, Zamora Valcarce G, Giménez M, Ruiz F, Martínez P, Bottesi G, Ramos VA (2010) Neogene to Quaternary extensional reactivation of a fold and thrust belt: the Agrio belt in the Southern Central Andes and its relation to the Loncopué trough (38°–39°S). Tectonophysics 92(1–4):279–294

Rojas Vera E, Folguera A, Zamora Valcarce G, Bottesi G Ramos VA (2013) Structure and development of the Andean system between 36–39°S. J Geodyn 73:34–52

Singer B, Hildreth W, Vincze Y (2000) 40Ar/39Ar evidence for early deglaciation of central Chilean Andes. Geophys Res Lett 27:1663–1666. doi:10.1029/1999GL011065

Stern C (1989) Pliocene to present migration of the volcanic front, Andean Southern Volcanic Front. Rev Geol Chile 16(2):145–162

Suárez M, Emparán G (1997) Hoja Curacautín, Regiones de la Araucanía y del Bío-Bío, scale 1:250,000, Servicio Nacional de Geología y Minería

Tašárová Z (2004) Gravity data analysis and interdisciplinary 3D modelling of a convergent plate margin (Chile, 36–42°S) (PhD thesis): Berlin, Germany, Freie Universität Berlin, pp 187

Varekamp J, Ouimette A, Herman S, Bermúdez A, Delpino D (2001) Hydrothermal element fluxes from Copahue, Argentina: a beehive volcano in turmoil. Geology 29(11):1059–1062

Vélez M, Euillades P, Caselli A, Blanco M, Martínez Díaz J (2011) Deformation of Copahue volcano: inversion of InSar data using a genetic algorithm. J Volcanol Geoth Res 202:117–126

Vergara M, Muñoz J (1982) La Formación Cola de Zorro en la alta cordillera Andina Chilena (36°–39° Lat. S), sus características petrográficas y petrológicas: una revisión. Rev Geol Chile 17:31–46

Yuan X, Asch G, Bataillek K, Bock G, Bohm M, Echtler H, Kind R, Oncken O, Wólbern I (2006) Deep seimic images of the Southern Andes. In: Kay S, Ramos VA (eds) Late Cretaceous to Recent magmatism and tectonism of the Southern Andean margin at the latitude of the Neuquen basin (36–39°S). Geol S Am S 407:61–72

Zech R, May J-H, Kull C, Ilgner J, Kubik PW, Veit H (2008) Timing of the late Quaternary glaciations in the Andes from ∼15 to 40°S. J Quaternary Sci 23 (6):635–647. doi:10.1002/jqs.1200

Active Tectonics and Its Interactions with Copahue Volcano

F.L. Bonali, C. Corazzato, F. Bellotti and G. Groppelli

Abstract

The aim of this review is to describe the state-of-art of the neotectonic setting of this area as well as to present new data resulting from a recent structural field survey. The integrated analysis of literature and new structural data shows incongruities mainly in some regional structures and in the ENE-WSW striking fault system that affects and controls the feeding system of Copahue volcano. In addition, taking into account the very recent volcanic activity, the structural constraints and the earthquakes occurred in the area close to the volcano, a static stress numerical model was applied to simulate the variations of the local stress perturbing the normal activity of the volcanic plumbing system favouring magma ascent and consequent eruptions. At present, a comprehensive structural model is lacking and more in-depth studies can furnish a complete tectonic framework of the area, which can provide fundamental information to assess volcanic hazard, forecast future volcanic activity, and to enhance the development of the associated geothermal field.

F.L. Bonali · C. Corazzato
Dipartimento di Scienze dell'Ambiente e del
Territorio e di Scienze della Terra, Università di
Milano-Bicocca, Piazza della Scienza 4, 20126
Milan, Italy

C. Corazzato
Dipartimento di Scienza e Alta Tecnologia,
Università dell'Insubria, Como, Italy

F. Bellotti
Tele-Rilevamento Europa T.R.E. s.r.l, Ripa di Porta
Ticinese 79, 21149 Milan, Italy

G. Groppelli (✉)
Istituto per la Dinamica dei Processi Ambientali—
Sezione di Milano, Consiglio Nazionale delle
Ricerche, via Mangiagalli 34, 20133 Milan, Italy
e-mail: gianluca.groppelli@cnr.it

2.1 Introduction

Active tectonics is capable of influencing activity at volcanoes both at local and regional scale, controlling the feeding system geometry, the magma rising, and the growth-dismantlement phases of volcanic edifices (Marzocchi et al. 1993; Barrientos 1994; Decker et al. 1995; Bautista et al. 1996; Nostro et al. 1998; Bellotti et al. 2006; Walter and Amelung 2006; Norini et al. 2008, 2010, 2013; Groppelli and Norini 2011; Bonali et al. 2013; Bonali 2013). Active tectonics also impacts the hydrothermal circulation and consequently geothermal fields in volcanic areas,

by developing faults and fractures in the upper crust (e.g. Cameli et al. 1993; Brogi et al. 2010; Giordano et al. 2013; Norini et al. 2013).

The purpose of this chapter is to present the state of the art on Copahue volcano, an active Andean volcano located in the eastern Andean Southern Volcanic Zone, where a close connection between tectonic control, volcanic activity and the associated geothermal field is well documented in previous works (e.g. Velez et al. 2011, and references therein). The resolution of the neotectonic setting around Copahue volcano has been improved in this chapter by means of a detailed structural field survey performed in 2007, mainly devoted to recognising the evidence of active tectonics and the relationship among the fault pattern, the volcanic feeding system and the eruptive history.

Moreover, for the reason that large earthquakes could trigger volcanic activity at both close and large distances from the epicentre at regional scale (Linde and Sacks 1998; Hill et al. 2002; Marzocchi 2002a, b; Marzocchi et al. 2002; Manga and Brodsky 2006; Walter and Amelung 2007; Eggert and Walter 2009; Bebbington and Marzocchi 2011) in a time-frame of a few days after the earthquake event (Linde and Sacks 1998; Manga and Brodsky 2006; Eggert and Walter 2009; Moreno and Petit-Breuilh 1999), a static stress numerical model was also applied to simulate the variations in the local stress induced by earthquakes on the plumbing system.

Structural data in combination with numerical modelling can provide fundamental information to forecast future volcanic activity and to assess volcanic hazard. Finally, the in-depth knowledge of the tectonic setting of Copahue volcano can enhance the development and exploitation of the geothermal field, because of the structural control on hydrothermal circulation (Giordano et al. 2013; Invernizzi et al. 2014).

2.2 Volcanotectonic Setting

As highlighted by Folguera et al. (2015), the 2997 m-high Copahue active stratovolcano is located in the eastern part of the Southern Volcanic Zone (SVZ) (Fig. 2.1). The deformation in the study area is partitioned in such a way that large thrust earthquakes dominantly occur in the subduction zone, whereas intra-arc transcurrent faulting events are observed (Barrientos and Ward 1990; Cisternas et al. 2005; Watt et al. 2009). Dextral strike-slip moment tensor solutions dominate between 34° and 46°S in the main cordillera (e.g. Chinn and Isacks 1983; Lange et al. 2008), although it is only south of 38°S that long-term strike-slip faulting shows surface evidence, represented by the 1200 km-long Liquiñe-Ofqui major intra-arc fault zone (LOFZ, Figs. 2.1 and 2.2; Cembrano et al. 1996; Folguera et al. 2002; Adriasola et al. 2006; Rosenau et al. 2006; Cembrano and Lara 2009). This dextral transpressional fault zone plays a fundamental role in controlling the magmatic activity along the volcanic front between 37° and 47°S (Lavenu and Cembrano 1999; Rosenau 2004). López-Escobar et al. (1995) and Cembrano and Lara (2009) suggested that, with respect to the more contractional setting further north in the SVZ, the LOFZ allows a more rapid magma ascent with lesser occurrence of crustal assimilation or magma mixing (Collini et al. 2013). Folguera et al. (2006, 2015) recognise a transition from the strike-slip fault zone to a thrust zone at approximately 37°S, testified by the merging of the LOFZ into the Agrio and the Malargue fold-and-thrust belts (Fig. 2.1). This transition also corresponds to a thickening and ageing of the continental crust (Rojas Vera et al. 2014), to longer crustal magma residence times, and to greater differentiation, crustal assimilation and magma mixing (Tormey et al. 1991).

The name "Caviahue-Agrio caldera", where Copahue volcano is located (Figs. 2.2a and 2.3), encompasses both names that this structure was given in the literature, Caviahue caldera (Melnick et al. 2006; Velez et al. 2011) and Agrio caldera (Melnick and Folguera 2001; Rosenau et al. 2006; Rojas Vera et al. 2009) respectively. It is described as a pull-apart basin, a transtensional structural system developed in the northeastern end of the LOFZ by dextral movements in the late Pliocene (Melnick and Folguera 2001;
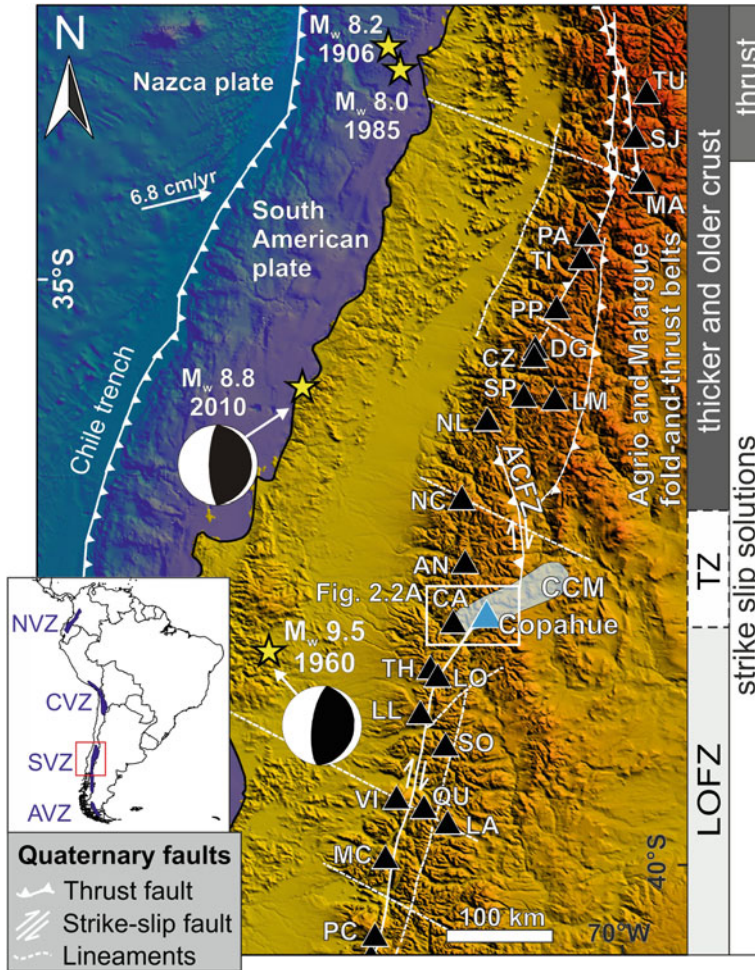
Fig. 2.1 Tectonic setting of the Southern Volcanic Zone (SVZ). *Triangles* locate active Holocenic volcanoes. The *white arrow* indicates the approximate convergence direction of the plates with estimated velocity. Main intra-arc faults with reverse motion (thrust faults) in the north, and right lateral strike-slip motion in the south are reported (redrawn after Melnick et al. 2006; Cembrano and Lara 2009; Bonali 2013). LOFZ-Liquiñe-Ofqui Fault Zone; TZ-Transition Zone; CCM-Callaqui-Copahue-Mandolegüe lineament, ACFZ-Antinir-Copahue regional thrust-fold system. NVZ, CVZ, SVZ and AVZ correspond to Northern, Central, Southern and Austral Volcanic Zones. TU-Tupungatito; SJ-San José; MA-Maipo; PA-Palomo; TI-Tinguiririca; PP-Planchón-Peteroa; DG-Descabezado Grande; CZ-Cerro Azul; NL-Nevado de Longavi, NC-Nevados de Chillán; AN-Antuco; CA-Callaqui; TH-Tolhuaca; LO-Lonquimay; LL-Llaima; VI-Villarrica; QU-Quetrupillan; LA-Lanin; MC-Mocho-Choshuenco; PC-Puyehue-Cordón Caulle. Yellow stars locate earthquakes with $M_w \geq 8$ occurred since 1900 AD, focal mechanisms of the modelled earthquakes are reported

Folguera et al. 2015) and part of the abovementioned transition zone between the Andean segments to the north and south (Lavenu and Cembrano 1999). The LOFZ shows clear evidence of Plio-Quaternary dextral kinematics, and the main active fault of this area is the NE-striking Lomìn fault (LF in Fig. 2.2), ending at the southwestern border of the Caviahue-Agrio caldera and representing the most relevant expression of a horsetail-like array and affecting Holocene lavas of Copahue volcano (Melnick 2000; Melnick et al. 2006).
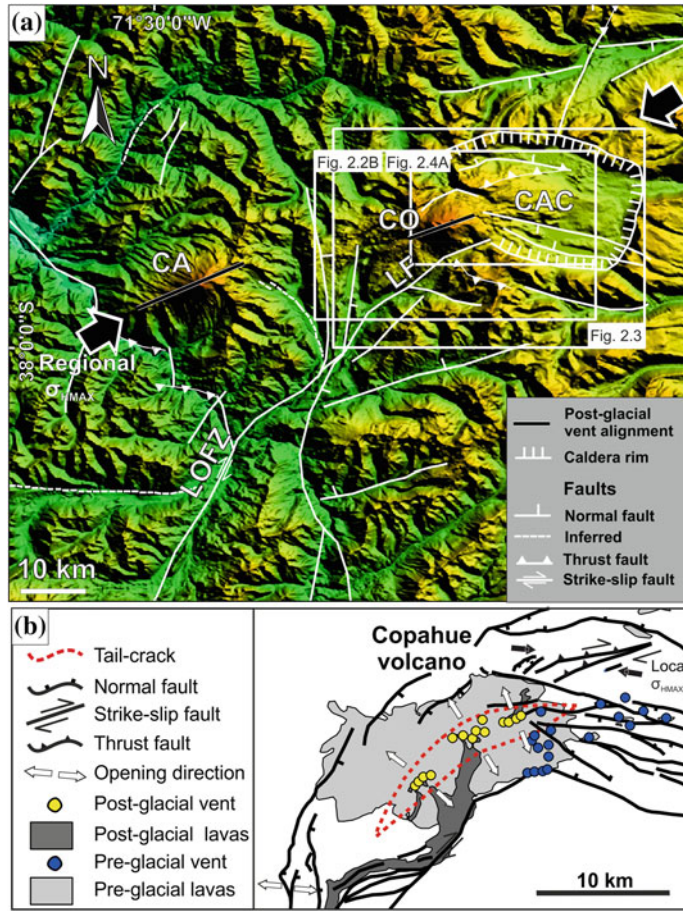
Fig. 2.2 a Tectonic map of the Callaqui-Copahue-Mandolegüe transfer zone (CCM). *CAC* Caviahue-Agrio Caldera; *LOFZ* Liquiñe-Ofqui fault zone; *LF* Lomìn fault; *CA* Callaqui volcano; *CO* Copahue volcano. *Thick black lines* represent the strike of volcano feeding systems, *while black arrows* represent the regional σ_{Hmax}. Shaded-relief digital elevation model is from SRTM90 data (datum WGS84) (http://srtm.csi.cgiar.org/). Boxes locate Figs. 2.2b, 2.3 and 2.4a. **b** Structural model of the Copahue volcanic complex characterized by a N60 °E trending post-glacial vent alignment. Redrawn from Melnick et al. (2006)

2.3 Active Tectonics – Literature Data

Several authors described the tectonics of the Caviahue-Agrio caldera—Copahue volcano complex, further on named as CAC as in Melnick et al. (2006), while in Velez et al. (2011) it is reported as CCVC (Caviahue caldera—Copahue stratovolcano). A recent structural synthesis is provided by Folguera et al. (2015) and references therein. Here, the focus is on the evidence of active tectonics in the CAC area as reported in the literature, and further original field data are provided to understand the tectonic structures presently controlling the volcanic activity of Copahue and the geothermal resources of the area.

The CAC represents an arc volcanic complex in an oblique subduction setting, and it is located in an important morphotectonic zone, transitional from strike-slip to thrust-dominated (Melnick et al. 2006). It represents the central sector of the NE-trending, 90-km-long Callaqui-Copahue-Mandolegue (CCM) volcanic alignment (Fig. 2.1), the longest Plio–
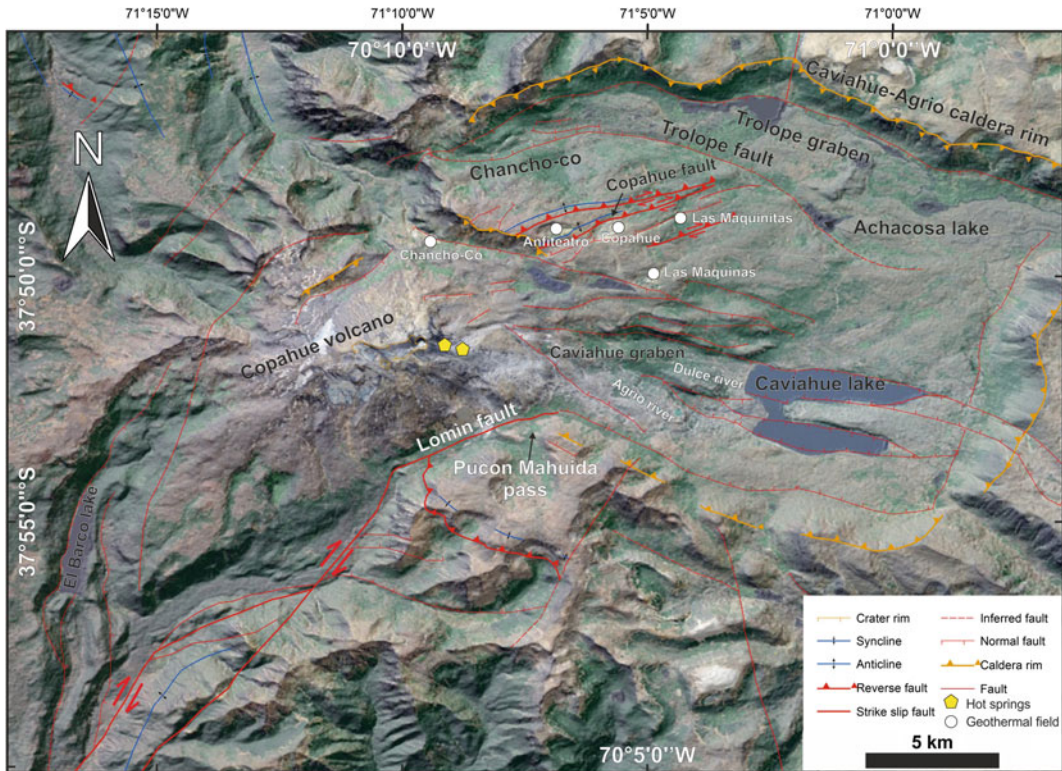
Fig. 2.3 Main structural features of the Caviahue-Copahue complex mapped on Aster DTM and Image (redrawn from Melnick et al. 2006). Geothermal fields are indicated after Velez et al. (2011)

Quaternary volcanic alignment of the SVZ (Melnick et al. 2006) and regarded as a transfer zone accommodating the step-wise configuration of the strike-slip LOFZ, controlled at the arc front, and the Antinir-Copahue regional thrust-fold system (ACFZ in Fig. 2.1, as defined in Folguera et al. 2004; Folguera and Ramos 2009; Velez et al. 2011, also named CAFS in Melnick et al. 2006), running through the inner retroarc (Melnick and Folguera 2001; Radic et al. 2002; Folguera et al. 2004; Melnick et al. 2006), with persistent activity in the Holocene. Melnick and Folguera (2001) described the Quaternary volcano-tectonic phase of activity of the area as mixed transtensional and transpressive, in close spatial relation with the CCM volcanic alignment. The following subsections describe in detail the state of the art on the active structures in the CAC, in particular the Caviahue-Agrio caldera, the structures located

south of Copahue volcano, the WNW-striking system, the Chancho-Co structures, and the Copahue Fault.

2.3.1 The Caviahue-Agrio Caldera

The Caviahue-Agrio caldera (Figs. 2.2 and 2.3), 15-km-long and 10-km-wide, formed as a volcanic feature with a strong structural control. Volcanic activity in the Caviahue-Agrio caldera area has been controlled by both the regional stress field imposed by plate convergence and by local structures formed at the intersection of regional fault systems (Melnick et al. 2006). The main structures of the Caviahue-Agrio caldera area are represented by (1) the normal faults of the caldera border, building up-to-400-m high scarps affecting Lower Pliocene units, (2) the right-lateral strike-slip faults affecting Copahue postglacial lava flows in the Lomín valley to the

south of the volcano, (3) the NE-trending fissure system controlling the effusive products of Copahue volcano and the hydrothermal manifestations inside the caldera, and (4) the NE-trending imbricated Chancho-Co fault system (Folguera and Ramos 2000, Mazzoni and Licitra 2000), (5) the WNW-trending Caviahue graben, hosting the Agrio lake, and (6) the NE-striking reverse fault affecting the Cola de Zorro formation to the south of the volcano (Melnick and Folguera 2001). Deflation processes at the intersection between the Caviahue graben and the Chancho-Co antiform have been recently recognized by radar interferometry (Ibáñez et al. 2008). Moreover, the CAC area includes several active geothermal fields, showing manifestations of boiling pools and bubbling pools (Velez et al. 2011), namely Las Máquinas, Maquinitas, Copahue, Anfiteatro and Chancho-Co (Fig. 2.3), which are aligned through the Chancho-Co frontal structures (Varekamp et al. 2001; Velez et al. 2011).

In the northern and central part of the Caviahue-Agrio caldera, Folguera et al. (2004) and Rojas Vera et al. (2009) recognise reverse faults with subordinate righ-lateral components, affecting post-glacial products and displacing Quaternary morphologies, and producing small pull-apart basins. These structures are associated with the ENE-trending Mandolegue fault system, which represents a transfer zone between the LOFZ and the ACFZ, and whose western edge is represented by the Chancho-Co uplift. Based on fault activity in unconsolidated deposits, Folguera et al. (2004) suggests ongoing deformation for the ACFZ, an E-vergent arrangement of high-angle dextral transpressive and transtensive faults.

2.3.2 The Structures South of Copahue

To the south of Copahue and SW of the Caviahue-Agrio caldera, the NNE-striking Lomín Fault corresponding to the northern edge of the LOFZ, is another Quaternary-active strike slip structure with minor normal component (LF in Figs. 2.2 and 2.3; Folguera et al. 2004), for

which Melnick et al. (2000) and Melnick et al. (2006) recognise neotectonic activity evidenced by 300–1000 m long and up to 5–10 m high fault scarps cutting Holocenic lavas erupted from the volcano, close to the Pucón-Mahuida Pass (Fig. 2.3). An at least Pleistocenic activity is recognized for the NE-striking structures affecting the southern flank of Copahue (Rojas Vera et al. 2009).

2.3.3 WNW-Striking Structures and Grabens

The WNW-striking normal fault system affects the eastern and central, as well as the northern and southern sectors of the caldera, cutting the Las Mellizas sequence and andesites from the base of Copahue volcano (Fig. 2.3). These faults have a strong topographic expression, and from N to S they form the Trolope and Caviahue grabens, controlling the elongated shape of Lake Caviahue (Melnick et al. 2006). The general strike of the Trolope and Caviahue grabens is parallel to the long axis of the rectangular Caviahue-Agrio caldera, and their formation is related to late Pliocene-Pleistocene reactivation of the caldera-pull-apart structure in response to dextral shear along the LOFZ (Melnick et al. 2006). The Quaternary extensional activity of these grabens represents the latest pulse of the caldera activity, and the Caviahue graben reveals a differential amount of extension from Copahue volcano to the east (Folguera et al. 2004). The Trolope graben affects the Las Mellizas formation, and its most recent control is over singlacial monogenetic cones (Rojas Vera et al. 2009). Copahue volcano is located at the intersection between two main structural systems, the WNW-trending Caviahue graben and the NE-trending Chancho-Co antiform (cfr. 2.3.4), the second main positive feature in the area (Fig. 2.3).

2.3.4 The Chancho-Co Structure

The Chancho-Co structure (Fig. 2.3) is located in the central to northern part of the CAC and is

considered to have been active during the Pleistocene and Holocene, controlling the main active geothermal systems in the area that form an en-echélon arrangement (Melnick et al. 2006). The Chancho-Co is a N60 °E trending elongated ridge (Folguera et al. 2004), representing a transpressive imbricated structure whose development is linked to a series of SE-vergent NE-trending thrusts and associated hanging-wall anticlines (Folguera and Ramos 2000), affecting Late Pliocene successions gathered in Las Mellizas Formation (Melnick et al. 2006). Its uplift would have preceded the extension that led to the Caviahue graben formation (Rojas Vera et al. 2009), and its front is in correspondence of the inhabited Copahue village. There is poor evidence of the potential Quaternary activity of these structures and of their relations with Copahue volcano, or of their deep control (Rojas Vera et al. 2009). The control on the Quaternary and present uplift of the Chancho-Co structure is exerted by a main NE-striking fault system and a subordinate WNW-striking system, coinciding with the geometry of the southernmost part of a gravimetric low (Rojas Vera et al. 2009).

Regarding neotectonic activity along this structure, several authors noticed that: (i) some reverse scarps, a few metres high, affect a glacial surface, together with open cracks (Folguera and Ramos 2000; Folguera et al. 2004); (ii) the southernmost of these reverse faults (defined as the "Copahue Fault" by Rojas Vera et al. 2009, cfr. 2.3.5 and Fig. 2.3) marks the main topographic break, thrusting ignimbrites over Quaternary till-like deposits near the Copahue village (Melnick et al. 2006); (iii) Rojas Vera et al. (2009) describe south-facing reverse fault scarps that uplift the Chancho-Co antiform and affect less than 1 Ma-old volcanics and postglacial Copahue products, as well as Pleistocene glacial morphologies; (iv) extensional faults and open cracks (extended for tens of meters and reaching depths of 15 m) along the axis of the Chancho-Co anticlines, with scarps up to 3-m high, were described by Melnick et al. (2006). They define small crestal grabens that trend slightly oblique to the reverse faults and the axis of the anticlines.

The Chancho-Co features do not fit with ground deformation contours determined from InSAR (Interferometric Synthetic Aperture Radar) studies observed by Velez et al. (2011), who describe an oval-shaped deflation feature whose location is partially coincident with Copahue volcano and also extends north-eastward over the Chancho-Co elevation. Their conceptual model is compatible with the present geochemical, geological and geophysical evidence, and deflation is regarded as a possible trigger mechanism for phreatic eruptions as those observed in the last eruptive cycles of Copahue in 1992, 1995 and 2000. The few fault-slip data measured along the reverse fault scarps indicate oblique dextral transpressional motion, consistent with the en-echélon arrangement formed by the Anfiteatro, Copahue, and Las Maquinitas depressions as well as the slightly oblique trend of the crestal grabens and open cracks with respect to the main reverse faults (Figs. 2.3 and 2.4). Melnick et al. (2006) explain the Chanco-Co kinematics due to a local rotation of the regional stress field, and they do not provide any justification for the hydrothermal activity and hot springs occurring along planes perpendicular to the greatest horizontal stress (σ_{Hmax}). In fact, Melnick et al. (2006) state that magma ascent has occurred along planes perpendicular to the least principal horizontal stress, whereas hydrothermal activity and hot springs also occur along parallel planes. The geometries of the Chanco-Co indicate that the direction of shortening was oblique to the trend of the main contractional structures (Burbank and Anderson 2001; Melnick et al. 2006). Finally, Melnick et al. (2006) suggest a tectonic control for the development of the caldera-related Chancho-Co block and of the N60 °E-trending compressive structures located on its upper part, whereas they advance the hypothesis of gravitational instability being the cause for the normal faults affecting the resurgent block.

2.3.5 The Copahue Fault

Rojas Vera et al. (2009) describe the main topographic break affecting the Chancho-Co system of reverse faults as the "Copahue
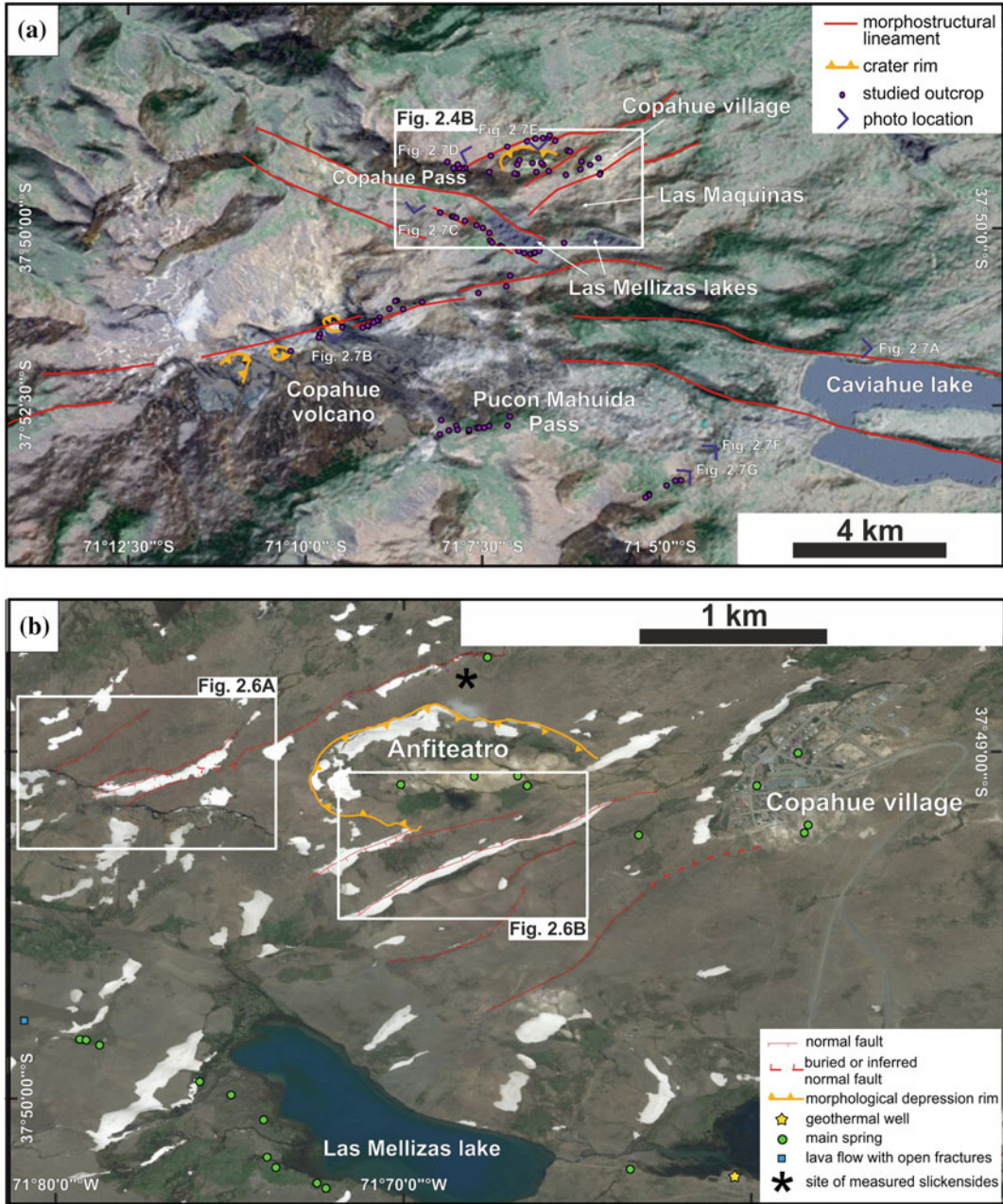
Fig. 2.4 a Morphostructural map showing the main lineaments of the area and the studied outcrops. The map contains the location of the photos illustrated in Fig. 2.7. Box locates Fig. 2.4b. **b** The Copahue Village Fault System: it affects the NE flank of Copahue volcano from Las Mellizas—Las Maquinas to Copahue Village. Boxes locate Fig. 2.6a, b

Fault", a system of reverse (thrust) scarps to the E of Las Mellizas lakes, some of them reaching the Trolope graben to the E (Fig. 2.3), and cutting the Copahue lavas to the SW. They also highlight a parallelism between the uplift structures of the Chancho-Co and the alignment of post-glacial monogenetic centres and the active crater of Copahue, giving rise, as a whole, to a

fault-and-scarp system extending more than 15 km. The study of uplifted Late Pliocene sequences over younger unconsolidated fluvial and colluvial deposits enabled Rojas Vera et al. (2009) to identify at least two periods of activity for the NE-striking Copahue Fault.

2.4 Active Tectonics – New Field Data

For a better understanding of the tectonic structures that control the volcanic activity of Copahue a structural survey in December 2007 mainly devoted to the neotectonic features was carried out. The frequent eruptions of Copahue volcano, the sharp scarps along its flanks and in the surroundings, as well as the presence of abundant springs, *spa* and geothermal wells and power plants (Fig. 2.4a) suggest the presence of recent and active tectonics in the area. During the field survey, the strike of fractures, fault scarps, dikes, eruptive fissures were measured, at the same time, the abundant evidence of a structural control linked to geothermal manifestations and alteration zones were considered. By plotting direction of all measured faults, fractures, eruptive fissures and dikes (Fig. 2.5), two main tectonic trends were recognized, a dominant one oriented ENE-WSW, and a secondary ESE-WNW trend (see also Fig. 2.4a). These two trends correspond to the well known structures

affecting the CAC, as described in the previous paragraph (e.g. Folguera et al. 2004; Melnick et al. 2006; Rojas Vera et al. 2009).

The ESE-WNW-oriented structures mainly crop out along the lower northeastern flank of Copahue volcano, where the springs are aligned along this trend (Fig. 2.4b) as well as the alteration zones due to hydrothermal circulation. Along the same structure a geothermal well is in operation (Las Mellizas lake, Fig. 2.4b), and a recent lava flow shows open fractures (Fig. 2.4b). This trend results parallel to a regional one that is affecting the northern border of Copahue and shows its morphological expression also in the Caviahue lake and at the Copahue pass (Fig. 2.4a). In addition, close to the Copahue village, in the large crateric depression called Anfiteatro, two N120 °E-aligned lava domes are emplaced.

The ENE-WSW-oriented structures show a more complex trend but, at the same time, they testify to the presence of more recent activity, with open fractures, soil displacement, etc (Figs. 2.4a, b, and 2.6a, b). They were defined as the Copahue Village Fault System (CVFS— Fig. 2.4a). Such fault system partially comprises the previous defined Chancho-Co structure and Copahue Fault (Melnik et al. 2006; Rojas Vera et al. 2009), but in this case it is characterised by a different kinematics. The system is affecting Copahue volcano (Fig. 2.4a), where the summit vents and craters are aligned along a N60–70 ° E-striking trend. More specifically, in the summit
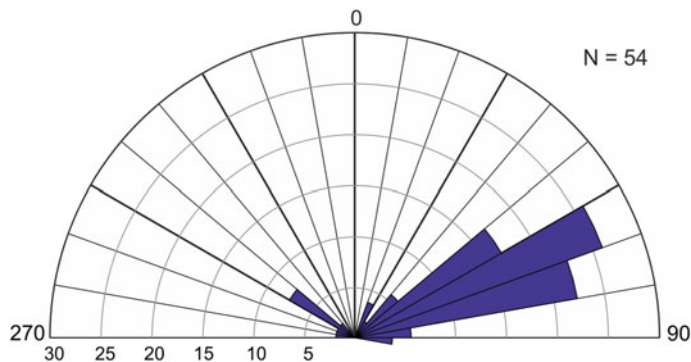
Fig. 2.5 Rose diagram showing the strike of the measured faults, fractures, eruptive fissures and dikes

area a dike strikes N60 °E (Fig. 2.7f, g). The southern rim of the summit crater lake (Fig. 2.7b) is affected by N55 °E-striking fractures, showing a left-step en-echelon arrangement. Following the same trend, on the NE flank of Copahue volcano numerous eruptive fissures are present, with a N65 °E–N78 °E-striking orientation. The Copahue village is located inside a graben with a general N60°–70 °E-striking trend and extending towards Copahue volcano (see Fig. 2.4a, b). The main graben, 3 km long and 2 km wide, is bordered by two main normal faults, along with some minor structures that form smaller asymmetric grabens. In detail, these smaller grabens are made of several discontinuous normal faults, whose trace is usually bent, locally forming a step morphology (Fig. 2.6a, b). All the faults show normal kinematics, striking from N50 °E–N70 °E, with a vertical displacement ranging from 50 cm to 30 m, and usually of some meters, often associated with open fractures unfilled by sediments or soil. Most faults and fractures are
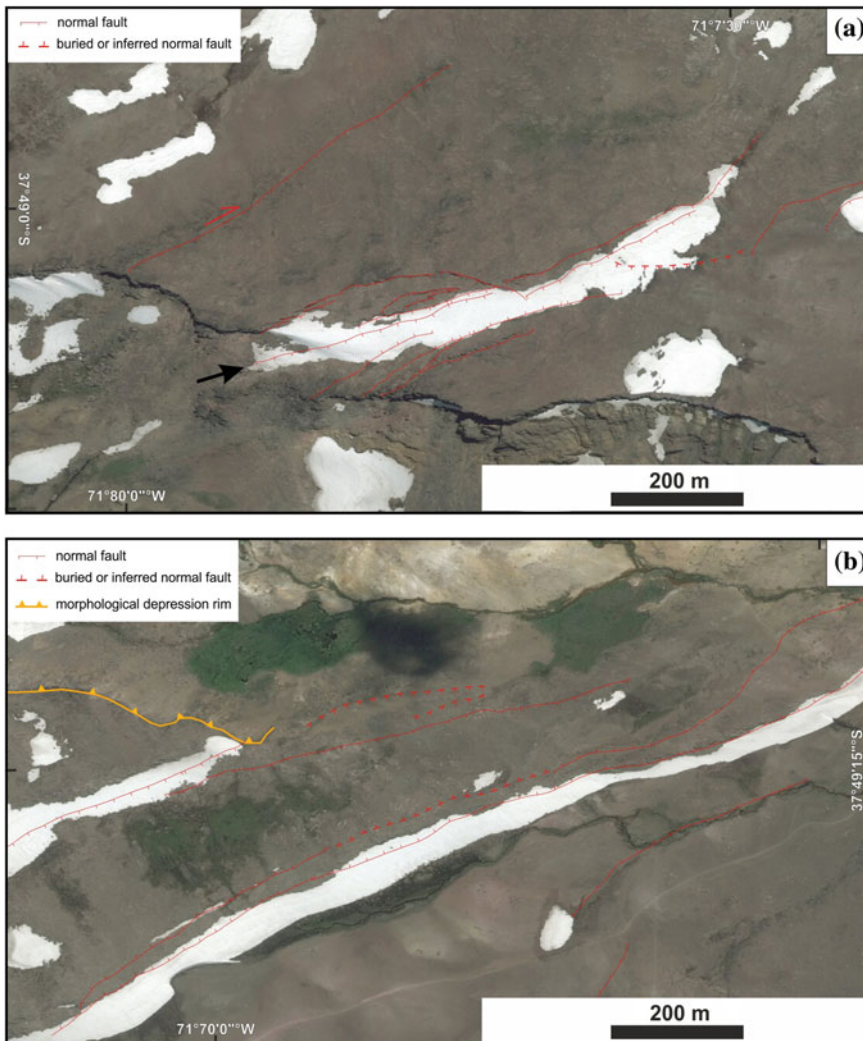
Fig. 2.6 a and **b** detailed sketch of the structures surveyed in two key areas. The *black arrow* in Fig. 2.6a indicates the trace of the main fault bordering the northern side of the graben. For further explanation, please see Sect. 2.4. Location in Fig. 2.4b

also recognisable on aerial photos (Fig. 2.6a, b). Frequently, the ground is also affected by open fractures, with opening up to 20 cm, or small faults with a maximum vertical displacement of 50 cm. This is a clear evidence of ongoing tectonic deformation, as shown also by interferometric data reported in Velez et al. (2011, this book).

In addition to the normal component, the main structure bordering the northern side of the graben (see arrow in Fig. 2.6a) also shows strike-slip kinematics. In particular, close to the scarp rim, this structure presents 30 m of vertical displacement associated with a dextral strike-slip component and an estimated offset of a few centimetres, not feasible to be measured in the field (Fig. 2.7c, d). 1.5 km eastward along the structure discussed above, a sub-vertical fault plane was measured, striking N75 °E and dipping 88°, affecting a lava flow. On this fault plane slickenlines are present, and a pitch angle of 45 °W (Figs. 2.4b and 2.7e) confirms its transtensive kinematics.

In addition, two dikes belonging to the same trend were recognized, which were intruded into a fault plane along the southern wall of the Caviahue caldera, close to the Pucón Mahuida pass. They strike N47 °E–N52 °E, with a left-stepping en-echélon arrangement. One of these dikes is aphyric and 2-m-thick, the second is porphyritic and 4-m-thick, with abundant phenocrysts of plagioclase, pyroxene and olivine (Fig. 2.7f, g).

The kinematics of CVFS is transtensive, characterized by metric extensional fault scarps that border an ENE-WSW striking graben (Fig. 2.4b), associated with a minor dextral strike-slip component indicated by slickenlines, en-echélon arrangements of dikes and fractures, as shown by field and morphological observations from our work, and interferometric data (Velez et al. 2011). Therefore, the tectonic extension of the CVFS has modelled the large graben that also affects the Copahue village. This kinematics is in agreement with the estimated direction of the maximum horizontal stress in this area (N80 °E–N90 °E, Cembrano and Lara 2009). In addition, the two tectonic trends

(ENE-WSW and ESE-WNW, Figs. 2.4a and 2.5) may represent a conjugate fault system and are responsible for driving hot fluids to the surface (geothermal springs) in the area of Copahue village and Las Mellizas Lakes.

2.5 Volcano Feeding System

During the Quaternary, the volcanic activity of Copahue has concentrated along the NE-trending, 90-km-long CCM (Fig. 2.1). Such lineament is the longest of the SVZ and it is interpreted as a crustal-scale transfer zone inherited from a Miocene rifted basin (Melnick et al. 2006). In particular, along this lineament are present the N60 °E-elongated Callaqui volcano to the SW, the Copahue stratovolcano, and the Caviahue-Agrio caldera to the NE (Fig. 2.2; Moreno and Lahsen 1986; Melnick et al. 2006). Local structures formed at the intersection of regional fault systems control the volcanic activity along the CAC alignment (Melnick et al. 2006). The N60 °E-striking structural control of the CCM transfer zone is also suggested at local scale by Holocenic fault scarps affecting the volcano eastern slopes as well as by post-glacial vent alignments (Fig. 2.2; Melnick et al. 2006). The Holocene activity of Copahue is testified by aligned parasitic cones, fissure-related pyroclastic flows, along with activity from the summit craters, with basaltic-andesitic products (Melnick et al. 2006). In particular, the volcano is formed by the superimposition of several emission centres along a main NE-striking fissure, and the volcano summit has nine craters aligned N60 °E, four of which post-glacial (Rojas Vera et al. 2009) and the eastern-most being presently active (Velez et al. 2011). The NE-striking fracture system affects the most recent lava flows in the NE flank of the volcano, together with the structures affecting the Chancho-Co (Rojas Vera et al. 2009). It has the same trend of the transtensive CVFS described in this chapter (cfr. 2.4). Based on the hypothesis that magmas rise along steeply-inclined intrusive sheets, propagating normal to the least principal
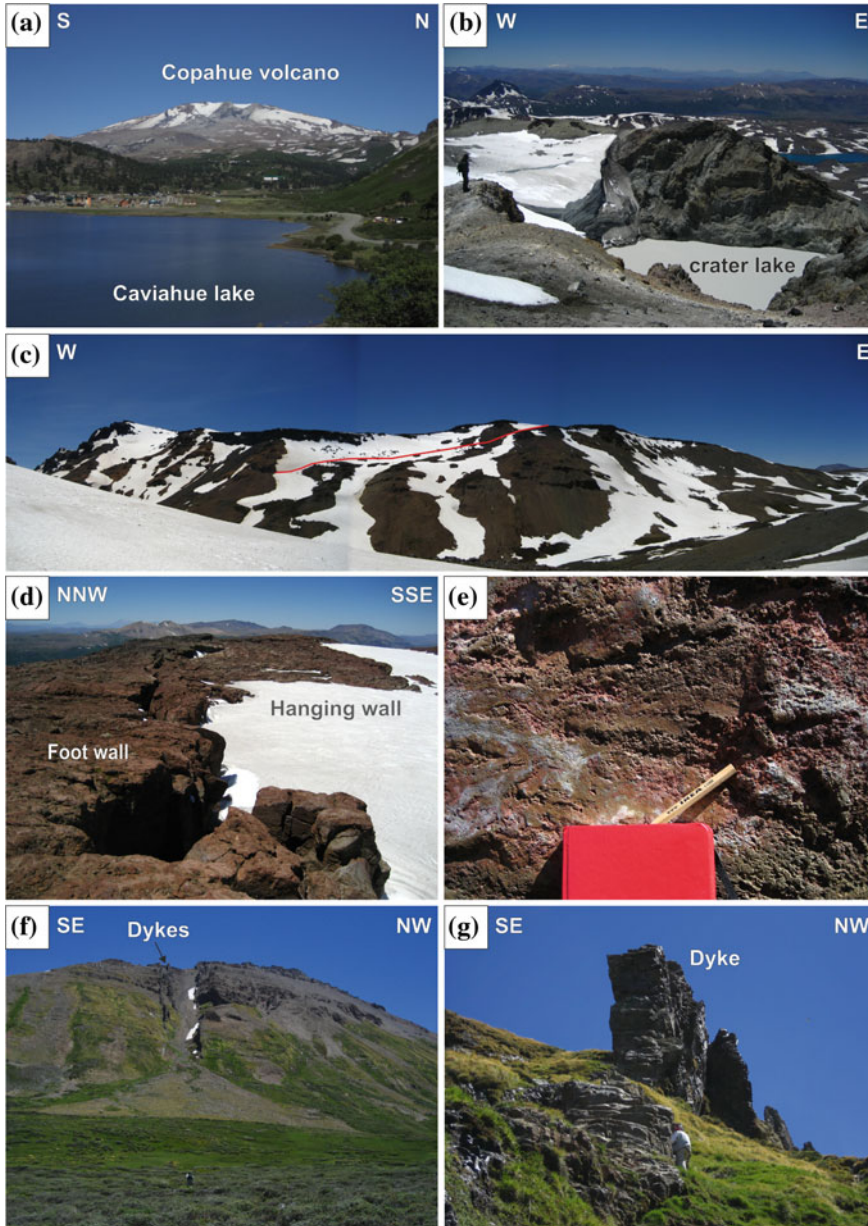
Fig. 2.7 Panoramic views and outcrops from Copahue volcano and surrounding areas. Photo location in Fig. 2.4a. **a** Copahue volcano western flank, with the village of Caviahue and the namesake lake in the foreground. **b** The summit crater of Copahue volcano, partially covered by a small ice cap. **c** Panoramic view of the Copahue Village Fault System striking ENE-WSW. The red dashed line outlines the fault plane, that corresponds to the fault indicated with black arrow in Fig. 2.6a. **d** Close-up view of the previous fault, showing the fault displacement: footwall to the left, hangingwall, partially covered by the snow, to the right. **e** Close-up view of Copahue Village fault plane: the pencil points out the direction of the slickensides (for location, see the star in Fig. 2.4b). **f** NE-striking fault. The fault plane is intruded by dikes. **g** Close-up view of the dike striking N50 °E. For further explanation, please see Sect. 2.4

horizontal stress (σ_{Hmin}), and form dyke swarms (Dieterich 1988; Walter and Schmincke 2002) and aligned parasitic cones (Nakamura 1977; Tibaldi 1995; Corazzato and Tibaldi 2006; Bonali et al. 2011). Bonali (2013) proposed that magma at Copahue rises along vertical or sub-vertical planes striking about N60 °E, perpendicular to σ_{Hmin} (in agreement with Melnick et al. 2006). This is supported by the evidence that the Quaternary least principal stress axis (σ_3) trends NW and it is mostly sub-horizontal, as suggested by the inversion of fault-slip data between 37 °S–46 °S in the SVZ (Lavenu and Cembrano 1999; Arancibia et al. 1999; Cembrano et al. 2000; Potent and Reuther 2001; Lara et al. 2006; Cembrano and Lara 2009). Furthermore Mamani et al. (2000), based on magnetotelluric soundings, suggest the possible presence of a magma chamber at a depth between 9 and 20 km.

2.6 Elastic Interactions Between Recent Faulting and Copahue

This section explores how active tectonics is capable of influencing the normal volcanic activity at Copahue volcano. Active tectonics along the SVZ is represented by faulting that produces earthquakes both along the subduction zone and along the intra-arc active faults. Such phenomena are capable of influencing the normal volcanic activity by inducing stress changes (static, quasi static and dynamic), as suggested in the literature (Hill et al. 2002; Marzocchi et al. 2002; Manga and Brodsky 2006). Several authors pointed out that the delay between the earthquake and the following volcanic events can be from seconds to years, because of the complexity of volcanic systems (Linde and Sacks 1998; Nostro et al. 1998; McLeod and Tait 1999; Walter and Amelung 2007; Eggert and Walter 2009), despite the present lack of a thorough constraint. Regarding the SVZ, Watt et al. (2009) noticed that the overall eruption rate in the Southern Volcanic Zone (SVZ) increased after the two Chilean earthquakes of August 1906 (M_w 8.2)

and May 1960 (M_w 9.5), and this increase occurred one and 3 years after the earthquakes.

The static stress change is the variation in the stress field from just before an earthquake to shortly after the seismic waves have decayed (Hill et al. 2002). Such change is invoked as an explanation for eruption-leading processes occurring in regions close to the fault rupture (e.g., Walter and Amelung 2007; Bonali 2013; Bonali et al. 2013). Quasi-static stress change occurs over a period of years to decades, and it is associated with slow viscous relaxation of the lower crust and upper mantle beneath the epicentre of a large earthquake (Freed and Lin 2002; Marzocchi 2002a, b; Marzocchi et al. 2002). Dynamic stress, associated with the passage of seismic waves, is often regarded as a possible eruption trigger at greater distances (Linde and Sacks 1998; Manga and Brodsky 2006; Delle Donne et al. 2010).

A new method, regarding the static stress changes imparted by the earthquakes on the reconstructed volcano magma pathway (e.g. Bonali et al. 2013; Bonali 2013), was followed.

2.6.1 Conceptual Model and Modelling Strategy

In order to study a possible relationship between earthquakes and volcanic activity in the Copahue area, the normal stress change, imparted on the volcano magma pathway (e.g. Nostro et al. 1998; Walter 2007; Bonali et al. 2012) by $M_w \geq 8$ earthquakes occurred in front of the SVZ, was calculated (Bonali et al. 2013). The numerical models using the Coulomb 3.3 software (Lin and Stein 2004; Toda et al. 2005) was performed. Calculations are made in an elastic half-space with uniform isotropic elastic properties following Okada's (1992) formulae that allow to calculate the static normal stress change resolved on a volcano magma pathway, independently from the rake angle of the receiver structure and from the friction coefficient used in the model. The reconstructed magma pathway of Copahue volcano was assumed as a N60 °E-striking vertical plane, as explained in Sect. 2.5, and different

Table 2.1 Characteristics for the four $M_w \geq 8$ earthquakes and finite fault models: date of the event, magnitude, search radius, fault rupture length (Comte et al. 1986; Lomnitz 1970; Kelleher 1972; Lomnitz 1985; Okal 2005; Watt et al. 2009; Lin et al. 2013; Servicio Sismológico de la Universidad de Chile, http://ssn.dgf.uchile.cl; USGS earthquake hazards program), fault-plane strike and dip angle, number of patches, averaged fault slip and rake angle, depth of top and bottom of the fault plane, trend and plunge of σ_1, σ_2, σ_3 (based on Barrientos and Ward 1990; Lin and Stein 2004; USGS earthquake hazards program, http://earthquake.usgs.gov; Okal (2011), written communication; Kanamori (2011), written communication)

Name	Valparaiso	Valdivia	Santiago	Maule
Date	8/17/2006	5/22/1960	3/3/1985	2/27/2010
Mw	8.2	9.5	8.0	8.8
Rupture length (km)	330	940	170	460
Fault geometry (strike/dip, °)	8/17	7/20	11/26	8–2°/12–14
N. of patches	1	864	153	292
Average slip (m)	2.6	3.8	1.6	2.5
Average rake angle (°)	117.0	105.0	105.0	105.0
Fault top (km)	20.5	0.0	21.8	2.9
Fault bottom (km)	47.5	153.9	61.3	50.1
σ1 (azimuth/plunge, °)	71/31	100/35	86/20	92/28
σ2 (azimuth/plunge, °)	157/7	10/0	174/9	178/5
σ3 (azimuth/plunge, °)	56/58	80/55	61/68	80/61

attitudes were also tested by changing the dip angles (50°, 70° and 90°). Its reconstructed geometry also mimics the Quaternary geometry of active faults reported in this work, striking ENE-WSW. The upper crust was modelled as an elastic isotropic half-space characterized by a Young's modulus E = 80 GPa and a Poisson's ratio ν = 0.25 based on Mithen (1982), King et al. (1994), Lin and Stein (2004) and Toda et al. (2005); a lower value of the Young's modulus would only have the effect of reducing the magnitude of static stress changes. Regarding the finite fault model used to simulate earthquake effects, for the 1960 earthquake the fault solutions proposed by Barrientos and Ward (1990) based on tsunami wave form inversion was used, whereas for the 2010 earthquake the fault solutions proposed by Lin et al. (2013), based on InSAR, GPS and teleseismic data, was used. The input stress field for both earthquakes is reported in Table 2.1, based on T, N and P axis of related focal mechanisms. Furthermore, it has been evaluated the possible contribution of earthquake-induced static stress changes due to crustal earthquakes occurred between the 1907

and the 2010 Chile earthquakes available in a digital database provided by USGS (http://earthquake.usgs.gov). Fault geometries and kinematics are based on focal mechanism solutions (http://earthquake.usgs.gov; http://www.gmtproject.it/) when available, and geometries and kinematics of active faults reported in the literature (Melnick et al. 2006; Cembrano and Lara 2009). Fault dimensions were based on empirical relations (Wells and Coppersmith 1994; Toda et al. 2011). The earthquake-induced normal stress changes on Copahue feeding system, possibly imparted by earthquakes with $M_w \geq 4$ and a depth between 0 and 70 km (http://earthquake.usgs.gov), was also resovled.

2.6.2 Interaction Between the Subduction Zone and the Volcano

It is commonly suggested that large subduction earthquakes are capable of inducing static stress perturbations on the fault hanging wall block, also promoting volcanic eruptions (Barrientos 1994; Lin and Stein 2004; Walter and Amelung

2007; Bonali 2013; Bonali et al. 2013). Static stress change is the difference in the stress field from just before an earthquake to shortly after the seismic waves have decayed (Hill et al. 2002), and it is proposed as a mechanism capable of leading eruptions in regions close to the fault rupture (e.g., Walter and Amelung 2007; Bonali et al. 2013). Altought a first theory suggested that magma could be squeezed upward by increased compressional stress in the crust surrounding a magma chamber close to its critical state (e.g. Bautista et al. 1996), more recent findings agreed that earthquake-induced static (permanent) normal stress reduction on magma pathway (unclamping) could promote dyke intrusion and following eruptions (e.g. Hill et al. 2002; Walter 2007). Furthermore, Walter and Amelung (2007) suggested that earthquake-induced volumetric expansion can increase the magma-gas pressure and encourage eruptions in a time frame of years. Finally, Bonali et al. (2013) advanced the hypothesis that unrest at volcanoes with deep magma chambers is encouraged by magma pathway unclamping.

Results of numerical modelling suggest that both the 1960 and 2010 subduction earthquakes were capable of inducing unclamping at vertical or subvertical magma pathway of Copahue volcano (Fig. 2.8). Regarding the 1960 earthquake-induced static stress changes (Fig. 2.8a, b), unclamping is higher for a vertical or SE-dipping magma pathway and it increases with depth, while it decreases with depth for a NW-dipping magma pathway, and it results in clamping at a depth between 5–9 km for the 50°-NW-dipping pathway (Fig. 2.8b). Regarding the 2010 earthquake-induced static stress changes, the magma pathway (Fig. 2.8c) is always affected by a normal stress reduction (unclamping) within a depth range of 1–9 km below the volcano base (Fig. 2.8d). Magnitude of unclamping slightly decreases with depth, and ranges from −0.258 to −0.147 MPa (Bonali 2013), and decreases with decreasing dip angle of the magma pathway (Fig. 2.8d). Although positive feedbacks due to dynamic and post-seismic stress changes could not be excluded, large subduction earthquakes seems to be capable of favouring volcanic

activity at Copahue due to earthquake-induced static (permanent) normal stress reduction on its magma pathway (e.g. Hill et al. 2002; Walter 2007) at a distance of 257–353 km and up to 3 years following subduction earthquakes (Bonali 2013; Bonali et al. 2013). Such hypothesis is supported by some suggestion proposed in Marzocchi (2002a, b) where coseismic stress changes are candidate to promote eruptions in the 0–5 years after earthquakes as far as 100–300 km from the epicentre (i.e. 38 h after the 1960 Valdivia 9.5 M_w earthquake the Cordon Caulle erupted; Moreno and Petit-Breuilh 1999, Collini et al. 2013). Regarding the time delay, Marzocchi (2002a, b) has proposed that: (i) the inertia of the volcanic system in reacting to the static stress changes, (ii) a non perfect elasticity of the crust and/or (iii) stress corrosion effect (e.g., Main and Meredith 1991), are processes candidate to explain a time delay of 0–5 years. Other mechanisms that could have promoted unrest at Copahue, following such earthquakes, regard postseismic-induced stress/strain (Marzocchi 2002a, b; Marzocchi et al. 2002) and dynamic stress changes (Manga and Brodsky 2006). As proposed by Marzocchi et al. (2002) and Freed and Lin (2002), quasi-static stress change, which is a post-seismically-induced effect, could promote eruptions over a period of years to decades. Marzocchi (2002a, b) suggested a time window of about 30–35 years after earthquakes, compatibly to the relaxation time of a viscous asthenosphere (Piersanti et al. 1995, 1997; Pollitz et al. 1998; Kenner and Segall 2000). Regarding the dynamic stress changes, such effects may excite and promote ascent of gas bubbles, and consequently magma ascent (Manga and Brodsky 2006), the details of the feedback mechanisms remaining unclear and are nowadays discussed in the literature. It is proposed that dynamic effects is capable of promoting bubble growth, including adjective overpressure (Linde et al. 1994), rectified diffusion (Brodsky et al. 1998; Ichihara and Brodsky 2006) and shear strain (Sumita and Manga 2008). Copahue experienced 9 eruptions since 1900 (Global Volcanism Program Digital Information Series), five of which in the last 21 years (Fig. 2.9). In
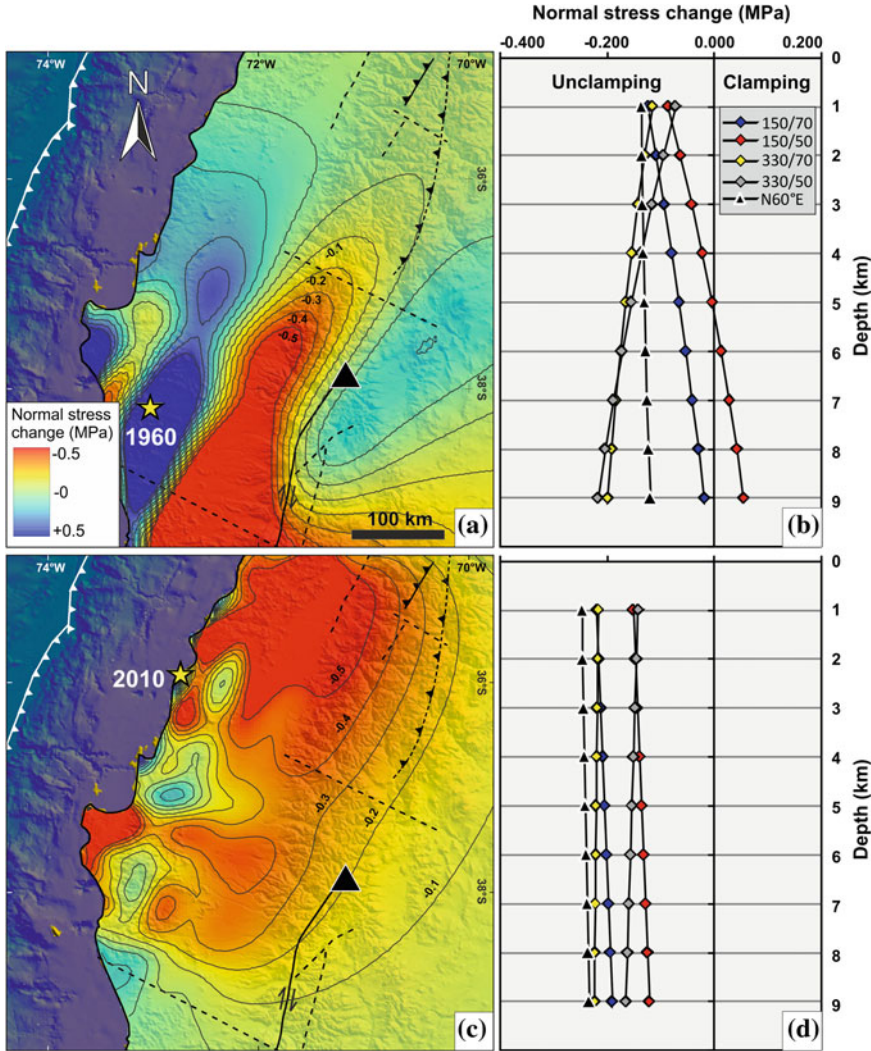
Fig. 2.8 a Contour map of the 1960 M_w 9.5 earthquake-induced normal stress change resolved on the N60 °E-striking Copahue magma pathway at a depth of 4.5 km below the volcano base. Red colours represent a normal static stress reduction on the receiver plane, blue colours represent an increase. The black triangle locates Copahue volcano. The finite fault model used is from Barrientos and Ward (1990), and **b** shows the normal stress change for vertical as well as inclined receiver surfaces (attitude expressed as dip direction/dip angle), in a depth range of 1–9 km below the volcano. **c** Contour map of the M_w 8.8 2010 earthquake-induced normal stress change resolved on the N60 °E-striking Copahue magma pathway at a depth of 4.5 km below the volcano base. The finite fault model used here is from Lin et al. (2013), and **d** shows the normal stress change for vertical as well as inclined receiver surfaces in a depth range of 1–9 km below the volcano

detail, four eruptions occurred in the time-frame 1992–2000, the recentmost eruption (2012) occurred instead after the 2010 Chile earthquake, under unclamping conditions of the magma pathway. The Copahue magma pathway was affected by normal stress reduction also after the 1960 Valdivia earthquake, and the volcano erupted certainly in 1961.
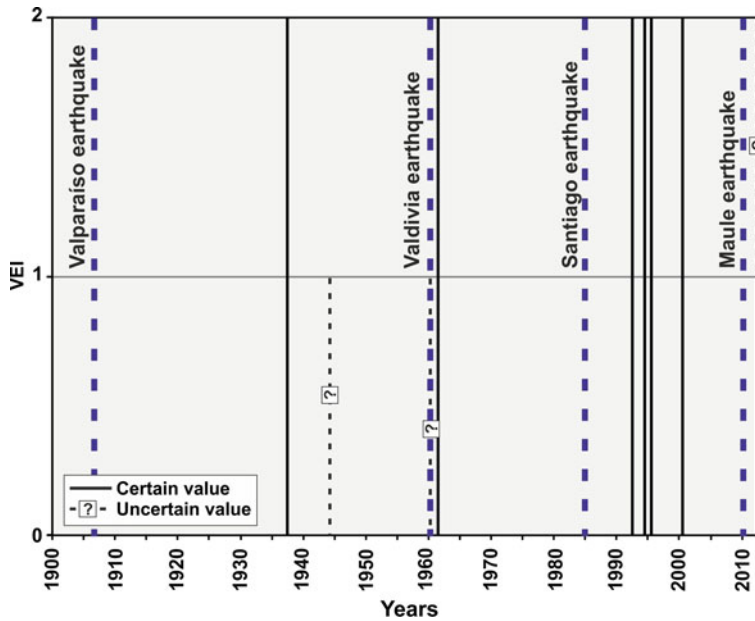
Fig. 2.9 The graph reports the eruptions occurred at Copahue since 1900 AD (Global Volcanism Program Digital Information Series) and significant earthquakes ($M_w > 8$) along the SVZ. Marks represent the first day of each reported year. VEI-Volcanic Explosivity Index

2.6.3 Effect of the Surrounding Structures on the Volcano

Our analysis of the possible contribution of earthquake-induced static stress changes due to crustal earthquakes with M_w 4–6.6 (http://earthquake.usgs.gov) reveals that only one out of 2727 earthquakes (Fig. 2.10a) was capable of inducing static normal stress changes on the Copahue magma pathway (Fig. 2.10b). Such earthquake occurred on 31/12/2006 with M_w of 5.6 at a distance of about 11 km from the volcano. The hypocenter was 20.6 km deep (http://earthquake.usgs.gov) and the kinematics was dextral strike-slip (Fig. 2.10a). Results of the numerical modelling carried out considering different dip angles of the N60 °E-striking magma pathway suggest that such surface suffered a normal stress reduction when vertical or subvertical, SE-dipping. A subvertical NW-dipping pathway is instead sometimes affected by normal stress increase with depth. When considering a less inclined NW-dipping pathway, no relevant normal stress changes are observed (Fig. 2.10b). Whatever the case, the stress change imparted by the 2010 earthquake is two orders of magnitude greater than the contribution of the 2006 seismic event.

2.7 Discussion

The role of structures in a volcanic area is unquestionable because they control the magma storage and drive the magma rising, as well as the location of vents and the evolution of a volcano (e.g. Bellotti et al. 2006; Norini et al. 2013). In this way, by examining the structural data published up to now on Copahue volcano (see Sect. 2.3), it is evident that a comprehensive model is lacking and a large discussion is ongoing. In this section, all these available data were summarised, showing that there are some divergences among them and the related models. In addition, the new field data presented here (see Sect. 2.4), which cover only some portions of the volcanic area and consider mainly the recent and present volcano-tectonic activity, were considered.
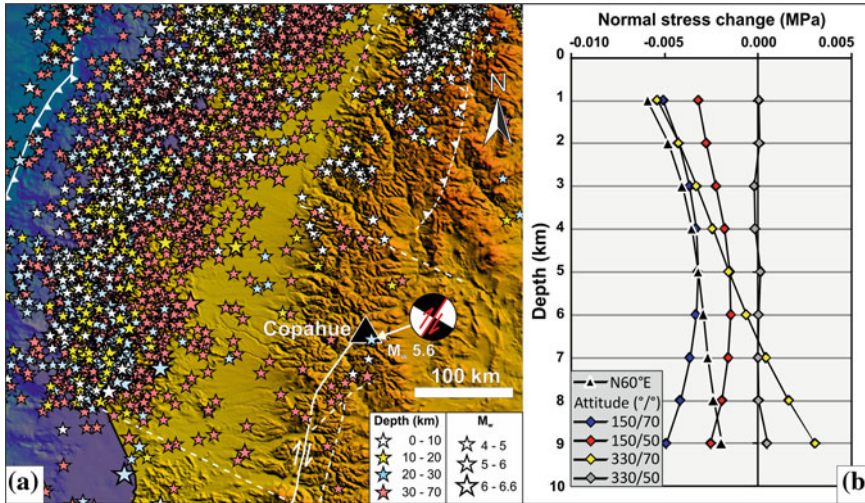
Fig. 2.10 a Stars represent the crustal earthquakes with $M_w \geq 4$ (http://earthquake.usgs.gov) occurred in the time-frame between the 1907 and the 2010 Chile earthquake. The focal mechanism of 31/12/2006 (M_w 5.6) is shown (http://earthquake.usgs.gov; http://www.gmtproject.it/), the red line representing fault strike and kinematics (Melnick et al. 2006; Cembrano and Lara 2009). **b** 2006 M_w 5.6 earthquake-induced normal stress change resolved on the N60 °E-striking reconstructed Copahue magma pathway. Vertical as well as inclined receiver surfaces are taken into account (attitude expressed as dip direction/dip angle), in a depth range of 1–9 km below the volcano

The long geological history of this sector of the Andes results in a really complex pattern of structures, with the superimposition of different tectonic phases. In detail, the complex structural setting displayed by Melnick et al. (2006) (Fig. 2.3) shows the presence of several generations of faults because of the variable position in time and somewhere in space of σ_{hmax} in the entire area. South of Copahue volcano there is a set of structures parallel to each others, striking NNE-SSW and with conflicting kinematics, as strike-slip faults parallel to normal faults and folds (anticlines and synclines). In addition, perpendicular to this direction a thrust system is emplaced. These features cannot be easily reconciled and could be explained to be the result of two or more generations of structures and/or of the heritage of older phases. Also in the Anfiteatro area, close to the Copahue village, there is another evident incompatibility between a set of reverse faults associated with fold anticlines and the normal faults parallel to them, and the geothermal field alignment (Melnick et al. 2006, Fig. 2.3).

In view of the main structures affecting Copahue volcano there is a general agreement among the authors that the ENE-WSW-striking lineament is the most important, because of active vents and summit craters alignment. This feature represents the local expression of the regional CMC structure (Figs. 2.1, 2.2, 2.3 and 2.4), a transfer fault system that links the LOFZ to the ACFZ (Folguera and Ramos 2009; Velez et al. 2011) along with three volcanoes are located (Callaqui, Copahue and Mandolegue). This fault system extends in the area close to the Copahue Village and Anfiteatro where vertical displacements, mainly reversal, associated with a right-lateral component have been identified. Some of these structures are named Chancho-Co and Copahue Fault (Fig. 2.3) (e.g. Folguera et al. 2004; Melnick et al. 2006; Rojas Vera et al. 2009 with some differences among their models). In our neotectonic survey (Figs. 2.4, 2.6 and 2.7) any evidence of recent reverse faults was identified; instead, based on our field data, they were considered as normal faults with a dextral strike-slip component. The subvertical geometry

of the faults (and their graben-like arrangement), the displacements, the presence of open fractures (up to 20 cm wide) and the few slickenlines suggest a normal-oblique kinematics for these structures. This normal fault system was named as Copahue Village Fault System (CVFS) was finally proposed. The CVFS kinematics is in agreement with the deflation observed by Velez et al. (2011), confirming that these are the re-centmost structures in the area, and thus they are more recent than the Chanco-Co structure. As suggested by Melnick et al. (2006), no evidence of folds on the topographic surface was identified; the lava flows display a tabular geometry, and local folding can be explained with the rotation due to the normal movements (drag) along the fault plane. The coeval presence of fold anticlines and parallel reverse faults can be related to the same stress field, but in this case the σ_{hmax} has to be rotated (about 90°) with respect to the regional one (N80 °E–N90 °E; Cembrano and Lara 2009). On the contrary, considering the new structural data, the resulting σ_{hmax} is in agreement with the regional one and the main geothermal sources are located in extensional and transtensional settings associated to a general deflation observed by InSAR data (Velez et al. 2011). Another evidence of extensional regime for the CVFS is suggested by the geometry of the plumbing system, striking almost parallel to this fault system. A previous shortening phase marked by folds and thrusts cannot be excluded, as recognised in the field and described in many outcrops by, among the others, Folguera et al. (2004), Melnick et al. (2006) and Rojas Vera et al. (2009). Conversely, the normal pattern recognised in our recent survey close to the Anfiteatro needs to be confirmed by more extensive surveys, also to recognise possibile diverse recent tectonic phases. Taking into account all the available data and models proposed for the area close to the Copahue village, an in-depth study appears necessary to better understand the structural setting and its evolution, allowing to recognise two or more possible tectonic phases. In addition, further studies should address the determination of the displacement rate of the active structures, because of

their importance for volcanic and seismic hazard and for geothermal exploitation.

Results of numerical models show that active tectonics is capable of perturbing the normal activity at Copahue due to static stress transfer. In the studied cases both 1960 and 2010 sub-duction earthquakes induced a normal stress reduction on volcano magma pathway, favouring dyke intrusion (e.g., Hill et al. 2002; Walter 2007; Walter and Amelung 2007). Minor events, occurred along intra-arc faults, were also capable of producing the same effect, but with minor intensity.

2.8 Final Remarks

This review presents the state-of-art about tectonic data in the CAC and surroundings area as well as includes some new neotectonic data around Copahue volcano. The main points are summarised as follow:

1. Different structural models have been proposed right now, but a comprehensive model is lacking and further in-depth studies are necessary.
2. A main ENE-WSW striking structure affects Copahue volcano and represents the local expression of the CCM transfer zone. This structure is inferred to control the magma pathway and the volcano evolution. There is no agreement on the normal or reverse kinematics related to the present activity of the CVFS. The possible reverse movement of this fault system needs a rotation of the regional σ_{hmax}, while the normal one is in agreement with it.
3. A better knowledge of the CVFS activity, the potential presence of two or more phases and the understanding of its Holocenic strain rate are fundamental goals for further and in-depth structural studies. In fact, a more detailed and complete tectonic setting of the CAC should represent a fundamental result also for the general geological-structural model of this area, providing structural constraints for the

magma storage, pathway and rising, and representing an essential issue also for volcanic hazard assessment, as well as for enancing the exploitation of the geothermal system.

4. Active tectonics is capable of perturbing the normal activity at Copahue volcano due to earthquake-induced static stress changes. As result of numerical modelling, both 1960 and 2010 large subduction earthquakes induced unclamping on Copahue feeding system, favouring following eruptions. Very low unclamping was also induced by one crustal earthquake occurred after the pre-2012 eruption and before the 2010 earthquake.

References

Adriasola AC, Thomson SN, Brix MR, Hervé F, Stockhert B (2006) Postmagmatic cooling and Late Cenozoic denudation of the North Patagonian Batholith in the Los Lagos Region of Chile, 41°S–42°S. Int J Earth Sci 95:504–528

Arancibia G, Cembrano J, Lavenu A (1999) Transpresión dextral y partición de la deformación en la Zona de Falla Liquiñe-Ofqui, Aisén, Chile (44–45°S). Rev Geol Chile 26(1):3–22

Barrientos SE, Ward SN (1990) The 1960 Chile earthquake; inversion for slip distribution from surface deformation. Geophys J Intern 103:589–598

Barrientos SE (1994) Large thrust earthquakes and volcanic eruptions. Pure appl Geophys 142(1):225–237

Bautista BC, Bautista MLP, Stein RS, Barcelona ES, Punongbayan RS, Laguerta AR, Rasdas EP, Ambubuyog G, Amin EQ (1996) Relationship of regional and local structures of Mount Pinatubo activity. In: Newhall CG, Punongbayan RS (eds) Fire and mud:

Eruptions and Lahars of Mount Pinatubo, Philippines. University of Washington Press, Seattle, pp 351–370

Bebbington MS, Marzocchi W (2011) Stochastic models for earthquake triggering of volcanic eruptions. J Geophys Res 116:B05204. doi.org/10.1029/2010JB008114

Bellotti F, Capra L, Groppelli G, Norini G (2006) Tectonic evolution of the central-eastern sector of trans Mexican volcanic belt and its influence on the eruptive history of the Nevado de Toluca Volcano (Mexico). In: Tibaldi A, Lagmay AMF (eds) Interaction between volcanoes and their basement. J Volcanol Geotherm Res 158:21–36

Bonali FL, Corazzato C, Tibaldi A (2011) Identifying rift zones on volcanoes: an example from La Réunion island. Indian Ocean Bull Volcanol 73(3):347–366

Bonali FL, Corazzato C, Tibaldi A (2012) Elastic stress interaction between faulting and volcanism in the Olacapato-San Antonio de Los Cobres area (Puna plateau, Argentina). Global Planet Change 90–91:104–120

Bonali FL (2013) Earthquake-induced static stress change on magma pathway in promoting the 2012 Copahue eruption. Tectonophysics 608:127–137

Bonali FL, Tibaldi A, Corazzato C, Tormey DR, Lara LE (2013) Quantifying the effect of large earthquakes in promoting eruptions due to stress changes on magma pathway: the Chile case. Tectonophysics 583:54–67

Brodsky EE, Sturtevant B, Kanamori H (1998) Earthquakes, volcanoes, and rectified diffusion. Geophys Res Lett 103:23827–23838

Brogi A, Liotta D, Meccheri M, Fabbrini L (2010) Transtensional shear zones controlling volcanic eruptions: the Middle Pleistocene Mt Amiata volcano (inner Northern Apennines, Italy). Terra Nova 22 (2):137–146

Burbank DW, Anderson RS (2001) Tectonic geomorphology. Blackwell Scientific, Oxford, p 270

Cameli GM, Dini I, Liotta D (1993) Upper crustal structure of the Larderello geothermal field as a feature of post-collisional extensional tectonics (southern Tuscany, Italy). Tectonophysics 224(4):413–423

Cembrano J, Hervé F, Lavenu A, Shermer E, Lavenu A, Sanhueza A (1996) The Liquiñe Ofqui fault zone: a long-lived intra-arc fault system in southern Chile. Tectonophysics 259(1–3):55–66

Cembrano J, Shermer E, Lavenu A, Sanhueza A (2000) Contrasting nature of deformation along an intra-arc shear zone, the Liquiñe-Ofqui fault zone, southern Chilean Andes. Tectonophysics 319:129–149

Cembrano J, Lara L (2009) The link between volcanism and tectonics in the Southern Volcanic Zone of the Chilean Andes: a review. Tectonophysics 471:96–113

Chinn DS, Isacks BL (1983) Accurate source depths and focal mechanisms of shallow earthquakes in western South America and in the News Hebrides islands arc. Tectonics 2:529–563

Cisternas M, Atwater BF, Torrejon T, Sawai Y, Machuca G, Lagos M, Eipert A, Youlton C, Ignacio S, Kamataki T, Shishikura M, Rajendran CP, Malik JK,

Rizal Y, Husni M (2005) Predecessors of the giant 1960 Chile earthquake. Nature 437:404–407

Collini E, Osores MS, Folch A, Viramonte JG, Villarosa G, Salmuni G (2013) Volcanic ash forecast during the June 2011 Cordon Caulle eruption. Nat Haz 66(2):389–412. doi:10.0007/s11069-012-0492-y

Comte D, Eisenberg A, Lorca E, Pardo M, Ponce L, Saragoni R, Singh SK, Suárez G (1986) The central Chile earthquake of 3 March 1985: a repeat of previous great earthquakes in the region? Science 233:449–453

Corazzato C, Tibaldi A (2006) Basement fracture control on type, distribution, and morphology of parasitic volcanic cones: an example from Mt. Etna, Italy. In: Tibaldi A, Lagmay M (eds) Interaction between Volcanoes and their Basement. J Volcanol Geoth Res Special issue, 158:177–194

Decker RW, Klein FW, Okamura AT, Okubo PG (1995) Forecasting eruptions of Mauna Loa Volcano, Hawaii. Mauna Loa revealed; structure, composition, history, and hazards. American Geophysical Union, Washington, DC, United States, pp 337–348

Delle Donne D, Harris AJL, Ripepe M, Wright R (2010) Earthquake-induced thermal anomalies at active volcanoes. Geology 38(9):771–774

Dieterich JH (1988) Growth and persistence of Hawaiian volcanic rift zones. J Geophys Res 93:4258–4270

Eggert S, Walter TR (2009) Volcanic activity before and after large tectonic earthquakes: observations and statistical significance. Tectonophysics 471:14–26

Folguera A, Ramos VA (2000) Control estructural del vólcan Copaue: Implicancias tectónicas para el arco volcánico Cuaternario (36°–39 °S): Rev Geol Arg 55:229–244

Folguera A, Ramos VA (2009) Collision of the Mocha fracture zone and a < 4 Ma old wave of orogenic uplift in the Andes (36°–38 °S). Lithosphere 1(6):364–369

Folguera A, Ramos VA, Melnick D (2002) Partición de la deformación en la zona del arco volcánico de los Andes neuquinos (36–39 °S) en los últimos 30 millones de años. Rev Geol Chile 29(2):151–165

Folguera A, Ramos VA, Hermans R, Naranjo J (2004) Neotectonics in the foothills of the southernmost central Andes (37°–38 °S): Evidence of strike-slip displacement along the Antiñir-Copahue fault Zone. Tectonics 23(5). doi:10.1029/2003TC001533

Folguera A, Ramos VA, Gonzalez Dıaz E, Hermanns R (2006) Late Cenozoic evolution of the Eastern Andean Foothills of Neuquén between 37° and 37°30'S. In: Kay SM, Ramos VA (eds) Late Cretaceous to recent magmatism and tectonism of the Southern Andean Margin at the latitude of the Neuquén Basin (36–39 ° S). Geol Soc Am 407:247–266

Folguera A, Rojas Vera E, Tobal J, Orts D, Ramos VA (2015) A review to the geology, structural controls and tectonic setting of the Copahue volcano in the Southern Volcanic Zone (in this volume 2015)

Freed AM, Lin J (2002) Accelerated stress buildup on the southern San Andreas Fault and surrounding regions caused by Mojave Desert earthquakes. Geology 30(6):571–574

Giordano G, Pinton A, Cianfarra P, Baez W, Chiodi A, Viramonte J, Norini G, Groppelli G (2013) Structural control on geothermal circulation in the Cerro Tuzgle-Tocomar geothermal volcanic area (Puna plateau, Argentina). J Volcanol Geotherm Res 249:77–94

Groppelli G, Norini G (2011) Geology and tectonics of the southwestern boundary of the unstable sector of Mt Etna (Italy). J Volcanol Geotherm Res 208:66–75

Hill DP, Pollitz F, Newhall C (2002) Earthquake-volcano interactions. Phys Today 55:41–47

Ibáñez JM, Del Pezzo E, Bengoa C, Caselli A, Badi G, Almendros J (2008) Volcanic tremor and local earthquakes at Copahue volcanic complex, Southern Andes, Argentina. J Volcanol Geotherm Res 174:284–294

Ichihara M, Brodsky EE (2006) A limit on the effect of rectified diffusion in volcanic systems. Geophys Res Lett 33:L02316. doi.org/10.1029/2005GL024753

Invernizzi C, Pierantoni PP, Chiodi A, Maffucci R, Corrado S, Baez W, Tassi F, Giordano G, Viramonte J (2014) Preliminary assessment of the geothermal potential of Rosario de la Frontera area (Salta, NW Argentina): insight from hydro-geological, hydro-geochemical and structural investigations. J South Am Earth Sci 54:20–36

Kelleher JA (1972) Rupture zones of large South American earthquakes and some predictions. J Geophys Res 77:2087–2103

Kenner SJ, Segall P (2000) Postseismic deformation following the 1906 San Francisco earthquake. J Geophys Res 105:13195–13209

King GCP, Stein RS, Lin J (1994) Static stress changes and the triggering of earthquakes. Bull Seismol Soc Am 84:935–953

Lange D, Cembrano J, Rietbrock A, Haberland C, Dahm T, Bataille K (2008) First seismic record for intra-arc strike-slip tectonics along the Liquiñe-Ofqui fault zone at the obliquely convergent plate margin of the southern Andes. Tectonophysics 455:14–24

Lara LE, Lavenu A, Cembrano J, Rodríguez C (2006) Structural controls of volcanism in transversal chains: resheared faults and neotectonics in the Cordón Caulle-Puyehue area (40.5 °S), southern Andes. J Volcanol Geotherm Res 158:70–86

Lavenu A, Cembrano J (1999) Compressional and transpressional-stress pattern for Pliocene and Quaternary brittle deformation in fore and intra-arc zones (Andes of Central and Southern Chile). J Structur Geol 21:1669–1691

Lin J, Stein RS (2004) Stress triggering in thrust and subduction earthquakes, and stress interaction between the southern San Andreas and nearby thrust and strike-slip faults. J Geophys Res 109:B02303

Lin YN, Sladen A, Ortega-Culaciati F, Simons M, Avouac J-P, Fielding EJ, Brooks BA, Bevis M, Genrich J, Rietbrock A, Vigny C, Smalley R, Socquet A (2013) Coseismic and postseismic slip

associated with the 2010 Maule earthquake, Chile: characterizing the Arauco Peninsula barrier effect. J Geophys Res 118(6):3142–3159

Linde AT, Sacks IS (1998) Triggering of volcanic eruptions. Nature 395:888–890

Linde AT, Sacks IS, Johnston MJS, Hill DP, Bilham RG (1994) Increased pressure from rising bubbles as a mechanism for remotely triggered seismicity. Nature 371:408–410

Lomnitz C (1970) Major earthquakes and tsunamis in Chile during the period 1535 to 1955. Geologische Rundschau Zeitschrift für Allgemeine Geologische 59:938–960

Lomnitz C (1985) Tectonic feedback and the earthquake cycle. Pageoph 123:667–682

López-Escobar L, Cembrano J, Moreno H (1995) Geochemistry and tectonics of the Chilean Southern Andes basaltic quaternary volcanism (37–46 °S). Rev Geol Chile 22(2):219–234

Main IG, Meredith PG (1991) Stress corrosion constitutive laws as a possible mechanism of intermediate-term and short-term seismic quiescence. Geophys J Int 107:363–372

Mamani MJ, Borzotta E, Venencia JE, Maidana A, Moyano CE, Castiglione B (2000) Electric structure of the Copahue Volcano (Neuquén Province, Argentina), from magnetotelluric soundings: 1D and 2D modellings. J South Am Earth Sci 13:147–156

Manga M, Brodsky EE (2006) Seismic triggering of eruptions in the far field: volcanoes and geysers. Annual Review of Earth and Planetary Science, 34, 263–291

Marzocchi W (2002a) Remote seismic influence on large explosive eruptions. J Geophys Res 107(B1): 2018

Marzocchi W (2002b) Remote seismic influence on the large explosive eruptions. J Geophys Res 107:EPM 6–1

Marzocchi W, Scandone R, Mulargia F (1993) The tectonic setting of Mount Vesuvius and the correlation between its eruptions and the earthquakes of the Southern Apennines. J Volcanol Geotherm Res 58(1–4):27–41

Marzocchi W, Casarotti E, Piersanti A (2002) Modeling the stress variations induced by great earthquakes on the largest volcanic eruptions of the 20th century. J Geophys Res 107(B11):2320

Mazzoni MM, Licitra DT (2000) Significado estratigráfico y volcanológico de depósitos de flujos piroclásticos neógenos con composición intermedia en la zona del lago Caviahue, provincia del Neuquén. Rev Asoc Geol Arg 55(3):188–200

McLeod P, Tait S (1999) The growth of dykes from magma chambers. J Volcanol Geotherm Res 92:231–246

Melnick D (2000) Geometría y estructuras de la parte norte de la zona de falla de Liquiñe-Ofqui (38°S): interpretación de sensores remotos. In: IX Congreso Geológico Chileno, Puerto Varas, Chile, vol 1, pp 796–799

Melnick D, Folguera A (2001) Geologia del complejo volcànico Copahue-Caldera Del Agrio, un sistema transtensional activo desde el Plioceno en la transiciòn de los Andes Patagònicos a los Andes Centrales (38 °S–71 °O). In: IX Congreso Geòlogico Latinoamericano, Montevideo, Uruguay, Universidad de Montevideo, pp 6–11

Melnick D, Folguera A, Ramos VA (2006) Structural control on arc volcanism: the Caviahue-Copahue complex, Central to Patagonian Andes transition (38 °S). J South Am Earth Sci 22:66–88

Moreno H, Lahsen A (1986) El volcán Callaqui: ejemplo de vulcanismo fisural en los Andes del Sur. Rev Asoc Geol Arg 42:1–8

Moreno H, Petit-Breuilh ME (1999) El volcán fisural CordónCaulle, Andes del Sur (40.5°S): geología general y comportamiento eruptivo histórico. In: XIV Congreso Geológico Argentino, Còrdoba, Argentina, vol 2, pp 258–260

Mithen DP (1982) Stress amplification in the upper crust and the development of normal faulting. Tectonophysics 83:121–130

Nakamura K (1977) Volcanoes as possible indicators of tectonic stress orientation: Principle and proposal. J Volcanol Geotherm Res 2:1–16

Norini G, Capra L, Groppelli G, Lagmay AMF (2008) Quaternary sector collapses of Nevado de Toluca volcano (Mexico) governed by regional tectonics and volcanic evolution. Geosphere 4(5):854–871

Norini G, Capra L, Groppelli G, Agliardi F, Pola A, Cortes A (2010) Structural architecture of the Colima Volcanic Complex. J Geophys Res 115(B12209):1–20. doi:10.1029/2010JB007649

Norini G, Baez W, Becchio R, Viramonte J, Giordano G, Arnosio M, Pinton A, Groppelli G (2013) The Calama-Olacapato-El Toro fault system in the Puna Plateau, Central Andes: geodynamic implications and stratovolcanoes emplacement. Tectonophysics 608:1280–1297

Nostro C, Stein RS, Cocco M, Belardinelli ME, Marzocchi W (1998) Two-way coupling between Vesuvius eruptions and southern Apennine earthquakes, Italy, by elastic stress transfer. J Geophys Res 103:24487–24504

Okada Y (1992) Internal deformation due to shear and tensile faults in a half-space. Bull Seismol Soc Am 82:1018–1040

Okal EA (2005) A re-evaluation of the great Aleutian and Chilean earthquakes of 1906 August 17. Geophys J Int 161:268–282

Piersanti A, Spada G, Sabadini R, Bonafede M (1995) Global postseismic deformation. Geophys J Int 120:544–566

Piersanti A, Spada G, Sabadini R (1997) Global postseismic rebound of a viscoelastic Earth: Theory for finite faults and application to the 1964 Alaska earthquake. J Geophys Res 102:477–492

Pollitz FF, Bürgmann R, Romanowicz B (1998) Viscosity of oceanic asthenosphere inferred from remote triggering of earthquakes. Science 280:1245–1249

Potent S, Reuther CD (2001) Neogene Deformations-prozesse im aktiven magmatischen Bogen Sudcentralchiles zwichen 37° und 39 °S. Mitteilungen aus dem Geologisch-Pala eontologischen Institut der Universitaet Hamburg 85:1–2

Radic JP, Rojas L, Carpinelli A, Zurita E (2002) Evolución tectónica de la cuenca terciaria de Cura-Mallín, región cordillerana chileno argentina (36°30′-39°00′S). XV Congreso Geológico Argentino, Calafate, Argentina 3:233–237

Rojas Vera E, Folguera A, Spagnuolo M, Gímenez M, Ruiz F, Martínez P. Ramos VR (2009) La neotectónica del arco volcánico a la latitud del volcán Copahue (38 °S), Andes de Neuquén. Rev Asoc Geol Arg 65(1):204–214

Rojas Vera EA, Folguera A, Valcarce GZ, Bottesi G, Ramos VR (2014) Structure and development of the andean system between 36 ° and 39°S. J Geodyn 73:34–52

Rosenau M (2004) Tectonics of the southern Andean intra-arc zone (38°–42°S). Ph.D. thesis, Free University, Berlin, Germany, pp 159

Rosenau M, Melnick D, Echtler H (2006) Kinematic constraints on intra-arc shear and strain partitioning in the Southern Andes between 38°S and 42°S latitude. Tectonics 25:TC4013

Sumita I, Manga M (2008) Suspension rheology under oscillatory shear and its geophysical implications. Earth Planet Sci Lett 269:468–477

Tibaldi A (1995) Morphology of pyroclastic cones and tectonics. J Geophys Res 100(B12):24521–24535

Toda S, Stein RS, Richards-Dinger K, Bozkurt S (2005) Forecasting the evolution of seismicity in southern California: animations built on earthquake stress transfer. J Geophys Res B05S16

Toda S, Stein RS, Lin J, Sevilgen K (2011) Coulomb 3.3 User Guide

Tormey DR, Hickey-Vargas R, Frey FA, López-Escobar L (1991) Recent lavas from the Andean volcanic front (33–42 °S); interpretations of along-arc compositional features. In: Harmon RS, Rapela CW (eds), Andean Magmatism and its Tectonic Setting. Geol Soc Am 265:57–77

Varekamp JC, Ouimette AP, Herman SW, Bermudez A, Delpino D (2001) Hydrothermal element fluxes from Copahue, Argentina: a "beehive" volcano in turmoil. Geology 29:1059–1062

Velez ML, Euillades P, Caselli A, Blanco M, Díaz JM (2011) Deformation of Copahue volcano: inversion of InSAR data using a genetic algorithm. J Volcanol Geotherm Res 202:117–126

Walter TR (2007) How a tectonic earthquake may awake silent volcanoes: Stress triggering during the 1996 earthquake-eruption sequence at the Karymsky Volcanic Group, Kamchatka. Earth Planet Sci Lett 264(3–4):347–359

Walter TR, Schmincke H-U (2002) Rifting, recurrent landsliding and Miocene structural reorganization on NW-Tenerife (Canary Islands). Int J Earth Sci 91:615–628

Walter TR, Amelung F (2006) Volcano-earthquake interaction at Mauna Loa volcano, Hawaii. J Geophys Res 111:B05204

Walter TR, Amelung F (2007) Volcanic eruptions following M ≥ 9 megathrust earthquakes: implications for the Sumatra-Andaman volcanoes. Geology 35:539–542

Wells DL, Coppersmith KJ (1994) New empirical relationships among magnitude, rupture length, rupture width, rupture area, and surface displacement. Bull Seismol Soc Am 84:974–1002

Watt SFL, Pyle DM, Mather TA (2009) The influence of great earthquakes on volcanic eruption rate along the Chilean subduction zone. Earth Planet Sci Lett 277:399–407

Prehistoric to Historic Volcanic Activity at Copahue Volcano

A.T. Caselli, M.L. Velez, M. Agusto, C. Liccioli and
O. Vaselli

Abstract

Copahue is one of the most active volcanic centers in Argentina. Despite the relatively intense volcanic activity its prehistoric events are poorly known. In this work, after a brief introduction on the geological and structural control on this volcanic complex, we have summarized the events that have led to the construction of the current volcanic edifice and its historical eruptive activity. Prehistoric events were divided into three main stages: pre-, sin- and post-glacial based on the stratigraphic relations observed in the field by previous authors. At least 13 eruptions were recorded during the last 260 years. Although the scarce detailed historical information, the eruptive style outlined by the available reports and data seems to indicate a general phreatic and phreato-magmatic character over the last two centuries, whereas the most recent (2000 and 2012) eruptive events, characterized by the occurrence of magmatic pulses, have a strombolian character.

3.1 Introduction

An exhaustive description of the geological and geodynamical context of the Copahue-Caviahue Volcanic Complex (CCVC) was provided by Folguera et al. (this book). The Copahue volcano edifice lies on a basement constituted by volcanic sequences belonging to the Cola de Zorro Formation, also described in literature as the Hualcupen Formation (González and Vergara 1962; Pesce 1989). According to available K-Ar ages (Muñoz and Stern 1988; Linares et al. 1999), this volcanic stage occurred in the Upper Pliocene (4.3 ± 0.2 Ma) under an extensional tectonic regime (Folguera et al. 2003). During the Upper

A.T. Caselli (✉)
LESVA, IIPG, Universidad Nacional de Río Negro, Roca 1242, 8332, General Roca, Argentina
e-mail: atcaselli@unrn.edu.ar

M.L. Velez · M. Agusto · C. Liccioli
GESVA - IDEAN, Dpto. Cs. Geológicas, FCEN, Universidad de Buenos Aires, 1428 Ciudad Universitaria, Pab.2, Buenos Aires, Argentina

M.L. Velez · M. Agusto · C. Liccioli
CONICET, Consejo Nacional de Investigaciones Científicas y Técnicas, Buenos Aires, Argentina

O. Vaselli
Department of Earth Sciences, University of Florence, Via La Pira, 4, 50121 Florence, Italy

O. Vaselli
Institute of Geosciences and Earth Resources of the National Research Council (CNR-IGG), Via La Pira, 4, 50121 Florence, Italy

Pliocene—Lower Pleistocene (ca. 2 Ma, Muñoz and Stern 1988; Linares et al. 1999; Folguera and Ramos 2000), a volcano-tectonic depression of about 20 × 15 and 0.5 km deep, known as Bajo de Caviahue (Groeber 1921) or Caldera del Agrio (Pesce 1989), was formed. Sruoga and Consoli (2011) excluded the collapse as a process responsible for the depression and recommended to avoid the term "caldera" due to lack of diagnostic evidences able to support of this interpretation. Inside this depression, two units were recognized (Fig. 3.1): trachyandesitic lava flows from "Derrames de Fondo de Valle" (or Trolope Lavas, Melnick et al. 2006) at Trolope and a widely distributed volcanic sequence called Las Mellizas (Pesce 1989). Ignimbrites from Las Mellizas sequence were dated by K-Ar at 0.4 ± 0.3 (Thiele and Pincheira 1987) and 2.6 ± 0.05 Ma (Linares et al. 1999). However, new radiometric ($^{40}Ar/^{39}Ar$) ages determined by Sruoga and Consoli (2011) yielded an age of 125 ka. These discordant ages raise several doubts on the timeline and evolution of the Copahue volcano (Fig. 3.2) and highlight the necessity of a complete stratigraphic revision.

The construction of the volcanic edifice began on the western sector of the depression at about 1.23 Ma ago (Muñoz and Stern 1988; Linares et al. 1999), covering the Las Mellizas Sequence. This area concentrated most of the recent volcanic activity in the CCVC. The volcanic edifice has a NE-SW elongated shape, gentle slopes and low aspect ratio. These morphological features allow to classify Copahue as a shield volcano (Sruoga and Consoli 2011). During its evolution, the emission centers migrated from the main central vent to lateral alignments of vents and fissures, enlightening a strong structural control of the volcanic activity (Folguera and Ramos 2000; Melnick et al. 2006; Sruoga and Consoli 2011). In the summit part of the volcano, nine N60°E-aligned craters were recognized, whereof only the easternmost one, characterized by the presence of an acidic hot crater lake, is currently active.

For a comprehensive study of an active volcano, the knowledge of its eruptive history is of fundamental importance in order to determine: (i) the eruptive mechanism involved and (ii) the current status of activity for monitoring purposes. This chapter shows that the historical eruptions of the Copahue volcano were mostly of low magnitude, phreatic and phreatomagmatic events, except for those occurred in 2000 and 2012 (Caselli et al. Chap. 4 this book), when magmatic pulses mostly strombolian in character were observed. On both occasions, volcanic activity showed a change in the eruptive style with an increase in magnitude and duration as major eruptions were occurring. Since no geochemical and geophysical data were available before 2004, i.e. when the very first types of these studies were performed, there are not enough discriminative tools to distinguish the different cycles among the reported eruptions. The 2012 eruption preceded by signals of magma
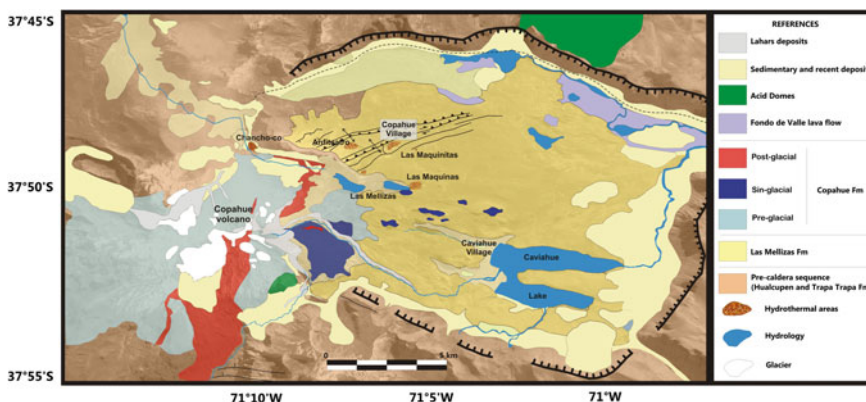
Fig. 3.1 Geological map showing the main litho-stratigraphic units of the CCVC (modified after Melnick et al. 2006)

		Pesce 1989			Delpino and Bermúdez 1993		Melnick et al. 2006		My	Sruoga and Consoli 2011		My
Holocene		3rd Effusive stage	Copahue Volcano		Copahue FM.	Copahue IV Eruptive Stage	Post-glacial	Copahue Volcanic Sequence (CVS)		Copahue FM.	Post-glacial	0.014
											Sin-glacial	
	Effusive Complex Copahue-Caviahue										Pre-glacial	
		2nd Effusive stage	Fondo de Valle flow			Copahue III Eruptive Stage				Las Mellizas FM.	Upper Andesitic Lavas	
			Acid dome				Sin-glacial		< 0.0115		Dacitic and Andesitic Ignimbrite	0.12
				Copahue Group					0.7-0.015		Lower Andesitic Lavas	
		1st. Effusive stage				Copahue II Eruptive Stage	Pre-glacial				?	
Pleistocene			Effusive Center Las Mellizas				Pucon Mahuida Dome		1.10 - 0.90			
						Copahue I eruptive Stage	Trolope Lavas		1.63 - 1.09			
							VS Las Mellizas		2.08 - 2.05?			
					Riscos Bayos				2.68 - 2.64			
Pliocene		Hualcupén FM.			Hualcupén FM.		Cola de Zorro FM.		5.6 - 4.0		Hualcupén FM.	

Fig. 3.2 Comparative chart of the identified litho-stratigraphic units recognized at Copahue

recharging of the plumbing system (as suggested by detected inflation of the volcanic edifice) likely represents the beginning of a new cycle (Caselli et al. Chap. 4 this book).

3.2 Prehistoric Eruptions

The prehistoric eruptions are related to the construction of the volcano edifice and can be divided into three main stages (Melnick et al. 2006): (i) pre-glacial, (ii) sin-glacial and (iii) post-glacial stage (Melnick et al. 2006; Sruoga and Consoli 2011) (Fig. 3.1). The pre-glacial sequence (up to 1,000 m thick) is mostly made up of aphiric lavas and minor pyroclastic flow deposits that form the edifice of the Copahue volcano (Fig. 3.3). These lavas have no significant textural variations and show homogeneous thickness and a basaltic–andesitic to andesitic composition (52.48–61.1 % SiO_2, Cecioni et al. 2000). Sruoga and Consoli (2011) suggested that this sequence was consisting of trachyandesite lavas interbedded with few pyroclastic surge deposits. Radiometric ages indicated that the Copahue edifice was built during Lower Pleistocene times, between 1.23 ± 0.18 and 0.76 ± 0.14 Ma (Muñoz and Stern 1988; Linares et al. 1999, respectively). Welded pyroclastic flow and surge deposits, 18 m width, outcrop on the eastern slope of the volcano (Fig. 3.4a, b). During this stage, when considerable volumes of volcanic
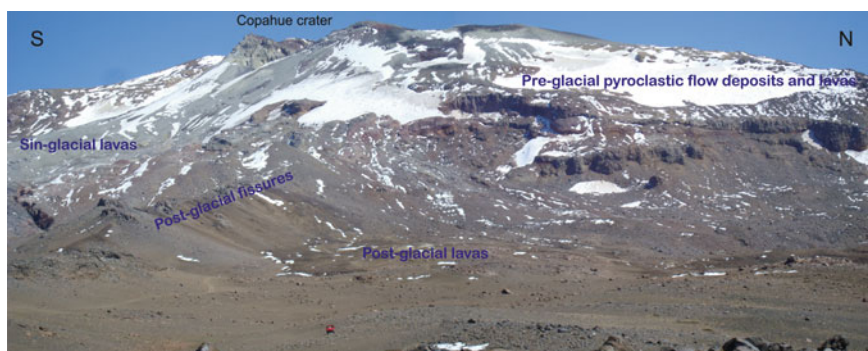
Fig. 3.3 View of the eastern slope of the Copahue volcano. The outcropping lavas and pyroclastic flow deposits belong to the pre-glacial volcanic sequence
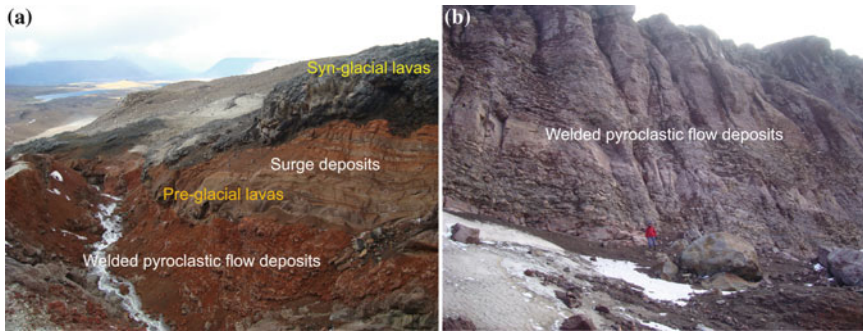
Fig. 3.4 **a** Volcanic sequence on the Agrio River valley showing folded pyroclastic flow and surge deposits belonging to the pre-glacial lavas, underlying the sin-glacial lavas; **b** welded pyroclastic flow deposits on the eastern flank of the Copahue volcano

products were emitted, the cone construction commenced. The volcanic material has striations and polished surfaces due to strong glacial abrasion (Fig. 3.5a, b) and is usually covered by thin drift layers or moraine deposits (Fig. 3.5c).

The main expression of the sin-glacial stage was characterized by the formation of several small eruptive centers aligned along fractures or dykes and randomly distributed in the eastern flank of the volcano (Fig. 3.1). The composition of these lavas ranges between andesitic to dacitic (58.2–63.6 % SiO_2, Cecioni et al. 2000), and they have typical features of magma–water interaction such as polygonal and hackly fractures, glassy margins with pseudo-pillow cracks, and well-developed pillow-lava like structures. Sub-glacial melting-related eruptions are likely the most suitable scenarios to explain the related volcanic products (Fig. 3.6a, b). They were formed during the last glacial period that is well constrained in the Patagonian Andes between 75 and 15 ka (e.g. Lowell et al. 1995).

The post-glacial stage is characterized by: (i) phreato-magmatic explosions with associated pyroclastic flow deposits erupted from the summit aligned craters, and (ii) emissions of relatively low volumes of lavas from summit craters and lateral fissures (Melnick et al. 2006). Sruoga and Consoli (2011) also recognized several lahar deposits related to this activity.

The phreato-magmatic activity is predominantly related to the numerous summit craters of Copahue. From here, pyroclastic flows have spread over the volcano slopes, reaching distances up to 14 km from the active crater and covering an area of about 22 km^2 (Polanco 2003). At least 6 events of pyroclastic flows, identified in a lapse of time between 8.770 and 2.280 years AD, generated deposits less than 2 m thick, matrix-supported and interbedded with fall deposits of lapilli, ash and scorias (Polanco 2003). In the Liay Valley (about 14 km NW from the volcano summit, outside of the caldera), three pyroclastic flow deposits, probably emitted from the western summit craters, occurred and they are interbedded with fluvial conglomerates to form a terrace. Radiocarbon ages of such flows ranged from 2,280 ± 50 to 2,630 ± 80 years BP (Polanco et al. 2000; Polanco 2003). Inside the caldera, Polanco et al. (2000) measured two ^{14}C ages from pyroclastic flow deposits: 8,770 ± 70 and 5,910 ± 50 years BP, probably emitted from the eastern craters. Thin and poorly consolidated pyroclastic surge deposits were recognized on the eastern flank of the eastern active crater, in the upper Agrio River. These deposits are mainly composed of ash and, at lesser extent, lapilli-sized clasts. The post-glacial pyroclastic flow deposits indicate that during the Holocene, the summit craters were intermittently active.

The post-glacial lava flows (Fig. 3.7) are "aa" type and are associated with either lateral fissures of the volcanic cone or temporary centers. The longest flow extends for approximately 20 km along the Lomin River valley in the Chilean territory. Other lava flows branch off the eastern

Fig. 3.5 Evidence of glacial erosion on lavas from the pre-glacial stage: **a** striation **b** polished surfaces, and **c** moraine deposits overlying the pre-glacial lavas

slope, with lengths ranging from 700 m to 3 km (Fig. 3.1). This stage is characterized by the deposition of homogeneous basaltic–andesitic blocky lava flows of uniform composition (54.9–56.9 % SiO_2, Cecioni et al. 2000).

The Copahue eruption rate since its formation age (1.23 Ma), considering a total volume of 375 km^3 of emitted material, was estimated in 0.03 km^3/century (Polanco 2003). According to this author, the eruptive style changed from mainly effusive in the Pliocene time to explosive in the Holocene. From a compositional point of view, the magmas related to the Copahue volcano activity belong to the medium to high K calc-alkaline series (Polanco 2003; Varekamp et al. 2006). Petrographic evidences revealing magmatic disequilibrium yielded Polanco (2003) to suggest that a magma-mixing process strongly affected the geochemical evolution of the Copahue system. A detailed review of petrological features of Copahue volcano is provided by Varekamp et al. (this book).
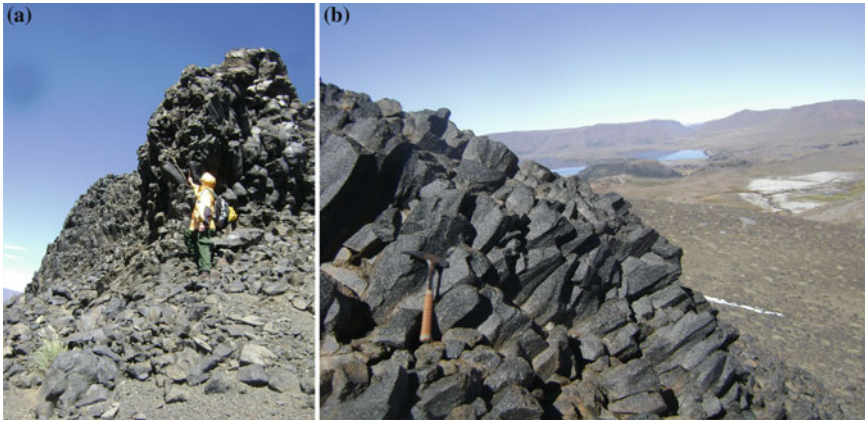
Fig. 3.6 Sin-glacial lavas in the eastern part of the volcano edifice (**a**) and contact with the pre-glacial lavas (**b**)
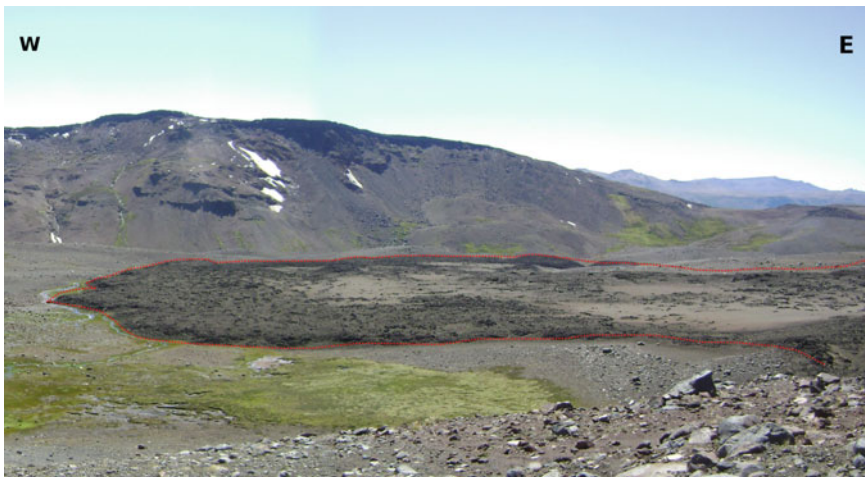
Fig. 3.7 Post-glacial "aa" lavas (*red line*) in the Las Mellizas area, NE of the volcanic edifice

3.3 Historic Eruptions

During the last 260 years, Copahue volcano has experienced at least 11 phreatic and phreato-magmatic eruptive episodes of low magnitude: 1750, 1759, 1867, 1937, 1944, 1960, 1961, 1992, 1993, 1994 and 1995 (Petit-Breuilh 1996; Naranjo and Polanco 2004 and references therein) and two phreato-magmatic to magmatic events of low magnitude in 2000 (Naranjo and Polanco 2004; Varekamp et al. 2001) and 2012 (Caselli et al. Chap. 4 this book).

The most ancient records, reported by Havestadt (1883), date back to 1750 and 1759 and described solfataric activity and a sequence of explosions that culminated with an eruption, which is not supported by any sedimentological description. In 1867 and 1876 eruptions likely occurred although with unknown characteristics (Petit-Breuilh 1996). The presence of a hot crater lake is known at least since 1937. Changes in the water temperatures of the crater-lake were reported until 1960, proving the persistent presence of the lagoon in this period. Herrero Doucloux (1938) pointed out that the
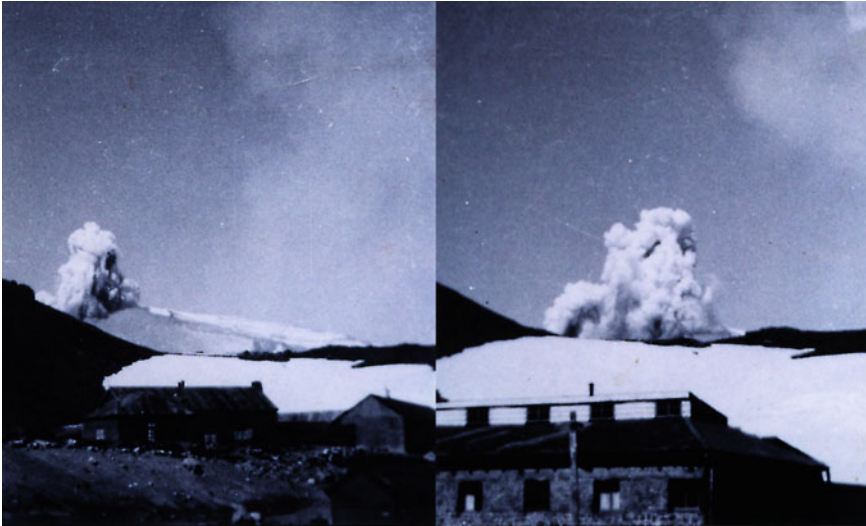
Fig. 3.8 Photographic sequence of one of the phreatic eruptions that occurred in 1960–61 (photos kindly provided by Juan Bravo) viewed from Copahue village

temperature of the lake was ranging between 20 and 25 °C. In 1940, temperature increased and achieved 52 °C along the shore-line and about 100 °C in the central zone (Groeber and Perazo 1941). In June 1944, the water temperature reached 90 °C and the acidity increased while the water level decreased of about 40 m (Casertano 1964). A small eruption occurred afterwards (Siebert and Simkin 2008), as supported by local witnesses. Temperatures started decreasing from 1945.

On December 24th 1960, a series of phreatic eruptions took place (Petit-Breuilh 1996; Siebert and Simkin 2008) and lasted until 1961 (Fig. 3.8). Tales from locals and photographic archives of the explosions allowed to assess the presence of a gas plume and the volcanic activity was centered in the volcanic crater. The 1960 eruption was preceded by the most powerful earthquake ever recorded in the area (known as the "Valdivia earthquake", Mw 9.5) occurred at approximately 200 km southwest of Copahue. The 1960 eruption at Copahue was likely induced by this seismic event, as also occurred in Cordon-Caulle volcanic complex (Watt et al. 2009). Later on, in January and February 1976, temperatures of 37 and 43 °C, respectively, were

measured in the crater lake (Mange 1978), asserting the normal conditions of the system with respect to the previous years.

One of the best-documented eruptions occurred in 1992, with several phreatic and phreato-magmatic explosions (Delpino and Bermudez 1993). A series of phreatic events, reported by Petit-Breuilh (1996) and Martini et al. (1997) took place in 1995. Between July and August 2000, the major and most prolonged eruptive "cycle" of Copahue volcano occurred, leading to the disappearance of the crater-lake (Naranjo and Polanco 2004). While Naranjo and Polanco (2004) identified the 2000 eruption as the beginning of a new cycle, previous works (Delpino and Bermúdez 2002), referred to that event as a prosecution of the cycle started in 1992.

3.3.1   The 1992–1995 Eruptive Activity

The eruption started on July 31, 1992 and was characterized by phreatic and phreato-magmatic activity. Three main eruptive phases were recorded (Delpino and Bermudez 1993). The first phase that lasted for 2 days produced a 300 m

Fig. 3.9 The 1995 phreatic eruption as from the Copahue sky-field (photo by courtesy of Antonio Huglich)

high white plume of steam and volcanic gases and various explosions from the active crater. This activity was accompanied by a strong sulfur smell and the ejection of pyroclastic material.

The second phase started on August 2nd and generated a 1.4 km high eruptive column that was the highest activity of this stage, producing ash-fall on Caviahue village. The tephra material was consisting of volcanic rock fragments (66 % of the total volume), the rest of material being sulfur-rich greenish-gray particles. Lahars, made up of ice, snow and solid fragments, flowed along the Agrio River (Delpino and Bermúdez 1994). Floating spots of oily appearance and brownish-grey color were observed on the surface of the crater-lake, while the water level decreased of several tens of meters. Fumarolic pulses caused vapor and gas clouds, which reached an altitude of 100 m over the crater rim. 6 days later the third phase started with a new explosion, giving rise to a mushroom-shaped plume of about 700 m high. The eruptive column spread tephra up to 20 km away from the crater draping the landscape with pyroclastic material, and triggering lahars up to 4 km length. The minimal estimated volume of the ejected material was 64,000 m^3 (Delpino and Bermudez 1993). According to these authors, the crater lake waters were rough, intense rhythmic fumarolic activity was observed giving rise to white vapor columns up to 50 m height. The 1994 eruption, as well as

that of 1995 (Fig. 3.9), was characterized by the emission of altered rock debris, siliceous dust, pyroclastic sulfur, and rare juvenile fragments (Varekamp et al. 2001; Delpino and Bermúdez 2002). Lahar deposits outcropping in the upper part of Rio Agrio River valley highlighted the occurrence of this kind of events also in the recent days. Lahars were mainly formed by the emission of remarkable amounts of solid fragments mixed with the hot water of the crater-lake. This mechanism was observed during the main explosions recorded between 1992 and 1995, when lahars reached distances of 5–6 km from the crater, but on September 12th 1995 one of the lahars extended up to 8 km along the Rio Agrio River.

3.3.2 The 2000 Eruption

On July 1st a new eruption started. It was characterized by low explosivity phreato-magmatic activity (VEI 1-2) and produced ash deposits that fall up to 50 km far from the volcano, bombs and sulfur fragments (Global Volcano Network 2000a, b). According to Varekamp et al. (2001), ash and gas plumes were detected up to 250 km from the vent. The eruptive process lasted approximately 4 months and, according to the description of Naranjo and Polanco (2004), it could be divided in 5 main stages. A summary of their detailed report is described here below.
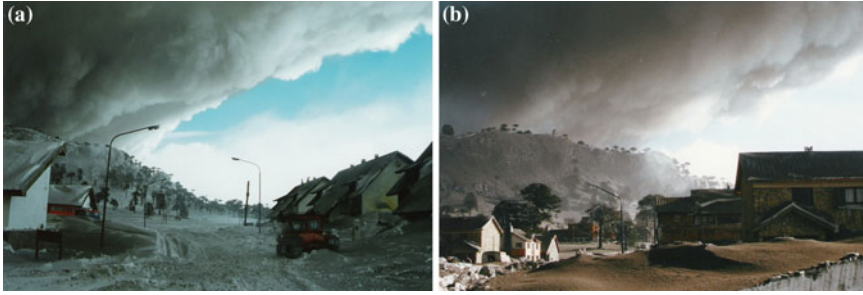
Fig. 3.10 View from Caviahue of the 2000 eruptive plume dropping ash on the village (**a**); ash deposit (*dark layer*) overlying the snow (**b**) (photo by courtesy of Antonio Huglich)

The first stage (1–11 July) was characterized by an intense activity during which phreatic and phreato-magmatic events repeatedly occurred. The opening phase (July 1st) was characterized by a strong sulfur smell followed by the deposition of 1 cm thick ash layer in the villages of Caviahue and Copahue. In the following days steam, ash, lapilli and bombs were ejected along with an eruptive column that reached the height of about 2,000 m. Lake Caviahue, characterized by a pH slightly above 3, increased its acidity (pH = 2.1). On July 3rd, a relatively strong explosion occurred at 16:20 (local time). Ash continued being deposited inside and around the volcano. About 30–40 explosions of decreasing intensity (as indicated by the height of the associated columns) were recorded on July 5th and the first pyroclastic flow was originated. In the Lomin River (10 km SW of Copahue), witnesses reported dead fishes. Lahars occurred in the Rio Agrio, whilst the Rio Dulce that enters Caviahue Lake, lowered its pH down to 2.5.

In the second stage (12–28 July) there was a renewal of sustained explosions and the eruptive column reached up to 3,000 m. Crater explosions continued and on July 12th, ash clouds up to about 500 m were recorded at intervals of 1–3 min. Incandescence in the crater was frequently observed and on July 14th brown-reddish clouds up to 3,000–5,000 m high were observed. On July 17th, the eruptive column reached 1,500 m above the crater and a thin (2 mm) film of ash deposited in the village of Copahue. During this phase, the volcanic plume was mostly dispersed to N, NE and NNE directions (Fig. 3.10a, b). From July

29th to August 8th (third stage) no significant activity was observed in the crater and 5 seismic events were reported on the 4th of August.

The fourth stage (August 9th–September 4th) was characterized by three cycles showing the following sequence of events: (i) explosive activity with relative columns up to 1,500 m high above the crater; (ii) associated seismic swarms which occurring few days later the explosions; (iii) presence of glowing in the crater interior during the following days.

The last phase (September 4th–October 31st) corresponded to a period of clear decrease of the eruptive activity, with scarce explosions and seismic events. In general, ash and steam explosions never exceeded 50–100 m above the crater rim. During October the eruptive died out and the normal fumarolic activity of Copahue volcano was re-established.

3.4 Final Remarks

- Copahue volcano corresponds to the recent expression of a persistent volcanic activity over the past ∼20 million years with a relatively homogeneous composition in this region.
- Although several historical eruptions were reported; however, information about the eruptive style and the related deposits is scarce or even absent.
- According to the best documented eruptive activities of 1992–1995 and 2000, the

behavior of this system consists of phreatic explosions with emission of (i) altered rock fragments, (ii) ash, (iii) important amounts of sulfur, and (iv) some low intensity phreato-magmatic eruptions with the emission of juvenile material.

- Lahars can be considered the most hazardous product of volcanic activity due to (i) velocity, (ii) water availability from crater lake and summit glaciers and (iii) the location of Caviahue village downstream Agrio River.

References

Casertano L (1964) Some reflections on the fumarolic manifestations of the Los Copahues crater. Bull Volcanol 27:197–215

Cecioni A, Alfaro G, Pincheira M, Pineda V, Arce M, Cares R, Reyes M, Valenzuela G, Melnick D (2000) Elaboración de Mapas Zonificados de Peligrosidad Volcánica. INGENDESA S.A. (Unpublished), Universidad de Concepción, pp 250

Delpino D, Bermudez A (1993). La actividad volcánica del volcán Copahue durante 1992. Erupción con emisión de azufre piroclástico. Provincia de Neuquén. In: XII Congreso Geológico Argentino, vol 4, Mendoza, pp 292–301

Delpino D, Bermúdez A (1994) Volcanismo post-glacial en el volcán Copahue (37° 45′ S), sector argentino. Peligros potenciales asociados. In: VII Congreso Geológico Chileno. vol 1, Puerto Varas, pp 260–264

Delpino DH, Bermúdez AM (2002). La erupción del volcán Copahue del año 2000. Impacto social y al medio natural. Provincia del Neuquén. Argentina. In: XV Congreso Geologico Argentino, vol 3, Calafate, pp 365–370

Folguera A, Ramos V (2000) Control estructural del volcán Copahue (38ºS-71ºO): implicancias tectónicas para el arco volcánico cuaternario (36–39º S). Rev Asoc Geol Arg 55(3):229–244

Folguera A, Ramos VA, Melnick D (2003) Recurrencia en el desarrollo de cuencas de intra-arco. Cordillera Neuquina (37°30′). Rev Asoc Geol Arg 58:3–19

Global Volcano Network (2000a) Frequent ash explosions and acidic mudflows starting on July 1. Glob Volcano Netw Bull 25:6

Global Volcano Network (2000b) Continued ash explosions and tremor during August–October. Glob Volcano Netw Bull 25:9

González O, Vergara M (1962) Reconocimiento geológico de la Cordillera de Los Andes entre los paralelos 35 y 38 S. Universidad de Chile, Instituto de Geología, Publicación 24, pp 119

Groeber P (1921) La región de Copahue y su glaciación diluvial. Rev Soc Arg Estudios Geográficos 1:92–110

Groeber P, Perazo R (1941) Captación y aprovechamiento de las aguas y fuentes de Copahue. Ministerio de Agricultura. Dirección de Parques Nacionales. Informe inédito, Buenos Aires

Havestadt B (1883) Chilidugú sive Tractatus Linguae Chilensis. Julio Platzmann, Leipzig

Linares E, Ostera H, Mas L (1999) Cronología potasio-argón del Complejo Efusivo Copahue-Caviahue, provincia de Neuquén. Rev Asoc Geol Arg 54 (3):240–247

Lowell TV, Heusser CJ, Andersen BG, Moreno PI, Hauser A, Heusser LE, Schlüchter C, Marchant DR, Denton GH (1995) Interhemispheric correlation of late pleistocene glacial events. Science 269:1541–1549

Mange J (1978) La laguna del cráter del volcán Copahue (Provincia de Neuquén). Dinámica de su mineralización y relaciones con otras manifestaciones geotérmicas locales. In: VII Congreso Geológico Argentino, vol 2, Neuquén, pp 151–175

Martini M, Bermúdez A, Delpino D, Giannini L (1997) The thermal manifestations of Copahue volcano area, Neuquen. In: VIII Congreso Geologico Chileno, Antofagasta, vol 1, pp 352–356

Melnick D, Folguera A, Ramos VA (2006) Structural control on arc volcanism: The Copahue-Agrio complex, Central to Patagonian Andes transition (38 S). J South Am Earth Sci 22:66–88

Muñoz JB, Stern CR (1988) The Quaternary volcanic belt of the southern continental margin of South America: Transverse structural and petrochemical variations across the segment between 38 °S and 39 °S. J S Am Earth Sci 1(2):147–161

Naranjo JA, Polanco E (2004) The 2000 AD eruption of Copahue Volcano, Southern Andes. Rev Geol Chile 31:279–292

Pesce A (1989) Evolución volcano-tectónica del complejo efusivo Copahue-Caviahue y su modelo geotérmico preliminar. Rev Asoc Geol Arg 44(1–4):307–327

Petit-Breuilh ME (1996) Cronología eruptiva histórica de los volcanes Planchón-Peteróa y Copahue, Andes del sur. Proyecto de Riesgo volcánico. Servicio Nacional de Geología y Minería, 45 p. Santiago, Chile

Polanco E (2003) Evolución del volcán Copahue (37 45'S), Andes del Sur. Tesis de Maestría (Unpublished), Instituto de Geofísica, Universidad Autónoma de México, México, p 90

Polanco E, Naranjo JA, Young S, Moreno H (2000) Volcanismo Explosivo Holoceno en la cuenca del alto Bio-Bio, Andes del Sur (37 45′–38 30′ S). IX Congreso Geológico Chileno, Puerto Varas, Chile 2:59–61

Sepúlveda ME (2004). La historia eruptiva de los volcanes hispanoamericanos (siglos XVI al XX). Servicio de Publicaciones del Exmo. Cabildo Insular de Lanzarote-Casa de los volcanes, pp 431

Siebert L, Simkin T (2008) Volcanoes of the world: an illustrated catalog of 691 Holocene volcanoes and their eruptions. Smithsonian institution, Global 692 volcanism program digital information series, GVP-3

Sruoga P, Consoli V (2011) Volcán Copahue. Relatorio Congreso Geológico Argentino, Neuquen

Thiele R, Pincheira M (1987) Tectonica transpresiva y movimiento de desgarre en el segmento Sur de la zona de falla Atacama Chile. Rev geol. Chile 31:77–94

Varekamp JC, Ouimette AP, Herman SW, Bermúdez A, Delpino D (2001) Hydrothermal element fluxes from Copahue, Argentina: a "beehive" volcano in turmoil. Geology 29:1059–1062

Varekamp JC, Maarten deMoor J, Merrill M, Colvin A, Goss A, Vroon P, Hilton D (2006) Geochemistry and isotopic characteristics of Caviahue-Copahue volcanic complex, Province of Neuquen, Argentina. En Kay S, y Ramos A (eds) Evolution of an Andean margin: a tectonic and magmatic view from the Andes to the Neuquen Basin (35º–39ºS lat): Geol Soc Am Special Paper 407:317–342

Watt S, Pyle D, Mather T (2009) The influence of great earthquakes on volcanic eruption rate along the Chilean subduction zone. Earth Planet Sci Lett 277:399–407

The 2012 Eruption

4

A. Caselli, M. Agusto, M.L. Velez, P. Forte, C. Bengoa,
R. Daga, J.M. Albite and B. Capaccioni

Abstract

This contribution is a detailed description of the precursory activity and the eruptive events that took place during July and December 2012 at Copahue volcano, based on field observations and geophysical and geochemical monitoring. After the Mw 8.8 Chilean earthquake on February 27th 2010, several signals of anomalous behavior were detected at Copahue, revealing the instability of the volcanic system. Starting from July 2012 a phreatic activity occurred with emission of a low amount of material mainly constituted by rocks from the volcanic conduit and sediments from the bottom of the crater lake. Seismic activity and degassing continued until December 22nd when the eruption started with an opening phreatic event that rapidly evolved to a phreatomagmatic, and finally a magmatic eruption.

A. Caselli (✉)
LESVA, IIPG, Universidad Nacional de Río Negro,
Roca 1242, 8332 General Roca, Argentina
e-mail: atcaselli@unrn.edu.ar

M. Agusto · M.L. Velez · P. Forte · C. Bengoa ·
J.M. Albite
GESVA-IDEAN, Dpto. Cs. Geológicas, FCEN,
Universidad de Buenos Aires, Ciudad Universitaria,
Pab.2, 1428 Buenos Aires, Argentina

M. Agusto · M.L. Velez · R. Daga · J.M. Albite
CONICET, Consejo Nacional de Investigaciones
Científicas y Tecnológicas, Buenos Aires, Argentina

B. Capaccioni
Department of Biology, Geology and Environmental
Sciences, Piazza Porta San Donato, 1, 40126
Bologna, Italy

R. Daga
Laboratorio de Análisis por Activación Neutrónica,
Centro Atómico Bariloche, CNEA, Av. Bustillo km
9.5, 8400 Bariloche, Argentina

4.1 Introduction

A new eruptive cycle started at Copahue volcano on 2012 after 12 years of quiescence. The previous eruption, on July 2000, involved the emission of ash, gases and volcanic bombs and it is considered the most important activity of the last 60 years (Naranjo and Polanco 2004). A detailed description of historic activity including the 2000 eruption is shown in Caselli et al. (Chap. 3, this book). This event was followed by several years of relatively constant activity characterized by continuous slow degassing. The explosive event on December 22nd 2012 was similar to the 2000 one, despite it was shorter and less material was emitted. Overall, the 2012 eruptive activity was characterized by short duration and low explosivity index (VEI 2).

Since 2004, Copahue volcano has been studied simultaneously from seismology, surface deformation and fluids geochemistry (fumarolic gases and thermal springs) in order to characterize the volcanic hydrothermal system and to establish a baseline behavior for future monitoring purposes (Caselli et al. 2005; Ibañez et al. 2008; Velez et al. 2011; Agusto et al. 2012, 2013).

After Maule earthquake occurred in Chile on February 27th 2010 (Mw 8.8), significant changes were registered in the seismic activity at Copahue volcano, with increasing high and low frequency signals (Bengoa et al. 2010; Forte et al. 2012). However, it was by the end of 2011 that major evidences where reported mainly related with an increase in the rate of fluid discharge from the Copahue summit and the formation of a column of vapour and acidic gases between 200 and 300 m height. A progressive increase in seismic signals, surface uplift deformation, diffuse acid steaming from the crater lake and variations in its physico-chemical parameters (temperature, pH and composition) were also registered. These signals were the evidence of the ongoing unrest of the volcanic system, which finally led to a series of phreatic and phreatomagmatic events on July 2012 and the phreatomagmatic–magmatic eruption on December 22nd 2012.

In this chapter, geochemical and geophysical data from the inter-eruptive period between the 2000 and 2012 eruptions are summarized. A detailed chronologically description of the 2012 eruptive activity and the preceding phenomena are given, including field observations and geophysical and geochemical studies. Geophysical information includes geodetic and seismological data. A brief description of surface deformation between 2002 and the 2012 is given throughout the chapter (for further details see Velez et al. this book). Seismological data incorporates information from the Chilean Volcano Observatory of the Southern Andes (OVDAS-SERNAGEOMIN), the Argentinean National Institute of Seismic Prevention (IN-PRES), and our seismic array installed near the Caviahue town.

4.2 Studies Between 2004 and 2010 (Inter-eruptive Period)

The Copahue-Caviahue region (Fig. 4.1) is characterized by a well developed magmatic-hydrothermal system whose most significant surface manifestations are related with the Copahue volcano edifice and involve: an acidic crater lake (pH 0.3 to 0.8, temperature 30–40 °C) and acidic hot springs on the eastern flank (pH 1–2 and temperatures between 60–70 °C) (Varekamp et al. 2001, 2009; Caselli et al. 2005; Agusto et al. 2012). Five geothermal areas (Fig. 4.1) are also recognized surrounding the volcano edifice with fumaroles and boiling pools (detailed geochemical information of the geothermal system is available in Agusto et al. 2013, and this book). During the 2000 eruption, the crater lake disappeared however the hydrothermal system keep flowing from the eastern springs during the entire eruptive period. After the eruption, the crater lake was renewed and completely stabilized during 2002–2003 (Varekamp et al. 2001, 2009).

Geochemical studies performed between 2004 and 2012 were mostly focused on the hyper-acidic waters of the volcano edifice. During May 2004, crater lake showed gray-green color with sulfur patches floating on its surface and low temperatures (13.5 °C). By July 2004, about 80 % of the lake surface was frozen, while hot springs displayed the highest temperatures up to 81 °C (Agusto et al. 2012, and this book). A decrease in total anion content was registered in both the crater lake water and the southern spring, while increased values were observed for the northern spring and Agrio river (Fig. 4.1). Saturation index from the lake waters suggests an increase in the deposition of gypsum, quartz, cristobalite and amorphous silica (Fazio et al. 2008).

An analysis of the seismic data recorded using three small-aperture seismic arrays between 2003 and 2010 (Ibañez et al. 2008; Bengoa et al. 2010) identified both volcanotectonic (VT) and long period events (tremor). Local VT events presented clear P and S wave arrivals, frequencies
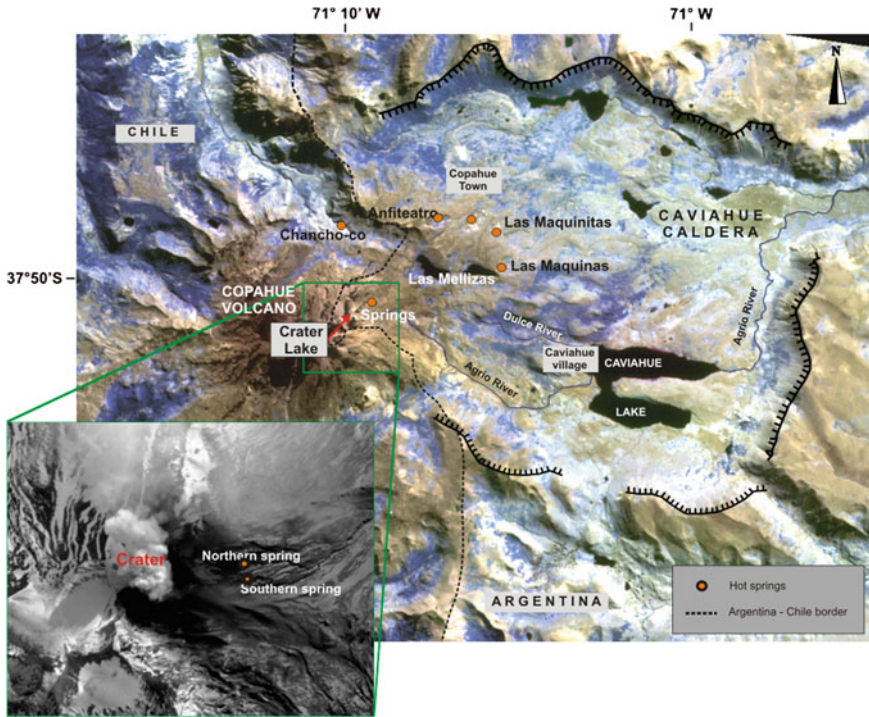
Fig. 4.1 Location map of the Copahue Caviahue Volcanic Complex showing the main features of the volcanic-hydrothermal system. Detailed image showing the summit area of Copahue volcano edifice: an emission column from the crater and the springs on the eastern flank

spectral content between 1 and 16 Hz and were related to brittle fractures. They concentrated near Caviahue village (63 events), most of them with focal depth less than 3 km and possibly related to fault system inside the caldera. Part of this VT activity occurred as a seismic swarm (24 low magnitude events) between January 22nd and 24th 2004 (Ibañez et al. 2008). Long period events had spectral energies concentrated at frequencies between 1–2 Hz, and array solutions showed a predominant slowness vector pointing to the geothermal field located about 6 km north of the array site (Ibañez et al. 2008).

Surface deformation between 2002 and 2007 was measured from Envisat images applying differential interferometry (DInSAR) technique (Velez et al. 2011). Results showed an area of deflation coincident with the volcanic edifice. According to temporal series, this phenomenon would have started in early 2004 at a mean deformation rate of almost 2 cm/year, and

continued with constant rate until 2007. Subsidence extended northward covering the geothermal areas with a deformation rate of 0.5 cm/year. Decomposition of displacements considering the ascending and descending passes for the same period confirmed a main vertical component of the deformation field. Inverse analytical models were applied in order to characterize the source of deformation. Best results were achieved for an ellipsoidal oblate source located at approximately 4 km beneath the volcanic edifice that suffers a volume change of -0.001 km^3/year during the time period under analysis (Velez et al. 2011, and this book).

During the following years (2005–2010) the crater lake had no significant change in temperature (30–40 °C) and volume, while the outlet temperature of the two hot springs dropped to a its usual value, between 40 and 60 °C. On the other hand, anions related to the dissolution of magmatic gases progressively increased

especially for crater lake waters (Agusto 2012, and this book). No significant changes were registered in seismic activity and there is no available information of the surface deformation between 2008 and 2010.

4.3 The 2012 Eruptive Event

4.3.1 Precursory Signals

After the Mw 8.8 Chilean earthquake on February 27th 2010, the number of local VT events at Copahue zone increased significantly up to 70 events per day. During the first week, around 180 VT earthquakes were identified. This number of events is equivalent to the total activity for the entire period 2003–2010. The amount of events slowly decreased throughout April. Low frequency seismic signals registered between May and August 2010, showed a change in back azimuth directions from those reported by Ibañez et al. (2008) from a north direction attributed to the geothermal areas to a northwest direction. According to Forte et al. (2012) this change could be associated with variations in the dynamics of the volcanic-hydrothermal system. There is a gap in seismic data from August 2010 due to registration problems of our seismic array. However, no significant information was reported by the Argentinean and Chilean Institutes.

On December 1st 2011, an increase in the number of seismic events was observed according to INPRES reports (INPRES, Araujo, personal communication). Simultaneously, a gradual increase in gas emission rates from the crater lake was recorded. A diffuse, visible steaming from the lake surface started. Effects of eyes and respiratory tract irritation suggest the presence of very acidic species (HCl, HF and SO_2). Diffuse steaming increased significantly on 2012 almost completely concealing the lake surface. Despite the intense steaming, on March 2012, according to a visual estimation, the crater lake did not showed a significant volume change. A complete geochemical sampling of crater lake and springs was performed, verifying an increase of water acidity (pH near 0) and temperature up to about 60 °C, as well as a significant increase in acidic species concentrations (SO_4^{2-}, Cl^-, F^-) (Agusto et al. this book). Usually, HCl and HF degassing can be promoted by lowering pH to values of 0 to 1 due to input of SO_2 followed by its disproportionation to H_2SO_4 and H_2S.

Ground deformation studies performed between 2011 and 2012 by DInSAR technique using Envisat Asar radar images revealed an uplift process. The identified inflation area is coincident with the volcano edifice and with the location of the deflation pattern detected during the 2002–2007 period. The uplift had possibly begun before August 2011, however a constant increasing rate is observed from October 2011 and remained constant until the beginning of 2012 (Velez et al. this book). From October 2011 until April 2012 inflation of 5 cm was observed. After April 2012 Envisat satellite was out of operation and Cosmo-Skymed images were used to evaluate surface deformation (Velez et al. this book).

4.3.2 Phreatic Events of July 2012

A small scale phreatic explosion throwing water and mud from the crater lake bottom up to 10 m high forming a cock's tail jet that was photographed on July 17th 2012 (Fig. 4.2a). Slurry filled vent masses were injected into the bottom of the crater lake and observed at the surface as burbles. On July 19th, a phreatomagmatic eruption emitted pyroclastic material and produced a small plume with E-SE direction of approximately 18 km length. Few blocks up to 20 cm in diameter were observed near the crater, most of them showing signs of the presence of liquid sulfur (Fig. 4.2b), a feature that was also observed in material ejected during the eruptions occurred in 1992 and 200. The presence of liquid sulfur in the blocks described, confirms high concentrations of molten sulfur in the volcano conduits and the existence of a sulfur pool.
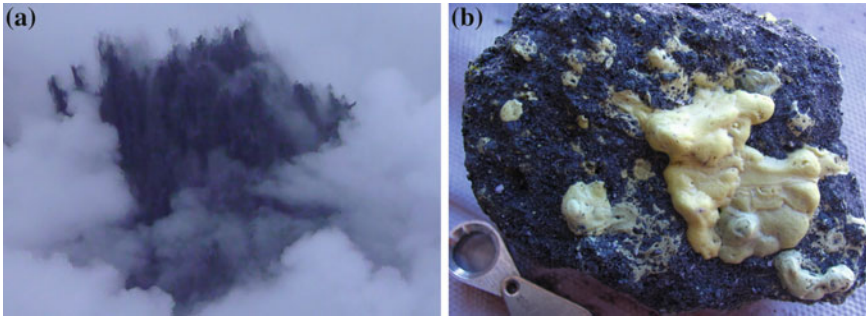
Fig. 4.2 a Phreatic explosion registered on July 17th 2012 at Copahue crater lake. Photograph from Nicolas Sieburger; **b** Pyroclastic material ejected during July 19th phreatic event, with evidences of liquid sulfur

Samples collected from the deposits on the crater rim, are composed of sulfur particles, shattered vitreous, pumice fragments, scoriaceous fragments and irregular fragments of white 'clay', accessorial and/or accidental fragments. A detailed description of the material emitted is available on Sect. 3.4.

Since May 2012, the Volcano Observatory of the Southern Andes (OVDAS -SERNAGEO-MIN) monitored the seismic activity at Copahue volcano. Between May and June, a stable behavior with moderate seismic activity characterized by the occurrence of volcano-tectonic (VT) and long period (LP) events, was reported (RAV N° 7 and 9—available on www.sernageomin.com.cl). During July, seismicity continued showing similar levels except for an increase registered on July 17th and 19th, which could be associated with the phreatic and phreatomagmatic explosions described above. For these days, seismic signals associated with fluid circulation (tremors) at the volcano were recorded with reduced displacements (DR) of 77.2 and 147.5 cm^2 (RAV N° 10).

Fumarolic activity and cyclic bubbling continued for several months, from two close vents observed at the crater (Fig. 4.3). A significant decrease in crater lake water level (about 20 m) was also reported. Continuous fumarolic activity with larger vapor columns every 1–2 min, exceeding the crater rim by about 200–300 m in height on the SW side of the crater lake. On July 26th, crater lake temperatures were measured at about 60 °C near the coast-line, low pH and high conductivity were also registered (Agusto et al. this book). The surface of the crater lake remained occasionally completely hidden by gas and steam clouds. The appearance of yellow sulfur spherules floating on the lake surface was reported in several days, being then deposited at the lake shore.

According to INPRES reports, VT earthquakes showed a small increment in the number of events for the period August–November 2012. Until mid-October the activity was stable, with less than 15 events per day except on August 26th, when a seismic swarm occurred (38 events). In the second half of October 184 VT events were recorded in 2 days (24th and 26th). After that, the level decreased to 10 events per day, weakly increasing again up to 20 events per day during the first days of November. The activity remained relatively stable at that level for the rest of that month. In the same period, also OVDAS-SERNAGEOMIN reported moderate activity, describing the occurrence of VT and low-frequency events. We recorded seismic data for the period August–October 2012 that include VT earthquakes, tremor displaying a variety of waveforms, LP and hybrid signals. Seismicity was dominated by a mix of VT and tremor events including a harmonic tremor episode lasting 5 h on August 5th. During December, INPRES data showed similar levels (number and magnitude of events) to those describe for previous months with 2 peaks occurring on the 9th and 16th, when a total of 51 and 39 events were recorded,

Fig. 4.3 Emission area on the southwest side of the crater lake (*right*) Bubbling of slurry filled vent masses from the emission point mission point

respectively. After this, a gradual decrease was registered until December 20th (only 1 VT was recorded). On December 21st a small increase in activity was reported, although it was not significant and remained below the average activity of the month. Finally, on December 22nd no VT events were registered, at least until the onset of the eruption.

DInSAR processing of Cosmo-Skymed radar images revealed that the uplift of about 2 cm per month registered between October 2011 and April 2012 continued with constant rate throughout 2012 (Velez et al. this book).

4.3.3 The Eruption of December 22nd

The eruptive activity began at 12:05 (GMT) on December 22nd with the emission of an 800 m high white colored vapor column that bent to the SE by wind (Fig. 4.4a). Several minutes later, the vapor column acquired a white-yellow color.

Initially, the eruptive column was sustained by a series of phreatic explosions which continues until the complete disappearance of the crater lake (by evaporation and possible partly emitted as liquid water in the eruptive plume). It is possible that after the disappearance of the lake, sulfur particles and sediments from the bottom of the crater were emitted, providing the yellow color of the plume. During that morning, a sudden increase in the seismic events was recorded by the OVDAS-SERNAGEOMIN. It was characterized by tremor signals with low frequency (around 0.35 and 1.9 Hz), which reached values of reduced displacement (DR) of 49 cm^2. These facts prompted the authorities to declare orange alert level (REAV N° 16).

At 12:48 (GMT) a dark grey color plume was observed (Fig. 4.4b) with the ballistic ejection of incandescent material forming cock's tail jets, as a result of water-magma interaction (hydromagmatic phase). A moderately convective grey and white colored plume with pyroclastic material
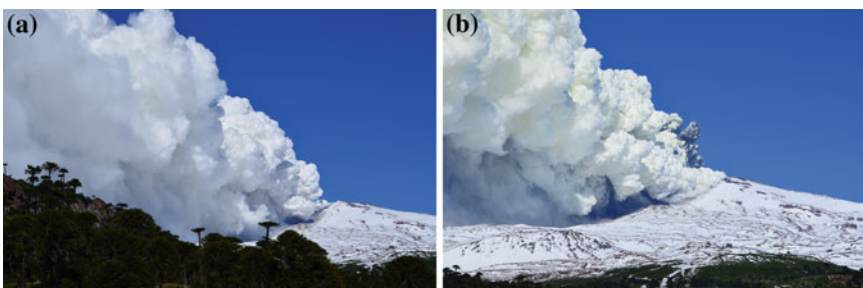
Fig. 4.4 **a** *White* colored vapor column of about 800 m produced at the beginning of the eruptive event on December 22nd 2012, reclined to the SE by wind; **b** *Dark grey* color plume observed during the initial phreatomagmatic phase. Photographs: Nicolas Elguero

was observed from this moment, reaching a height of approximately 3000 m (Fig. 4.5a). Subsequently, the column turned to grey, emitting incandescent pyroclastic material in a ballistic projection (Fig. 4.5b). The material from this plume was deposited by fallout on the SE flank of the volcano and following a SE direction reaching 320 km length (covering an area of about 8700 km^2, Fig. 4.6) Several pyroclastic flows were observed descending from the crater vertex ("V" shaped lower sector of crater rim) flowing down the valley of the Agrio river (Fig. 4.7). Moreover, small explosions of vapor similar to geysers were emitted from the eastern springs.

At 18:30 (GMT) the emission of convective, incandescent dark-grey clouds ejection of pyroclastic material were reported from the crater (Fig. 4.8a). Since 19:00 (GMT) the tremor signals started to decrease their energy, stabilizing at values of 12 cm^2 (REAV N°17). At night time, ballistic projections of juvenile incandescent material were observed (Fig. 4.8b) being responsible of impact craters at distances up to 1 km from vent. A harmonic tremor signal with

duration of 5 min and explosions were also reported. These variations in the evolution of the eruptive process led the authorities to raise the alert level to red (REAV No. 18).

On December 23rd afternoon, seismic activity began to decline and the eruptive process gradually decreases in intensity, although an important plume of vapor and gases still continued with intermittent explosions involving juvenile material. During the following days, December 24th and 25th, the eruptive process could not be observed due to adverse meteorological conditions. On December 26th, a significant gas emission was still detected and incandescence was observed during night time.

On December 30th, during a hike to the crater from the eastern flank, a large quantity of pyroclasts, scoria fragments, blocks and bombs of different sizes and impact craters were recognized (detailed description in Sect. 3.4). A particular feature was the presence of conduit rocks with globular sulfur (Fig. 4.9). Liquid sulfur would probably be present in the fractures or porosity of conduit rocks which, after being ejected would escape to block surface as globules, due to
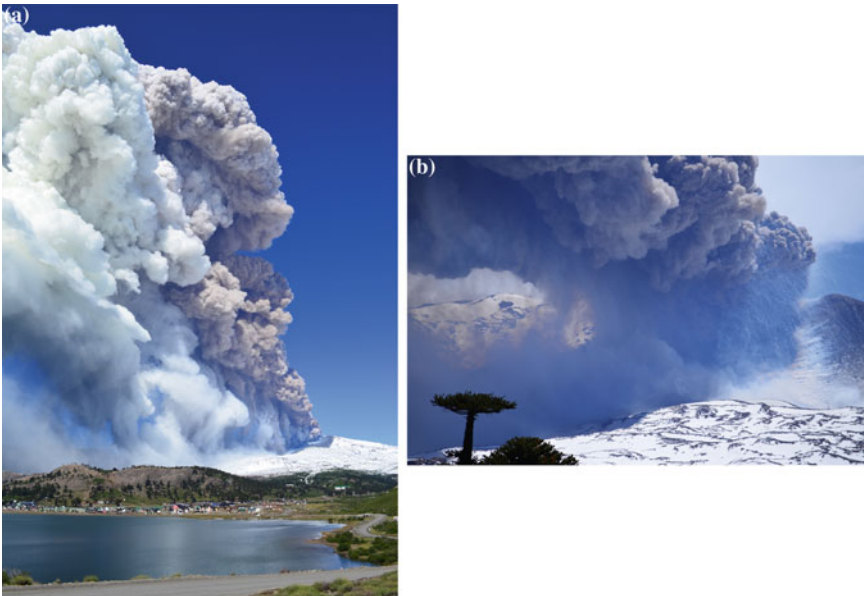
Fig. 4.5 **a** *Grey* and *white* colored convective eruptive column reaching approximately 3000 m high; **b** *Grey* color column emitting incandescent pyroclastic material in a ballistic projection. Photographs: Nicolas Elguero
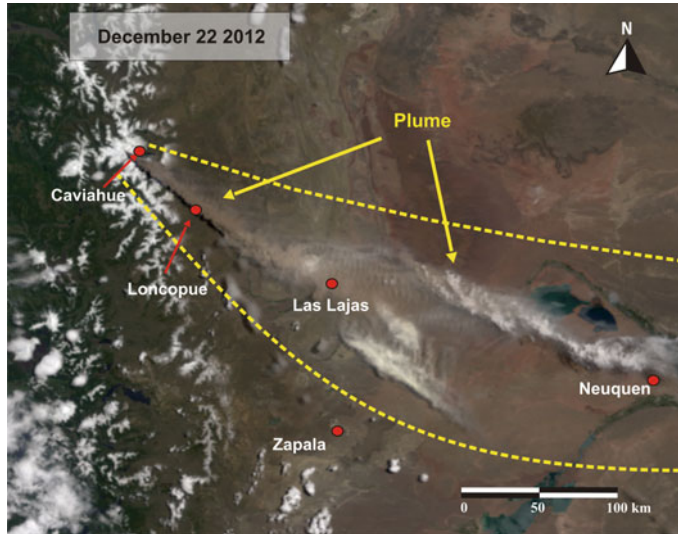
Fig. 4.6 Emission plumes during the December 22nd eruptive event, showing a white colored plume corresponding to the first pulse at a distance between about 300 and 600 km from the active center, and the current emission characterized by a grey colored plume with about 60 km length

Fig. 4.7 Pyroclastic flow observed descending from the crater vertex ("V" shaped lower sector of crater rim) to the valley of the Agrio river. Photograph: Pablo Pantiga

decompression and the consequent quenching process as observed in material ejected by Ruapehu volcano (Christenson et al. 2010). Some of these fragments showed pyroclasts of juvenile material attached, which could be evidence of a plastic state of sulfur during deposition. Hot springs on the eastern flank were completely covered by deposits from pyroclastic flows and fall and possible landslides from the eastern flank.

Inside the crater, the disappearance of the lake was confirmed and explosion craters with emission of dense fumaroles were reported (Fig. 4.10). Fractures were observed both inside the crater and on the eastern flank with fumaroles and sulfur deposits. Temperatures between 180 and 220 °C were measured using a digital thermometer in one of the fumaroles from the crater rim, while the crater floor temperature was about 420 °C (Agusto et al. 2013). Fumaroles from the crater showed emission of yellow color gases related with sulfur and bluish grey color gases (associated with SO_2 and water vapor). During
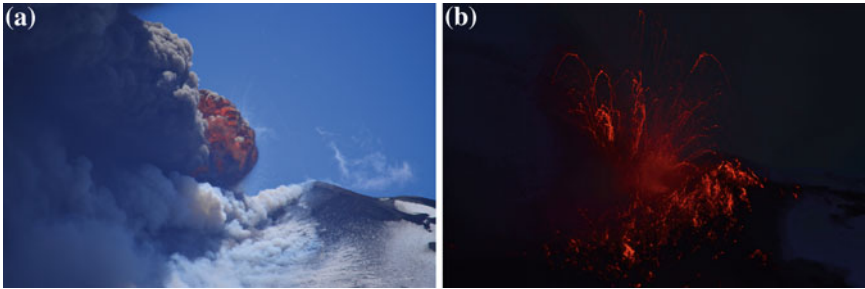
Fig. 4.8 a Convective incandescent *dark-grey* clouds observed from the crater resulted from a mixed between incandescent pyroclastic material and burned gases; **b** Ballistic projection of juvenile incandescent material observed at night time. Photographs: Nicolas Elguero
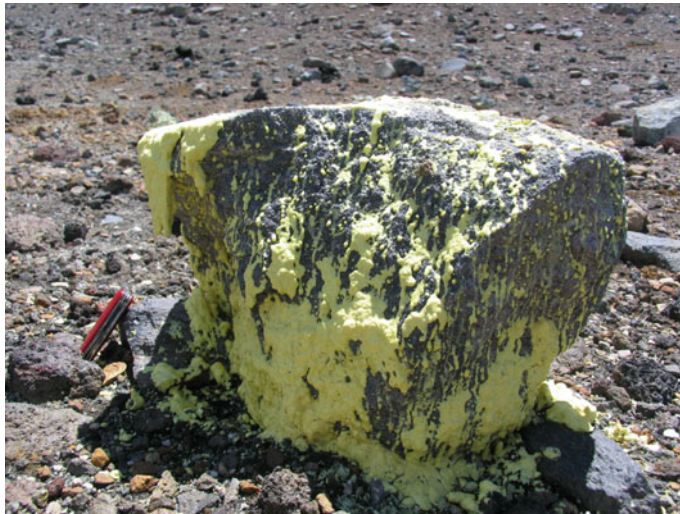
Fig. 4.9 Pyroclastic block with evidence of liquid sulfur ejected during December 22nd 2012

the days of increased seismic activity, reddish flames from the fumaroles (associated with gas combustion) and mud geysers were observed.

4.4 Description of Material Ejected During the Eruption

4.4.1 Phreatomagmatic Events of July 2012

Samples obtained from the 19th July, 2012 eruptive event corresponds to a coarse ash fraction (0.062–2 mm) composed of sulfur particles (23 %), glass shards (21 %), scoriaceous fragments (4 %), abundant whitish irregular argillaceous fragments (19 %), and an important proportion of lithics, crystals and crystal fragments (33 %). The coarser population in the coarse ash fraction mostly consists of sulfur particles, which provide a general greenish aspect to the sample. Such particles, indeed, form more than 70 % of components between 0.5–2 mm grain sized. Argillaceous fragments, lithics, and crystals, even high in proportion, are concentrated in the smaller grains sizes of the coarse ash fraction.

Fig. 4.10 Photograph from December 30th 2012 showing the crater situation after the eruption. Fumaroles exposed without crater lake

Sulfur particles are the most abundant particles in the deposit, with a particular greenish color (with slight variations between yellowish green and grayish green) and variable size from less than 0.5 up to 3–4 mm. They also show distinctive morphologies, as globular or spherical with inner vesicles, like more or less deformed 'droplets', or elongated shapes (Fig. 4.11a, b), resembling particles erupted as melted material. This kind of fragments would have been also generated in previous eruptions of Copahue volcano, particularly during 1993, 1995, and 2000 eruptive events. Even though these materials are not so frequently found in volcanic systems, its morphology resembles the dark and markedly vesicular pyroclastic sulfur ejected during phreatic bursts in Poás volcano in 1970s (Oppenheimer 1992), but different to the euhedral orthorhombic sulfur crystals erupted during the construction of small sulfur cones in 1990 in the same volcano (Oppenheimer 1992). In addition, a myriad of small sulfur spheres were described on Poás volcano in 1978, formed by the interaction of molten sulfur with water from crater lake (Francis et al. 1980). If these particles are observed in detail, under scanning electron microscope, the external surface of these particles, which seem to be expelled as molten material, shows the formation of numerous small crystals, approximately up to 30 μm in size (Fig. 4.11c–h).

Different kind of glassy particles were identified, mainly due to the presence and variation in size and shape of vesicles, as highly vesicular, plate-like, cuspate and Y-shaped, and massive blocky glass shards (Fig. 4.12). It is possible to observe vesicular and fluidal textures, brown color and vitreous luster in these particles (Fig. 4.12a, b). Vesicular particles are sub-rounded to highly irregular, depending on vesicle shape and size, generally with moderate-high vesicularity degree, and domain of spheric-subspheric vesicles varying between micrometers to millimeters in size (Fig. 4.12c). The irregular concave-convex edges correspond to wall bubbles, which become thinner as the particle vesicularity increases. Fragments irregularly shaped are given by tortuous vesicles, due to the bubble coalescence. Fluidal textures are given by dominant elongated vesicles, with moderate-high vesicularity degree, with tortuous shapes in some cases too. Tubular vesicles form straight edged particles, conferring blocky shapes to the fragments (Fig. 4.12d). Plate-like, cuspate, Y-shaped, and blocky shards are brown colored and irregularly shaped (Fig. 4.12e, f). In finer grain size fraction these particles are light colored and translucent.
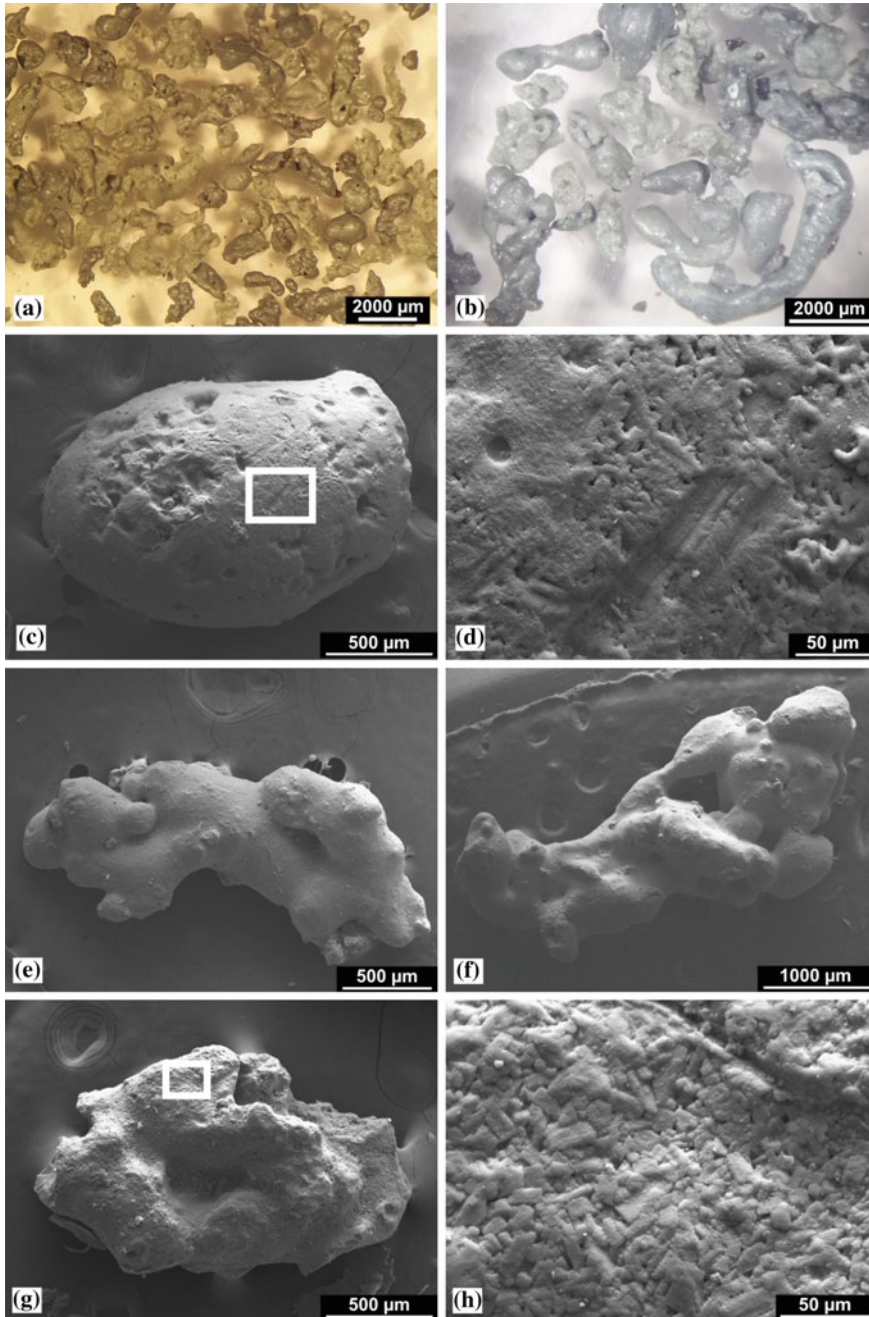
Fig. 4.11 Pyroclastic sulphur particles from July 2012 eruption, collected near volcano Copahue; **a** Sulphur particles isolated from the ejected tephra, where it is possible to observe the distinctive morphologies and the slight color variation between *yellowish green* and *grayish green*; **b** more detail of the same sulphur particles showing the irregular shapes and fragments inner vesicularity, some spherical or drop-like shapes, resembling particles ejected as molten material; **c**, **d** sub-spherical sulphur particle with irregular surface, and surface detail showing the small crystals forming the fragment; **e**, **f** highly irregular sulphur particles with sub-rounded surfaces; they seem to be formed by the joint of smaller fragments still during plastic/semi-molted state; **g**, **h** irregular sulphur particle and surface detail showing the small crystals forming the fragment, as in **d**. **a**, **b** Photographs under binocular magnifying glass; **c–h** Images from Scanning Electron Microscope (SEM, Grupo de Caracterización de Materiales, Centro Atómico Bariloche)
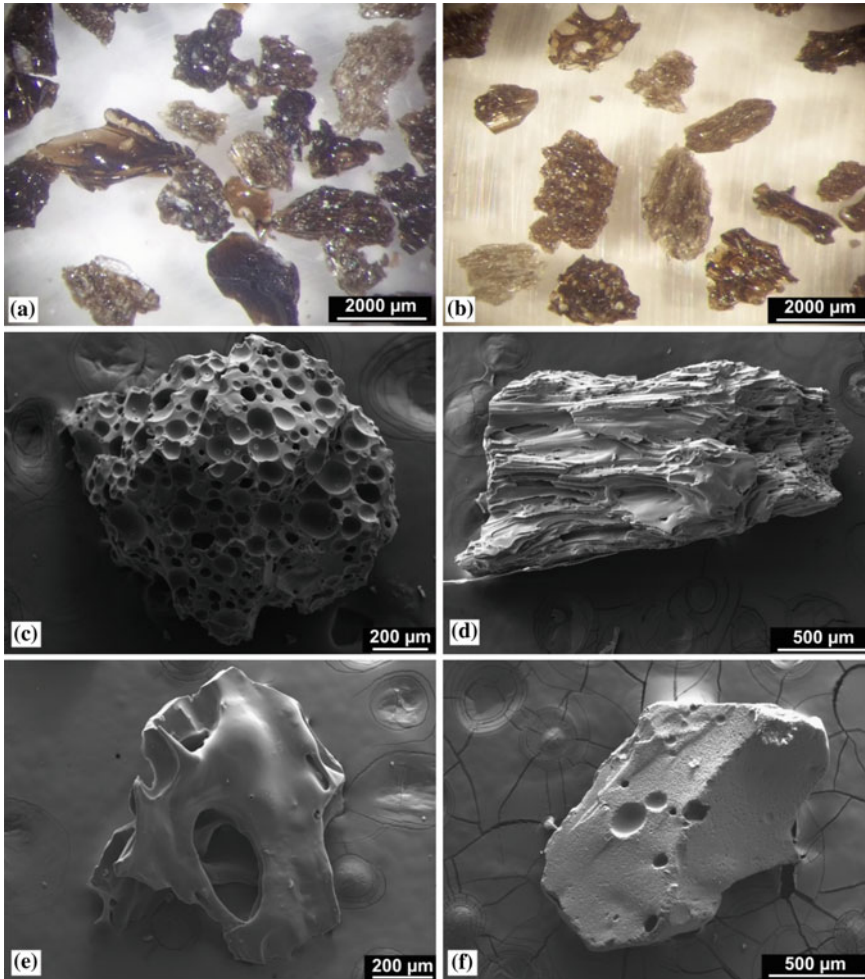
Fig. 4.12 Glass shards from July 2012 eruption, collected near volcano Copahue; **a**, **b** Photographs under binocular magnifying glass of glass shards isolated from the ejected tephra; different shard morphologies, *brown color*, and vitreous luster are observed; **c–f** Images from Scanning Electron Microscope (SEM, Grupo de Caracterización de Materiales, Centro Atómico Bariloche) of glass shards of variable shapes: moderately vesicular, fluidal with elongated and tortuous vesicles, Y-shaped edges, and blocky with low vesicularity glass shards, respectively

Scoria particles: they are found in low proportion relative to sulfur and glassy particles. The dark scoriaceous fragments have irregular to subrounded shapes, with smooth and irregular surface, metallic luster in some cases, and moderate-low vesicularity degree with subspherical vesicles of variable size. Low vesicular fragments have block shape, with wall bubbles determining the borders, while moderate vesicular fragments have subrounded morphologies.

4.4.2 The Eruption of December 22nd

The material emitted was sampled 1.0 km northeastwards from the eruptive center consisting in basaltic-andesitic volcanic bombs (Fig. 4.13) and the highly vesiculated volcanic fragments with identical composition, i.e. similar to that of products from the 2000 eruption (Delpino and Bermudez 2002) and the post-glacial lavas.

Fig. 4.13 Pyroclastic bomb on the eastern flank at a distance of about 500 m from the crater

Table 4.1 Geochemistry of major elements (% wt) of the two samples analyzed

Sample	SiO$_2$	TiO$_2$	Al$_2$O$_3$	Fe$_2$O$_3$	MnO	MgO	CaO	Na$_2$O	K$_2$O	P$_2$O$_5$
BM1212	54.95	1.19	16.87	9.18	0.145	4.37	7.65	3.52	1.84	0.281
P1212	54.22	1.09	17.85	8.41	0.134	4.1	7.97	3.56	1.67	0.262

The basaltic-andesitic volcanic bombs (BM 1212; 54.95 % SiO$_2$, Table 4.1) have elongated shapes with moderate vesicularity in the outer crust. Microscopically they are characterized by a porphyritic texture that turns to glomeroporphyritic by sectors (Fig. 4.14).

Dark brown highly vesiculated fragments (P 1212) are flat and reach up to 5 cm length. They are characterized by its light weight and floatability. Under the microscope, these fragments showed porphyritic texture, where phenocrysts represent less than 1 % and consist of andesine (90 %) and clynopiroxene (10 %). According to field observations, this ejects were thrown up by a grey plume that preceded the strombolian event (Fig. 4.5). The geochemical aspect was also considered, in order to reach a better understanding of the processes that controlled the 2012 eruptive event. Both samples are geochemically consistent with the petrographic description. They are classified as Basaltic Andesites (TAS diagram, Fig. 4.15a). According to the K$_2$O versus SiO$_2$ diagram (Peccerillo and Taylor 1976, Fig. 4.15b) these rocks corresponds to high K calc-alkaline series. The geochemistry obtained is consequent with the mineralogy observed under the microscope, with mafic anhydrous minerals (olivines and clynopiroxenes), intermediate plagioclases.

4.5 Discussion

The multidisciplinary studies performed after the 2000 eruption allowed to interpret the anomalous process occurring during 2004 (Ibañez et al. 2008; Caselli et al. 2009; Velez et al. 2011; Agusto et al. 2012, 2013). This process was related to a possible magmatic input that did not lead to an eruption (called "failed eruption" by Varekamp et al. 2009). Variations in steam
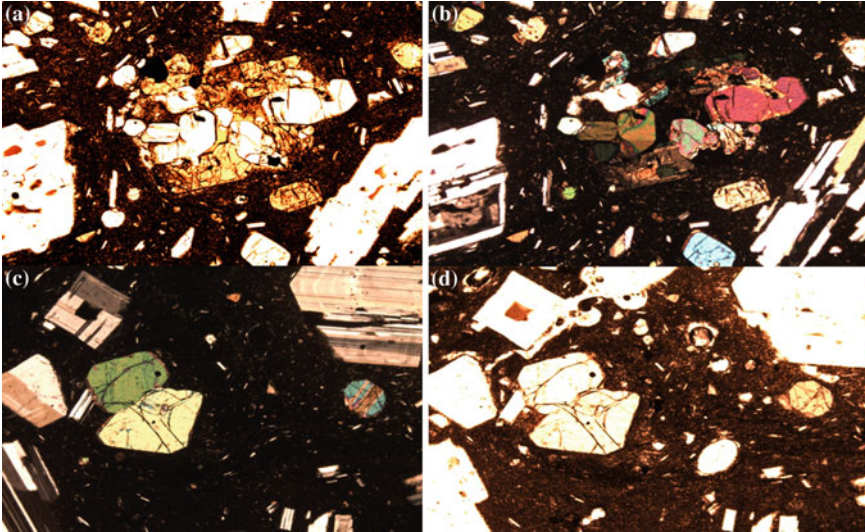
Fig. 4.14 Thin sections under the petrographic microscope showing phenocrysts of Plagioclase intergrowth with clynopiroxene in glomerules; olivines with reaction crowns and a hialopilitic matrix, with parallel Nichols (**a**) and crossed Nichols (**b**), and showing euhedral phenocrysts of Plagioclase, clinopyroxenes and Olivines with crossed Nichols (**c**) and with parallel Nichols (**d**)
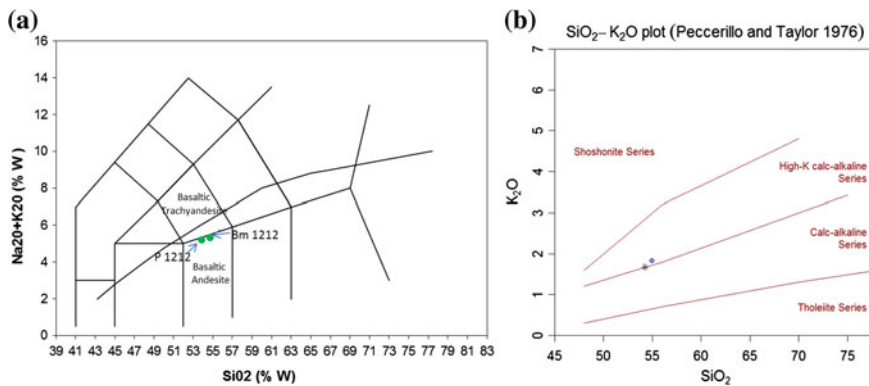
Fig. 4.15 **a** Plot in TAS diagram of the 2012 eruption's products (*green circles*); **b** SiO2 versus K2O plot (Peccerillo and Taylor 1976). The samples analyzed plot in the High K calc-alkaline series field

discharge rates are commonly observed in volcanic-hydrothermal systems and could occur without any input of new magma from the deeper system (Agusto et al. 2012). According to the model proposed by Founier et al. (2006) severe increase of degassing at the surface could result from the fracturing of the sealed zone in the ductile-brittle region (carapace) that surrounds the magma chamber. Leakages across the brittle–plastic boundary can range from slow diffusion

of non-condensable gases or minor discharges of steam through small fractures quickly resealed, up to large explosive events that vent to the surface. The rupture process could be associated with the increment in the number of seismic activity and the seismic swarm registered at the beginning of 2004. This release of fluids from lenses hosted in the ductile region would be responsible for the deformation observed at surface by DInSAR (Velez et al. 2011, and this

book). The arrival of these fluids at the subsurface volcanic-hydrothermal system would have generated the oversaturation of hydrothermal silica and sulfur species, partially sealing the conduits that fed the crater lake (Caselli et al. 2005; Agusto et al. 2012, and this book). The decrease in permeability could have produced a partial disconnection of the crater lake with the underlying volcanic-hydrothermal system leading to a decrease contents of ionic solutes, of waters temperature and, finally, to freezing of the lake surface. It is also important to consider the behavior of sulfur in the system. According to the geochemical modeling performed in Kawah Ijen and Ruapehu volcanoes, the alteration assemblage of predominantly liquid elemental sulfur with anhydrite, alunite and quartz readily develops in the hydrothermal envelope enclosing the conduit (Delmelle and Bernard 1994; Christenson et al. 2010). This condition is consistent with the silica alteration of the material ejected during the 1992 phreatic event of Copahue described by Delpino and Bermudez (1993). The authors also reported the occurrence of pyroclastic sulfur that indicated temperatures higher than 120 °C and suggested the existence of a molten sulfur pool at the bottom of the crater lake (Francis et al. 1980; Varekamp et al. 2001). A sulfur pool could have favored the decrease in permeability during the 2004. A possible explanation is related with the behavior of molten sulfur as temperature increases. Several authors (Hurst et al. 1991; Oppenheimer 1992; Takano et al. 1994) proposed that the viscosity of molten sulfur increases with an increment in temperature over 120–150 °C, and this could result in a partial sealing of the vent system. We consider that possibly both mechanisms, mineral precipitation and an increment in molten sulfur viscosity, have favored the partial sealing developed in the upper portion of the conduits controlling the permeability of the system.

The significant variations observed since 2011 in seismic activity, temperature, chemical contents of acidic species, crater lake volume together with the increase of diffuse acid steaming and surface uplift (Fig. 4.16), allowed us to infer a disturbance of the volcanic-hydrothermal system and constitute a successful example of precursory signals (Caselli et al. 2012). Surface uplift registered from October 2011 could be associated with the migration of magmatic fluids from depth. Generally inflation processes took place before volcanic eruptions, as magma is accumulated in or ascending from magmatic chambers (Dvorak and Dzurisin 1997). Geochemical variations in the crater lake for this period clearly indicate an increase in the flux of heat and acidic magmatic species from a magmatic source. The recorded geophysical and geochemical changes allowed to infer the beginning of a new eruptive cycle for the Copahue volcano. The most important pulse of the eruptive process started during July 2012 took place on December 22nd 2012. Due to the continuous magmatic degassing from crater lake between July and December 2012, we can assume that during a progressive ascent of magma, volatiles from the melt were concentrated on the upper part of the conduit. The increased heat flux firstly resulted in an eruptive phreatic pulse. The interaction between the magmatic body and the superficial waters would produce the phreatomagmatic event with the emission of pyroclastic material associated to hydromagmatic fragmentation. Once there is no more water on the superficial system, the process gradually evolved to purely magmatic. Incandescence could be indicating the absence of water and the transition from a hydromagmatic to magmatic eruptive style with moderate strombolian characteristics. An outstanding feature for this volcanic center is the abundance of liquid sulfur in the material emitted at the beginning of the eruption. This was also observed during previous eruptive processes in 1992 and 2000 (Delpino and Bermudez 1993; Varekamp et al. 2001). The existence of a sulfur pool at the bottom of the crater lake could also play an important role, controlling the permeability of the upper part of the conduit.

Concerning the trigger mechanism of the 2012 eruption, the increased seismic activity registered for Copahue volcano and surrounding areas at the beginning of 2010 (Fig. 4.16) could suggest a significant role of the February 27th
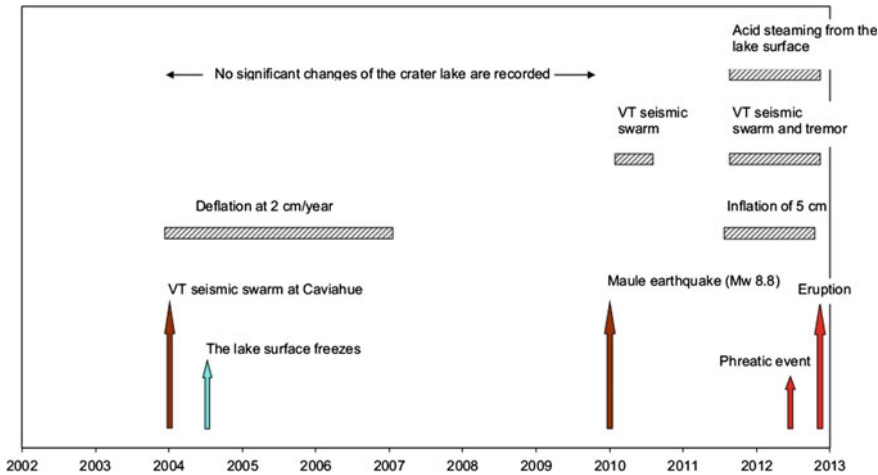
Fig. 4.16 Schematic diagram showing the chronology of eruptive activity and the preceding phenomena

2010 Maule earthquake (Mw 8.8) in the volcano unrest. A detailed analysis of the earthquake-induced static stress/strain changes on Copahue volcano was performed by Bonali et al. (2013). Numerical modeling indicates that the vertical N60ªE striking magma pathway below Copahue was affected by a normal stress reduction of about −0.258 to −0.147 MPa induced by the 2010 Chilean earthquake. Other then Copahue, other volcanoes started new eruptive cycles after this seismic event (Planchón-Peteroa volcano during September 2010 until 2012, Cordón Caulle on June 2011 and Hudson on October 2011). On the basis of a numerical modeling, Walter and Amelung (2007) suggested that earthquakes of great magnitude induce volumetric expansion on active volcanic areas. Sudden decompression due to overpressure of the magmatic chamber and/or its plumbing system could initiates processes that lead to an eruption.

References

Agusto M, Caselli A, Tassi F, Dos Santos Alfonso M, Vaselli O (2012) Seguimiento geoquimico de las aguas acidas del sistema volcan Copahue – Rio Agrio: Posible aplicacion para la identificacion de precursores eruptivos. Rev As Geol Arg 689(4):481–495

Agusto M, Tassi F, Caselli AT, Vaselli O, Rouwet D, Capaccioni B, Caliro S, Chiodini G, Darrah T (2013) Gas geochemistry of the magmatic-hydrothermal fluid reservoir in the Copahue-Caviahue Volcanic Complex (Argentina). J Volcanol Geotherm Res 257:44–56

Bengoa C, Caselli AT, Ibáñez JM (2010) Volcanic seismology studies at Copahue volcano—Argentina. In: VI Cities on Volcanoes, Tenerife, Spain, 1.3 52:95

Bonali FL (2013) Earthquake-induced static stress change on magma pathway in promoting the 2012 Copahue eruption. Tectonophysics 608:127–137

Caselli AT, Agusto M, Fazio A (2005) Cambios térmicos y geoquímicos del lago cratérico del volcán Copahue (Neuquén): posibles variaciones cíclicas del sistema volcánico. XVI Congreso Geológico Argentino, La Plata, Argentina 1:332–336

Caselli A, Agusto M, Capaccioni B, Tassi F, Chiodini G, Tardani D (2012) Aumento térmico y composicional de las aguas cratéricas del Volcán Copahue registradas durante el año 2012 (Neuquen, Argentina). XIII Congreso Geológico Chileno. Antofagasta, Actas: 441–442

Caselli A, Vélez ML, Agusto MR, Bengoa CL, Euil-lades PA, Ibáñez JM (2009) Copahue volcano (Argentina): a relationship between ground deformation, seismic activity and geochemical changes. In: Bean CJ, Braiden AK, Lockmer I, Martini F, O'Brien GS (eds) The volume project. Volcanoes: understanding subsurface mass movement. Jaycee Printing, Dublin, pp 309–318

Christenson BW, Reyes AG, Young R, Moebis A, Sherburn S, Cole-Baker J, Britten K (2010) Cyclic processes and factors leading to phreatic eruption events: insights from the 25 September 2007 eruption through Ruapehu Crater Lake, New Zealand. J Volcanol Geotherm Res 191:15–32

Delmelle P, Bernard A (1994) Geochemistry, mineralogy, and chemical modeling of the acid crater lake of Kawah Ijen volcano. Indonesia. Geochim Cosmochimi Acta 58(11):2445–2460

Delpino D, Bermudez A (1993) La actividad volcánica del volcán Copahue durante (1992). Erupción con emisión de azufre piroclástico. Provincia de Neuquén. In: XII Congreso Geológico Argentino, vol 4, Mendoza, pp 292–301

Delpino DH, Bermúdez AM (2002) La erupción del volcán Copahue del año (2000). Impacto social y al medio natural. Provincia del Neuquén, Argentina. In: XV Congreso Geológico Argentino, 3:365–370

Dvorak J, Dzurisin D (1997) Volcano geodesy: The search for magma reservoirs and the formation of eruptive vents. Rev Geophys 35. doi: 10.1029/97RG00070

Fazio AM, Agusto M, Farías SS, Caselli AT (2008) Evaluación de posibles fases minerales en equilibrio en el sistema volcánico Copahue (Neuquén) y su vinculación con parámetros químicos. In: XVII Congreso Geológico Argentino, Jujuy. Actas, pp 1343–1344

Forte P, Bengoa C, Caselli A (2012) Análisis preliminar de la actividad sísmica del complejo volcánico Copahue-Caviahue mediante técnicas de array. In: XIII Congreso Geológico Chileno, Antofagasta, pp 574–576

Fournier RO (2006) Hydrothermal systems and volcano geochemistry. In: Dzurisin D (ed) Volcano deformation, pp 153–194

Francis PW, Thorpe RS, Brown GC, Glasscock J (1980) Pyroclastic sulphur eruption at Poa´s volcano Costa Rica. Nature 283:754–756

Hill DP, Dzurisin D, Ellsworth WL, Endo ET, Galloway DL, Gerlach TM, Johnston MSJ, Langbein J, McGee KA, Miller CD, Oppenheimer D, Sorey ML (2002) Response plan for volcano hazards in the long valley Caldera and Mono Craters region. Geol Surv Bull 2185:65. California

Hurst AW, Bibby HM, Scott BJ, McGuinness MJ (1991) The heat source of Ruapehu Crater Lake; deductions from the energy and mass balances. J Volcanol Geotherm Res 46:1–20

Ibañez JM, Del Pezzo E, Bengoa C, Caselli A, Badi G, Almendros J (2008) Volcanic tremor and local earthquakes at Copahue volcanic complex, Southern Andes, Argentina. J S Am Earth Sci 174:284–298

Linde AT, Sacks LS (1998) Triggering of volcanic eruptions. Nature 395:888–890

Naranjo JA, Polanco E (2004) The 2000 AD eruption of Copahue volcano. Southern Andes. Rev Geol Chile 31 (2):279–292

Oppenheimer C (1992) Sulfur eruptions at Volcán Poás, Costa Rica. J Volcanol Geotherm Res 49:1–21

OVDAS-SERNAGEOMIN (2013a) Reporte de Actividad Volcánica (RAV). http://www.sernageomin.cl/reportesVolcanes

OVDAS-SERNAGEOMIN (2013b) Reporte Especial de Actividad Volcánica (REAV). http://www.sernageomin.cl/reportesVolcanes

Peccerillo A, Taylor SR (1976) Geochemistry of Eocene calc-alkaline volcanic rocks from the Katamonu area, northern Turkey. Contrib Mineral Petrol 58:63–81

Takano B, Saitoh H, Takano E (1994) Geochemical implications of subaqueous molten sulfur at Yugama crater lake, Kusatsu-Shirane volcano, Japan. Geochem J 28:199–216

Velez ML, Euillades P, Caselli A, Blanco M, Martínez Díaz J (2011) Deformation of Copahue volcano: Inversion of InSAR data using a genetic algorithm. J Volcanol Geotherm Res 202(1–2):117–126

Varekamp J, Ouimette A, Hermán S, Bermúdez A, Delpino D (2001) Hydrothermal element fluxes from Copahue, Argentina: a "beehive" volcano in turmoil. Geology 29(11):1059–1062

Varekamp JC, Ouimette AP, Herman SW, Flynn KS, Bermudez A, Delpino D (2009) Naturally acid waters from Copahue volcano, Argentina. Appl Geochem 24:208–220

Walter T, Amelung F (2007) Volcanic eruptions following M ≥ 9 megathrust earthquakes: implications for the Sumatra-Andaman volcanoes. Geology 35:539–542

Watt SF, Pyle DM, Mather TA (2009) The influence of great earthquakes on volcanic eruption rate along the Chilean subduction zone. Earth Planet Sci Lett 277 (3):399–407

Copahue Volcano and Its Regional Magmatic Setting

5

J.C. Varekamp, J.E. Zareski, L.M. Camfield and E. Todd

Abstract

Copahue volcano (Province of Neuquen, Argentina) has produced lavas and strombolian deposits over several 100,000s of years, building a rounded volcano with a 3 km elevation. The products are mainly basaltic andesites, with the 2000–2012 eruptive products the most mafic. The geochemistry of Copahue products is compared with those of the main Andes arc (Llaima, Callaqui, Tolhuaca), the older Caviahue volcano directly east of Copahue, and the back arc volcanics of the Loncopue graben. The Caviahue rocks resemble the main Andes arc suite, whereas the Copahue rocks are characterized by lower Fe and Ti contents and higher incompatible element concentrations. The rocks have negative Nb-Ta anomalies, modest enrichments in radiogenic Sr and Pb isotope ratios and slightly depleted Nd isotope ratios. The combined trace element and isotopic data indicate that Copahue magmas formed in a relatively dry mantle environment, with melting of a subducted sediment residue. The back arc basalts show a wide variation in isotopic composition, have similar water contents as the Copahue magmas and show evidence for a subducted sedimentary component in their source regions. The low $^{206}Pb/^{204}Pb$ of some backarc lava flows suggests the presence of a second endmember with an EM1 flavor in its source. The overall magma genesis is explained within the context of a subducted slab with sediment that gradually looses water, water-mobile elements, and then switches to sediment melt extracts deeper down in the subduction zone. With the change in element extraction mechanism with depth comes a depletion and fractionation of the subducted

J.C. Varekamp (✉) · J.E. Zareski · L.M. Camfield
Earth and Environmental Sciences, Wesleyan
University, Middletown, CT 06459, USA
e-mail: jvarekamp@wesleyan.edu

E. Todd
Alaska Science Center, U.S. Geological Survey,
4210 University Drive, Anchorage, AK 99508, USA

complex that is reflected in the isotope and trace element signatures of the products from the main arc to Copahue to the back arc basalts.

5.1 Introduction

As highlighted in Chap. 1 of the present book, the active Volcán Copahue occurs in the Andean Southern Volcanic Zone (SVZ) $\sim$ 30 km east of the main volcanic front defined by the NNE-trending active volcanic centers of Antuco, Callaqui, and Llaima in Chile (Fig. 5.1). It is located on the southwestern edge of an elliptic Pliocene depression (19 × 15 km), known as the Caviahue caldera or Agrio caldera (Fig. 5.2), 30 km west of the town of Loncopué, Argentina. Unlike many of the stratovolcanoes in the SVZ, Copahue has a concave-down shape, resembling a Hawaiian shield volcano from afar. This rounded shape may be the result of glacial action (Delpino and

Bermúdez 1993), repeated flank collapses as a result of hydrothermal weakening of the interior (Varekamp et al. 2001) or simply the result of repeated eruptions of small lava flows and small explosive eruptions (many hydromagmatic) that dispersed fine ash away from the volcano. The volcanic series can be subdivided into: lavas of the Caviahue caldera walls, the Riscos Bayos ignimbrite sequence on the SE flanks of the Caviahue caldera slopes, intra- and extra-caldera silicic rocks, and the Copahue volcano rock sequence itself, including the volcanic products of the 2000 and 2012 eruptions. The zone east of the caldera contains many Holocene lava flows and cinder cones (Fig. 5.2), forming the back arc suite of Copahue volcano (Muñoz and Stern 1989; Kay et al. 2004; Hesse 2007; Varekamp et al. 2006).
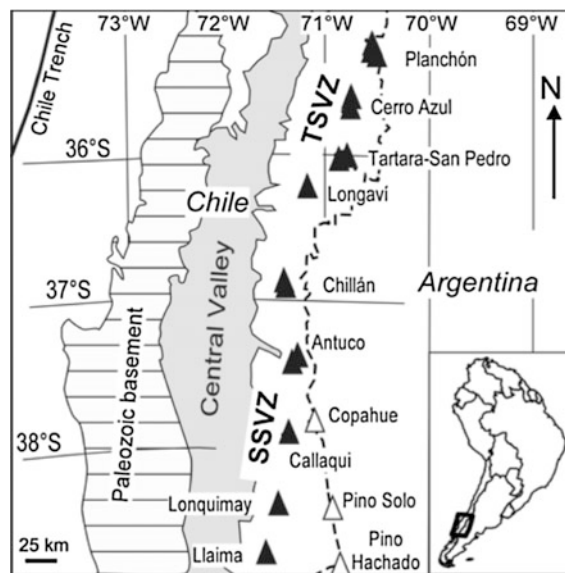
Fig. 5.1 Copahue and its regional geography; *dashed line* is border of Argentina and Chile
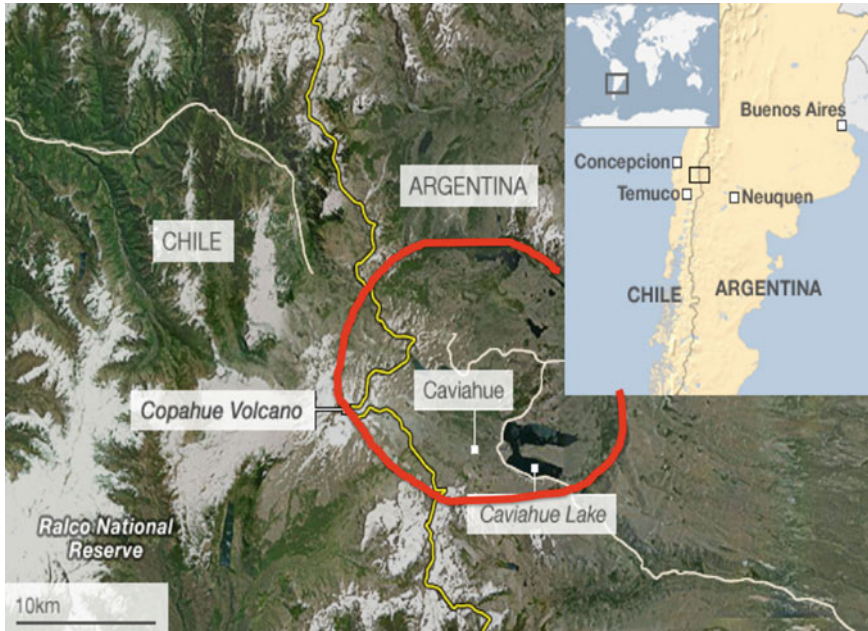
Fig. 5.2 Copahue volcano on the western rim of the Caviahue caldera (*red line*) with Lake Caviahue. *Yellow line* is the border between Chile and Argentina

The volcanic stratigraphy and geology of the Caviahue and Copahue Volcano Complex (CCVC) have been characterized by Bermúdez et al. (1993, 2002), Bermúdez and Delpino (1995; 1999), Colvin (2004), Delpino and Bermúdez (1993, 2002), deMoor (2003), Merrill (2003), Moreno et al. (1986), Goss (2001), Linares et al. (1999), Melnick et al. (2006), Hesse (2007), Todd (2005), Todd and Ort (2012), Varekamp et al. (2006, 2010) and Zareski (2014). A small young cone occurs NE of Copahue (Troncon) and further to the northeast, the volcanoes Tromen and Domuyo are found, surrounded by many small lava flows and cinder cones (Zareski 2014). Some studies (Jacques et al. 2013, 2014) have documented regional cross arc trends over the Andes between 36° and 39°S, from the volcanic front volcanoes in Chile, through Copahue/Caviahue, to the back arc basalts all the way in the Payenia province, a more cratonic domain of volcanism (Soager et al. 2013).

In this chapter, the geochemistry of the products of Copahue volcano, the Caviahue caldera, as well as a comparison with the main arc in Chile and nearby back-arc rocks are

presented. The Copahue eruptions of 2000 and 2012 are discussed in some detail, as is the tectonic setting of Copahue and this part of the Andean subduction zone.

5.2 Tectonic Setting

5.2.1 Regional Tectonic Setting

The Caviahue and Copahue volcanoes are related to the eastward subduction of the Nazca Plate below the South American continent. The Nazca Plate is currently being subducted beneath South America between 0° and 49°S in a roughly east-west compressional direction of $77 \pm 12°$ at a rate of 9.2–10.8 cm/year with little variation along strike in both direction and rate (Pardo-Casas et al. 1987). The subducting slab has a relatively constant dip of 30° along the entire length of the SVZ. Volcanic gaps separate the SVZ from the non-magmatic Chilean "low-inclination-slab" to the north and the Austral Volcanic Zone to the south (Jordan et al. 1983; Bevis and Isacks 1984; Kay et al. 1987).

The SVZ is commonly divided into the Southern South Volcanic zone (SSVZ) from about 37°S southwards, the Transitional South Volcanic Zone (TSVZ, from 37°S to 35°S) and the Northern South Volcanic Zone (NSVZ) from 35° S north. The Mocha oceanic fracture zone collides with the trench at 37°S and separates 36 Ma oceanic crust to the north from younger, 18 Ma crust to the south (Swift and Carr 1974; Herron 1981). Seismic profiles taken across the SVZ indicate that earthquakes defining the Benioff-Wadati zone below the SVZ initiate approximately 270–285 km east of the trench. Intermediate depth earthquakes in the SVZ occur directly beneath the modern volcanic arc and under Copahue volcano cluster at 90–120 km depth (Barazangi and Isacks 1976; Bevis and Isacks 1984; Cahill and Isacks 1992). Back-arc earthquakes are sparse in the SVZ, suggesting that the slab is relatively warm below that region (Cahill and Isacks 1992). The thickness of the overriding continental crust changes markedly at the 37°S Mocha Fracture Zone boundary (Beck et al. 1996). South of 37°S, the crustal thickness is relatively uniform at 35 km (Hildreth and Moorbath 1988; Volker et al. 2011), but gravity data show a steady increase in crustal thickness to 55 km at 34.5°S (Dragicevic et al. 1961; Diez-Rodriguez and Introcaso 1986). The age of the crustal rocks also increases to the North, providing a more radiogenic isotopic end member for magmas that may have reacted with the upper crust in this zone. Geochemical and isotopic signatures of crustal contamination are evident in magmas from volcanic edifices north of 37°S (Hickey et al. 1986; Hildreth and Moorbath 1988), although Davidson et al. (1987, 1988) argued for a strong crustal influence south of 37°S as well. Subduction erosion may occur along this part of the Andean subduction zone (Stern 1991) and steepening of the subduction angle over time may have occurred (Ramos 1978; Folguera et al. 2008). During the early to mid-Miocene eastward migration of the arc front accelerated, culminating at its eastern-most extent during the late Tertiary, a result of a shallower subduction of the Nazca plate beneath South America. The position of the volcanic front in the Quaternary occurs to the west of the Late Tertiary front between 38 and 39°S (Muñoz and Stern 1988). Migration to the west is suggested to be a result of roll back with a general steepening of the subduction angle in this region. This roll back may have produced retro-arc basaltic magmatism of alkaline composition in the Southern Central Andes (Muñoz and Stern 1988, 1989; Jordan et al. 1983). Discontinuity in Nazca plate segment ages and strike of axial magnetic anomalies also occur at the Valdivia Fracture Zone-trench interface at ∼40°S. The age of the subducting slab age is ∼18 Ma south of 40°S. This section was formed at the Chile Ridge, whereas the segment to the north of 40°S (at 26 Ma) was formed at the East Pacific Rise (Tebbens et al. 1997).

Copahue volcano is found about 320 km east of the subduction trench, and is situated on the western margin of the older Caviahue caldera (∼2.0 Ma). Copahue also sits on the transition from SSVZ to TSVZ, where the thickness and age of the upper plate changes and the subducted plate is separated by the Moccha fracture zone (Folguera et al. this book). The Caviahue volcanic complex may be related to a slightly less steep subduction geometry that was prevalent here several million years ago, and the steepening may have led to the westward retreat of the main volcanic front to the line Callaqui-Antuco (Muñoz and Stern 1989).

5.2.2   Local Tectonic Setting

The CCVC marks the northern extent of the Copahue-Pino Hachado precordilleran uplift. This uplift diverges to the southeast from the main Andean Cordillera south of 38°S. Its western limit is delineated by the Bío Bío/Aluminé fault system, which merges with the northernmost extension of the Liquiñe-Ofqui Fault just south of the CCVC (Cembrano et al. 1996; Cembrano and Lara 2009; Muñoz and Stern 1988, 1989). The north-south running Agrio Valley bounds the uplift to the east and is marked by the NNW-SSE trending Cordillera del Viento Fault. Normal faults form the boundaries of the Pino Hachado

Uplift, with the eastern low area sometimes called the "Graben of Loncopué" (Ramos 1978), which has scoria cones and lava flows of back arc basalts (Kay et al. 2006; Muñoz and Stern 1989; Varekamp et al. 2010). Quaternary volcanic centers are absent along the Cordillera del Viento fault at this latitude, yet ∼150 km north along the fault are the massive Quaternary volcanic complexes of Tromen and Domuyo.

Throughout the Pliocene and early Pleistocene, magmatism persisted within and along the margins of the Copahue–Pino Hachado uplift, evidenced by NNW trending centers between the CCVC in the north and Palao Mahuida in the south (Muñoz and Stern 1989). A number of these Plio-Pleistocene centers have experienced caldera collapse, including the CCVC, Pino Hachado and Palao Mahuida. In the early Pleistocene, volcanic centers on the southeast part of the uplift erupted alkali basaltic lavas and by the late Pleistocene, volcanic activity had largely shifted to the west (Muñoz and Stern 1989). Quaternary volcanism persists at the CCVC and at fissure-aligned back arc cones in the valleys flanking the Copahue–Pino Hachado uplift.

There is minor evidence for post-Miocene compression south of 34°S, although north of 34°S high-angle reverse and Quaternary thrust faults in the Argentine Precordillera testify to a compressional regime existing since the Mid-Miocene (Jordan et al. 1983; Garcia Morabito et al. 2011; Folguera et al. 2007, 2012; Orts et al. 2012). Since this time, the SSVZ region has only undergone regional extension, as the Quechua compressional phase of the Andean Orogeny ended in the late Miocene (Charrier and Vicente 1972). The Pleistocene lavas that fill the Loncopue Graben probably reflect this extensional regime.

5.3 Character of the Subduction Zone

The Benioff Wadati zone can be characterized from earthquake data. Two sources were used to establish the subduction geometry in the band from 35° to 39°S and 66° to 76°W (400 km × 600 km). The NEIC (National Earthquake Data Center) hypocenter database consists of 2000 earthquake events, which plot as a diffuse downward curving planar feature of approximately 30–40 km in thickness that extends to a depth of 210 km (Fig. 5.3). The EHB hypocenter database (Engdahl et al. 1998) consists of a smaller number of earthquake events but with better spatial resolution, providing a Wadati-Benioff Zone with a 10–20 km thickness) but no data below 150 km. The geometry of the subducting plate was approximated using the inverse distance weighting interpolation algorithm (Spatial Analyst in Arc GIS) to convert the array of hypocenters into a plane (Fig. 5.3). This method does not identify the top of the subducting plate. Inconsistencies in fault plane depth can cause hypocenter location errors of up to 30 km in the NEIC database (Engdahl et al. 1998) and the reconstruction of the subducting Nazca plate thus has uncertainties. The subduction angle of the Nazca Plate in both models is very similar. The positions of the volcano centers on the surface are extrapolated down to intersect with the subducting plate model establishing the subduction zone geometry (Fig. 5.3, bottom). The estimated depths to the Benioff zone of individual volcanoes are: Llaima: 85 km, Tolhuaca: 90 km, Callaqui: 105 km, Copahue: 120 km and LBAB: 180 km. Since Caviahue volcanism (Pliocene) predates Copahue (Quaternary), the position of the Benioff zone in relation to Caviahue at that time is uncertain.

5.4 Regional Volcanology

Earlier volcanological studies (Pesce 1989; Delpino and Bermúdez 1993, 2002; Bermúdez and Delpino 1995, 1999; Bermúdez et al. 2002; Linares et al. 1999, Muñoz and Stern 1988, 1989; Mazzoni and Licitra 2000, Melnick et al. 2006) have named the CCVC as Volcan Copahue and the Copahue-Caviahue volcano and have drawn up schemes of evolution with a number of
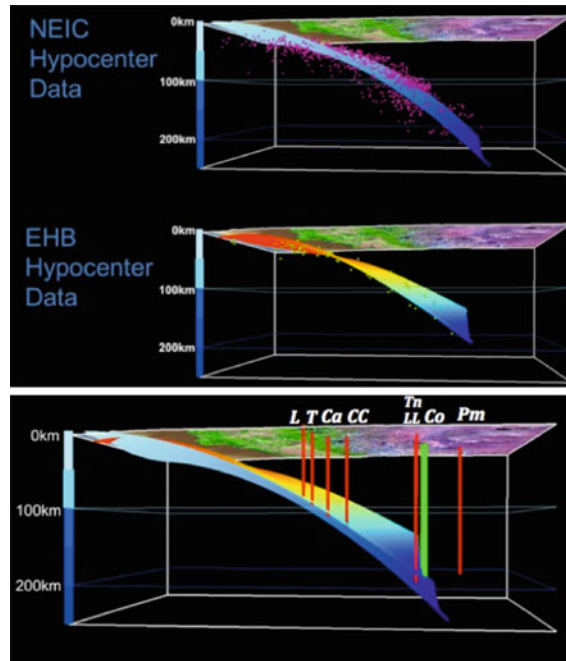
Fig. 5.3 Reconstruction of the "twisted" plane of subduction at ∼37°S with the two sets of seismic data (*top panel*) and the depth to the Benioff zone (*bottom panel*). Volcanic centers *left* to *right* (west to east); Llaima (L), Tolhuaca (T), Callaqui (Ca), Copahue-Caviahue (CC), Las Lajas and Laguna Blanca cinder cones (LL) and the back arc volcanoes further to the northeast Tromen (Tn), Cochiquito (Co) (*green bar*) and Payun Matru (Pm)

local stratigraphic units (Table 5.1). The following broad nomenclature was used: the CCVC consists of the older pre-caldera Caviahue sequences (e.g., Hualcupen formation of Pesce), the intracaldera volcanic rocks, the Riscos Bayos ignimbrite sequence, the Cerro Bayo dome complex, the modern Copahue volcano, and the cinder cones and flows in the Loncopue graben area (Fig. 5.2). Pesce (1989) and Delpino and Bermúdez (1993) describe four general eruptive episodes (EE) of volcanic activity at the CCVC labeled Copahue eruptive episodes I, II, III, and IV. The Copahue I phase began in the early Pliocene (4.3 ± 0.6 Ma, although Linares et al. (1999) also report some ages of ∼5 Ma) with the growth of numerous polygenetic strato-volcanoes characterized by large Plinian eruptions. Andesitic to rhyolitic pyroclastic and debris flow deposits of this volcanic stage are widely distributed in both Argentine and Chilean territory.

The Caviahue caldera formed during the Plio-Pleistocene, probably around 2.0 Ma (Linares et al. 1999; Folguera and Ramos 2000). The main exposed ignimbrite deposits on the Argentine side of the region are the Riscos Bayos flows near Loncopue, with additional outcrops along the south wall of the Caviahue caldera (Todd 2005). The caldera forms a major collapse structure in this region, and formed the basement for the later evolutionary stages of Volcán Copahue (Muñoz and Stern 1988). Rhyolitic domes that intruded into the floor of the caldera terminated this phase of magmatism (Niermeyer and Muñoz 1983).

Copahue II commenced during the Pleistocene (0.8 ± 0.1 Ma) with the nucleation of a new volcanic edifice on the southwest rim of the caldera. This new volcanic cone forms the underlying structure of the present day Volcán Copahue. Deposits from this eruptive stage are

Table 5.1 Stratigraphic schemes used for the CCVC area (after Todd 2005)

Delpino and Bermúdez (1993)	Niermeyer and Muñoz (1983) / Suarez and de la Cruz (1998)	Pesce (1989)	Linares et al. (1999) / Folguera and Ramos (2000)
Holocene	Post 1 Ma Stratovolcanoes	Copahue Stratovolcano	Post-caldera Rocks
E.E. IV	Pleistocene to Late-Holocene	Upper Pleistocene and Holocene	Bayo and Trolope domes (0.6 Ma)
		Stratovolcanoes and domes:	Trolón (0.6 Ma)
		Del Bayo, Trolope, Cerro Trolón, and valley floor flows	Copahue stratovolcano (<1 Ma)
E.E. III	Lower Pleistocene stratovolcanoes	Las Melizas	Trolope lava flows (1.6 Ma)
		Lower Pleistocene	Riscos Bayos P.F. (2 Ma)
		Riscos Bayos	
Pleistocene			Pre-caldera rocks
E.E. II			Cerro Chancho-Co (2.6 Ma)
Lower Pliocene to Lower Pleistocene	Cola de Zorro Formation	Pliocene (Pre-caldera)	Extra-caldera rocks (4.5 Ma)
E.E. I	Associated with Pre-Cordillera		
	Pliocene-Lower Pleistocene	Hulcapén Formation	Some dates are from 11 to 2.5 Ma
	Miocene		Miocene to Permo-Triassic
	Trapa Trapa Formation		
	Cura Mallín		Volcanicbasement to Neogene rocks

found within the caldera in Argentine territory and outside of the caldera in Chile (Muñoz and Stern 1988). During this eruptive episode, much of the volcanic cone was completely glaciated leaving U-shaped valleys and striated lava flows (Rabassa and Clapperton 1990). Evidence from striations on the exposed caldera walls and on intracaldera lava flows (on the peninsula) suggest that the entire caldera could have been filled with ice during this period.

Copahue III began as the glacial cap began to recede. Lava flows and pyroclastic eruptions originated at the base of the then still fully glaciated Volcán Copahue and flowed into river valleys. A 100 m thick glacier is currently present at the summit of the volcano (Delpino and Bermúdez 1993).

Copahue IV composes the post-glacial Holocene lava and pyroclastic deposits erupted largely from a NW-SE trending 2.5 km long fissure near the summit of Volcán Copahue. Aligned along this fissure are several cones located inside the larger extinct crater. The youngest lava flows belong to this stage and were erupted from a fissure on the north margin of the Rio Agrio (Delpino and Bermúdez 1993). The 2000 and 2012 Copahue eruptions produced mainly ashes and larger (10–20 cm-sized) clasts, which form a surface deposit mantling ice and older topography, with minor preservation potential.

In this chapter, the Copahue EE I volcanic rocks were labeled the 'Caviahue series' and Copahue EE III, II and I the 'Copahue series'. Folguera and Ramos (2000) suggested that subsidence of the Caviahue Caldera occurred as a tectonic manifestation of trans-tensional stress associated strike-slip motion of the faults bounding the Copahue–Pino Hachado uplift. Pesce (1989), Delpino and Bermúdez (1993), and Linares et al. (1999) argue for a possible volcanic caldera collapse after the eruption of the Riscos Bayos ash flows, although the relations between caldera volume and estimated ash flow volume are uncertain (Colvin 2004; Todd 2005).

5.5 The Recent Eruptions of Copahue Volcano

Copahue volcano had phreato-magmatic eruptions in the 1990s (1992–1995), which led to the ejection of the crater lake, vigorous steam plumes (evaporated hydrothermal fluids), emissions of copious amounts of liquid sulfur, debris from the

hydrothermal system, and some scoria of primary magmatic material (Delpino and Bermúdez 1993). Goss (2001) described one of these scoria from a lahar deposits of the 1995 eruption. The 2000 eruption was preceded by thermal activity in late 1999 (Varekamp et al. 2001) and also started with ejection of the crater lake followed by a sustained column that spread ashes well beyond Caviahue village, which had accumulations of several cm of ash. The snow-covered slopes surrounding the crater had coarser ashes and large scoria and cinders (several dm), which were sampled and analyzed (Goss 2001; Varekamp et al. 2006; Camfield 2014). The 2000 eruption was discussed by Naranjo and Polanco (2004) and Delpino and Bermúdez (2002).

The character of the 1995 and 2000 eruptions has been documented before (Velez et al. 2011; Ibañez et al. 2008). A summary for the 2012 eruption, which can be classified as a violent Strombolian event (Pioli et al. 2008), is given here (Fig. 5.4) and more extensively described in Chap. 4 of this book. The deposits of the 2012 eruption can not be found in one location in
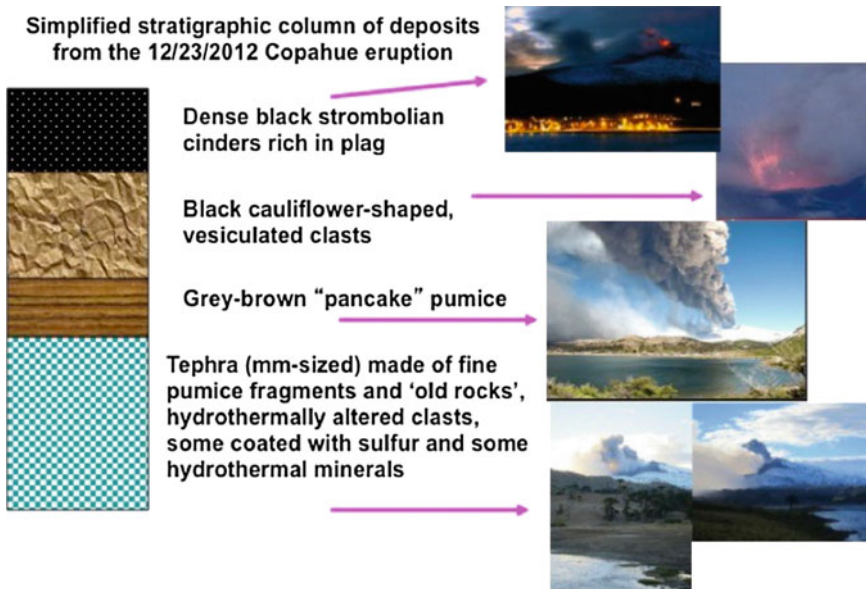
Fig. 5.4 Stratigraphic diagram of the December 2012 eruption of Copahue volcano, with the phreato-magmatic phase overlain by the pancake pumices and the scoria and cinders during the later phases. Stratigraphic thickness in this figure is not proportional to volume or duration

superposition, but the general stratigraphy is as follows: the initial phreato-magmatic phase deposited mm-sized ash in the area directly south of Copahue (the 'four cascades' area) in a narrow lobe of a few 100 m wide that reached a maximum thickness of a few cm at most. The dark ashes are juvenile material mixed with debris of the hydrothermal system, mainly white and yellow, fine-grained fragments. On top of this deposit and mixed-in at places are 3–10 cm large flat pumice fragments that consist of a quenched, pale rim with sub-mm sized vesicles and a highly inflated core (mm to cm sized bubbles), with a maximum thickness of 1–2 cm. These flat pumice fragments were described by Pioli et al. (2008) as "pajaritos" (small birds) and have been described by others as "flat pumices". These small "pancake-shaped" clasts have a large diameter relative to the mm-sized ashes among which they are found. Their low density made them travel relatively far from source through their disc-like morphology and low weight relative to their maximum dimension. The scoria and denser cinders from the Strombolian phase are only found near-source on the slopes along the crater. The vesicularity decreased during the eruption from the pumice-like clasts (they float), to the scoria (density >1) to the denser cinders (density $\sim$2.5; Camfield 2014).

5.6 Methods of Analyses

Bulk rock samples were analyzed by wave-length dispersive X-ray flurorescence (WD-XRF, Bruker S-4) at Wesleyan University. Major elements were analyzed against a suite of USGS SRMs and precision for these analyses is better than 1 %. Finely ground samples were initially heated to 1040 °C to oxidize all Fe to Fe^{3+} and release volatiles (LOI). Only samples with LOI less than 1.5 % were used and analyses are reported on an anhydrous basis. The heated samples were fused with a La-rich Li-metaborate flux (0.5 g sample, 2.5 g flux GF-47) at 1040 °C and poored as small beads. Variations in the quality of fusion and bead-pooring add

uncertainty, giving a reproducibility between various beads of the same sample of 1–2 %.

Trace element analyses were done with the WD-XRF instrument using the Bruker GeoQuant program that has been re-calibrated by us for volcanic arc rock samples using similar USGS SRMs as used for the major elements. The powdered samples are pressed at 5 tonnes pressure with a binder (Bruker supplied binder pills) into a small Al cup and then run in the instrument with an ultra-thin foil to prevent dust contamination. An excellent accuracy was obtained for the elements Sc, Ti, V, Cr, Mn, Fe, Co, Ni, Cu, Zn, Ga, Rb, Sr, Y, Zr, Nb, Pb and Th. The detection of U, Cs, La, Ce was less satisfactory ($\sim$10 % noise) and for Ba an extra correction was added to fully correct for the Ti peak overlap. Precision of the instrument was 1–3 % but accuracy depended on the matrix. Overall, the elements listed above have an accuracy of $\sim$5–8 %.

Most samples were analyzed by SGS Laboratories, Toronto, Ontario, Canada for 54 trace element concentrations. Sodium peroxide fusion of the powdered samples was followed by acid digestion, and trace elements were analyzed using both ICP-MS (Inductively Coupled Plasma Mass Spectrometer) and ICP-AES (Inductively Coupled Plasma Atomic Emission Spectrometer). Duplicate analyses indicate a deviation from 0.2 to 6.7 % for the majority of trace elements measured and analyses of standard reference materials also yielded results within 6 % of the reported data (Rea 2009). Comparison of the XRF and ICP-MS/ICP-AES data show good agreement for most elements, except for U, Th, and Cs which were ultimately all drawn from the ICP-MS data set. The ICP-MS data were used when available but those that had only XRF trace element analyses, only elements that showed good agreement with the ICP-MS data in the other sample suite were used from the XRF data base (Camfield 2014).

Radiogenic isotope data are after Varekamp et al. (2006, 2010) for most of the Copahue, Caviahue and back-arc samples, and the methods, laboratories and precision/accuracy of these data are discussed in those articles. The Caviahue

sample suite from Todd was analyzed at the same time as his samples from the Fiji Basin and their precision and accuracy is provided in Todd et al. (2011).

Several back arc samples, Copahue samples and Callaqui samples were analyzed for $^{87}Sr/^{86}Sr$, $^{143}Nd/^{144}Nd$, $^{206}Pb/^{204}Pb$, $^{207}Pb/^{204}Pb$ and $^{208}Pb/^{204}Pb$ at the University of Florida, Gainesville (details in Rea 2009; Zareski 2014). Samples were analyzed using a Nu-Plasma Multi Collector-Inductively Coupled Plasma Mass Spectrometer. The sample powders were dissolved in strong acids, dried, re-dissolved in acid and centrifuged. The resulting supernatant was injected into cation exchange columns and target elements were separated. Standard NBS 981 was used for Pb isotope analyses, NBS 987 for Sr isotope analyses (0.71024; error ∼0.000012) and JNDi1 for Nd isotope analyses (0.512115; error ∼0.00005). Details of the precision are shown in Table 5.2.

5.6.1 Electron Microprobe Analyses

Compositions of individual mineral grains, matrix glasses and glass inclusions were analyzed at the American Museum of Natural History, New York, NY, using a 5-spectrometer Cameca SX-100 Electron Microprobe and some of the 2012 pumices were also analyzed at the University of Bristol (UK) microprobe facility. A 5 μm beam diameter was used with a voltage of 15 kV and a 10 nA beam current. Counts were made for 30 s on all elements except Na, for which a 20 s counting time was used. Five known standard compositions—Lake County Plagioclase USNM 115900, Augite 164905, San Carlos Olivine, OPX 25-25, and Augite (209) were analyzed before the samples to calibrate the instrument accurately.

For analyses of matrix glass and glass inclusions, a 10 μm-diameter beam was used at 15 kV. Na and K were analyzed with a 5 nA beam

Table 5.2 Precision and accuracy of Pb, Sr, and Nd isotope measurements by MCICPMS at the University of Florida (Gainsville, FL) for standards analyzed in the course of this study

Suite	Sample ID	$^{206}Pb/^{204}Pb$	In-run error[a]	$^{207}Pb/^{204}Pb$	In-run error	$^{208}Pb/^{204}Pb$	In-run error
Standard	NBS 981	16.935	0.001	15.488	0.001	36.689	0.001
	NBS 981	16.934	0.001	15.486	0.001	36.683	0.002
	NBS 981	16.936	0.001	15.488	0.001	36.688	0.002
	NBS 981, U of F long-term average	16.936		15.488		36.688	
	NBS 981, Abouchami et al. (2000)	16.941		15.496		36.722	

	Sample ID	$^{87}Sr/^{86}Sr$	In-run error[b]				
Standard	NBS 987-Sr	0.710223	0.000014				
	Sample ID	$^{143}Nd/^{144}Nd$	In-run error[c]				
Standard	JNdi-1	0.512103	0.000007				

[a]In-run error is the statistical internal precision (2 standard error) of all accepted integrations within a single analysis. Long-term external reproducibility (2 standard deviation) of many analyses of standard solutions of NBS-981 over several analytical sessions were 0.003, 0.003, and 0.009 for $^{206}Pb/^{204}Pb$, $^{207}Pb/^{204}Pb$, and $^{208}Pb/^{204}Pb$

[b]In-run error provided is internal precision for typical analysis of standard solution. Long-term external reproducibility (2 standard deviation) of many analyses of standard solutions of NBS-987 over several analytical sessions was ±0.000030 for $^{87}Sr/^{86}Sr$. Sr results in Table 5.8 are normalized to NBS 987 = 0.710250

[c]In-run error provided is internal precision for typical analysis of standard solution. Long-term external reproducibility (2 standard deviation) of many analyses of standard solutions of JNdi-1 over several analytical sessions was ±0.000014 for $^{143}Nd/^{144}Nd$. Nd isotope results in Table 5.8 are normalized to JNdi-1 = 0.512115 (LaJolla = 0.511858) (Tanaka et al. 2000)

current, S and Cl with a 20 nA current. Calibrations were tested on andesite glass (AGV-1), Macusani glass, and AMNH andesite (H2VF) and dacite (R121) samples. The Cl and S analyses have a precision of about 10 %, and water in matrix glass and glass inclusions was estimated with the "by difference method" (difference from 100 % totals). An additional suite of mineral phases was analyzed at the University of Massachusetts microprobe (Cameca SX50), again using natural standards for calibration. Cross correlation of the same samples with the three different microprobes gave excellent results (Camfield 2014).

5.7   Samples and Petrography of the CCVC Volcanic Rocks Copahue

The stack of lavas and scoria from Copahue volcano are made up mainly of basaltic andesites and trachy-andesites that carry olivine, clino- and ortho-pyroxene, abundant plagioclase and rare oxides (Goss 2001). Hydrous phases are lacking in all studied specimen. Some microprobe data are available from mineral phases of the 1995 Copahue scoria (sample JM95, Goss 2001), and numerous analyses are presented here for the 2000 and 2012 eruptive products. The 2000 and 2012 scoria, cinders, and pumices are basaltic andesites, with two pyroxenes, olivine, plagioclase and

one oxide. Many olivine crystals are broken and resorbed, and in some rare instances rimmed by orthopyroxene. Two plagioclase types occur in the 2000 and 2012 samples (Fig. 5.5): clean blocky, twinned crystals, and large crystals that display sieve texture with clean rims; the latter are probably xenocrystic. Some 2000 scoria samples carried large unidentified SiO_2 crystals that have the optical properties of Cristobalite with small brown glass inclusions, presumably the result of interaction of the magma with the hydrothermal reservoir rocks (Goss 2001). The 1995 juvenile clasts show evidence for mixed magmas ranging in composition from high-K basaltic andesite to high-K andesite. Plagioclase is the most abundant phase, with about one quarter of phenocrysts displaying sieve textures. Clinopyroxene (augite) and orthopyroxene (hypersthene) are also common (Fig. 5.5) along with olivine, oxides, and trace amounts of apatite (Goss 2001).

Olivine crystals have a narrow compositional range in the 2000 and 2012 samples (Fo = 64–67 %) and have few if any spinel inclusions. Clinopyroxene crystals are diopsitic augites (Mg# = 67–81 %) with ~ 2 % Al_2O_3, 0.7–0.9 % TiO_2, whereas the orthopyroxenes are hypersthenes with up to 2 % CaO. Plagioclase crystals in the 2000 samples range in composition from 51 to 62 % An, whereas the 2012 samples range from 42 to 63 % An, with the large corroded plagioclase crystals from 64 to 91 % An. Only a single oxide (titanomagnetite) has been found in
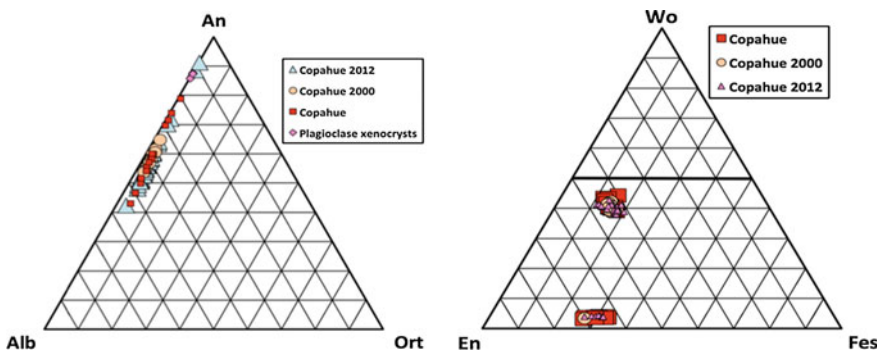
Fig. 5.5 *Left* compositional variation in plagioclase crystals for the 1995, 2000, and 2012 eruptions; *Right* the same for the two pyroxene phases. Data of the 1995

scoria sample are from Goss (2001) and those of the 2000 and 2012 scoria and pumices are after Camfield (2014)

all the recent products. The pyroxenes and pla-
gioclases from the products of the two eruptions
overlap in composition (Fig. 5.5).

5.8 Caviahue

The Caviahue samples show much more com-
positional and mineralogical variation than
Copahue volcano, with rocks ranging from
basaltic andesite to rhyolite. The more evolved
magmas have hornblende and biotite as hydrous
minerals. The compositional range of the min-
erals in these rocks was described by Todd
(2005), deMoor (2003) and Merrill (2003), and
data from the latter two summarized in Var-
ekamp et al. (2006). The intermediate rocks are
two-pyroxene andesites (Fig. 5.6), with olivine in
the more mafic endmembers and intermediate
plagioclase crystals (Fig. 5.6). The rock samples
from the Riscos Bayos pyroclastic flow series
have plagioclase, two pyroxenes, Fe-oxides,
biotite, and quartz in the rhyolitic endmembers,
with abundant variation between the various
stratigraphic units within these flows (Colvin
2004; Varekamp et al. 2006; Todd 2005). The
intra-caldera rocks are mainly dacites and rhyo-
lites, with orthopyroxenes, plagioclase and oxi-
des. The silicic dome on the north rim of the
Caviahue caldera (Cerro Bayo) is a dacitic rock.
Rocks from the southern caldera wall (Todd
2005) consist of volcanoclastic breccias, lava

flows, dikes, and a few ignimbrites that range
from basaltic andesite to andesite in composition.
Plagioclase is most abundant, followed by
clinopyroxene with opaques, with rarer olivine
and orthopyroxene.

The compositional variation in minerals from
the analyzed rock samples from the Caviahue
caldera walls shows plagioclase with 50–70 An
%, with slightly more albite-rich crystals in
sample NB6 (dacite). The clinopyroxenes have
Mg# 62–74, and sample NB6 has some
groundmass pyroxene grains with 9–10 % Wo.
These could be pigeonites but more detailed
work is needed to further prove this.

5.9 Loncopue Back Arc Basalts

The back arc volcanics in the Loncopue graben
(LBAB) are largely basalts and trachybasalts and
were sampled over an area stretching just North
of Loncopue in the North to the nature preserve
of Laguna Blanca south of Zapala (Fig. 5.7).
These scoria cones and basalts were originally
subdivided (Hesse 2007; Varekamp et al. 2010)
into the geographic groups LP north of Lon-
copue, LL (near Las Lajas) and LB, the latter
surrounding the Laguna Blanca.

Analytical data indicate that the evolved LP
samples (samples AH-1, AH-6, and AH-7, Var-
ekamp et al. 2010) belong stratigraphically to the
top part of the Caviahue sequence, and as argued
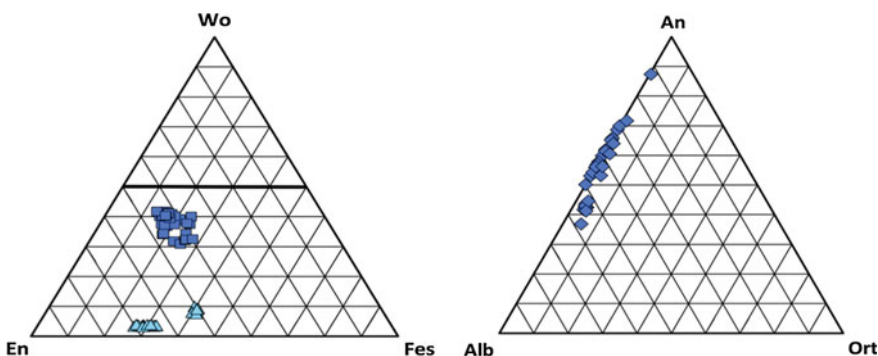
Fig. 5.6 Pyroxene (*left*) and plagioclase (*right*) compo-
sitions of the Caviahue north and east caldera wall rocks

(Merrill 2003; deMoor 2003). *Blue squares* clinopyrox-
enes; *light blue triangles* orthopyroxenes

Fig. 5.7 Geography of a section of the LBAB area directly southeast of CCVC, with cinder cones and small lava flows around the Laguna Blanca (6 km wide in E-W direction). Exact sampling locations in Varekamp et al. (2010) and Camfield (2014)

later on, the other LP samples are transitional between the Caviahue and LBAB magmas. An additional 12 rock samples from the LB area were collected and analyzed by Camfield (2014). The LP samples (AH-1 to AH-7) are trachy-andesites rich in plagioclase phenocrysts with small amounts of olivine, clinopyroxene and opaques. The LP cinder cone and its associated small dike (AH-2 and AH-3) are the most mafic and olivine-rich samples of this group. The LL samples (AH-8 to AH-15) have abundant olivine, some clinopyroxene, and only minor amounts of plagioclase microphenocrysts. These equant small plagioclase crystals could be late-stage phenocrysts or large groundmass

crystals. The LB samples have abundant phenocrysts of olivine, clinopyroxene and no plagioclase. The euhedral shape of the olivine crystals suggests that these were in equilibrium with the host magma. Many olivine phenocrysts carry swarms of small enclosed cubes and octagons of pale green to dark spinel. The groundmass of these basalts consists of fine laths of clinopyroxene, plagioclase, alkali feldspar, and rare olivine with a dusting of opaques.

The Fo-values in olivine range from 79 to 87 %, whereas olivines in more evolved samples have Fo contents down to 67 %. The most magnesian olivines have between 100–550 ppm Cr, and 1000–3000 ppm Ni. The chemistry of the
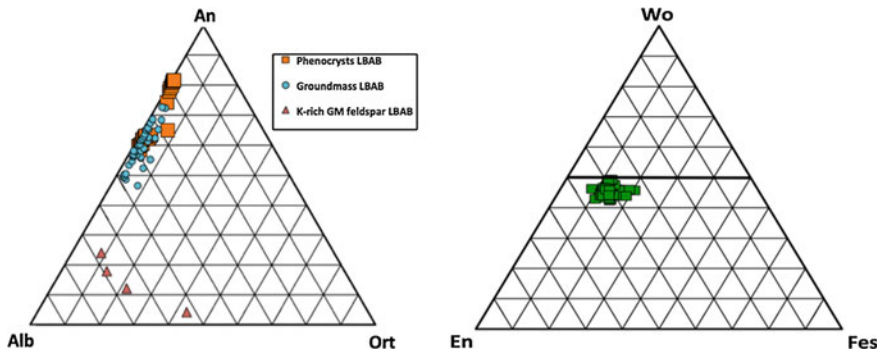
Fig. 5.8 Mineral compositions from LL and LB samples from the LBAB series: *Left* plagioclase with groundmass and phenocryst data; *Right* clinopyroxene phenocryst compositions. Data after Hesse (2007)

Cr-Al-rich spinel phases included in the Mg-rich olivines was discussed by Hesse (2007) and Varekamp et al. (2010). Plagioclase phenocryst compositions range from 60 to 82 % An, whereas the groundmass crystals range from 50–72 % An. A few flows have K-rich groundmass feldspars with up to 43 % Or (Fig. 5.8). The plagioclase microphenocrysts overlap in composition in several flows with ground mass plagioclase compositions and most likely are late-stage crystals. The clinopyroxene compositions have a narrow compositional range in the diopsitic augite field (Fig. 5.8), with relatively high non-quadrilateral components (2–8 % Al_2O_3, up to 3 % TiO_2).

5.10 Geochemistry of the CCVC and LBAB Rocks

5.10.1 Major Elements

The CCVC rocks form a calc alkaline suite (Varekamp et al. 2006) with distinct differences between Copahue and Caviahue rocks. Major element analyses of the Copahue rocks show a limited compositional range from 54–61 % SiO_2 and 2.2–4.8 % MgO and they form a high-K calc-alkaline series running from basaltic andesite to trachyandesite (Table 5.3; Figs. 5.9 and 5.10). The samples from the Caviahue caldera walls have 52–74 % SiO_2 and 1–5 % K_2O and

form a suite from basalts to basaltic andesites to trachyandesites, trachydacites and rhyolites. These rocks are a medium-K calc-alkaline series (Fig. 5.10), although many samples plot just in the arc tholeiite field on a Miyashiro diagram (Todd 2005). The LBAB have a wide range in MgO (4–10 %) and form a suite of basalts to basaltic trachyandesites.

Local chemical variations between the three suites show the following at similar MgO level: Copahue rocks are lower in Fe and Ti compared to the Caviahue series but enriched in K and Ca. The LBAB samples are enriched in K and Ti but relatively depleted in Al_2O_3 and CaO compared to the CCVC rocks (Fig. 5.11).

The chemical composition of the Copahue 2012 and 2000 eruptive products have only minor differences. The 2012 rocks are slightly less evolved than the 2000 scoria: higher in MgO, CaO, Fe_2O_3, Al_2O_3 and lower in SiO_2. The 2000 and 2012 samples were run simultaneously with the same standards on the Wesleyan University WD-XRF, so these small differences are probably real. The 2012 products are the most mafic rocks of the whole Copahue series ($\sim$800,000 years sequence; Goss 2001).

The more mafic endmembers of the Riscos Bayos pyroclastic flows overlap in composition with many of the lava flows of the Caviahue series, but the bright white top unit (RB3 of Varekamp et al. 2006) is a rhyolite (with quartz and biotite) and quite distinct from all other

Table 5.3 Normalized anhydrous major element compositions of Copahue rocks (samples with < 1.5 % LOI)

Sample ID	SiO$_2$	Al$_2$O$_3$	MgO	Na$_2$O	Fe$_2$O$_3$	TiO$_2$	CaO	K$_2$O	MnO	P$_2$O$_5$
JM 1995	58.19	16.63	3.40	3.78	7.78	1.24	6.65	2.00		0.33
COP1 2000	55.29	17.24	4.09	3.94	8.98	1.21	7.26	1.98	0.15	0.33
COP3 2000	55.26	17.14	4.31	4.10	8.72	1.22	7.23	2.02		0.31
CE2000 B	55.77	17.13	4.23	3.57	8.33	1.16	7.42	1.94	0.13	0.31
CE2000 C	55.68	16.98	4.16	3.93	8.36	1.17	7.30	1.98	0.13	0.31
CM 1 2012	55.31	17.26	4.28	3.54	8.61	1.19	7.50	1.86	0.14	0.29
CM 4 2012	54.65	17.35	4.50	3.56	8.76	1.19	7.69	1.86	0.15	0.29
CM 5 2012	54.43	17.39	4.59	3.48	8.99	1.21	7.57	1.89	0.15	0.30
SC 1 2012	53.91	17.20	4.67	3.88	9.08	1.19	7.71	1.88	0.15	0.30
CE2012 B	54.65	17.58	4.40	3.46	8.73	1.18	7.77	1.81	0.14	0.28
CE2012 C	55.38	17.51	4.24	3.25	8.58	1.18	7.64	1.80	0.14	0.28
CE2012 D	54.54	17.42	4.36	3.33	8.94	1.20	7.89	1.88	0.15	0.29
8-271199	55.55	17.82	3.70	4.21	8.86	1.17	6.95	1.73	0.12	0.30
4-281199	56.95	17.28	3.69	3.85	7.98	1.13	7.11	2.01	0.14	0.29
8-261199	58.29	17.53	3.08	4.34	6.96	1.14	6.16	2.51		
4-271199	59.56	16.87	2.87	4.31	7.15	1.19	5.24	2.81		
7-271199	61.30	16.76	2.39	3.73	7.08	1.20	4.55	2.99		
CL563[a]	56.97	16.62	3.86	4.02	10.26	1.37	6.36	2.25	0.14	0.38

[a]Sample and analyses from Jacques et al. (2013)

Fig. 5.9 Classification diagram for the CCVC and LBAB rocks, with members of the Riscos Bayos ignimbrite series in the rhyolite field. The Copahue rocks are largely basaltic trachyandesites to trachy-andesites (After LeBas et al. 1991)
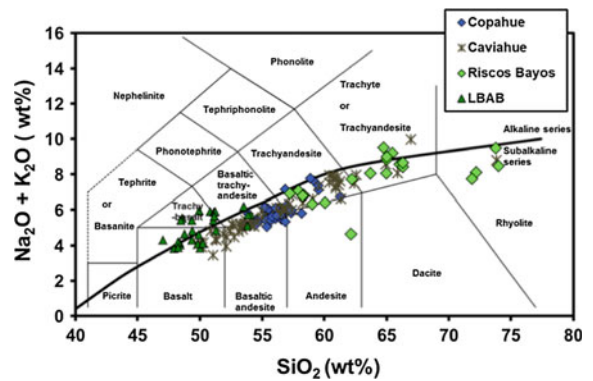
Fig. 5.10 Classification diagram, with the Copahue rocks straddling the medium K-high-K border. Samples with MgO > 3.5 % shown only
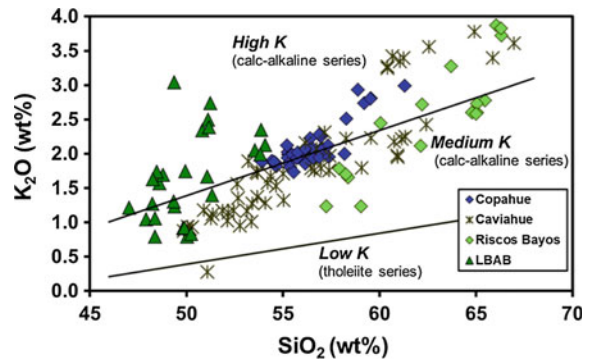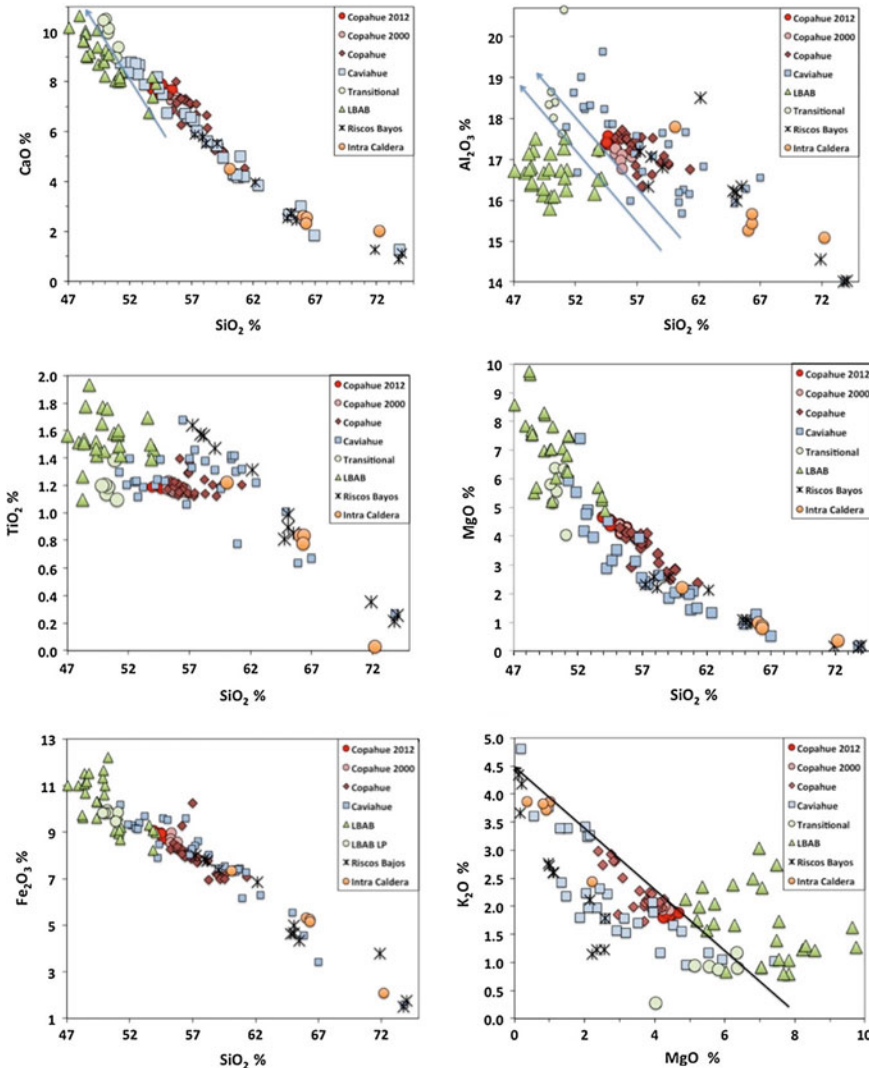
Fig. 5.11 Major element variation diagrams with the volcanic stratigraphic units. The *arrows* separate the back arc basalts from the arc rocks. Note the small differences in the products of the 2000 and 2012 eruptions. The RB samples plot largely with the Caviahue series, except for the rhyolitic members (RB3) of which one sample overlaps with a pumice sample from the eastern caldera wall

flows. A pumice sample collected from the top of the eastern Caviahue caldera wall has a very similar composition as the RB3 units, suggesting a genetic connection between the Riscos Bayos ignimbrites and the Caviahue volcano.

The LBAB samples were described in detail by Hesse (2007) and Varekamp et al. (2010). The LP series of the LBAB rocks (samples taken north of Loncopue) are chemically transitional between the Caviahue and LBAB series, plotting alternately with each group in the different diagrams. These five samples of cinder cones and small lava flows occur east of the Caviahue caldera along the northern extension of the Loncopue graben and have Ca, Fe and Al similar to the Caviahue series, but K and Ti like the LBAB.

The "evolved" LP samples of Varekamp et al. (2010) are lava flows that belong to the top of the Caviahue sequence and are here plotted with the Caviahue series.

5.10.2 Trace Elements

Trace element concentrations in the CCVC and LBAB samples vary widely (Table 5.4), with the following systematics: the LILE (large ion lithophile elements) such as Rb, U, Th, Ba, and Cs and the HFSE (high field strength elements; Nb, Ta, Hf, Zr) are enriched in the Copahue rocks compared to the Caviahue series at similar MgO levels.

Many LBAB samples show still greater enrichments in these elements compared to the CCVC suite. The compatible elements Cr, Ni and Co are low in all CCVC samples but present in much higher concentrations in the more mafic LBAB suite. A clear grouping of the three rock suites (Copahue, Caviahue, LBAB) emerges in most MgO vs trace element diagrams (Fig. 5.12). The Copahue 2000–2012 rocks have the lowest Rb, Ba, Zr and Y with respect to the older Copahue rocks. The silicic RB and the dacitic-rhyolitic intra caldera samples have the highest LILE concentrations of the Caviahue series.

A relative abundance diagram for trace elements (Fig. 5.13) at 4.5–5 % MgO shows the characteristic Nb-Ta depletions in all CCVC samples, but these are much less pronounced or absent in the LBAB samples. Some LBAB have overall slightly lower incompatible trace element concentrations than the CCVC rocks, but also many samples with anomalously high concentrations. Most samples have negative P and Ti anomalies and extreme Sr depletion in the RB sample.

The REE analyses of Copahue samples are shown in Table 5.5. The chondrite normalized REE diagram (at 4.5 % MgO) shows LREE enrichment in all rocks but variable patterns in the HREE (Fig. 5.14). The LBAB rocks have sloping HREE trends whereas the CCVC rocks have flatter HREE. The arc rocks all have strong negative Eu anomalies whereas the LBAB lack these, in agreement with the absence of modal plagioclase in most of them. The Copahue rock sample has a stronger LREE enrichment than the Caviahue sample, and the LBAB sample has slightly lower overall REE concentrations.

In conclusion, the trace element data confirm the grouping based on major elements into the older Caviahue rocks with lower LILE concentrations compared to the Copahue suite. The mafic end-members of the Caviahue and Copahue series overlap in some binary diagrams with the LBAB suite, whereas in others as well as several element ratio diagrams they occupy completely separate compositional fields. The LP samples plot with the Caviahue series for Ba, Rb, Nb, and Nb/Y. whereas they plot with the LBAB series for the HFSE.

5.10.3 Glass Compositions

The 2012 pumices (CE2012B, most vesiculated material) provided material for precise glass analyses by microprobe (Table 5.6). The quenched liquid in the pumices is presumably the melt that was in equilibrium with some of the mineral phases in these rocks. The available pumice glass analyses are in good agreement for the two microprobe data sets (Bristol University, UK and American Museum of Natural History, NY) and have an andesitic composition with ∼56–57 % SiO_2 (Fig. 5.15). The cinder samples of the 2012 eruption (CE2012C, D) have many glassy veins with no microlites in it, and these tan glasses have more evolved compositions (Table 5.6; Fig. 5.15). Fractionation lines of clinopyroxene and plagioclase are indicated and various degrees of groundmass crystallization may have given rise to these matrix glasses in the denser scoria and cinder samples. The glass veins represent extrusions of groundmass liquid into cracks of crystals, possibly when the cinders started to freeze, filtering out the groundmass crystals. The water concentrations in the pumice matrix glasses ('by difference' method) range from 0.5 to 1.5 % H_2O and the more evolved glasses show a

Table 5.4 Trace element analyses of Copahue rocks

Sample ID	Ba	Sc	Sr	Cs	Th	U	Rb	Cr	Ni	V	Co	Zr	Ta	Hf	Nb	Pb
JM 1995	500		490	5	10	2.2	79				19.9	226	0.7	8	7	21
COP1 2000	446		488	4	10.7	2.6	60				26.9	194			10	14
COP3 2000	376		404	3	7.9	2.1	56				21.1	179	0.5	5	6	12
CE2000 B	440	23	496	3	8.8	2.4	60	45	23	185	28.1	215		6	8	17
CE2000 C	430	22	499	3	8.6	2.3	59	45	26	182	25.7	199		5	8	16
CM 1 2012	413	19	499				56	41	22	195		203			9.3	13
CM 4 2012	416	26	509				57	47	26	206		202			9.3	13
CM 5 2012	411	18	492				56	42	27	206		200			8.2	12
SC 1 2012	408	26	496				55	52	27	207		196			9.3	13
CE2012 B	430	23	496	3	8.6	2.2	54	48	29	204	28.1	190		5	7	17
CE2012 C	440	23	499	3	8.3	2.2	54	53	27	202	25.7	201		5	7	16
CE2012 D	410	23	487	3	8.5	2.3	56	48	29	196	24.6	211		5	7	16
8-271199	441		545	2	9	1.6	48				24.8	200		7	12	18
4-281199	503		543	4	8	2	68				22.3	188	1.5	7	7	19
8-261199	546		545	3	12	2.8	94				16.3	253	2.1	9	12	20
4-271199	625		443	6	12	3	107				15.2	303	1.1	9	14	21
7-271199	633		411	4	14	2.9	116				14.1	315	0.8	10	15	27
CL563[a]	512		464	4	9.7	2.5	68				25.3	269	0.6	6.3	9.4	14

[a]Sample and analyses from Jacques et al. (2013)
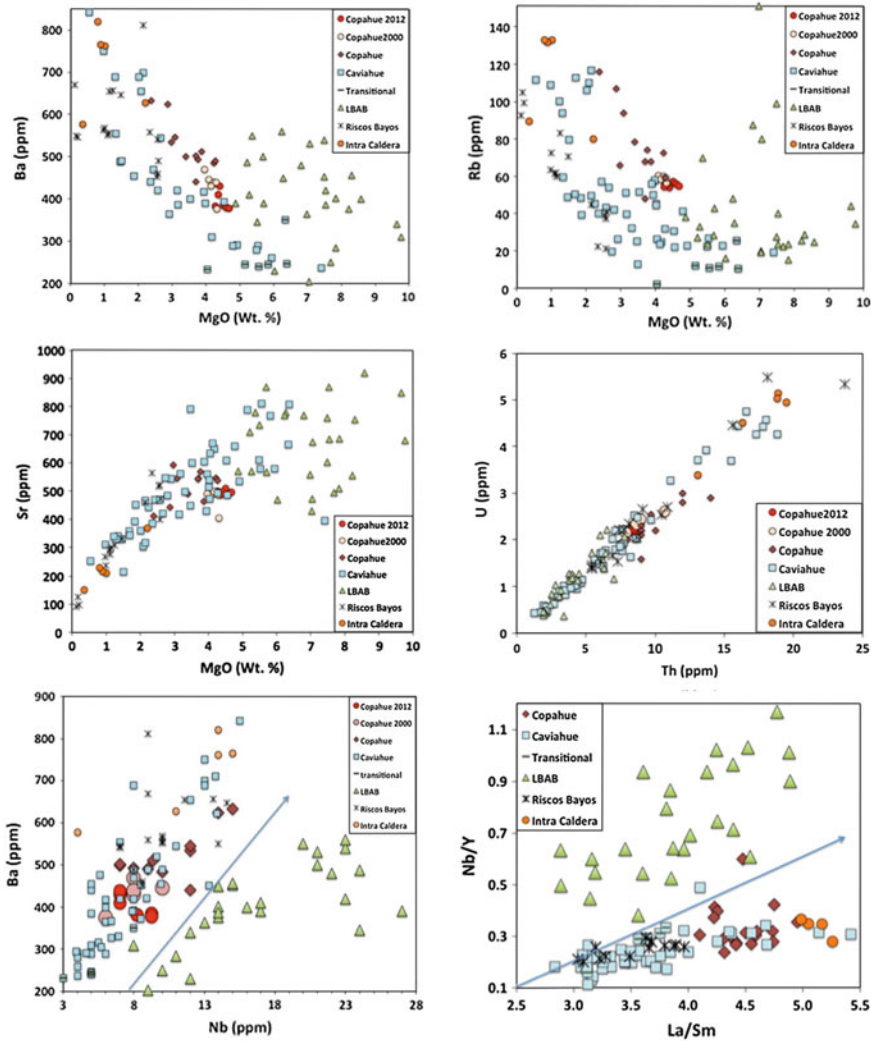
Fig. 5.12 *Top left* and right MgO versus Ba and Rb. The Copahue rocks are enriched in Ba and Rb relative to the Cavahue samples, while the LBAB show a wide range. Note the small differences in the 2000 and 2012 eruption products; *Mid-left* wide range of Sr concentrations in LBAB, with decreasing Sr with decreasing MgO. The rhyolites have the lowest Sr concentrations; *Mid-right* near constant U/Th raios in the three suites; *Bottom left* Ba-Nb, showing a sharp distinction between the LBAB and the CCVC rocks. The transitional rocks plot with the Caviahue series; *Bottom right* La/Sm versus Nb/Y, showing a sharp separation between the LBAB and CCVC rocks. The LBAB and CCVC have similar range of La/Sm, whereas the LBAB have much higher Nb/Y values. The Copahue samples have higher La/Sm than the Caviahue samples. The RB3 samples plot outside the graph to the *right*. *Lines* separate fields for LBAB and CCVC samples

similar range. The 2012 bulk rock values plot on a plagioclase fractionation line in Fig. 5.15, which is reasonable given that plagioclase is modally the dominant phase.

Matrix glasses of the 2000 cinders (no pumice available) show a comparable compositional range as the 2012 matrix glasses of scoria and cinders. Glass inclusions in olivine and
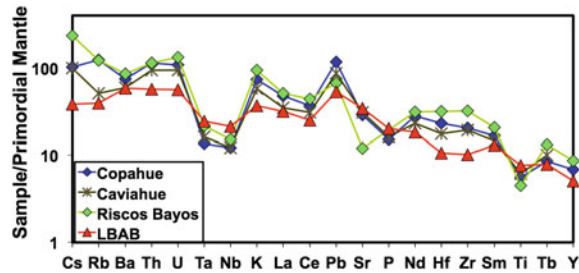
Fig. 5.13 Relative abundance diagram with strong Nb-Ta anomalies for the arc rocks, less deep anomalies for the LBAB, which also have slightly lower overall trace element concentrations. Normalization after McDonough and Sun (1995)

plagioclase of the 2000 scoria (Goss 2001) show relatively low and variable water contents (by difference method), up to 1.5 % H_2O.

The Cl concentrations in glass inclusions in plagioclase from rocks from the 1995 eruption range from 1115 to 1650 ppm (Goss 2001), and glass inclusions in plagioclase from the samples from the 2000 and 2012 eruptions carry 1250–1840 ppm Cl (Table 5.7). The 2012 pumice groundmass glass has 1010–1150 ppm Cl in one sample and 50–590 ppm Cl in another, more vesicular part of the same sample (Fig. 5.15).

The overall range of Cl concentrations in glasses shows a positively correlated array with K_2O, except for the small group of low-Cl pumice matrix glasses. The latter probably represent the inflated cores of pumice clasts that have undergone syn-eruptive degassing, whereas the higher Cl concentrations were measured in the quench rims of the pumice clasts. The sulfur concentrations range from 100 to 600 ppm in glass inclusions and matrix glass, with no simple systematics. The data suggest that part of the crystallization may have happened when magma was already degassing, given the overlap in volatile concentrations in inclusions and matrix glasses.

5.10.4 Radiogenic Isotope Ratios in CCVC Rocks

Twenty eight rocks from Copahue, Caviahue and back arc rocks have data for $^{87}Sr/^{86}Sr$,

$^{143}Nd/^{144}Nd$ and the three radiogenic Pb isotope ratios (Table 5.8). Some of these data have not yet been published, others are from the literature (see footnotes). The Copahue rocks have Sr isotope ratios (Table 5.8) that range from 0.703820 to 0.703954, whereas the Caviahue rocks show a wider range (0.703295–0.704122). The Riscos Bayos ignimbrites fall in the same range as the Caviahue rocks. The LBAB samples are isotopically not distinct and have the widest range of Sr isotope ratios (0.703511–0.704599). No systematic relationships exist between degree of magmatic evolution and Sr isotope ratios for any of these suites. The Nd isotope ratios plot in a linear array with the Sr isotope values (Fig. 5.16), with again the widest range in the LBAB samples. The Copahue 2000 scoria are among the isotopically most evolved of the Copahue series with the highest $^{87}Sr/^{86}Sr$ while chemically being the least evolved (Figs. 5.11 and 5.12). The Pb isotope compositions of the Copahue rocks show a limited range (Fig. 5.16), but are at the high end of all samples analyzed from the region. A wider Pb isotope range is encountered for the Caviahue samples, but with generally lower Pb isotope ratios. The RB samples plot at the high end of the Caviahue range in all Pb isotope diagrams. The widest range in Pb isotope ratios is found again in the LBAB samples, which overlaps for $^{206}Pb/^{204}Pb$ with the Caviahue and Copahue rocks, with a tail to low $^{206}Pb/^{204}Pb$ ratios.

The transitional samples plot with the LBAB samples in the low $^{206}Pb/^{204}Pb$ tail, well away

Table 5.5 REE and Yttrium analyses of Copahue rocks

Sample ID	La	Ce	Pr	Nd	Sm	Eu	Gd	Tb	Dy	Ho	Er	Tm	Yb	Lu	Y
JM 1995	29	62.7	8.1	33.8	6.2	1.7	6.5	0.9	5.8	1	3.1	0.4	2.8	0.4	25
COP3 2000	23	50.6	6.54	29.3	5.4	1.3	4.8	0.71	4.5	0.93	2.8	0.36	2.4	0.36	25
CE2000 B	28	60	7.07	28.7	6.1	1.57	5.71	0.87	5.13	0.99	2.9	0.4	2.7	0.4	26
CE2000 C	26.2	57.2	6.73	27.5	5.7	1.52	5.5	0.83	4.77	0.96	2.76	0.4	2.5	0.4	25
CE2012 B	24.2	54.7	6.5	26.6	5.5	1.52	5.43	0.81	4.73	0.95	2.74	0.39	2.6	0.38	25
CE2012 C	24.1	54	6.34	26.1	5.6	1.53	5.19	0.79	4.68	0.93	2.66	0.36	2.6	0.37	24
CE2012 D	25.2	57.1	6.73	27.3	5.7	1.57	5.48	0.84	4.96	0.96	2.8	0.4	2.7	0.4	25
8-271199	30	61.3	8.8	37.9	7	1.9	6.4	0.9	5.9	1.1	3.4	0.5	3.3	0.4	29
4-281199	26	52.1	7.8	30.6	5.8	1.6	5.3	0.9	5.4	1	3.1	0.5	3.2	0.3	26
2-271199L	27	58.5	7.8	31	6.3	1.6	6	0.9	5.7	1	3.3	0.4	2.8	0.4	30
8-261199	38	80	11.6	44.3	8.9	1.8	7.4	1.1	6.6	1.2	4	0.5	3.3	0.5	32
4-271199	38	75.2	10.3	41.3	8	1.7	7.4	1	6.4	1.2	3.9	0.4	3	0.5	33
7-271199	27	56.5	7.5	32.2	6.1	1.7	5.1	0.7	5.3	1	3.3	0.5	2.7	0.4	25
CL563	30	65.5	8.46	35	7.22	1.62	6.63	0.98	5.65	1.12	3.03	0.45	2.95	0.44	31
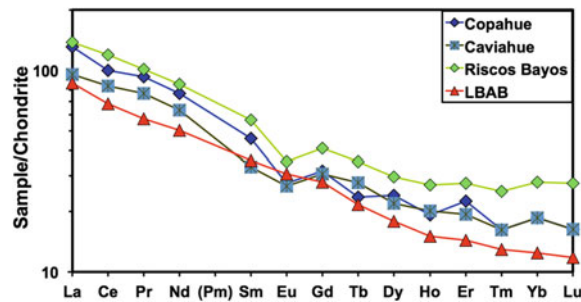
Fig. 5.14 Chondrite-normalized relative abundance diagrams for the REE

Table 5.6 Representative matrix glass analyses by microprobe (Bristol University, UK) of samples CE2012 B (MG of pumice), C and D (glass veins in scoria and cinder)

SAMPLE	SiO$_2$	Al$_2$O$_3$	MgO	CaO	FeO	TiO$_2$	Na$_2$O	K$_2$O	P$_2$O$_5$	H$_2$O
CE2012B	56.9	15.4	3.2	6.4	8.4	1.7	3.5	2.6	0.4	1.2
CE2012B	55.7	15.4	3.4	6.4	8.9	1.7	3.8	2.5	0.5	1.5
CE2012D	58.0	15.2	1.4	5.1	9.3	2.3	4.0	3.6	0.5	0.3
CE2012D	59.5	15.1	1.0	4.0	8.1	2.3	4.1	4.2	0.6	0.6
CE2012D	60.2	15.1	1.0	4.0	8.2	2.3	2.9	4.3	0.6	1.1

H$_2$O contents are 'by difference'

from the Caviahue grouping. The Copahue samples have a well defined field in the ^{207}Pb/^{204}Pb versus ^{206}Pb/^{204}Pb diagram (Fig. 5.16), with the Caviahue samples in their own field at slightly lower values and the LBAB showing a wide field, but rather distinct from the other two series.

The Copahue samples have a distinct field in the ^{208}Pb/^{204}Pb versus ^{206}Pb/^{204}Pb diagram (Fig. 5.16), whereas the Caviahue and LBAB samples show a fair degree of overlap. Lead isotope ratios measured in the acid hydrothermal fluids of Copahue are similar to the isotope data from the 2000 rock sample (Varekamp et al. 2006). The 2000 Copahue sample is isotopically the most radiogenic rock of Copahue volcano with the highest ^{206}Pb/^{204}Pb and ^{208}Pb/^{204}Pb and also the samples with the highest Pb isotope ratios of the whole CCVC area. The ^{87}Sr/^{86}Sr versus ^{206}Pb/^{204}Pb graph (Fig. 5.16) shows a low ^{206}Pb/^{204}Pb field with the LBAB and transitional samples, but with a wide range of Sr isotope ratios. The more radiogenic LBAB samples fully overlap with the Caviahue and Copahue samples.

There are no simple relationships between major or trace elements with the radiogenic isotope ratios, and the various potential mixing endmembers involved in the magma genesis are discussed later on.

The Nd isotope ratio versus ^{206}Pb/^{204}Pb diagram (Fig. 5.17) shows a data array along a mixing curve drawn between the endmembers of MORB mantle (Vermeesch 2006) and subducted sediment (Pacific Detrital Sediment, PDS, Kilian and Behrmann 2003). Several of the LBAB and one transitional sample do not plot within this array but are offsett towards low ^{206}Pb/^{204}Pb (green arrows), suggesting a third endmember for those magmas (Varekamp et al. 2010).

The He isotope ratios of the Copahue magmatic system were measured in 2003 in the volcano hydrothermal fluids (Rs/Ra = 6.7; Varekamp et al. 2006) and are slightly more radiogenic than average MORB values ($\sim$8). Measurements on the ^{129}I composition of the acid waters from Copahue (Fehn et al. 2004) indicate the presence of a subducted sediment component in the Copahue magmatic fluids, in
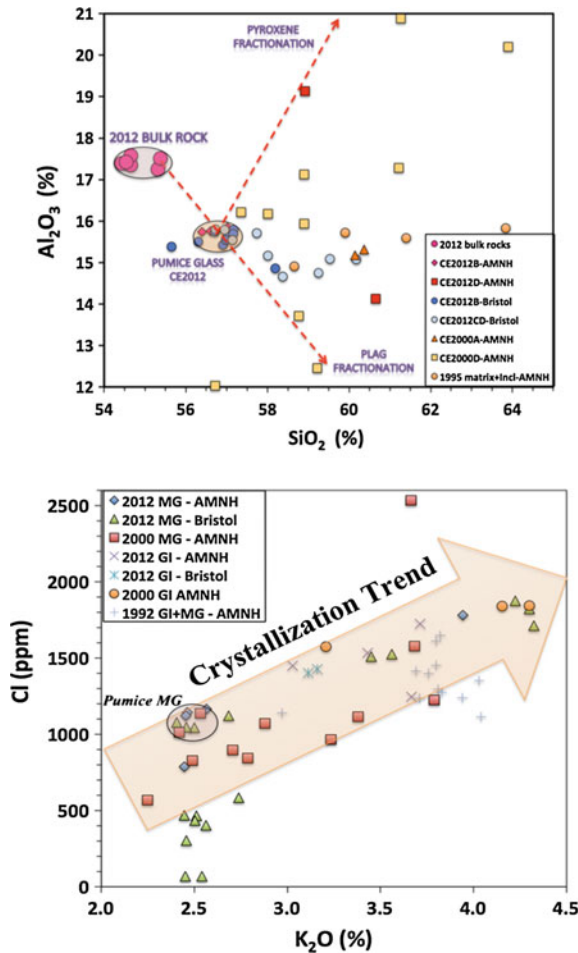
Fig. 5.15 *Top* Microprobe (AMNH, NY and Bristol University, UK) glass analyses of 2012 eruption products (MG = matrix glass; GI = glass inclusion; CE2012B = pumice; C, D are scoria) and CE2000 eruption products (CE2000A, D—cinders). Glass inclusion data and matrix glasses from the 1995 eruption are shown as well. The 2012 bulk rock data plot on the plagioclase fractionation line with the MG; *Bottom* Microprobe glass analyses for the incompatible elements K and Cl. The pumice matrix glasses (MG) have ∼1000–1150 ppm Cl at 2.5 % K$_2$O, and the remainder of the glasses plots on a fractionation trend (*large arrow*) as a result of groundmass crystallization of mainly plagioclase and pyroxene. The MG with 50–500 ppm Cl (*green triangles*) represents more degassed glasses that presumably lost volatiles during the eruption

broad agreement with the radiogenic and He isotope data discussed above.

5.11 Regional Comparisons

The CCVC and LBAB volcanic centers are positioned east of the main Andes arc in Chile. In this section, data from the Andean volcanoes Llaima, Tolhuaca, and Callaqui were compared with those from the CVCC and LBAB suites (Fig. 5.1). Of the modern arc volcanoes, Llaima is closest to the trench, followed by Tolhuaca-Callaqui, and then Copahue, the farthest east from the trench (Fig. 5.3). The Caviahue suite resembles the modern Andes suite in many respects (Varekamp et al. 2006) but its geographic position with respect to the trench is not directly comparable to that of the active volcanoes in Chile because of the presumably shallower subduction angle at 5 Ma.

Table 5.7 Cl-S data (microprobe analyses) for glasses from the 2000 and 2012 scoria

Sample	Glass type	SiO$_2$	Cl	S
CE2000A	Matrix glass (with microlites)	60.1	1115	41
CE2000A	Matrix glass (with microlites)	60.4	2535	99
CE2000D	Matrix glass (with microlites)	56.7	828	426
CE2000D	Matrix glass (with microlites)	61.2	896	225
CE2000D	Matrix glass (with microlites)	59.2	1224	
CE2000D	Matrix glass (with microlites)	61.3	569	
CE2000D	Matrix glass (with microlites)	63.9	964	
CE2000D	Matrix glass (with microlites)	58	1070	36
CE2000D	Matrix glass (with microlites)	58.9	1136	22
CE2000D	Matrix glass (with microlites)	58.9	843	54
CE2000D	Matrix glass (with microlites)	57.4	1012	92
CE2000D	Matrix glass (with microlites)	58.8	1577	137
CE2012B	Matrix glass pumice	56.4	1164	129
CE2012B	Matrix glass pumice	56.6	1143	178
CE2012B	Matrix glass pumice	57	1121	69
CE2012B	Bubble wall	57	301	566
CE2012B	Bubble wall	56.3	466	545
CE2012B	Bubble wall	56.7		547
CE2012B	Bubble wall	56.9	402	559
CE2012B	Glass rim	55.6	435	495
CE2012B	Bubble wall	57.2	467	570
CE2012B	Bubble wall	57	67	545
CE2012B	Dark glass	58.2	585	765
CE2012B	Dark glass	57.2	67	558
CE2012D	Matrix glass	58.9	786	60
CE2012D	Matrix glass	60.7	1780	19
CE2012D	Glass vein	58	1526	175
CE2012D	Glass vein	58.4	1510	184
CE2012D	Glass vein	59.5	1875	201
CE2012D	Glass vein	60.2	1711	201
CE2012D	Glass vein	59.3	1823	168
CE2012C	Glass patch	57.1	1044	
CE2012C	Glass patch	56.7	1047	75
CE2012C	Glass patch	57.7	1077	

SiO$_2$ concentrations are in %, Cl and S concentratons are in ppm

The trace element relative abundance diagram (at ~4 % MgO; Fig. 5.18) for the various arc volcanoes shows roughly similar patterns for these magmas, with the lowest concentrations at Llaima and the highest at Copahue. The LBAB samples show less deep negative Nb and Ti anomalies. All rocks show typical arc patterns although the LBAB patterns are overall flatter.

Table 5.8 Radiogenic isotope ratios in CCVC and LBAB rock samples

Suite	Sample ID	$^{87}Sr/^{86}Sr$	$^{143}Nd/^{144}Nd$	$^{206}Pb/^{204}Pb$	$^{207}Pb/^{204}Pb$	$^{208}Pb/^{204}Pb$
Copahue						
	COP3[c]	0.703954	0.512795	18.593	15.606	38.502
	1-251199[a]	0.703820	0.512836	18.576	15.599	38.446
	CL563[e]	0.703922	0.512780	18.589	15.611	38.501
	8-261199[a]	0.703854	0.512814	18.584	15.600	38.465
	7-271199[a]	0.703871	0.512771	18.578	15.602	38.467
Caviahue						
	EB8[c]	0.703781	0.512846	18.557	15.598	38.435
	LPE3[d]	0.703886	0.512788	18.581	15.596	38.452
	E5a[b]			18.544	15.599	38.426
	F9a[b]			18.563	15.593	38.408
	C5b[b]			18.567	15.600	38.447
	C1a[b]			18.578	15.599	38.430
	G1a[b]			18.547	15.599	38.430
Transitional						
	AE3D[c]	0.703295	0.512928	18.485	15.570	38.268
	AH-4[d]	0.704122	0.512768	18.532	15.597	38.434
	AH-5[d]	0.703713	0.512857	18.530	15.581	38.354
Riscos Bayos						
	RB1-1[c]	0.703776	0.512849	18.554	15.600	38.440
	RB1-4[c]	0.703783	0.512854			
	RB2-1[c]	0.703761	0.512857	18.560	15.602	38.449
	RB3-2[c]	0.703985	0.512823	18.558	15.607	38.461
	IGN-A[b]			18.551	15.600	38.436
	VC-13[b]			18.554	15.603	38.442
Callaqui						
	CA-3[a]			18.580	15.598	38.458
	CA-7[a]			18.626	15.596	38.467
	CA-1[a]			18.580	15.596	38.454
	CA-6[a]			18.580	15.600	38.465
	CA-8b[a]			18.483	15.591	38.370
LBAB						
	AH-9[a]	0.703844	0.512800	18.527	15.589	38.383
	AH-11[d]	0.703511	0.512857	18.563	15.583	38.377
	AH-13[d]	0.703724	0.512830	18.435	15.569	38.275
	AH-15[a]	0.704599	0.512630	18.530	15.595	38.393
	AH-16[d]	0.703933	0.512758	18.593	15.592	38.456

(continued)

Table 5.8 (continued)

Suite	Sample ID	$^{87}Sr/^{86}Sr$	$^{143}Nd/^{144}Nd$	$^{206}Pb/^{204}Pb$	$^{207}Pb/^{204}Pb$	$^{208}Pb/^{204}Pb$
	AH-17[d]	0.704332	0.512729	18.547	15.590	38.433
	AH-18[d]	0.703863	0.512798	18.582	15.586	38.410

[a]New, analyzed at University of Florida by MCICPMS. Typical internal precision for Sr and Nd isotopes was similar to results for standard solutions as reported on Table 5.2. Internal precision for Pb isotopes was typically 0.001, 0.001, and 0.002 for $^{206}Pb/^{204}Pb$, $^{207}Pb/^{204}Pb$, and $^{208}Pb/^{204}Pb$

[b]New, analyzed at UCSC around the same time as results presented in Todd et al. (2011). Analytical methods and performance provided therein

[c]Varekamp et al. (2006); Analytical methods and performance provided therein

[d]Varekamp et al. (2010); Analytical methods and performance provided therein

[e]Sample and analyses from Jacques et al. (2013)
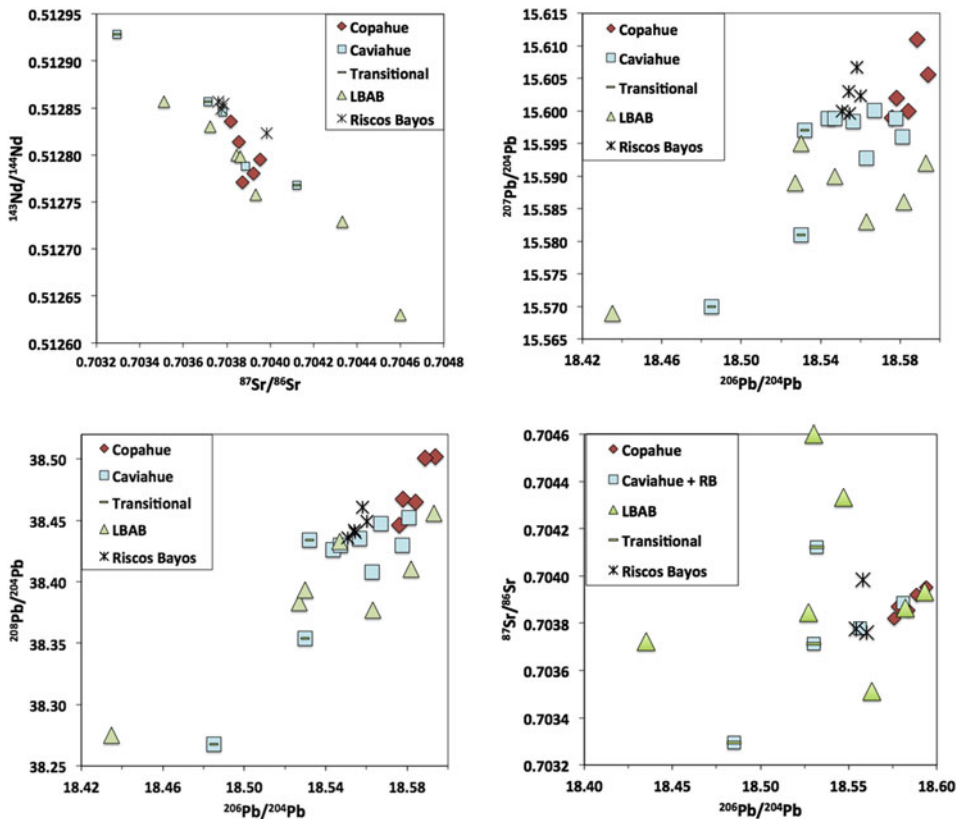
Fig. 5.16 Isotopic compositions of CCVC and LBAB rocks. *Top left*: Sr and Nd isotope ratios, showing a linear array with full overlap of LBAB values with CCVC; *Top right* $^{206}Pb/^{204}Pb$ versus $^{207}Pb/^{204}Pb$, showing the low $^{206}Pb/^{204}Pb$ group (LBAB +transitional), the high ratios for Copahue rocks and intermediate values for Caviahue and Riscos Bayos samples; *Bottom left* $^{206}Pb/^{204}Pb$ versus $^{208}Pb/^{204}Pb$ which shows a similar pattern as $^{206}Pb/^{204}Pb$ versus $^{207}Pb/^{204}Pb$; *Bottom right* $^{206}Pb/^{204}Pb$ versus $^{87}Sr/^{86}Sr$ with overlap between LBAB, Copahue, RB and Caviahue samples, with the low $^{206}Pb/^{204}Pb$ samples with a wide range of Sr isotope ratios

This diagram is expanded upon by plotting the depth of the Nb anomaly (Nb measured) divided by Nb*, the latter value recalculated from linear extrapolation between K and U in the spider diagram) in Fig. 5.18 against Ba/Nb (Fig. 5.19). The Llaima and Tolhuaca samples have high
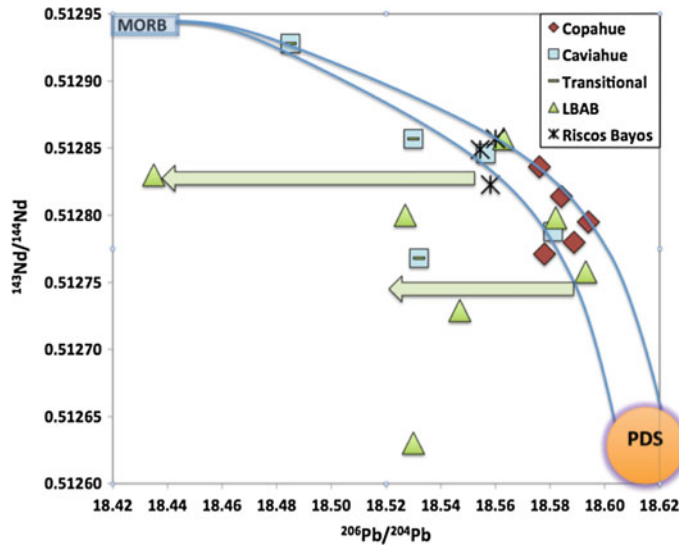
Fig. 5.17 The ^{206}Pb/^{204}Pb versus Nd isotope ratio diagram shows Copahue and Caviahue samples that plot along a gently curved trend, symbolized by an envelope of mixtures of subducted sediment (PDS) and MORB mantle (Vermeesch 2006). Four of the LBAB and one transitional sample (*blue box* with *green strip*) plot outside this array at lower Pb isotope ratios
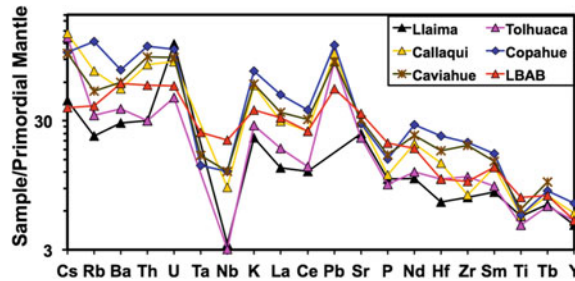
Fig. 5.18 Regional variations in trace element patterns from Llaima to LBAB

Fig. 5.19 Across arc trends with decreasing Nb anomalies with increasing depth to the Benioff zone. The Ba/Nb values also drop from Llaima to Caviahue to LBAB
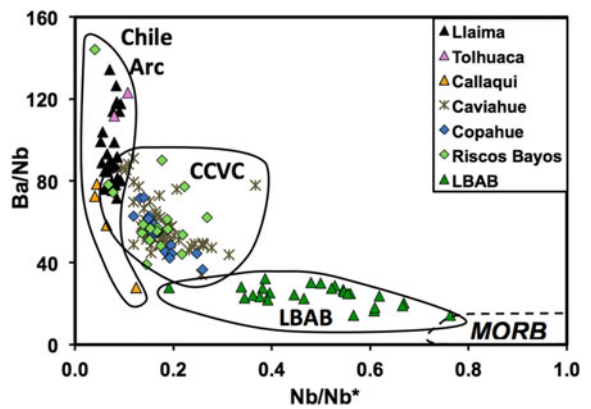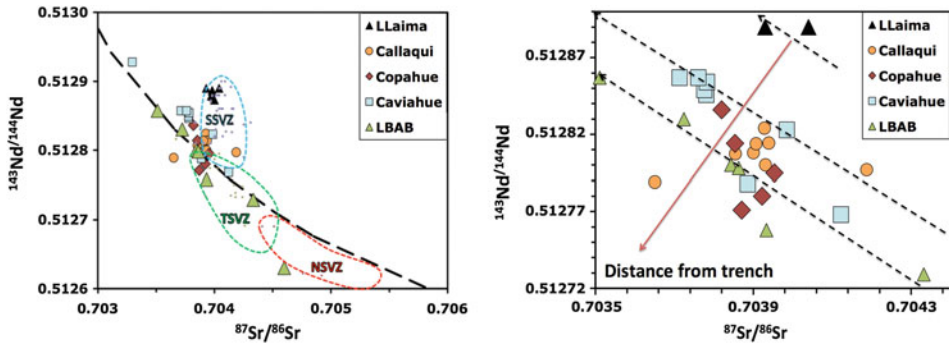
Fig. 5.20 *Left* The Sr–Nd isotope graph shows the wide array of compositions among the studied samples, ranging from NSVZ to SSVZ characteristics, with outlying data from Llaima and Callaqui above the MORB-PDS mixing curve and some data below this curve; *Right* trend from Llaima to LBAB (distance to trench or depth to Benioff zone) with lower $^{143}Nd/^{144}Nd$ at similar or slightly lower

$^{87}Sr/^{86}Sr$. The *dashed line* segments portray different mixing lines connecting the same endmembers but with different degree of curvature as a result of decreased element abundance in the subducted complex as a result of element loss during subduction. *Top line* Sr rich-Nd poor—Llaima; *bottom* Nd enriched

Ba/Nb and a deep negative Nb anomaly, with the Callaqui samples at lower Ba/Nb. With increasing depth to the Benioff zone, the Nb anomaly becomes less negative whereas the Ba/Nb values decrease to 40–90 for the Copahue rocks. The Ba and Nb concentrations in the LBAB are higher than in mafic CCVC rocks, but Ba/Nb is lower (Fig. 5.19).

In the Sr-Nd isotope diagram, the Llaima data plot within the overall field of the SSVZ samples, but well above the CCVC-LBAB array (Fig. 5.20). This is the result of higher Nd isotope values, which are closer to MORB than in the CCVC-LBAB rocks, whereas the Sr isotope values overlap between the two volcanic regions. The Callaqui samples plot close to the Caviahue data, with one sample also above the CCVC-LBAB array, and the tholeiitic dike plots below the array (Rea 2009). The dashed line is a bulk mixing curve between PDS (Killian and Behrmann 2003) and MORB mantle, which covers broadly most of the CCVC, LBAB and Callaqui samples. The LBAB sample AH-15 and the Callaqui dike sample plot below the curve and have a different mix of sources.

A more detailed view of the Sr-Nd isotope diagram of Fig. 5.20 (right) shows a crude trend of samples from Llaima-Caviahue-Callaqui-

Copahue-LBAB that represents depth to the Benioff zone (Fig. 5.20 right). The dashed line segments are different mixing lines between the MORB mantle and the same PDS subducted source, but representing changing concentrations in the PDS endmember as a result of element extraction in the shallower part of the subduction zone. The Nd contributions increase with depth when the element release switches from fluid fluxing to sediment melting. In contrast, progressive loss of Sr from the subducted aggregate may have occurred from the shallow to the deeper part of the subduction zone.

The Pb-Nd isotope diagram (Fig. 5.21) shows two mixing curves: one for Callaqui and Llaima and one for the Copahue-Caviahue samples. The different degree of curvature derives once more from the different amounts of elements released from the subducted complex in the different volcanoes, with high Pb and low Nd contributions below Llaima (fluxing of LIL elements and Pb) and more Nd and less Pb contributions below the Copahue and LBAB centers. The Pb isotope diagram (Fig. 5.22) also shows the mixing array between PDS and MORB mantle, with 1–3 % bulk sediment contribution for most rock samples, and for some of the LBAB well below 1 % sediment contributions.
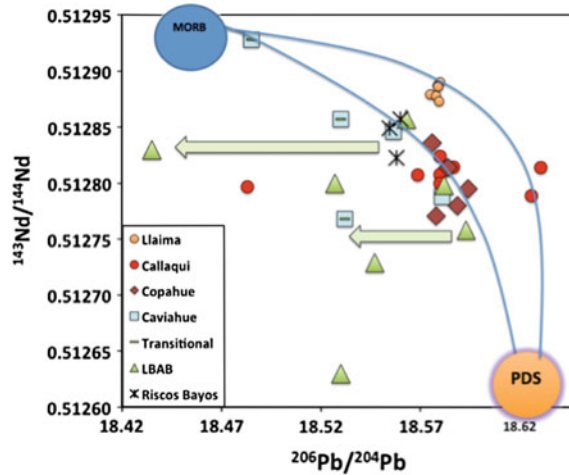
Fig. 5.21 The $^{206}Pb/^{204}Pb$ versus Nd isotope diagram shows two mixing lines using the same endmembers with a more strongly *curved line* connecting the Llaima and some Callaqui data and a less *curved line* for the Copahue and Caviahue data. Some of the LBAB are offset (*green arrows*) as a result of the contributions of the EM1 endmember
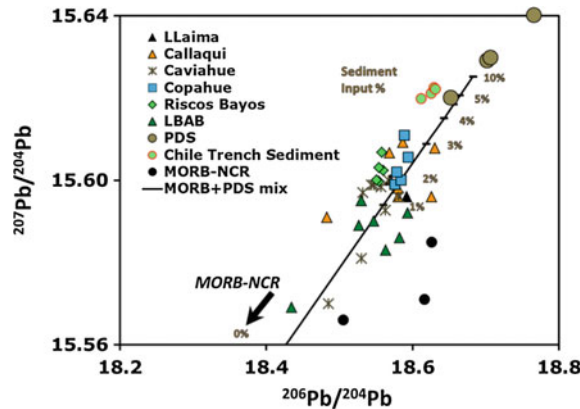
Fig. 5.22 $^{207}Pb/^{204}Pb$ versus $^{206}Pb/^{204}Pb$ isotope diagram with % bulk sediment mixing (PDS) indicated

5.12 Discussion

The chemical and isotope data presented above provide evidence for significant chemical and isotopic differences between the three studied magma suites (Copahue, Caviahue, LBAB). The older Caviahue series resembles the modern southern volcanic zone arc magmas (Varekamp et al. 2006), and has close geochemical similarities with the Callaqui-Tolhuaca rocks. The across-arc compositional variation shows near

trench magmas with lower LIL element concentrations, and their isotope compositions may plot on mantle-sediment mixing lines that are more strongly curved than those of the CCVC and LBAB samples. What are the processes underlying these across-arc trends? Assuming that the more mafic rocks in the CCVC area have limited evidence for crustal assimilation (Varekamp et al. 2006, 2010), the fractionation in elements and isotopes during the subduction process, as well as variations in mantle sources, were considered.
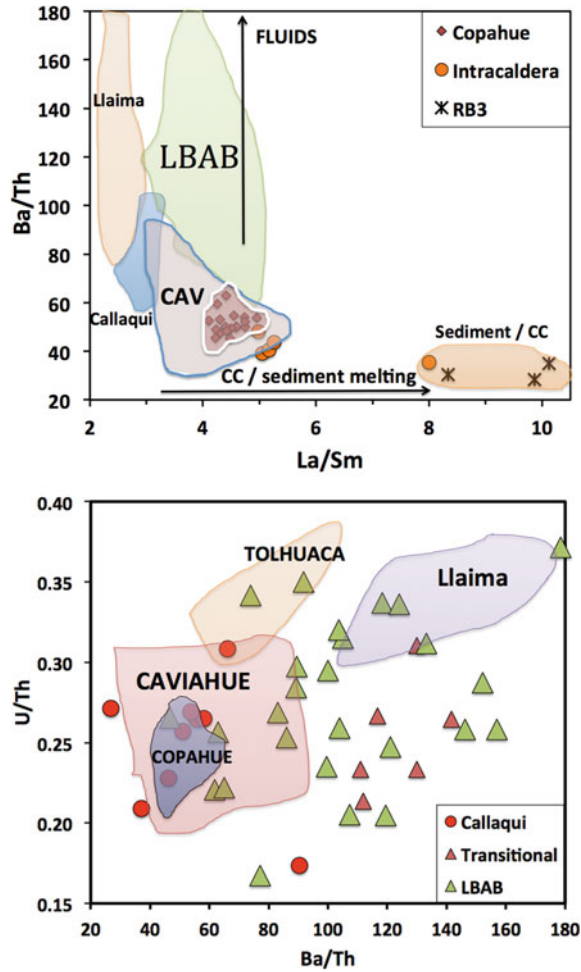
Fig. 5.23 *Top* Trace element ratio diagrams across the arc: La/Sm (indicator for sediment contributions) versus Ba/Th (aqueous fluxes versus melting of sediment). Note the steady increase in La/Sm from Llaima to Tolhuaca to Callaqui to Copahue to the crustal melts and the decrease in Ba/Th as a result of declining aqueous fluxing with depth to the Benioff zone. The LBAB have the La/Sm of the Caviahue rocks but reach Ba/Th comparable to Llaima rocks, suggesting the dual influence of fluid releases and partial melts of subducted sediments in their source regions; BOTTOM: The U/Th versus Ba/Th diagram shows a stepwise decrease in U/Th, suggesting that U is less fluid mobile than Ba. The transitional samples plot with the LBAB sample group, away from the Caviahue samples

The La/Sm versus Ba/Th diagram (Fig. 5.23) shows tight clusters for all the volcano groups. Aqueous fluids will transport Ba, whereas Th is largely mobilized through sediment melting (Labanieh et al. 2010; Plank 2005; Johnson and Plank 1999). The La/Sm value is influenced by the degree of partial melting of the mantle, fractional crystallization in the magma chamber, crustal assimilation, and by the quantity of added components from the subducted slab/sediment. Studies from the Carribean arc have shown that the La/Sm value in arc magmas can be used as a qualitative "sediment melt" (or crustal contamination) indicator, processes that overwhelm the others (Labanieh et al. 2010).

High Ba/Th is found in Llaima rocks, in combination with low La/Sm (large % partial melting, no sediment-partial melt addition). With

increasing depth to the Benioff zone, the La/Sm increases (smaller % partial melting) and possibly the first sediment-melt addition occurs, with less aqueous fluxing.

The Ba/Th values decrease from Llaima to Tolhuaca (Ba depletion in subducted complex, sediment melts have much lower Ba/Th values than aqueous fluids). The Caviahue and Callaqui rocks have still lower Ba/Th and higher La/Sm while Copahue has the highest La/Sm. Extremely high La/Sm values are reached in the silicic intra-caldera rocks and the RB3 rhyolitic ignimbrites, which have the chemistry and mineralogy of magmas with contributions from partial crustal melts. The highest U/Th is found in Llaima and Tolhuaca rocks, with lower values in Caviahue-Copahue (Fig. 5.23, bottom). The LBAB and the transitional samples cover the full range of U/Th and Ba/Th values observed in all other rocks.

The Pearce diagram (Fig. 5.24) shows the relations between mantle melts and magmas contaminated with subducted sediment material (Pearce 1982), using elements that are not aqueous mobile. The LBAB have the smallest contributions of sediment melts, whereas the RB3 ignimbrites and intracaldera rocks have the highest contributions of crustal materials. The Copahue rocks plot further from the mantle line than the Caviahue rocks and presumably have more subducted sediment contributions (as melt extracts) than most Caviahue rocks.

Isotope ratio plots show systematic differences between the near-trench arc rocks and the behind-the-main-arc rocks: the Nd isotope ratio versus $^{206}Pb/^{204}Pb$ (Fig. 5.21) shows two mixing lines using the same isotopic values for the two endmembers, MORB and PDS. The Llaima-Callaqui curve is based on high Pb with low Nd in the PDS endmember whereas the CCVC and LBAB line is based on lower Pb and higher Nd concentrations in the PDS component, providing the different curvatures in the mixing lines. Some LBAB and transitional samples are further impacted by the third (EM1) source component, which displaces them from the binary mixing lines. A similar picture emerged in a Sr-Nd isotope ratio plot (Fig. 5.20), with different mixing lines indicated for Llaima, Callaqui, Caviahue, Copahue and LBAB. There is overlap between the various suites, but nonetheless, there seems to be a trend that can be related to the changing concentrations of these elements (and their isotopes) during subduction in the sediment endmembers.
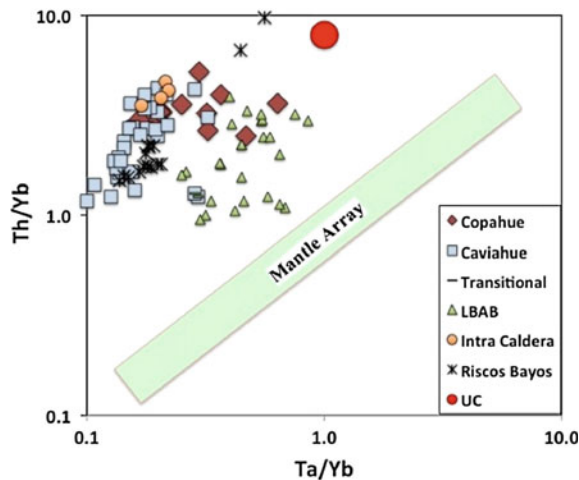
Fig. 5.24 In the Th/Yb versus Ta/Yb diagram (Pearce 1982), the LBAB rocks are near the "within plate volcanic basalt field", with high Th/Yb values in the CCVC rocks at the high end of the Active Continental Margin field (Gorton and Schandl 2000). The Upper Crustal (UC) endmember is after Rudnick and Ghao (2003). The highest Th/Yb ratios occur in the RB3 siliceous ignimbrites (crustal components) and the Copahue magmas have among the highest Th/Yb of the three CCVC-LBAB magma zones
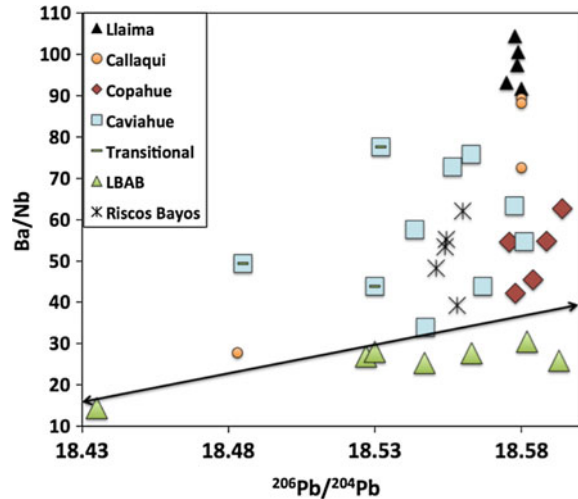
The Llaima and Callaqui rocks have the highest Ba/Nb (aqueous flushing of the subducted complex) but a very narrow range of Pb isotope ratios, overlapping with Caviahue, Copahue, and some LBAB samples (Fig. 5.25). The transitional rocks of Caviahue-LBAB have the low Nb of the Caviahue series and the low $^{206}Pb/^{204}Pb$ like some of the LBAB. The LBAB rocks have features both of element transport by fluids (like the main arc rocks) as well as sediment melting (as found at Copahue). Possibly, during subduction the water in the subduction complex is locked up in amphibole-like phases which release fluids at shallow depth and in mica-like phase which only destabilize at much greater depth (e.g., Winter 2001). As a result, some fluid fluxing occurs in the deeper mantle wedge, which is also hot enough for sediment melt extraction processes.

5.13 Comprehensive Model for the Regional Magmatic Setting

The Copahue rocks form a series of basalts and basaltic andesites that were largely erupted as lava flows, scoria and, through violent strombolian eruptions, as lapillis and ashes. The resulting structure is a rather rounded, somewhat flat-topped volcano, probably the combined result of lava flow emplacement, possibly intrusions inside the mountain, minor flank collapse with lahar transport downslope, all modified by glacial activity. The 1995, 2000 and 2012 magmas are very similar in composition, with the 2012 magma slightly more mafic than the 2000 magma. The mineralogy of the scoria of the three eruptions is similar, with olivine, clinopyroxene, orthopyroxene, plagioclase and magnetite. The constancy of composition over a ~ 20 years period suggests that the volcano stores that magma at several levels, and injects it at shallow level just prior to eruption. The 1995 eruptive events were preceded by magma mixing several weeks to months prior to the eruption (Goss 2001). The magma is continuously degassing in between eruptions, and these magmatic gases are largely trapped at 1–2 km depth in the hydrothermal reservoir (Varekamp et al. 2009; Agusto et al. 2012, 2013).

The magma chemistry of the Copahue series is distinct from that of neighbouring volcanoes. The older Caviahue complex has a much wider compositional range (basalt to rhyolite) and differs at the mafic compositional realm from Copahue by lower K and Ca and higher Fe and Ti. Compared to the main Andes arc volcanoes of Callaqui, Tolhuaca and Llaima, Copahue is enriched in the LIL elements, has less deep negative Nb anomalies, and has relatively low Ba/Nb values (40–60). The back arc basalts of

the Loncopue graben (LBAB) are much more mafic, and enriched in Nb as well as the LIL elements. The back arc rocks north of Loncopue positioned on the flank of the old Caviahue structure are transitional in chemistry between the Caviahue and LBAB series. Mantle enrichment related to subduction several million years ago still persists when tapped again during the LBAB magmatic phase, as also suggested by Hickey-Vargas et al. (2002) for centers further south in the Andes.

The isotope geochemistry of the Copahue rocks is distinct from that of the Caviahue series, whereas the LBAB rocks show a wide range that encompasses all the data of the CCVC rocks. The Copahue magmas have the highest Pb isotope ratios relative to all surrounding volcanoes. The LBAB and transitional series have some samples with unusually low $^{206}Pb/^{204}Pb$ as does the large tholeiitic dike of Callaqui volcano (Rea 2009). The overall rock chemistry and isotope compositions in this section of the Andes arc point to the usual source mixture of subducted Pacific Ocean sediment (PDS) and MORB type mantle (0.5–3 % bulk sediment mixing), with an additional low $^{206}Pb/^{204}Pb$ component in some magmas. This third component has EM1 characteristics and may represent the continental lithospheric mantle, lower crust, or other EM1-type mantle domains (Varekamp et al. 2010; Soager et al. 2013; Jacques et al. 2013, 2014).

Our interpretation of the chemical composition of Copahue lavas is as follows: these Copahue magmas formed from a mantle wedge influenced by an already "fractionated" subducted sediment-slab complex, which had already lost water and easily mobile elements such as Ba, Sr, Pb and U below the currently active main arc in Chile. The magmas formed in a relatively water-poor environment, leading to smaller % melting compared to the main arc magmas in Chile, which also resulted in largely effusive magma extrusions. The small violent strombolian eruptions were probably caused by local volatile enrichment in the tops of small pods of magma after shallow emplacement of magma from a deeper storage region. The isotope

data also indicate that a slightly different sediment mix was involved at Copahue than what created the Caviahue magmas a few million years earlier. The presence of $^{129}Iodine$ in the modern magmato-hydrothermal fluids (Fehn et al. 2004) and the slightly low He isotope ratios with respect to MORB values leave little doubt about the involvement of subducted sediments in these magmas (Hilton et al. 2002). As argued before (Varekamp et al. 2006), limited crustal assimilation may have taken place during storage in the lower and or middle crust.

The central Andes arc magmas are generated once fluids from the subducted complex are released, adding the water-soluble elements to the magma generation zone (e.g., Ba, Cs, Th, U, R, Pb, Sr). These magmas were generated with a large % of partial melting and they also plot on strongly curved mixing lines in e.g., Nd-Pb isotope ratio plots because of the strong concentration contrast between Pb in the sediment extract and mantle source. The Copahue rocks would be generated deeper in the Benioff zone in a less water-enriched mantle wedge, and as a result would have smaller % of partial melting. As a result of the prior Pb loss, less curved mixing lines are present in the same isotope plots. The LBAB are even dryer ($\sim$1 % water; Varekamp et al. 2010), but contain a third source component that displaces these rocks from the sediment-mantle mixing curves to low $^{206}Pb/^{204}Pb$. The less-water soluble elements like the REE increase in concentration down dip in the subduction zone and their release is related to incipient melting of the sediment and slab materials or breakdown limits of a specific mineral phase. The combined effects of early release of water and fractionation of the associated elements causes the trends down dip, a result of changing % of melting and shift from aqueous element transport to melt-derived element additions. Possibly, the LBAB source region may have seen both addition of sediment melts as well as fluid element transfer as a result of the breakdown of a more thermally stable hydrous mineral deep in the subduction zone, resulting in a wide range of trace element and isotope ratios.

The discrete differences in chemical and isotopic composition between main arc (Chile), Copahue and LBAB suggest that if a MASH zone exists below this region of the Andes, it is not widespread. Callaqui and Copahue volcanoes are separated by about 25 km and have very different compositions. A large regional MASH zone would not allow these differences to persist at this scale. This is even more true for the monogenetic basaltic volcanoes of the Loncopue graben (LBAB), which commonly vary in chemical and isotopic composition from cinder cone to the next lava flow at distances of only a few kilometers.

Alternative models to explain the east west compositional trends at this latitude in the Andes as e.g., proposed by Hickey et al. (1986), Hickey-Vargas et al. (1989), and Hickey-Vargas (1991) are viable as well. A combination of progressive depletion in mobile elements of the subducted complex in combination with decreasing degrees of partial melting in deeper parts of the subduction zone (dryer conditions), combined with limited crustal assimilation and fractional crystallization can explain most of the observed features. The LBAB rocks demand involvement of an additional component with the EM1 flavour.

References

Abouchami W, Galer SJG, Hofmann AW (2000) High precision lead isotope systematics of lavas from the Hawaiian Scientific Drilling Project. Chem Geol 169:187–209

Agusto MR, Tassi F, Caselli A, Vaselli O, dos Santos Afonso M (2012) Seguimiento geoquímico de las aguas ácidas del sistema volcán Copahue – Río Agrio: posible aplicación para la identificación de precursores eruptivos. Rev As Geol Arg 69(4):481–495

Agusto MR, Tassi F, Caselli AT, Vaselli O, Rouwet D, Capaccioni B, Caliro S, Chiodini G, Darrah T (2013) Gas geochemistry of the magmatic-hydrothermal fluid reservoir in the Copahue-Caviahue Volcanic Complex (Argentina). J Volcanol Geotherm Res 257:44–56

Barazangi M, Isacks BL (1976) Spatial distribution of earthquakes and subduction of the Nazca plate beneath South America. Geology 4(11):686–692

Beck SL, Zandt G, Myers SC, Wallace TC, Silver PG, Drake L (1996) Crustal-thickness variations in the central Andes. Geology 24(5):407–410

Bermúdez A, Delpino D (1995) Mapa de los peligros potenciales en el area del Volcàn Copahue, Sector Argentino: Neuquen, Argentina. Province of Neuquen Geological Survey, scale 1:50 000

Bermúdez A, Delpino D (1999) Erupciones subglaciales y en contacto con el hielo en la región volcánica de Copahue, Neuquén. XIV Congreso Geológico Argentino, Còrdoba, Argentina, vol 2, pp 250–253

Bermúdez A, Delpino D, Frey F, Saal A (1993) Los basaltos de retroarco extraandinos. XII Congreso Geológico Argentino, Mendoza, Argentina, vol 1, pp 161–172

Bermúdez A, Delpino D, López-Escobar L (2002) Caracterización geoquímica de lavas y piroclastos holocenos del volcán Copahue, incluyendo los originados en la erupción del año 2000. Comparación con otros volcanes de la Zona Volcánica Sur de los Andes. XV Congreso Geológico Argentino, Calafate, Argentina, pp 377–382

Bevis M, Isacks BL (1984) Hypocentral trend surface analysis: probing the geometry of Benioff zones. J Geophys Res 89(B7):6153–6170

Cahill T, Isacks BL (1992) Seismicity and shape of the subducted Nazca plate. J Geophys Res 97 (B12):17503–17529

Camfield L (2014) Copahue volcano, (Province Neuquen, Argentina): the 2012 eruption and its regional magmatic setting. MA Thesis, Wesleyan University, Middletown CT, p 187

Cembrano J, Lara L (2009) The link between volcanism and tectonics in the southern volcanic zone of the Chilean Andes: a review. Tectonophysics 471(1):96–113

Cembrano J, Hervé F, Lavenu A (1996) The Liquiñe-Ofqui fault zone; a long-lived intra-arc fault system in southern Chile: geodynamics of the Andes. Tectonophysics 259(1–3):55–66

Charrier R, Vicente J (1972) Liminary and geosyncline Andes: major orogenic phases and synchronical evolutions of the central and Magellan sectors of the Argentine Chilean Andes. In: Solid Earth problems conference, Upper Mantle Project, vol 2, pp 451–470

Colvin AS (2004) Trace element and isotope geochemistry of the Caviahue-Copahue volcanic complex. MA Thesis, Middletown, Connecticut, Wesleyan University, p 207

Davidson JP, Dungan MA, Ferguson KM, Colucci MT (1987) Crust-magma interactions and the evolution of arc magmas: the San Pedro-Pellado volcanic complex, southern Chilean Andes. Geology 15(5):443–446

Davidson JP, Ferguson KM, Colucci MT, Dungan MA (1988) The origin and evolution of magmas from the San Pedro-Pellado volcanic complex, S. Chile: multicomponent sources and open system evolution. Contr Mineral Petrol 100(4):429–445

Delpino D, Bermúdez A (1993) La actividad del volcán Copahue durante 1992. Erupción con emisión de azufre piroclástico. XII Congreso Geológico Argentino, Mendoza, Argentina, vol 1, pp 292–301

Delpino D, Bermúdez A (2002) La erupción del volcán Copahue del año 2000. Impacto social y al medio

natural. XXV Congreso Geológico Argentino, Cala-tafe, Argentina, pp 365–370

deMoor JM (2003) The magmatic evolution of Caviahue caldera: Implications for subduction processes and caldera formation. MA Thesis, Middletown, Connecticut, Wesleyan University, p 205

Diez Rodríguez A, Introcaso A (1986) Perfil transcontinental sudamericano en el paralelo 39 S. Geoacta 13 (2):179–201

Dragicevic M, Kausel E, Lomintz C, Meirnardus H, Silva L (1961) Levantamiento gravimetrito de Chile. Anales de la Facultad de Ciencias Físicas y Matemáticas, Universidad de Chile, vol 18, pp 221–242

Engdahl ER, van der Hilst R, Buland R (1998) Global teleseismic earthquake relocation with improved travel times and procedures for depth determination. Bull Seismol Soc Am 88(3):722–743

Fehn U, Snyder G, Varekamp JC (2004) Detection of recycled marine sediment components in crater lake fluids using ^{129}I. J Volc Geotherm. Res 115:451–460

Folguera A, Ramos V (2000) Control estructural del volcán Copahue (38 S-71 O): implicancias tectónicas para el arco volcánico cuaternario (36-39): Rev As Geol Arg 53(3):229–244

Folguera A, Introcaso A, Gimenez M, Ruiz F, Martinez P, Tunstall C, Garcia Morabito E, Ramos VA (2007) Crustal attenuation in the Southern Andean retroarc (38°–39°30′S) determined from tectonic and gravimetric studies: The Lonco-Luán asthenospheric anomaly. Tectonophysics 439:129–147

Folguera A, Bottesi G, Zapata T, Ramos VA (2008) Crustal collapse in the Andean backarc since 2 Ma: Tromen volcanic plateau, Southern Central Andes (36°40′-37°30′S). Tectonophysics 459:140–160

Folguera A, Alasonati Tasarova Z, Gotze HJ, Rojas Vera E, Gimenez M, Ramos V (2012) Retroarc extension in the last 6 Ma in the South-Central Andes (36°S–40°S) evaluated through a 3-D gravity modelling. J South Am Earth Sci 40:23–37

Garcia Morabito E, Gotze HJ, Ramos VA (2011) Tertiary tectonics of the Patagonian Andes retro-arc area between 38°15′ and 40°S latitude. Tectonophysics 499:1–21

Gorton MP, Schandl ES (2000) From continents to island arcs: a geochemical index of tectonic setting for arc-related and within-plate felsic to intermediate volcanic rocks. Canadian Mineralogist 38:1065–1073

Goss A (2001) Magmatic evolution of Volcan Copahue: Neuquen, Argentina. MA Thesis, Middletown, Connecticut, Wesleyan University

Herron E (1981) Chile Margin near lat 38°S: evidence for a genetic relationship between continental and marine geologic features or a case of curious coincidences? Geol Soc Am Mem 154:755–760

Hesse A (2007) Back arc basalts from the Loncopue Graben, Province Neuquen, Argentina (38–39°S). MA thesis, Wesleyan University, Middletown CT, p 213

Hickey RL, Frey FA, Gerlach DC, Lopez-Escobar L (1986) Multiple sources for basaltic arc rocks from the southern volcanic zone of the Andes (34–41°S): trace element and isotopic evidence for contributions from subducted oceanic crust, mantle, and continental crust. J Geophys Res 91(B6):5963–5983

Hickey-Vargas R (1991) Andean magma; peeled or MASHed? Nature 350:381–382

Hickey-Vargas R, Moreno Roa H, Lopez-Escobar L, Frey FA (1989) Geochemical variations in Andean basaltic and silicic lavas from the Villarrica- Lanin volcanic chain (39.5°S); an evaluation of source heterogeneity, fractional crystallization and crustal assimilation. Contr Mineral Petrol 103:361–386

Hickey-Vargas R, Sun M, Lopez-Escobar L, Moreno-Roa H, Reagan MK, Morris JD, Ryan JG (2002) Multiple subduction components in the mantle wedge: evidence from eruptive centers in the Central Southern volcanic zone. Geology 30:199–202

Hildreth W, Moorbath S (1988) Crustal contributions to arc magmatism in the Andes of Central Chile. Contr Mineral Petrol 98(4):455–489

Hilton DR, Fischer TP, Marty B (2002) Noble gases and volatile recycling at subduction zones. Rev Mineral Geochem 47(1):319–370

Ibáñez JM, Del Pezzo E, Bengoa C, Caselli A, Badi G, Almendros J (2008) Volcanic tremor and local earthquakes at Copahue volcanic complex, Southern Andes, Argentina. J Volcanol Geotherm Res 174:284–294

Jacques G, Hoernle K, Gill J, Hauff F, Wehrmann H, Garbe-Schonberg D, van den Bogaard P, Bindeman I, Lara LE (2013) Across-arc geochemical variations in the Southern Volcanic Zone, Chile (34.5–38.0°S): constraints on mantle wedge and slab input compositions. Geochim Cosmochim Acta 123:218–243

Jacques G, Hoernle K, Gill J, Wehrmann H, Bindeman I, Lara LE (2014) Geochemical variations in the Central Southern Volcanic Zone, Chile (38-43°S): the role of fluids in generating arc magmas. Chem Geol 371:27–45

Johnson MC, Plank T (1999) Dehydration and melting experiments constrain the fate of subducted sediments. Geochem Geophys Geosys 1. doi:10.1029/1999GC000014

Jordan TE, Isacks BL, Allmendinger RW, Brewer JA, Ramos VA, Ando CJ (1983) Andean tectonics related to geometry of subducted Nazca plate. Geol Soc Am Bull 94(3):341–361

Kay SM, Maksaev V, Moscoso R, Mpodozis C, Nasi C (1987) Probing the evolving Andean Lithosphere: mid-late tertiary magmatism in Chile (29°–30°30′S) over the modern zone of subhorizontal subduction. J Geophys Res 92(B7):6173–6189

Kay SM, Gorring M, Ramos VA (2004) Magmatic sources, setting and causes of Eocene to recent Patagonian plateau magmatism (36° to 52°S latitude). Rev Asoc Geol Argent 59:556–568

Kay SM, Burns WM, Copeland P, Mancilla O (2006) Upper Cretaceous to Holocene magmatism and evidence for transient Miocene shallowing of the Andean subduction zone under the northern Neuquén Basin. Geol Soc Am 407:19

Kilian R, Behrmann JH (2003) Geochemical constraints on the sources of Southern Chile Trench sediments and their recycling in arc magmas of the Southern Andes. J Geol Soc London 160:57–70

Labanieh S, Chauvel C, Germa A, Quidelleur X, Lewin E (2010) Isotopic hyperbolas constrain sources and processes under the Lesser Antilles arc. Earth Planet Sci Lett 298:35–46

Le Bas MJ, Le Maitre RW, Woolley AR (1991) The construction of the Total Alkali-Silica chemical classification of volcanic rocks. Contrib Mineral Petrol 46:1–22

Linares E, Ostera HA, Mas L (1999) Cronología potasio-argón del Complejo Efusivo Copahue-Caviahue, Provincia de Neuquen. Rev As Geol Arg 54(3):240–247

Mazzoni L, Licitra DT (2000) Significado estratigráfico y volcanológico de depósitos de flujos piroclásticos neógenos con composición intermedia en la zona del lago Caviahue, Provincia del Neuquén. Rev As Geol Arg 55(3):247–249

McDonough WF, Sun SS (1995) Composition of the Earth. Chem Geol 120:223–253

Melnick D, Folguera A, Ramos VA (2006) Structural control on arc volcanism: the Copahue-Agrio complex, South-Central Andes (37°50′S). J. South Am. Earth Sci. 22:66–88

Merrill M (2003) Petrogenesis of the Caviahue caldera. MA Thesis, Middletown, Connecticut, Wesleyan University

Moreno H, Thiele R, Lahsen A, Vareta J, López L, Vergara M (1986) Geocronología de rocas volcánicas cuaternarias en los Andes del Sur entre las latitudes 37 y 38pS. Chile. Rev As Geol Arg 15(3–4):297–299

Muñoz BJ, Stern CR (1988) The quaternary volcanic belt of the southern continental margin of South America: Transverse structural and petrochemical variations across the segment between 38°S and 39°S. J South Am Earth Sci 1(2):147–161

Muñoz JB, Stern CR (1989) Alkaline magmatism within the segment 38–39 S of the Plio-Quaternary volcanic belt of the southern South American continental margin. J Geophys Res 94(B4):4545–4560

Naranjo JA, Polanco E (2004) The 2000 AD eruption of Copahue volcano Southern Andes. Rev Geol Chile 31 (2):279–292

Niermeyer H, Muñoz J (1983) Geología de la Hoja Laguna de La Laja, Región del Biobío. Servicio Nacional de Geología y Minería, Carta Geológica de Chile

Orts DL, Folguera A, Encinas A, Ramos M, Tobal J, Ramos VA (2012) Tectonic development of the North Patagonian Andes and their related Miocene foreland basin (41°30′-43°S). Tectonics 31(TC3012). doi:10.1029/2011TC003084

Pardo-Casas F, Molnar P (1987) Relative motion of the Nazca (Farallon) and South American plates since Late Cretaceous time. Tectonics 6(3):233–248

Pearce JA (1982) Trace element characteristics of lavas from destructive plate boundaries. In: Thorpe RS (ed), Andesites: orogenic andesites and related Rocks. Wiley, Chichester, pp 525–548

Pesce A (1989) Evolución volcano-tectónica del complejo efusivo Copahue-Caviahue y su modelo geotérmico preliminar. Rev As Geol Arg 44(1–4)307–327

Pioli L, Erlund E, Johnson E, Cashman K, Wallace P, Rosi M, Delgado Granados H (2008) Explosive dynamics of violent Strombolian eruptions: the eruption of Parícutin Volcano 1943–1952 (Mexico). Earth Plan Sc Lett 271:359–368

Plank T (2005) Constraints from thorium/lanthanum on sediment recycling at subduction zones and the evolution of the continents. J Petrol 46:921–944

Rabassa J, Clapperton CM (1990) Quaternary glaciations of the southern Andes. Quat Scie Rev 9(2):153–174

Ramos V (1978) Relatório: Estructura, Geológia y Recursos Naturales del Neuquén: Buenos Aires. In: Proceedings Asociación Geológica Argentina, VII Congreso Geológico Argentino, pp 99–118

Rea JC (2009) The petrology and geochemistry of volcan Callaqui, Chile. MA Thesis, Wesleyan University, Middletown, CT, USA, p 162

Rudnick RL, Gao S (2003) Composition of the continental crust. In: Holland HD, Turekian KK (eds) Treatise on geochemistry, vol 3. Elsevier, Amsterdam, pp 1–64

Søager N, Holm PM, Llambías EJ (2013) Payenia volcanic province, southern Mendoza, Argentina: OIB mantle upwelling in a backarc environment. Chem Geol 349–350:36–53

Suarez M, de la Cruz R (1998) Hoja Curacautin (38°–39°). Servicio Nacional de Geologia y Mineria de Chile, Mapa escala 1:250,000, p 105

Stern CR (1991) Role of subduction erosion in the generation of Andean magmas. Geology 19(1):8–81

Swift SA, Carr MJ (1974) The segmented nature of the Chilean seismic zone. Phys Earth Planet Inter 9 (3):183–191

Tanaka T, Togashi S, Kamioka H, Amakawa H, Kagami H, Hamamoto T, Yuhara M, Orihashi Y, Yoneda S, Shimizu H, Kunimaru T, Takahashi K, Yanagi T, Nakano T, Fujimaki H, Shinjo R, Asahara Y, Tanimizu M, Dragusanu C (2000) JNdi-1: a neodymium isotopic reference in consistency with LaJolla neodymium, Chem Geol 168:279–281

Tebbens S, Cande S, Kovacs L, Parra J, LaBrecque J, Vergara H (1997) The Chile ridge: a tectonic framework. J Geophys Res 102(B6):12035–12059

Todd E (2005) Geochemical evolution of pre-caldera magmas at Caviahue caldera, Neuquén province, Argentina. MA Thesis, Flagstaff, Arizona, Northern Arizona University, p 252

Todd E, Ort MH (2012) Variable sources and differentiation of lavas from the Copahue-Caviahue eruptive complex, Neuquen Argentina. Fall meeting, AGU, San Francisco, USA, Abstract V11D, p 2804

Todd E, Gill JB, Wysoczanski RJ, Hergt JM, Wright IC, Leybourne MI, Mortimer N (2011) Hf isotopic evidence for small-scale heterogeneity in the mode of mantle wedge enrichment: Southern Havre Trough

and South Fiji Basin back-arcs. Geochem Geophys Geosys 12(9):34

Varekamp JC, Ouimette AP, Herman SW, Bermúdez A, Delpino D (2001) Hydrothermal element fluxes from Copahue, Argentina: a "beehive" volcano in turmoil. Geology 29(11):1059–1062

Varekamp JC, deMoor JM, Merrill MD, Colvin AS, Goss AR, Vroon PZ, Hilton DR (2006) Geochemistry and isotopic characteristics of the Caviahue-Copahue volcanic complex, Province of Neuquén, Argentina. Geol Soc Am 407:317–342

Varekamp JC, Ouimette A, Herman S, Flynn K, Bermúdez A, Delpino D (2009) Naturally acid waters from Copahue volcano Argentina. Appl Geochem 24 (2):208–220

Varekamp JC, Hesse A, Mandeville C (2010) Back-arc basalts from the Loncopue graben (Province of Neuquen, Argentina). J Volcanol Geotherm Res 197 (1):313–328

Velez ML, Euillades P, Caselli A, Blanco M, Díaz JM (2011) Deformation of Copahue volcano: inversion of InSAR data using a genetic algorithm. J Volcanol Geotherm Res 202:117–126

Vermeesch P (2006) Tectonic discrimination diagrams revisited. Geochem Geophys Geosys 7(Q06017). doi:10.1029/2005GC001092

Völker D, Kutterolf S, Wehrmann H (2011) Comparative mass balance of volcanic edifices at the southern volcanic zone of the Andes between 33°S and 46°S. J Volcanol Geotherm Res 205(3):114–129

Winter JD (2001) Introduction to igneous and metamorphic petrology. Prentice and Hall, Englewood Cliffs, p 699

Zareski JE (2014) An east-west transect through the Andes at 35-39°S. MA thesis Wesleyan Univ, Middletown CT, p 248

Geochemistry of the Magmatic-Hydrothermal Fluid Reservoir of Copahue Volcano (Argentina): Insights from the Chemical and Isotopic Features of Fumarolic Discharges

6

F. Tassi, M. Agusto, O. Vaselli and G. Chiodini

Abstract

In this chapter the chemical (inorganic and organic) and isotopic compositions (δ^{13}C-CO_2, δ^{15}N, ^{3}He/^{4}He, ^{40}Ar/^{36}Ar, δ^{13}C-CH_4, δD-CH_4, and δD-H_2O and δ^{18}O-H_2O) of gas discharges, collected during 6 campaings carried out from 1976 to 2012, located at the foot of Copahue volcano are presented and discussed. Gas composition is typical of hydrothermal fluids from volcanic areas, since it consists of dominant CO_2 and relatively high concentrations of H_2S, H_2, CH_4 and N_2. The helium isotopic ratios are the highest ones (R/R$_a$ up to 7.94) observed in whole South America continent. This feature is not common for gases from a classic arc-like setting, and is possibly related to an extensional regime subdued to asthenospheric thinning. The CO_2/^{3}He ratios (from 1.4 to 8.8×10^9), slightly exceeding that of MORB gases, and the δ^{15}N values (+1.7 to +5.5 ‰ vs. air) point to the occurrence of an additional crustal source for CO_2 and N_2. Gas discharges of the northern sector of the volcanic edifice are likely produced by mixing of hydrothermal gases with fluids from a shallow source permeating through the local fault systems. Gas geothermometry based on chemical reactions characterized by slow kinetics, such as those involving the $CO[\log(X_{H_2}/X_{H_2O}) = -2.8)]_2$-$CH_4$ redox pair, are quenched at temperatures of $\sim$260 °C and redox conditions consistent with those measured in the geothermal wells. On the contrary, the C_3H_6-C_3H_8 pair, H_2 and CO tend to re-adjust at decreasing temperatures and more oxidizing conditions $[\log(X_{H_2}/X_{H_2O}) \leq -3.4]$ in the uprising vapor phase. The hydrothermal reservoir is mainly recharged

F. Tassi (✉) · O. Vaselli
Department of Earth Sciences, University of Florence, Via La Pira 4, 50121 Florence, Italy
e-mail: franco.tassi@unifi.it

F. Tassi · O. Vaselli
Institute of Geosciences and Earth Resources of the National Research Council (CNR-IGG), Via La Pira 4, 50121 Florence, Italy

M. Agusto
IDEAN-GESVA Dpto. Cs. Geológicas, FCEN Universidad de Buenos Aires. Ciudad Universitaria, Pab.2, 1428 Buenos Aires, Argentina

G. Chiodini
Istituto Nazionale di Geofisica e Vulcanologia, sez. Di Napoli "Osservatorio Vesuviano", Via Diocleziano 328, 82124 Naples, Italy

by meteoric water whose isotopic signature is modified by water-rock interactions. The N_2/He ratios measured in 2006–2007 were significantly lower than those of 2012, possibly due to variable input of N_2-bearing species from sediments interacting with the magmatic source. Considering that the R/R_a values of the 2006–2007 period were significantly higher than those measured in 2012, such compositional variation may also be explained by the injection of fresh N_2- and ^{3}He-rich magma that triggered the 2000 eruption. This hypothesis, although speculative since no geochemical data of fumaroles are avalaible from 1997 to 2006, implies that a geochemical monitoring of inert gas compounds discharged from the hydrothermal emissions could be used to detect the occurrence at depth of injections of new magma batches.

6.1   Introduction

Copahue volcano is one of the more active volcanoes of the central sector of the Volcanic chain along the border between Argentina and Chile. Frequent phreatic to phreato-magmatic eruptions (e.g., Delpino and Bermúdez 1993, 2002; Bermúdez et al. 2002; Naranjo and Polanco 2004) have recently occurred (Caselli et al. this volume). During quiescent periods, an intense degassing occurs at the easternmost summit crater, where the hyperacidic Lake Copahue is hosted (Agusto et al. 2012), and along the flanks of the volcano. Notwithstanding, relatively few data of chemical and isotopic compositions of gases discharged from this volcanic system are currently available. Geochemical investigations in this area were mainly focused on the chemical-physical features of the geothermal reservoir, in the framework of the first stage of geothermal exploration carried out by private companies (Jurío 1977; Panarello et al. 1986, 1988; JICA 1992; Sierra et al. 1992; Fujita et al. 1996; Mas et al. 2000; Panarello 2002). These studies were mostly based on the chemistry of fluids from three geothermal wells (COP1, COP2 and COP3) that were drilled at the

beginning 1980s (Mas et al. 2000, and references therein), whereas the geochemistry of fluids discharged from the natural emissions of this system was recently described and discussed in detail by Agusto et al. (2013). This chapter is dedicated to the description of the chemical and isotopic features of fumaroles and bubbling pools from five hydrothermal areas located at the foot of the Copahue cone, which were collected before the 2000 phreatomagmatic eruption, in 1976, 1986 and 1996 (Jurío 1977; Martini et al. 1997; Panarello 2002) and after it in 2003, 2006, 2007 and 2012 (Varekamp et al. 2006; Agusto et al. 2011, 2013). Geochemical data of fluids discharged from the geothermal wells (JICA 1992; Panarello 2002; Agusto et al. 2013) were also reported for comparison, although a complete characterization and a detailed description of these fluids is carried out in another chapter of the present book (Mas et al. this volume). The chapter thus recompile the available geochemical data to show a comprehensive geochemical conceptual model for fluid circulation describing (i) primary fluid sources, (ii) chemical-physical conditions controlling gas chemistry at different depths and (iii) secondary processes controlling the chemistry of fluid discharges.

6.2 Fluid Discharges at CCVC

The crater lake hosted in the easternmost of the 9 NE-oriented summit craters of Copahue volcano is generally characterized by a relatively high temperature (up to 63 °C) and low pH (<1), although in the last two decades these two chemical-physical parameters have shown strong variations likely related to changes of the volcanic activity (Varekamp et al. 2001; Varekamp 2008; Agusto 2011; Agusto et al. 2012). Acidic gases are typically released from the lake surface, especially during the summer season when the lake temperature increases. However, no fumaroles were found in the summit area during the sampling campaigns, with the exception of steaming ground emissions showing a strong air contamination. Two springs located on the eastern flank of the volcano, at a short distance from the active crater rim (Fig. 6.1), discharge hot (up to 80 °C) and acidic (pH = 1–2) water giving rise to the Rio Agrio river that flows down to Lake Caviahue (Varekamp et al. 2001, 2009; Parker et al. 2008). No free gas emergences were present from these springs neither along Rio Agrio. The Copahue gas discharges basically consist of boiling, bubbling and mud pools and fumaroles distributed in 5 different areas on the N and NE sectors of the external flanks of the volcanic edifice (Fig. 6.1): (1) Las Máquinas, (2) Las Maquinitas, (3) Termas de Copahue,

(4) Anfiteatro, and (5) Chanco-Co. These natural manifestations have outlet temperatures (up to 95 °C) approaching that of boiling water at the altitude of the emissions ($\sim 2,000$ a.s.l.), with the only exception of one jet fumarole at La Maquinitas, where temperatures up to 160 °C were measured (Mas et al. 1996, 2000; Linares et al. 1999; Vallés et al. 2004; Agusto et al. 2013).

6.3 Gas Chemical Composition

The gas chemical composition (in mmol/mol) is referred to the dry gas fraction, whereas water vapor concentrations (for fumaroles) are expressed as molar percentages (Table 6.1). The fumaroles collected from the 5 thermal areas in the volcano surroundings (LM1, LMM1, PC2, AF1, AF2, CC1, CC2 and CC3) are mainly constituted by water vapor (>96 %), whereas the dry gas phase of both fumaroles and bubbling gases (LM2, RB, TE, AL CH, LN and PC1) mostly consists of CO_2 (up to 989 mmol/mol), with variable concentrations of H_2S (from 2.5 to 155 mmol/mol), N_2 (from 2.5 to 105 mmol/mol), CH_4 (from 0.68 to 55 mmol/mol) and H_2 (from 1 to 40 mmol/mol). Helium, Ar, CO and Ne are present in minor amounts (up to 0.089, 0.11, 0.0042 and 0.000036 mmol/mol, respectively). Light hydrocarbons pertain to the alkane, alkene,

Fig. 6.1 CCVC area with location of the gas sampling sites

aromatic and S-substituted groups and they show relatively low concentrations, their total contents being <54 μmol/mol (Table 6.2). Ethane and C_6H_6 have concentrations one order of magnitude higher than those of the other hydrocarbons of their functional groups, i.e. alkanes and aromatics, respectively, a compositional feature commonly found in hydrothermal fluids (e.g., Capaccioni et al. 1995; Darling 1998; Taran and Giggenbach 2003; Tassi et al. 2009a).

The chemical composition of the dry gases from the COP1 COP2 and COP3 geothermal wells is basically similar to that of the natural fluid discharges (Table 6.1), whereas water vapor concentrations, calculated by Panarello et al. (2002) on the basis of gas chemical composition according to the theoretical approach proposed by Saracco and D'Amore (1989), are significantly higher (99.9 %), possibly due to vapor condensation affecting the fumarolic fluids.

6.4 Isotopic Composition of Gases (δ^{13}C-CO$_2$, δ^{15}N, R/R$_a$, ^{40}Ar/^{36}Ar, δ^{13}C-CH$_4$ and δD-CH$_4$) and Steam (δ^{18}O-H$_2$O and δD-H$_2$O)

The δ^{13}C-CO$_2$ values, analyzed in those gas samples collected in 2003, 2006, 2007 and 2012, ranged from −8.8 to −6.8 ‰ versus V-PDB (Varekamp et al. 2006; Agusto et al. 2013). Gases collected from Las Maquinas (LM1 and LM2), Las Maquinitas (LMM1) and Piedra Copahue (PC2 and PC3) in 2003, 2006 and 2012 showed relatively high R/R$_a$ values, ranging from 6.97 to 7.94 (Varekamp et al. 2006; Agusto et al. 2013). On the contrary, R/R$_a$ values of gas samples collected in 2007 and 2012 from Anfiteatro (AF1 and AF2) and Cancho Co (CC2 and CC3) were from 4.04 to 5.02 (Agusto et al. 2013). Analogous differences were also shown by the δ^{15}N values collected from LM1, PC2 and LMM1, which were from 5.3 to 5.5 ‰ versus air, and those of the CC3 and AF2 gases ranging from 1.7 to 2.5 ‰ versus air, respectively (Agusto et al. 2013). The

^{40}Ar/^{36}Ar ratios, available for the 2006–2007 samples where the R/R$_a$ values were also determined, spanned from 298 to 450. Both the δ^{13}C-CH$_4$ and δD-CH$_4$ values, analyzed in the 2012 gases, were in narrow ranges, from −24.5 to −20.3 ‰ versus V-PDB and from −143 to −121 ‰ versus V-SMOW, respectively. The values of δ^{18}O-H$_2$O and δD-H$_2$O of steam were from −17.9 to −10.6 ‰ and from −109 to −84 ‰ versus V-SMOW, respectively.

Fluids from the geothermal wells showed δ^{13}C-CO$_2$, R/R$_a$, ^{40}Ar/^{36}Ar, δ^{18}O-H$_2$O and δD-H$_2$O values consistent with those of the fumaroles and bubbling pools (Table 6.3).

6.5 Gas Geothermometry

The occurrence of a vapor-dominated hydrothermal system located northeast of the main Copahue edifice was firstly suggested by JICA (1992) in the framework of a feasibility study carried out for a geothermal exploration project (ARG-3988/IG). Measured temperatures of fluids from the COP1, COP2 and COP3 geothermal wells were up to ∼250 °C (Mas and Mas, this volume). Panarello (2002) used the chemical composition of the geothermal fluids and those from Las Maquinas and Las Maquinitas fumaroles (Martini et al. 1997) for geothermometric evaluation in the H$_2$O-CO$_2$-CH$_4$-H$_2$S-H$_2$ system (D'Amore and Panichi 1980). The results of this theoretical approach confirmed the hypothesis suggested by previous authors (Panarello et al. 1986, 1988; D'Amore et al. 1988; Sierra et al. 1992) indicating the occurrence of two different reservoirs, located at 800-1000 m and 1400 m depth, having temperatures up to 200 and 260 °C, respectively.

Following the approach proposed by Chiodini and Marini (1998), an estimation of equilibrium temperature independent on redox conditions can be provided by geothermometric calculations in the H$_2$O-CO$_2$-CH$_4$-CO-H$_2$ system, based on the combination of the two following reactions:

Table 6.1 Outlet temperature (in °C), chemical composition of the dry gas fraction (in mmol/mol) and steam concentrations (in%) of the CCVC gases

Sample	Achronym	Reference	Type	Date	T°C	CO$_2$	SO$_2$	H$_2$S	N$_2$	CH$_4$	Ar	O$_2$	Ne	H$_2$	He	CO	Vapor %
Las Maquinas 1	LM1	1	Fumarole	1976	n.m.	831	n.d.	4.5	105	32	0.080	n.a.	n.a.	24	0.013	0.0042	–
Las Maquinas 1	LM1	2	Fumarole	1986	85	927	n.d.	6.2	28	22	0.110	n.a.	n.a.	14	0.013	0.0014	–
Las Maquinas 1	LM1	3	Fumarole	1997	n.m.	965	n.d.	6.1	24	1.1	0.006	n.a.	n.a.	1.0	0.002	0.0001	–
Las Máquinas 1	LM1	4	Fumarole	Nov-06	95	971	n.d.	11	6.7	5.8	0.028	0.19	0.000015	5.5	0.028	n.a.	97.0
Las Máquinas 2	LM2	4	Bubbling gas	Nov-06	75	922	n.d.	64	6.5	3.5	0.020	0.066	0.000013	4.0	0.028	n.a.	–
Las Máquinas 2	LM2	4	Bubbling gas	Feb-07	74	989	n.d.	2.5	2.7	3.7	0.010	0.025	0.000006	2.5	0.015	n.a.	–
Las Máquinas 1	LM1	4	Fumarole	Mar-12	96	938	n.d.	8.1	17	20	0.023	0.009	0.000015	16	0.015	0.0021	97.9
Las Maquinitas 1	LMM1	1	Fumarole	1976	n.m.	905	n.d.	16	55	15	0.070	n.a.	n.a.	16	0.014	0.0020	–
Las Maquinitas 1	LMM1	2	Fumarole	1986	130	944	n.d.	14	24	13	0.090	n.a.	n.a.	14	0.010	0.0013	–
Las Maquinitas 1	LMM1	3	Fumarole	1997	n.m.	936	n.d.	3.0	26	21	0.042	n.a.	n.a.	3	0.003	0.0004	–
Las Maquinitas 1	LMM1	4	Fumarole	Nov-06	135	974	n.d.	7.8	8.7	4.0	0.026	0.087	0.000017	6.2	0.029	n.a.	96.2
Las Maquinitas 2	LMM1	4	Fumarole	Mar-12	160	944	n.d.	8.6	21	13	0.021	0.006	0.000012	13	0.019	0.0021	97.1
Rio Blanco	RB	2	Bubbling gas	1986	n.m.	926	n.d.	5.2	25	25	0.083	n.a.	n.a.	18	0.013	n.a.	–
Termas	TE	2	Bubbling gas	1986	n.m.	936	n.d.	6.2	23	10	0.107	n.a.	n.a.	16	0.011	0.002	–
Agua Limon	AL	2	Bubbling gas	1986	n.m.	935	n.d.	4.4	32	13	n.a.	n.a.	n.a.	16	n.a.	0.002	–
Chancho	CH	4	Bubbling gas	Nov-06	27	969	n.d.	9.4	12	3.6	0.038	0.25	0.000024	6.3	0.041	n.a.	–
Limon Negro	LN	4	Bubbling gas	Nov-06	83	958	n.d.	9.9	15	6.5	0.049	0.12	0.000032	10	0.064	n.a.	–
Piedra Copahue 1	PC1	4	Bubbling gas	Nov-06	96	973	n.d.	11	8.4	3.2	0.031	0.31	0.000018	4.5	0.032	n.a.	–
Piedra Copahue 2	PC2	4	Fumarole	Nov-06	93	961	n.d.	10	15	6.4	0.055	0.19	0.000031	7.1	0.061	n.a.	96.0
Piedra Copahue 2	PC2	4	Fumarole	Mar-12	95	947	n.d.	8.9	19	10	0.013	0.008	0.000007	14	0.011	0.0021	97.0
Anfiteatro 1	AF1	4	Fumarole	Feb-07	92	864	n.d.	90	13	27	0.061	0.23	0.000036	5.0	0.089	n.a.	96.2
Anfiteatro 2	AF2	4	Fumarole	Mar-12	92	870	n.d.	24	35	55	0.025	0.013	0.000013	26	0.030	0.0029	98.3
Chancho Co 1	CC1	4	Fumarole	Feb-07	86	911	n.d.	68	3.8	0.68	0.018	0.23	0.000011	16	0.035	n.a.	98.4
Chancho Co 2	CC2	4	Fumarole	Feb-07	93	876	n.d.	109	2.5	2.1	0.015	0.16	0.000008	9.2	0.016	n.a.	98.0
Chancho Co 3	CC3	4	Fumarole	Mar-12	95	789	n.d.	155	14	2.1	0.035	0.011	0.000018	40	0.016	0.0023	99.2

(continued)

Table 6.1 (continued)

Sample	Achronym	Reference	Type	Date	T°C	CO_2	SO_2	H_2S	N_2	CH_4	Ar	O_2	Ne	H_2	He	CO	Vapor %
COP-1	COP1	2	Geothermal well	1981	n.m.	940	n.d.	3.0	12	25	n.a.	n.a.	n.a.	n.a.	n.a.	n.a.	99.9
COP-1	COP1	2	Geothermal well	1982	n.m.	936	n.d.	2.8	18	16	n.a.	n.a.	n.a.	n.a.	n.a.	n.a.	99.9
COP-1	COP1	2	Geothermal well	1982	n.m.	923	n.d.	2.2	43	10	n.a.	n.a.	n.a.	n.a.	n.a.	n.a.	99.9
COP-1	COP1	2	Geothermal well	1986	242	938	n.d.	5.1	21	20	0.022	n.a.	n.a.	17	0.014	0.0075	99.9
COP-1	COP1	5	Geothermal well	1991	n.m.	905	n.d.	7.6	30	33	n.a.	n.a.	n.a.	30	n.a.	n.a.	99.9
COP-2	COP2	2	Geothermal well	1986	n.m.	952	n.d.	9.0	16	12	0.020	n.a.	n.a.	12	0.003	0.0070	99.9
COP-3	COP3	5	Geothermal well	1991	n.m.	958	n.d.	3.9	24	5.2	n.a.	n.a.	n.a.	9.3	n.a.	n.a.	99.9

n.a.: not analyzed. References for chemical and isotopic data are: (1) Jurío 1977, (2) Panarello (2002), (3) Martini et al. (1997) (4), Agusto et al. (2013), (5) JICA (1992), (6) Varekamp et al. (2006)

Table 6.2 Chemical composition of light hydrocarbons (in μmol/mol) of the CCVC gases

Achronym	Reference	Type	Date	C_2H_6	C_3H_6	C_3H_8	$n-C_4H_{10}$	$i-C_4H_8$	$n-C_5H_{12}$	$n-C_6H_{14}$	C_2H_6S	C_6H_6	C_4H_4S	C_7H_8	C_5H_6S	$m-p-C_8H_{10}$
LM1	4	Fumarole	Nov-06	6.5	0.0005	0.56	0.29	0.12	0.039	0.017	0.012	0.074	0.007	0.013	0.006	0.008
LM2	4	Bubbling gas	Nov-06	1.6	n.d.	0.17	0.049	0.062	0.008	0.008	0.010	0.13	0.006	0.011	0.006	0.007
LM2	4	Bubbling gas	Feb-07	2.9	0.0004	0.30	0.19	0.14	0.008	0.005	0.004	0.049	0.004	0.006	0.003	0.004
LM1	4	Fumarole	Mar-12	23	0.0016	2.3	0.43	0.22	0.043	0.022	0.021	0.17	0.009	0.018	0.007	0.009
LMM1	4	Fumarole	Nov-06	6.1	0.0006	0.67	0.38	0.10	0.042	0.016	0.009	0.17	0.013	0.016	0.009	0.009
LMM1	4	Fumarole	Mar-12	11	0.0009	1.1	0.11	0.13	0.015	0.016	0.018	0.14	0.011	0.017	0.007	0.008
CH	4	Bubbling gas	Nov-06	0.8	n.d.	0.11	0.022	0.013	0.003	0.003	0.012	0.034	0.003	0.003	0.001	0.002
LN	4	Bubbling gas	Nov-06	1.8	n.d.	0.24	0.053	0.081	0.008	0.011	0.014	0.31	0.002	0.029	0.014	0.018
PC1	4	Bubbling gas	Nov-06	0.52	n.d.	0.075	0.015	0.009	0.002	0.002	0.013	0.093	0.007	0.011	0.006	0.007
PC2	4	Fumarole	Nov-06	9.0	0.0006	0.89	0.44	0.14	0.053	0.025	0.016	0.27	0.013	0.024	0.010	0.014
PC2	4	Fumarole	Mar-12	8.4	0.0007	0.75	0.22	0.24	0.012	0.011	0.0067	0.17	0.006	0.011	0.004	0.005
AF1	4	Fumarole	Feb-07	2.5	0.0003	0.30	0.097	0.14	0.020	0.020	0.025	0.49	0.010	0.023	0.006	0.075
AF2	4	Fumarole	Mar-12	47	0.0036	5.1	0.46	0.27	0.064	0.025	0.016	0.20	0.019	0.020	0.012	0.013
CC1	4	Fumarole	Feb-07	7.5	0.0004	0.84	0.47	0.24	0.019	0.016	0.005	0.30	0.008	0.008	0.007	0.010
CC2	4	Fumarole	Feb-07	2.4	0.0002	0.44	0.078	0.051	0.007	0.006	0.008	0.40	0.003	0.051	0.008	0.036
CC3	4	Fumarole	Mar-12	2.6	0.0003	0.21	0.041	0.011	0.005	0.006	0.005	0.16	0.003	0.004	0.002	0.002

References as in Table 6.1

Table 6.3 $\delta^{13}C\text{-}CO_2$ (‰ V-PDB) and $\delta^{13}C\text{-}CH_4$ (‰ V-PDB), $\delta D\text{-}CH_4$ (‰ V-SMOW), R/R_a, $\delta^{15}N$ (‰ ATM), $\delta^{18}O\text{-}H_2O$ (‰ V-SMOW) and $\delta D\text{-}H_2O$ (‰ V-SMOW) values and $^{40}Ar/^{36}Ar$, $CO_2/^3He$ and $CH_4/^3He$ ratios of the CCVC gas discharges

Achronym	Reference	Type	Date	$d^{13}C\text{-}CO_2$	R/Ra	$^{40}Ar/^{36}Ar$	He/Ne	$d^{15}N$	$d^{13}C\text{-}CH_4$	$dD\text{-}CH_4$	$CO_2/^3He$ (x10⁹)	$CH_4/^3He$ (x10⁷)	$d^{18}O$	dD	f_S	f_A	f_M
LM1	2	Fumarole	1986	n.a.	n.a.	n.a.	n.a.	n.a.	n.a.	n.a.	n.a.	n.a.	−10.6	−85	–	–	–
LM1	4	Fumarole	Nov-06	−8.2	7.72	306	1898	n.a.	n.a.	n.a.	3.2	1.9	n.a.	n.a.	–	–	–
LM2	6	Bubbling gas	2003	−8.3	7.5	n.a.	729	n.a.	n.a.	n.a.	9.0	n.a.	n.a.	n.a.	–	–	–
LM2	4	Bubbling gas	Nov-06	−7.9	n.a.	n.a.	n.a.	n.a.	n.a.	n.a.	n.a.	n.a.	n.a.	n.a.	–	–	–
LM2	4	Bubbling gas	Feb-07	−8.8	n.a.	n.a.	n.a.	n.a.	n.a.	n.a.	n.a.	n.a.	n.a.	n.a.	–	–	–
LM1	4	Fumarole	Mar-12	−7.3	7.04	385	1215	5.3	−21.1	−124	6.4	14	−11.2	−90	0.84	0.05	0.11
LMM1	2	Fumarole	1986	n.a.	n.a.	n.a.	n.a.	n.a.	n.a.	n.a.	–	n.a.	−10.8	−84	–	–	–
LMM1	4	Fumarole	Nov-06	−7.7	7.94	299	1679	n.a.	n.a.	n.a.	3.0	1.3	n.a.	n.a.	–	–	–
LMM1	4	Fumarole	Mar-12	−7.1	6.97	436	1330	5.5	−20.3	−127	5.1	7.1	−10.8	−88	0.86	0.03	0.11
TE	2	Bubbling gas	1986	n.a.	n.a.	n.a.	n.a.	n.a.	n.a.	n.a.	n.a.	n.a.	−12.8	−90	–	–	–
AL	2	Bubbling gas	1986	n.a.	n.a.	n.a.	n.a.	n.a.	n.a.	n.a.	n.a.	n.a.	−11.9	−85	–	–	–
CH	4	Bubbling gas	Nov-06	−7.3	n.a.	n.a.	n.a.	n.a.	n.a.	n.a.	n.a.	n.a.	n.a.	n.a.	–	–	–
PC3	6	Bubbling gas	2003	−8.3	7.6	n.a.	1228	n.a.	n.a.	n.a.	9.8	n.a.	n.a.	n.a.	–	–	–
PC2	4	Fumarole	Nov-06	−7.7	7.36	332	1957	n.a.	n.a.	n.a.	1.5	1.0	n.a.	n.a.	–	–	–
PC2	4	fumarole	Mar-12	−7.0	7.01	450	1048	5.5	−22.4	−121	8.8	9.3	−11.8	−91	0.83	0.11	0.06
AF1	4	Fumarole	Feb-07	−6.8	5.01	297	2445	n.a.	n.a.	n.a.	1.4	4.4	n.a.	n.a.	–	–	–
AF2	4	Fumarole	Mar-12	−7.0	4.93	303	1996	2.5	−24.5	−143	4.4	27	−17.9	−109	0.43	0.47	0.11
CC2	4	Fumarole	Feb-07	n.a.	5.02	291	914	n.a.	n.a.	n.a.	7.9	1.9	n.a.	n.a.	–	–	–
CC3	4	Fumarole	Mar-12	−8.1	4.04	298	1058	1.7	−23.2	−137	8.8	2.3	−8.6	−89	0.27	0.69	0.04
COP1	2	Geothermal well	1981	n.a.	n.a.	n.a.	n.a.	n.a.	n.a.	n.a.	n.a.	n.a.	−10.5	−84	–	–	–

(continued)

Table 6.3 (continued)

Achronym	Reference	Type	Date	$d^{13}C$-CO_2	R/Ra	$^{40}Ar/^{36}Ar$	He/Ne	$d^{15}N$	$d^{13}C$-CH_4	dD-CH_4	$CO_2/^3He$ ($\times 10^9$)	$CH_4/^3He$ ($\times 10^7$)	$d^{18}O$	dD	f_S	f_A	f_M
COP1	2	Geothermal well	1985	n.a.	n.a.	n.a.	n.a.	n.a.	n.a.	n.a.	n.a.	n.a.	−9.6	−83	–	–	–
COP1	2	geothermal well	1987	n.a.	n.a.	n.a.	n.a.	n.a.	n.a.	n.a.	n.a.	n.a.	−9.1	−80	–	–	–
COP2	2	Geothermal well	1986	n.a.	n.a.	n.a.	n.a.	n.a.	n.a.	n.a.	n.a.	n.a.	−10.1	−85	–	–	–
COP2	5	Geothermal well	1991	n.a.	n.a.	n.a.	n.a.	n.a.	n.a.	n.a.	n.a.	n.a.	−9.4	−85	–	–	–
COP2	4	Geothermal well	Feb-07	−7.5	7.37	298	672	n.a.	n.a.	n.a.	57	1.0	n.a.	n.a.	–	–	–
VAF2	2	Cold spring	1985	n.a.	n.a.	n.a.	n.a.	n.a.	n.a.	n.a.	n.a.	n.a.	−12.5	−90	–	–	–
VAF3	2	Cold spring	1985	n.a.	n.a.	n.a.	n.a.	n.a.	n.a.	n.a.	n.a.	n.a.	−12.9	−94	–	–	–

Calculated N_2 fractions from (i) air (f_A), (ii) mantle (f_M), and (iii) subducted sediments (f_S) are also reported. References as in Table 6.1

$$CO_2 + H_2 \Leftrightarrow CO + H_2O \qquad (6.1)$$

$$3CO_2 + CH_4 \Leftrightarrow 4CO + 2H_2O \qquad (6.2)$$
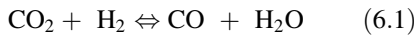
whose temperature dependence is given by:

$$\begin{aligned} \log(X_{CO}/X_{CO_2}) - \log(X_{H_2}/X_{H_2O}) \\ = -2248/T + 2.485 \end{aligned} \qquad (6.3)$$

$$\begin{aligned} 3\log(X_{CO}/X_{CO_2}) + \log(X_{CO}/X_{CH_4}) \\ = -17813/T + 19.605 \end{aligned} \qquad (6.4)$$

The $[\log(X_{H_2O}/X_{H_2}) + \log(X_{CO}/X_{CO_2})]$ versus $[3\log(X_{CO}/X_{CO_2}) + \log(X_{CO}/X_{CH_4})]$ binary diagram (Fig. 6.2) shows that the Copahue fumarolic gases (Agusto et al. 2013) attained equilibrium in a single vapor phase at temperature ranging from 200 to 220 °C, whereas fluids from the geothermal wells (Panarello et al. 2002) seem to equilibrate in a liquid phase at ~275 °C. This confirms the occurrence of a deep liquid dominated reservoir releasing a vapor phase that fed the fumarolic discharges. As the hydrothermal fluids are uprising through their natural pathways,

Fig. 6.3 $\text{Log}(X_{H_2}/X_{H_2O})$ versus $\log(X_{CO}/X_{CO_2})$ binary diagram for gas samples from Copahue volcano. The theoretical compositions for chemical equilibrium attained in a single saturated vapor phase (vapor) and single saturated liquid phase (liquid) at different temperatures and redox conditions controlled by the FeO-FeO$_{1.5}$ redox buffer (Giggenbach 1987), are shown. Symbols as in Fig. 6.2

re-equilibration of gas compounds occurs at different degrees, depending on the kinetics of the chemical reactions of the H_2O-CO_2-CH_4-CO-H_2 system. Both CO and H_2 rapidly respond to changes of chemical-physical conditions (Giggenbach 1987, 1996; Chiodini et al. 1993). Accordingly, in the $\log(X_{H2}/X_{H2O})$ versus $\log(X_{CO}/X_{CO2})$ diagram (Fig. 6.3) constructed on the basis of the dissociation constant of H_2O and CO_2 (Stull et al. 1969) and assuming that redox conditions are controlled by the typical hydrothermal FeO-FeO$_{1.5}$ redox buffer (Giggenbach 1987), the composition of fumarolic gases plot at temperatures ~180 °C in a vapor+liquid field, whereas that of the geothermal wells equilibrated in the liquid phase at temperatures consistent with those of H_2O-CO_2-CH_4-CO-H_2 system.

Chemical equilibria in the CO_2-CH_4 system are less affected than the CO-H_2 pair by re-equilibration at decreasing temperatures (Giggenbach 1987, 1991, 1997), thus they can be adopted to evaluate chemical-physical conditions of the deep hydrothermal system using the compositional data of the fumaroles. Assuming that water-rock interaction in the hydrothermal reservoir can be expressed, as follows (Giggenbach 1988):

Fig. 6.2 $3\log(X_{CO}/X_{CO_2}) + \log(X_{CO}/X_{CH_4})$ versus $\log(X_{H_2O}/X_{H_2}) + \log(X_{CO}/X_{CO_2})$ binary diagram for gas samples from Copahue volcano. The theoretical compositions for chemical equilibria attained in a single saturated vapor phase (vapor) and single saturated liquid phase (liquid) are shown. The composition of fumarolic gases (*open circles*) are from Agusto et al. (2013), whereas that of geothermal wells (*open triangles*) is from Panarello (2002)

Ca-Al-silicate $+$ K-feldspar $+$ CO_2
$\quad \Leftrightarrow$ K-mica $+$ calcite $\qquad$ (6.5)

f_{CO2} is fixed by the following equation:

$$\log f_{CO2} = 0.0168 \text{ T(K)} - 8.369 \qquad (6.6)$$

The CO_2-CH_4 reaction can be described, as follows:

$$CH_4 + 2H_2O \Leftrightarrow CO_2 + 4H_2 \qquad (6.7)$$
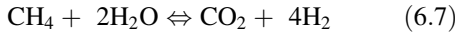
According to reaction (6.7), the dependence of X_{CH_4}/X_{CO_2} log-ratio on temperature and redox conditions in a single vapor phase is:

$$\log(X_{CH_4}/X_{CO_2}) = 5181/\text{T(K)} \\ + 4\log(X_{H_2}/X_{H_2O}) \quad (6.8)$$

whereas in a liquid phase is:

$$\log(X_{CH_4}/X_{CO_2}) = -5181/\text{T(K)} \\ + 4\log(X_{H_2}/X_{H_2O}) \\ + \log(B_{CO_2}) - \log(B_{CH_4})$$
$$(6.9)$$

where B_{CO_2} and B_{CH_4} are the vapor-liquid distribution coefficients for CO_2 and CH_4, respectively.

In the $\log(X_{CH_4}/X_{H_2O})$ versus $\log(X_{CO_2}/X_{H_2O})$ binary diagram, constructed on the basis of Eqs. (6.6), (6.8) and (6.9) and assuming the FeO-FeO$_{1.5}$ pair as the dominant redox buffer system (Giggenbach 1987) and that $f_{CO_2} = X_{CO_2}$, the Copahue fumaroles plot at temperatures ranging from 220 to 300 °C between the liquid and the vapor equilibrium lines (Fig. 6.4). The difference between the CO_2-CH_4 temperatures and the measured temperature of the reservoir (~ 260 °C) depends on the relatively low steam concentrations of the fumaroles (from 96 to 99.2 %) with respect to that of the reservoir (99.9 %). In fact, using $X_{H_2O} = 99.9$ % for all the Copahue gas 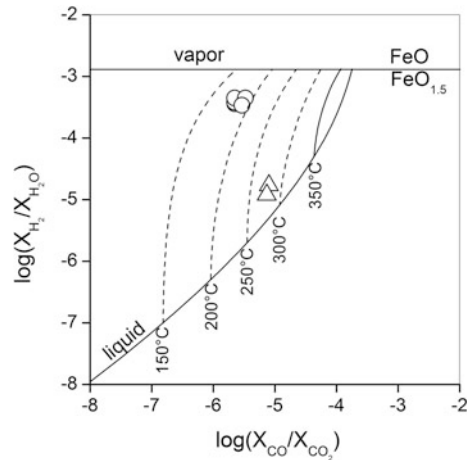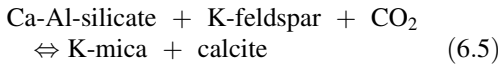samples, the position of fumarolic fluids in Fig. 6.4 is consistent with that of the geothermal wells, i.e. indicating the attainment of equilibrium in a liquid phase at ~ 260 °C.

Dehydrogenation processes involving the C_3 alkene-alkane pair can also be used to obtain
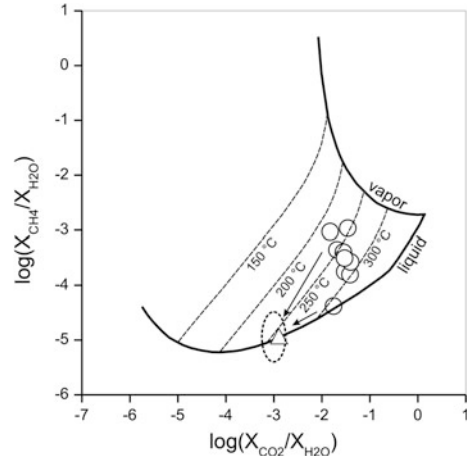
Fig. 6.4 $\log(X_{CH_4}/X_{H_2O})$ versus $\log(X_{CO_2}/X_{H_2O})$ binary diagram for gas samples from Copahue volcano. The theoretical compositions of equilibrated vapor and liquid phases at redox conditions controlled by the FeO-FeO$_{1.5}$ redox buffer (Giggenbach 1987) are reported. Symbols as in Fig. 6.2

insights on chemical-physical conditions of the deep fluid source regions (Capaccioni and Mangani 2001; Seewald et al. 1994, 2001; Taran and Giggenbach 2003; Capaccioni et al. 2004; Tassi et al. 2005). Dehydrogenation of C_3H_8 to produce C_3H_6 is given by:

$$C_3H_8 \Leftrightarrow C_3H_6 + H_2 \qquad (6.10)$$
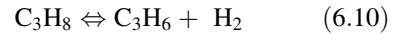
Assuming that the temperature dependency of C_3H_8 dehydrogenation is (Taran and Giggenbach 2003):

$$\log K = 6.32 - 5676/T - 222490/T^2 \quad (6.11)$$

theoretical molar $X_{C_2H_6}/X_{C_3H_8}$ log-ratios of the single vapor phase can be computed, as follows:

$$\log(X_{C_3H_6}/X_{C_3H_8})_V + \log(X_{H_2}/X_{H_2O})_V \\ = \log K - \log X_{H_2O} \qquad (6.12)$$

Considering that $B_{C_3H_6}$ and $B_{C_3H_8}$, i.e. the vapor-liquid distribution coefficients of C_3H_6 and C_3H_8, are basically identical (Wilhelm et al. 1977; Plyasunov and Shock 2003; Tassi et al. 2007), equilibrium of reaction (6.10) in a liquid phase can be expressed, as follows:

$$\log\left(X_{C_nH_{2n}}/X_{C_nH_{2n+2}}\right)_L + \log\left(X_{H_2}/X_{H_2O}\right)_L$$
$$= \log K - \log X_{H_2O} - \log B_{H_2}$$

$$(6.13)$$

where B_{H_2} is the vapor-liquid distribution coefficient of H_2 and $\log X_{H_2O} = 5.51 - 2048/T(K)$ (Giggenbach 1980). The advantage of this approach is that in the correlation plot between the sum of $\log(X_{C_3H_6}/X_{C_3H_8}) + \log(X_{H_2}/X_{H_2O})$ and temperature (Fig. 6.5), redox conditions need not be fixed externally. At 260 °C, i.e. the reservoir temperature, measured $\log(X_{C_3H_6}/X_{C_3H_8}) + \log(X_{H_2}/X_{H_2O})$ values seem to be controlled by chemical equilibrium attained in a vapor phase at measured R_H values (~ -3.4). Thus, the C_3-C_3 equilibrium was achieved at more oxidizing conditions with respect to those controlling reactions (6.5) and (6.7) (Fig. 6.4). Coincidence of CO_2-CH_4 equilibrium temperature in the liquid phase with that attained by the C_3-C_3 pair in the vapor phase implies that vapor separated from the liquid reservoir isothermally, a process that can occur in high-enthalpy hydrothermal systems (Chiodini et al. 2004). Using the measured R_H values for the construction of the $\log(X_{H_2}/X_{H_2O})$ versus $\log(X_{CO}/X_{CO_2})$ binary diagram (Fig. 6.6), the fumarolic gases plot in correspondence of the vapor line, suggesting that the redox conditions

Fig. 6.6 $\log(X_{H_2}/X_{H_2O})$ versus $\log(X_{CO}/X_{CO_2})$ binary diagram for fumaroles from Copahue volcano (Agusto et al. 2013). The theoretical compositions for chemical equilibrium attained in a single saturated vapor phase (vapor) and single saturated liquid phase (liquid) at different temperatures and redox conditions fixed at $R_H = -3.4$, are reported

controlling the C_3-C_3 pair in the uprising vapors are consistent with those regulating the H_2-CO equilibrium at 200–220 °C (Fig. 6.6).

6.6 Origin of Gas Compounds and Steam

6.6.1 Water Vapor

The origin of steam in the Copahue fluid reservoirs was investigated on the basis of the isotope ratios of water in the condensate samples. As shown by the δD-H_2O versus $\delta^{18}O$-H_2O diagram (Fig. 6.7), most of the samples from the Copahue fumaroles are slightly enriched in ^{18}O with respect to water from cold streams of the area (Panarello 2002) that plot on the Global Meteoric Water Line (GMWL; Craig 1961). Such a positive ^{18}O-shift was likely caused by that interaction of the fumarolic steam, having a meteoric origin, with rocks. At a first approximation, significant contribution of "andesitic" water (Taran et al. 1989; Giggenbach 1992a) from the magmatic source seems to be unlike, although it

Fig. 6.5 $\log(X_{C_3H_6}/X_{C_3H_8}) + \log(X_{H_2}/X_{H_2O})$ binary diagram for fumaroles from Copahue volcano (CF). The theoretical compositions of equilibrated vapor and liquid phases are reported
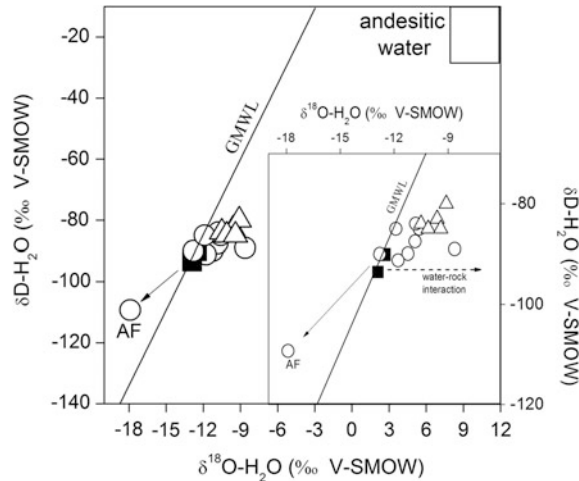
Fig. 6.7 δD-H_2O versus δ^{18}O-H_2O binary diagram for gas samples from Copahue volcano. The Global Meteoric Water Line (GMWL; Craig 1961), and the "andesitic" water field (Taran et al. 1989; Giggenbach 1992b) were reported. Fumarolic gases (Agusto et al. 2013): *open circles*; geothermal wells (Panarello 2002): *open triangles*; cold streams (Panarello 2002): closed squares

cannot completely discarded since the isotopic signature for meteoric water recharging the Copahue hydrothermal system is not univocally determined (Panarello 2002). The negative shift of both the δD-H_2O and δ^{18}O-H_2O values in the AF gas sample (Fig. 6.7) was presumably produced by secondary boiling of meteoric water at shallow depth, masking the contribution of ^{18}O-rich vapors from the hydrothermal reservoir (Agusto et al. 2013). Steam discharged from the geothermal wells has a heavier isotopic signature with respect to that of the fumaroles (insect in Fig. 6.7). This is possibly due to isotope fractionation caused by vapor extraction during the exploitation of the reservoir that was carried out when the condensate samples were collected (Panarello 2002).

6.6.2 CO_2 and He

The isotope signature of He is consistent with a dominant mantle source, since the PC, LM and LMM fumaroles show the highest R/R_a values (up to ∼8; Table 6.3) reported for a South American volcano (Hilton et al. 1993; Hoke and Lamb 2007; Ray et al. 2009; Tassi et al. 2009b, 2010a; Capaccioni et al. 2011; Aguilera et al.

2012), excepting those of Galeras volcano in Colombia (Sano et al. 1997) that, however, were strongly affected by air contamination (^{4}He/^{20}Ne < 1) making those values strongly uncertain. Such an isotopic signature is likely related to transtensional tectonics acting in this area that produced crustal attenuation and upwelling of mantle asthenosphere (Folguera et al. 2007). A significantly lower He mantle fraction (R/R_a ≤ 5) is shown by the CC and AF gas discharges, located in the northern sector of the CCVC (Fig. 6.1), suggesting addition of ^{4}He-rich fluids from the shallow environment.

The δ^{13}C-CO_2 values of the Copahue gases are slightly more negative than those of mantle-related fluids (∼−5‰ versus V-PDB; Pineau and Javoy 1983), possibly due to significant CO_2 contribution from organic material buried in subducting pelagic sediments, in agreement with the hypothesis of a mantle contaminated source based on ^{129}I data of Lake Copahue (Fehn et al. 2002). Accordingly, most of the CO_2/^{3}He ratios, ranging from 1.4 to 57×10^9, are higher than those of MORB gases (1.41×10^9; Marty and Jambon 1987; Sano and Marty 1995) (Fig. 6.8). A relatively large variation of the CO_2/^{3}He ratios could be caused by
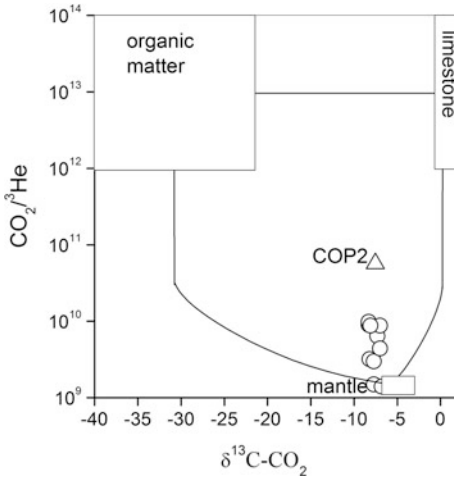
Fig. 6.8 $CO_2/^3He$ versus $\delta^{13}C$-CO_2 binary diagram for gas samples from Copahue volcano. Boxes and mixing curves between the three end-members (organic matter, limestone and MORB) are from Sano and Marty (1995). Symbols as in Fig. 6.2

Fig. 6.9 a, **b** $^{40}Ar^*/^{40}Ar$ versus **a** N_2/Ar and **b** $\delta^{15}N$ binary diagrams for gas samples from Copahue volcano. The composition of the Deep Component (DC) was estimated at $^{40}Ar^*/^{40}Ar = 0.99$

secondary processes, such as gas-liquid interaction at shallow depth, affecting at different degrees these two gas species.

6.6.3 N_2 and Ar

Following the approach firstly proposed by Kennedy et al. (1985) and subsequently modified by Chiodini et al. (2012), potential sources for N_2 and Ar of the Copahue gases were investigated by using the $^{40}Ar^*/^{40}Ar$ ratio, i.e. the ratio between total ^{40}Ar and non-atmospheric Ar ($^{40}Ar^*$) calculated assuming that ^{36}Ar completely derives from the atmosphere, as follows:

$$^{40}Ar* = ^{40}Ar - ^{40}Ar/^{36}Ar_{atm} \times ^{36}Ar_{meas}$$
(6.14)

where $^{40}Ar/^{36}Ar_{atm} = 295.5$ (Marty 1995). As shown by the $^{40}Ar^*/^{40}Ar$ versus N_2/Ar diagram (Fig. 6.9a), the Copahue gases seems to be produced by mixing between a deep component (DC) characterized by $^{40}Ar^*/^{40}Ar = 0.99$, a value that can be assumed as representative for mantle sources, being the typical $^{40}Ar/^{36}Ar$ ratios in a upper mantle up to 40,000 source (Burnard et al.

1997; Graham 2002; Marty and Dauphas 2003), and $N_2/Ar \sim 3,500$, and shallow (meteoric) fluids having $^{40}Ar^*/^{40}Ar = 0$ and $N_2/Ar = 40$, the latter being the N_2/Ar ratio of Air Saturated Water (ASW). Using the same diagnostic method, the $\delta^{15}N$ value of the DC for the Copahue fluids was estimated at 5.5‰ versus air (Fig. 6.9b), i.e. a value that is consistent with the average $\delta^{15}N$ value of sediments of Central America (Li et al. 2003), suggesting that the extremely high N_2/Ar ratios of these gases depend on N_2 production from N-rich hemipelagic sediments (Giggenbach 1992b; Sadofsky and Bebout 2004). Accordingly, the estimated $N_2/^4He$ (Fig. 6.10a) and $N_2/^3He$ (Fig. 6.10b) DC ratios ($\sim 1,500$ and 1.5×10^8, respectively) are consistent with those of a wide variety of arc settings (Jenden et al. 1988; Giggenbach and Poreda 1993; Giggenbach et al. 1993; Fischer et al. 1998; Sano et al. 2001; Hilton et al. 2002), whereas the relatively low DC $^4He/^{40}Ar$ ratio (2.25; Fig. 6.10c), typically found in mantle fluids (Ozima and Posodek 2002; Graham 2002), seems to indicate that the N_2- and CO_2-rich sediments contaminating the mantle source feeding the Copahue fumaroles do not contain significant amounts of crustal He.

To further investigate the origin of the strong N_2-excess in the Copahue fumarolic fluids, contributions from extra-atmospheric N_2 sources, i.e.
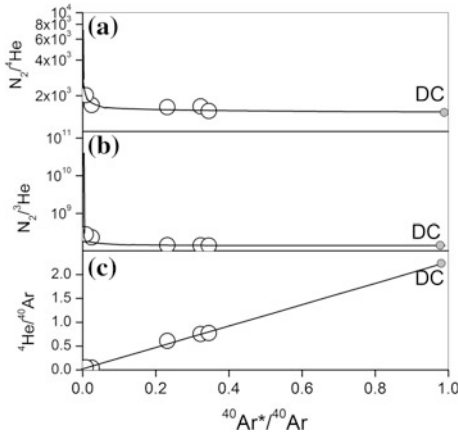
Fig. 6.10 **a–c** $^{40}Ar*/^{40}Ar$ versus **a** $N_2/^4He$, **b** $N_2/^3He$ and **c** $^4He/^{40}Ar$ binary diagrams for gas samples from Copahue volcano. The composition of the Deep Component (DC) was estimated at $^{40}Ar*/^{40}Ar = 0.99$

Fig. 6.11 $\delta^{15}N_2$ versus N_2/He binary diagram for gas samples from Copahue volcano. Boxes and mixing curves between the three end-members (Sediment, Mantle and Air) are from Sano et al. (2001) and Fischer et al. (2002)

mantle (f_M) and subducted sediments (f_S), can also be evaluated on the basis of the $\delta^{15}N$ values and N_2/He ratios (Sano et al. 1998, 2001; Fischer et al. 2002), as described by the following equations:

$$(\delta^{15}N)_{meas} = f_A \times (\delta^{15}N)_A + f_M \times (\delta^{15}N)_M + f_S \times (\delta^{15}N)_S \tag{6.15}$$

$$1/(N_2/He)_{meas} = f_A \times 1/(N_2/He)_A + f_M \times 1/(N_2/He)_M + f_S \times 1/(N_2/He)_S \tag{6.16}$$

$$1 = f_A + f_M + f_S \tag{6.17}$$

where (f_A) is the N_2 fraction from air. The following reference values were considered: $(\delta^{15}N)_M = -5‰$ versus Air; $(\delta^{15}N)_S = +7‰$ versus Air; $(\delta^{15}N)_A = 0‰$ versus Air; $(N_2/He)_M = 150 \pm 30$; $(N_2/He)_S = 1.05 \times 10^4$; $(N_2/He)_A = 1.49 \times 10^5$ (Marty and Zimmermann 1999; Elkins et al. 2006).

As shown in Fig. 6.11, the PC3, LM1 and LMM2 gas discharges are mainly fed by a

sediment source (~ 85 %), whereas the N_2 fractions from air are low (from 3 to 11 %), in agreement with the high $^{40}Ar/^{36}Ar$ values (up to 450). The relatively low N_2 contribution from mantle (from 6 to 11 %) is supported by the $^{87}Sr/^{86}Sr$, $^{143}Nd/^{144}Nd$, $^{207}Pb/^{204}Pb$ and $^{206}Pb/^{204}Pb$ ratios measured in basaltic-andesitic lavas and pyroclastic rocks from the CCVC (Varekamp et al. 2006), indicating a significant sediments contamination of the magma source. The relatively high N_2 air fractions (47 and 69 %, respectively) characterizing the AF2 and CC2 gases, consistent by their low $^{40}Ar/^{36}Ar$ values (<303), were interpreted as related to addition of atmospheric gases, which in the northern sector of the volcano is likely added to uprising gases by meteoric water permeating through local fault systems (Agusto et al. 2013).

The N_2-He-Ar ternary diagram (Fig. 6.12; Giggenbach 1992b) shows that the N_2/He ratios of gases sampled in 2006 and 2007 have N_2/He ratios significantly lower than those collected in 2012 and prior to 2000. It is worth noting that the R/R_a values in 2003, 2006 and 2007 were significantly higher than those measured in 2012 (Table 6.3), possibly in relation to the intrusion of mafic magma occurred prior to the 2000 eruption (Varekamp et al. 2001, 2006). A similar evolution of the He isotopic signature was
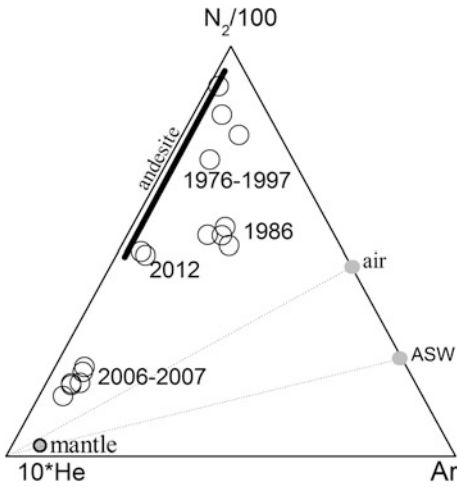
Fig. 6.12 10*He-N$_2$/100-Ar ternary diagram for gas samples from Copahue volcano. Compositional field for "Andesitic", "Mantle" (Giggenbach 1992b) and N$_2$/Ar ratios of "Air" and "ASW" (Air Saturated Water) are reported

already observed in fluids discharged from Galeras volcano (Colombia) in 1993 (Fischer et al. 1996, 1997), in concomitance with a magmatic injection that triggered the eruptive events occurred in the following period (Stix et al. 1997). These evidences may suggest that the N$_2$/He variations observed in the Copahue fumarolic fluids were caused by addition to the

hydrothermal system of fluids released from a new magma batch characterized by a relatively low N$_2$/He ratio, being N$_2$ less soluble than He (Lux 1987). A new magma injection is consistent with the lack of any specific temporal trend of the CO$_2$/^{3}He ratios and δ^{13}C-CO$_2$ values, as expected in case of variation of deep slab sediments. However, the lack of information about the composition of fumaroles from 1997 to 2006 makes this hypothesis only speculative. Moreover, it is unclear how clues of this process were still recognizable in fumarolic fluids in 2007, 7 years after the 2000 eruption, but not in 2012. An alternative explanation is that the temporal evolution of the inert gas composition depends on a high variability contents of N$_2$-bearing compounds in the sediments contaminating the magma at the source of the volcanic-hydrothermal activity of this volcano.

6.6.4 CH$_4$ and Light Hydrocarbons

Processes regulating formation and behavior of CH$_4$ in fluid discharges from natural systems are commonly investigated on the basis of δ^{13}C-CH$_4$ and δD-CH$_4$ ratios (Schoell 1980, 1988). The isotopic signatures of CH$_4$ in the Copahue fumaroles (Fig. 6.13) seem to indicate that this gas is produced by thermal degradation of parental

Fig. 6.13 δ^{13}C-CH$_4$ versus δD-CH$_4$ binary diagram for gas samples from Copahue volcano. Values for gases of biogenic and thermogenic origin (Schoell 1980, 1988) are reported
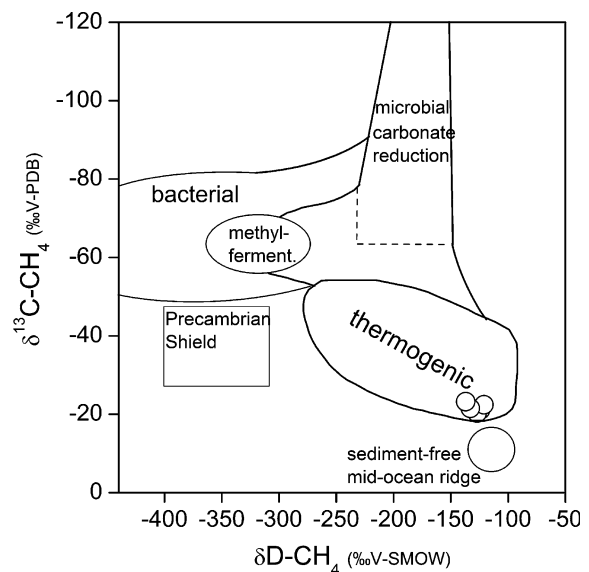
organic material, a process that typically occur at hydrothermal conditions (e.g., Des Marais et al. 1981; Darling 1998; Mango 2000). However, the data points plot near the compositional field of gases supposed to have an abiotic origin, i.e. those from sediment-free mid-oceanic ridges (McCollom and Seewald 2007, and references therein). Moreover, recent studies (Fiebig et al. 2007, 2009; Tassi et al. 2012) have reported geochemical evidences suggesting that CH_4 in hydrothermal gases characterized by high CH_4/C_{2+} ratios (>250) and $\delta^{13}C$-CH_4 values >−25‰ versus V-PDB (Table 6.3), such as those of the Copahue fumaroles (Tables 6.1 and 6.2), are produced by abiogenic processes, such as Fischer–Tropsch Type (FTT) synthesis (Fischer and Tropsch 1926; Anderson 1984). Thus, it seems reasonable to suppose that the origin of CH_4 in the Copahue hydrothermal reservoir is related to mixing of thermogenic and abiogenic contributions. This hypothesis is in agreement with the composition of heavier organic volatiles, characterized by the occurrence of C_6H_6 and sulfur heterocycles (Table 6.2), indicative of thermogenic hydrocarbon production (Tassi et al. 2010b), and C_3-C_4 alkenes, likely formed through dehydrogenation of alkanes at temperature and redox conditions typical of a hydrothermal-magmatic environment (Capaccioni et al. 1995; Taran and Giggenbach 2003; Tassi et al. 2005, 2010a).

6.7   The Conceptual Model of Copahue Volcano

Recent geochemical investigations provided a strong contribution to the knowledge of the chemical-physical features of fluids discharged from fumaroles of the five thermal areas located in the surroundings of this extremely active volcano. A conceptual model describing the Copahue hydrothermal-magmatic system is reported in Fig. 6.14. Magmatic fluids released from a magma body located at a depth of ∼4–5 km (Velez et al. 2011) interact with a perypheral hydrothermal aquifer mostly recharged by meteoric water. Acidic gases, mostly consisting of SO_2, HCl and HF, are dissolved in this aquifer, where production of reduced gas species, such as H_2, H_2S, CO, CH_4 and light hydrocarbons, occurs. On the contrary, the central part of the volcanic system, where the hyperacid crater lake and the hot springs are located, is directly connected with a magmatic-dominated fluids reservoir (Varekamp et al. 2004). Carbon dioxide, N_2 and noble gases, which are not significantly affected by secondary processes, mantain their magmatic isotopic signatures even in the hydrothermal discharges. Most of the R/R_a values mimic those typical of MORB fluids, whereas the $CO_2/^3He$ ratios and the $\delta^{13}C$-CO_2 and $\delta^{15}N_2$ values indicate a significant fluid contribution from sediments of the subducting
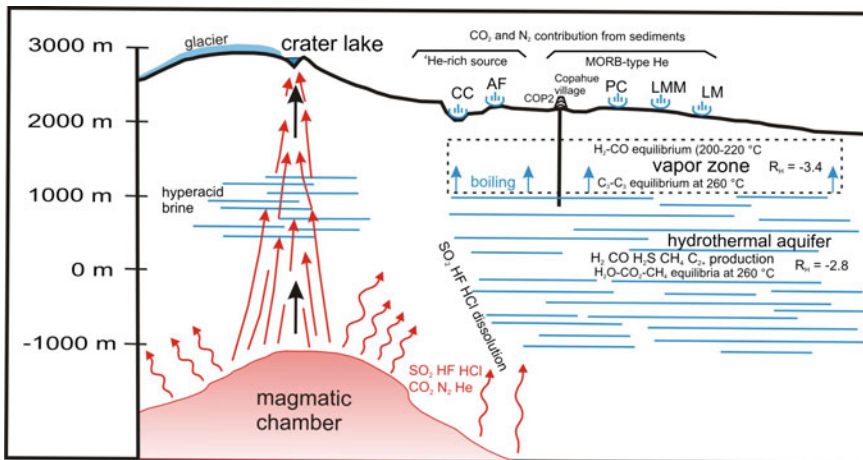
Fig. 6.14   Geochemical conceptual model of magmatic–hydrothermal system of Copahue volcano

slab and/or directly interacting with the magmatic source within the crust. According to the Ar, N_2 and He isotope values in the hydrothermal discharges, a deep end-member characterized by $N_2/Ar = 3500$, $\delta^{15}N = 5.5‰$ versus Air, $^4He/^{40}Ar = 2.2$, $N_2/^4He = 1,500$, and $N_2/^3He = 1.5 \times 10^8$ can be recognized (Agusto et al. 2013). Significant contribution from a shallow and ^4He-rich aquifer, likely permeating through a local fault system, affects gas discharges emerging in the northern sector of the volcanic edifice. Temperature estimations based on chemical equilibria in the H_2O-CO_2-CH_4 system, attained at redox conditions typical of a hydrothermal reservoir, are consistent with those measured in the geothermal wells (~ 260 °C) and similar to those possibly characterizing of the magmatic fluid reservoir feeding the hyperacid crater lake and hot springs (Varekamp et al. 2004). On the contrary, the C_3H_6-C_3H_8 pair, H_2 and CO tend to re-adjust at decreasing temperatures and more oxidizing conditions in a uprising vapor phase produced by the boiling hydrothermal aquifer (Agusto et al. 2013). Steam condensation, affecting these fluids at decreasing temperatures, controls the outlet fumarolic temperatures.

According to this model, the hydrothermal discharges investigated in this chapter would not be sensitive to changes related to rejuvenating activity of Copahue volcano, since magmatic gases are buffered by the liquid-dominated reservoir feeding these emissions. However, the temporal behavior of inert gas compounds (N_2, Ar and He) observed in the last decades suggests that the geochemical monitoring of these parameters may provide important information for the interpretation of mechanism triggering a possible volcanic unrest.

References

Aguilera F, Tassi F, Darrah T, Moune S, Vaselli O (2012) Geochemical model of a magmatic-hydrothermal system at the Lastarria volcano, northern Chile. Bull Volcanol 74:119–134

Agusto M (2011) Estudio geoquímico de los fluidos volcánicos e hidrotermales del Complejo Volcánico Copahue Caviahue y su aplicación para tareas de seguimiento. Ph.D. Thesis, Universidad de Buenos Aires, p 270

Agusto M, Caselli A, Tassi F, Dos Santos Alfonso M, Vaselli O (2012) Seguimiento geoquimico de las aguas acidas del sistema volcan Copahue—Rio Agrio: posible aplicacion para la identificacion de precursores eruptivos. Rev As Geol Arg 689(4):481–495 (in Spanish)

Agusto M, Tassi F, Caselli AT, Vaselli O, Rouwet D, Capaccioni B, Caliro S, Chiodini G, Darrah T (2013) Gas geochemistry of the magmatic-hydrothermal fluid reservoir in the Copahue-Caviahue Volcanic Complex (Argentina). J Volcanol Geotherm Res 257:44–56

Anderson RB (1984) The Fischer-Tropsch synthesis. Academic Press, New York

Bermúdez A, Delpino D, López Escobar L (2002) Caracterización geoquímica de lavas y piroclastos holocenos del volcán Copahue, incluyendo los originados en la erupción del año 2000. Comparación con otros volcanes de la Zona Volcánica Sur de los Andes. XV Congreso Geológico Argentino, Calafate, Argentina, pp 377–382

Burnard P, Graham D, Turner G (1997) Vesicle-specific noble gas analyses of "popping rock": implications for primordial noble gases in earth. Science 276:568–571

Capaccioni B, Mangani F (2001) Monitoring of active but quiescent volcanoes using light hydrocarbon distribution in volcanic gases: the results of 4 years of discontinuous monitoring in the Campi Flegrei (Italy). Earth Planet Sci Lett 188:543–555

Capaccioni B, Martini M, Mangani F (1995) Light hydrocarbons in hydrothermal and magmatic fumaroles: hints of catalytic and thermal reactions. Bull Volcanol 56:593–600

Capaccioni B, Taran Y, Tassi F, Vaselli O, Mangani F, Macias JL (2004) Source conditions and degradation processes of light hydrocarbons in volcanic gases: an example from El Chichón volcano (Chiapas State, Mexico). Chem Geol 20:81–96

Capaccioni B, Aguilera F, Tassi F, Vaselli O (2011) Geochemistry of gas emissions from Tacora volcano (northern Chile): evidences of magmatic fluid input into a hydrothermal reservoir. J Volcanol Geotherm Res 208:77–85

Chiodini G, Marini L (1998) Hydrothermal gas equilibria: The H_2O-H_2-CO_2-CO-CH_4 system. Geochim Cosmochim Acta 62:2673–2687

Chiodini G, Cioni R, Marini L (1993) Reactions governing the chemistry of crater fumaroles from Vulcano Island, Italy, and implications for volcanic surveillance. Appl Geochem 8(4):357–371

Chiodini G, Avino R, Brombach T, Caliro S, Cardellini C, de Vita S, Frondini F, Granirei D, Marotta E, Ventura G (2004) Fumarolic and diffuse soil degassing

west of Mount Epomeo, Ischia, Italy. J Volcanol Geotherm Res 133:291–309

Chiodini G, Caliro S, Lowenstern JB, Evans WC, Bergfeld D, Tassi F, Tedesco D (2012) Insights from fumarole gas geochemistry on the origin of hydrothermal fluids on the Yellowstone Plateau. Geochim Cosmochim Acta 89:265–278

Craig H (1961) Isotopic variations in meteoric waters. Science 133:1702–1703

D'Amore F, Panichi C (1980) Evaluation of deep temperature of hydrothermal systems by a new gas-geothermometer. Geochim Cosmochim Acta 44:549–556

D'Amore F, Sierra JL, Panarello H (1988) Informe Avance del Contrato de Investigación OIEA N. 3988/IG (in Spanish)

Darling WG (1998) Hydrothermal hydrocarbons gases: 1. Genesis and Geothermometry. Appl Geochem 13:815–824

Delpino D, Bermúdez A (1993) La actividad del volcán Copahue durante 1992. Erupción con emisiones de azufre piroclástico. Provincia de Neuquen, Argentina. XII Congreso Geológico Argentino, Mendoza, Argentina, pp 292–301

Delpino D, Bermúdez A (2002) La erupción del volcán Copahue del año 2000. Impacto social y al medio natural. Provincia del Neuquén. Argentina. XIII Congreso Geológico Argentino, Buenos Aires, Argentina, pp 365–370

Des Marais DJ, Donchin JH, Truesdell AH, Nehring NL (1981) Molecular carbon isotopic evidence for the origin of geothermal hydrocarbons. Nature 292:826–828

Elkins LJ, Fischer TP, Hilton DR, Sharp ZP, McKnight S, Walker J (2006) Tracing nitrogen in volcanic and geothermal volatiles from the Nicaraguan volcanic front. Geochim Cosmochim Acta 70:5215–5235

Fehn U, Snyder GT, Varekamp JC (2002) Detection of recycled marine sediment components in crater lake fluids using ^{129}I. J Volcanol Geotherm Res 115:451–460

Fiebig J, Woodland AB, Spangenberg J, Oschmann W (2007) Natural evidence for rapid abiogenic hydrothermal generation of CH_4. Geochim Cosmochim Acta 71:3028–3039

Fiebig J, Woodland A, D'Alessandro W, Puttmann W (2009) Excess methane in continental hydrothermal emissions is abiogenic. Geology 37:495–498

Fischer F, Tropsch H (1926) Die Erodölsynthese bei gewöhnlichem druck aus den vergangsprodukten der kohlen. Brennstoff-Chemie 7:97–116

Fisher T, Arehart G, Sturchio N, Williams S (1996) The relationship between fumarole gas composition and eruptive activity at Galeras Volcano. Colombia Geol 24(6):531–534

Fischer T, Sturchio N, Stix J, Arehart G, Counce D, Williams S (1997) The chemical and isotopic composition of fumarolic gases and spring discharges from Galeras Volcano. Colombia J Volcanol Geotherm Res 77:229–253

Fischer TP, Giggenbach WF, Sano Y, Williams SN (1998) Fluxes and sources of volatiles discharged from Kudryavy, a subduction zone volcano, Kurile Islands. Earth Planet Sci Lett 160:81–96

Fischer TP, Hilton DR, Zimmer MM, Shaw AM, Sharp ZD, Walker JA (2002) Subduction and recycling of nitrogen along the Central American Margin. Science 297:1154–1157

Folguera A, Introcaso A, Giménez M, Ruiz F, Martinez P, Tunstall C, García Morabito E, Ramos VA (2007) Crustal attenuation in the Sourthern Andean retroarc (38°-39°30' S) determined from tectonic and gravimetric studies: The Lonco-Luán asthenospheric anomaly. Tectonophysics 239:129–147

Fujita T, Abe M, Yamada M, Nakanishi S, Tokada N (1996) Feasibility study of Copahue geothermal development project. Argentina. J Jap Geotherm En Ass 33(1):39–55

Giggenbach WF (1980) Geothermal gas equilibria. Geochim Cosmochim Acta 44:2021–2032

Giggenbach WF (1987) Redox processes governing the chemistry of fumarolic gas discharges from White Island, New Zealand. Appl Geochem 2:143–161

Giggenbach WF (1988) Geothermal solute equilibria. Derivation of Na-K-Mg-Ca geoindicators. Geochim Cosmochim Acta 52(12):2749–2765

Giggenbach WF (1991) Chemical techniques in geothermal exploration. Application of geochemistry in geothermal reservoir development. UNITAR, New York, pp 253–273

Giggenbach WF (1992a) Isotopic shifts in waters from geothermal and volcanic systems along convergent plate boundaries and their origin. Earth Planet Sci Lett 113(4):495–510

Giggenbach WF (1992b) The composition of gases in geothermal and volcanic systems as a function of tectonic setting. Final proceedings of international symposium. Water-Rock Interaction, WRI-8, pp 873–878

Giggenbach WF (1996) Chemical composition of volcanic gases. In: Scarpa R, Tilling R (eds) Monitoring and mitigation of volcano hazard. Springer, Berlin, pp 222–256

Giggenbach WF (1997) Relative importance of thermodynamic and kinetic processes in governing the chemical and isotopic composition of carbon gases in high-heatflow sedimentary basins. Geochim Cosmochim Acta 61:3763–3785

Giggenbach WF, Poreda RJ (1993) Helium isotopic and chemical composition of gases from volcanic-hydrothermal systems in the Philippines. Geothermics 22:369–380

Giggenbach WF, Sano Y, Wakita H (1993) Isotopic composition of helium, CO_2, and CH_4 contents in gases produced along the New Zealand part of a convergent plate boundary. Geochim Cosmochim Acta 57:3427–3455

Graham DW (2002) Noble gas isotope geochemistry of midocean ridge and ocean island basalts: characterization of mantle source reservoirs. In: Porcelli D,

Ballentine CJ, Wieler R (eds) Noble gases in geochemistry and cosmochemistry, Reviews in mineralogy and geochemistry. Society of America, Washington, DC., vol 47, pp 247–317

Hilton DR, Hammerschmidt K, Teufel S, Friedrichsen H (1993) Helium isotope characteristics of Andean geothermal fluids and lavas. Earth Planet Sci Lett 120:265–282

Hilton DR, Fischer TP, Marty B (2002) Noble gases and volatile recycling at subduction zones, in noble gases. In: Procelli D, Ballentine CJ, Wieler R (eds) Cosmochemistry and Geochemistry, Mineral. Society of America, Washington D. C., vol 9, pp 319–370

Hoke L, Lamb S (2007) Cenozoic behind-arc volcanism in the Bolivian Andes, SouthAmerica: implications for mantle melt generation and lithospheric structure. J Geol Soc Lond 164:795–814

Jenden PD, Kaplan IR, Poreda RJ, Craig H (1988) Origin of nitrogen-rich natural gases in the California Great Valley: evidence from helium, carbon, and nitrogen isotope ratios. Geochim Cosmochim Acta 52:851–861

JICA (Japan International Cooperation Agency) (1992) The feasibility study on the northern Neuquén geothermal development project. Ente Provincial de Energía de la Provincial del Neuquén, Argentina, p 89

Jurío RL (1977) Características geoquímicas de los fluidos termales de Copahue (Neuquén—Argentina). Principales implicancias geotérmicas. Minería 172:1–11 (in Spanish)

Kennedy BM, Lynch MA, Reynolds JH, Smith SP (1985) Intensive sampling of noble gases in fluids at Yellowstone: i early overview of the data; regional patterns. Geochim Cosmochim Acta 49:1251–1261

Li L, Sadofsky SJ, Bebout GE (2003) Carbon and nitrogen input fluxes in subduction sediments at the Izu-Bonin and Central America convergentmargins. EOS. Transact Am Geophys Union 84(46) (FallMeet. Suppl., Abstract T32A-0908)

Linares E, Ostera HA, Mas LC (1999) Cronología K-Ar del Complejo Efusivo Copahue-Caviahue, Provincia del Neuquén. Rev Assoc Geol Arg 54(3):240–247

Lux G (1987) The behavior of noble gases in silicate liquids: solution, diffusion, bubbles, and surface effects, with applications to natural samples. Geochim Cosmochim Acta 51:1549–1560

Mango FD (2000) The origin of light hydrocarbons. Geochim Cosmochim Acta 64:1265–1277

Martini M, Bermúdez A, Delfino D, Giannini L (1997) The thermal manifestation of Copahue volcano area. Final Proc. VIII Congreso Geológico Chileno, Antofagasta, Chile, pp 352–356

Marty B (1995) Nitrogen content of the mantle inferred from N2-Ar correlation in oceanic basalts. Nature 377:326–328

Marty B, Jambon A (1987) C/^{3}He in volatile fluxes from the solid earth: implications for carbon geodynamics. Earth Planet Sci Lett 83:16–26

Marty B, Dauphas N (2003) The nitrogen record of crust–mantle interaction and mantle convection from Archean to present. Earth Planet Sci Lett 206:397–410

Marty B, Zimmermann L (1999) Volatiles (He, N, C, Ar) in mid-ocean ridge basalts: assessment of shallow-level fractionation and characterization of source composition. Geochim Cosmochim Acta 63:3619–3633

Mas GR, Mas LC, Bengochea L (1996) Alteración ácido-sulfática en el Campo Geotérmico Copahue, Provincia del Neuquén. Rev Asoc Geol Arg 51 (1):78–86

Mas LC, Mas GR, Bengochea L (2000) Heatflow of Copahue geothermal field, its relation with tectonic scheme. Final Proc World Geothermal Congress, Tohoku, Japan, pp 1419–1424

McCollom TM, Seewald JS (2007) Abiotic synthesis of organic compounds in deep-sea hydrothermal environments. Chem Rev 107:382–401

Naranjo JA, Polanco E (2004) The 2000 AD eruption of Copahue Volcano. Southern Andes Rev Geol Chile 31 (2):279–292

Ozima M, Podosek FA (2002) Noble gas geochemistry. Cambridge University Press, Cambridge

Panarello HO (2002) Características isotópicas y termodinámicas de reservorio del campo geotérmico Copahue-Caviahue, provincia del Neuquén. Rev As Geol Arg 57(2):182–194

Panarello HO, Sierra JL, Gingins MO, Levin M, Albero MC (1986) Estudio geoquímico e isotópico de los sistemas geotermales de la Provincia del Neuquén, República Argentina, primera parte: área Copahue. Informe anual de avance del contrato OIEA N. 3988 IG (B) (in spanish)

Panarello HO, Levin M, Albero MC, Sierra JL, Gingins MO (1988) Isotopic and geochemical study of the vapour dominated geothermal field of Copahue (Neuquén, Argentina). Rev Brasil Geofís 5(2):275–282

Parker SR, Gammons CH, Pedrozo FL, Wood SA (2008) Diel changes in metal concentrations in a geogenically acidic river: Rio Agrio, Argentina. J Volcanol Geotherm Res 178:213–223

Pineau F, Javoy M (1983) Carbon isotopes and concentration in mid-oceanic ridge basalts. Earth Planet Sci Lett 62:239–257

Plyasunov AV, Shock EL (2003) Prediction of the vapor-liquid distribution constants for volatile nonelectrolytes in water up to its critical temperature. Geochim Cosmochim Acta 67:4981–5009

Ray MC, Hilton DR, Muñoz J, Fischer TP, Shaw AM (2009) The effects of volatile recycling, degassing and crustal contamination on the helium and carbon geochemistry of hydrothermal fluids from the Southern Volcanic Zone of Chile. Chem Geol 166:38–49

Sadofsky SJ, Bebout GE (2004) Nitrogen geochemistry of subducting sediments: new results from the Izu-Bonin-Mariana margin and insights regarding global nitrogen subduction. Geochem Geophys Geosys 5, doi:10.1029/2003GC000543

Sano Y, Marty B (1995) Origin of carbon in fumarolic gases from island arcs. Chem Geol 119:265–274

Sano Y, Gamo T, Williams SN (1997) Secular variations of helium and carbon isotopes at Galera volcano, Colombia. J Volcanol Geotherm Res 77:255–265

Sano Y, Takahata N, Nishio Y, Marty B (1998) Nitrogen recycling in subduction zones. Geophys Res Lett 25:2289–2292

Sano Y, Takahata N, Nishio Y, Fischer TP, Williams SN (2001) Volcanic flux of nitrogen from the earth. Chem Geol 171:263–271

Saracco L, D'Amore F (1989) CO₂B, a computer program for applying a gas-geothermometer to geothermal systems. Comput Geosci 15(7):1053–1065

Schoell M (1980) The hydrogen and carbon isotopic composition of methane from natural gases of various origins. Geochim Cosmochim Acta 44:649–661

Schoell M (1988) Multiple origins of methane in the Earth. Chem Geol 71:1–10

Seewald JS (1994) Evidence for metastable equilibrium between hydrocarbons under hydrothermal conditions. Nature 370:285–287

Seewald JS (2001) Aqueous geochemistry of low molecular weight hydrocarbons at elevated temperatures and pressures: constraints from mineral buffered laboratory experiments. Geochim Cosmochim Acta 65:1641–1664

Sierra J, D'Amore F, Panarello H, Pedro G (1992) Reservoir characteristics of the vapour dominated geothermal field of Copahue, Neuquén, Argentina, as established by isotopic and geochemical techniques. Geothermal investigations with isotope and geochemical tecniques in Latin America. Nuclear Techniques in Geothermal Resources Investigation. San José, Costa Rica, pp 13–30

Stix J, Torres R, Narváez L, Cortés GP, Raigosa J, Gómez D, Castonguay R (1997) A model of vulcanian eruptions at Galeras volcano, Colombia. J Volcanol Geotherm Res 77:285–303

Stull DR, Westrum EF, Sinke GG (1969) The Chemical thermodynamics of organic compounds. Wiley, New York

Taran YA, Giggenbach WF (2003) Geochemistry of light hydrocarbons in subduction-related volcanic and hydrothermal fluids. In: Simmons SF, Graham IJ (eds), Volcanic, geothermal, and ore-forming fluids: Rulers and witnesses of processes within the Earth, Littleton, Colorado, Society of Economic Geology Special Publications, vol 10, pp 61–74

Taran YA, Pokrovsky BG, Esikov AD (1989) Deuterium and oxygen-18 in fumarolic steam and amphiboles from some Kamchatka volcanoes: 'andesitic waters'. Dokl Akad Nauk SSSR 304:440–443

Tassi F, Martinez C, Vaselli O, Capaccioni B, Viramonte J (2005) The light hydrocarbons as new geoindicators of equilibrium temperatures and redox conditions of geothermal fields: evidence from El Tatio (northern Chile). App Geochem 20:2049–2062

Tassi F, Vaselli O, Capaccioni B, Montegrossi G, Barahona F, Caprai A (2007) Scrubbing processes and chemical equilibria controlling the composition of light hydrocarbons in natural gas discharges: an example from the geothermal fields of Salvador. Geochem Geophys Geosyst 8:Q05008. doi:10.1029/2006GC001487

Tassi F, Capaccioni B, Capecchiacci F, Vaselli O (2009a) Non-methane volatile organic compounds (VOCs) at El Chichon volcano (Chiapas, mexico): geochemical features, origin and behavior. Geofis Intern 48(1):85–95

Tassi F, Aguilera F, Vaselli O, Medina E, Tedesco D, Delgado Huertas A, Poreda R, Kojima S (2009b) The magmatic- and hydrothermal-dominated fumarolic system at the Active Crater of Lascar volcano, northern Chile. Bull Volcanol 71:171–183

Tassi F, Aguilera F, Darrah T, Vaselli O, Capaccioni B, Poreda RJ, Delgado Huertas A (2010a) Fluid geochemistry of hydrothermal system in the Arica-Parinacota, Tarapacá and Antofagasta regions (Northern Chile). J Volcanol Geotherm Res 192:1–15

Tassi F, Montegrossi G, Capaccioni B, Vaselli O (2010b) Origin and distribution of thiophenes and furans in thermal fluid discharges from active volcanoes and geothermal systems. Int J Mol Sci 11:1434–1457

Tassi F, Fiebig J, Vaselli O, Nocentini M (2012) Origins of methane discharging from volcanic, hydrothermal and cold emissions in Italy. Chem Geol 310–311:36–48

Vallés J, Baschini M, Pettinati G, García N (2004) Characterization of muds and waters of the Copahue geothermal field, Neuquen province, Patagonia, Argentina. ICAM-Brasil, pp 507–510

Varekamp JC (2008) The volcanic acidification of glacial Lake Caviahue, Province of Neuquen. Argentina J Volcanol Geotherm Res 178:184–196

Varekamp JC, Ouimette A, Hermán S, Bermúdez A, Delpino D (2001) Hydrothermal element fluxes from Copahue, Argentina: a "beehive" volcano in turmoil. Geology 29(11):1059–1062

Varekamp JC, Ouimette AP, Kreulen R (2004) The Magmato System at Copahue Volcano, Argentina. In: Wanty RB, Seal RB II (eds) Water-rock interaction, 11. Bakema Publishers, Leiden, pp 215–218

Varekamp JC, deMoor JM, Merrill MD, Colvin AS, Goss AR, Vroon PZ, Hilton DR (2006) Geochemistry and isotopic characteristics of the Caviahue-Copahue volcanic complex, Province of Neuquen, Argentina. Geol Soc Am 407:317–342

Varekamp JC, Ouimette AP, Herman SW, Flynn KS, Bermudez A, Delpino D (2009) Naturally acid waters from Copahue volcano, Argentina. App Geochem 24:208–220

Velez ML, Euillades P, Caselli AT, Blanco M, Martinez Diaz J (2011) Deformation of Copahue volcano: inversion of InSAR data using a genetic algorithm. J Volcanol Geotherm Res 202:117–126

Wilhelm E, Battino R, Wiicock RJ (1977) Low-pressure solubility of gases in liquid water. Chem Rev 77:219–262

Acid Rivers and Lakes at Caviahue-Copahue Volcano as Potential Terrestrial Analogues for Aqueous Paleo-Environments on Mars

A. Rodríguez, J.C. Varekamp, M.J. van Bergen,
T.J. Kading, P. Oonk, C.H. Gammons and M. Gilmore

Abstract

Mars carries primary rock with patchy occurrences of sulfates and sheet silicates. Both Mg- and Fe- sulfates have been documented, the former being rather uncommon on Earth. To what extent can a natural acidic river system on Earth be a terrestrial analog for early Mars environments? Copahue volcano (Argentina) has an active acid hydrothermal system that has precipitated a suite of minerals in its hydrothermal reservoir (silica, anhydrite, alunite, jarosite). Leakage from this subterranean system through hot springs and into the crater lake have formed a strongly acidified watershed (Río Agrio), which precipitates a host of minerals during cooling and dilution downstream. A suite of more than 100 minerals has been found and conditions for precipitation of the main phases are simulated with speciation/saturation routines. The lower part of the watershed (Lake Caviahue and the Lower Río Agrio) have abundant deposits of ferricrete since 2003: hydrous ferric oxides and schwertmannite occur, their precipitation being mediated by Fe-oxidizing bacteria and photochemical processes. Further downstream, at greater degrees of dilution, hydrous aluminum oxides and sulfates form and create 'alcretes' lining the river bed. The watershed carries among others jarosite, hematite, anhydrite, gypsum and silica minerals and the origin of all these minerals

A. Rodríguez · M.J. van Bergen · P. Oonk
Department of Earth Sciences, Utrecht University,
Budapestlaan 4, 3584 CD Utrecht, The Netherlands

J.C. Varekamp (✉) · T.J. Kading · M. Gilmore
Earth and Environmental Sciences, Wesleyan
University, 265 Church Street, Middletown, CT
06459, USA
e-mail: jvarekamp@wesleyan.edu

C.H. Gammons
Department of Geological Engineering,
1300 W. Park Street, Montana Tech, Butte
MT 59701, USA

could be modeled through cooling/dilution of the primary hot spring fluids. Single evolution (acidification through capture of volcanic gases, water rock interaction to acquire the dissolved cations) through cooling of the primary fluids could explain most of the Fe-bearing minerals, but to precipitate Mg-sulfates, evaporation and renewed interaction with olivine-rich rocks is needed to saturate some common Mg-sulfates (e.g., epsomite). The schwertmannite beds formed through processes involving Fe-oxidizing bacteria, which may be significant if this mineral was common on Mars in the past. Photochemical processes on Mars are commonly discussed in terms of photo-oxidation of Fe, but photo-reduction may be a common process as well, as was found to be the case in the Río Agrio watershed. A model of waters acidified by the capture of S-rich volcanic gases that have reacted with basaltic rocks, and then evaporated or were neutralized by higher alkalinity surface fluids may explain the origin of the sulfate mineral suites on Mars quite well.

Keywords

Water geochemistry · Acidic waters · Mineral precipitation · Rio agrio

7.1 Introduction

The discovery of iron sulfate minerals in Martian meteorites (McSween 1999) and on the Martian surface (e.g., Klingelhöfer et al. 2004; Ming et al. 2006; Ehlmann and Edwards 2014) has stimulated research on the climate and hydrology of ancient environments at Mars. Was there water from which these minerals could precipitate and were these waters acid? On Earth, sulfate minerals are common in hydrothermal lakes (Delmelle and Bernard 1994; Delmelle et al. 2000), acid-mine drainage systems, and evaporites, which must also be considered for Mars. The presence of jarosite on Mars was first measured in outcrops by the Opportunity rover (Klingelhöfer et al. 2004) and later measured regionally by spectroscopy from orbit (e.g., Farrand et al. 2009). Terrestrial jarosite has been found in volcanic-hydrothermal settings (Delmelle and Bernard 2000; Van Hinsberg et al. 2010; Cousins et al. 2013), in alteration suites in volcanic craters (Africano and Bernard 2000) and in acid-mine drainage systems (e.g., Fernández-Remolar et al. 2004). Martian sulfates are associated with a

number of non-igneous minerals including alunite, anhydrite, goethite, hematite and kaolinite (e.g., Ehlmann and Edwards 2014). Formation of all these minerals requires specific conditions, for example jarosite needs sulfate rich, acidic (pH < 4.0) and oxidizing conditions to form (Stoffregen 1993; Stoffregen et al. 2000) and the specific environment for each mineral is reasonably well known from theory and terrestrial occurrences (Bishop et al. 2005; Papike et al. 2006). In this chapter, the possibility to interpret active acid hydrothermal systems with their crater lakes, rivers and ponds as found at Copahue volcano as terrestrial analogues for some of these early Mars environments that formed sulfates (e.g., Oonk 2013), was evaluated. Shallow hydrothermal reservoir rocks on Mars may have been exposed during cratering, so mineral formation both at the surface and at shallow depth was considered. Chemical analyses of acid waters and XRD studies of secondary minerals in and around the rivers and lakes of Copahue are combined with saturation calculations under a variety of conditions to constrain the origin of these minerals on Earth. At the end, the sulfate

mineral suites at Mars and Copahue and point out potential reasons for observed differences were compared.

7.2   Mars Mineralogy

The mineralogy of the Martian surface derived from in situ measurements by landers and rovers, remote observations by spectrometers in orbit and by studies of the Martian meteorites (Chevrier and Mathé 2007). The geological history of Mars has been described through a global stratigraphy, initially based on the occurrence of different rock formations and later also through crater counts and can be divided into the Noachian (>3.7 Ga), Hesperian (3.7–3.1 Ga), and Amazonian (<3.1 Ga) epochs (e.g., Hartmann and Neukum 2001; Tanaka et al. 2014). The lander and particularly orbital data have identified a plethora of igneous and aqueous minerals that can be placed in temporal context.

The crust of Mars is generally basaltic with various proportions of pyroxenes, plagioclases and olivine (e.g., Christensen et al. 2000; Mustard et al. 2005). The aqueous minerals of Mars are thus derived from the weathering of basalts in a range of environments. Global assessments of the spatial and temporal distribution of aqueous minerals show an evolution from early phyllosilicates to sulfates to the oxides that dominate the surface today (Bibring et al. 2005; Chevrier and Mathé 2007; Ehlmann and Edwards 2014).

7.3   Martian Primary Rocks and Minerals

Compositions of unaltered Hesperian Martian rock are considered to range from basalt to andesite (Fig. 7.1; Bandfield et al. 2000; Chevrier and Mathé 2007; McSween et al. 2009). This range is based on orbital observations, in situ characterizations and studies on Martian meteorites. Two end-member types of surface rock (I and II) were distinguished based on the thermal emission spectra from the Mars Global

Surveyor orbiter (Bandfield et al. 2000). Type I is associated with the southern part of Mars whereas the northern part is dominated by type II. Spectral data of type I match with terrestrial basalts (42–52 wt% SiO_2), while the type II rocks are similar to terrestrial high-SiO_2 basaltic-andesite (52–57 wt% SiO_2) to andesitic rocks (57–63 wt% SiO_2) (Bandfield et al. 2000). Modal mineralogies were obtained from a least-square fit using 45 mineral end-members (Bandfield et al. 2000). Type I is dominated by feldspar (50 %), pyroxene (25 %) and sheet silicates (15 %). Orthopyroxene is more common in the Noachian terrains and clinopyroxene in the younger Hesperian terrains, while both pyroxenes coexist in other areas (Chevrier and Mathé 2007). Endmember type II is dominated by feldspar (35 %), potassium-rich glass (25 %), sheet silicates (15 %) and pyroxene (10 %). Others have interpreted the type II rock spectra as a partially altered basalt (Wyatt et al. 2004).

In situ measurements by Mars rovers of rocks in its vicinity were analyzed using cleaning tools like the Rock-Abrasion Tool (RAT) on the Spirit Rover to create fresh surfaces. Gusev Crater rocks are similar to primitive terrestrial basalts (Gellert et al. 2004; 2006). A compilation of rock compositions from all sources of information such as soils, in situ rock analyses, spectral imaging and Martian meteorites is given in Fig. 7.1 (McSween et al. 2009).

7.4   Martian Aqueous Minerals

Phyllosilicate minerals are widespread in the Noachian crust of Mars, indicating persistent weathering by fluids (Poulet et al. 2005; Mustard et al. 2008; Bishop et al. 2009). The climate was presumably warm and mild, and an atmosphere was presumably present, although a simple H_2O-CO_2 rich atmosphere would have been unlikely to keep it warm enough to maintain water liquid at this distance from the sun. During the Hesperian, phyllosilicate minerals are less abundant, and sulfate minerals are dominant. Sulfates have been found in various

Fig. 7.1 Variation of primary volcanic rocks present at some Mars locations (McSween et al. 2009). Most rocks are relatively unevolved and range from basalt to andesite, with a notable absence of rhyolite
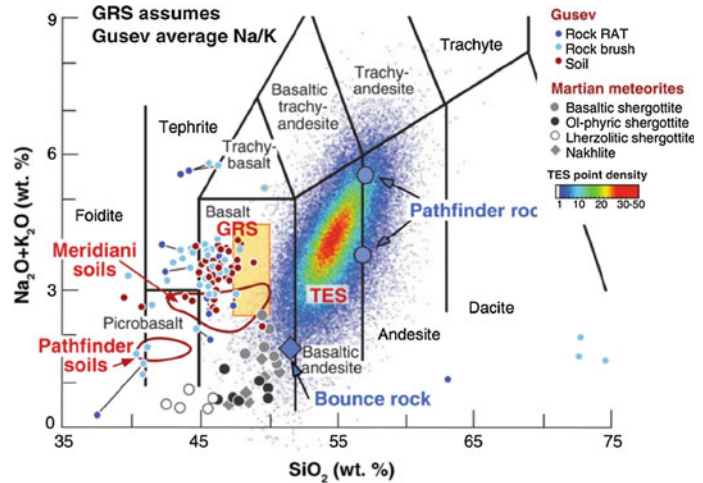
environments: (1) Gypsum has been identified in dunes surrounding the North Pole and has been attributed to polar processes in the Amazonian (Horgan et al. 2009 and references therein), (2) Meridiani-type layered deposits of sulfates, silica and hematite; these have been interpreted to be sulfate-rich sandstones that were diagenetically altered due to rising groundwater, producing the hematite and sulfate crusts (McClennan et al. 2005; Arvidson et al. 2006). Similar deposits have been discovered in locations throughout the Valles Marineris system, where monohydrated (kieserite and szomolokite) and polyhydrated sulfates (epsomite and other Mg-rich sulfates) occur with hematite (Glotch et al. 2006; Bishop et al. 2009; Roach et al. 2009). The correlation of many of these regions to areas inferred to be sites of groundwater upwelling (Andrews-Hanna et al. 2010) suggests that groundwater diagenesis may have been widespread. The sites where aqueous minerals have been recognized in the Martian surface are shown in Fig. 7.2.

Acid sulfates have been detected at a number of places on Mars. Jarosite was identified by the Mössbauer spectrometer onboard Opportunity as one of the sulfates at Meridiani Planum (Klingelhöfer et al. 2004). It has also been identified from orbit in association with opaline silica (Milliken et al. 2008; Weitz et al. 2011), phyllosilicates, goethite and ferrihydrite (Farrand

et al. 2009), and with alunite (Wray et al. 2011). The presence of schwertmannite has been hypothesized for Mars (e.g., Bishop and Murad 1996) but this mineral may have turned into Fe-(hydr)oxides such as goethite, ferrihydrite and magnetite over time. All of these minerals occur on Earth as well, but Ca and Fe sulfates are much more common on Earth than Mg sulfates. Ferric oxides are common in many terrestrial environments as well, given the prevalence of Fe^{3+} in waters in full exchange with the O_2-rich atmosphere. Mars is a planet with no evidence for free O_2 today, but most of the iron on its surface appears to be in the Fe^{3+} form. Because surface renewal through sea floor spreading-subduction presumably has not occurred, the buildup of Fe^{3+} may have proceeded very slowly through photochemical processes.

Several processes inferred from terrestrial analogues have been proposed to explain the jarosite-rich assemblages on Mars, including evaporation of saline lakes (Benison and LaClair 2003; Baldridge et al. 2009; McHenry et al. 2011), acid fog weathering (Morris et al. 1996; McCanta et al. 2014), acid-mine type drainage (Fernández-Remolar et al. 2004), and fluid-rock interaction in hydrothermal systems (Papike et al. 2006). These mechanisms involve the weathering of rocks by H_2SO_4 generated either by dissolution of sulfides or conversion of volcanic SO_2 (e.g., Chevrier and Mathé 2007). Perhaps the
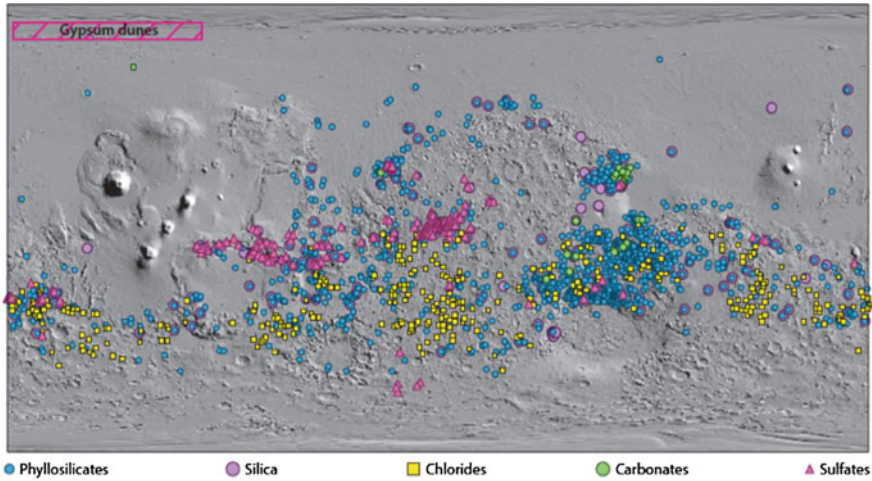
Fig. 7.2 Location of aqueous minerals on the Martian surface (Ehlmann and Edwards 2014)

best-known sulfate occurrence on Mars is at Meridiani Planum, where jarosite, gypsum and Mg-sulfates are found within sedimentary outcrops. The sedimentary record suggests that the rocks are aeolian sandstones later cemented by sulfate-rich groundwater (e.g., Grotzinger et al. 2005; McClennan et al. 2005). There is an argument as to how much water was in the system (Fig. 7.3; Chevrier and Mathé 2007): Some models call for open hydrological systems with long-range transport, where rivers supply soluble elements, leached from basaltic rock to a shallow lake or bay, and subsequent evaporation induces the precipitation of sulfate minerals (Tosca et al. 2004; Chevrier and Mathé 2007). Recent chemical modeling (Hurowitz and Fischer 2014) supports such a model where S-rich fluids are produced by long-term weathering. Alternatively, sulfates are formed in cracks and fissures as a product of interaction between primary

mineral phases and relatively water-limited acid fluids percolating through and/or over the surface. This model explains the presence of highly water-soluble minerals such as kieserite and chlorides next to poorly soluble Si-minerals at the Opportunity site (Chevrier and Mathé 2007; Morris et al. 2008; Niles and Michalski 2009).

The hydrothermal environment of Copahue volcano in Argentina has been proposed as a terrestrial analogue to the Opportunity landing site on Mars (Varekamp 2004). Here, the association of volcanic lakes, acid stream waters and hot springs in a dynamic volcanic-hydrothermal setting provides an opportunity to test evidence for fossil shallow Martian hydrothermal systems with acid fluids as a third class of models for the origin of sulfate-bearing mineral assemblages on Mars (Grotzinger et al. 2005; McClennan et al. 2005). If applicable, it would be a hybrid of the main existing models, with water/rock interaction
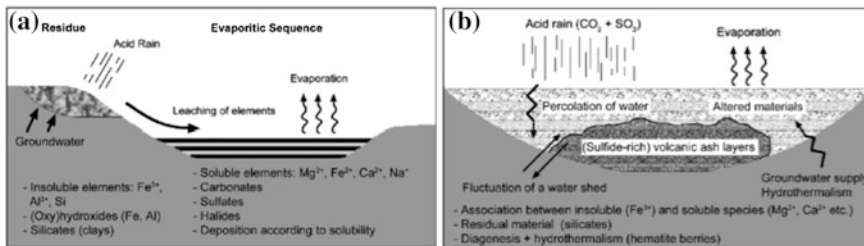
Fig. 7.3 Two common models for sulfate genesis on Mars (from Chevrier and Mathé 2007)

at depth, local precipitation of sulfates, coupled with escape and accumulation of fluids in rivers and lakes, where further water-rock interaction and evaporation may lead to the precipitation of Mars-type mineral assemblages.

In the following, the mineralogy of surface deposits surrounding Copahue volcano that formed from leakage of the hydrothermal system (mineralized acid hot springs), dilution with glacial melt waters, or local evaporation is described. The observed fluid compositions were modeled to determine how the various minerals could have formed in the ambient environment or under shallow hydrothermal conditions.

7.5 Copahue Minerals and Rocks

Copahue is an andesitic volcano in the eastern Andes, and much of its characteristics are described in this volume. The unusual aspect of Copahue is the presence of the highly acidic hydrothermal system at depth below the volcano (Agusto and Varekamp, this volume) from which concentrated acid brines are emitted at the surface, forming springs, acid streams and the crater lake. The direct mineral precipitates of these fluids as well as the minerals that they would precipitate upon cooling and evaporation are modelled and compared with field data of minerals. The suggestion of Copahue as a terrestrial analogue of early Mars environments was originally inspired by the presence of hematite, jarosite and gypsum in one of the local riverbeds (Varekamp 2004). Another river bed has been covered with schwertmannite for several years (Kading and Varekamp 2009, 2011), a mineral considered as a potential precursor mineral on Mars (Bishop and Murad 1996). The copious quantities of elemental sulfur emitted by Copahue during phreato-magmatic eruptions are a specific feature of this volcano (Bermúdez and Delpino 1995).

As a first approximation, the Copahue volcanic rocks are compositional proxies for the Martian rocks. The mineralogy of recent Copahue ejecta and older lava flows is dominated by plagioclase, with two pyroxenes, olivine and one Fe-oxide. Some of the recent ashes and pumices have a glass phase with about 57 % SiO_2 (Varekamp et al., this volume) and the bulk composition (Varekamp et al. 2006) is similar to that of type II Martian rocks. The following section presents and discusses the new data collected from the Copahue streams, springs and lakes, the minerals identified in the watershed, and modelling results that show under which conditions these minerals could have formed from the local fluids.

7.6 Fieldwork and Analytical Techniques

Samples were collected during March 11th to 22th, 2013 and other samples were collected on earlier field trips described by Gammons et al. (2005a, b) and Varekamp et al. (2009). The geographical coordinates and altitude were taken with a handheld GPS at each sampling location. Temperature (°C), pH, electrical conductivity (C) and redox potential (Eh) were measured using a WTW® 3430 portable multimeter. Conductivity, pH and redox potential were also measured again at room temperature in the cabin after daily fieldwork. Fluids with measured pH values below 1 were calculated through charge balance with PHREEQC software (Parkhurst and Appelo 1999) taking into account Pitzer and Mayorga (1973) ion interaction parameters. The reason for this approach is that linearity of the pH versus potential (mV) curve from the electrode is strongly reduced when pH values are below zero (Nordstrom et al. 2000). Water samples were collected from rivers and hot springs for IC (ion-chromatography) and ICP-OES (inductively coupled plasma optical emission spectrometry) analyses and were filtered on site through 0.2 µm pore size cellulose acetate membranes with the aid of a hand vacuum pump. Samples for IC analyses were collected in 250 ml HDPE bottles. For ICP-OES analyses, 60 mL HDPE bottles were used and samples were treated with 1 ml Suprapur® HNO_3 per 100 mL sample. For pH determinations at room temperature, unfiltered samples were collected in 20 mL amber glass air-tight bottles. Samples for Si analyses were diluted 10 times on site with deionized water in

pre-weighed 60 ml HDPE bottles. Rocks and volcanic ejecta samples were collected in plastic bags, whereas sediments and mineral samples were collected in 50 mL Greiner® tubes.

The concentration of the anions Cl^-, F^-, and SO_4^{2-} in untreated, undiluted and diluted samples were determined with a Dionex® ICS-3000 ion chromatograph (IC), equipped with a Dionex® IonPac® AS 19 column. Concentrations of Al, B, Ca, Fe, K, Mg, Mn, Na, P, Si, Sr, Ti, V and Zn in acidified samples were determined using a Spectro® Ciros® ICP-OES. Rock samples were analysed by wavelength dispersive X-ray fluorescence (XRF) at Wesleyan University (Bruker S-4 Pioneer).

Minerals, sediments and hydrothermally altered rocks were dried several days at ∼40 °C until a constant weight (<1 % mass difference) was measured between two consecutive weight readings. Then, the samples were ground in an agate mortar to a very fine grain size (approximately No. 40 mesh). These powders were analysed by X-ray diffraction (XRD) at the Department of Inorganic Chemistry and Catalysis of Utrecht University with a Bruker® AXS D2 Phaser powder X-ray diffractometer, in Bragg-Brentano mode, equipped with a LYNXEYE® detector. The radiation used is cobalt $K_{\alpha1,2}$ (1.79026 Å), operated at 30 kV, 10 mA. The patterns from these analyses were processed and interpreted with DIFFRAC.SUITE software. Thin sections were made from rocks and volcanic ejecta and the samples were observed under the polarizing microscope. Some of these samples were selected for electron microprobe analyses (EPMA). EPMA work was done on carbon coated samples on a JEOL® 8600 instrument. The microprobe was equipped with an energy-dispersive spectrometer (EDS). Normal operating conditions were 15 kV accelerating voltage, 10 nA beam current and 30 s counting time. PROZA software provided by JEOL® was used to convert the raw data into elemental and oxide weight %. All analyses, with the exception of XRF and XRD, were carried out at the Department of Earth Sciences of Utrecht University.

7.6.1 Geochemical Modelling

The geochemical modelling software PHREEQC (Parkhurst and Appelo 1999), version 3.1. was used to calculate aqueous species distributions, mineral saturation states and reaction path simulations. Lawrence Livermore National Laboratories thermodynamic database (llnl.dat) was used. This database was expanded with recent available thermodynamic data on sulfates and halides. Additionally, Pitzer and Mayorga (1973) ion interaction parameters from many ion pairs were included.

7.7 Water Chemistry of Copahue Fluids

The waters from Copahue crater lake and hot springs consist of SO_4-Cl hyperacid brines (pH < 1). These fluids are produced by the condensation of magmatic gases (SO_2, H_2S, HCl, and HF) in meteoric waters, mainly originating through melting of the local glacier. The aqueous dissolution of $SO_{2(g)}$ and its disproportionation create the acidity of these waters with H^+ and the bisulfate ion (HSO_4^-) as products (Kusakabe et al. 2000; Symonds et al. 2001):

$$3SO_{2(g)} + 2H_2O \rightarrow 2HSO_4^- + 2H^+ + S_{(s)}$$
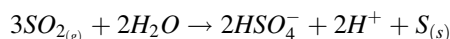
The species $HCl_{(g)}$ and $HF_{(g)}$ are also important contributors to the H^+ concentrations because of their almost complete dissociation in water at low temperatures (Delmelle and Bernard 1994; Delmelle et al. 2000; Symonds et al. 2001). Such hyperacid waters readily react with the surrounding rocks (e.g., Wolff-Boenish et al. 2004), leaching cations from minerals and glasses and partially dissolve the silica matrix (Agusto and Varekamp, this volume; Varekamp 2015). Samples from the Vertiente hot spring, about 100 meters below the crater lake, provide good aliquots from the hydrothermal system, because no boiling or evaporation occurs. The Upper Río Agrio waters are largely mixtures of the Vertiente spring waters with glacial melt
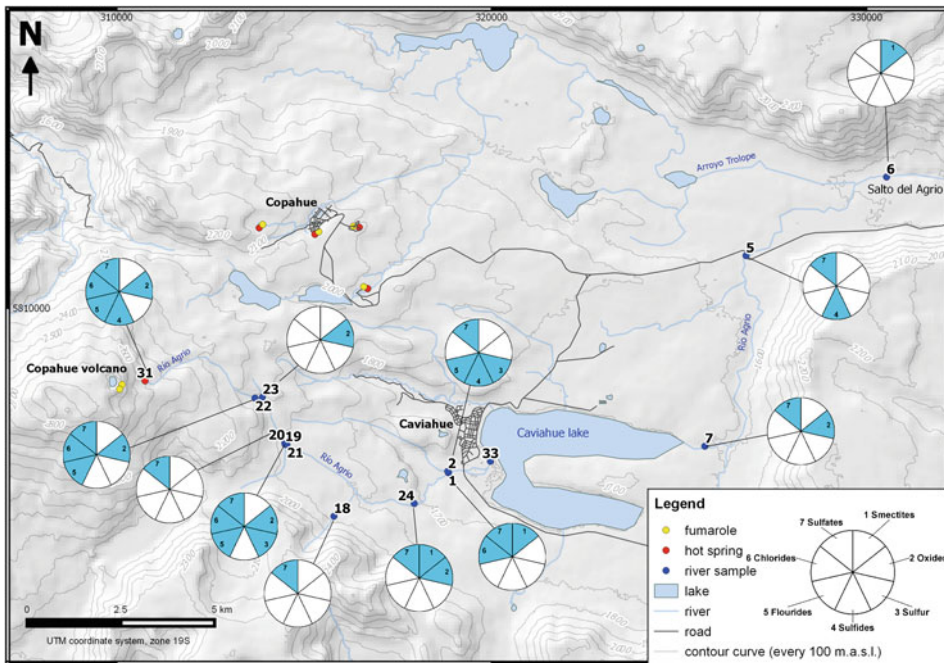
Fig. 7.4 Sampling locations and rose diagrams with mineral occurrences

water and/or local precipitation (rain and snow; Ouimette 2000; Varekamp et al. 2001, 2009). A summary of water analyses of the Vertiente spring and the upper reaches of the Upper Río Agrio is given in Agusto and Varekamp (this book). The water sampling locations of the March 2013 expedition are shown in Figs. 7.4 and 7.5, and the chemical composition of these samples is presented in Tables 7.1 and 7.2.

Copahue volcano erupted in December 2012 (Caselli et al. Chap. 4 this book) and the water samples were collected in March 2013, just three months after the eruption. At that time, the flow of the hot springs was relatively modest, the fluids were slightly less concentrated and acidic as in some earlier years, and showed some compositional differences with earlier fluid compositions of the same hot spring (Alexander 2014). The hot spring waters (Site 31) had more than 2.5 % sulfate and close to 1 % Cl, at a pH of 0.65 and a temperature of 52.4 °C (Table 7.1). A large fraction of these waters is of magmatic origin, with up to 60 % magmatic water in some years (Varekamp et al. 2004; Agusto and

Varekamp, this volume). The main rock-forming cations in the fluids are high in concentration (between 1000 and 3000 ppm of Fe, Al and Ca). The Al/Cl decreased after the 2012 eruption, similar to a decrease in 2001 after the 2000 eruption, which is explained with the retention of Al in alunite in the hydrothermal reservoir (Agusto and Varekamp, this book). The compositions of the Upper Río Agrio (Tables 7.1 and 7.2) are largely diluted versions of the hot springs with admixtures of smaller hot springs and mineralized tributaries and glacial melt water dilution. The pH value of the river increases downstream from 0.5 to 2.5 just before entering Lake Caviahue. That lake represents a further dilution of the Upper Río Agrio waters with pH 2.2–3, and has a significant compositional lag time when the composition of the Upper Río Agrio changes over time because of non-steady state effects (Varekamp 2008). The outflow of Lake Caviahue (Lower Río Agrio) is further diluted by meltwater tributaries and the pH reaches values >3 near the large water fall just outside the caldera (Salto, Site 6). The riverbed
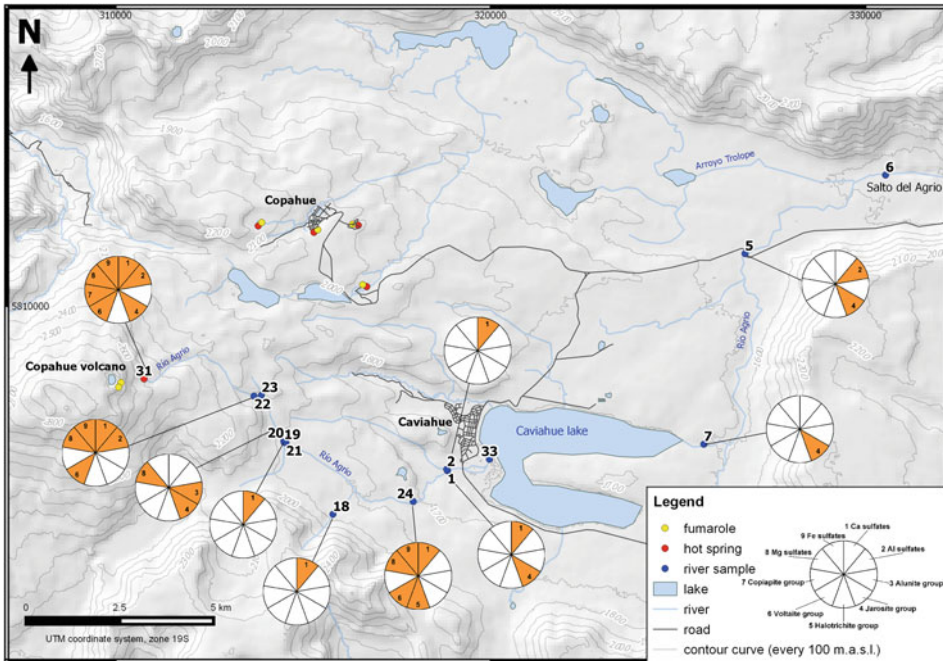
Fig. 7.5 Rose diagrams of sulfate mineral occurrences in the field

7.8 Alteration Mineralogy in the Field

More than 140 secondary minerals were found in the field based on powder XRD determinations. The sampling sites covered the Río Agrio course from its origin at the hot spring (Site 31) to just before the Salto del Agrio (Site 6). Some small tributaries were also included in the sampling campaign. The minerals have been grouped in families as an aid to visualize their distributions in a qualitative way (Figs. 7.4 and 7.5). The radial graphs (rose diagrams; Figs. 7.4 and 7.5) only depict the presence of mineral groups, not their abundance. Sulfates, silica minerals (tridymite, cristobalite-α, quartz), and oxides of Fe, Ti, Mn

of the Lower Río Agrio has been covered in red ochre deposits since at least 2003, which was determined to be a mixture of schwertmannite and ferrihydrite phases (Kading and Varekamp 2011). Lake Caviahue supports an acidophile ecosystem (Baffi et al. 2004).

and Al are the most common minerals identified along the Río Agrio. Hematite and ferrohexahydrite were only found at Sites 7 and 24, respectively. Some iron oxides were poorly crystalline and could not be determined by the XRD technique. Chlorides (Fe and Mg-rich) and Fe-fluorides were observed at the Vertiente hot spring (Site 31), just before Río Colorado (Site 22) and near the junction with Río Blanco (Site 19). Smectites were only found near Site 1 and Site 6. Sulfates occurred in the stretch between the Vertiente spring (Site 31) and Site 5, behind Lake Caviahue. The most common sulfates were gypsum, K-jarosite, Na-jarosite, voltaite-pertlikite and the Mg-sulfates epsomite and hexahydrite. In most sites, the Na and K jarosites were found together. No obvious geographic abundance trends could be derived from the data.

The 2012 ashes carried abundant hydrothermal debris, in which the following minerals were found: cristobalite, quartz, tridymite, pyrite, elemental sulfur, K- and Na-alunite, hematite, anhydrite, gypsum, kaolinite and montmorillonite, among others.

Table 7.1 Sampling sites and locations with pH, temperature (°C), electrical conductivity (E.C., micro-siemens/cm) and anion contents (ppm)

Site	Location	Date	pH	T (°C)	C (μS/cm)	ORP$_H$ (mV)	F (ppm)	Cl (ppm)	Br (ppm)	SO4 (ppm)
1	Upper Rio Agrio (Before A° Jarra joins)	2013/03/11	2.33	10.5	4100	–	7.6	346	0.60	1119
2	A° Jarra	2013/03/11	7.46	11.5	373	–	0.29	20	b.d.l.	92
5	Lower Rio Agrio (bridge)	2013/03/12	2.88	9.2	1023	–	2.2	66	b.d.l.	233
6	Lower Rio Agrio (before Salto del Agrio)	2013/03/12	3.38	11.2	624	–	1.3	39	b.d.l.	138
7	Lower Rio Agrio (Lago Caviahue outlet)	2013/03/12	2.70	9.1	1600	785.1	3.0	90	b.d.l.	318
18	Reddish river (Upper Rio Agrio)	2013/03/17	7.50	12.4	43	-	0.20	0.91	b.d.l.	3.4
19	Río Blanco (Upper Río Agrio)	2013/03/17	5.88	10.8	698	402.5	2.1	61	b.d.l.	225
20	Upper Rio Agrio (before Rio Blanco junction)	2013/03/17	1.72	16.5	11480	648.3	21	879	1.7	2714
21	Upper Rio Agrio (after Rio Blanco junction)	2013/03/17	1.92	14.4	7610	651.6	12	514	0.95	1584
22	Upper Rio Agrio (before Rio Colorado junction)	2013/03/17	1.57	14.5	14820	647.0	29	1230	2.3	3708
23	Rio Colorado (Upper Río Agrio)	2013/03/17	3.53	20.2	2690	594.2	4.4	276	b.d.l.	1046
24	Upper Rio Agrio (betweem Cascadas del Agrio)	2013/03/18	2.30	10.0	4190	669.4	6.6	346	b.d.l.	1115
25	Lower Rio Agrio (before Rio Ñorquín junction)	2013/03/17	6.99 (24.1 °C)	–	361	470.5	0.61	27	b.d.l.	93
26	Lower Rio Agrio (after Río Ñorquín junction)	2013/03/17	7.01 (24.6 °C)	–	361	470.3	0.82	25	b.d.l.	85
27	Lower Rio Agrio (500 m after Río Ñorquín junction)	2013/03/17	7.86 (24.4 °C)	–	338	545.0	0.77	22	b.d.l.	73
31	Upper Rio Agrio (hot spring)	2013/03/19	0.65 (23.9 °C)	52.4	75500	635.8	198	9412	17.7	26855
33	Upper Rio Agrio (Lago Caviahue)	2013/03/20	2.43	19.7	3450	689.2	6.2	305	b.d.l.	1004
CVLSAA 0	Caviahue Lake (surface)	2013/03/13	2.82	11.7	–	–	n.a.	n.a.	n.a.	n.a.

T = temperature, C = conductivity, ORP$_H$ = redox potential referred to the H electrode, b.d.l. = below detection limit, n.a. = not analyzed

7.9 Schwertmannite in the Copahue Volcano Watershed

The Upper and Lower Río Agrio had no macroscopic mineral deposits in the riverbeds or suspended in the water column prior to 2000. This all changed after the 2000 eruption, when intrusion of new magma into the hydrothermal system led to highly mineralized fluid emissions into the ambient environment (Varekamp et al. 2001). The Lower Río Agrio riverbed was covered with a yellow ochre just after the confluence of the Río Trolope and Lower Río Agrio for the first time in 2003 (Fig. 7.6). The pH of the mixed fluids was

Table 7.2 Major and trace element contents of analysed fluids

Site	Al (ppm)	B (ppm)	Ca (ppm)	Fe (ppm)	K (ppm)	Mg (ppm)	Mn (ppm)	Na (ppm)	P (ppm)	Si (ppm)	Sr (ppm)	Ti (ppm)	V (ppm)	Zn (ppm)
1	91	0.13	113	53.1	21	99	7.1	56	0.79	31	0.63	0.13	0.13	0.14
2	0.16	b.d.l.	20	0.12	4.3	17	0.16	18	0.02	17	0.11	b.d.l.	b.d.l.	b.d.l.
5	23	b.d.l.	20	14	5.3	15	0.78	13	0.14	15	0.15	0.03	0.03	0.03
6	13	b.d.l.	16	5.8	3.9	12	0.46	9.8	0.04	13	0.13	0.01	0.01	0.01
7	32	0.01	25	20	6.3	20	1.1	15	0.26	15	0.19	0.04	0.04	0.04
18	b.d.l.	b.d.l.	3.2	0.62	b.d.l.	1.71	*0.01*	2.7	b.d.l.	13	0.01	b.d.l.	b.d.l.	b.d.l.
19	2.1	b.d.l.	45	0.27	5.9	43	1.97	19	b.d.l.	19	0.10	b.d.l.	b.d.l.	b.d.l.
20	236	0.34	220	132	50	192	15	118	2.6	36	1.4	0.38	0.36	0.31
21	138	0.20	145	72	31	130	9.5	77	1.4	29	0.86	0.22	0.21	0.19
22	382	0.43	236	189	72	187	12	143	4.2	39	1.8	0.63	0.59	0.45
23	14	0.15	176	12	18	175	19	74	b.d.l.	25	0.56	b.d.l.	b.d.l.	0.08
24	89	*0.13*	113	47	21	100	7.3	57	0.79	29	0.62	0.13	0.12	0.13
25	*0.25*	b.d.l.	26	*0.01*	4.4	13	0.10	8.9	*0.02*	20	0.16	b.d.l.	b.d.l.	b.d.l.
26	b.d.l.	b.d.l.	26	*0.01*	*4.4*	13	0.10	9.2	0.01	20	0.17	b.d.l.	b.d.l.	b.d.l.
27	*0.26*	b.d.l.	28	*0.01*	4.2	13	0.06	10	*0.02*	20	0.16	b.d.l.	b.d.l.	b.d.l.
31	2946	3.2	1087	1318	600	585	23	799	40	76	13.5	2.6	4.4	2.94
33	80	*0.11*	104	52	19	94	6.54	52	0.69	33	0.58	0.11	0.11	0.12
CVLSAA 0	28	n.a.	25.9	20.1	6.4	20	n.a.	16	0.19	15	n.a.	n.a.	n.a.	n.a.

Values in italics can have an error of analysis > 10 % and should be seen as an approximate; b.d.l. = below detection limit; n.a. = not analyzed

Fig. 7.6 Hydrous ferric oxide-sulfate mineral phases in the river bed of the Lower Río Agrio (*Left*) and at the Salto waterfall (*Right*) post 2003

Table 7.3 Common mineral phases used in the modelling and observed in the field

Rhomboclase	$HFe^{3+}(SO_4)_2 \cdot 4(H_2O)$	Alunite	$KAl_3(SO_4)_2(OH)_6$
Kieserite	$MgSO_4 \cdot H_2O$	Na-alunite	$NaAl_3(SO_4)_2(OH)_6$
Hexahydrite	$MgSO_4 \cdot 6H_2O$	Jarosite	$KFe_3(SO_4)_2(OH)_6$
Epsomite	$MgSO_4 \cdot 7H_2O$	Na-jarosite	$NaFe_3(SO_4)_2(OH)_6$
Halite	$NaCl$	H-jarosite	$(H_3O)Fe_3(SO_4)_2(OH)_6$
Sylvite	KCl	Anhydrite	$CaSO_4$
Ferrohexahydrite	$FeSO_4 \cdot 6H_2O$	Gypsum	$CaSO_4 \cdot 2H_2O$
Siderotile	$FeSO_4 \cdot H_2O$	Jurbanite	$AlSO_4(OH) \cdot 2H_2O$
Diaspore	$AlO(OH)$	Sulfur	S
Rozenite	$FeSO_4 \cdot 4H_2O$	Pyrite	FeS_2
Hematite	Fe_2O_3	Szolmolnokite	$FeSO_4 \cdot H_2O$
Schwertmannite	$Fe_8O_8(OH)_6SO_4 \cdot nH_2O$	Melanterite	$FeSO_4 \cdot 7H_2O$

close to or exceeded three and the riverbed of the large Salto waterfall turned from bare rock to a cover of fluffy brown-yellow precipitate. The Lower Río Agrio turned brown downstream from the Salto for many kilometers, until further dilution by the Río Ñorquín waters led to pH values of 4–5 (Gammons et al. 2005a). Chemical analyses of the brown ochre (Table 7.3) revealed it to be a mixture of bacterial organic matter, with small flakes of the mineral schwertmannite and several Fe-oxides, presumably ferrihydrite or goethite (Kading and Varekamp 2009). The identification of schwertmannite is not easy because it tends to be a poorly crystallizine mineral: XRD patterns were compatible with schwertmannite, the stoichiometry of the Fe/S was obtained from SEM-EDAX analyses and was largely compatible with the pure mineral or mixed with ferrihydrite (Fig. 7.7a). In addition, the reflectance spectrum of the ochres strongly resemble that of schwertmannite (Fig. 7.7b), and as Schwertmann himself argued after discussing the many techniques to detect schwertmannite, its colour is actually quite characteristic (Schwertmann and Cornell 2000). Definite evidence was provided by TEM studies, showing the characteristic spacings in an electron diffractogram (Fig. 7.8a). The bright field images show the crystallinity of the sample (fine spacings) but also small domains of 50–100 nm that may reflect the fine-grained nature of the mineral or maybe related to its mode of precipitation (Fig. 7.8b).

Chemical analyses of the ochres show strong enrichments in the oxyanion forming elements V,

Fig. 7.7 Fe/S versus S in the ochres from the Lower Río Agrio as determined by SEM-EDX; the red lines delineate the zone with schwertmannite stoichiometry and many samples have Fe excess, presumably ferrihydrite (*Top*). The reflectance spectra show the pattern for the ochre (LRA008) and literature reference spectra (Clarke et al. 2007) for schwertmannite and goethite (*Bottom*)
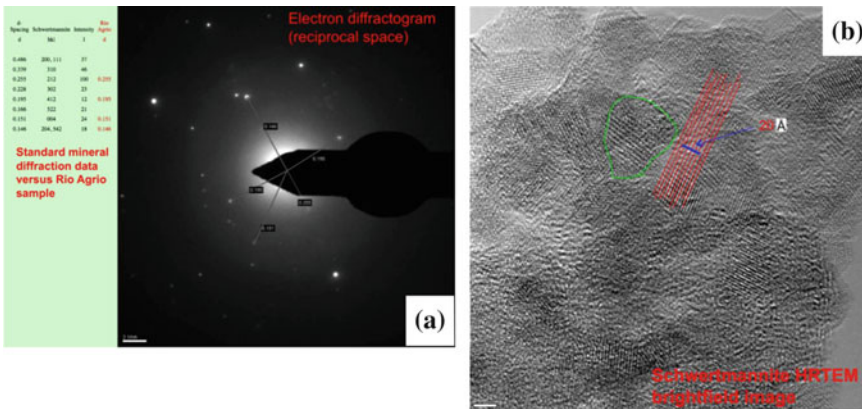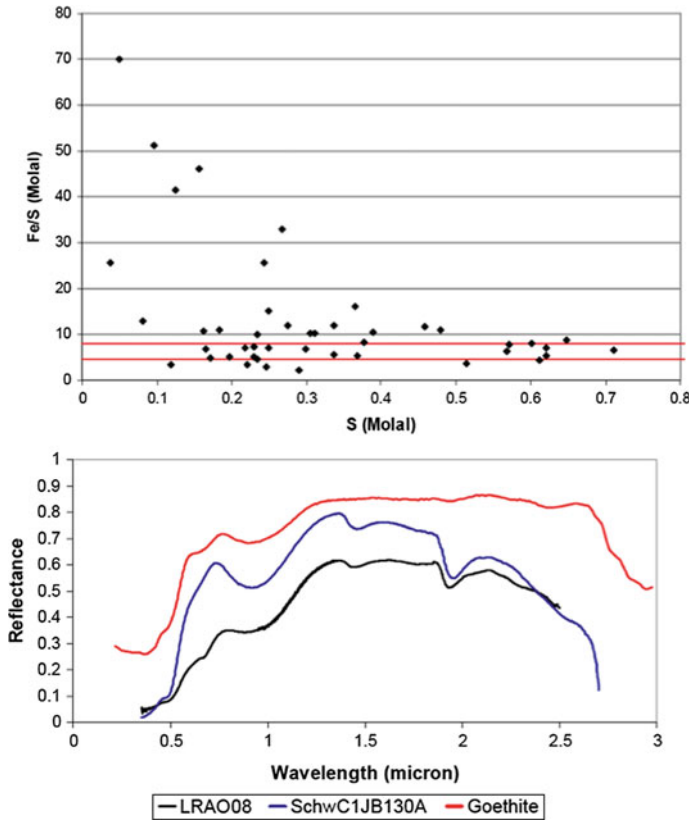
Fig. 7.8 Transmission Electron micrographs of schwertmannite samples from the Lower Río Agrio. *Left* Electron diffractogram with some of the characteristics spacings labeled. *Right* Bright field image, showing small patches (green outline, 50–100 nm) of crystalline mineral with some of the spacings indicated

P and As (Table 7.4). The arsenic may be adsorbed on the surface of the mineral or may be part of its structure, substituting for the SO_4 group (Acero et al. 2006; Regensburg and Peiffer 2005; Schroth and Parnell 2005; Webster et al. 1998). The Lower Río Agrio waters that precipitated these ochres became strongly depleted in dissolved As, V and P (Kading 2010). Since

Table 7.4 Chemical composition of ochres in the Lower Río Agrio

Sample	Al	Ca	Mg	K	Mn	Ti	Fe	P	As	V	C	N
	(%)	(%)	(%)	(%)	(%)	(%)	(%)	(ppm)	(ppm)	(ppm)	(%)	(%)
SPZO09	7.4	3.7	1.7	1.2	0.08	0.6	8	4500	890	480	8	0.6
SPZO08	4.9	2.1	1	0.7	0.06	0.5	20	6000	620	970	6.4	0.6
SALTOA08	0.4	0.1	0.1	0.3	0.01	0.1	21	2300	70	210	20	1.9
LRA08	1.4	0.2	0.1	0	0.02	0.1	30	5800	1040	1130	–	–
SALTO08	2.2	0.6	0.3	0.3	0.03	0.2	27	5400	820	1100	8.9	1.1

2003, the precipitation front of ochres in the Lower Río Agrio moved from the Salto gradually upstream to almost reach the exit of Lake Caviahue. In 2010, yellow precipitates started to form at the lake exit and some lake water filters had a yellowish precipitate (Kading and Varekamp 2011).

The P enrichment on the schwertmannite led to a secondary ecosystem in the Lower Río Agrio: extensive fields of green algae grew on the brown schwertmannite oozes, using both the decaying bacterial matter and phosphorus as a fertile substrate. The isotopic composition of the organic matter in one of the Lower Río Agrio ochre samples has a $\delta^{13}C$ of −21.1 ‰ (C = 31.3 %) and $\delta^{15}N$ of + 7.7 ‰ (N = 2.63 %) with C/N (wt) = 11.9. These samples were mixtures of the fresh yellow flocculate with bacterial matter and some debris of the green algae. The source of the nitrogen may be related to effluents of local wastewater into the lake (Pedrozo et al. 2001, 2008), while the $\delta^{13}C$ and C/N values suggest that the sample contains abundant bacterial organic matter (Cowie et al. 2009).

The total amount of schwertmannite that precipitated along the Lower Río Agrio is on the order of 60 tonnes/month, leading to the retention of large quantities of Fe, As, P and V in the watershed (Kading and Varekamp 2009). The fluid emissions from Copahue became more acidic prior to the 2012 eruption and the waters in the lake and Lower Río Agrio were no longer saturated with schwertmannite. The river bed ochres have started to redissolve since 2012 or even earlier, which also released their toxic load of arsenic to areas downstream, while leaving behind a matte brown Fe-oxide coating on the rocks. In conclusion, the schwertmannite deposits at Caviahue occur in a natural setting instead

of in an acid mine drainage field where the mineral is commonly encountered (Yu et al. 1999; Kumpulainen et al. 2007; Jonsson et al. 2005; Gagliano et al. 2004; Brady et al. 1986; Blodau and Knorr 2006), and are ephemeral because of changing water composition trends.

7.10 Saturation States of Fluids Collected Before 2012

The composition of local Copahue rocks (Varekamp et al. 2006) and the composition of products from the 2012 eruption were used for the numerical water-rock equilibration experiments (Varekamp et al., this book). Water analyses from samples taken at the Vertiente spring between 1997 and 2009 (Gammons et al. 2005a, b; Varekamp et al. 2009; Kading 2010) were used in a first set of models that predict the saturation state of relevant minerals (following Stefansson et al. 2001) at the exit temperature and higher temperatures (Fig. 7.9). The spring waters were always close to saturation with gypsum and anhydrite, and slightly undersaturated with jurbanite. Jarosite species were generally far below saturation, except in 2003 when the spring water was also oversaturated in the H-jarosite endmember.

Saturation indices for alunites vary strongly, although they never reach saturation at spring exit temperatures. Increasing saturation levels with temperature (up to ca. 200 °C) predict that alunite occurs in the hotter and deeper parts of the volcanic-hydrothermal system where temperatures up to 280 °C have been estimated (Varekamp et al. 2004). In 2000, 2001 and 2004, however, the waters could have been saturated with alunite at temperatures as low as 75–100 °C.
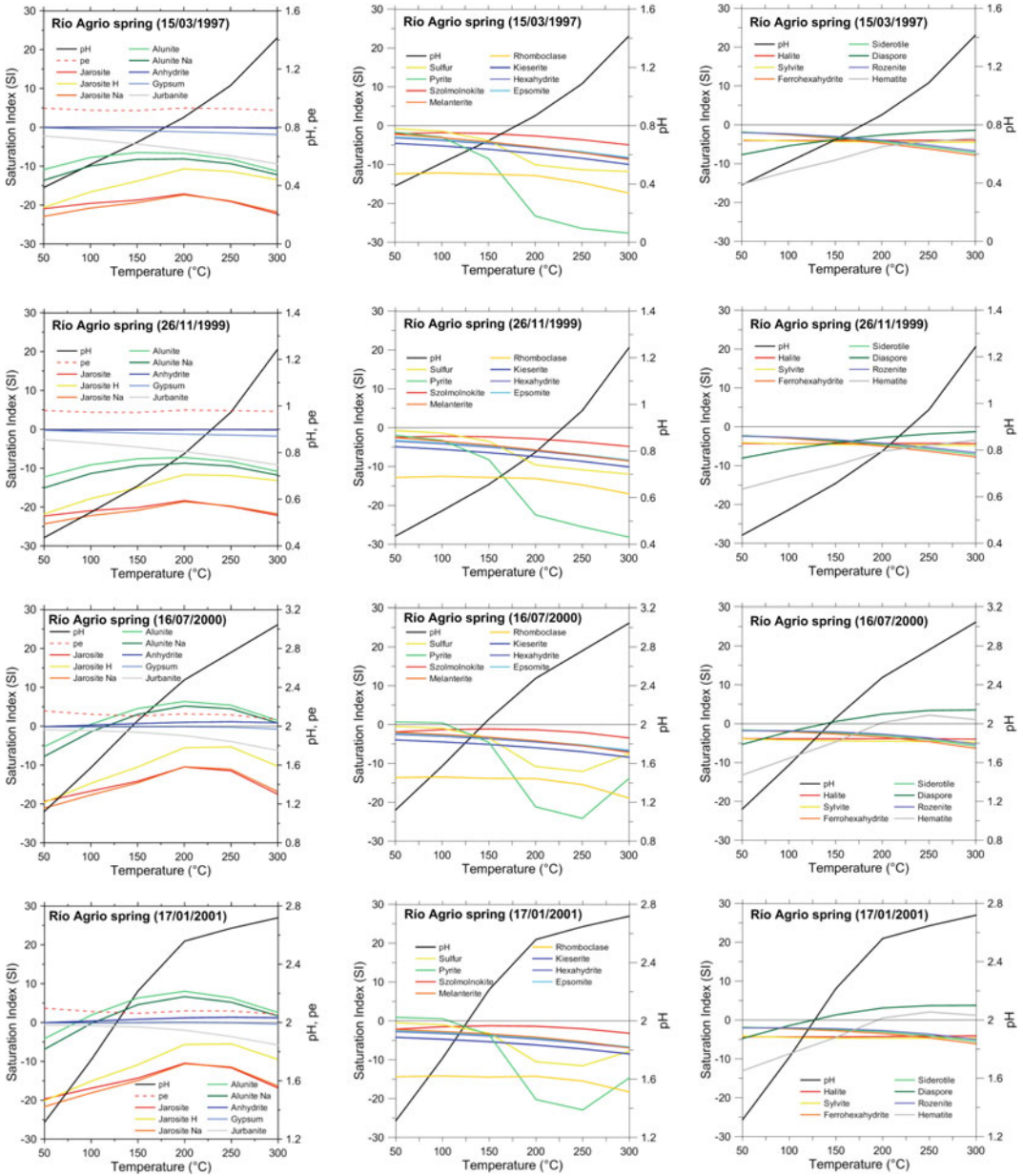
Fig. 7.9 Summary of 6 runs modelling mineral saturation states for selected minerals as a function of temperature for Vertiente spring-water compositions between 1997 and 2004

Hydrothermally altered andesites expelled during the 2012 eruption contained alunite inside vesicles, which according to EMPA has the following approximate composition: (Na0.5K0.5)(AI2.8Fe0.1)(SO4)2(OH)6, testifying that this mineral is potentially stable at depth. Likewise, fluids are expected to be saturated in diaspore,

kaolinite, and hematite (not shown) at temperatures higher than measured at the spring. As an exception, hematite was also saturated below the spring-water temperature in 2003, which was confirmed by its presence along the streambed in the vicinity of the spring (Varekamp 2004). In the same year, jarosite was close to saturation in
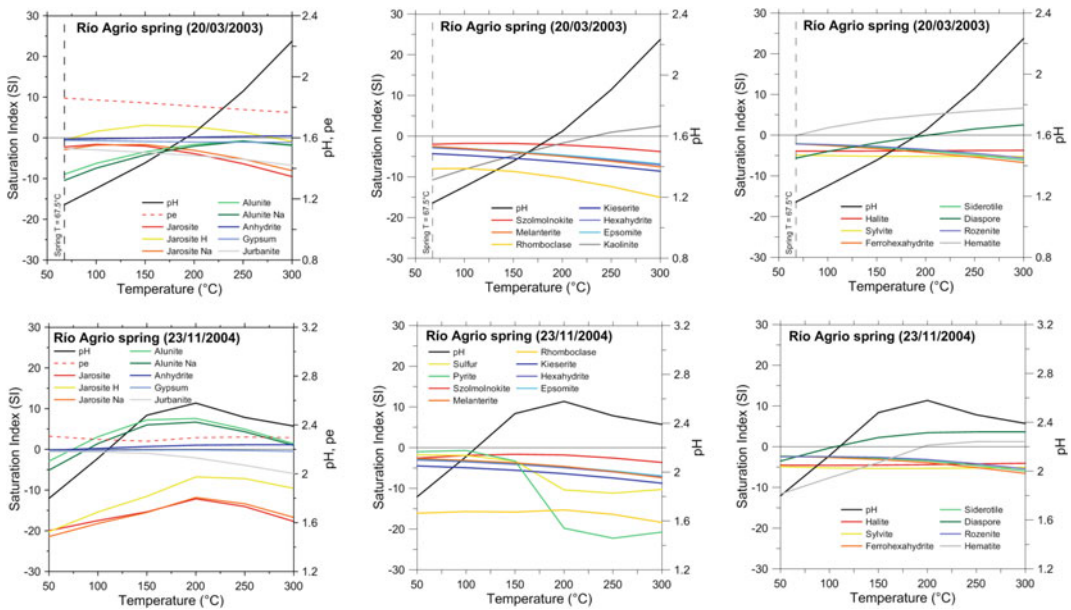
Fig. 7.9 (continued)

the spring fluid as well. The hydrous Fe and Mg-sulfate minerals szolmolnokite, melanterite, rhomboclase, rozenite, kieserite, hexahydrite, epsomite, ferrohexahydrite, and siderotile were undersaturated in the spring fluids during the entire period, as were the chlorides halite and sylvite. Elemental sulfur and pyrite (not shown) were occasionally close to equilibrium.

7.11 Mineral Saturation Trends Along the Río Agrio

In a second set of hydrogeochemical models, changes in saturation indices downstream along the Río Agrio were explored, based on the compositions of stream-water samples taken in 2013 at 14 locations. These changes are largely controlled by cooling, and mixing with near-neutral and more dilute tributary waters which induces pH shifts. The pH values of the Upper Río Agrio waters increased steadily from 0.49 at the Vertiente spring, to ca. 1 at the entrance of Lake Caviahue, and to pH = 3.38 just before the Salto del Agrio at the rim of the Caviahue caldera (Table 7.1 and Fig. 7.10). Further downstream,

after the junction between the Lower Río Agrio and the Río Ñorquín, there is a step increase to values close to pH = 6. The 2013 spring waters (52.4 °C) were oversaturated in quartz, in equilibrium with gypsum and anhydrite, and slightly undersaturated in K-jarosite, amorphous silica, goethite, hematite, and Mg-nontronite. While the saturation state of quartz and amorphous silica remained fairly constant along the river, the indices for gypsum and anhydrite decreased because of dilution and cooling.

K-jarosite was oversaturated from the Cascadas del Agrio area (Site 24) on down to Site 5, after which the entrance of near-neutral water from the Arroyo Trolope tributary induces dilution and a pH increase, leading to undersaturation of this mineral. The Na and H-jarosite end-members followed the same tendencies. Goethite, hematite, ferrihydrite and Mg-nontronite reached saturation higher up in the URA watershed, and their indices further increased after dilution with near-neutral waters below the Salto del Agrio. The pH increase after the Salto was also associated with oversaturation of new phases suchs as gibbsite, kaolinite, Mg-montmorillonite, leonhardite and stilbite. In summary,
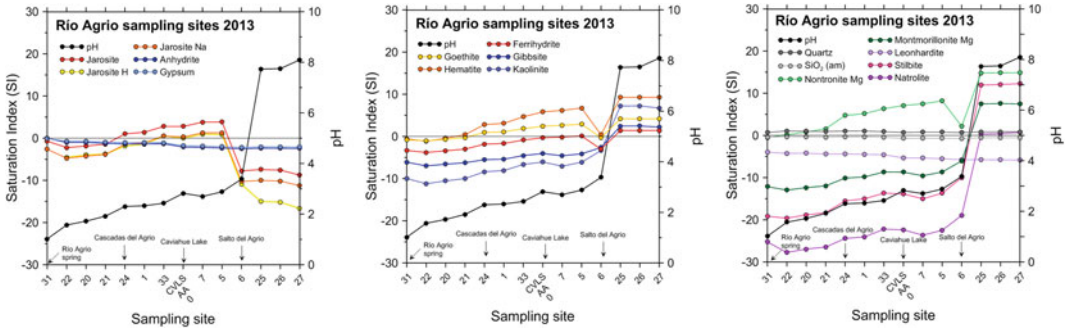
Fig. 7.10 Downstream trends in pH and saturation indices for selected minerals in the Río Agrio from its source (Vertiente spring) to the lower reaches past the Salto. Modelled indices are based on the composition of samples collected in March 2013

from the Río Agrio spring (Vertiente) to the point where the stream mixes with the Arroyo Trolope (just before the Salto), the modelled secondary mineralogy was dominated by jarosite, goethite, hematite, ferrihydrite and Mg-nontronite. Downstream from the Salto, goethite, hematite, ferrihydrite, gibbsite, kaolinite, Mg-montmorillonite and eventually stilbite and leonhardite were oversaturated.

7.12 Modelling Schwertmannite Stability

The Fe and sulfate concentrations in the Lake Caviahue and the Lower Río Agrio waters leads to conditions suitable for hydrous ferric iron precipitates (Bigham et al. 1990, 1996a, b;

Bigham and Nordstrom 2000). Speciation models for the Lake Caviahue and Lower Río Agrio water analyses between 1997 and 2009 were run and we entered the ion activities into the equilibrium expression for schwertmannite saturation (e.g., Fig. 7.11; Kading 2010). The lake was undersaturated in schwertmannite for the first decade but started to enter the stability field of this mineral in 2008 and 2009 (Fig. 7.11). The Lower Río Agrio was also schwertmannite saturated at that time, as documented by the precipitates in the river. The whole lake was expected to turn bright yellow-brown in 2010, but the onset of new volcanic activity led to a depression of the pH values in the Upper Río Agrio and then in Lake Caviahue, and first the lake and then the Lower Río Agrio became undersaturated in schwertmannite again.

Fig. 7.11 Schwertmannite saturation state of Lake Caviahue and the Lower Río Agrio (sample SPZ-LRA); saturation occurred in 2008–2009

$$8\ Fe^{3+} + SO_4^{2-} + 14\ H_2O \rightleftharpoons Fe_8O_8(OH)_6SO_4 + 22\ H^+ \quad,\quad K_{Schwert} = \frac{\{Fe^{3+}\}^8\{SO_4^{2-}\}}{\{H^+\}^{22}}$$
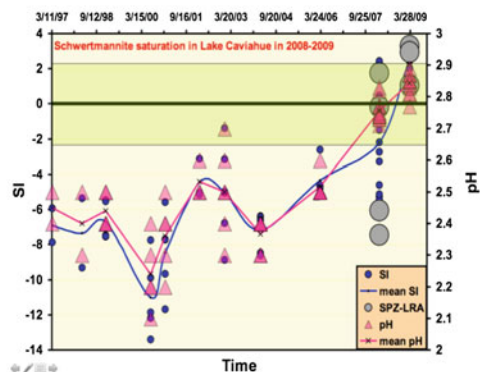
Schwertmannite is a common but ephemeral mineral at Copahue and its stability is strongly influenced by pH variations ($[H^+]$). Relative minor dilutions or mixing with fluids with a higher alkalinity will push the fluids out of the schwertmannite stability field. Much of this increase in pH is caused by the influx of tributary streams, in particular the Trolope and Norquin rivers (Gammons et al. 2005a; Parker et al. 2008). Alkalinity is also added by groundwater influx, especially below the Salto del Agrio where irrigation water applied to fields in the river valley returns to the stream as diffuse seepage with neutral pH and elevated HCO_3^- alkalinity (Parker et al. 2008). The spatial gradients in pH cause precipitation of these hydrous ferric oxides (HFO, including amorphous ferric hydroxide, ferrihydrite, and schwertmannite) and hydrous aluminum oxide (HAO, including amorphous $Al(OH)_3$, as well as hydrous Al-sulfates, such as basaluminite). Precipitation of HFO is most pronounced at pH transitions from <2.5 to >3. In summer low-flow periods, this pH transition is often located immediately below the confluence of the Río Trolope, where abundant, freshly-formed HFO stain the river and its banks a bright orange-red color (compare photographs in Fig. 7.12a, b). Because of photo-redox cycling (discussed below), HFO may dissolve and re-precipitate over the entire length of the Río Agrio below this point. Extensive outcrops of ferricrete (goethite-cemented alluvium) exist along the stream banks as far as 10 km below the Trolope confluence (Fig. 7.12c), and show that Fe precipitation must have been a dominant characteristic of the Río Agrio well into pre-historic times. Because of the higher solubility of Al relative to Fe, HAO precipitation does not occur until the pH > 4.5.

Evidence of this reaction is seen below the Salto del Agrio by the localized accumulation of white HAO precipitates along the edges of the Río Agrio where irrigation return water enters the stream. Precipitation of HAO proceeds to completion after the confluence of the Río Norquin, a large tributary with high alkalinity, where a prominent white ledge of Al-cemented boulders ("alcrete") exists in the mixing zone between the two rivers (Fig. 7.12d).

Previous workers (McKnight and Bencala 19971988; McKnight et al. 1988, 2001; Kimball et al. 1992; Voelker et al. ; Sullivan et al. 1998; Emmenegger et al. 2001; McKnight and Duren 2004; Gammons et al. 2005b, 2008; Sherman 2005; Parker et al. 2008; Nimick et al. 2011) have documented diel (24-h) cycles in the concentration and redox speciation of dissolved iron in streams that are acidic due to pyrite oxidation. These cycles are caused by day-time photo-reduction of dissolved or colloidal Fe^{III} to dissolved Fe^{2+} (reactions 7.1, 7.2) and re-oxidation of Fe^{2+} to dissolved or colloidal Fe^{III} compounds at night (reactions 7.3, 7.4), as follows:

$$\textbf{Day}: Fe(OH)^{2+} + h\upsilon \rightarrow Fe^{2+} + OH\cdot \quad (7.1)$$

$$Fe(OH)_3(s) + h\upsilon + 2H^+ \\ \rightarrow Fe^{2+} + OH\cdot + 2H_2O \quad (7.2)$$

$$\textbf{Night}: Fe^{2+} + \tfrac{1}{4}O_2 + \tfrac{1}{2}H_2O \rightarrow Fe(OH)^{2+} \\ (7.3)$$

$$Fe^{2+} + \tfrac{1}{4}O_2 + 5/2H_2O \\ \rightarrow Fe(OH)_3(s) + 2H^+ \quad (7.4)$$
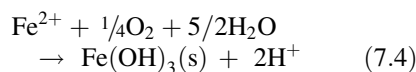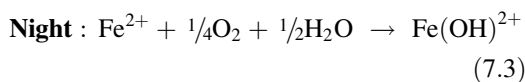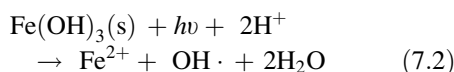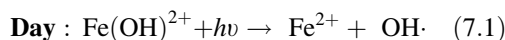
Fe(III) photo-reduction via reactions (Eq. 7.1) or (Eq. 7.2) creates a short-lived $OH^\cdot$ radical which is destroyed by reaction with other redox-sensitive species (Collienne 1983; Kimball et al. 1992; Voelker et al. 1997), such as dissolved organic carbon (DOC). David and David (1976) showed that photo-reduction of Fe(III) occurs in the ultraviolet (UV) to near-UV region of 200 to 450 nm, with a local maximum near 300 nm, and is sensitive to changes in pH, temperature, light intensity, major solute chemistry, and Fe(II) concentration. Collienne (1983) found that maximum Fe(III) photo-reduction rates take place in the pH range 2 to 4 where $Fe(OH)^{2+}$ is the dominant dissolved ferric species. This is also the pH range of the Río Agrio for many km below the outlet to Lake Caviahue, usually extending well below the confluence of the Río Trolope. Parker et al. (2008) conducted diel sampling along the Río Agrio just
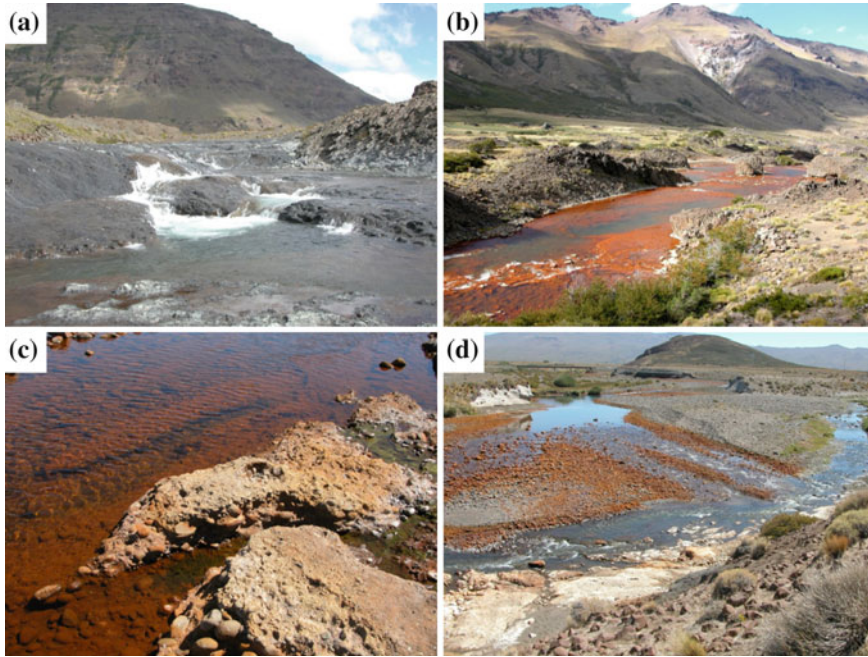
Fig. 7.12 Photographs (taken in February, 2009) of the lower Río Agrio in low-flow conditions. **a** Río Agrio above confluence with R. Trolope. **b** R. Agrio below confluence with R. Trolope. **c** Ferricrete deposits (center, bottom) along the bank of the river. **d** Confluence of R. Agrio (*left*) and R. Norquin (*right*), with large, cream-colored ledge of Al-cemented boulders (alcrete)

upstream of the Salto, as well as at two sites with higher pH further downstream. Results for dissolved Fe^{II}, Fe^{III}, and total dissolved Fe are summarized in Fig. 7.13a, along with data for photosynthetically-active radiation (PAR). The results show the predicted photo-reduction trends, i.e., a decline in dissolved Fe^{III} concentration during the day (high PAR) coincident with an increase in dissolved Fe^{II}, and a reversal of these trends at night. Because the rate of abiotic oxidation of Fe^{II} is very slow at low pH (Singer and Stumm 1970), Parker et al. (2008) attributed the night-time increase in Fe^{III} to iron-oxidizing bacteria (IOB). The IOB oxidize Fe^{II} during the daytime hours as well, but at a rate that is slower than the production of Fe^{II} by photo-reduction.

Gammons et al. (2008) quantified the amount of free energy made available to iron-oxidizing bacteria by daytime photo-reduction in the Tinto and Odiel Rivers of southern Spain. The same approach is used here to investigate the

bioenergetics of Fe^{II}-oxidation in the Río Agrio, using data collected by Parker et al. (2008). The amount of free energy consumed or released during Fe^{II} oxidation via reaction (7.3) is dependent on the concentrations of reactants and products and can be determined as follows:

$$\Delta G_r = \Delta G_r^\circ + RT\ln Q \text{ where } Q$$
$$= \left\{ Fe(OH)^{2+} \right\}$$
$$\cdot \left\{ Fe^{2+} \right\}^{-1} \cdot \{O_2\}^{-1/4} \cdot \{H_2O\}^{-1/2}$$
$$(7.5)$$

where ΔG_r^o is the standard state free energy change (-32.0 kJ mol^{-1} for reaction 7.3 based on data in Faure 1997), R is the gas constant, T is absolute temperature, Q is the ion-activity quotient, and the brackets {} refer to species activities (Faure 1997). To calculate the activities of Fe$(OH)^{2+}$ and Fe^{2+} (and thence Q), the chemical composition of each hourly river water sample at

Fig. 7.13 Diel changes in iron chemistry in the lower Río Agrio at Salto del Agrio in February, 2009. **a** Changes in concentration of dissolved Fe(II), Fe(III), total dissolved Fe, and photosynthetically active radiation (Parker et al. 2008). **b** Diel changes in the "exergonicity" of Fe^{2+} oxidation (reaction i) and precipitation of hydrous ferric oxide (reaction ii)
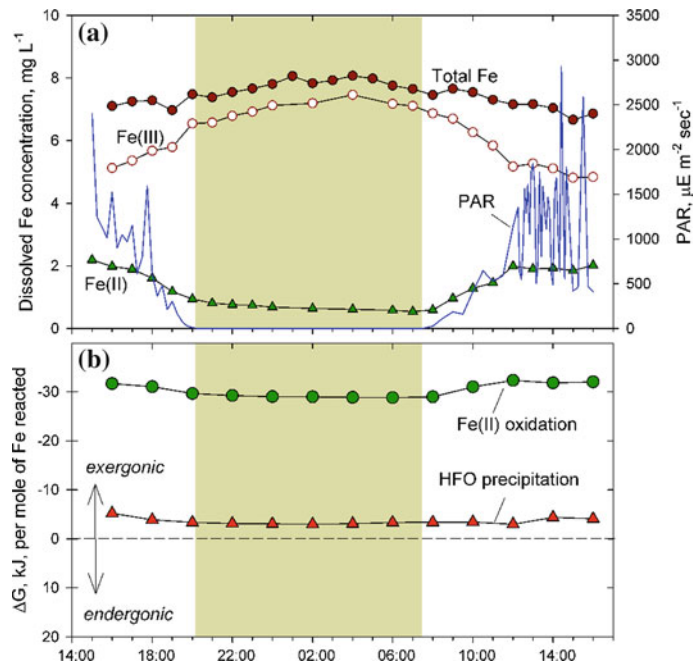
the Salto site (Parker et al. 2008) was entered into the program Visual Minteq (Vers. 3.0, a recent version of the original MINTEQA2 program of Allison et al. (1991)). The activity of water was taken as unity, and the activity of O_2 was assumed to reflect saturation with atmospheric O_2. In the study of Parker et al. (2008), the Río Agrio remained well-oxygenated above the Salto throughout the day and night. The results (Fig. 7.13b) indicate a range in ΔG of -28.8 to -31.7 kJ per mole of Fe^{2+} oxidized, with a 24-h average of -30.3 kJ mol^{-1}. These values are strongly exergonic (thermodynamically favorable), and overlap with the reported free energy changes of -25 to -37 kJ mol^{-1} for Fe(II) oxidation in the Río Tinto and Río Odiel, Spain (Gammons et al. 2008). As discussed by Gammons et al. (2008) and Lees et al. (1969), the disequilibrium created by sunlight and Fe^{III} photo-reduction is sufficient to support a thriving population of IOBs in the Río Tinto, as is also evidently the case in the Río Agrio. The amount of energy potentially gained by a micro-organism that catalyzes the oxidation of Fe^{2+} using O_2 is ~ 10 times greater than the amount of energy gained by precipitation of HFO.

7.13 Scenarios Involving Evaporation and Water-Rock Interaction

Evaporation of splash water or standing pools, as well as interaction with rocks in the streambed or on the borders are ubiquitous features along the Río Agrio, so a set of models was run to investigate the relevance of these processes to the formation of a suite of secondary minerals. In evaporation models, waters from the Vertiente hot spring, collected in 2003 (Gammons et al. 2005a, b) and 2013, were first titrated with O_2 to create equilibrium with local atmospheric conditions (10 °C, pressure corresponding to 2483 m a.s.l.), and were then evaporated at the same conditions. The results for 1 kg of water with compositions equal to the 2003 and 2013 samples (Fig. 7.14) show that evaporation has the most obvious effects on the formation of gypsum and iron (III) fluoride. Gypsum was already saturated in the 2013 sample at 10 °C before evaporation was imposed, whereas it only reaches saturation in the 2003 sample after ca. 60 % water loss. Iron (III) fluoride (FeF_3)
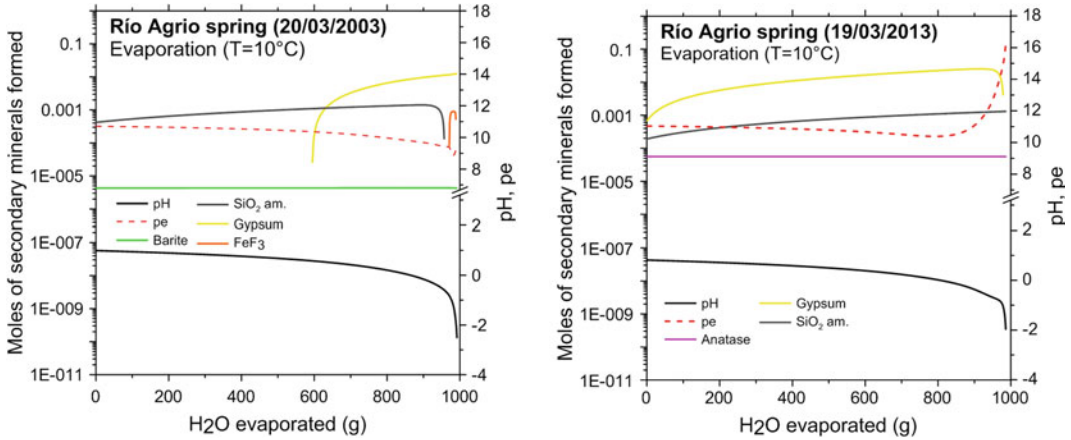
Fig. 7.14 Simulations predicting the formation of minerals during progressive evaporation of Vertiente spring water for 2003 and 2013 samples. Associated changes in pH and pe are also shown. Note that Ba was not analysed in the 2013 sample and Ti not in the 2003 sample, precluding the calculation for barite and anatase saturation in these cases

becomes stable in the 2003 sample when most of the water is evaporated, whereas saturation is not reached in the 2013 sample. FeF_3 in solid samples collected at the Vertiente Site 33 and at Site 23 (before the junction with the Río Colorado) during our 2013 campaign were detected. In view of the strong undersaturation of the mineral in the 2013 waters, the solid product can be considered a residue from an earlier period when dissolved Fe and F concentrations were much higher and the mineral could form during evaporation of splash or standing pool water.

In our water-rock interaction models, 1 mol (110 g) of andesite from the 2012 eruption of Copahue (Varekamp et al., this volume) was reacted with 1 kg of the 2013 sample of the Vertiente spring. Where necessary, the number of theoretically stable phases was restricted in model outcomes by allowing the formation of only those phases that are most consistent with our field observations. Figure 7.15 illustrates the results for a run at 24 °C, 1 atm and a water/rock (W/R) ratio of 0.1. Amorphous silica and anatase, saturated from the start, were the only phases precipitating

Fig. 7.15 Water-rock interaction model simulating the reaction between andesite rock (composition similar to products of the Copahue 2012 eruption) and water from the Vertiente hot spring at 24 °C
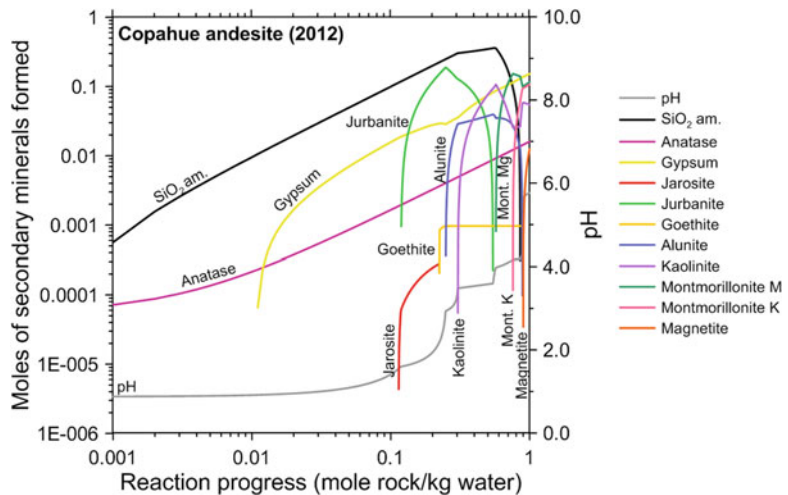
at low reaction progress, followed first by gypsum and then by jarosite and jurbanite. Goethite, alunite (K-endmember) and kaolinite appeared afterwards. Finally, at the highest reaction-progress values, montmorillonites (Mg and K endmembers) and magnetite formed. Interaction models (not shown) for lower water/rock ratios or higher temperatures were also tested. A run for a 10-fold lower W/R ratio (0.01) yielded a similar mineral sequence as in Fig. 7.15, but more clays and eventually zeolites appeared at high reaction-progress values. The main outcome of the temperature evaluation is that, above ca. 50 °C, neither jarosite nor jurbanite are formed, and Na-alunite becomes dominant over K-alunite.

7.14 Modelled Scenarios for the Formation of Mg-Sulfates

Since Mg-sulfates did not form in any of the above experiments, additional interaction models for hypothetical Mg-enriched systems were explored, based on the assumption that the Vertiente spring water and Copahue's andesitic rocks contain insufficient magnesium to create these minerals via simple pathways. In a first scenario, the interaction between acid fluid and olivine was modelled as the only reactive solid material available. It has been proposed that olivine dissolution was possibly an important process on Mars (Bandfield and Rogers 2008). An olivine composition of $Fa_{34}Fo_{66}$ was adopted, based on EPMA analysis of phenocrysts in a fresh sample collected after the Copahue 2012 eruption. One mole of olivine (160.7 g) was reacted with the 2013 Vertiente spring water at 24 °C. The resulting secondary mineral assemblage (Fig. 7.16a) was largely similar to that found in the water-andesite model (Fig. 7.16b), except that K-montmorillonite did not form and higher pH values (> 10) were ultimately reached. The saturation indices for Mg-sulfates show maxima (highest for epsomite) but without reaching saturation levels (Fig. 7.16b). A decrease in the saturation indices near the end of the reaction is presumably due to Mg^{2+} consumption by Mg-montmorillonite at the highest pH conditions.

In a more complex scenario, a multiple-step process involving both solid-fluid interaction and evaporation to create sufficiently magnesian conditions for the formation of Mg-sulfates was simulated. An open system in which fluid, after reaction with an Mg-rich solid, evaporates to some extent, was envisaged after which the more concentrated residue reacts again with a fresh aliquot of the same solid. As input for the evaporation step, a fluid with a composition simulated in the previous water-olivine reaction model was used just before jarosite started to precipitate (i.e. at a reaction progress value of ca. 0.05; Fig. 7.16a), when much of the cation budget needed to form sulfates (other than gypsum) in the ultimate products was still in solution. With progressive evaporation, the saturation indices for Mg-sulfates increased only slowly until the final stages when most of the fluid was evaporated and epsomite reached saturation (Fig. 7.17). In a subsequent step, the liquid from the last stage of this evaporation experiment was let to react again with Fo_{66} olivine, which produced epsomite ($MgSO_4 \cdot 2H_2O$) and ferrohexahydrite ($FeSO_4 \cdot 6H_2O$) together with anatase, gypsum and amorphous silica (Fig. 7.18). Even though both the evaporation and the second interaction model could not be completed because of convergence problems with PHREEQC (due to the high ionic strengths of the solutions), our findings suggest that the formation of Mg-sulfates in the Copahue environment requires interaction between relatively small volumes of acid fluid and Mg-rich solid in combination with evaporation.

7.15 Comparison Between Mineralogical Features of Copahue-Caviahue and Mars

The occurrences of sulfate-bearing mineral assemblages on Mars was retrieved to evaluate in how far the mineralogy at Copahue-Caviahue shows similarities with the documented and
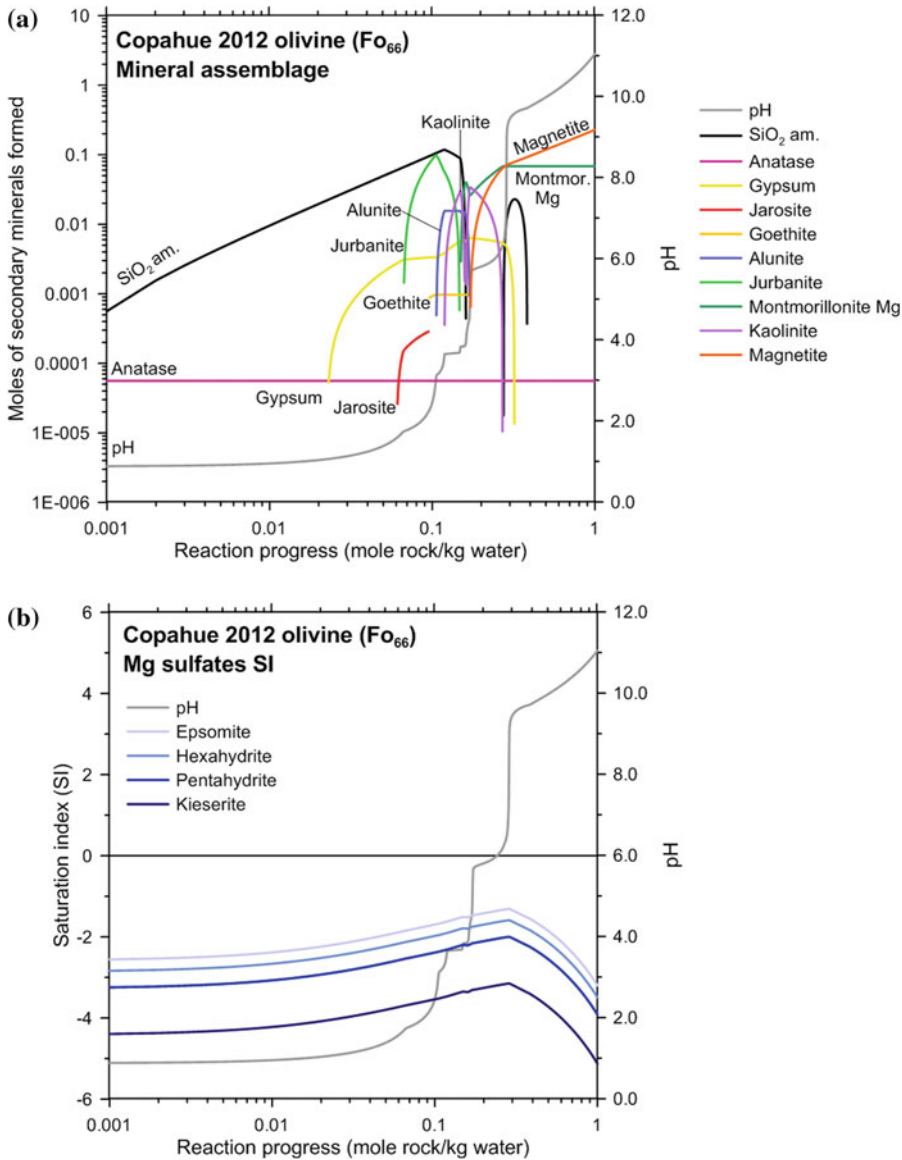
Fig. 7.16 Modelled interaction between olivine (Fo_{66}) and water from the Vertiente hot spring (2013) at T = 24 °C. **a** Types and amounts of secondary minerals formed with increasing interaction. **b** Saturation indices for inferred Mars minerals. Under which conditions can these Copahue fluids crystallize minerals that occur on Mars but are currently rare or absent at Copahue? The absorption of hot volcanic gases by shallow ground waters, in this case glacial melt waters, leads to hot and acid hydrothermal fluids inside Copahue volcano. These aggressive fluids dissolve and react with the surrounding rock matrix producing fluids that are saturated in anhydrite, some sulfides and hydrothermal silica. When the fluids react with newly intruded chilled magma, alunite starts to crystallize, and in some cases the various forms of jarosite become stable. The main minerals in the hydrothermal reservoir

Fig. 7.17 Evaporation model for Vertiente hot spring water previously modified by interaction with olivine (fluid composition before formation of jarosite, cf., Fig. 7.16). **a** Saturation indices for amorphous silica, anatase and gypsum. **b** Saturation indices for magnesium sulfates. Note that epsomite reaches equilibrium near the end of this run. See text for details
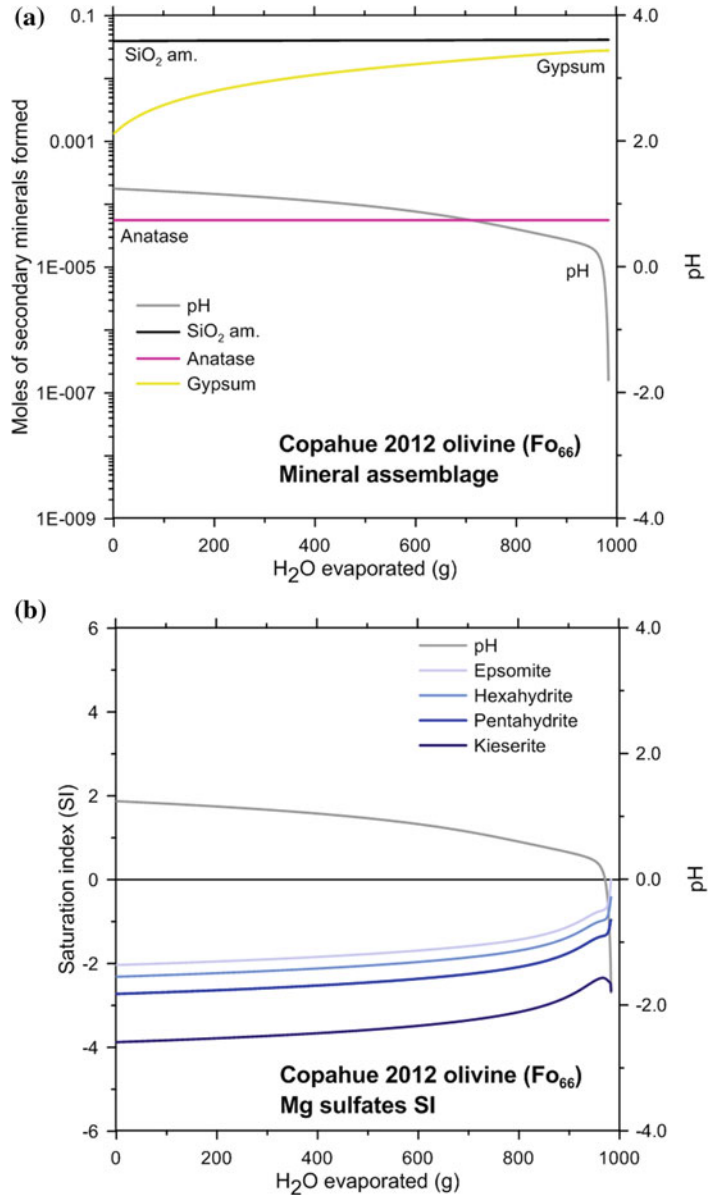
rock thus are silica, anhydrite, alunite and possibly jarosite as also shown by lithics ejected during recent Copahue eruptions. When the fluids escape from the hydrothermal system into the ambient environment (hot springs, crater lake), cooling, dilution, evaporation and oxidation through atmospheric oxygen may occur, leading to another suite of minerals becoming saturated as detailed above. Further downstream, after substantial dilution to pH values around

three, microbiotic reactions as well as photo-reduction processes, may occur, cycling some dissolved components through various aqueous species and creating conditions for the saturation with schwertmannite. The crystallization of those HFO-sulfates then leads to adsorption and incorporation of the trace elements arsenic, phosphorus and vanadium. Ultimately, schwertmannite may convert to hydrous ferric oxides such as ferrihydrite and goethite, which

Fig. 7.18 Final step in a hypothetical model showing the formation of epsomite and ferrohexahydrite as products of interaction between the fluid residue of evaporation (as modelled in Fig. 7.17) and olivine
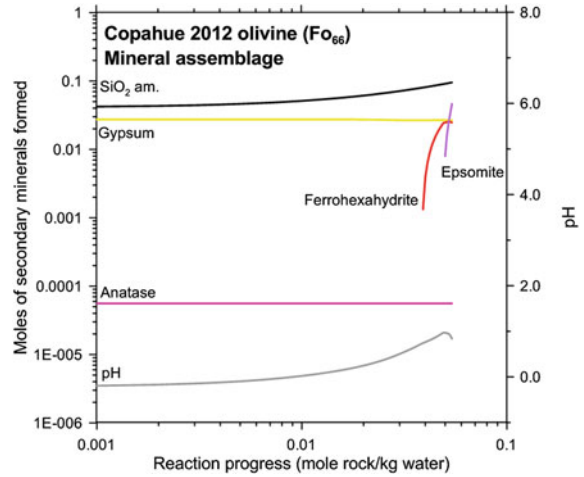
may over time turn into hematite. At Copahue it appears that schwertmannite crystallization is conditioned or at least modulated by Fe-oxidizing acidophilic bacteria, as found in the Lower Río Agrio. The Copahue hydrothermal fluids are rich in Mg and Fe^{2+}, especially directly following intrusive events, and these cations are probably largely derived from dissolution of mafic phases such as olivine and pyroxenes. Oxidation of the Fe^{2+} leads to the precipitation of ferric oxides and sulfates, whereas Mg sulfates are rare. Combination of acid water-rock interaction with evaporation and subsequent reaction with olivine may lead to Mg sulfate crystallization.

Weathering experiments of basaltic rocks (Nesbith and Young 1984; Nesbith and Wilson 1992; Gislasson and Arnolsson 1993; Tosca et al. 2004; Golden et al. 2005; Hausrath et al. 2013) and olivine (King et al. 2011) suggest that the bulk composition of the starting material, low water/rock ratios and incongruent rock or glass dissolution may lead to the formation of magnesium sulfates. Mars is largely a basaltic planet (Baratoux et al. 2009; Carr and Head 2010; Grott et al. 2013) whereas silicic and intermediate rocks predominate on the continents of the earth. Some of these major differences in surface rocks between the two planets are reflected in their secondary minerals. While on Earth secondary mineral assemblages are dominated by clay minerals, aluminium hydroxides, and iron

oxi/hydroxides, on Mars the secondary mineralogy is primarily represented by magnesium, iron and calcium sulfates and iron oxides (Hurowitz and Mc Lennan 2007). Nevertheless, the rivers and lakes at Caviahue-Copahue formed secondary mineral associations that resemble some Mars terrains and their mechanisms of formation was documented by our analytical studies and constrained by the modelling above.

With regard to the search for Mars analogues at Copahue, several features of the Lower Río Agrio are significant. The acidity of the Agrio watershed has a volcanic source, unlike other putative Mars analogues, such as the Río Tinto, Spain, which owe their acidity to mining and accelerated weathering of sulfide bedrock minerals. The spatial distribution of active HFO-sulfate precipitates and ancient ferricrete deposits along the lower Río Agrio may be examples of the types of mineral deposits that could conceivably exist on Mars in paleo-fluvial environments. The thickest accumulations of ferricrete along the Río Agrio exist along the margins of the stream where alkaline groundwater mixes with acidic river water, not within the main channel of the river. Most of the HFO that precipitates in the main channel is swept downstream during periods of high flow, leaving a thin (<1 cm), transient coating of orange-red "muck" on boulders and outcrops when the river levels recede. Thirdly, the existence of HAO flocs and Al-cemented gravel in the lower

reaches of the Río Agrio suggest that similar geologic deposits could exist on Mars. In the absence of active volcanic-hydrothermal systems, groundwater under the Martian regolith would most likely have a neutral to alkaline pH through interaction with basalt, just as it does on Earth. By mixing with this groundwater, or mixing with non-acidic tributary streams, the "pH endpoint" of titration of an acidic Martian river with distance away from its volcanic-hydrothermal source could have been >5, resulting in precipitation of dissolved Al as HAO. Such precipitates could be preserved as alcrete deposits along paleo-river banks, as sediment in a terminal playa lake, or as coatings on mineral surfaces beneath the paleo-river channel in the event that the surface water soaked into the ground before it evaporated or froze.

It has been postulated that schwertmannite was an important mineral on Mars (Bishop and Murad 1996), either in its far past or even still occurring today. If the analogy with Caviahue holds, the mineral formation on Mars may also have been facilitated by Fe-oxidizing bacteria and photo-reduction and/or photo-oxidation processes. The disequilibrium created by sunlight and Fe^{III} photo-reduction is sufficient to support a thriving population of IOBs in the Río Tinto (Gammons et al. 2008), and similar processes occur in the Río Agrio. The effectiveness of the IOBs to oxidize Fe^{II} to Fe^{III} is a function of O_2 concentrations in the water and thus in air (reaction 7.3). For early Mars, the partial pressure of O_2 is poorly constrained, but reaction (7.3) is thermodynamically favorable ($\Delta G > 0$) for water with the same chemistry as the Salto del Agrio samples as long as pO_2 is greater than 10^{-22} to 10^{-24} bars. The question then becomes: could partial O_2 pressures have been this high in an early Martian atmosphere?

Astrobiologists have speculated that a significant amount of organic carbon could have been deposited on Mars by comets, and yet empirical data that have been returned from orbital and land-based probes show only few traces of organic compounds on Mars (Benner et al. 2000; Ming et al. 2013). Iron photo-reduction may have provided a means to break down DOC or solid organic carbon molecules. Following the Río Agrio analogy, organic carbon delivered to the surface of Mars could have been largely oxidized by free radicals such as OH· that formed via the Fe^{III} photo-reduction reactions (7.1) and (7.2) presented earlier. This assumes that: (1) water existed on the Martian surface; and (2) the water was acidic enough to mobilize ferric iron. The importance of Fe^{III} photo-reduction on Mars is rarely discussed in the astrobiology literature. Most researchers discuss Fe^{II} photo-*oxidation* (Cairns-Smith 1978, and the later work of Braterman et al. 1983; Borowska and Mauzerall 1986; Lundgreen et al. 1989; Kim et al. 2013). Short wave-length UV-C light (maximum at 267 nm; Kim et al. 2013) in controlled laboratory experiments created Fe^{II} photo-oxidation, as opposed to Fe^{III} photo-reduction, which is induced by light over a wider range of wavelengths (200 to 450 nm, maximum at 300 nm, David and David 1976). In the absence of a protective ozone layer in the upper atmosphere, UV-C radiation could have easily penetrated Mars' thin atmosphere, as it presumably did the atmosphere of early Earth. It is unknown if Fe^{II} photo-oxidation occurs simultaneously with Fe^{III} photo-reduction in full-spectrum sunlight, and what the relative rates of these two opposing reactions are over a wide range of pH, and in the presence of other solutes, such as possibly dissolved organic carbon.

Obviously, if firmer evidence of schwertmannite presence from the Mars surface can be supplied, this may lead to many inferences regarding the presence of bacteria as well the atmospheric composition at the time. Our modelling and observations make it likely that schwertmannite may have formed on Mars in analogy to the processes documented in the Río Agrio watershed. The key parameters here are that the waters are both acidic and sulfate-rich because of absorption of volcanic gases, and Fe-rich because of high temperature water-rock interaction at depth. The schwertmannite stability zone at Copahue is distal from the hot springs and caused both by an increase in pH through dilution and the Fe-cycling discussed above. If schwertmannite was common at the surface of

early Mars, adsorption of As, V and P is also expected, which would probably create an overall surface enrichment in these elements. Greenwood and Blake (2006) suggested that Mars surface rocks are indeed enriched in phosphorus.

Hurowitz et al. (2010) designed an inverse schwertmannite precipitation scheme, where neutral groundwaters became enriched in Fe^{II} through interaction with basaltic basement. Once at the surface, photo-oxidation processes reduced the pH which then led to schwertmannite saturation while coming from the higher pH values (the sulfate source is not obvious in this model). The precipitation of schwertmannite would then lead to even lower pH values, creating conditions of acid surface waters on Mars. Our observations and modelling shows that in the Río Agrio the opposite occurs: strongly acid fluids become neutralized and once the pH = 3 limit is exceeded schwertmannite starts to crystallize as discussed above.

Summarizing, many minerals observed on the surface in the Copahue-Caviahue watershed are also thought to occur on Mars: silica, jarosite, gypsum, hematite, various hydrous Fe-oxides and hydrous Fe-sulfates such as schwertmannite. Alunite is uncommon at the surface at Copahue but is an important mineral that formed inside the hydrothermal reservoir at elevated temperatures. In analogy, alunite on Mars may be found at the surface near impact craters that de-roofed former volcanic hydrothermal systems. The abundance of many Mg-sulfates on Mars is in contrast with their limited occurrence in the Río Agrio watershed, where Mg is an almost conservative element. Modelling suggests that more extensive interaction between acid fluids and olivine-rich basement rocks, possibly coupled with evaporation could easily lead to Mg-sulfate formation. Mars is largely a basaltic planet, rich in olivine, whereas Copahue is an andesitic volcano where the most mafic rocks were the 2012 scoria with some olivine and a bulk rock magnesium content of 4.5 % MgO (Varekamp et al. this book). The potential presence of schwertmannite on Mars leads to many speculations regarding presence of bacteria, composition of the atmosphere as well as surface enrichments in the oxyanions of V,

As and P. At first sight, Copahue appears to be a good terrestrial analogue for some Martian environments that carry sulfate minerals (Varekamp 2004).

References

Acero P, Ayora C, Torrento C, Nieto JM (2006) The behaviour of trace elements during schwertmannite precipitation and subsequent transformation into goethite and jarosite. Geochim Cosmochim Acta 70:4130–4139

Africano F, Bernard A (2000) Acid alteration in the fumarolic environment of Usu volcano, Hokkaido, Japan. J Volcanol Geotherm Res 97:475–495

Agusto MR, Varekamp JC (2015) Geochemistry of the acidic waters of the Copahue volcano-hydrothermal system with applications for volcanic surveillance, this volume

Allison JD, Brown DS, Novo-Gradak KJ (1991) MINTEQA2/PRODEAFA2, a geochemical assessment model for environmental systems. U.S. Environmental Protection Agency, Washington DC, EPA/600/3-91/021

Alexander EW (2014) Aqueous geochemistry of an active magmato-hydrothermal system: Copahue Volcano, Río Agrio, and Lake Caviahue, Neuquén, Argentina. Undergraduate thesis, Wesleyan University, Middletown CT, USA, pp 1–100

Andrews-Hanna JC, Zuber MT, Arvidson RE, Wiseman SM (2010) Early Mars hydrology: Meridiani playa deposits and the sedimentary record of Arabia Terra. J Geophys Res 115:E06002

Arvidson R, Poulet F, Morris RV, Bibring J-P, Bell III JF, Squyres SW, Christensen PR, Bellucci G, Gondet B, Ehlmann BL, Farrand WH, Fergason RL, Golombek M, Griffes JL, Grotzinger J, Guinness EA, Herkenhoff KE, Johnson JR, Klingelhöfer G, Langevin Y, Ming D, Seelos K, Sullivan RJ, Ward JG, Wiseman SM, Wolff M (2006) Nature and origin of the hematite-bearing plains of Terra Meridiani based on analyses of orbital and Mars Exploration Rover data sets. J Geophys Res 11:E12S08. doi:10.1029/2006JE002728

Baffico GD, Diaz MM, Wenzel MT, Koschorreck M, Schimmele M, Neu TR, Pedrozo F (2004) Community structure and photosynthetic activity of epilithon from a highly acidic (pH 2) mountain stream in Patagonia, Argentina. Extremophiles 8:463–473

Baldridge AM, Hook SJ, Crowley JK, Marion GM, Kargel JS, Michalski JL, Thomson BJ, de Souza Filho CR, Bridges NT, Brown AJ (2009) Contemporaneous deposition of phyllosilicates and sulfates: using Australian acidic saline lake deposits to describe geochemical variability on Mars. Geophys Res Lett 36:L19201. doi:10.1029/2009GL040069

Bandfield JL, Hamilton VE, Christensen PR (2000) A global view of Martian surface compositions from MGS-TES. Science 287:1626–1630

Bandfield JL, Rogers AD (2008) Olivine dissolution by acidic fluids in Argyre Planitia, Mars: evidence for a widespread process? Geology. doi:10.1130/G24724A.1

Baratoux D, Pinet P, Toplis MJ, Mangold N, Greeley R, Baptista AR (2009) Shape, rheology and emplacement times of small Martian shield volcanoes. J Volcanol Geotherm Res 185:47–68

Benison KC, LaClair DA (2003) Modern and ancient extremely acid saline deposits: terrestrial analogs for Martian environments? Astrobiology 3:609–618

Benner SA, Devine KG, Matveeva LN, Powell DH (2000) The missing organic molecules on Mars. Proceed Nat Acad Sci 97:2425–2430

Bermúdez A, Delpino D (1995) Mapa de los peligros potenciales en el área del Volcán Copahue—sector Argentino. Volcanic Hazard Map. The Geological Survey of the Province of Neuquén, Argentina

Bibring J-P, Langevin Y, Gendrin A, Gondet B, Poulet F, Berthé M, Soufflot A, Arvidson R, Mangold N, Mustard J, Drossart P, the OMEGA team (2005) Mars surface diversity as revealed by the OMEGA/Mars Express observations. Science 307:1576–1581

Bigham JM, Schwertmann U, Carlson L, Murad E (1990) A poorly crystallized oxyhydroxysulfate of iron formed by bacterial oxidation of Fe(II) in acid mine waters. Geochim Cosmochim Acta 54:2743–2758

Bigham JM, Schwertmann U, Traina SJ, Winland RL, Wolf M (1996a) Schwertmannite and the chemical modeling of iron in acid sulfate waters. Geochim Cosmochim Acta 60:2111–2121

Bigham JM, Schwertmann U, Pfab G (1996b) Influence of pH on mineral speciation in a bioreactor simulating acid mine drainage. Appl Geochem 11:845–849

Bigham JM, Nordstrom DK (2000) Iron and aluminium hydroxysulfates from acid sulfate wateres. In Alpers CN, Jambor JL, Nordstrom DK (eds) Sulfate minerals, crystallography, geochemistry, and environmental significance, vol 40. Reviews in Mineralogy and Geochemistry, Mineralogical Society of America, Washington, D.C., pp 351–403

Bishop JL Murad E (1996) Schwertmannite on Mars? Spectroscopic analyses of schwertmannite, its relationship to other ferric minerals, and its possible presence in the surface material of Mars. In: Dyar MD, McCammon C, Schaefer MW (eds) Mineral spectroscopy: a tribute to Roger G Burns, vol 5. Geochemical Society Special Publications, Houston, pp 337–358

Bishop JL, Parente M, Wietz CM, Noe Dobrea EZ, Roach LH, Murchie SL, McGuire PC, McKeown NK, Rossi CM, Brown AJ, Calvin WM, Milliken R, Mustard JF (2009) Mineralogy of Juventae Chasma: sulfates in the light-toned mounds, mafic minerals in the bedrock, and hydrated silica and hydroxylated ferric sulfate on the plateau. J Geophys Res 114: E00D09

Bishop JL, Dyar MD, Lane MD, Banfield JF (2005) Spectral identification of hydrated sulfates on Mars and comparison with acidic environments on Earth. Int J Astrobiol 3:275–285

Blodau C, Knorr KH (2006) Experimental inflow of groundwater induces a biogeochemical regime shift in iron-rich and acidic sediments. J Geophys Res 111: G02026

Borowska Z, Mauzerall D (1986) Formation of hydrogen on irradiation of aqueous ferrous iron by UV-light at neutral pH. Orig Life Evol Biosph 16:194–195

Brady KS, Bigham JM, Jaynes WF, Logan TJ (1986) Influence of sulfate on Fe-oxide formation: compositions with a stream receiving acid mine drainage. Clays Clay Mineral 34:266–274

Braterman P, Cairns-Smith AG, Sloper RW (1983) Photo-oxidation of hydrated Fe^{2+}−significance for banded iron formations. Nature 303:163–164

Cairns-Smith AG (1978) Precambrian solution photo-chemistry, inverse segregation, and banded iron formations. Nature 276:807–808

Carr MH, Head JW (2010) Geologic history of Mars. Earth Planet Sci Lett 294:185–203

Chevrier V, Mathé PE (2007) Mineralogy and evolution of the surface of Mars: a review. Plan Space Sci 55:289–314

Christensen PR, Banfield JL, Clark RN, Edgett KS, Hamilton VE, Hoefen T, Kieffer HH, Kuzmin RO, Lane MD, Malin MC, Morris RV, Pearl JC, Pearson R, Roush TL, Ruff SW, Smith MD (2000) Detection of crystalline hematite mineralization on Mars by the thermal emission spectrometer: evidence for near-surface water. J Geophys Res 105(E4):9623–9642

Clark RN, Swayze GA, Wise RA, Eric Livo K, Hoefen TM, Kokaly RF, Sutley SJ (2007) USGS digital spectral library splib06a. U.S. Geological Survey, Digital Data Series 231

Collienne RH (1983) Photo-reduction of iron in the epilimnion of acidic lakes. Limnol Oceanogr 28:83–100

Cousins CR, Crawford IA, Carrivick JL, Gunn M, Harris J, Kee TP, Karlsson M, Carmody L, Cockell C, Herschy B, Joy KH (2013) Glaciovolcanic hydrothermal environments in Iceland and implications for their detection on Mars. J Volcanol Geotherm Res 256:61–77

Cowie BR, Slater GF, Bernier L, Warren LA (2009) Carbon isotope fractionation in phospholipid fatty acid biomarkers of bacteria and fungi native to an acid mine drainage lake. Org Geochem 40:956–962

David F, David PG (1976) Photoredox chemistry of iron (III), chloride and iron(III) perchlorate in aqueous media. A comparative study. J Phys Chem 80:579–583

Delmelle P, Bernard A (1994) Geochemistry, mineralogy and chemical modeling of the acid crater lake of Kawah-Ijen Volcano, Indonesia. Geochim Cosmochim Acta 58:2445–2460

Delmelle P, Bernard A, Kusakabe M, Fischer TP, Takano B (2000) Geochemistry of the magmatic-hydrothermal system of Kawah Ijen

volcano, East Java, Indonesia. J Volcanol Geotherm Res 97:31–53

Delmelle P, Bernard A (2000) Downstream composition changes of acidic volcanic waters discharged into the Banyupahit stream, Ijen caldera, Indonesia. J Volcanol Geotherm Res 97:55–75

Ehlmann BL, Edwards CS (2014) Mineralogy of the Martian surface. Ann Rev Earth Plan Sci 42:291–315

Emmenegger L, Schönenberger R, Sigg L, Sulzberger B (2001) Light-induced redox cycling of iron in circum-neutral lakes. Limnol Oceanogr 46:49–61

Farrand WH, Glotch TD, Rice JW Jr, Hurowitz JA, Swayze GA (2009) Discovery of jarosite within the Mawrth Vallis region of Mars: implications for the geologic history of the region. Icarus 204:478–488

Faure G (1997) Principles and Applications of Geochemistry, 2nd edn. Prentice Hall, Upper Saddle River, NJ

Fernandez-Remolar D, Gomez-Elvira J, Gomez F, Sebastian E, Martiin J, Manfredi JA, Torres J, Gonzalez Kesler C, Amils R (2004) The Tinto River, an extreme acidic environment under control of iron, as an analog of the Terra Meridiani hematite site of Mars. Planet Space Sci 52:239–248

Gagliano WB, Brill MR, Bigham JM, Jones FS, Traina SJ (2004) Chemistry and mineralogy of ochreous sediments in a constructed mine drainage wetland. Geochim Cosmochim Acta 68:2119–2128

Gammons CH, Wood SA, Pedrozo F, Varekamp JC, Nelson B, Shope CL, Baffico G (2005a) Hydrogeochemistry and rare earth element behavior in a volcanically acidified watershed in Patagonia, Argentina. Chem Geol 222:249–267

Gammons CH, Nimick DA, Parker SR, Cleasby TE, McClesky RB (2005b) Diel behavior of iron and other heavy metals in a mountain stream with acidic to neutral pH: Fisher Creek, MT, USA. Geochim Cosmochim Acta 69:2505–2516

Gammons CH, Nimick DA, Parker SR, Snyder DM, McCleskey RB, Amils R, Poulson SR (2008) Photo-reduction fuels biogeochemical cycling of iron in Spain's acid rivers. Chem Geology 252:202–213

Gellert R, Rieder R, Anderson R, Bruckner J, Clark B, Dreibus G, Economou T, Klingelhofer G, Lugmair G, Ming D, Squyres S, d'Uston C, Wanke H, Yen A, Zipfel J (2004) Chemistry of rocks and soils in Gusev crater from the alpha particle x-ray spectrometer. Science 305: 829–832

Gellert R, Rieder R, Brückner J, Clark BC, Dreibus G, Klingelhöfer G, Lugmair G, Ming DW, Wänke H, Yen A, Zipfel J, Squyres SW (2006) Alpha Particle X-Ray Spectrometer (APXS): Results from Gusev crater and calibration report. J Geophys Res 111 (E2):2156–2202

Gíslasson SR, Arnórsson S (1993) Dissolution of primary basaltic minerals in natural waters—saturation state and kinetics. Chem Geol 105:117–135

Glotch TD, Bandfield JL, Christensen PR, Calvin WM, McLennan SM, Clark BC, Rogers AD, Squyres SW (2006) Mineralogy of the light-toned outcrop at Meridiani Planum as seen by the Miniature Thermal Emission Spectrometer and implications for its formation. J Geophys Res 111:E12S03

Golden DC, Ming DW, Morris RV, Mertzman SA (2005) Laboratory-simulated acid-sulfate weathering of basaltic materials: Implications for formation of sulfates at Meridiani Planum and Gusev crater, Mars. J Geophys. Res-Planets 110:E12

Greenwood JP, Blake RE (2006) Evidence for an acidic ocean on Mars from phosphorus geochemistry of Martian soils and rocks. Geology 34:953–956

Grott M, Baratoux D, Hauber E, Sautter V, Mustard J, Gasnault O, Ruff SW, Karato SI, Debaille V, Knapmeyer M, Sohl F, Van Hoolst T, Breuer D, Morschhauser A, Toplis MJ (2013) Long-term evolution of the Martian crust-mantle system. Space Sci Rev 174:49–111

Grotzinger JP, Arvidson RE, Bell JF III, Calvin W, Clark BC, Fike DA, Golombek M, Greeley R, Haldemann AFC, Herkenhoff KE, Joliff BL, Knoll AH, Malin MC, McLennan SM, Parker T, Soderblom LA, Sohl-Dickstein JN, Squyres SW, Tosca NJ, Watters WA (2005) Stratigraphy and sedimentology of a dry to wet eolian depositional system, Burns formation, Meridiani Planum, Mars. Earth Planet Sci Lett 240:11–72

Hartmann WK, Neukum G (2001) Cratering chronology and the evolution of Mars. Space Sci Rev 96:165–194

Hausrath EM, Golden DC, Morris RV, Agresti DG, Ming DW (2013) Acid sulfate alteration of fluorapatite, basaltic glass and olivine by hydrothermal vapors and fluids: implications for fumarolic activity and secondary phosphate phases in sulfate-rich Paso Robles soil at Gusev Crater. Mars. J Geophys Res-Planets 118:E1

Horgan BH, Bell JF III, Noe Dobrea EZ, Cloutis EA, Bailey DT, Craig MA, Roach LH, Mustard JF (2009) Distribution of hydrated minerals in the north polar region of Mars. J Geophys Res 114:E01005

Hurowitz JA, McLennan SM (2007) A ∼ 3.5 Ga record of water-limited, acidic weathering conditions on Mars. Earth Planet Sci Lett 260:432–443

Hurowitz JA, Fischer WW (2014) Contrasting styles of water–rock interaction at the Mars Exploration Rover landing sites. Geochim Cosmochim Acta 127:25–38

Hurowitz JA, Fischer WW, Tosca NJ, Milliken RE (2010) Origin of acidic surface waters and the evolution of atmospheric chemistry on early Mars. Nat Geosci 3:323–326

Jonsson J, Persson P, Sjoberg S, Lovgren L (2005) Schwertmannite precipitated from acid mine drainage: phase transformation, sulfate release and surface properties. Appl Geochem 20:179–191

Kading TJ, Varekamp JC (2009) Schwertmannite precipitation in glacial Lake Caviahue, Neuquén, Argentina. Geol Soc Am Abstr Programs 43:77

Kading TJ, Varekamp JC (2011) Lake Caviahue (Argentina) as a source-sink for volcanic arsenic and phosphorus. Geol Soc Am Abstr Programs 41:645

Kading TJ (2010) Natural pollutant attenuation by schwertmannite at Copahue Volcano, Argentina [M. A. thesis]: Middletown, Wesleyan University, Middletown CT USA, pp 247

Kim JD, Yee N, Nanda V, Falkowski PG (2013) Anoxic photochemical oxidation of siderite generates molecular hydrogen and iron oxides. Proc Natl Acad Sci 110:10073–10077

Kimball BA, McKnight DM, Wetherbee GA, Harnish RA (1992) Mechanisms of iron photo-reduction in a metal-rich, acidic stream (St. Kevin Gulch, Colorado, USA). Chem Geol 96:227–239

King HE, Plumper O, Geisler T, Putnis A (2011) Experimental investigations into the silicification of olivine: Implications for the reaction mechanism and acid neutralization. Am Mineral 96:1503–1511

Klingelhöfer G, Morris RV, Bernhardt B, Schroder S, Rodionov DS, de Souza Jr PA, Yen A, Gellert R, Evlanov EN, Zubkov B, Foh J, Bonnes U, Kankeleit E, Gütlich P, Ming DW, Renz F, Wdowiak T, Squyres SW, Arvidson RE (2004) Jarosite and hematite at Meridiani Planum from Opportunity's Mössbauer spectrometer. Science 306:1740–1745

Kumpulainen S, Carlson L, Raisanen M-L (2007) Seasonal variations of ochreous precipitates in mine effluents in Finland. Appl Geochem 22:760–777

Kusakabe M, Komoda Y, Takano B, Abiko T (2000) Sulfur isotopic effects in the disproportionation reaction of sulfur dioxide in hydrothermal fluids: implications for the delta S-34 variations of dissolved bisulfate and elemental sulfur from active crater lakes. J Volcanol Geotherm Res 97:287–307

Lees H, Kwok SC, Suzuki I (1969) The thermodynamics of iron oxidation by the Ferrobacilli. Can J Microbiol 15:43–46

Lundgreen B, Jensen HG, Knudsen JM, Olsen M, Vistisen L (1989) Photostimulated oxidation of Fe^{2+} (aq): a Mars simulation experiment studied by Mössbauer spectroscopy. Phys Scr 39:670

McCanta MC, Dyar MD, Treiman AH (2014) Alteration of Hawaiian basalts under sulfur-rich conditions: applications to understanding surface-atmosphere interactions on Mars and Venus. Am Mineral 99:291–302

McHenry LJ, Vhevrier V, Schröder C (2011) Jarosite in a Pleistocene East African saline-alkaline paleolacustrine deposit: implications for Mars aqueous geochemistry. J Geophys Res 116:E04002

McLennan SM, Bell JF III, Calvin WM, Christensen PR, Clark BC, De Souza PA, Farmer J, Farrand WH, Fike DA, Gellert R, Ghosh A, Glotch TD, Grotzinger JP, Hahn BC, Herkenhoff KE, Hurowitz JA, Johnson JR, Johnson SS, Joliff BL, Klingelhoefer G, Knoll AH, Learner ZA, Malin MC, McSween Jr HY, Pocock J, Ruff SW, Soderblom LA, Squyres SW, Tosca NJ, Watters WA, Wyatt MB, Yen A (2005) Provenance and diagenesis of the evaporite-bearing Burns formation, Meridiani Planum, Mars. Earth Planet Sci Lett 240:95–121

McKnight D, Bencala KE (1988) Diel variations in iron chemistry in an acidic stream in the Colorado Rocky Mountains, USA. Arctic Alpine Res 20:492–500

McKnight DM, Kimball BA, Bencala KE (1988) Iron photo-reduction and oxidation in an acidic mountain stream. Science 240:637–640

McKnight DM, Kimball BA, Runkel RL (2001) The pH dependence of iron photo-reduction in a rocky mountain stream affected by acid mine drainage. Hydrol Proc 15:1979–1992

McKnight DM, Duren SM (2004) Biogeochemical processes controlling midday ferrous iron maxima in stream waters affected by acid rock drainage. Appl Geochem 19:1075–1084

McSween HY Jr (1999) Meteorites and their parent planets, Revised 2nd edn, Cambridge University Press, New York, pp 310

McSween HY Jr, Taylor GJ, Wyatt MB (2009) Elemental composition of the Martian Crust. Science 32:736–739

Milliken RE, Swayze GA, Arvidson RE, Bishop JL, Clark RN, Ehlmann BL, Green RO, Grotzinger JP, Morris RV, Murchie SL, Mustard JF, Weitz C (2008) Opaline silica in young deposits on Mars. Geology 36:847–50

Ming DW, Mittlefehldt DW, Morris RV, Golden DC, Gellert R, Yen A, Clark BC, Squyres SW, Farrand WH, Ruff SW, Arvidson RE, Klingelhofer G, McSween HY, Rodionov DS, Schröder C, de Souza PA, Wang A. (2006) Geochemical and mineralogical indicators for aqueous processes in the Columbia Hills of Gusev crater, Mars. J Geophys Res 111:E02S12, doi:10.1029/2005JE002560

Ming DW, Archer Jr PD, Glavin DP, Eigenbrode JL, Franz HB, Sutter B, Brunner AE, Stern JC, Freissinet C, McAdam AC, Mahaffy PR, Cabane M, Coll P, Campbell JL, Atreya SK, Niles PB, Bell III JF, Bish DL, Brinckerhoff WB, Buch A, Conrad PG, Des Marais DJ, Ehlmann BL, Fairén AG, Farley K, Flesch GJ, Francois P, Gellert R, Grant JA, Grotzinger JP, Gupta S, Herkenhoff KE, Hurowitz JA, Leshin LA, Lewis KW, McLennan SM, Miller KE, Moersch J, Morris RV, Navarro-González R, Pavlov AA, Perrett GM, Pradler I, Squyres SW, Summons RE, Steele A, Stolper EM, Sumner DY, Szopa C, Teinturier S, Trainer MG, Treiman AH, Vaniman DT, Vasavada AR, Webster CR, Wray JJ, Yingst RA, MSL Science Team (2013) Volatile and Organic Compositions of Sedimentary Rocks in Yellowknife Bay, Gale Crater, Mars. Science 343, doi:10.1126/science.1245267

Morris RV, Ming DW, Golden DC, Bell III JF (1996) An occurrence of jarosite tephra on Mauna Kea, Hawaii: Implications for the ferric mineralogy of the Martian surface. In MD Dyar, C McCammon, MW Schaefer (eds), Mineral Spectroscopy: a tribute to Roger G. Burns, The Geochemical Society, Special Publication 5:327–336

Morris RV, Klingelhöfer G, Schroeder C, Fleischer I, Ming DW, Yen AS, Gellert R, Arvidson RE, Rodionov DS, Crumpler LS, Clark BC, Cohen BA,

McCoy TJ, Mittlefehldt DW, Schmidt ME, de Souza PA, Jr. and Squyres SW (2008) Iron mineralogy and aqueous alteration from Husband Hill through Home Plate at Gusev Crater, Mars: Results from the Mössbauer instrument on the Spirit Mars Exploration Rover. J Geophys Research-Planets 113, E12S42.

Mustard JF, Poulet F, Gendrin A, Bibring J-P, Langevin Y, Gondet B, Mangold N, Bellucci G, Altieri F (2005) Olivine and pyroxene diversity in the crust of Mars. Science 307:1594–1597

Mustard JF, Murchie SL, Pelkey SM, Ehlmann BL, Milliken RE, Grant JA, Bibring J, Poulet F, Bishop J, Dobrea EN, Roach L, Seelos F, Arvidson RE, Wiseman S, Green R, Hash C, Humm D, Malaret E, McGovern JA, Seelos K, Clancy T, Clark R, Des Marais D, Izenberg N, Knudson A, Langevin Y, Martin T, McGuire P, Morris R, Robinson M, Roush T, Smith M, Swayze G, Taylor H, Titus T, Wolff M (2008) Hydrated silicate minerals on mars observed by the Mars reconnaissance orbiter CRISM instrument. Nature 454:305–309

Nesbitt HW, Young GM (1984) Prediction of some weathering trends of plutonic and volcanic rocks based on thermodynamic and kinetic considerations. Geochim Cosmochim Acta 48:1523–1534

Nesbitt HW, Wilson RE (1992) Recent chemical weathering of basalts. Am J Sci 292:740–777

Niles PB, Michalski J (2009) Meridiani Planum sediments on Mars formed through weathering in massive ice deposits. Nature Geosciesce 2:215–220

Nimick DA, Gammons CH, Parker SR (2011) Diel biogeochemical processes and their effect on the aqueous chemistry of streams: a review. Chem Geol 283:3–17

Nordstrom DK, Alpers CN, Ptacek CJ, Blowes DW (2000) Negative pH and extremely acidic mine waters from Iron Mountain, California. Environ Sci Technol 34:254–258

Oonk PBH (2013) Volcanic crater lake systems: a terrestrial analogue for the sulphate terrains on Mars. MSc thesis, Utrecht University, The Netherlands, pp 71

Ouimette AP (2000) Hydrothermal processes at an active volcano, Copahue, Argentina. M.A. Thesis, Wesleyan University, Middletown, CT, USA, pp 219

Papike JJ, Karner JM, Shearer CK (2006) Comparative planetary mineralogy: Implications of Martian and terrestrial jarosite: a crystal chemical perspective. Geochim Cosmochim Acta 70:1309–1321

Parker SR, Gammons CH, Pedrozo F, Wood SA (2008) Diel changes in metal concentrations in a geogenically acidic river: Río Agrio, Argentina. J Volcanol Geotherm Res 178:213–223

Parkhurst DL, Appelo CAJ (1999) User's guide to PHREEQC (Version 2)-A computer program for speciation, batch-reaction, one-dimensional transport, and inverse geochemical calculations. USGS Report 99–4259, pp 312

Pedrozo F, Kelly L, Diaz M, Temporetti P, Baffico G, Kringel R, Friese K, Mages M, Geller W, Woelfl S (2001) Water chemistry, plankton and trophic status of an Andean acidic lake of volcanic origin in Patagonia. Hydrobiologia 452:129–137

Pedrozo FL, Temporetti PF, Beamud G, Diaz MM (2008) Volcanic nutrient inputs and trophic state of Lake Caviahue, Patagonia, Argentina. J Volcan Geotherm Res 178:205–212

Pitzer KS, Mayorga G (1973) Thermodynamics of electrolytes. II. Activity and osmotic coefficients for strong electrolytes with one or both ions univalent. J Phys Chem 77:2300–2308

Poulet F, Bibring JP, Mustard JF, Gendrin A, Mangold N, Langevin Y, Arvidson RE, Gondet B, Gomez C, Berthé M, Erard S, Forni O, Manaud N, Poulleau G, Soufflot A, Combes M, Drossart P, Encrenaz T, Fouchet T, Melchiorri R, Bellucci G, Altieri F, Formisano V, Fonti S, Capaccioni F, Cerroni P, Coradini A, Korablev O, Kottsov V, Ignatiev N, Titov D, Zasova L, Pinet P, Schmitt B, Sotin C, Hauber E, Hoffmann H, Jaumann R, Keller U, Forget F, Team Omega (2005) Phyllosilicates on Mars and implications for early Martian climate. Nature 438:623–627

Regenspurg S, Peiffer S (2005) Arsenate and chromate incorporation in schwertmannite. Appl Geochem 20:1226–1239

Roach LH, Mustard JF, Murchie SL, Bibring J-P, Forget F, Lewis KW, Aharonson O, Vincendon M, Bishop JL (2009) Testing evidence of recent hydration state change in sulfates on Mars. J Geophys Res 114: E00D02, doi:10.1029/2008JE003245

Schroth AW, Parnell RA (2005) Trace metal retention through the schwertmannite to goethite transformation as observed in a field setting, Alta Mine, MT. Appl Geochem 20:907–917

Schwertmann U, Cornell RM (2000) Iron oxides in the laboratory. Preparation and characterisation, Wiley-VCH, Weinheim pp 188

Sherman DM (2005) Electronic structures of iron(III) and manganese(IV) (hydr)oxide minerals: thermodynamics of photochemical reductive dissolution in aquatic environments. Geochim Cosmochim Acta 69:3249–3255

Singer PC, Stumm W (1970) Acidic mine drainage: the rate-determining step. Science 167:1121–1123

Stefánsson A, Gislason SR, Arnórsson S (2001) Dissolution of primary minerals in natural waters—II mineral saturation state. Chem Geol 172:251–276

Stoffregen RE (1993) Stability relations of jarosite and natrojarosite at 150–250 °C. Geochim Cosmochim Acta 57:2417–2429

Stoffregen RE, Alpers CN, Jambor JL (2000) Alunite–jarosite crystallography, thermodynamics, and geochronology. In: Alpers CN, Jambor JL, Nordstrom DK (eds) Sulfate minerals: crystallography, geochemistry, and environmental significance. Mineralogical Society of America, Washington, DC, pp 453–479

Sullivan AB, Drever JI, McKnight DM (1998) Diel variation in element concentrations, Peru Creek,

Summit County, Colorado. J Geochem Explor 64:141–145

Symonds RB, Gerlach TM, Reed MH (2001) Magmatic gas scrubbing: implications for volcano monitoring. J Volcanol Geotherm Res 108:303–341

Tanaka KL, Skinner JA, Dohm JrJM, Irwin RPIII, Kolb EJ, Fortezzo CM, Platz T, Michael GG, Hare TM (2014) Geologic map of Mars: U.S. Geol Survey Scientific Investigations Map 3292, scale 1:20,000,000, pamphlet p 43, http://dx.doi.org/10.3133/sim3292

Tosca NJ, McLennan SM, Lindsley DH, Schoonen MAA (2004) Acid-sulfate weathering of synthetic Martian basalt: the acid fog model revisited. J Geophys Res-Planets 109:E5

Van Hinsberg V, Berlo K, Van Bergen M, Williams-Jones A (2010) Extreme alteration by hyperacidic brines at Kawah Ijen volcano, East Java, Indonesia: I. Textural and mineralogical imprint. J Volcanol Geotherm Res 198:253–263

Varekamp JC (2004) Copahue Volcano: A Modern Terrestrial Analogue for the Opportunity Landing Site? EOS 85(41):401–407

Varekamp JC (2008) The acidification of glacial Lake Caviahue, Province of Neuquen, Argentina. J Volcanol Geotherm Res, Special issue Volcanic Lakes and Environmental Impacts of Volcanic Fluids 178:184–196

Varekamp JC (2015) The chemical composition and evolution of volcanic lakes. In D Rouwet, B Christenson, F Tassi, J vandeMeulenbrouck, (eds) Volcanic Lakes, Springer-Verlag, Chapter 4, 93–124

Varekamp JC, Ouimette AP, Herman SW, Bermudez A, Delpino D (2001) Hydrothermal element fluxes from Copahue, Argentina: a beehive volcano in turmoil. Geology 29:1059–1062 Varekamp JC, Ouimette A, Kreulen R (2004) The magmato-hydrothermal system of Copahue volcano, Argentina. In: Proceedings of the 11th International Conference Water-Rock Interaction, WRI-11, vol 1, pp 215–218

Varekamp JC, de Moor MJ, Merrill M, Colvin A, Goss A, Vroon P, Hilton D (2006) The geochemistry and isotopic characteristics of the Caviahue Copahue volcanic complex, Province of Neuquen, Argentina. Geol Soc Am Special Paper 407:317–342

Varekamp JC, Ouimette AP, Herman SW, Flynn KS, Bermudez A. and Delpino D. (2009) Naturally acid waters from Copahue volcano, Argentina. Appl Geochem 24:1354–1354

Varekamp JC, Zareski JE, Camfield LM, Todd E (2015) Copahue volcano and its regional magmatic setting, this volume

Voelker B, Morel FMM, Sulzberger B (1997) Iron redox cycling in surface waters: effects of humic substances and light. Environ Sci Technol 30:1106–1114

Webster JG, Swedlund PJ, Webster KS (1998) Trace metal adsorption onto an acid mine drainage iron (III) oxyhydroxysulfate. Environ Sci Technol 32:1361–1368

Weitz CM, Milliken RE, Grant JA, McEwen AS, Williams RME, Bishop JL, Thompson BJ (2011) Mars Reconnaissance Orbiter observations of light-toned layered deposits and associated fluvial landforms on the plateaus adjacent to Valles Marineris. Icarus 205:73–105

Wolff-Boenisch D, Gíslason SR, Oelkers EH, Putnis CV (2004) The dissolution rates of natural glasses as a function of their composition at pH 4 and 10.6, and temperatures from 25 to 74 °C. Geochim Cosmochim Acta 63:4843–4858

Wray JJ, Milliken RE, Dundas CM, Swayze GA, Andrews-Hanna JC, Baldridge AM, Chojnacki M, Bishop JL, Ehlmann BL, Murchie SL, Clark RN, Seelos FP, Tornabene LL Squyres SW (2011). Columbus crater and other possible groundwater-fed paleolakes of Terra Sirenum, Mars. J Geophys Res 116:E01001

Wyatt MB, McSween HY, Tanaka KL, Head JW (2004) Global geologic context for rock types and surface alteration on Mars. Geology 32:645–648

Yu JY, Heo B, Choi IK, Cho JP, Chang HW (1999) Apparent solubilities of schwertmannite and ferrihydrite in natural stream water polluted by mine drainage. Geochim Cosmochim Acta 63:3407–3416

Ground Deformation Between 2002 and 2013 from InSAR Observations

M.L. Velez, P. Euillades, M. Blanco and L. Euillades

Abstract

Ground deformation is one of the main geophysical methods for volcano monitoring. Surface deformation patterns can provide important insights into the structure, plumbing system, and state of restless volcanoes. Copahue volcano is one of the most active eruptive centers in Argentina, and a major risk factor for the nearby towns of Caviahue and Copahue. Historic eruptive activity involved low intensity phreatic and phreatomagmatic events in 1992, 1995 and 2000. A new eruptive cycle is ongoing since June 2012, with several phreatic explosions and one phreatomagmatic—magmatic eruption on December 22nd, 2012. In this work, the Small Baseline Subsets (SBAS) DInSAR-based technique is successfully applied to compute surface displacements using the ENVISAT ASAR radar imagery during quiescent and pre-eruptive periods. Our purpose is to investigate possible sources of ground deformation to better understand the system behavior. Analytical models are used to interpret geodetic data and to constrain the parameters that characterize the source responsible for the observed deformation.

M.L. Velez (✉)
Departamento de Geología, Facultad de Ciencias Exactas, Instituto IDEAN UBA-CONICET, Universidad de Buenos Aires, Ciudad Universitaria, Buenos Aires, Argentina
e-mail: mlauravelez@gmail.com

P. Euillades · L. Euillades
Facultad de Ingeniería, Centro Universitario, CONICET and Instituto CEDIAC, Universidad Nacional de Cuyo, Ciudad Mendoza, Argentina

M. Blanco
Facultad de Ingeniería, Centro Universitario, Instituto CEDIAC, Universidad Nacional de Cuyo, Ciudad Mendoza, Argentina

8.1 Introduction

Several eruptive cycles have occurred at Copahue volcano during the last decades. Historical eruptions occurred in 1992, 1995 and 2000, and were characterized by moderate central vent explosive activity. The 2000 eruptive cycle is considered to be the most vigorous activity for the past hundred years and involved both ash and gas emissions (Caselli et al. this book). Copahue and Caviahue villages are located approximately 4 and 9 km
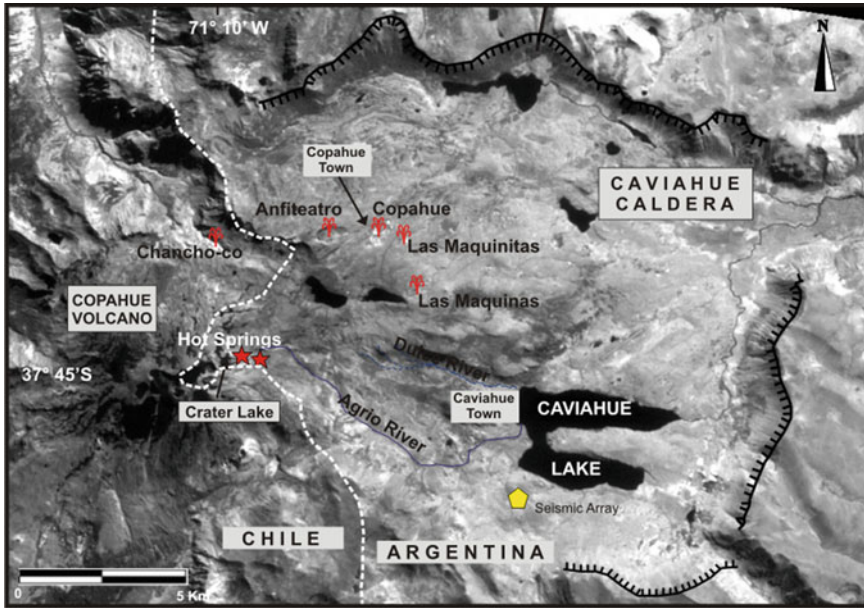
Fig. 8.1 Location map of the Caviahue–Copahue Volcanic Complex showing geothermal fields and seismic array

from the volcano crater, respectively (Fig. 8.1). The high vulnerability of these areas and the hazards imposed by the volcano enhance the importance of studying and monitoring this volcanic system. A new eruptive cycle began on July 2012 with several phreatic explosions and one phretomagmatic-magmatic eruption on December 22nd, and is still ongoing as of April 2013.

Ground deformation at active volcanic areas is a usual phenomenon and a consequence of the dynamic behavior of volcanic systems. In many cases, ground deformation may constitute a valuable eruptive precursor for early-warning systems (Sparks 2003; Vogfjörd et al. 2005). Usually uplift displacements are related to the migration of magmatic fluids before an eruptive process. Deflation typically occurs during or after eruptive events and may be associated with pressure release in the magma reservoir or the volcano hydrothermal system (e.g. Dzurisin 2006). Measuring and interpreting volcano-related deformation can be helpful to constrain the eruptive mechanisms, magma sources and ultimately the behavior of a volcanic system. However, the pattern of deformation prior to and/or during eruptions can be quite variable and complex in terms of magnitude, location and timing (e.g. Fournier et al. 2010).

Subtle ground deformation that might occur when magma accumulates or depressurizes near the brittle-ductile transition can be characterized by modern geodetic techniques. Traditional leveling provides sparse measurements at low temporal resolution depending on campaign frequency. Differential GPS and tilt-meters also provide sparse spatial measurements but high temporal resolution is achievable. DInSAR-based techniques do not require field access, except for validation purposes, and provide medium temporal resolution at very high spatial density. The last technique allows obtaining deformation fields that are of great importance for understanding the volcanic processes. A usual approach is to assume that displacements are produced by a magmatic source embedded in the crust at specific depth. The source is approximated by mathematical models representing simple geometries like pressure points, ellipsoidal cavities or dislocations to emulate the plumbing system. Key model parameters are estimated from inversion of the observed displacements (see Dzurisin 2006 and references therein).

This chapter presents a review of existing results for surface deformation and source modeling of Copahue volcano between 2002 and

2007 (Velez et al. 2011), and new results for the 2011–2012 period. DInSAR time series revealed a change in the deformation from subsidence during 2002–2007 to inflation in 2011–2012.

8.2 DInSAR Processing: Datasets and Results

8.2.1 Processing Algorithm

Differential SAR Interferometry (DInSAR) technique exploits phase information provided by Synthetic Aperture Radar (SAR) scenes acquired under strictly controlled conditions. Images acquired before and after a deformation event are combined to form a phase difference map, which, after topographic compensation via an external digital elevation model (DEM), is called differential interferogram. Differential interferometric phase is proportional to the Line of Sight (LOS) projection of the ground deformation accumulated during the time span between the scene acquisitions. Potential sources of noise affecting the DInSAR results are large spatial baselines between the two scenes, changes in the distribution of scatterers inside the resolution cell, non-compensated atmospheric phase contributions and DEM errors. The former two possibilities provoke noisy and potentially unusable interferograms and are quantified through the interferometric coherence coefficient (Zebker and Villasenor 1992). Atmospheric contribution and DEM errors do not introduce noise in the differential phase, but can generate phase components that may be confused with deformation (Massonnet and Feigl 1998). DInSAR has proven to be very useful for studying volcano deformation as it can detect small (<1 cm) surface displacements at high spatial resolution (e.g. Dzurisin and Lu 2006).

The well-known DInSAR-based SBAS algorithm (Berardino et al. 2002) was used for computing deformation time series. In this approach, $N + 1$ co-registered SAR scenes of the area of interest are combined to form a number M of interferograms that ranges between $(N + 1)/$

2 and $N*((N + 1)/2)$. In order to deal with decorrelation phenomena, interferograms corresponding to those combinations with short spatial and temporal baselines were created. The spatial baseline threshold value is usually set to about a third of the system's critical baseline, whereas the temporal baseline depends heavily on SAR wavelength and the physiographical characteristics of the studied area.

Subsequently, M differential interferograms are computed and unwrapped by using the minimum cost flow technique described by Costantini (1998). Considering a generic point located at the azimuth and range coordinates (a, r) the unwrapped differential phase of the j-th interferogram can be expressed as:

$$\delta\varphi_j(a,r) = \varphi(t_{m,j},a,r) - \varphi(t_{s,j},a,r) \atop \forall j = 1,\ldots,M \qquad (8.1)$$

where $t_{m,j}$ and $t_{s,j}$ refers to the acquisition time of the j-th inteferogram's master and slave images respectively. Note that $\varphi(t,a,r)$ represents the differential phase of the pixel located in (a, r) at time t measured with respect to an arbitrarily selected time origin that is common for all scenes. Equation (8.1) can be written for every point and interferogram, creating, for each pixel, a system of equations where the unknowns are the functions $\varphi(t_j,a,r)$. In vector notation:

$$A\varphi = \delta\Phi \qquad (8.2)$$

where A is an incident-like matrix already described in Berardino et al. (2002). By solving the system (8.2), a vector of unknowns $\varphi_i \forall i = 1,\ldots,N+1$ is obtained that can be used to compute the line of sight (LOS) displacements through the expression:

$$d_{LOS} = \frac{\lambda}{4\pi}\varphi \qquad (8.3)$$

It is convenient to write the system (8.2) in terms of phase velocity between adjacent acquisitions instead of phase change. Considering $v_i = (\varphi_{i+1} - \varphi_{i+1})/(t_{i+1} - t_{i+1}) \qquad \forall i = 0,\ldots,N-1$ then:

$$Bv = \delta\Phi \qquad (8.4)$$

where the vector φ is obtained after the integration of the phase velocities. This formulation gives robustness to the solution when baseline distribution generates two or more independent interferogram subsets (Berardino et al. 2002; Pepe et al. 2005).

In order to assess the retrieved solution's quality, the concept of temporal coherence, γ, as described in Tizzani et al. (2007) was used. Temporal coherence is calculated on a pixel by pixel basis using the following expression:

$$\gamma = \frac{\left|\sum_{k=1}^{M} \exp\left[j\left(\delta\varphi_k^{wrap} - \delta\bar{\varphi}_k\right)\right]\right|}{M}, 0 \leq \gamma \leq 1 \qquad (8.5)$$

where $\delta\varphi_k^{wrap}$ is the kth original wrapped interferogram and $\delta\varphi_k$ is the wrapped phase reconstructed from the estimated results. When $\gamma \to 1$ the original phase can be almost perfectly reconstructed from the results. Using (8.5), the pixels where the temporal coherence is greater than a threshold high enough for ensuring the reliability of the results (typical values are higher than 0.8 and depends on the overall coherence of the processed area) were accepted.

Finally, atmospheric contribution is estimated providing that it is well correlated spatially but poorly in time (Hanssen 2001). The correction for atmospheric artifacts is implemented through a cascade of low pass filtering (spatial) followed by a high pass temporal filtering (Tizzani et al. 2007).

8.2.2   Dataset

The complete dataset comprises 67 ENVISAT ASAR radar images divided into two datasets acquired between December 2002 and April 2012 (Table 8.1). The first dataset (December 2002—December 2007) consists of 54 images acquired in ascending (32 scenes) and descending (26 scenes) passes (Velez et al. 2011). Acquisition mode is IS2 (23° look-angle) in all cases. The second dataset contains 13 images acquired in descending passes between April 2011 and April 2012 in mode I6 (40º look angle).

The second dataset was acquired during the ENVISAT Phase E3 which began in October 2010 and lasted until April 2012. During this phase a new orbit control strategy was applied for extending the satellite's lifetime that sacrificed inclination drift compensation in favor of enforcing attitude stability. As a consequence, DInSAR performance/capabilities were degraded compared with the E1 and E2 phases. Inclination angle diminished constantly making perpendicular baselines greater in successive cycles and leading to increasing geometrical decorrelation between images further apart in time. However, baselines were held at a minimum value in two predefined points: latitude 38ºN for descending pass and latitude 38ºS for ascending pass (Miranda et al. 2010). Copahue volcano's location is well within the valid DInSAR latitude bands for Phase E3.

The main problem for DInSAR processing in the Copahue region, and the volcano edifice in particular is winter snowfall, which causes almost complete temporal decorrelation. The snow season typically lasts from June to November but the date of first snowfall as well as the duration and percentage of soil coverage are highly variable from year to year. Snow coverage using archived optical images before discarding scenes were checked. Table 8.1 lists the employed and discarded scenes.

Additionally, two COSMO-Skymed scenes from December 2011 and March 2013, for evaluating surface deformation during the entire 2012 eruptive period, were employed.

8.3   Results

According to Velez et al. (2011), the first dataset (2002–2007) allowed the construction of 72 interferograms, 43 ascending (Table 8.2) and 29 descending (Table 8.3), using SBAS constraints on both spatial and temporal baselines (300 m

Table 8.1 List of scenes used for SBAS processing

	Orbit	Day	Month	Year
Track 239 swath I2 descending	4301	26	December	2002
	5303	6	March	2003
	5804	10	April	2003
	6806[a]	19	June	2003
	7307[a]	24	July	2003
	7808[a]	28	August	2003
	8309	2	October	2003
	8810	6	November	2003
	9812	15	January	2004
	10,814	25	March	2004
	11,315	29	April	2004
	11,816	3	June	2004
	14,321	25	November	2004
	14,822	30	December	2004
	15,323	3	February	2005
	16,826[a]	19	May	2005
	17,327[a]	23	June	2005
	17,828[a]	28	July	2005
	18,329[a]	1	September	2005
	18,830[a]	6	October	2005
	22,337[a]	8	June	2006
	25,343	4	January	2007
	26,846	19	April	2007
Track 261 swath I2 ascending	4323	28	December	2002
	5325	8	March	2003
	5826	12	April	2003
	6828[a]	21	June	2003
	7329[a]	26	July	2003
	8331[a]	4	October	2003
	8832	8	November	2003
	9333	13	December	2003
	9834	17	January	2004
	11,337	1	May	2004
	11,838[a]	5	June	2004
	12,840[a]	14	August	2004
	13,341[a]	18	September	2004
	13,842[a]	23	October	2004
	14,343	27	November	2004
	15,345	5	February	2005
	15,846	12	March	2005

(continued)

Table 8.1 (continued)

	21	May	2005
17,850[a]	30	July	2005
18,351[a]	3	September	2005
18,852[a]	8	October	2005
19,353[a]	12	November	2005
19,854	17	December	2005
20,355	21	January	2006
20,856	25	February	2006
21,357	1	April	2006
22,359[a]	10	June	2006
22,860[a]	15	July	2006
23,862[a]	23	September	2006
29,373	13	October	2007
29,874	17	November	2007
Track 219 swath I6 ascending	46,785	10	February	2011
47,216	12	March	2011
47,647	11	April	2011
48,078	11	May	2011
48,940	10	July	2011
49,371	9	August	2011
50,233[a]	8	October	2011
50,664	7	November	2011
51,095	7	December	2011
51,526	6	January	2012
51,957	5	February	2012
52,388	6	March	2012
52,819	5	April	2012

[a]in the orbit field mark discarded scenes due to snowfall

and 1500 days) on each data pair. Furthermore, precise orbital information and a Shuttle Radar Topography Mission (SRTM) DEM were used to compensate for the effect of topography. Interferograms with an elliptical deformation signal centered in the volcano edifice are shown in Fig. 8.2. Deformation time series and mean velocity deformation maps were calculated following a complex multilook operation with 4 looks in range and 20 in azimuth, giving a ground projected pixel area of approximately 100 × 100 m.

The second dataset (2011–2012) allowed the construction of 66 interferograms (Table 8.4), some of which were depict in Fig. 8.3. Since the critical baseline is much longer than for the first dataset, due to a higher look angle, the interfering pairs using a 700 m long spatial baseline were constrained. The longest baseline, 522 m was well below this limit (Table 8.4). The temporal baseline length is irrelevant because the time span between the first and last scene is only 420 days. Multilooking factors were the same as for the first dataset, but the resulting pixel

Table 8.2 List of interferograms. Track 261, swath I2, ascending, 2002–2007

#	Master_slave [ddmmyyyy]	Bperp [m]	Btemp [days]
0	28122002_17012004	0.47	385
1	28122002_05022005	234	770
2	28122002_27112004	218	700
3	28122002_17122005	260	1085
4	28122002_25022006	171	1155
5	08032003_05022005	88	700
6	08032003_13122003	242	280
7	08032003_01052004	118	420
8	08032003_21022004	295	350
9	08032003_25022006	152	1085
10	12042003_12112005	59	945
11	12042003_27112004	288	595
12	12042003_12032005	11	700
13	12042003_17122005	246	980
14	08112003_21012006	85	804
15	08112003_21022004	212	105
16	08112003_13122003	265	35
17	08112003_01042006	33	874
18	13122003_01052004	124	139
19	13122003_21022004	53	69
20	13122003_01042006	298	839
21	17012004_05022005	235	385
22	17012004_25022006	171	769
23	17012004_13102007	115	1365
24	17012004_27112004	217	315
25	17012004_17122005	260	699
26	21022004_01042006	245	769
27	21022004_01052004	177	70
28	21022004_21012006	297	699
29	01052004_05022005	207	280
30	01052004_25022006	270	664
31	27112004_17122005	42	384
32	27112004_12032005	276	104
33	27112004_17112007	167	1084
34	05022005_25022006	63	384
35	05022005_13102007	120	979
36	12032005_12112005	71	245
37	12032005_17112007	109	979
38	12032005_17122005	234	279

(continued)

Table 8.2 (continued)

39	12112005_17112007	180	734
40	17122005_17112007	124	699
41	21012006_01042006	51	69
42	25022006_13102007	56	595

Table 8.3 List of interferograms. Track 239, swath I2, descending, 2002–2007

#	Master_slave [ddmmyyy]	Bperp [m]	Btemp [days]
0	26122002_03062004	239	525
1	26122002_25032004	106	455
2	06032003_06112003	92	245
3	06032003_25112004	10	630
4	06032003_10042003	52	35
5	06032003_29042004	168	420
6	06032003_06022005	106	700
7	10042003_25112004	41	595
8	10042003_06112003	145	210
9	10042003_06022005	220	385
10	10042003_03022005	158	665
11	02102003_30122004	54	454
12	02102003_04012007	294	1189
13	06112003_25112004	103	385
14	06112003_03022005	13	455
15	06112003_29042004	75	175
16	06112003_25032004	281	140
17	06112003_19042007	207	1260
18	15012004_04012007	27	1085
19	15012004_30122004	267	349
20	25032004_29042004	205	34
21	25032004_19042007	73	1119
22	25032004_03022005	267	314
23	29042004_19042007	131	1085
24	29042004_03022005	62	280
25	29042004_25112004	179	210
26	25112004_03022005	116	69
27	30122004_04012007	240	735
28	03022005_19042007	194	804

resolution was 40 × 100 m. Temporal coherence for both datasets is shown in Fig. 8.4.

The 2002–2007 interferograms show an oval-shaped area of deflation partially coincident with the volcano edifice but also extending northeastward over the geothermal fields (Fig. 8.1). The semi-major axis is 7.5 km long and strikes NE, and semi-minor axis is 3.25 km long and strikes NW. Mean deformation velocities estimated using the ascending and
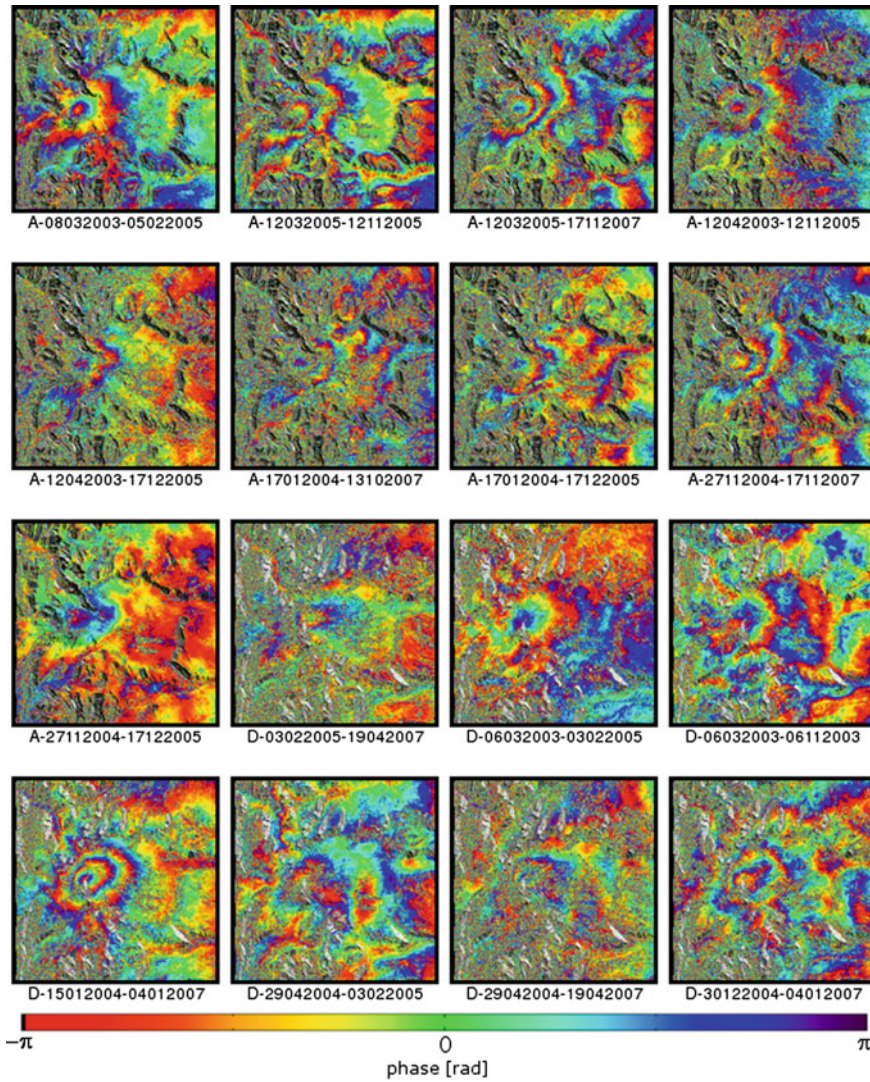
Fig. 8.2 Differential interferograms from ascending and descending pass 2002–2007. Dates are expressed as DDMMYYY. Deflation pattern is clearly appreciable in A-12032005-17112007 and D-15012004-04012007

descending acquisitions provide an overall picture of the deformation (Fig. 8.5). They have been calibrated with respect to a reference pixel (identified by the red square) that is located on the northern sector of the Caviahue caldera. The deformation time series (Fig. 8.6) indicate that the displacement rate remained nearly constant from March 2004 until December 2007. The maximum mean LOS deformation velocity,

approximately −2 cm/year, occurs near the volcano's summit, dropping to about −0.5 cm/year at Copahue village located at roughly 7.2 km to the northeast. The subsidence pattern is not observed at Caviahue village, located about 10 km east of the volcano summit.

The availability of SAR data acquired from ascending and descending orbits allows us to retrieve the east–west and vertical displacement

Table 8.4 List of interferograms. Track219, swathI6, ascending, 2011–2012

#	Master_Slave [ddmmyyy]	Bperp [m]	Btemp [days]
0	10022011_11042011	296	60
1	10022011_11052011	6	90
2	10022011_06032012	140	390
3	10022011_12032011	153	30
4	10022011_10072011	262	150
5	10022011_08102011	38	240
6	10022011_07112011	81	270
7	10022011_07122011	382	300
8	10022011_06012012	4	330
9	10022011_05022012	132	360
10	10022011_05042012	124	420
11	12032011_07112011	72	240
12	12032011_08102011	115	210
13	12032011_10072011	109	120
14	12032011_05022012	21	330
15	12032011_11042011	142	30
16	12032011_11052011	160	60
17	12032011_07122011	228	270
18	12032011_06012012	149	300
19	12032011_06032012	294	360
20	12032011_05042012	29	390
21	11042011_07122011	85	240
22	11042011_10072011	33	90
23	11042011_11052011	302	30
24	11042011_08102011	258	180
25	11042011_07112011	215	210
26	11042011_06012012	291	270
27	11042011_05022012	164	300
28	11042011_06032012	437	330
29	11042011_05042012	171	360
30	11052011_06012012	10	240
31	11052011_06032012	134	300
32	11052011_08102011	44	150
33	11052011_10072011	269	60
34	11052011_07112011	87	180
35	11052011_07122011	388	210
36	11052011_05022012	138	270
37	11052011_05042012	130	330
38	10072011_05022012	130	210
39	10072011_07122011	119	150

(continued)

Table 8.4 (continued)

40	10072011_08102011	224	90
41	10072011_07112011	181	120
42	10072011_06012012	258	180
43	10072011_06032012	403	240
44	10072011_05042012	138	270
45	08102011_06012012	33	90
46	08102011_07112011	43	30
47	08102011_07122011	343	60
48	08102011_05022012	94	120
49	08102011_06032012	178	150
50	08102011_05042012	86	180
51	07112011_05022012	50	90
52	07112011_05042012	43	150
53	07112011_06012012	76	60
54	07112011_07122011	300	30
55	07112011_06032012	221	120
56	07122011_05022012	249	60
57	07122011_05042012	257	120
58	07122011_06012012	377	30
59	07122011_06032012	522	90
60	06012012_06032012	145	60
61	06012012_05042012	119	90
62	06012012_05022012	127	30
63	05022012_05042012	7	60
64	05042012_06032012	272	30
65	06032012_05042012	265	30

components. According to Lungdren et al. (2004) and Borgia et al. (2005), the difference between ascending and descending velocity maps over common coherent pixels cancels the vertical and north velocity vectors and shows the east-west component of the surface velocity of deformation only (Fig. 8.7). However, adding velocity maps from both passes allows us to retrieve the vertical component (Fig. 8.7). This simple calculation is valid because both the ascending and descending pass look angles are equal. However, it gives only the direction of displacement but not the magnitude, which can be calculated by applying a calibration factor that considers the acquisition geometry. In our case, the sum-and-difference methodology allowed us to confirm the nature of the observed deformation, i.e. a deflation bowl.

$$
\begin{aligned}
d_{E-O} &\approx \frac{(d_{LOS\_Desc} - d_{LOS\_Asc})/2}{\sin\theta} \\
d_V &\approx \frac{(d_{LOS\_Desc} + d_{LOS\_Asc})/2}{\cos\theta}
\end{aligned}
\tag{8.6}
$$

Figure 8.8 (left) shows the mean velocity of deformation from 2011–2012, which peaks near the volcano's summit as it did during the prior deflation, being the signal noisier than the one obtained in the 2002–2008 period. This may be a consequence of approximating the time series' non-linear behavior (see Fig. 8.9) with a linear trend like the deformation rate. Inflation of 5 cm
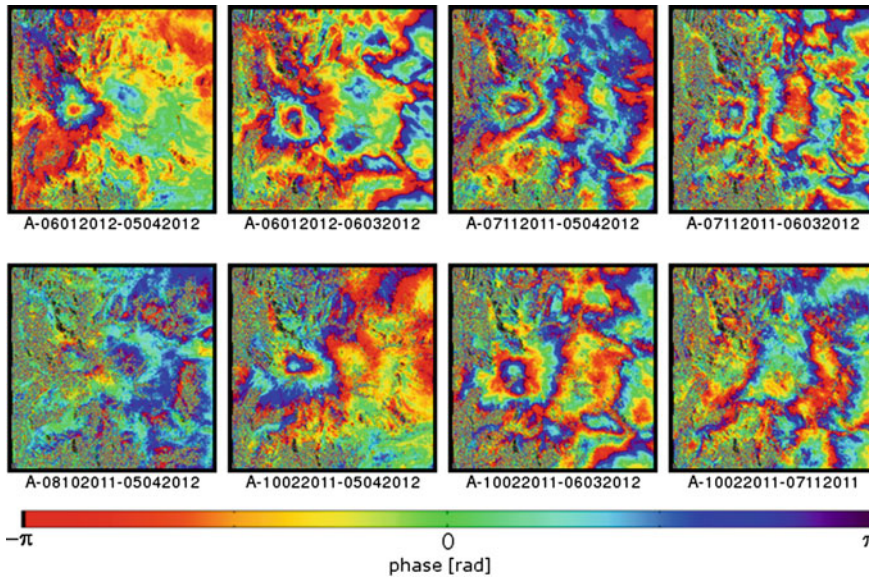
Fig. 8.3 Differential interferograms from 2011–2012 ascending pass scenes. Inflation pattern centered in the northern flank of Copahue is visible although somewhat obscured by atmospheric noise
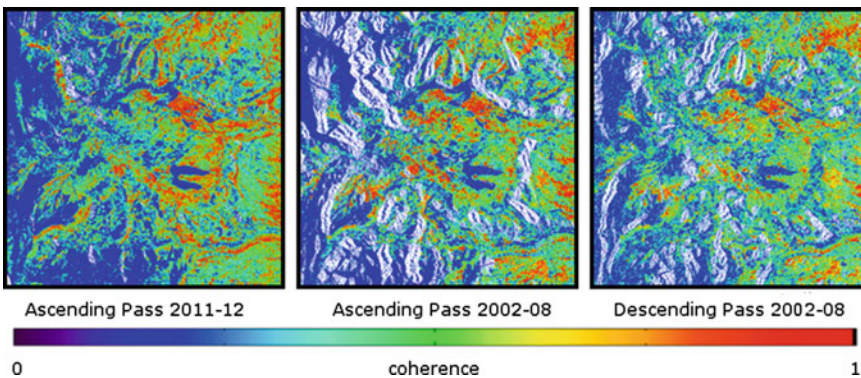
Fig. 8.4 Temporal coherence computed for the SBAS elaborations. Color scale ranges from *purple* (complete decorrelation) to *red* (no decorrelation). *White* areas are layover zones where the spatial resolution is severely diminished. Low coherence values are coincident with snow-covered areas. Note how the results from swath I6 (ascending pass 2011–2012) present less layover due to higher look angle

in 6 months is observed from October, 2011 until the end of available data, April, 2012, so computing the deformation velocity from only this period gives a clearer picture of the pattern (Fig. 8.8 right). Since the scenes between May 2011 and October 2011 were missing, a detailed description of the inflation behavior's initial stage was not provided, but the interferogram computed from CSK scenes acquired in December 29th 2011 and January 20th 2013 show that by the last date it accumulated 17 cm of deformation (Fig. 8.10).

8.3.1 Modeling Surface Deformation

Models provide the linkage between observed deformation and the inaccessible deformation source. Simplified analytical models are widely
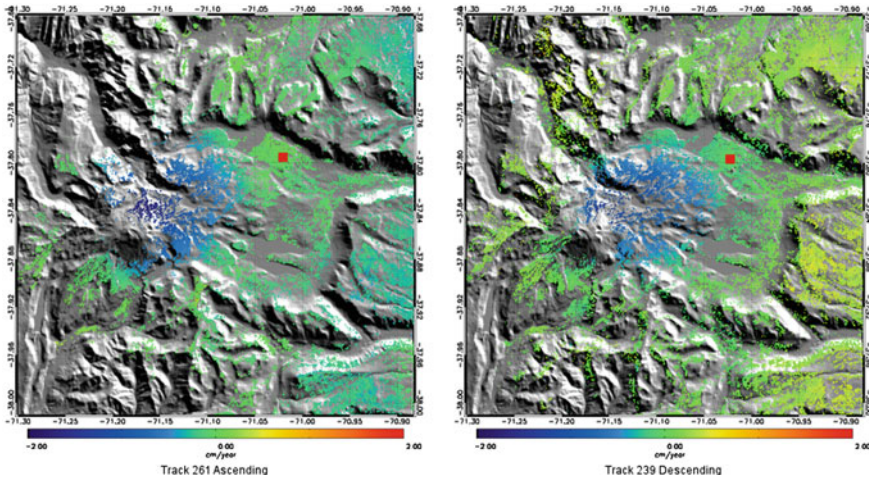
Fig. 8.5 Mean deformation velocity map computed from 2002–2007 ascending (*left*) and descending (*right*) pass scenes. *Red squares* show the location of the reference pixel where deformation is considered zero
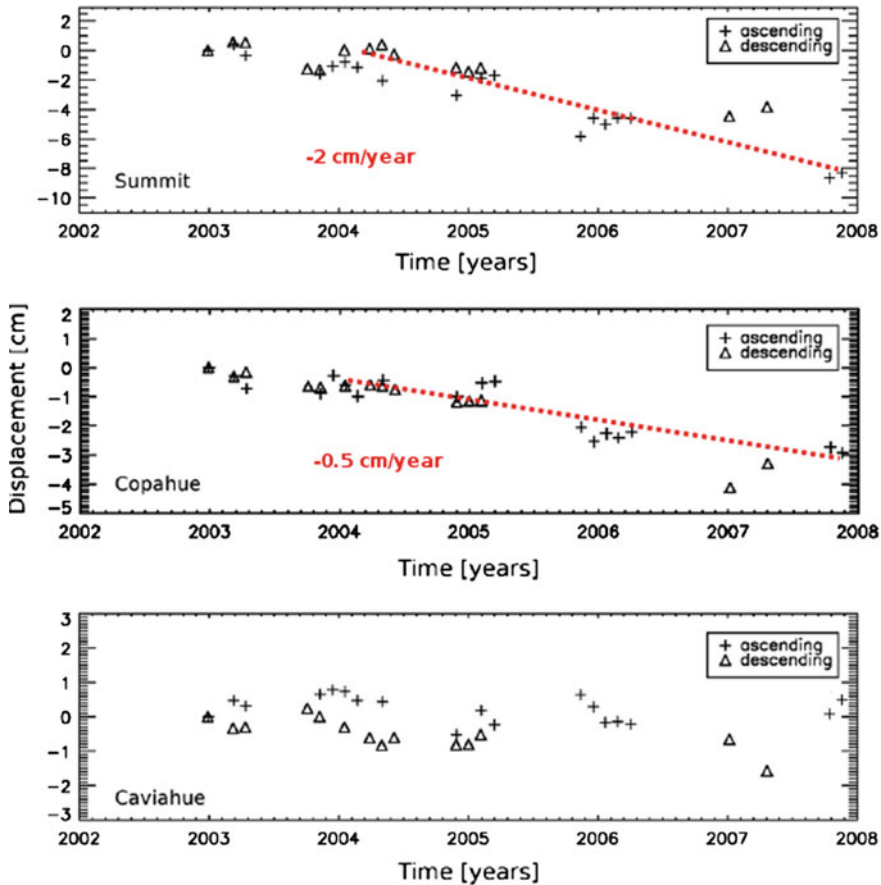
Fig. 8.6 2002–2007 deformation time series extracted at three significant points: (1) Summit, i.e. maximum deformation area, (2) Copahue geothermal field and (3) Caviahue, where no volcanic-related deformation is observed. Deflation evolution shows a linear constant trend of −2 cm/year at the summit. In the Caviahue series the seasonal pattern could be related to groundwater level change in the vicinity of Caviahue lake
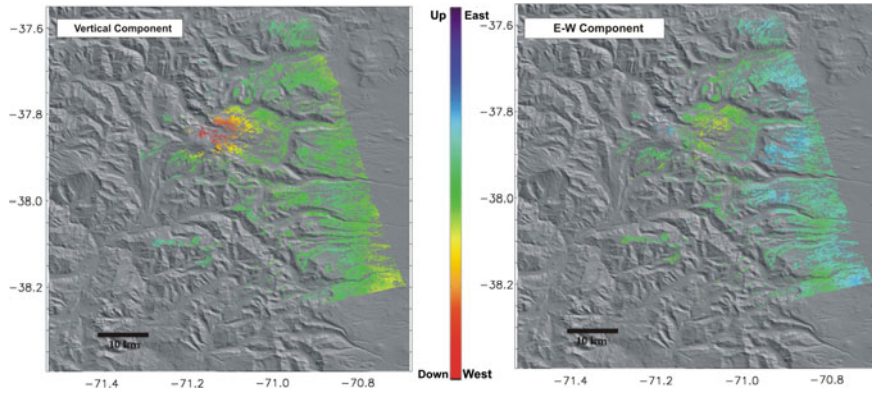
Fig. 8.7 2002–2007 mean velocity components: east–west and vertical projections, modified from (Velez et al. 2011)
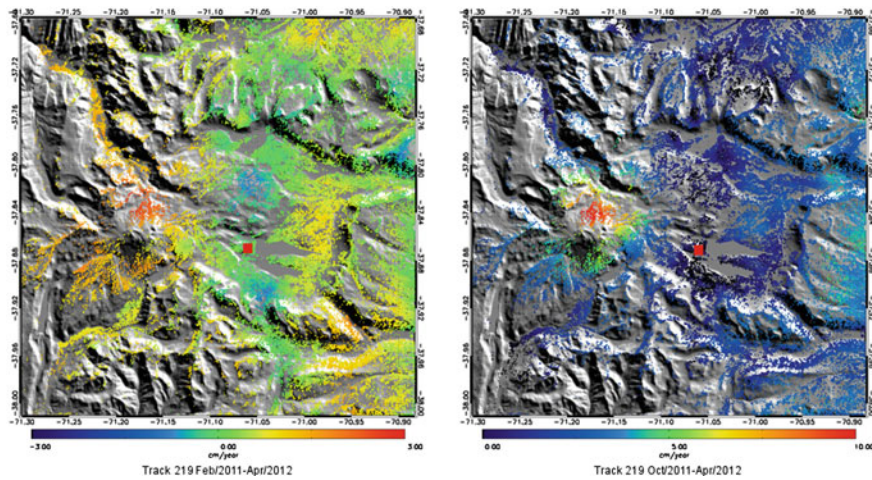
Fig. 8.8 Mean deformation velocity maps computed from February 2011–April 2012 period (*left*), and from October 2011–April 2012 (*right*). *Red squares* show the location of the reference pixel. Mean velocity computed considering the whole period (*left*) is affected by non-linearity of the time series (see Fig. 8.9) and appears contaminated by atmospheric fringes. Computing the mean velocity from October 2011 allows capturing an almost linear inflation trend still on-going in April 2012
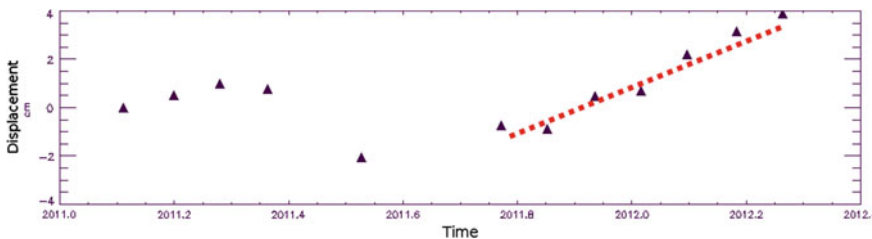
Fig. 8.9 Deformation time series computed from 2011–2012 ascending pass scenes. At the Copahue summit., *Red trend line mark* the inflation process beginning between July 2011 and October 2011
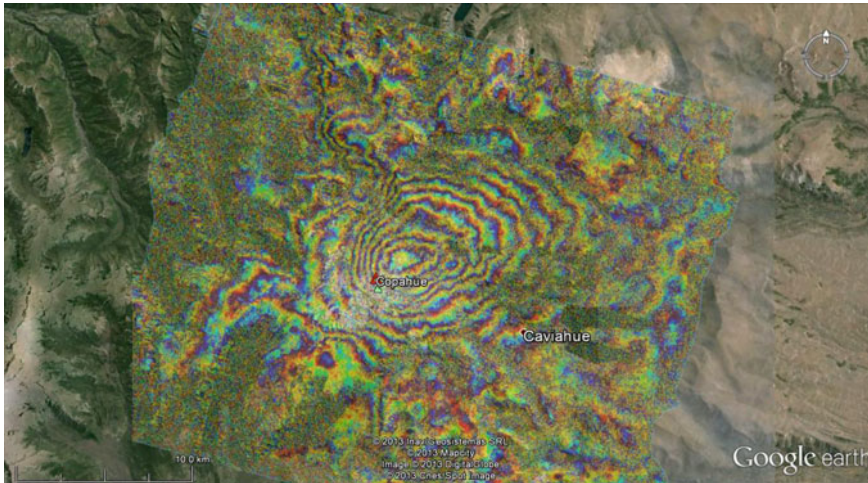
Fig. 8.10 Interferogram from December 29th 2011 to January 20th 2013

used for studying volcanoes around the world, and can provide rough estimates of important parameters related to the behavior of volcanic systems. However, several simplifications and assumptions could affect the results and must be considered. Mechanical heterogeneities and topographic effects usually affect the pattern and magnitude of ground deformation, and could produce some erroneous estimation of magma chamber depth and volume change (Manconi et al. 2007). In addition, using only one deformation component, a common situation when DInSAR data are available, can result in a weak constrain of source dimensions and geometry (Dieterich and Decker 1975).

More realistic and complex results can be obtained by using numerical techniques that account for the effect of topography and medium heterogeneities. However, increasing the number of parameters in absence of detailed knowledge of the medium's geophysical properties can produce poorly constrained and/or inconsistent results.

8.3.2 Direct Modeling

A range of simple analytical sources for approximating the pressurized reservoir was explored.

Sources are embedded in an elastic homogeneous Poissonian flat half-space ($v = 0.25$, i.e. $\lambda = G$) with a rigidity modulus G estimated in 30 GPa. First, a point pressure source or Mogi source (Mogi 1958) was tested, which is a simple analytical solution but has successfully reproduced the vertical deformation pattern of many uplifting and/or subsiding volcanic areas. This dilatation source is characterized by four parameters: horizontal location (easting x, northing y), depth d, and strength s. Assuming that the source radius (α) is small compared with the depth, the strength can be computed in terms of a change in pressure or volume as:

$$s = \Delta P(1 - v)\alpha^3/G \quad s = \Delta V \frac{(1 - v)(1 + v)}{2\pi(1 - 2v)} \quad (8.7)$$

where v is Poisson's ratio and expansion is positive (Masterlark 2007, and references therein). In the Mogi source approximation the radius of the source cannot be separated from the pressure change (ΔP), and there is also a limiting α/d condition meaning that the solution becomes less accurate as this ratio increases. McTigue (1987) provides an analytical solution that includes higher-order terms taking into account the finite shape of a spherical body. Pressure variation in a spherical cavity produces a change $\Delta\alpha$ in its radius.

It can be expressed as $\Delta\alpha = \frac{1}{4}\Delta P/G\alpha$. Volume change resulting from $\Delta\alpha$ is $\Delta V \approx \Delta P/G\pi\alpha^3$ (McTigue 1987). Other geometries were also modeled, including a prolate spheroidal source (Yang et al. 1988) and a dislocation (Okada 1985). The spheroidal source is an arbitrarily oriented cavity of finite dimensions characterized by its semi-major and semi-minor axis, depth, dip angle, azimuth angle of the major axis, location x-y, and pressure change (ΔP). The volume change (ΔV) caused by a pressure change in the ellipsoidal cavity is usually estimated by $\Delta V \approx (\Delta P/G)*\pi ab^2$, according to Tiampo et al. (2000), where **a** is the semi-major axis and **b** is the semi-minor axis of the ellipse. However, according to Amoruso and Crescentini (2009) this equation always underestimate the volume change, instead a correct empirical formula available in Battaglia et al. (2013) was tested: $\Delta V = V.(\Delta P/G).(A^2/3 + 0.7A + 1.37)$ where A is the aspect ratio Finally, a finite rectangular dislocation sources characterized by length L, width w, dip angle δ, depth d, strike slip ($U1$), dip slip ($U2$) and tensional opening ($U3$), was tested. The case for tensile faults only ($U3 \neq 0$ and $U1 = U2 = 0$) was considered, since this is usually the most relevant in volcanic areas. The volume change estimated for a dislocation surface considering only uniform opening is given by $\Delta V = U3.w.L$.

8.3.3 Inversion Method

Given a source model (point source, cavity, dislocation), the inverse methods search for a set of parameters that minimize the misfit between the model and the data in a L2 norm sense. Considering that the problem is non-linear and characterized by several parameters, solving it requires sophisticated techniques (Snieder and Trampert 2010). Methods usually applied consist of algorithms with a random component like genetic algorithms or simulated annealing. A genetic algorithm (GA) was employed as a probabilistic, global optimization method. It is based on rules defined by the laws of evolutionary genetics (Holland 1975; Goldberg 1989), i.e. reproduction, natural selection and diversity of the species.

GA starts with a set of randomly selected potential solutions, called individuals, that comprise an initial population. It must represent the entire range of possible solutions sampled according to a uniform distribution. To achieve this, and considering that the initial population is generated by pseudo random numbers, the number of individuals must be high. Parameter independency was tested by using a correlation coefficient and running test for uniform random distribution.

Each individual represents a set of model parameters. N deformation fields are computed by using the governing equations of the selected source and the model parameters represented by each individual. They are then compared with the deformation data provided by the DInSAR results using a fitness function. In our case, the fitness function (F) for the j-th individual is:

$$F_j = \sqrt{\frac{\sum_{i=0}^{M}(Um_i - Ud_i)}{M}} \quad \forall j = 1 \ldots N \quad (8.8)$$

where Um_i and Ud_i are the i-th modeled and DInSAR observation points respectively. M represents the number of observations and N the number of individuals.

In the next step, individuals are assigned with a probability P_j computed from the fitness function as:

$$P_j = \frac{F_j}{\sum_{j=1}^{N} F_j} \quad (8.9)$$

The next generation's population is constructed as follows: (1) a number of individuals are selected by the montecarlo method (Holland 1975) according to its probability Pj for preserving the better information; (2) single point crossover operation over the selected individuals occurs for optimizing the new individual and (3) mutation occurs for maintaining genetic diversity. In the present case, 0.6 and 0.05 as

crossover and mutation factors, respectively, was used. This procedure was repeated through a large number of generations until the best solution is obtained according to a given convergence criteria. In this case, the employed criterion is: $|F_j - F_{j-1}| < 1 \times 10^{-6}$ for 50 consecutive generations.

8.4   Modeling Results

8.4.1   Subsidence 2002–2007

The mean deformation velocity (LOS) computed from the SBAS processing of the 2002–2007 ascending dataset, already described in Sect. 8.2, was used to estimate the source parameters by inverting 12,910 data points. The best fit results suggest that source is a deflating oblate ellipsoid, located at approximately 4 km depth beneath the volcano edifice. The volume change caused by pressure variation in the ellipsoidal cavity is 0.0013 km^3/year (Velez et al. 2011). Residuals between measured (DInSAR) and modeled displacements are shown in Fig. 8.11. Similar results were obtained by Fournier et al. (2010)

from an inversion of two ALOS interferograms.

This ellipsoidal source is probably related with the oscillating brittle– plastic boundary beneath the volcano, where leakages of brines and steam take place, producing a depressurization of the system (Velez et al. 2011). These results are consistent with the variations observed in thermometry and geochemical contents of the crater lake waters and springs (Agusto et al. 2012). Anomalous seismicity was also registered as increased volcano tectonic signals, including a seismic swarm on January 2004 (Ibañez et al. 2008).

8.4.2   Pre-eruptive Deformation 2011–2012

Mean deformation velocity (LOS) computed from the SBAS processing of 2011–2012, already described in Sect. 8.2, was used for estimating source parameters through inversion of 33,507 data points. The velocity computed for the period between October 2011 and April 2012 was considered, already shown in Fig. 8.8 (right).

Three different sources were tested: (1) a point source, (2) a finite ellipsoidal source and (3) a finite horizontal rectangular dislocation. Volume change was estimated over the 6 month period.
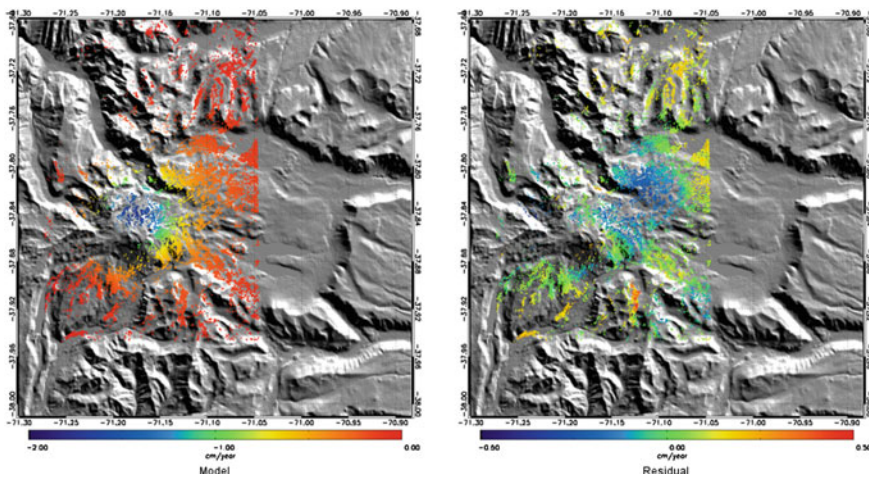
Fig. 8.11 Model (*left*) and residuals (*right*) for ellipsoidal cavity inversion for the 2002–2007 period
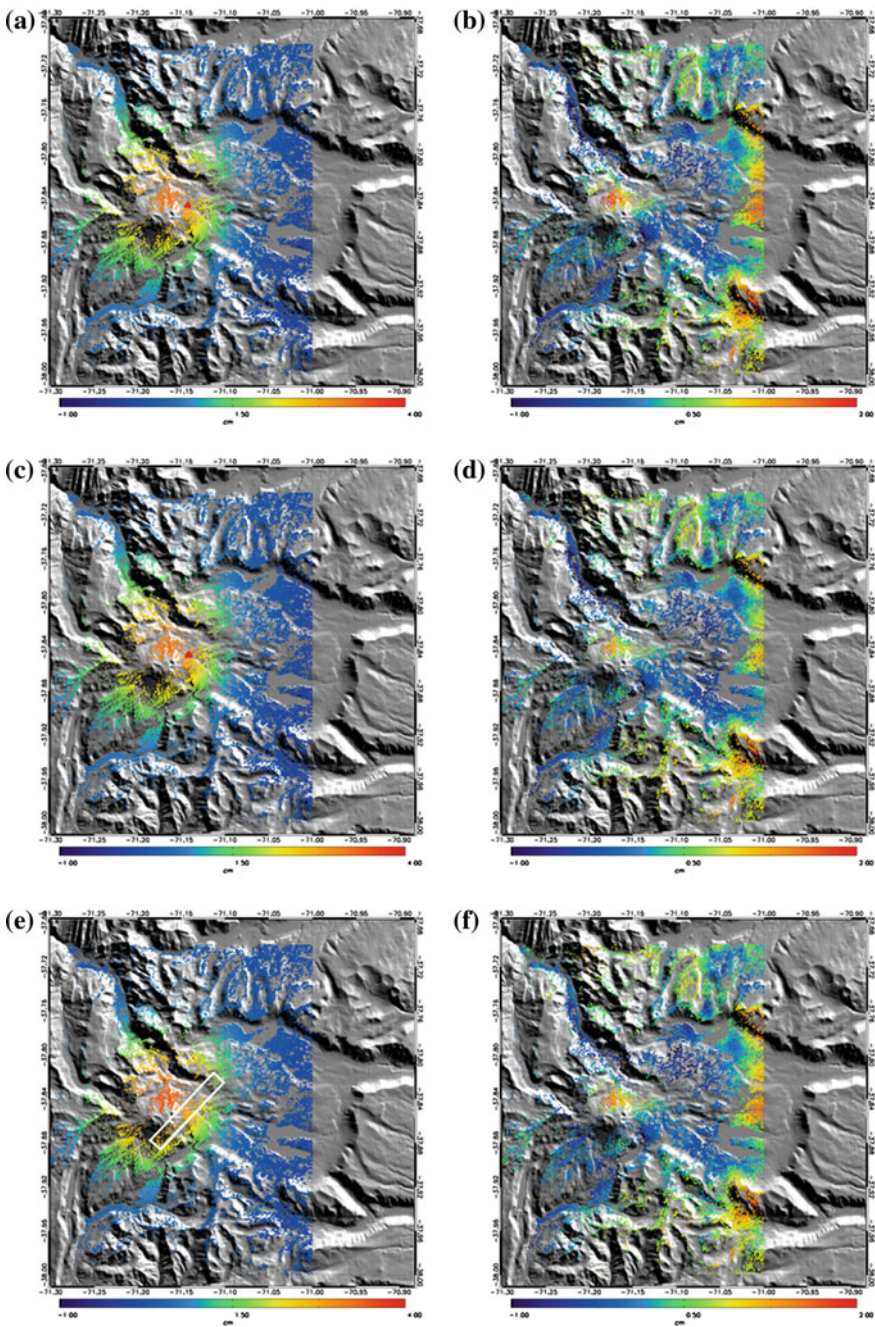
Fig. 8.12 Models (*left*) and residuals (*right*) for (**a**, **b**) point pressure source inversion (**c**, **d**) ellipsoidal cavity inversion and (**e**, **f**) finite horizontal rectangular dislocation inversion for the October 2011–April 2012 period. *Red triangles mark* the source center location. *White rectangle* is the surface projection of the dislocation source

Modeled displacements and residuals are shown on Fig. 8.12. Best fit parameters obtained for a point source are: latitude 37.85°S, longitude 71.15°W, depth 8000 m and volume change estimated at about 0.01 km^3 (Fig. 8.12a). However, when results are compared to measured data, significant residuals remain (Fig. 8.12b). Although this spherical expansion source is intended to simulate the change in storage of a magma caused by a magmatic input, it produces circular deformation patterns that are inconsistent with the oval-shaped observation.

The best fit solution for the ellipsoidal source is a nearly horizontal prolate geometry located at latitude 37.85°S, longitude 71.14°W and 7580 m depth. The semi-major axis is about 1.1 km long (strike 87.4°E, dip 5°) and semi-minor axis is 210.9 m long. Pressure change versus rigidity modulus ($\Delta P/G$) equals to 0.05 and volume change is estimated at 0.015 km^3 (Fig. 8.12c). This source performs slightly better than the point source in representing the observed deformation according to the residuals shown in Fig. 8.12d and Table 8.5.

The best fit solution for the horizontal dislocation is a 9.3 km long by 1.4 km width rectangular sill, striking N43.5°E, located at 9 km depth, with a uniform opening of 0.75 m (Fig. 8.12e). Volume change is estimated in 0.009 km^3. The residuals shown in Fig. 8.12f and Table 8.5 are on the same order of magnitude than those obtained with the ellipsoidal cavity.

Both sill geometries (ellipsoidal cavity and finite rectangular dislocation) show a positive localized residue located in the volcano northern flank. For accommodating this feature, a conduit represented by a prolate inclined ellipsoid with high aspect ratio (Bonaccorso and Davis 1999) was added. Best fit solution was obtained using a source with a semi-major axis of 1.1 km inclined 40°, a semi-minor axis of 46.4 m, and located beneath the volcano edifice at ∼2 km depth. Model results and residuals are shown in Fig. 8.13 and Table 8.5. A schematic diagram considering the chamber-conduit system is shown in Fig. 8.14.

Parameter sets obtained by using different model types are summarized in Table 8.5.

8.5 Final Considerations

According to the data presented in this chapter, at Copahue volcano was affected by a deflation process active between at least March 2004 and December 2007, followed by an inflation process beginning in February 2011 and continuing until the end of the available data in January 2013. Lack of data prevents us from knowing how the volcano behaved during 2008–2010. The deflation rate reached −2 cm/year at the summit of the volcano edifice. Inflation reached ∼6 cm in total between October 2011 and April 2012 and was coincident with the former deflation pattern.

The observed subsidence can be explained by a deflating horizontal prolate spheroidal source at 4 km depth beneath the volcano edifice with a volume change estimated at −0.0013 km^3/year. The modeled location, volume change and geochemical observations (Agusto et al. 2012) are compatible with the conceptual model proposed by Fournier (2006). Deflation at Copahue had been associated with leakage of hyperconcentrated fluids across the brittle–plastic boundary (Velez et al. 2011). This mechanism has the potential to trigger phreatic eruptions, possibly accounting for those that occurred in the 1990s.

The inflation observed since October 2011 has been followed by an eruptive cycle (Caselli et al. this book). Increased activity was reported beginning in July 2012, including phreatic explosions and a phreato-magmatic eruption on December 22nd, 2012. Inflation continued after the eruption, indicating that process was still ongoing and the system have not stabilized. Several physicochemical indicators changed significantly in this period including:

Table 8.5 Parameter sets obtained by using different geometries for 2011–2012 inflation period

2011–2012 period	Latitude	Longitude	Depth (km)	Radius	Length	Width	a	b	Strike	Dip	U3	ΔP/G	ΔV (km^3)
Mogi source	−37.8461°	−71.1422°	7.99	1 km	–	–	–	–	–	–	–	0.027	0.0106
Ellipsoidal source	−37.8470°	−71.1410°	7.5	–	–	–	1.14 km	0.21 km	87.6°	5.6°	–	0.057	0.015
Dislocation source	−37.8446°	−71.1577°	9.0	–	9.3 km	1.47 km	–	–	43.5°	1.6°	0.75 m	–	0.009
conduit source	−37.8418°	−71.1683°	1.98	–	–	–	1.1 km	0.46 km	78°	40°	–	0.0108	0.01
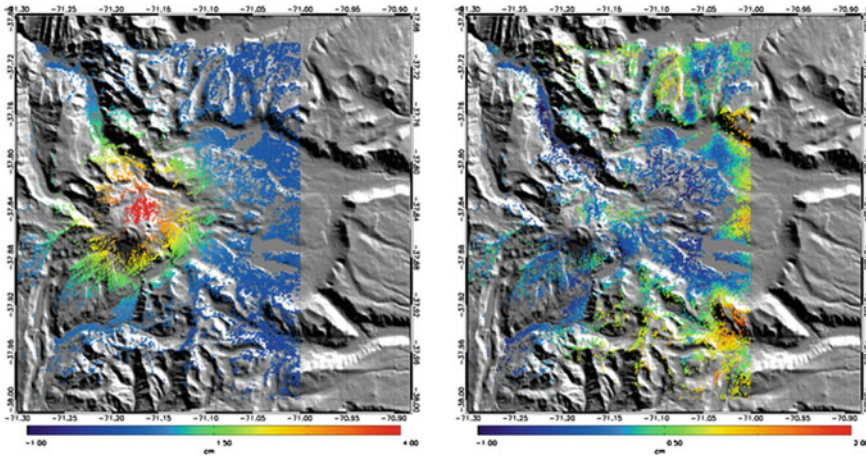
Fig. 8.13 Model (*left*) and residuals (*right*) for an ellipsoidal magma chamber plus a conduit inversions

a progressive decrease of water level in the crater lake, increment changes in magmatic species content and temperature, and also an increase in volcano-seismicity signals. Source parameters obtained by inversion (see results section) locate a magma reservoir between 7.5 km depth (point and ellipsoidal source) and 9 km depth (rectangular horizontal dislocation). The spheroidal sources, and in particular the ellipsoidal one, are preferred because they are located directly beneath the deformation pattern, whereas the dislocation seems too long and extends far outside the volcano edifice. Hence, a horizontal ellipsoidal sill would represent the pressurized magmatic chamber. The pressure/volume change suffered by this source results from new magmatic input. A summit-localized positive residual was well accounted for by considering a volcanic conduit represented by a prolate inclined ellipsoid with a high aspect ratio. It would have also enabled increased gas transport to the surface. Both the deflation and inflation sources are located approximately at the same position, differing only in depth and size. The deflation source, at 4 km depth and 4 km long (major axis), is shallower and larger than the inflation one, located at 7.5 km and 2.2 km long. This is consistent with the conceptual model proposed

by Fournier (2006); the shallower source represents the carapace through which degassing is producing pressure release observed as surface deflation in 2002–2007, while the deeper source represents the expanding magmatic chamber that creates the observed surface uplift in 2011–2012 due to new magma input. This conceptual model is graphically represented in Fig. 8.14.

The positive anomaly observed in the residuals of the deep source allowed us to postulate a conduit linking the chamber with the surface. The best fit solution is located between 1 and 3 km depth, not strictly reaching the modeled shallower ellipsoidal source. However, this idea is attractive given the increased gas output to the crater lake reported for this period (Agusto et al. this book). Furthermore, in December 22nd, 2012 an eruption took place, so magmatic fluids actually reached the surface.

In summary, Copahue volcanic hydrothermal system shows surface deformation during both quiescent (subsidence) and pre-eruptive periods. The signal is strong enough to be measured by DInSAR time series based techniques. The advent of high revisit SAR sensors like present COSMO-Skymed's and future SAOCOM's could make possible a satellite-based ground deformation monitoring system at Copahue.
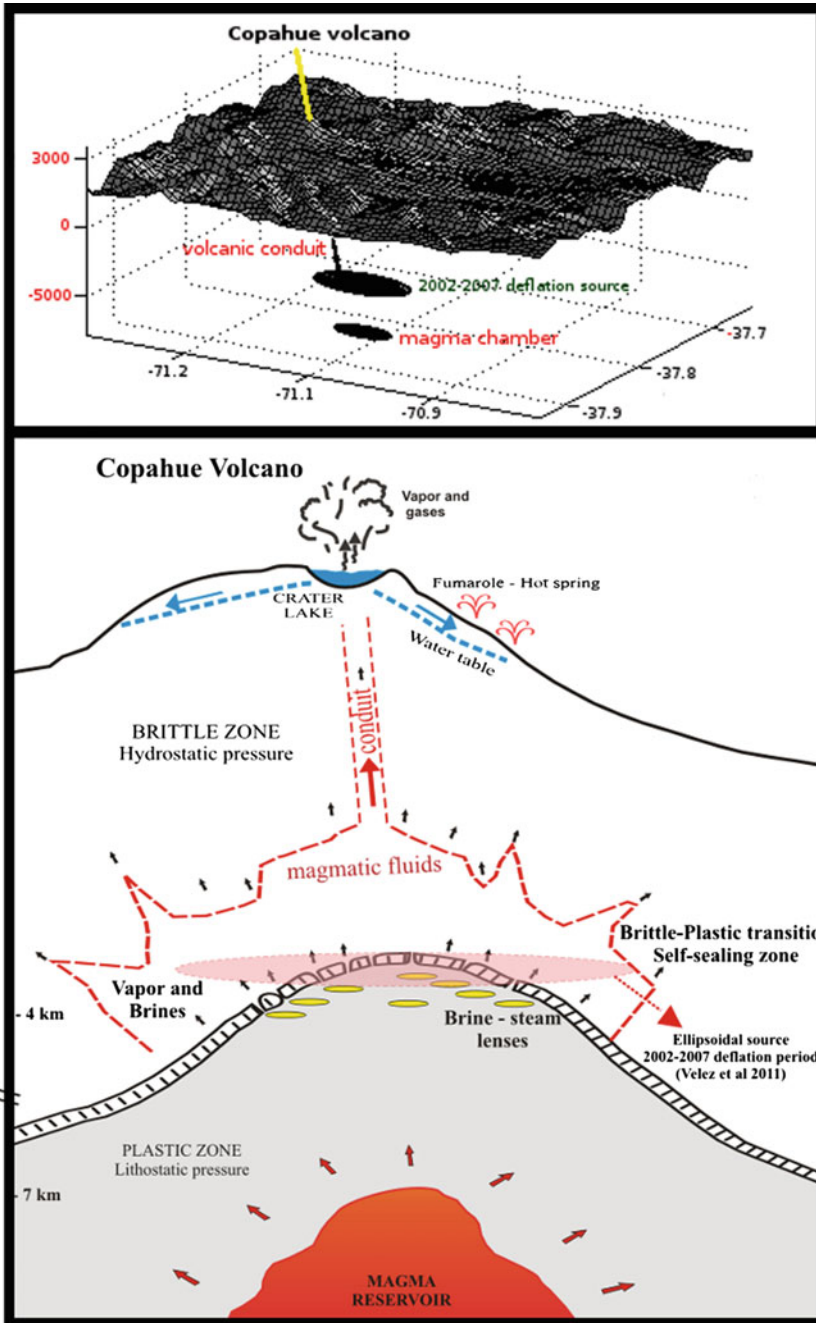
Fig. 8.14 Schematic block diagram showing the 2002–2008 and 2011–2012 sources and conduit locations (*up*) and conceptual model of the volcanic system (*down*)

References

Agusto M, Caselli A, Tassi F, Dos Santos Alfonso M, Vaselli O (2012) Seguimiento geoquimico de las aguas acidas del sistema volcan Copahue—Rio Agrio: posible aplicacion para la identificacion de precursores eruptivos. Rev As Geol Arg 689(4):481–495

Amoruso A, Crescentini L (2009) Shape and volumen change of pressurized elipsoidal cavities from deformation and seismic data. J Geophys Res 14:B02210

Berardino P, Fornaro G, Lanari R, Sansosti E (2002) A new algorithm for surface deformation monitoring based on small baseline differential SAR interferograms. IEEE Trans Geosci Remote Sens 40(11):2375–2382

Battaglia M, Cervelli P, Murray J (2013) Modeling crustal deformation near active faults and volcanic centers. A catalog of deformation models: U.S. Geological Survey Techniques and Methods, book 13, chap. B1, pp 96, http://pubs.usgs.gov/tm/12/b1

Bonaccorso A, Davis P (1999) Models of ground deformation from vertical volcanic conduits with application to eruptions of Mount St. Helens and Mount Etna. J Geophys Res 104(B5):10531–10542. doi:10.1029/1999JB900054

Borgia A, Tizzani P, Solaro G, Manzo M, Casu G, Luongo G, Pepe A, Berardino P, Fornaro G, Sansosti E, Riciardi GP, Fusi N, Di Donna G, Lanari R (2005) Volcanic spreading of Vesuvius, a new paradigm for interpreting its volcanic activity. Geophys Res Lett 32(3):L03303. doi:10.1029/2004GL022155

Costantini M (1998) A novel phase unwrapping method based on network programming. Geosci Remote Sens, IEEE Trans 36(3):813–821

Dieterich JH, Decker RW (1975) Finite element modeling of surface deformation associated with volcanism. J Geophys Res 80:4094–4102

Dzurisin D (2006) Volcano deformation: new geodetic monitoring techniques. Springer, Berlin

Dzurisin D, Lu Z (2006) Interferometric synthetic-aperture radar (InSAR). In: Dzurisin D (ed) Volcano Deformation. Springer, pp 153–194. http://dx.doi.org/10.1007/978-3-540-49302-0_5

Fournier RO (2006) Hydrothermal systems and volcano geochemistry. In: Dzurisin D (ed), Volcano Deformation. Springer, pp 153–194. http://dx.doi.org/10.1007/978-3-540-49302-0_5

Fournier TJ, Pritchard ME, Riddick SN (2010) Duration, magnitude and frequency of subaerial volcano deformation events: new results from Latin America using InSAR and a global synthesis. Geochem Geophys Geosyst 11(1):Q01003. doi:10.1029/2009GC002558

Goldberg DE (1989) Genetic algorithm in search. Optimization and Machine Learning, Addison-Wesley, Reading

Hanssen RF (2001) Radar interferometry—data interpretation and error analysis. Available from: Kluwer Academic Publishers, U.S. http://kluweronline.com

Holland J (1975) Adaptation in natural and artificial systems. The University of Michigan Press, Ann Arbor

Ibañez JM, Del Pezzo E, Bengoa CL, Caselli AT, Badi G, Almendros J (2008) Volcanic tremor and local earthquakes at Copahue volcanic complex, southern Andes, Argentina. J Volcanol Geoth Res 174:284–294. doi:10.1016/j.jvolgeores.2008.02.005

Lundgren P, Casu F, Manzo M, Pepe A, Berardino P, Sansosti E, Lanari R (2004) Gravity and magma induced spreading of Mount Etna volcano revealed by satellite radar interferometry. Geophys Res Lett 31(4):L04602

Manconi AT, Walter R, Amelung F (2007) Effects of mechanical layering on volcano deformation. Geophys J Int 170(2):952–958. doi:10.1111/j.1365-246X.2007.03449.x

Massonnet D, Feigl K (1998) Radar interferometry and its application to changes in the Earth's surface. Rev Geophys 36:441–500

Masterlark T (2007) Magma intrusion and deformation predictions: sensitivities to the mogi assumptions. J Geophys Res 112:B06419. doi:10.1029/2006JB004860

McTigue DF (1987) Elastic stress deformation near a finite spherical magma body: resolution of the point source paradox. J Geophys Res 92:12931–12940

Miranda N, Duesman B, Pinol M, Giudici D, D'Aria D (2010) Impact of Envisat Mission Extension on SAR data. Technical note 1.0. European Space Agency

Mogi K (1958) Relations between the eruptions of various volcanoes and the deformations of the ground surface around them. Bull Earthq Res Inst Univ Tokyo 36:99–134

Okada Y (1985) Surface deformation due to shear and tensile faults in a half-space. Bull Seism Soc Am 75:1135–1154

Pepe A, Sansosti E, Berardino P (2005) On the generation of ERS/ ENVISAT DInSAR time2series via the SBAS technique[J]. IEEE Geosci Remote Sens Lett 2(3):265–269

Snieder R, Trampert J (2010) Inverse problems in geophysics. http://samizdat.mines.edu/snieder_trampert

Sparks RSJ (2003) Forecasting volcanic eruptions. Earth Planet Sci Lett 210:1–15. doi:10.1016/S0012-821X(03)00124-9

Tiampo KF, Rundle JB, Fernandez J, Langbein JO (2000) Spherical and ellipsoidal volcanic sources at Long Valley caldera, California, using a genetic algorithm inversion technique. J Volcanol Geotherm Res 102:189–206

Tizzani P, Berardino P, Casu F, Euillades P, Manzo M, Ricciardi GP, Zeni G, Lanari R (2007) Surface deformation of Long Valley caldera and Mono Basin, California, investigated with the SBAS-InSAR approach. Remote Sens Environ 108:277–289

Velez ML, Euillades P, Caselli AT, Blanco M, Martinez Diaz J (2011) Deformation of Copahue volcano:

inversion of InSAR data using a genetic algorithm. J Volcanol Geotherm Res 202:117–126

Vogfjörd KS et al (2005) Forecasting and monitoring a subglacial eruption in Iceland. EOS Trans AGU 86:245. doi:10.1029/2005EO260001

Yang XM, Davis PM, Dieterich JH (1988) Deformation from inflation of a dipping finite prolate spheroid in a elastic half-space as a model for volcanic stressing. J Geophys Res 93:4249–4257

Zebker HA, Villasenor J (1992) Decorrelation in interferometric radar echoes. IEEE Trans Geosci Remote Sens 30:950–959

The Copahue Volcanic-Hydrothermal System and Applications for Volcanic Surveillance

9

M. Agusto and J. Varekamp

Abstract

During the last two decades, Copahue and its active acidic crater lake have shown different magmatic, phreatomagmatic, and hydrothermal manifestations. Geochemical data of waters from Copahue springs, lakes and rivers provide new insights into the behavior of its volcano-hydrothermal system. Temporal variations in the chemical (major anions and cations) compositions, element fluxes, and isotopic fluctuations (δD and $\delta^{18}O$; stable Pb isotopes, $^{129}I/^{127}I$, $\delta^{37}Cl$, $\delta^{7}Li$, $\delta^{34}S$) of surface waters from Copahue for the period 1997–2012 can be related to processes in the underlying hydrothermal system. The 2000 and 2012 eruptive periods and the 2004 thermal anomaly showed increases in SO_4, Cl and F contents in the waters as a result of ascending magmatic fluids. The changing chemical compositions also showed evidence for enhanced water/rock interaction during these magmatic periods, with increased concentrations of the major rock forming elements such as Al, K and Mg. Soon after the magmatic events, the elemental fluxes from the hydrothermal system decreased strongly, especially for K and Al. The latter is related to a decrease in permeability in the system through crystallization of alunite. Stable isotopic data (δD and $\delta^{18}O$) indicate that the hydrothermal fluids consist of a mixture of meteoric and magmatic waters that are affected by evaporation and water/rock interaction processes. The $\delta^{7}Li$ values, polythionate concentrations and water stable isotope ratios indicate that the hot spring

M. Agusto (✉)
GESVA-IDEAN (UBA-CONICET),
Dpto. Cs. Geológicas, FCEN,
Universidad de Buenos Aires,
Ciudad Universitaria, Pab.2,
1428 Buenos Aires, Argentina
e-mail: magusto@gl.fcen.uba.ar

J. Varekamp
Department of Earth and Environmental Sciences,
Wesleyan University, 265 Church Street,
Middletown, CT 06459-0139, USA

on the flank of the crater does not carry simple seepage from the crater lake. The crater lake and hot spring are fed by different sections from the underlying hydrothermal system. Temperatures of ~ 260 °C in the deeper part of the volcano-hydrothermal reservoir were estimated based on $\delta^{34}S$ values in sulfur and dissolved sulfate. The upper part of the system is possibly more dilute and cooler at ~ 175 °C, based on silica geothermometry. The presence of ^{129}I in the hydrothermal fluids indicates that subducted sediment with organic matter is one source for the magmatic volatiles. Stable Pb isotope ratios showed that the acidic hydrothermal fluids are dissolving local host rocks from the Copahue volcano edifice. The pyroclastic material ejected during the eruptive events carried the hydrothermal alteration phases silica, jarosite, alunite, and anhydrite/gypsum; liquid and particulate native sulfur was also emitted in large quantities. The chemical composition of the Upper Rio Agrio is controlled by the emissions of the feeding volcanic hot springs and mixing with glacial melt water. The compositional evolution of the large Lake Caviahue reflects inputs from the Upper Rio Agrio and melt water dilution, as well as mineral precipitation from the lake waters. The Lower Rio Agrio had copious amounts of Fe-sulfates in the river bed since 2003, which started to disappear again during the period of the 2012 eruption. Monitoring of SO_4/Cl, Mg/Cl and Al/Cl in the Upper Rio Agrio waters may constitute an efficient mode of volcanic surveillance, complementing the ongoing multidisciplinary volcano monitoring and forecasting at Copahue.

9.1 Introduction

The chemical composition of volcanic fluids is of great interest to volcanologists because fluctuations in composition and elemental fluxes may aid in volcano activity monitoring. Extensive and detailed geochemical investigations of fluid discharges are part of many volcano geochemical monitoring programs (Stoibert and Rose 1970; Giggenbach 1987; Martini et al. 1991; Takano et al. 1994a, b; Vaselli et al. 2010). Many active volcanic systems have crater lakes, dependent on the local hydrology and climate (Pasternack and Varekamp 1997). They can be viewed as the uppermost manifestation of a hydrothermal reservoir situated between the surface and the top of the underlying magma chamber. The physical-chemical features of a crater lake depend strongly on the inputs of magmatic-volcanic fluids apart from meteoric waters, so changes in lake chemistry can be interpreted in terms of precursors to pending volcanic activity. Moreover, crater lakes may also constitute a volcanic hazard because interaction between lake water and uprising magmas may produce phreatomagmatic or Surtseyan eruptions that can threaten the surrounding areas through ash fall-out and lahars (Healy et al. 1965; Brown et al. 1989; Cronin et al. 1997; Christenson 2000; Christenson et al. 2007, 2010). In addition, the large volumes of
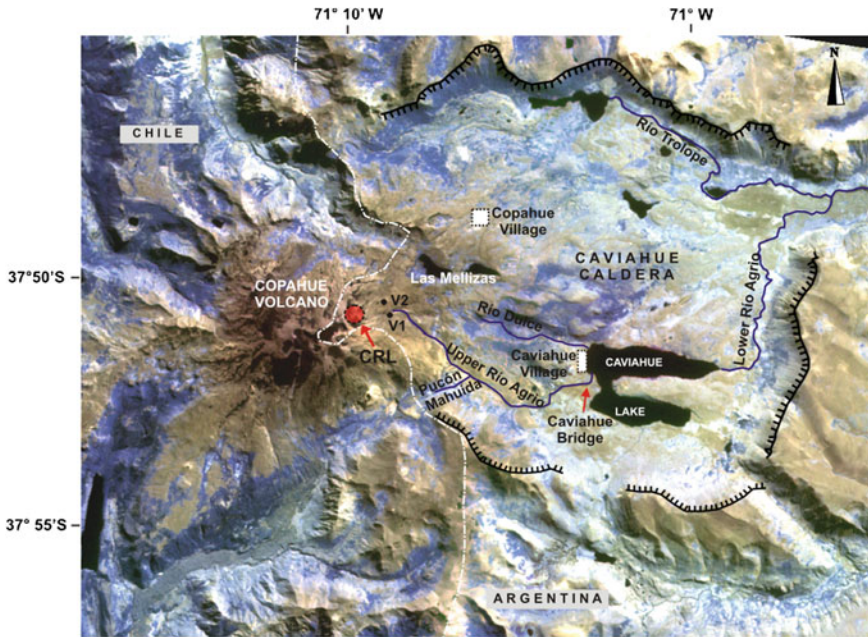
Fig. 9.1 Location map of Copahue volcano and sampling sites of the volcanic-hydrothermal manifestations (CRL, V1 and V2 hot springs), the hydrological system (acid waters URA, CVL and LRA) and snowmelt waters (Río Dulce, Pucón Mahuida and Río Trolope)

toxic hot acid waters in crater lakes can become a danger if a retaining wall fails and lake expulsion and lahars may result, sending the hot and toxic fluids downhill into villages and rural lands. Many acid crater lakes are saturated with elemental sulfur, as indicated by floating sulfur spherules on the lake surface, and some of them have a pool of liquid sulfur at their bottom (Takano and Watanuki 1989; Takano et al. 1994a, b; Ohba et al. 2008). The sealing capacity of a molten sulfur pool at a lake bottom is a function of sulfur composition and temperature (Takano et al. 1994a, b; Kusakabe et al. 2000). Other minerals that may seal the lake bottom in ultra-acidic crater lakes are kaolinite, natroalunite, anhydrite, gypsum, pyrite, halite, barite, anglesite, celestite, amorphous silica, which may be expulsed during phreatic eruptions (Christenson and Wood 1993; Delmelle and Bernard 1994; Varekamp et al. 2004; Christenson et al. 2010). The occurrence of a sealing zone may affect the mass and pressure of an injected, superheated vapor, and consequently, phreatic eruption modalities (Morrissey et al. 2010).

The Copahue active crater hosts a hot acidic lake, periodically with a floating sulfur slick, and several acidic hot springs (some below the summit glacier), which seep out from the eastern summit flank, and merge together downstream to form the Upper Río Agrio (Fig. 9.1). These features are the surface expressions of the volcanic-hydrothermal system of Copahue volcano; other hydrothermal areas around the volcano have geothermal pools and fumarolic emissions fed by a largely meteoric geothermal aquifer (Tassi et al. this book). This chapter deals with the variations in temperature and chemical composition of the Copahue crater lake (CRL), the flank thermal springs (called Vertientes, V), the Upper Río Agrio (URA), Lago Caviahue (CVL) and the Lower Rio Agrio over the last 20 years as well as gas variations in elemental fluxes from the hot springs. The aim was to find relationships between these parameters and the ongoing volcanic activities of Copahue. All the available geochemical data for the magmatic-influenced waters were compiled and a conceptual model was proposed to explain

observed changes in the hydrological and geo-chemical regimes of the Copahue summit system over time. Strategies on how a safe and frequent monitoring program of the Upper Río Agrio were outlined to help to decipher possible variations in the summit magmatic-hydrothermal system within the context of volcanic surveillance.

9.2 Copahue Volcano: Hydrothermal Manifestations and Historical Activity

Copahue volcano hosts an acid brine-like crater lake (CRL) with a diameter of approximately 200 m (Fig. 9.2a). Acidic hot springs on the eastern flank, Vertiente 1 and 2 (V1 and V2), are located ∼200 m below the crater rim and flow

into the Upper Río Agrio (URA) that discharges into Lago Caviahue (CVL), an acidified lake of glacial origin (Fig. 9.2b) (Varekamp et al. 2001, 2009; Gammons et al. 2005; Parker et al. 2008; Pedrozo et al. 2008; Varekamp 2008). Lago Caviahue has two arms and an outlet at the northern arm, the Lower Río Agrio (LRA), which joins the Río Trolope, which is largely meteoric water with some discharges from the geothermal system near Copahue village. The LRA exits the caldera in the NE corner and then passes through a large waterfall (Salto del Agrio) and then continues to merge 30 km further with the Río Ñorquín, and then goes further south towards Loncopué to ultimately discharge into the Río Neuquén (Gammons et al. 2005; Agusto et al. 2012). Representative tributaries to the acidic hydrological system are the Río Dulce (RD), Pucón Mahuida (PM) and Río Trolope

Fig. 9.2 **a** Photograph of Copahue crater lake, **b** Photograph taken from Copahue crater lake showing Vertientes (V1 and V2) hot springs, Upper Río Agrio and Lago Caviahue
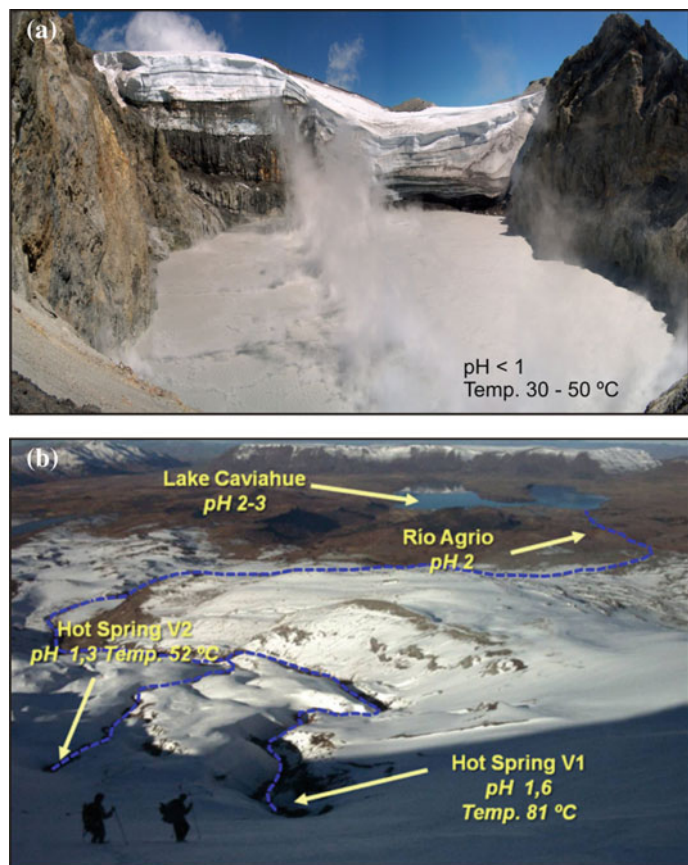
(Fig. 9.1). The area north-northeast of Copahue volcano hosts several hydrothermal emissions, which do not seem to be related to direct magmatic degassing, but are rather structurally controlled and fed by a separate, largely meteoric geothermal aquifer (Mas et al. 2000; Agusto et al. 2013a, b; Tassi et al. this book).

The recent activity of Copahue volcano involved a phreatic eruption cycle from the active crater that occurred from July 1992 to September 1995 (Delpino and Bermúdez 1993; Bermúdez and Delpino 1995). An initial phreatomagmatic eruption occurred in July 2000, followed by magmatic eruptions for several months (Delpino and Bermúdez 2002; Naranjo and Polanco 2004; Varekamp et al. 2001, 2004, 2009). The next phase of activity had the normally warm to hot (30–40 °C) crater lake surface become frozen from July to September 2004 (Caselli et al. 2005; Agusto 2011; Agusto et al. 2012), labeled here the 2004 negative thermal anomaly (NTA). The crater lake returned to its usual state in early 2005 and remained relatively constant until late 2011, when the discharge rate of fluids from the Copahue summit started to increase. During 2012 the crater lake water temperature increased and the water level decreased (Caselli et al. 2013; Agusto et al. 2013a), with a phreatic (phreatomagmatic?) event in July 2012, and finally a major phreatomagmatic-magmatic eruption that

took place in late December 2012 (Caselli et al. this book).

9.3   Analytical Data and Results

9.3.1   Temporal Evolution of the CRL, V1 and V2 Water Temperatures

The crater lake water temperature varied from 21 to 54 °C for the period 1997–2000, (Varekamp et al. 2001). A few months prior to the July 2000 eruption, the temperature of the crater lake water was extremely low: 8 °C in January and 5 °C in April 2000 (Pedrozo et al. 2008). Two years prior to the 2000 eruption hot spring temperatures were between 63–83 °C, and at 75 °C during the July 2000 events (Varekamp et al. 2001, 2004). No information on the lake water temperature is available for the period 2000–2003. In May 2004, the lake had a temperature of 13.5 °C with a gray-green color with sulfur patches floating on the lake surface (Fig. 9.3a). In July 2004, ∼80 % of the lake surface was frozen (Fig. 9.3b) (Caselli et al. 2005; Agusto 2011; Agusto et al. 2012). The following months the frozen portion of the lake surface reduced to ∼40 % (Fig. 9.3c). Freezing of an active crater lake is a rare feature, and was never reported before for the Copahue crater lake

Fig. 9.3 Photographs of the acid crater lake of Copahue volcano and changes of temperature from May 2004 to December 2005 (modified from Agusto et al. 2012)
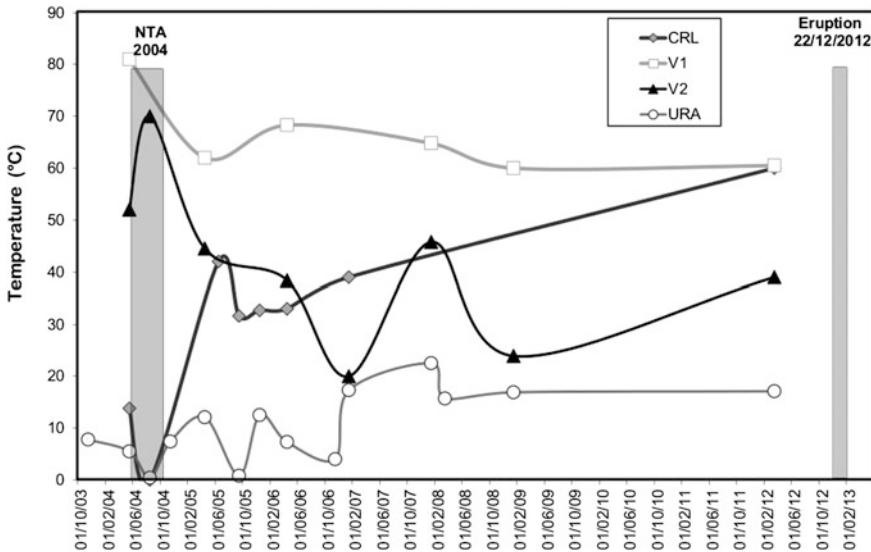
Fig. 9.4 Temporal variations in water temperatures from CRL, V1, V2 and URA

although the lake temperature before the 2000 eruption also approached the freezing point. The 2004 NTA was not followed by an eruption. During the crater lake NTA, the Vertientes hot springs showed the highest temperatures measured since 2003: 81 °C (V1) and 69 °C (V2). Afterwards, the V1 and V2 temperatures remained relatively constant (T_{V1} = 60–70 °C, and T_{V2} = 40–50 °C) (Agusto et al. 2012). The hot springs that feed the Upper Río Agrio do not affect the temperature of the river greatly because it is largely snowmelt water. The URA water temperature varies from 2 °C in winter to 13 °C in summer (Fig. 9.4). The crater lake and hot spring water temperatures are less sensitive to seasonal temperature changes than the URA (Fig. 9.4), whose waters receive large amounts of snow and ice melt water from tributary streams during southern spring-summer period (October-December) and small meteoric water inputs during the low rainfall of austral summer-autumn period (December–April). During 2004–2005 the weather was not anomalous at the region (AIC 2007), thus the 2004 lake NTA cannot be ascribed to climatic conditions. By the end of that year, the crater lake returned to its usual appearance (Fig. 9.3d), and during the following years (2005–2011) it had temperatures between 30 and 40 °C. During 2012 the crater lake temperature increased up to 63 °C in

March, and the water level decreased. Two weeks after a phreatic explosion event in July 2012 the temperature of CRL was similar to the previous measurement (60 °C) while the water level continued to fall (Agusto et al. 2013a). When the major phreatomagmatic eruptions occurred in December 2012 (Caselli et al. this book) the CRL diameter was reduced to approximately 20 m.

9.3.2 Chemical Composition of the Copahue Volcanic-Hydrothermal System

The CRL water is characterized by a low pH (<1–1.7), and specific conductivity up to 102 mS/cm. The crater lake has high contents of SO_4, Cl and F, up to 66,000, 9,100, and 950 mg/L, respectively 7 months prior to the 2000 eruption, and up to 42,000, 18,000 and 2,000 mg/L respectively 8 months prior to the 2012 eruption. These contents are comparable to those of the hot springs V1 and V2 (concentrations of SO_4, Cl and F up to 45,400, 6,800, and 500 mg/L, respectively prior to the 2000 eruption, and up to 28,000, 8,500 and 600 mg/L respectively prior to the 2012 eruption). The pH values of the V1 and V2 springs also range from <1 to 1–2. The specific conductivity of the URA waters decreases from 284 to 1.05 mS/cm from source to

the entrance of Lago Caviahue, as a result of the inputs of tributary streams that are largely fed by snowmelt (Agusto et al. 2012). These tributaries such as Pucón Mahuida have a higher pH and lower SC (pH = 6.3 and SC = 0.03 mS/cm). The Río Dulce stream is largely made of snow-melt water (pH = 6.65, SC = 0.01 mS/cm), and discharges into CVL, which has pH values that ranged over time from 2.2 to ∼3 and relatively low SC (1.06 mS/cm). A similar decrease in the concentration of major and trace elements downstream in the URA was documented by earlier workers (Gammons et al. 2005; Ouimette 2000). The acidic hydrological system thus changes from hyperacidic (pH < 1–2) at the source to a pH between 2.55 and 3 in the CVL, and ultimately reaching a pH of 6 near Loncopué, after joining the Río Neuquén. Below CVL, the pH of the LRA remains near 3 until the con-fluence of the Río Trolope, below which point the pH rises and Fe-sulfates precipitated in abun-dance. The precipitation front of the sulfate mineral suite slowly moved from the confluence of the Rio Trolope upstream in the LRA until it almost reached the outflow point of CVL in 2008–2009. Since 2012, the yellow brown pre-cipitates have started to disappear and dissolve again.

Gammons et al. (2005) documented a similar spatial pattern of changes in water chemistry downstream in the LRA, with additional data on the concentration of major and trace elements, including the rare earth elements. The authors showed that the overall trends in Fe, Al and other rock-forming elements followed predicted pat-terns based on mineral solubilities, with precipi-tation of Fe-rich minerals occurring in the pH range 2.5–4, and precipitation of Al-bearing compounds in the pH range 4.5–6.

The CRL, V1, V2 and URA waters have a $SO_4(Cl)$-Ca(Fe, Al) composition, whereas CVL waters are SO_4/Cl-Na(Mg, Ca) type. The RD water has a HCO_3-Ca composition, whereas PM water shows a SO_4-Ca composition that is dif-ferent with respect to the typical meteoric water likely due to the influence of the volcanic ash plumes from Copahue volcano (Agusto 2011). Waters from the system (CRL, V1, V2 and URA)
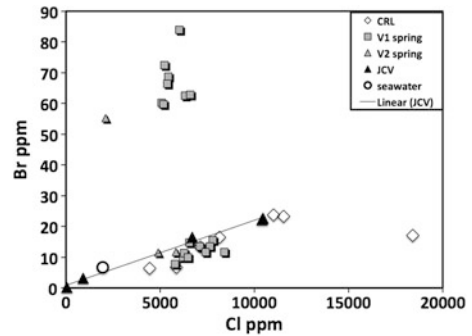
Fig. 9.5 Cl–Br data from V and CRL and CVL

have Σanions/salinity molar ratios of 0.8–0.9, and Σcations/salinity molar ratios of 0.1–0.2, where anions are SO_4, Cl, F, Br and cations Na, K, Al, Ca, Fe and Mg. The total anion content (hereafter TAC) is thus a good approximation for the total salinity. The S/Cl values range from 1 to 9 and Br/Cl values show bimodal distribution (Fig. 9.5). Br/Cl ratios scatter shows an upper cluster and a lower linear trend, the high Br values are in V1 fluids and one high value in V2, while all the CRL values plot on the linear trend with sea-water Br/Cl. High Br values in V1 and V2 are related with a period of TAC increment (see below).

The volcanic elements (VE) derive from the input of magmatic gases into the hydrothermal cell with condensation and recirculation of the fluids between the degassing magma and the shallow zone. Magmatic gases such as CO_2, SO_2, HCl and HF (and minor volatile elements such as As, Hg and B) are absorbed into the hydrother-mal cell by scrubbing processes (Symonds et al. 2001) acidifying the waters of the system, except for the CO_2 which may escape into the geother-mal aquifer. The condensation of the magmatic water in the hydrothermal cell creates a mixture of glacial melt water that seeped into the super structure of the mountain and magmatic water. The rock forming elements (RFE) derive from water rock interaction between the very hot and acid fluids and the volcanic rocks at depth. At temperatures >200 °C and pH values near zero, rock dissolution is probably near congruent, although some minerals may dissolve faster than
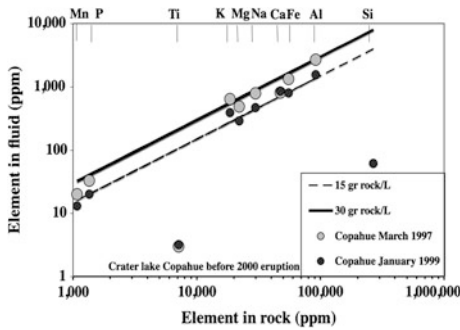
Fig. 9.6 Isosol diagram with 15 and 30 g isosols and CRL compositions in 1997 and 1999. The off sets of Ti and S indicate retention of these two elements in the reservoir (or for Ti also precipitation in the lake). The distance Si–Si* is the amount of Si retained (8 g silica per 15 g rock dissolved)

others. A simple way to express the element relations for near congruent rock dissolution is the isosol diagram (Varekamp 2015), which shows the element concentrations in the rock protoliths versus the same elements in the fluids. The isosols are lines of equal dissolution (grams rock/liter fluid), and an example is given for crater lake fluids of 1997 and 1999 (Fig. 9.6). The diagram indicates 30 g rock dissolved/liter in 1997 and 15 g/L in 1999. In the lake, this drop in rock contents can be simply the result of dilution with glacial melt water. Both patterns show strong depletions in Ti and Si, indicating that either Ti is not completely dissolved from the source rocks or precipitated in the lake through a Ti-rich mineral. The silica was never completely dissolved in the hydrothermal fluids and precipitated while rock dissolution was ongoing (Varekamp 2015). The amount of hydrothermal silica retained by the system can be calculated from the isosol value minus the observed Si value (the vertical intercept on Fig. 9.6 for Si), which for the 1999 fluids is 4000 ppm Si expected and 61 ppm Si observed. This implies that with 15 g rock dissolved per liter, 8 g of hydrothermal silica are retained in the system.

Speciation saturation calculations on the V and CRL fluids indicate that hydrothermal silica, anhydrite and possibly some Cu sulfides are almost always saturated in the fluids (Varekamp et al. 2001, 2009). During some periods the fluids

became more concentrated and jarosite and alunite were predicted to be stable phases (Ouimette 2000; Varekamp et al. 2004, 2009; Fazio et al. 2008). These potential relationships can be documented in molar triangular diagrams such as Na-5 K-Mg with the minerals olivine, albite and alunite indicated (Fig. 9.7a). The bulk rock composition (2000 basaltic andesite of Copahue, Varekamp et al. 2004) is shown and most fluid compositions cluster around this andesitic rock index point (ARIP). Many compositions plot away from the alunite pole, indicating crystallization of that phase, whereas some fluid compositions plot towards the alunite phase, suggesting redissolution in the fluids of older alunite deposits. The diagrams with Fe-Ca-Na+K (Fig. 9.7b) and Mg-Na+K-Al (Fig. 9.7c) show similar relations for crystallization of anhydrite, jarosite and alunite. There are no fluid compositions trending towards albite-plagioclase suggesting no preferential dissolution of that mineral, but a few data points lay towards early dissolution of olivine (Mg enrichment in fluids). In summary, the volcanic-hydrothermal system underlying Copahue active crater consists of glacial meltwater that is acidified by magmatic gases. That mixture dissolves the host rock near congruently, while silica and anhydrite precipitate and at certain periods jarosite and alunite crystallize. The crystallization of the latter phases and the occurrence of liquid native sulfur may lead to reduced permeability in the system, as discussed below. The V fluids discharge into the URA and then afterward are released into Lake Caviahue, to be discussed in detail later.

9.3.3 Isotope Compositions

9.3.3.1 δD and δ^{18}O of Water

The stable isotope compositions of water in term of δD and δ^{18}O are a good tracer for hydrological processes such as mixing of magmatic waters with meteoric waters and evaporation. The springs, rivers and lakes at Copahue show a wide range of isotopic compositions, ranging from pure meteoric waters to highly evolved waters with high values of δD and δ^{18}O (Table 9.1, after
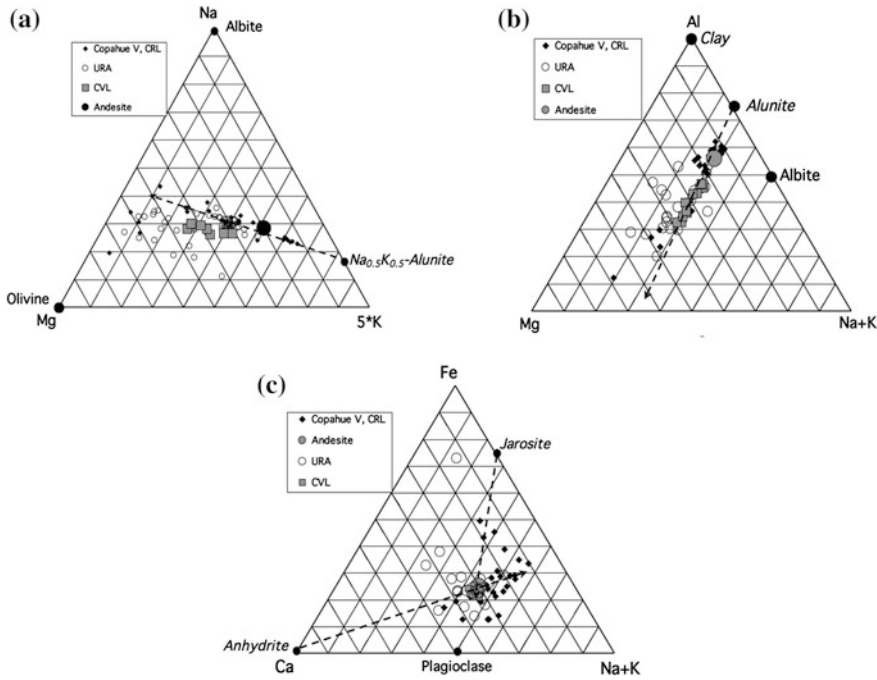
Fig. 9.7 Molar triangular diagrams: **a** Al-Mg-Na+K, showing the ARIP and the tail of water compositions in V and CRL that indicate alunite crystallization; **b** Fe-Ca-Na +K, showing the ARIP and anhydrite crystallization; **c** Na-Mg-5 K, showing evidence for alunite crystallization and a slight offset between the V and URA compositions

Ouimette 2000; Varekamp et al. 2001, 2004; Agusto 2011). The $\delta^{18}O$ values for acidic waters ranged between −12.1 and −5.9 ‰ V-SMOW, andδD values between −90 and −22.5 ‰ V-SMOW (URA and CRL, respectively). Snowmelt waters (PM and RD) show the lowest isotopic values, with $\delta^{18}O$ values ranging between −10.8 and −12.1 ‰ V-SMOW, and δD values between −77 and −88 ‰ V-SMOW; these are the meteoric end member waters for this volcanic-hydrothermal system.

The $\delta^{18}O$–δD diagram (Fig. 9.8a) shows the Local Meteoric Water Line (LMWL: δD ‰ = 7.8 * $\delta^{18}O$ ‰ −0.21 ‰), based on data from the regional precipitation network in Mendoza. The LMWL differs slightly from the global meteoric water line (Craig 1961), which is the result of local atmospheric fractionation processes. The OIPC web site (Bowen and Revenaugh 2003) provides values for local meteoric water at Caviahue and Copahue (OIPC-http://www.waterisotopes.org), in good agreement with

the empirical LMWL (Caviahue: δD = −70 ‰, $\delta^{18}O$ = −9.9 ‰; Copahue summit: δD = −90 ‰, $\delta^{18}O$ = −12.6 ‰). Local meteoric water (Table 9.1) plot on a line with the equation δD ‰ = 4.95 * $\delta^{18}O$ ‰ −26.32 ‰ (Fig. 9.8b) which include data from meteoric water ponds that show extreme evaporation (pond near airport of Caviahue and the Laguna Auquinco (Lat −37.357486; Long −69.992266, elev. 1400 m) in the desert near Chos Malal. This line shows the effects of evaporation of pure meteoric waters at mean ambient temperatures (about 11 °C) and local relative humidity (60 %). The intersection of the evaporation line and LMWL gives a value similar to the OIPC value for mean LMW in Caviahue and close to those defined by Panarello (2002) (−80 ± 5 ‰ for δD, and −11.2 ± 0.4 ‰ for $\delta^{18}O$). Andesitic waters (AW), as defined by Taran et al. (1989) and Giggenbach and Corrales Soto (1992), have $\delta^{18}O$ and δD values of +10 ± 3 ‰ and −20 ± 10 ‰, respectively. The CRL and V water samples plot on a line with

Table 9.1 Temperatures (°C), pH and Specific Conductivity (SC, mS/cm) values, chemical (mg/L) and isotopic ($\delta^{18}O$ and δD, ‰V-SMOW) composition from regional waters

Sampling Point	Date	Reference	T °C	pH	SC	HCO$_3^-$	SO$_4^=$	Cl$^-$	F$^-$	Br$^-$	Na	K	Ca	Mg	Fe	Si	Al	δD	δ¹⁸O
Crater Lake (CRL)																			
	3/15/1997	1	54*	0.3	n.a	n.a	64200	10300	960	n.a	790	640	810	490	1320	n.a	2700	−26	3.6
	3/20/1998	1	33*	0.3	n.a	n.a	59600	8600	840	n.a	590	480	800	370	960	n.a	2020	−36	1.5
	1/6/1999	1	21*	0.3	n.a	n.a	55400	8000	720	n.a	470	390	850	290	800	n.a	1560	−37	0.4
	11/26/1999	1	33*	0.2	n.a	n.a	66000	9100	950	n.a	430	370	840	270	750	n.a	1490	−30	3.5
	1/17/2001	1	n.a	1.1	n.a	n.a	20000	4300	230	n.a	460	50	450	1830	1780	n.a	360	−54.6	−3.3
	3/21/2002	1	n.a	0.6	n.a	n.a	34900	9000	740	n.a	700	80	680	1430	2100	n.a	1040	n.a	n.a
	1/18/2003	1	n.a	0.6	n.a	n.a	31700	14500	970	n.a	1200	260	1020	1470	1890	n.a	2400	−22.5	5.9
	5/5/2004	2	14	0.8	n.a	n.a	9590	3805	423	n.a	280	79	419	296	262	n.a	416	−62.6	−6
	8/20/2004	2	0?	0.6	n.a	n.a	11915	4385	249	n.a	609	178	375	324	337	41	585	n.a	n.a
	11/23/2004	1	n.a	0.8	n.a	n.a	20700	6700	520	n.a	560	170	900	590	760	n.a	1190	n.a	n.a
	4/13/2005	2	n.a	n.a	n.a	n.a	8875	6498	1134	n.a	417	201	715	311	292	64	817	−48.6	−2
	6/13/2005	2	42	n.a	n.a	n.a	9903	6668	768	n.a	366	188	745	282	355	84	914	n.a	n.a
	9/15/2005	2	32	0.8	60500	n.a	10127	7164	864	n.a	290	181	636	232	327	101	878	n.a	n.a
	12/6/2005	2	33	0.4	101500	n.a	17134	7486	932	n.a	364	246	570	232	313	64	451	n.a	n.a
	4/8/2006	2	33	0.6	65200	n.a	17326	7135	568	13	1006	186	834	397	314	61	566	n.a	n.a
	1/29/2007	2	39	1.7	9500	n.a	22476	8145	625	16	422	202	689	293	n.a	n.a	n.a	n.a	n.a
	11/30/2007	2	n.a	n.a	n.a	n.a	32016	11012	766	24	399	242	802	276	n.a	n.a	n.a	n.a	n.a
	12/11/2007	2	n.a	n.a	n.a	n.a	33003	11552	851	23	448	275	898	321	n.a	n.a	n.a	n.a	n.a
	3/14/2008	2	n.a	n.a	n.a	n.a	18980	5874	450	7	227	163	565	207	n.a	n.a	n.a	n.a	n.a
	3/18/2009	3	n.a	n.a	n.a	nd	12873	4442	407	6	177	104	368	127	n.a	n.a	n.a	n.a	n.a
	3/6/2012	3	63	<0	n.a	n.a	41748	18404	1917	17	84	36	143	98	619	n.a	n.a	n.a	n.a

(continued)

Table 9.1 (continued)

Sampling Point	Date	Reference	T °C	pH	SC	HCO_3^-	$SO_4^=$	Cl^-	F^-	Br^-	Na	K	Ca	Mg	Fe	Si	Al	δD	δ18O
Hot Spring (V)																			
	3/15/1997	1	68*	0.4	n.a	n.a	64200	10600	nd	n.a	940	790	1100	640	2190	n.a	3870	−33	1.9
	3/20/1998	1	63*	0.4	n.a	n.a	64000	10200	nd	n.a	1020	930	1420	640	2270	n.a	3690	−38	0.9
	1/6/1999	1	83*	0.3	n.a	n.a	65400	9800	700	n.a	910	880	770	500	1860	n.a	3250	−33	1.7
	11/26/1999	1	72*	0.2	n.a	n.a	45400	6800	500	n.a	520	470	800	300	970	n.a	1940	−49	−2.1
	7/16/2000	1	75*	0.8	n.a	n.a	51400	8400	700	n.a	1500	710	610	1870	2780	n.a	5320	−33.4	1.1
	1/17/2001	1	n.a	2.4	n.a	n.a	30900	4300	230	n.a	900	660	710	960	1580	n.a	2950	−76.3	−9.8
	3/21/2002	1	n.a	1.5	n.a	n.a	24500	7800	1300	n.a	1180	190	860	2830	3590	n.a	1720	−48.9	−2.4
	1/18/2003	1	n.a	1.7	n.a	n.a	11100	6600	750	n.a	1010	60	600	1870	2140	n.a	1010	n.a	n.a
	3/14/2004	1	n.a	2.3	n.a	n.a	15600	9800	840	n.a	1540	130	680	1720	2610	n.a	2210	n.a	n.a
	11/23/2004	1	n.a	1.5	n.a	n.a	8800	3800	220	n.a	540	120	630	640	780	n.a	1020	n.a	n.a
Hot Spring (V1)																			
	2/25/2004	2	n.a	n.a	n.a	n.a	2746	2192	287	n.a	245	34	203	405	367	n.a	443	n.a	n.a
	1/15/2004	2	n.a	n.a	n.a	n.a	2190	1747	246	n.a	73	9	89	120	135	n.a	126	−46	−1.4
	5/5/2004	2	81	1.6	n.a	n.a	14995	2140	441	n.a	1562	225	989	703	495	n.d	1492	−52.5	−3.8
	4/13/2005	2	62	1.4	n.a	n.a	11988	7026	524	n.a	759	263	735	814	672	49	1510	n.a	n.a
	4/8/2006	2	68	0.9	28400	n.a	12236	5025	419	n.a	950	262	516	814	765	39	911	n.a	n.a
	1/29/2007	2	n.a	n.a	n.a	n.a	14587	4929	406	n.a	981	214	589	599	n.a	n.a	n.a	n.a	n.a
	5/31/2007	2	n.a	n.a	n.a	n.a	20050	7107	357	14	1035	322	803	819	n.a	n.a	n.a	n.a	n.a
	11/30/2007	2	n.a	n.a	n.a	n.a	19643	5798	290	8	792	377	736	602	n.a	n.a	n.a	n.a	n.a
	12/11/2007	2	n.a	n.a	n.a	n.a	20687	6211	314	10	851	416	800	599	n.a	n.a	n.a	n.a	n.a
	12/15/2007	2	n.a	n.a	n.a	n.a	20887	6280	294	11	828	403	762	583	n.a	n.a	n.a	n.a	n.a
	1/5/2008	2	n.a	n.a	n.a	n.a	21651	6477	309	10	893	446	794	601	n.a	n.a	n.a	n.a	n.a
	1/12/2008	2	65	1.7	33500	n.a	21538	6558	306	15	787	445	755	572	n.a	n.a	n.a	n.a	n.a
	2/12/2008	2	n.a	n.a	n.a	n.a	25703	7804	307	16	1006	537	735	677	n.a	n.a	n.a	n.a	n.a

(continued)

Table 9.1 (continued)

Sampling Point	Date	Reference	T °C	pH	SC	HCO₃⁻	SO₄⁼	Cl⁻	F⁻	Br⁻	Na	K	Ca	Mg	Fe	Si	Al	δD	δ¹⁸O
	3/2/2008	2	n.a	n.a	n.a	n.a	25757	7651	326	14	1011	525	748	722	n.a	n.a	n.a	n.a	n.a
	3/11/2008	2	n.a	n.a	n.a	n.a	26084	7424	317	12	1028	535	741	823	n.a	n.a	n.a	n.a	n.a
	12/7/2008	2	n.a	n.a	n.a	n.a	18748	5065	146	60	587	359	764	462	n.a	n.a	n.a	n.a	n.a
	12/9/2008	2	n.a	n.a	n.a	n.a	19218	5182	78	60	616	380	791	475	n.a	n.a	n.a	n.a	n.a
	1/2/2009	2	n.a	n.a	n.a	n.a	21905	6326	153	63	706	430	742	495	n.a	n.a	n.a	n.a	n.a
	1/22/2009	2	60	0.8	32200	n.a	22700	6598	221	63	753	456	738	511	n.a	n.a	n.a	n.a	n.a
	29/02/10	4	n.a	n.a	n.a	n.a	16880	5218	470	72	591	408	825	390	n.a	n.a	n.a	n.a	n.a
	3/9/2010	4	n.a	n.a	n.a	n.a	19798	5427	502	69	611	411	766	399	n.a	n.a	n.a	n.a	n.a
	3/18/2010	4	n.a	n.a	n.a	n.a	20598	6010	590	84	783	447	745	529	n.a	n.a	n.a	n.a	n.a
	3/31/2010	4	n.a	n.a	n.a	n.a	19512	5384	493	66	611	993	763	407	n.a	n.a	n.a	n.a	n.a
	3/6/2012	3	60.5	0.6	n.a	n.a	27934	8411	594	12	820	587	826	549	770	n.a	n.a	n.a	n.a
Hot Spring (V2)																			
	5/5/2004	2	52	1.3	n.a	n.a	16260	1825	139	n.a	1010	161	985	628	485	n.a	1141	n.a	n.a
	8/20/2004	2	70	1.4	n.a	n.a	20590	8283	232	n.a	997	211	720	1469	678	n.a	1991	n.a	n.a
	4/13/2005	2	45	1.5	n.a	n.a	9700	5341	375	n.a	537	171	670	622	653	40	1123	−62.6	−6.1
	4/8/2006	2	38	1.5	23800	n.a	18085	7468	604	n.a	769	129	587	588	480	27	689	n.a	n.a
	1/29/2007	2	20	2.3	21200	n.a	5701	1641	169	n.a	219	72	181	252	n.a	n.a	n.a	n.a	n.a
	1/12/2008	2	46	1.7	23700	n.a	15158	4901	272	12	630	267	634	474	n.a	n.a	n.a	n.a	n.a
	1/22/2009	2	24	1.1	39000	n.a	6688	2113	114	55	232	99	318	204	n.a	n.a	n.a	n.a	n.a
	3/6/2012	3	39	1.2	n.a	n.a	19234	5848	381	12	550	343	712	420	585	n.a	n.a	n.a	n.a
Upper Rio Agrio (URA)																			
	1/7/1999	1	n.a	n.a	n.a	n.a	4740	950	46	n.a	100	65	170	100	170	36	280	−64	−7.2
	11/25/1999	1	n.a	n.a	n.a	n.a	1060	180	15	n.a	24	14	49	25	31	15	55	−54	−3.3
	7/6/2000	1	n.a	n.a	n.a	n.a	1220	130	21	n.a	33	7	88	130	130	n.a	76	−85.2	−11.5
	1/13/2001	1	n.a	n.a	n.a	n.a	790	120	11	n.a	27	9	72	58	34	23	45	−76.6	−10.3

(continued)

Table 9.1 (continued)

Sampling Point	Date	Reference	T °C	pH	SC	HCO_3^-	$SO_4^=$	Cl^-	F^-	Br^-	Na	K	Ca	Mg	Fe	Si	Al	δD	$\delta^{18}O$
	3/24/2002	1	n.a	n.a	n.a	n.a	1170	280	36	n.a	26	5	45	71	53	19	44	−80.8	−10.8
	1/21/2003	1	n.a	n.a	n.a	n.a	460	170	17	n.a	30	6	44	62	23	20	27	−82.8	−11.6
	11/6/2003	2	8	2.4	1560	n.a	n.a	n.a	n.a	n.a	29	5	47	48	n.d	27	102	n.a	n.a
	1/15/2004	2	n.a	3	n.a	n.a	585	457	57	n.a	51	6	79	93	74	n.a	81	n.a	n.a
	1/25/2004	2	n.a	3	n.a	n.a	737	594	70	n.a	66	6	89	120	96	n.a	111	n.a	n.a
	2/24/2004	2	n.a	2	n.a	n.a	1438	1135	123	n.a	131	22	160	247	219	n.a	236	n.a	n.a
	3/12/2004	1	n.a	n.a	n.a	n.a	2790	1490	120	n.a	210	34	160	310	320	n.a	260	n.a	n.a
	5/5/2004	2	6	2	n.a	n.a	1604	614	57	n.a	88	15	161	152	137	n.d	123	n.a	n.a
	8/20/2004	2	0	2.3	n.a	n.a	1720	890	30	n.a	40	15	79	103	617	n.a	136	n.a	n.a
	11/12/2004	2	7	2.4	n.a	n.a	598	238	15	1.3	29	10	58	49	50	n.a	59	n.a	n.a
	11/22/2004	1	n.a	n.a	n.a	n.a	560	180	11	n.a	28	6	36	40	32	n.a	41	n.a	n.a
	4/13/2005	2	12	2	n.a	n.a	1977	1067	70	n.a	122	35	166	153	170	23	230	−83.3	−10.8
	9/15/2005	2	1	2.2	5100	n.a	799	437	38	n.a	49	17	56	59	79	16	106	n.a	n.a
	12/6/2005	2	13	2.7	1438	n.a	391	123	11	n.a	6	10	22	22	23	9	29	n.a	n.a
	4/8/2006	2	7	2.5	9685	n.a	2255	834	90	n.a	116	41	153	108	121	17	164	n.a	n.a
	11/14/2006	2	4	2.7	1975	n.a	490	174	14	0.3	9	4	33	31	36	n.a	42	−86.4	−11.9
	1/29/2007	2	17	2.7	3420	n.a	983	312	23	n.a	54	13	68	62	n.a	n.a	n.a	−89.6	−11.2
	11/12/2007	2	30	2.5	5370	n.a	1109	344	25	0.6	53	19	69	56	n.a	n.a	n.a	n.a	n.a
	11/19/2007	2	n.a	n.a	n.a	n.a	994	303	26	0.5	51	18	71	56	n.a	n.a	n.a	n.a	n.a
	11/28/2007	2	n.a	n.a	n.a	n.a	692	202	21	0.3	32	12	43	34	n.a	n.a	n.a	n.a	n.a
	12/27/2007	2	n.a	n.a	n.a	n.a	1303	388	28	0.6	62	24	82	67	n.a	n.a	n.a	n.a	n.a
	1/13/2008	2	23	2.7	7200	n.a	2342	696	58	1.3	103	42	137	104	n.a	n.a	n.a	n.a	n.a
	1/27/2008	2	17	n.a	n.a	n.a	2229	655	54	1.2	99	39	128	101	n.a	n.a	n.a	n.a	n.a
	2/10/2008	2	n.a	n.a	n.a	n.a	2711	791	59	1.5	116	49	147	116	n.a	n.a	n.a	n.a	n.a
	2/19/2008	2	n.a	n.a	n.a	n.a	3463	979	96	2	137	60	168	130	n.a	n.a	n.a	n.a	n.a

(continued)

Table 9.1 (continued)

Sampling Point	Date	Reference	T °C	pH	SC	HCO$_3^-$	SO$_4^=$	Cl$^-$	F$^-$	Br$^-$	Na	K	Ca	Mg	Fe	Si	Al	δD	δ^{18}O
	3/2/2008	2	n.a	n.a	n.a	n.a	4496	1239	95	2.5	n.a	n.a	n.a	n.a	n.a	n.a	n.a	n.a	n.a
	3/16/2008	2	16	1.5	23760	n.a	6656	1794	176	6.7	250	114	285	240	n.a	n.a	n.a	n.a	n.a
	4/30/2008	2	n.a	n.a	n.a	n.a	4670	1342	186	2.4	184	86	236	201	n.a	n.a	n.a	n.a	n.a
	5/4/2008	2	n.a	n.a	n.a	n.a	5840	1637	127	4.2	218	101	283	227	n.a	n.a	n.a	n.a	n.a
	6/24/2008	2	n.a	n.a	n.a	n.a	1513	443	73	0.8	55	26	92	57	n.a	n.a	n.a	n.a	n.a
	7/20/2008	2	n.a	n.a	n.a	n.a	6266	1744	121	3.2	62	29	103	67	n.a	n.a	n.a	n.a	n.a
	7/27/2008	2	n.a	n.a	n.a	n.a	1752	493	74	0.9	64	29	104	69	n.a	n.a	n.a	n.a	n.a
	8/8/2008	2	n.a	n.a	n.a	n.a	844	232	21	0.4	31	15	53	34	n.a	n.a	n.a	n.a	n.a
	8/26/2008	2	n.a	n.a	n.a	n.a	1790	496	73	1	62	27	102	68	n.a	n.a	n.a	n.a	n.a
	9/9/2008	2	n.a	n.a	n.a	n.a	863	232	21	0.4	31	14	51	34	n.a	n.a	n.a	n.a	n.a
	9/23/2008	2	n.a	n.a	n.a	n.a	861	229	21	0.4	32	15	53	35	n.a	n.a	n.a	n.a	n.a
	9/30/2008	2	n.a	n.a	n.a	n.a	861	230	21	0.4	31	15	53	35	n.a	n.a	n.a	n.a	n.a
	10/7/2008	2	n.a	n.a	n.a	n.a	874	231	21	0.4	31	14	52	34	n.a	n.a	n.a	n.a	n.a
	12/29/2008	2	n.a	n.a	n.a	n.a	1138	321	17	3.6	43	19	73	52	n.a	n.a	n.a	n.a	n.a
	1/17/2009	2	17	1.9	10140	n.a	2271	633	29	4.2	80	37	130	97	n.a	n.a	n.a	n.a	n.a
	3/6/2012	3	17	1.4	n.a	n.a	2394	689	44	1.4	84	36	143	98	75	n.a	n.a	n.a	n.a
Lake Caviahue (CVL)																			
	19/03/1998 N	1	n.a	2.3	n.a	n.a	370	85	nd	n.a	13	7	20	14	18	n.a	29	n.a	n.a
	06/07/2000 S	1	n.a	2.2	n.a	n.a	480	104	9	n.a	12	8	22	14	19	n.a	26	−76.3	−10
	11/6/2003	2	15	2.2	980	n.a	n.a	n.a	n.a	n.a	8	4	19	12	n.d	24	45	n.a	n.a
	5/5/2004	2	11	2.4	n.a	n.a	n.a	n.a	n.a	n.a	8	7	49	22	16	n.d	14	−81	−10.8
	8/20/2004	2	5	2.9	n.a	n.a	n.a	n.a	n.a	n.a	n.d	6	15	18	20	n.a	17	n.a	n.a
	11/12/2004	2	9	3.1	n.a	n.a	n.a	n.a	n.a	n.a	8	5	30	16	19	n.a	17	n.a	n.a
	21/11/2004 N	1	n.a	2.6	n.a	n.a	330	80	8	n.a	15	5	20	22	22	n.a	22	n.a	n.a
	4/13/2005	2	12	2.8	n.a	n.a	260	91	13	n.a	15	9	17	17	24	13	22	n.a	n.a

(continued)

Table 9.1 (continued)

Sampling Point	Date	Reference	T °C	pH	SC	HCO$_3^-$	SO$_4^=$	Cl$^-$	F$^-$	Br$^-$	Na	K	Ca	Mg	Fe	Si	Al	δD	δ^{18}O
	9/15/2005	2	6	2.9	1050	n.a	178	60	9	n.a	3	9	9	12	19	13	16	−82.2	−10.2
	12/6/2005	2	9	2.6	1344	n.a	305	70	9	n.a	n.d	7	8	14	18	7	15	n.a	n.a
	4/8/2006	2	12	3.0	1205	n.a	326	77	5	0.1	10	14	23	17	18	8	15	n.a	n.a
	11/14/2006	2	9	2.8	1110	n.a	225	59	6	n.a	13	4	18	20	15	n.a	12	−88	−10.7
	14/11/06 S	2	10	3.2	930	n.a	186	52	5	n.a	10	3	14	16	6	n.a	10	−82.1	−11.1
	14/11/06 N	2	7	3.1	1060	n.a	229	65	6	n.a	12	4	18	19	16	n.a	14	n.a	n.a
	2/7/2007	2	12	3.1	n.a	n.a	314	66	6	n.a	12	4	18	20	n.a	n.a	n.a	n.a	n.a
	11/12/2007	2	9	2.8	1110	n.a	317	76	5	0.1	13	4	19	18	n.a	n.a	n.a	n.a	n.a
	1/17/2009	2	15	2.9	1260	n.a	277	76	4	1.6	14	5	20	18	n.a	n.a	n.a	n.a	n.a
Lower Río Agrio (LRA)																			
Puente NE	11/14/2006	2	10	3.1	1050	n.a	218	60	5	0.06	11	4	17	18	17	n.a	12	n.a	n.a
Salto del Agrio	11/14/2006	2	12	3.5	380	n.a	85	23	2	0.05	7	2	11	9	5	n.a	5	−86.7	−11.7
Puerta de Trolope	11/14/2006	2	13	3.6	330	n.a	83	23	2	0.02	5	2	9	7	2	n.a	4	n.a	n.a
Puente - Rio Ñorquin	11/14/2006	2	13	3.7	240	n.a	73	20	2	0.03	5	2	13	7	n.a	n.a	3	n.a	n.a
Loncopue	11/14/2006	2	14	6.7	110	13	34	9	1	0.01	1	2	11	5	n.a	n.a	n.a	n.a	n.a
Snowmelt waters																			
Río Dulce (RD)	11/14/2006	2	4	6.7	10	9	4	0.8	2	n.a	0.6	1	1	0.1	n.a	n.a	n.a	−84.6	−11
Las Mellizas	11/14/2006	2	1	6.3	290	7	44	11	0.5	0.015	7	2	10	9	n.a	n.a	n.a	n.a	n.a
Hualcupen	11/14/2006	2	12	7	10	15	0.8	0.4	0.1	0.002	2	0.8	2	1	n.a	n.a	n.a	−88.39	−12.08
Pucón Mahuida (PM)	11/14/2006	2	5	6.3	30	4	12	1	0.2	n.d	2	1	2	2	n.a	n.a	n.a	n.a	n.a
Río Trolope	11/14/2006	2	11	6.2	30	17	8	2	0.1	0.004	3	1	3	2	n.a	n.a	n.a	−86.7	−11.7

n.a not analyzed. Reference data; * Varekamp et al. (2001), (1) Varekamp et al. (2009), (2) Agusto et al. (2012), (3) Agusto et al.(2013a), (4) this work

a lesser slope that trends towards the AW field (Fig. 9.8a), labeled here the VHS line (volcano-hydrothermal system) with the equation δD ‰ = 3.6 * $\delta^{18}O$ ‰ −41.65 ‰. The VHS line intersects with the LMWL roughly at the same point as the meteoric water evaporation line. The slope of evaporation lines is defined by:

$$S = [h*(\delta atm − \delta w)+\varepsilon]D/[h*(\delta atm − \delta w)+\varepsilon]^{18}O \tag{9.1}$$

where the ε parameters are the total fractionation factors for a given h* and temperature, δw are the isotopic values of the waters that are evaporating and δatm are the isotopic values of atmospheric moisture (Gat 1995). The latter can be taken as in equilibrium with the precipitation at the ambient temperature or can be approximated from an empirical relationship with ambient temperature, which was done here (Gibson et al. 1999). The common relative humidity h is applicable for waters at similar temperature as the atmosphere, but for waters well above ambient temperatures, h* is the water temperature- normalized relative humidity, defined as (Pw(atm) at T atm at h)/(Pw(water) at Twater at saturation) (Gat 1995; Varekamp and Kreulen 2000). The slope of the meteoric water evaporation line of 4.95 can be obtained from the above equation at a mean annual ambient temperature of 11 °C and h ∼0.6. The VHS line is largely the result of mixing between meteoric and magmatic/andesitic waters (V fluids), with the CRL fluids having an additional evaporation component. Some fluids from the geothermal system also plot near the VHS line, which is the result of evaporation at an elevated temperature (Varekamp and Kreulen 2000), not the result of mixing with andesitic fluids. The V fluids are most likely binary mixtures between magmatic fluids ("andesitic waters" or AW) and glacial melt water, and this would suggest that the V fluids may consist of >50 % of magmatic fluids (Varekamp et al. 2004), with a range over time based on our total data from highs of 70 % to extreme lows of 10 %. The low % values occurred during and after eruptive activity, thus

the enhanced W/R interaction during intrusive/extrusive events likely led to a reduced permeability in the upper part of the system as a result of mineral precipitation. That led to a diminished rise of the deep hydrothermal fluids and as a result the effluents at the Vertientes springs and feeders into the crater lake became more dilute. These mixing calculations for the V fluids assume that the glacial melt waters mix with pure magmatic fluids, but the W/R interaction will also add ^{18}O to the mix (no ^{2}H because rocks are poor in hydrogen). Average rock consists of about 45 % (wt) of oxygen, and the V waters have up to 10 % TDS. A simple calculation for congruent dissolution of 10 % rock yields ∼4.5 % of oxygen with $\delta^{18}O$ = +8 ‰, which would make the V water possibly 1 ‰ heavier in $\delta^{18}O$ then simple binary mixing of meteoric/glacial water and andesitic water. The composition of the CRL is most likely a combination of mixing between a hydrothermal component from the underlying reservoir and glacial meltwater, with simultaneous evaporation. The geothermal pools in the geothermal/fumarolic areas around the volcano edifice seem to be largely steam-heated waters close to meteoric in origin and the evaporation effect dominates there, (e.g., Panarello 2002; Agusto 2011; Tassi et al. this book). The slope of the line for the geothermal samples (about coincident with the VHS line) indicates that evaporation occurred at about 30 °C, which is the typical low-end range temperature of the crater lake and the typical temperature of the geothermal pools. The effects of mixing and evaporation can be further separated for the CRL samples, in a Cl versus $\delta^{18}O$ plot, where the Cl contents are less strongly influenced by evaporation than the $\delta^{18}O$ values. The CRL values plot on a line, which is a combined mixing-evaporation line (Varekamp and Kreulen 2000). The V samples plot on a simple mixing line for the more concentrated samples but show more scatter in the more dilute V compositions. The latter are the result of the temporal changes in the hydrothermal reservoir that led to variations in Cl concentration and $\delta^{18}O$ values (Fig. 9.8c). The evaporation of warm CRL waters would be accompanied by HCl
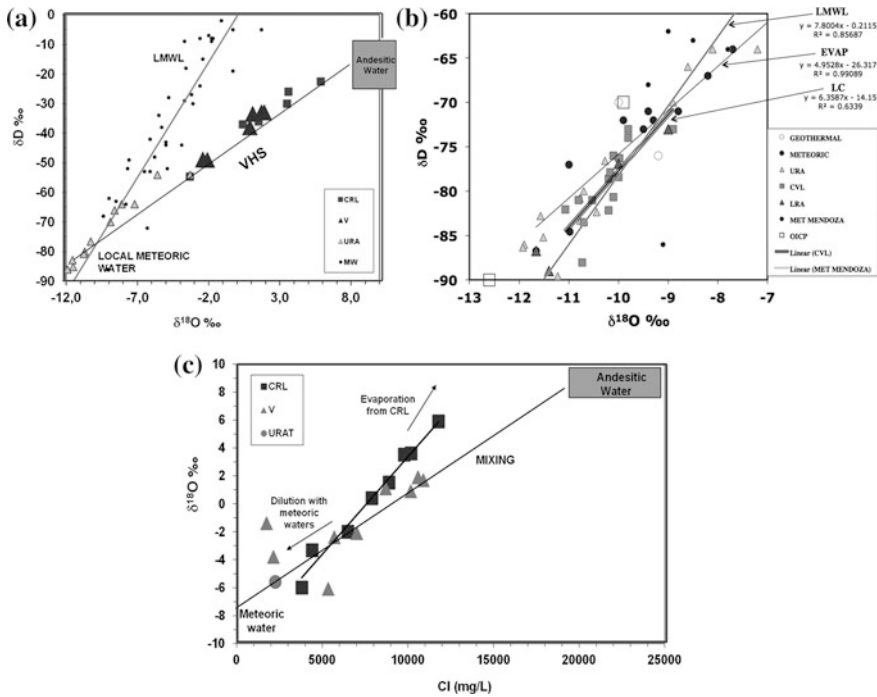
Fig. 9.8 Stable isotopes of water: **a** a. $\delta^{18}O$—δD diagram with CRL, V fluids on mixing line and URA fluids near meteoric water. Also indicate the LMWL; **b** URA-CVL-LRA and MW data, showing the range of values in CVL as a result of both in situ precipitation (Geothermal and Meteroric data from Varekamp et al. 2004); **c** mixing and evaporation for CRL and V samples in Cl-$\delta^{18}O$ diagram. Note the evaporation line for CRL samples

escape, while the evaporation of water would concentrate the Cl^-. More detailed data are needed to model quantitatively the combined water and HCl evasion from the lake.

The Upper Rio Agrio and Lago Caviahue samples are all close to the meteoric water endmember but in detail the effects of mixing (URA) and evaporation (CVL) can be detected (Fig. 9.8b). The E/I value (Evaporation over Input; Gat and Levy 1978) for Lago Caviahue was calculated from the CVL isotope data array and the meteoric water endmember, using the same evaporation parameters as that for the meteoric water evaporation line (see also Mayr et al. 2007). This provides a range of E/I = 4–6 %, indicating that evaporation is only a small component in the CVL water balance. The range of isotope values for CVL (−88 to −73 ‰ for δD) can be explained as follows: glacial melt water has a δD of −87 ‰ and theoretical

precipitation at the summit of Copahue (~ 3000 m elevation) has a δD of −90 ‰ (OIPC). Observed URA water with the lightest composition has δD −89.6 ‰. This water enters the lake and mixes with the lake fluids and the isotopically lightest lake values are −88 ‰. The CVL array of data points ends near −73 ‰, which is also close to the theoretical mean value for precipitation around Caviahue (1600 m elevation, OICP). Mixing between those meteoric endmember values as well as evaporation creates the array of isotope data for CVL with a slope of 6.4, which as a result of the evaporation component is slightly less than the slope of the pure LMWL of 7.8.

The URA has up to 8 % magmatic water in its higher reaches, which then decreases downstream because of dilution of the Vertiente spring waters with glacial melt waters. The geothermal fluids from the pipe from the geothermal drill
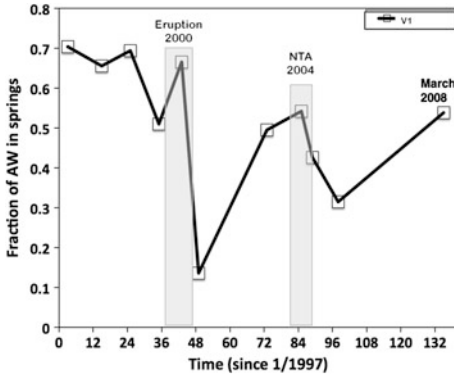
Fig. 9.9 Mixing diagram of AW versus MW in V fluids versus time. Note the two drop off events after the 2000 eruption and the 2004 NTA

hole show an offset to heavier $\delta^{18}O$ from LMW (more details Tassi et al. this book), typical for non-magmatic hydrothermal systems (Craig et al. 1963).

The V waters can provide the closest estimate of the isotopic composition of the volcano-hydrothermal reservoir fluids, which consist for >50 % of magmatic fluids (AW). The time trend of the AW % in the V fluids shows a strong decrease after the 2000 eruption and after the 2004 NTA (Fig. 9.9), indicating the decrease in the flux of deep hydrothermal fluids to the surface as a result of the reduced permeability in the system. The freezing of the crater lake at that

time was a direct result of the decreased input of hot deep hydrothermal waters into the lake.

In summary, the V fluids are binary mixtures between magmatic fluids and meteoric waters, whereas the other mineralized waters are impacted by mixing with V type fluids and evaporation processes, be it at ambient or at slightly elevated temperatures. The fluids from the pools in Copahue village and the geothermal steam pipe stem from the geothermal aquifer are dominated by meteoric water. That system on the north flank of the mountain seems to be spatially well-separated from the acid volcano-magmatic hydrothermal system that occurs directly below the Copahue summit and its crater lake.

9.3.3.2 $\delta^{34}S$ and Sulfur Speciation

The sulfur isotopic composition of fluids at Copahue has been measured in several samples at different times. The $\delta^{34}S$ for dissolved sulfate in V, CRL, URA, CVL and elemental sulfur samples from the slicks on the crater lake, from the crater lake wall as well as from the crater lake sediment were collected and analyzed (Table 9.2). In general, the $\delta^{34}S$ in bisulfate or sulfate is rather high, ranging from +13.7 to +21.2 ‰ over time. The elemental sulfur is much lighter, ranging from −8.2 to −11.4 ‰. The difference in $\delta^{34}S$ between the oxidized and

Table 9.2 Sulfur isotope data and $\delta^{18}O$ (‰) in sulfate

Sampling point	1993	1995	1997	1999	2000	2001	2002	2003
CRL	n.a.	n.a.	14.2	14.2	n.a.	13.6	16.6	21.2
V	n.a.	n.a.	14.5	14.2	15	14.8	18.3	14.8
URA-P	n.a.	n.a.	14.4	13.9	14.3	n.a.	n.a.	n.a.
URA-D	n.a.	n.a.	14.1	n.a.	14	n.a.	n.a.	n.a.
CVL	n.a.	n.a.	14.1	13.7	14.3	n.a.	n.a.	n.a.
CVL	n.a.	n.a.	14	n.a.	14.4	n.a.	n.a.	n.a.
URAT	n.a.	n.a.	n.a.	14	n.a.	n.a.	n.a.	n.a.
S°	−10.5	−11.4	n.a.	−8.2	−10.9	n.a.	n.a.	n.a.
S in sediment	−8.4	n.a.	n.a.	n.a.	n.a.	n.a.	n.a.	n.a.
$\Delta\delta^{34}S$ V	n.a.	n.a.	24.5	24.2	25	24.8	28.3	24.8
ΧΠ $\delta^{18}O$-SO_4	n.a.	n.a.	20.6	19.6	16.8	n.a.	n.a.	n.a.
ΧΠ $\delta^{18}O$-H_2O	n.a.	n.a.	1.9	1.7	1.1	n.a.	n.a.	n.a.

n.a not analyzed

reduced sulfur species is created during the disproportionation of SO_2 in water according to:

$$3SO_2 + 2H_2O \rightarrow HSO_4^- + S_o + 2H^+ \quad (9.2)$$
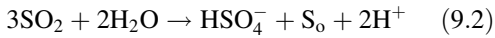
The isotopic fractionation is determined by temperature and in the lower temperature range also by the kinetics of the process (Kusakabe et al. 2000). The calculated temperatures of the $\delta^{34}S$ system for the hydrothermal system range from 250–280 °C (Varekamp et al. 2004) assuming that the native sulfur stems from the deep reservoir. The copious amounts of liquid sulfur ejected during phreatic events in the 1990s and 2012 eruption (Delpino and Bermudez 1993; Agusto et al. 2013a) indicates that the hydrothermal system contains a vast reservoir of liquid sulfur that may escape with the fluids into the lake. The $\delta^{34}S$ in dissolved sulfate decreases downstream in the URA and CVL, although the effect is close to the data precision. This may be caused by the oxidation of reduced sulfur species in the water during its flow down the mountain, precipitation of sulfates along the way, or mixing with tributaries with isotopically lighter sulfur. More data are needed to establish the exact reason, but the trend is consistent over the years.

The $\delta^{18}O$ in sulfate is a tracer for the origin of the sulfate oxygen when it formed from less oxidized sulfur species (Boschetti 2013). At high temperature, magmatic SO_2 reacts with water to form HSO_4 (Eq. 9.2), and the $\delta^{18}O$ of the water and temperature determine the $\delta^{18}O$ value in sulfate. This value will reset rapidly during cooling and dilution at relatively high temperatures and low pH values, but it will be "frozen in" at ambient temperatures. Equilibration temperatures can be calculated for the hot spring using the $\delta^{18}O$ of the water and the $\delta^{18}O$ in bisulfate (Table 9.2). Using the expressions of Seal et al. (2000), temperatures of 93, 99, and 117 °C were obtained for the years 1997, 1999 and 2000. The $\delta^{18}O$ of the acid reservoir fluids is a mixture of water close to magmatic values (+8 ‰) and glacial melt water (−11 ‰) and the hot springs provide fluids of various mixtures between the two. An extreme endmember temperature can be calculated assuming that the

lowest section of the volcanic-hydrothermal reservoir was at the magmatic $\delta^{18}O$ value of +8 ‰, yielding an equilibration temperature of 183 °C, still well below the ∼260 °C calculated earlier from sulfur isotope equilibrium considerations. Most likely, the waters have re-equilibrated during cooling and dilution with glacial melt water in the subsurface, and the obtained range of temperatures is close to the exit temperature of the V hot spring in these years (see Table 9.1). The temperatures calculated from the sulfur isotope fractionation (250–270 °C) probably provide the closest estimate to the true temperature of the magmatic fluid reservoir feeding the hyperacid crater lake and hot springs. These temperature estimations are similar to those based on gas chemical equilibria for the hydrothermal reservoir feeding fumarolic areas northeastern of the volcano (Tassi et al. this book), and consistent with those measured in the geothermal wells (∼260 °C) located near these areas (Mas et al. this book).

In 1996, 1997 and 2004, polythionate species were analyzed both in the crater lake waters and in the Vertientes hot spring (Table 9.2). The concentrations in 1996 and 1997 were very low compared to those documented in other acid volcanic lakes (Takano and Watanuki 1989; Takano et al. 1994a; Kusakabe et al. 2000; Delmelle and Bernard 2000a, b), whereas much higher concentrations were found in late 2004. Polythionate levels in the V springs were always below detection. The latter suggests that the CRL and V fluids draw from different parts of the underlying hydrothermal fluids, or alternatively, the CRL fluids have an active SO_2 input and the polythionates are generated within the lake environment. Either way, it is obvious from these data as well differences in cation ratios and stable isotope ratios between CRL and V fluids, that the V fluids are not direct seepage from the crater lake but have a source at depth independent of the crater lake fluids. The 2004 polythionate data show an order of magnitude higher polythionate concentrations than the late 1990s data, which has been interpreted at other lakes as an indicator of pending eruptions (Takano and Watanuki 1989). The November 2004 sampling of the

crater lake took place after the 2004 NTA, and hydrothermal input into the lake had been restored by that time. Possibly, SO_2 rich vapors were again entering the lake at that time, related to the input of deep magmatic fluids or even a small magmatic intrusion earlier that year ("failed eruption" of Varekamp et al. 2009; Velez et al. 2011; Agusto et al. 2012).

9.3.3.3 Stable Pb Isotope Ratios, ^{129}I, ^{36}Cl, δ^{37}Cl, and δ^7Li

Some more exotic isotope ratios and their elemental values were also analyzed in the Copahue acidic waters: ^{129}I, δ^7Li, ^{36}Cl and stable Pb isotopes, be it that the number of analyses is very limited (Table 9.3). The isotope ^{129}Iodine is cosmogenic with a $T_{1/2} = 16.5$ Ma. Upon rain-out from the atmosphere into the ocean, the iodine gets largely incorporated into organic matter and then ends up in marine sediment. With its long half life time, it survives the subduction process and may then be released again during sediment devolatilization in the arc-magma generation zone. As such, the isotope is like ^{10}Be one of the "smoking guns" of sediment subduction (Fehn et al. 2002). Nuclear industry contamination and weapons testing has raised the modern levels of ^{129}I above cosmogenic background levels, which needs to be considered in systems open to the atmosphere such as volcanic lakes. Measurements of ^{129}I were reported for CRL, V and CVL as well as local non-volcanic lakes (Fehn et al.
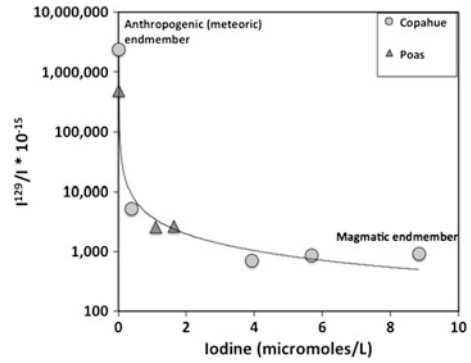

Fig. 9.10 Mixing diagram for magmatic fluids (I = 15 mmol, and 129I/I = versus meteoric fluids (I = 0.00015 mmol and 129I/I = 12,450,000 × 10^{-15})., CRL, URA and V fluids from Copahue indicates as well as some crater lake fluids from Póas crater lake (after Fehn et al. 2002)

2002). Mixing curves of I versus ^{129}I/^{127}I show that the V and CRL fluids have excess amounts of ^{129}I (Fig. 9.10), suggesting the presence of a volatile component derived from degassing of subducted sediments in the magmatic fluids. The mixing curve is based on a magmatic endmember with 15 micromolar iodine and ^{129}I/I ratio of 700 10^{-15}. Some data from Poas crater lake in Costa Rica are shown for comparison, which shows potentially a very similar magmatic endmember (Fehn et al. 2002). Crustal contamination with organic-rich sediments was assumed to not occur and that these are "deep" signals. The presence of a volatile component derived from subducted

Table 9.3 I, Cl and Br concentrations (mg/L) in Copahue fluids and δ^7Li, δ^{37}Cl (‰) and Iodine and Pb isotope ratios

Sampling point	Date	I	Cl	Br	δ^7Li	δ^{37}Cl	^{207}Pb/^{206}Pb	^{208}Pb/^{206}Pb	^{129}I/I × 10^{-15}
URA	1997	0.04826	911	3.1	n.a.	+0.5	n.a.	n.a.	5160 ± 380
CVL	1997	0.007366	55	0.2	n.a.	+0.3	n.a.	n.a.	n.a.
CRL	1997	0.49784	10412	22.2	+8.4	+0.5	n.a.	n.a.	701 ± 59
V	1997	n.a.	n.a.		+3.4	+0.4	n.a.	n.a.	n.a.
CRL	1999	112,141	6695	16.5	n.a.	n.a.	0.8394	20,692	921 ± 49
V	1999	0.72009	10462	22.7	n.a.	n.a.	0.8390	20,702	860 ± 90
Lago Verde	1999	0.000152	n.a.	n.a.	n.a.	n.a.	n.a.	n.a.	2367580 ± 1320050
Pool V	1999	n.a.	n.a.	n.a.	n.a.	+0.7	n.a.	n.a.	n.a.

n.a not analyzed

organic material was also suggested by Agusto et al. (2013b) based on the measurements of $\delta^{13}C\text{-}CO_2$ and $\delta^{15}N\text{-}N_2$ in fumarolic gas samples from geothermal areas of Copahue (Tassi et al. this book).

The isotope ^{36}Cl also forms in the upper atmosphere, but its halflife is too short to survive the subduction process. However, it also forms during the spontaneous fissioning of U and Th isotopes (Fehn et al. 1992). Subducted sediment rich in U and Th thus has the potential to generate ^{36}Cl during the subduction process that is then released in the arc magma generation zone. If the transfer from mantle wedge to magma reservoir and magmatic degassing is not too long (several 1000 years at most), one can expect an inventory of ^{36}Cl in these magmatic fluids. The ^{36}Cl data in the Copahue crater lake and V fluids were relatively low (3 ± 3) and no clear constraints on magma residence time can be derived from these data.

The two δ^7Li values for the crater lake and V fluids, sampled in 1997, are +8.4 ‰ and +3.4 ‰, respectively (referenced to NIST 8545). Most arc rocks have δ^7Li values at 4 ± 1.5 (White 2013). During W/R interaction, ^7Li is preferentially removed from the rock matrix, creating higher δ^7Li values in the fluid relative to the protolith. The value in the CRL fluids is higher than the mean value in arc rocks, and thus may suggest a less complete degree of rock digestion below the lake. The V fluids may stem from a part of the hydrothermal system where more complete rock digestion takes place. Other explanations are possible as well, such as digestion of rocks that have undergone earlier W/R interaction which would constitute a Li-poor but ^6Li-enriched protolith. Most importantly, these isotopes confirm the earlier data on sulfur speciation that the crater lake and the hot springs draw fluids from spatially diverse sections of the overall hydrothermal system.

The stable Pb isotopes ^{206}Pb, ^{207}Pb and ^{208}Pb were measured in fluids from the crater lake and V spring (1999 samples). The two samples have comparable values for the ratios $^{207}Pb/^{206}Pb$ and $^{208}Pb/^{206}Pb$ (Table 9.3; ^{204}Pb was not measured with the ICP-MS because of interference of

^{204}Hg), which are also very close to these ratios in rock sample COP3 (2000 eruption cinders, Varekamp et al. 2006). These data show beyond any doubt that the volcanic-hydrothermal fluids below Copahue summit are dissolving and reacting with lava flows and pyroclastic rocks from Copahue volcano. The Pb isotope ratio in the Caviahue rock series is different (Varekamp et al. 2006), which makes those less likely protoliths for the fluids.

Stable Cl isotopes were measured in several samples (Table 9.3), and these $\delta^{37}Cl/^{35}Cl$ show small positive deviations from 0 (referenced to the seawater standard), ranging from +0.3 to +0.7 ‰. Most subducted sediments have small negative stable chlorine isotope values (Sharp et al. 2007; Barnes et al. 2009). Chlorine isotope fractionations occur during fluid—gas partitioning (Liebscher et al. 2006; Sharp et al. 2007) and the acid hydrothermal fluids may have lost some HCl that escaped into the hydrothermal aquifers in the flanks of the volcano, leaving the acid fluids slightly enriched in ^{37}Cl. Alternatively, the degassing of HCl from the magma may have fractionated the isotopes, leading to a ^{37}Cl enriched component in the hydrothermal fluids; volcanic gas samples from many other volcanoes show slightly positive values as well (Eggenkamp et al. 1994). The +0.5 ‰ value for the CRL sample may also be related to the observed loss of HCl vapors from the lake favored by the elevated temperature and salinity and the extremely low pH of lake waters (Rouwet and Ohba 2015).

9.4 Temporal Variations in Fluid Chemical Compositions

9.4.1 Variations in Chemistry of Copahue Crater Lake, Vertientes Hot Springs and Upper Río Agrio

The erupted products of the period 1992–2000, (Delpino and Bermudez 1993; Varekamp et al. 2001) showed the presence of hydrothermal silica and liquid native sulfur on the lake floor and

Fig. 9.11 Temporal variations of SO_4/Cl ratios in CRL, V and URA. Note the increase values during 2000 eruption and NTA 2004
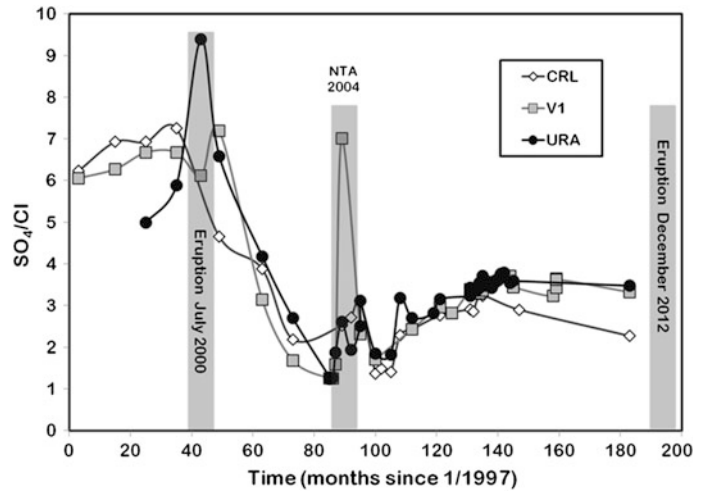
probably in the underlying system as well. Varekamp et al. (2004) suggested that the saturation indices of the fluid system became more complex during the 2000 eruptive period, with a larger number of saturated mineral phases that included alunite. Vertientes hot springs and crater lake RFE compositions before the 2000 eruptions show low pH values with high concentrations of Al, K, Ca, Ti and P. These elements drop significantly in concentration after the 2000 eruptions; the pH values rose in the V fluids, whereas the CRL remained very acidic. The Mg and Mn concentrations increased during and after the eruptions (Varekamp et al. 2001), whereas the Fe concentrations show no clear time trends. During the July 2000 eruption of Copahue, an increase of Salinity/Cl by mass was associated with a marked increase in the relative proportion of SO_4 with respect to Cl (Fig. 9.11). After the eruptive period, the relative values of the more soluble species Cl and F gradually increased with respect to SO_4 (Varekamp et al. 2009) consistent with the newly injected degassing magma in the system.

The total anion content (TAC) of CRL and V1 spring shows a temporal pattern for 2003–2012 consistent with that of lake surface temperature (Agusto et al. 2012). Lower TAC_{CRL} and TAC_{V1} values were observed during the NTA period and increase afterwards (Fig. 9.12). On the contrary, the V2 spring shows an opposite behavior:

TAC_{V2} is highest during the NTA period and decreases afterwards. This suggests that CRL and V1 were directly affected by the input of a hot SO_4-Cl rich fluid, whereas the V2 spring had an independent fluid source for this period (Fig. 9.12). Saturation indices were determined for polymorphs of silica, gypsum and sulfur for the normal conditions of the crater lake (2005) and anomalous conditions in May and August 2004 (Fazio et al. 2008). For the NTA period, the crater lake waters were saturated or supersaturated in gypsum, quartz, cristobalite and amorphous silica. When normal conditions were reestablished in 2005, the crater lake only showed saturation in quartz and cristobalite.

Simultaneously, the URA water shows a period with a lower TAC (stage 1), and a second period with a higher TAC (stage 2) contemporary with increases in TAC in CRL and V1 (Fig. 9.12). During both stages, even with different TAC, the URA waters display seasonal behavior controlled by dilution processes. It shows the highest TAC in the dry summer, a lower TAC in correspondence with snowfall in winter, and lowest TAC during the snowmelt spring-summer period. Note that during the first stage, the URA shows a relatively constant seasonal pattern only disturbed during the NTA interval (Fig. 9.12).

Comparing the ionic groups (anions and cations) respect to major magmatic species (SO_4,

Fig. 9.12 Temporal variations in TAC for CRL, V1, V2 and URA
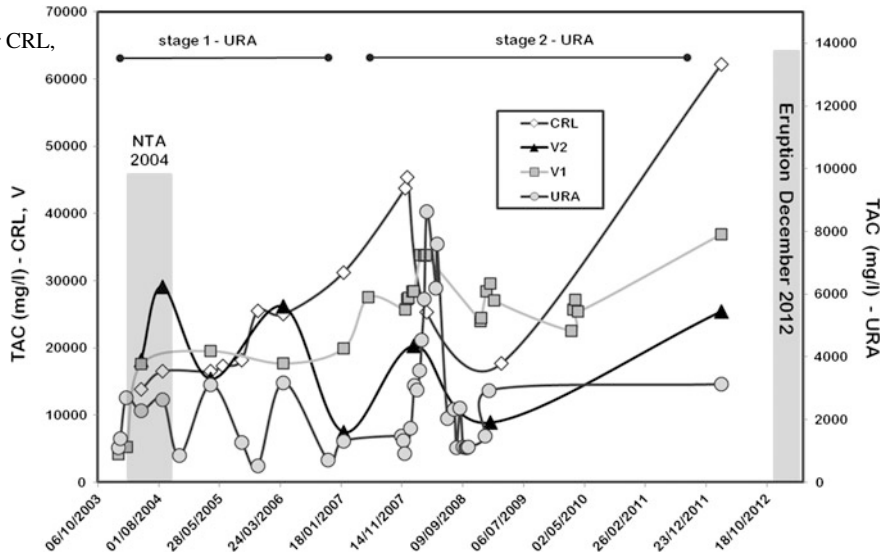
Cl, F) allows the identification of variations filtering the effects of seasonality and dilution by rainfall. They also indicate variations in the degassing regime of a magmatic system and in the water-rock interaction processes (Giggenbach and Glover 1975; Rowe et al. 1992a, b, Christenson and Wood 1993; Delmelle and Bernard 1994).

During the NTA interval, a negative excursion in Anions/SO$_4$ (mass) is documented for all members of the system (CRL, V springs and URA), indicating a relative increase in SO$_4$ compared to the rest of the anions in the waters (Fig. 9.13a). After the NTA interval, positive peaks occur in that ratio and then the whole system stabilizes with Anions/SO$_4$ at ∼1.3−1.4. The positive peaks after the NTA interval indicate a relative increase of Cl and F. This alternation of peaks in ratios points out that during the NTA initially SO$_4$ enrichment occurred followed by a relative Cl and F increase. As observed during the 2000 eruption, the order of enrichment of magmatic species (anions) is consistent with the order of degassing of these species from a rising melt or a degassing fluid (Giggenbach 1996; Symonds et al. 2001; Aiuppa et al. 2002).

The anomalous behavior of the system during the NTA interval (2004) is associated with just a disturbance of the shallow hydrothermal environment, because no eruptive event occurred. High values of Cations/SO$_4$ (mass) were observed prior to, and a marked decrease during the NTA interval, stabilizing towards the end of the sampling period (Fig. 9.13b). The relatively high RFE concentrations suggest increased primary rock leaching before the NTA. During the NTA interval, Cations/SO$_4$ values decrease as a result of a marked increase in SO$_4$, and/or precipitation of secondary minerals, which involve both the leached material and fluids coming from deep environments. Towards the end of the high frequency sampling period (2009–2010), despite a significant increase in TAC (stage 2 in Fig. 9.12), the element ratios remained constant (Fig. 9.13a, b), indicating a stabilization of the system.

The changes in cation concentrations over time are best illustrated through fluctuations in the concentrations in the V1 spring. The element-time patterns do not change dramatically when normalized to Cl (Fig. 9.14), indicating that these variations are not simply dilution effects but true inputs and withdrawals in the major cation contents through W/R interaction and secondary
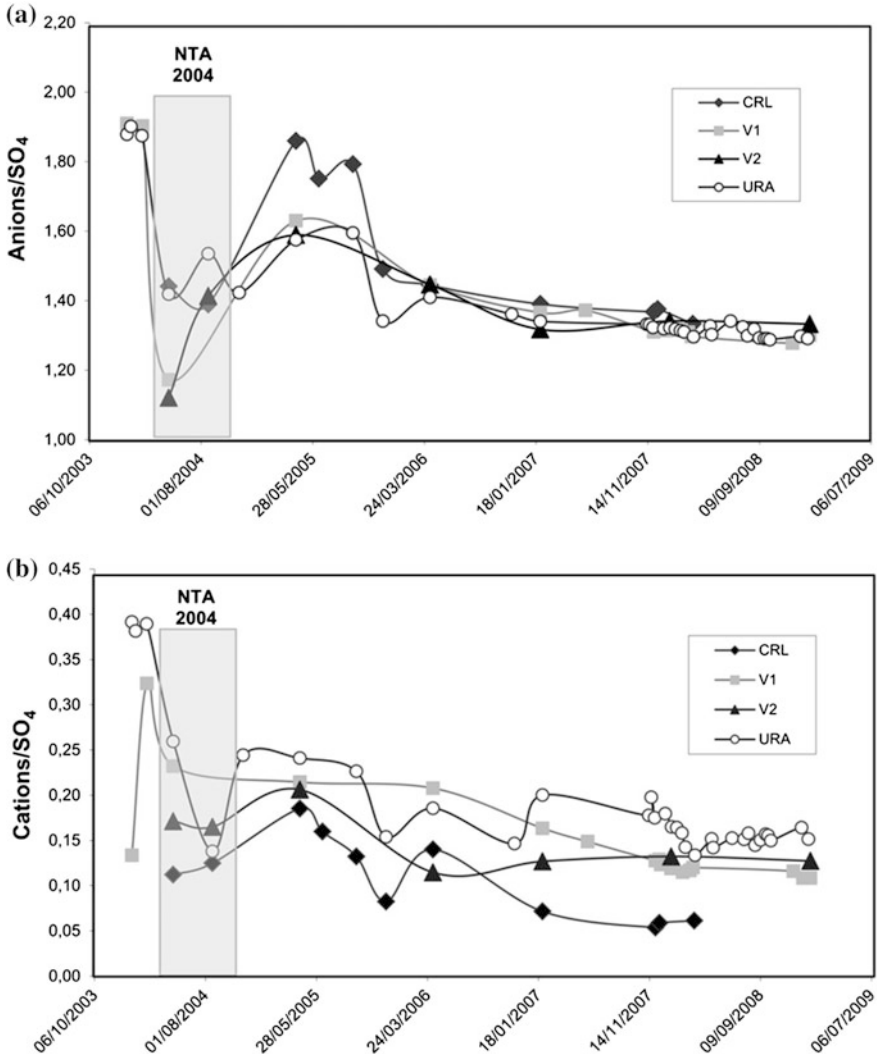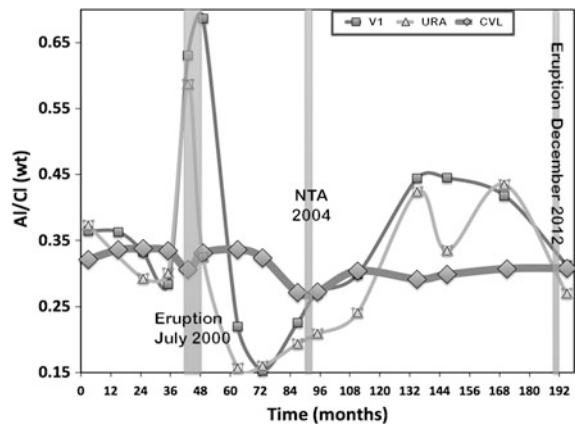
Fig. 9.13 Temporal variations in **a** Anions/SO$_4$ ratios, and **b** Cations/SO$_4$ ratios for CRL, V1, V2 and URA

Fig. 9.14 Al/Cl in the V spring, the URA and in a composite of Lake Caviahue profiles by year, showing the sharp drop after the 2000 eruption and the start of a drop after the 2012 eruption

mineral precipitation. The Al concentration in the springs and URA (and Al/Cl) drops precipitously after the 2000 eruption, which was related to the alunite crystallization in the hydrothermal reservoir. The K concentration versus time pattern is very similar.

The decrease in Al/Cl in Lake Caviahue is much more muted (Fig. 9.14), and lags those in the V spring and the URA. The large volume of CVL and its mixing properties cause these delayed responses (see below).

9.4.2 Variations in Chemistry of Lago Caviahue and the Lower Río Agrio

Lago Caviahue is a large volume (0.47 km^3) glacial lake that is kept acidic by the URA effluents. The URA discharges in between the two arms of the lake, and at this time there is uncertainty towards the mixing behavior of these fluids with respect to depth and between the two lake arms. The river water may be colder than the lake water during the spring snow melting, and more concentrated and warmer during the hot summer. A plume of cold, dilute water may descend while mixing with the lake waters in spring and the more concentrated, but slightly warmer water in summer may also descend and mix. Despite these uncertainties, the data show only minor compositional differences between the southern and northern arm of the lake at a given time, and the vertical compositional gradients are small, so these waters do mix thoroughly over time. The lake is probably fully mixed during the winter season but is thermally stratified during the summer. The water residence time was estimated at 2.5 years by Rapacioli (1985) and at ∼3.5–4.0 years by Varekamp (2003). The lake stratification negates the quantification of the mean whole-lake water residence times somewhat, but still, it indicates that the compositional variation of CVL will be lagging the compositional fluctuations in the URA. The composition of CVL is not a good aid in volcanic

surveillance, but provides a broad average of compositional trends over time without all the small compositional variations that the URA, CRL and V waters present (see above).

Secular trends in lake water composition from 1997–2006 capture the 2000 eruption and the 2004 NTA (Varekamp 2008). The compositional trends from 1997 to 2013 provide an extension of these earlier data. The pH of the lake decreased during and following the 2000 eruption, followed by a long period of relative dilution and gently increasing pH values. The pH crossed the value of 3 in 2009, but then became more acidic again in 2012, possibly prior to and after the 2012 eruption (Alexander 2014). The TDS shows a strong peak during the 2000 eruption and a small "bump" during the 2004 NTA. Overall, the lake became more dilute past 2004, but some elements started to increase again in 2006. Examples of time versus Cl, K and Mg concentrations are shown (Fig. 9.15), together with data from the Lower Rio Agrio. The mean whole lake data show a smooth trend whereas the CVL depth profiles show more scatter as they probably represent different mixing events and inputs over time in the lake. The surface water samples (A series from Agusto et al. 2012) show more variation in Cl as a result of a higher frequency sampling and the local dilution controlled by the seasonal behavior, as observed for URA. The K concentrations of Agusto et al. (2012) are mostly higher whereas the Mg values are all lower than the Varekamp (2008) data, probably a consequence of the different sampling points and imperfect mixing of the lake, although some analytical variability in either data set cannot be totally excluded.

Most striking in the pattern is the very strong dilution that takes place after the 2000 eruption: the hydrothermal system almost 'shut down' in 2001, which was documented with strongly decreased element fluxes through the URA and dilution trends in the lake, especially for Al, Fe, K, and SO_4 (Varekamp 2008). The dilution in the lake could be the same for all elements if simply the discharge from the springs decreased. The
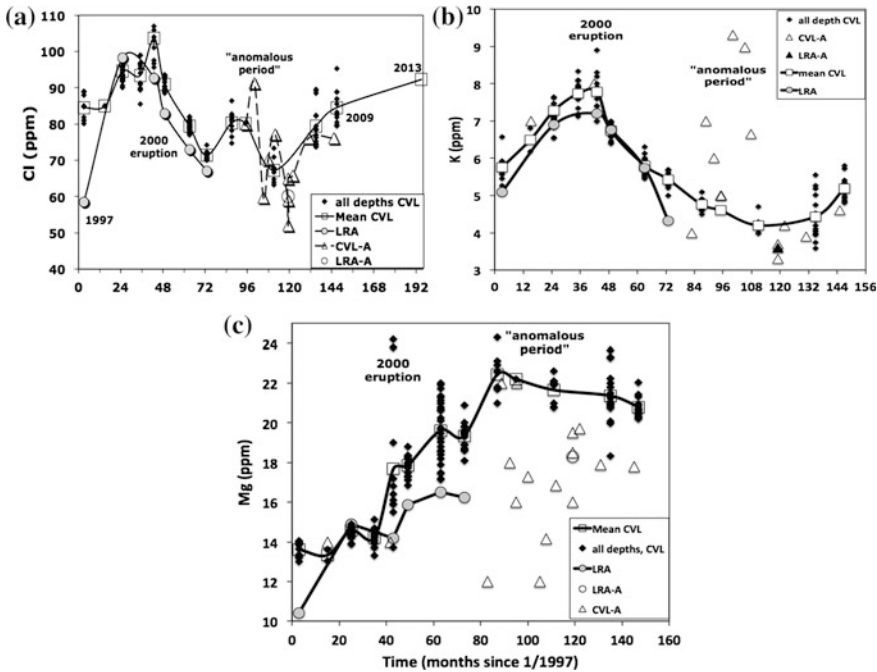
Fig. 9.15 Secular trends: **a** Trend of Cl concentration in CVL with build up to eruption followed by rapid drop off. Then again an increase during the 2004 NTA followed by a drop off and then a slow rise to 2013 values; **b** trend of K versus time, with sharp drop off after 2000 eruption and

minor to no effects during the NTA. Steep rise during the 2008–2009 period; **c** trend of Mg versus time, with an increase during the 2000 eruption but followed by a long term rise, with a slight decrease after the 2004 NTA

percentage drop was calculated from the 2000 high values for all elements and the following grouping appears: a 40–46 % drop for Cl, Al, Mg and Na whereas a bigger relative drop for K, Fe and SO_4 (56–66 %) is found. This is also shown in a 100 K/Cl versus time plot (Fig. 9.16),

indicating that after the eruption the 100 K/Cl value dropped from highs of 9 to 5.5–6, suggesting that K decreased more than Cl. The 100 K/Cl values of the A data series shows a close coherence with the other data, suggesting that local dilution effects in the surface waters

Fig. 9.16 Trend of 100 K/Cl over time, showing the drop off after the 2000 eruption and the strong decrease during the 2004 NTA. This is related to the saturation of alunite-jarosite in the hydrothermal cell below Copahue
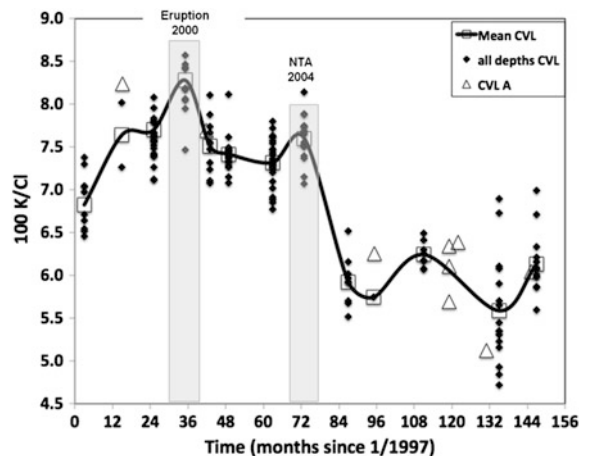
Fig. 9.17 Brown yellow Schwertmannite mineral precipitates in the riverbed near the Salto del Agrio (picture from J.C. Varekamp)

indeed played a role here. So the reduction in element fluxes into the lake is not just a diminished discharge of the V springs: also the composition of the springs changed, as discussed above in Sect. 4.1. During this period directly following the eruption, the V fluids were saturated with jarosite and alunite, and as a result the fluxes of Fe, Al, K and SO_4 diminished greatly. Assuming that the hydrothermal fluids had reacted extensively with freshly intruded plugs of new magma during the eruption, leading to higher cation contents in the fluids, a higher degree of neutralization, and oversaturation in a range of minerals. The resulting mineral precipitation reduced the permeability in the system considerably, diminishing the flow rate of the springs. The 2004 NTA saw an increase in some element fluxes but a total shut off of fluids into CRL, suggesting again a strong mineral precipitation event during early 2004, but this time localized in the upper part of the hydrothermal system. This may have been preceded by intrusions of stringers of new magma into the hydrothermal system ("failed eruptions" of Varekamp et al. 2009) or may have been just a rise of hyperconcentrated deep fluids generating a local perturbation into the shallow hydrothermal system (Agusto 2011; Vélez et al. 2011; Agusto et al. 2012).

The LRA is a diluted expression of the outflow of CVL as it receives water from small melt water streams along its course. It passes through a small water fall at the exit of the caldera (near

bridge) and then is joined by the Río Trolope, which discharges largely groundwater and meltwater, with some effluents from the Copahue village thermal areas. The rivers flow then jointly towards the large cascade of the Salto del Agrio and then further to join the Río Ñorquín and then south to Loncopue. The pH of the LRA was <3 before and during the 2000 eruption but then with the dilution of the lake the pH became close to 3.1–3.2 in the area of the confluence before the Salto. Around 2002–2003, the riverbed near the Salto del Agrio turned deep brown yellow from fresh mineral precipitates (Fig. 9.17). The riverbed further down to the confluence with the Río Ñorquín also became coated with similar 'ocher' materials. The front of mineral precipitation moved slowly upstream to very near the outlet of CVL and CVL itself became saturated with the ocher phases in 2008–2009 (Kading 2010). With the renewed acidification starting in 2011 or 2012, no more new yellow precipitates formed and the existing minerals started to dissolve again. In 2013, much of the LRA near the lake outlet had lost most of the precipitates that formed earlier. The expectation was that CVL itself would become fully saturated with the yellow mineral and would turn bright yellow-brown in 2011. The renewed acidification prevented a lake wide mineral precipitation event.

The yellow brown mineral consists of an organic slurry with small mineral particulates, suggesting the involvement of bacterial reactions

in its precipitation. Studies with Xray diffraction, SEM-EDX, reflectance spectroscopy and TEM indicated that the mineral is Schwertmannite $(Fe_8O_8(SO_4)(OH)_6nH_2O)$, which is a strong adsorbent for the polyvalent oxyanions of As, P and V (and also may build these elements into its structure on the SO_4 site). The main driver for saturation of Schwertmannite in the Fe and SO_4 rich CVL and LRA fluids is the pH: when the pH exceeds 3, the mineral will start to precipitate (Kading 2010). The ocher mineral assemblage may be a mixture of goethite-ferrihydrite and Schwertmannite because the Fe/S values are slightly higher than the stoichiometric value of Schwertmannite alone (Kading 2010). The concentrations of P, As and V on the Schwertmannite are respectively 5700, 1040 and 1800 ppm. The bacterial species ferrooxidans sp. oxidizes the Fe^{2+} in the water to Fe^{3+}, which may cycle in a diel pattern through photoreduction (Parker et al. 2008). The thick brown C_{org}-rich deposits just before the Salto del Agrio are hosting abundant green macroflora that flourish on this P-rich substrate. The N-C concentrations and stable isotope values of these organic-rich deposits are N = 2.6 %, $\delta^{15}N$ = +7.7 ‰, C = 31.3 % and $\delta^{13}C$ = −21.1, with a resulting C/N (weight) of 11.9. These analyses indicate a strong bacterial organic component in the mineral deposit, with debris of subaquatic vegetation (SAV). The bacterial chemosynthesis and the C3 photosynthesis pathway of the SAV yield the intermediate $\delta^{13}C$ value. The nitrogen possibly derived from the effluents of the sewage treatment plant of Caviahue that discharges into the lake. The dissolution of the Schwertmannite in the last few years is releasing the P and As again, possibly with harmful effects downstream. The confluence of the Lower Río Agrio and Río Ñorquín has whitish mineral precipitates, presumably Al-oxides, which may have influenced the REE patterns in the river (Gammons et al. 2005).

The chemical data of CVL waters show a general similarity with those of the URA fluids, but in detail, some differences exist, as shown above. The meltwater streams also have their impact on the chemical composition of CVL, despite their high degree of dilution. The range of composition in the URA is greater than in the CRL and V fluids as a result of the contributions of several tributaries. The issue of in situ weathering of the bedrock in the URA that may contribute to the dissolved load and ultimately to the compositional evolution of CVL has not been researched in detail and remains a topic to be explored (e.g., van Hinsberg et al. 2010).

9.5 Element Fluxes from the Copahue Hydrothermal System

Element fluxes were measured annually over the last 15 years at the URA bridge in Caviahue and near the Mapuche settlement just above the cascades area of the URA. The LRA was monitored at the bridge near the exit from the caldera. The URA data (water composition multiplied by water discharge rate) provide a good quantitative insight into chemical discharges that enter Lago Caviahue, which were tested with non-steady state models for the lake (Varekamp et al. 2009). The general agreement between the evolution of the CVL composition and measured fluxes suggests that these annual measurements provide a first order quantification of element export rates from the hydrothermal system. From these element export rates, dissolved rock export rates, which are then recast into pore space created in the reservoir, were estimated. Detailed flux estimates for each element and their variation over time were presented by Varekamp et al. (2009). The total element export rate (in tonnes/month) shows variations over time (Fig. 9.18), with strong reductions in flux just after the 2000 eruption and with the 2004 NTA. This is true for both RFE and VE, and as argued before based on element concentrations, the VE flux is much larger than the RFE flux. The response to these flux variations is clearly reflected in the compositional trends of Lake Caviahue (Fig. 9.19), providing a coherent picture. The total RFE mass flux curve also shows a strong similarity with the %AW curve based on $\delta^{18}O$ in the V fluids

Fig. 9.18 Trend in the total mass fluxes into the lake for VE and RFE. Strong pulse during the 2000 eruption and drop off afterwards (shut down) with a smaller scale repeat during the 2004 NTA
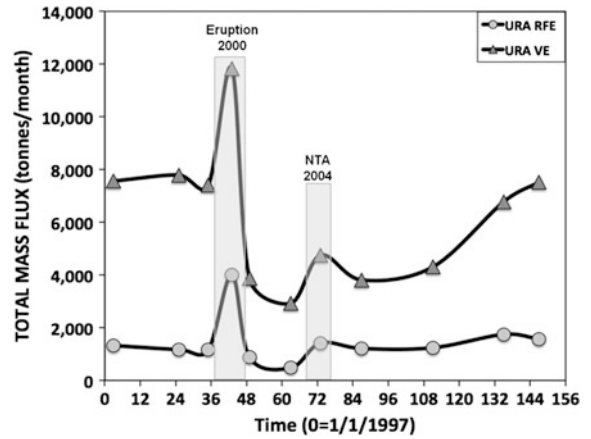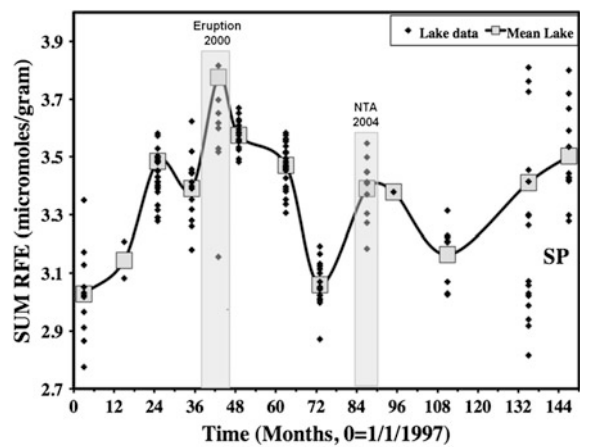

Fig. 9.19 Trend in the sum of the RFE against time, showing the 2000 eruption and 2004 NTA as positive excursions and a renewed increase in 2008–2009

(Fig. 9.9). When the hydrothermal component in the V fluids decreases, the measured fluxes in the URA decrease in a similar pattern.

The VE element export rate (Fig. 9.18) can be recast as an equivalent SO_2 flux (e.g., tonnes SO_2/day) which is the conventional parameter determined on passively degassing volcanoes that do not have a hydrothermal system that scrubs the magmatic volatiles. A mean of ~ 100 tonnes SO_2/day was exported as dissolved SO_4 through the Río Agrio over the main 12 year period of observation. Through the disproportionation reaction (Eq. 9.2), an additional fraction of magmatic sulfur is retained in the hydrothermal system as liquid sulfur and only emitted periodically as sulfur pyroclastics during phreatomagmatic events (e.g., 1992, 1995, 2000, 2012 eruptions). An estimate of this fraction,

using Eq. 9.2 is another 150 tonnes SO_2/day, for a mean total of 250 tonnes SO_2/day as the estimated magmatic sulfur flux. This is similar to many passively degassing volcanoes (http://so2.gsfc.nasa.gov), but here none of that SO_2 reaches the atmosphere because all is scrubbed as SO_4 and SO (Symonds et al. 2001). In this calculation the precipitation of anhydrite has not been considered, but is considered relatively small because Ca does not show a significant offset in the iso sol diagram (Fig. 9.6).

The RFE fluxes are a measure of rock dissolution rates in the hydrothermal system. The mean rock removal rate, using Mg as a conservative index element together with an average of all Copahue rocks (Varekamp et al. 2004) as the rock protolith is about 11,000 tonnes rock/month. That value does not consider that a

significant fraction of the rock (~ 55 %) is retained as hydrothermal silica. As a result, the net rock export rate is thus $\sim 5,000$ tonnes rock/month. This amount of rock is resupplied during the small intrusive events that occur periodically, as referred to earlier. The total amount of rock removed during the 12 year period of observation is $\sim 800,000$ tons, which would occupy a volume of about 300,000 m^3 (at a density of 2.5 g/cm^3) that is equivalent to a 500 m deep hole with a 20 m diameter. Assuming the size of the hydrothermal system at ~ 1 km^3 (underlying the whole Copahue volcanic cone), the porosity or void space created by this dissolution process can be estimated. The 'dissolution porosity' is on the order of a few % in the 12 year period. This relatively small value suggests that other processes may create more permeability and porosity, such as seismic activity and associated faulting. The total amount of dissolved rock contained in Lago Caviahue is on the order of 160,000 tonnes (corrected for silica retention in the hydrothermal system).

Of interest is also the contents of nutrients and toxins in CVL (As and P, both largely derived from the hydrothermal system) and their associated in and outfluxes. On average, 1450 tonnes F, 6 tonnes As and 2 tonnes Li per year carried into Lake Caviahue, were measured, most of which leaves again through the Lower Río Agrio. Most of the As was locked up in the Schwertmannite beds in the LRA, but F and Li probably behaved close to conservative and were further transported downstream.

9.6 Events that Impacted the Hydrothermal System at Copahue Volcano

9.6.1 The 1993, 1995 and 2000 Eruptions

Volcanic activity at Copahue has been reported since the eighteenth century, but good documentation of activity started only with the eruptive cycle beginning July 1992. That cycle continued into 1993, with major eruptions in December 1994 and September 1995. The crater lake explosions ejected hydrothermally altered rock fragments, siliceous white dust, copious amounts of green and yellow liquid sulfur and some basaltic-andesitic fragments (Delpino and Bermudez 1993, 1995). Unfortunately, no data were provided on the geochemistry of the hydrothermal fluids during this period. From 1997 to 2000, the Cl concentrations in the crater lake initially decreased, but during 1999 the concentrations and lake water temperatures increased considerably. By early 2000 the temperature of the CRL was extremely low (5–8 °C), while the Vertientes springs remained at high temperatures (70–75 °C). During July 2000 magmatic eruptions (VEI 1–2) occurred, starting with phreatomagmatic events and continuous degassing between eruptive phases until October 2000. Explosions ejected incandescent bombs and dark ash with chilled sulfur fragments covered an area up to 50 km from the crater (Global Volcano Network 2000a, b).

The RFE/Cl values and the 'degree of neutralization' (Varekamp et al. 2000) of the fluids declined in the crater lake and hot spring during the few years prior to 2000 eruption. Varekamp et al. (2001) suggested that this resulted from increased water/rock ratios in the hydrothermal system as a result of rock dissolution as well as that the rock protolith possibly became covered with liquid sulfur and/or cristobalite, slowing water-rock reaction. The REE patterns during this period showed enrichment in LREE relative to the rock. The degree of neutralization was ~ 50 % but then decreased towards lower values by late 1999, possibly signaling enhanced volcanic gas inputs from rising magma.

The July 2000 fluids show a dramatic change, the RFE/Cl ratios increased, and RFE ratios in the fluids differed from those in the older Copahue rocks and in the 2000 magma. The 2000 intrusion of fresh magma into the hydrothermal system led to increased RFE/Cl values in the fluids, and water compositions became specially enriched in Mg. During the 2000 eruption, the hot spring fluids became more concentrated, the REE pattern became closer to that of the bulk rock, and the

fluxes of Mg, Na, Fe and Al increased strongly. The composition of these fluids resulted from the incongruent dissolution of the newly intruded magma with saturation of alunite, anhydrite, and silica phases at temperatures of 150 °C and up (Varekamp et al. 2009). The retention of these secondary phases may explain why the K, Al and Ca concentrations in the fluids have increased less than those of Fe, Mg, and Na.

In the years following the 2000 eruption, strong variations in element ratios occurred, and the REE became heavily fractionated in both the HREE as well as the LREE. The negative Eu anomaly in the pre-eruptive fluids decreased in magnitude (Eu/Eu* increased) during the 2000 eruption and in late 2004, suggestive of preferential plagioclase dissolution in the fluids.

9.6.2 The 2004 NTA Event

The temperature of the CRL waters decreased in early 2004, reaching 13 °C in May 2004. By July 2004, ~ 80 % of the lake surface was frozen probably for the first time (Fig. 9.3), while hot springs displayed high water temperatures: 81 °C_{V1} and 69 °C_{V2}. During the NTA, the Anions/SO_4 ratio indicated initially a relative SO_4 enrichment followed by a relative Cl and F increase. The V2 showed an increase in TAC, while TAC_{CRL} and TAC_{V1} showed the lowest values at that time (Fig. 9.12). The temperature and TAC decrease in CRL, and simultaneous increase in V2, suggest that a decrease in the mass and heat flux occurred in the shallow part of the underlying hydrothermal system (Agusto 2011). Saturation indices of the lake water during the NTA increased for gypsum, quartz, cristobalite and amorphous silica (Fazio et al. 2008), probably the result of the arrival of a hyperconcentrated deep fluid that cooled in the shallow part of the hydrothermal system. Most likely, hydrothermal inputs into the lake ceased temporarily during the NTA as a result of partial sealing of the upper conduit and crater floor below the lake due to mineral precipitation in the fractures (Agusto et al. 2012). The permeability of the upper reaches of the hydrothermal system also may have been influenced by increased viscosity of molten sulfur present there. The viscosity of liquid sulfur increases at temperatures 150−250 °C (Oppenheimer 1992; Takano et al. 1994a, b) and a viscous cap of sulfur may have partly isolated the lake from uprising magmatic fluids

Fig. 9.20 Deflation of the Copahue volcano: **a** mean velocity deformation map 2002–2008; **b** deformation temporal serie volcano summit showing 2 cm/year subsidence since 2004. Start of deflation volcano during NTA interval
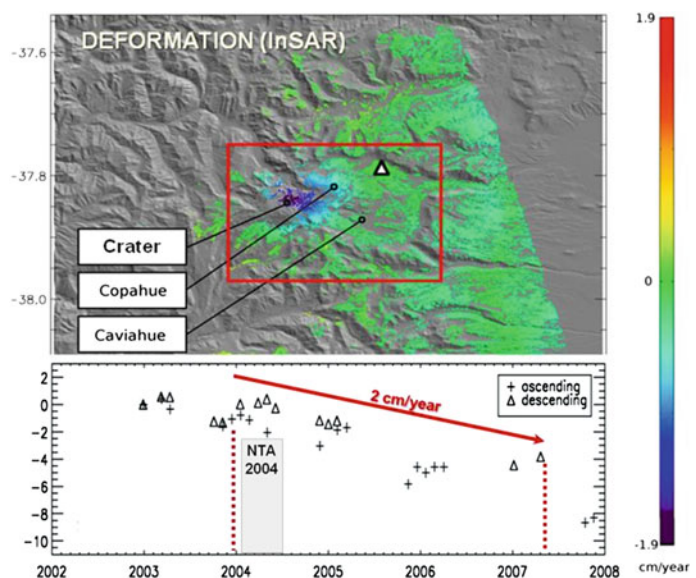
(Takano et al. 1994a, b; Delmelle et al. 2000; Christenson et al. 2010), which would be an additional explanation for the frozen lake at that time.

Deflation (negative surface deformation) was also observed since early 2004 on the Copahue volcanic edifice, with a maximum subsidence rate of 2 cm/year (Fig. 9.20; Vélez et al. 2011). Analytical models indicated that the source of deformation was located at ~ 4 km depth below the volcanic edifice, with an estimated decrease in volume of 0.0015 km^3/year (Vélez et al. this book). Deflation processes on volcanoes are sometimes associated with the release of magmatic brines from the plastic to the brittle zone (Fournier 2006), resulting in strong degassing trough the conduit toward surface. Such a process could have caused a release of hot and concentrated deep fluids into the shallow Copahue volcanic-hydrothermal system, leading to: (i) increased TAC in the V springs and URA, |(ii) secondary mineral precipitations in fractures below the crater lake, (iii) increased temperature of the molten sulfur increasing the viscosity, and thus (iv) decreased permeability in the upper part of the system ultimately leading to the freezing over of the lake (Agusto et al. 2012). The increased element export fluxes during 2004 (Varekamp et al. 2009) may support the contention that a small magmatic intrusion could have been involved as well ("failed eruption"?), although the deflation of the volcanic edifice can not be explained by such an event alone.

By the end of 2004 the crater lake icy surface melted again (Fig. 9.3), and during the following years (2005–2010) it had temperatures between 30 and 40 °C, while the outlet temperature of the two hot springs had dropped and remained relatively constant (T_{V1} = 60–70 °C, and T_{V2} = 40–50 °C). Between 2005 and 2011, the crater lake had no significant changes in temperature, and water level. On the other hand, the concentrations of anions related to the input of magmatic gases increased progressively.

9.7 Changes Affecting the Crater Volcanic-Hydrothermal System Related to the 2012 Eruption

Phreatic and phreatomagmatic eruptions occurred in 2012 after 12 years of a solfataric state. A column of water vapour and acidic gases was observed some 200–300 m above the crater in November-December 2011, indicating an increased fluid discharge rate from the volcano summit. By March 2012, the waters from the hot springs and crater lake showed (1) the highest acidity (pH < 0), (2) high temperatures (~ 65 °C), (3) highest contents of magmatic VE species (SO_4^{2-}, Cl^-, F^-) since the 2000 eruption (Fig. 9.12), and (4) a significant decrease of the crater lake water level due to enhanced evaporation (Agusto et al. 2013a).

A phreatic eruption occurred on July 17, manifested by vertical jets 10 m above the crater lake level. On July 19, a minor phreatomagmatic event occurred with the expulsion of pyroclastic material. During the following months, fumarolic activity and intense bubbling continued, the crater lake waters remained at high temperatures ($\sim 60°$), with high acidity (pH < 0), and extremely high electrical conductivity. The lake water level continued to decrease until becoming a boiling pool only ~ 20 m in diameter just before the December 2012 eruption.

A bigger phreatomagmatic eruption occurred on December 22nd (Caselli et al. this book). Chilled liquid sulfur was recognized in the erupted pyroclastic material, suggesting the presence of molten sulfur at the lake bottom or below in the hydrothermal system. As the eruption continued, the last remnants of the crater lake disappeared, the hot springs were covered by a pyroclastic surge, and the course of the URA was modified. High temperature fumaroles and liquid sulfur ponds formed inside the crater. The maximum measured fumarole temperature (420 °C) was close to the local boiling temperature of liquid sulfur (440 °C) (Agusto et al. 2013a). Two

months later, the crater lake began to reform and in March–April 2013, two water pools with intense gas bubbling were observed. During the 12 years prior to the 2012 eruption, the frequency of sampling monitoring of Copahue acidic waters (CRL, V and URA) had decreased, and not much chemical water data is available.

9.8 Conceptual Model of the Copahue Crater Volcanic-Hydrothermal System

The wealth of chemical and physical data presented above has led to a conceptual model for Copahue crater and its hydrothermal system (Fig. 9.21). Prior to and during eruptions, stringers of new magma intrude into the hydrothermal system, creating a higher pressure and temperature, and therefore a higher flow rate of the V springs and CRL input. This then is accompanied by an increase in magmatic VE species like SO_4 and Cl. The fresh rock protolith reacts with the hot acid fluids which become enriched in RFE (symbolized by e.g., much higher Mg). The fluids then evolve towards secondary mineral saturation involving sulfate bearing minerals like jarosite, alunite, anhydrite/gypsum and hydrothermal silica. The precipitation of these minerals reduces the porosity and permeability of the upper part of the system, and the formation of liquid sulfur leads to the filling of pore spaces and vents (Fig. 9.21b). This reduction in permeability after an intrusive event or eruptive period, leads to strongly reduced fluxes of all elements (reduced permeability-reduced flow rates) and especially reduced fluxes of K-Al-Fe (jarosite-alunite retention), as observed after the 2000 eruption and after the 2004 NTA. The latter was not associated with an eruption, but probably as result of an input of deep magmatic fluids and/or a small magmatic intrusion. This event caused precipitation of minerals in the high part of the system, cutting off the pathways to the crater lake which then froze over. The flow rates of the springs may have first increased (increased element fluxes) but then also decreased when further mineral precipitation reduced permeability in the system. The recovery of the system may be that with ongoing "flushing" through the system of magmatic volatiles and exhaustion of the protolith, the secondary minerals start to dissolve again (enhanced TAC and Al-K-Fe fluxes) as seen in 2008–2009, creating new permeability and enhanced fluid flow (Figs. 9.12 and 9.17).

The sealing of fractures that vent into the crater lake decreases the intensity of convection in the lake. The lake may form an incipient stratification,
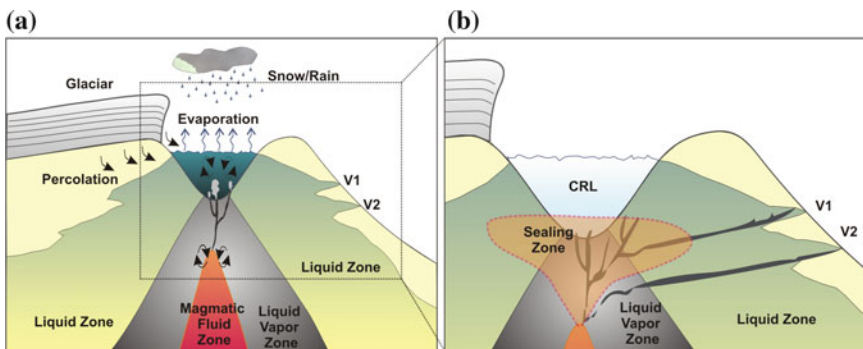
Fig. 9.21 Conceptual model for fluid circulation patterns at the Copahue crater: **a** Indication of the area affected by permeability changes in the fractures that feed the upper volcanic-hydrothermal system, physical steady-state situation: open fracture system and free movement of fluids prior to NTA period; **b** decreased permeability by fracture sealing that feed Cr and V1 during NTA period, generating the lake freezing and reduced salinity of Cr and V1 waters, channeling the flow of deep origin through V2

with warmer concentrated bottom waters affected by hydrothermal inflow, and cooler but more dilute surface waters exposed to the low atmospheric temperatures. Lake water color changes and variations in turbidity may indicate these variations in degree of stratification (Delmelle and Bernard 2000a). The combined effect of decreased heat input into the lake, with enhanced stratification may have led to the frozen lake water surface during the NTA in July 2004 (Agusto 2011).

A drop in permeability by the filling of fractures results in a gradual pressure increase in the shallow volcano-hydrothermal system. Decompression can occur through (1) a sudden pressure release through a phreatic explosion (the 1992 and 1995 phreatic eruptions), or (2) a more gradual pressure release by changes in the fluid circulation in the summit system (post-NTA period) (Agusto et al. 2012). The return to "normal" degassing then reestablishes the convective mechanism in the lake leading to thermal and compositional homogenization, manifested in the crater lake by its more normal appearance (Fig. 9.21a).

The permeability decrease of the upper part of the system, by partial or complete sealing of fractures may control the phreatic eruption dynamics. When the pressure buildup in the shallow volcanic-hydrothermal system reaches a critical value, and the decompression process does not take place by fluid drainage through flank springs, phreatic explosions are necessary to relieve the excess pressure in the summit volcanic-hydrothermal system, as occurred between 1992 and 1995.

This hypothesis is consistent with the composition of pyroclastic material ejected during the 1992 and 1995 phreatic explosions (Delpino and Bermúdez 1993, 1995) and the hydrothermally altered fragments involved in 2000 and 2012 eruptions (Delpino and Bermúdez 2002; Caselli et al. this book). In addition, the 1992 phreatic eruptions González Ferrán (1995) indicated that explosions also took place through a smaller crater outside the lake-bearing crater. This suggests that the sealing effect can become so efficient that the pressure release took place adjacent to the main volcanic duct.

9.9 Recommendations for Monitoring of Volcanic Activity at Copahue Volcano

During the last two decades, a discontinuous geochemical sampling program was carried out by various investigators on effluent waters of the Copahue volcanic-hydrothermal system. The available compiled geochemical data provide several new insights into the behavior of this system and make suggestions for improved volcanic surveillance. The Copahue crater lake is a typical example of a hyperacidic lake whose water composition may serve as a direct sensor for the hydrothermal and possibly eruptive activity of the underlying volcanic system. Traditional geochemical monitoring (e.g., SO_2 flux monitoring) is not feasible at Copahue due to the absence of summit fumaroles and the occurrence of the well-developed hydrothermal aquifer below the crater where magmatic gases are almost completely scrubbed. On the contrary, URA is a very suitable place for volcano monitoring due to its easy access throughout the year (including the winter period) and its direct relationship with the water coming downslope from the volcano that impact the RFE and VE contents as observed during the 2000 eruption (Figs. 9.11 and 9.16). The URA at the "bridge of Caviahue" (Fig. 9.1) has been most frequently sampled for waters associated with the volcanic-hydrothermal system. The URA is sensitive to seasonal changes because of inputs of snowmelt waters and rain but its seasonal behavior is predictable and reasonably well known. Temporal variations of major RFE cation contents (Fig. 9.22a) follow the seasonal pattern. Compositional variations in the magmatic-hydrothermal system are easily detected as significant deviations from the seasonal trends in the river.

Compositional variations superposed on seasonal trends were particularly noticeable during the 2004 NTA interval (Fig. 9.22). The contents of K, Mg and Al deviated from the seasonal pattern, with higher values than expected during high rainfall periods (AIC 2007). Minor elements such as Mn and B (Agusto 2011) also increased
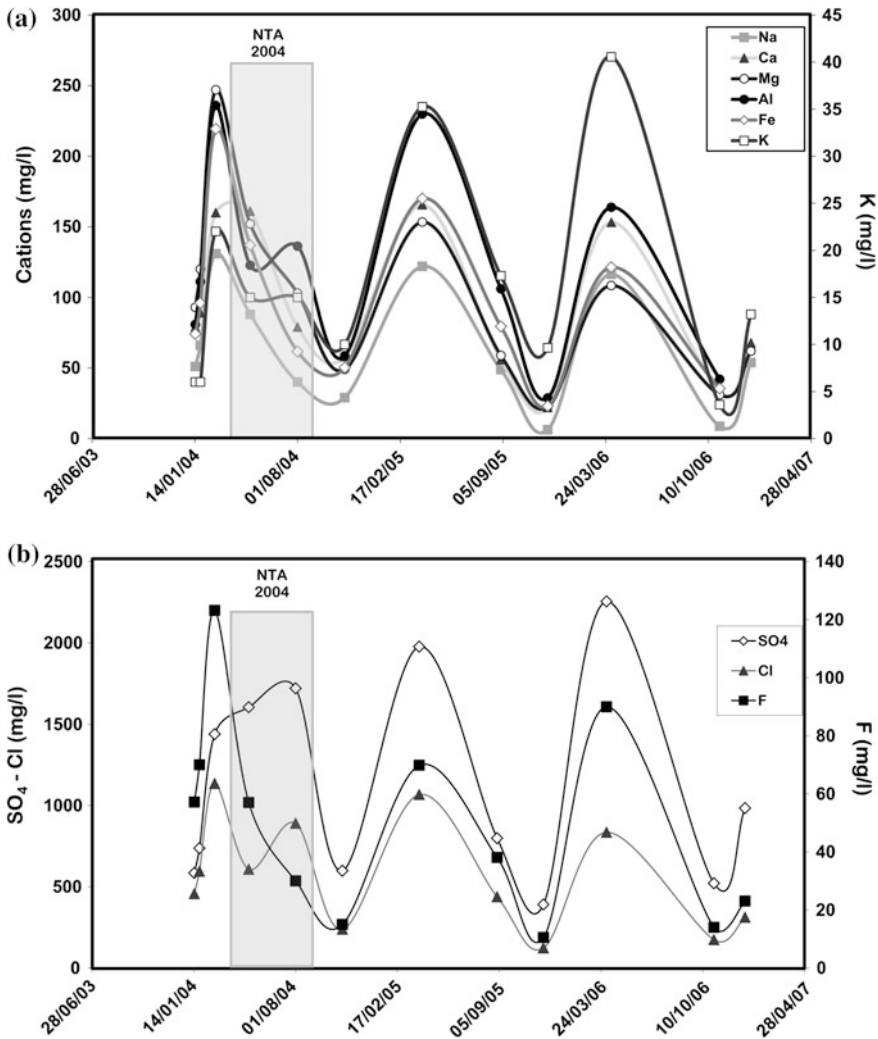
Fig. 9.22 Temporal variations in URA waters: **a** RFE, elements in mg/l; **b** aions in mg/l

at that time, suggesting enhanced hydrothermal effluxes from the system. Boron is enriched in magmatic fluids and behaves conservatively (Tonani 1970; Palmer et al. 1987; Martini 1989; Tassi et al. 2005, 2009), and an increase in B concentrations indicates a pulse of concentrated deep fluids that is transported to the surface and emitted into the URA. The increased B values were associated with enhanced VE concentrations during the NTA, with an especially sharp increase in SO_4 values, followed by Cl and to a lesser extent F (Fig. 9.21b).

SO_4/Cl, Mg/Cl and Mg/SO_4 values would make suitable indicators of disturbance

(precursors?) in the volcanic-hydrothermal environment: enhanced releases of deep hydrothermal fluids to the surface and/or enhanced water-rock interaction. An increase in SO_4/Cl ratio was observed in the system during the 2000 eruption (Fig. 9.11; Varekamp et al. 2009) which may have been related to an intrusion of new magma in the system with degassing of deep fluid during ascent. The lower solubility of SO_2 with respect to HCl in magmas may make the SO_4/Cl value a useful indicator for rising magma batches (Martini 1993; Giggenbach 1996).

The Mg/Cl ratio is a parameter widely applied in geochemical monitoring of active crater lakes

(Giggenbach 1974; Christenson 2000; Ohba et al. 2008; Tassi et al. 2009; Christenson et al. 2010; Rouwet and Tassi 2011). This ratio showed a rapid increase during the eruption of 2000, particularly in the URA (Varekamp et al. 2004). An increase in Mg/Cl in the crater lake environment can also indicate increased loss of HCl by evaporation from the lake surface (Rowe et al. 1992a; Christenson and Wood 1993; Delmelle and Bernard 2000a, b; Rouwet and Ohba 2015), making the lake environment less suitable for this parameter.

Varekamp et al. (2006) identified a less negative Eu anomaly and a correlation between the LREE enrichment pattern of erupted rocks and waters from the 2000 eruptive period, and during 2004. Accordingly, the authors explained these observations by intrusions of small magma stringers into the volcanic-hydrothermal system, with preferential dissolution of plagioclase in the early stages. These intrusions then continued with the 2000 phreatomagmatic eruption. The Eu anomaly variation during the NTA of 2004 was not followed by an eruption ("failed eruption",

Fig. 9.23 Temporal variations CRL, V and URA waters: **a** SO_4/Cl ratio; **b** Mg/Cl ratio; **c** Mg/SO_4 ratio
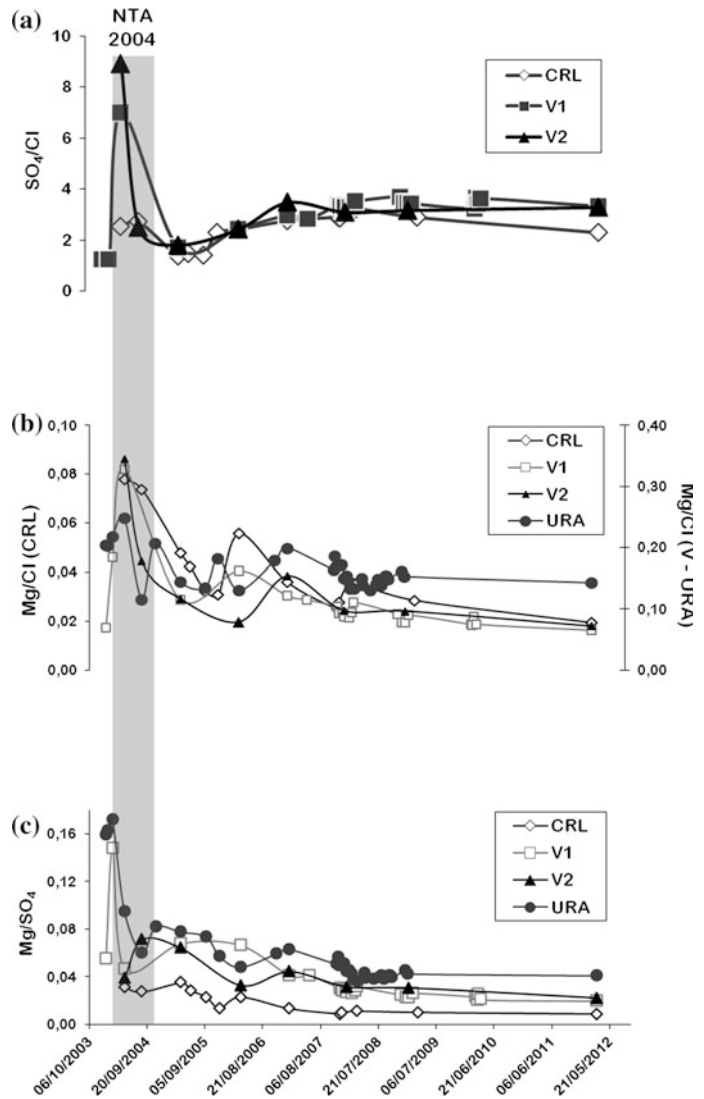
Varekamp et al. 2009), but provided evidence for a perturbation of the hydrothermal system (Agusto 2011). The enhanced SO_4/Cl and Mg/Cl values prior to the NTA interval (Fig. 9.23a,b) were excellent precursors of "hydrothermal perturbance" (Agusto et al. 2012). The SO_4/Cl seems to be a more effective predictor in V1 and V2 than in the CRL and URA, while Mg/Cl is also significant in the CRL, and Mg/SO_4 clearly indicated the upcoming NTA in the URA and V springs (Fig. 9.23c). The Al/Cl parameter may be useful to signal the beginning of the 'plugging' of the hydrothermal system and heralding a period of post-eruptive activity following an active period (Fig. 9.14).

In conclusion, the establishment of a small monitoring post with regular sample collection at the bridge of the URA at Caviahue would be the most efficient mode of starting a regular volcano monitoring program at Copahue volcano.

References

Agusto M (2011) Estudio geoquímico de los fluidos volcánicos e hidrotermales del Complejo Volcánico Copahue Caviahue y su aplicación para tareas de seguimiento. Ph.D. Thesis, Buenos Aires, Argentina, Universidad de Buenos Aires, pp 294

Agusto M, Tassi F, Caselli A, Vaselli O, Rouwet D, Capaccioni B, ChiodiniG (2013a) Thermal and chemical changes in the crater lake of Copahue volcano (Argentina) prior to the December 2012 phreatomagmatic eruption. IAVCEI General Assembly 2013, Kagoshima Japan, pp 1019

Agusto M, Tassi F, Caselli A, Vaselli O, Rouwet D, Capaccioni B, Caliro S, Chiodini G, Darrah T (2013b) Gas geochemistry of the magmatic-hydrothermal fluid reservoir in the Copahue-Caviahue Volcanic Complex (Argentina). J Volcanol Geoth Res 257:44–56

Agusto M, Tassi F, Caselli A, Vaselli O, dos Santos Afonso M (2012) Seguimiento geoquímico de las aguas ácidas del sistema volcán Copahue – Río Agrio: posible aplicación para la identificación de precursores eruptivos. Rev As Geol Arg 69(4):481–495

Aiuppa A, Federico C, Paonita A, Pecoraino G, Valenza M (2002) S, Cl and F degassing as an indicator of volcanic dynamics: the 2001 eruption of Mount Etna. Geophys Res Lett 29. doi: 10.1029/2002GL0150322004

Alexander E (2014) Aqueous geochemistry of an active magmato-hydrothermal system: Copahue Volcano, Río Agrio, and Lake Caviahue, Neuquén, Argentina.

BA Thesis Middletown, CT USA, Wesleyan University, pp 100

AIC (2007) Autoridad Interjurisdiccional de las Cuencas de los ríos Limay, Neuquén y Negro. Datos meteorológicos de la región de Caviahue entre los años 2003 y 2007. Cipolletti, Río Negro, Informe Inédito, pp. 5

Barnes JD, Sharp ZD, Fischer TP (2009) Variations in chlorine stable isotopes along the Central American volcanic front. Geochem Geophys Geosys 7:Q08015. doi:10.1029/2009GC002587

Bermudez A, Delpino D (1995) Mapa de los peligros potenciales en el área del Volcán Copahue – sector Argentino. Volcanic Hazard Map. The Geological Survey of the Province of Neuquen, Argentina

Boschetti T (2013) Oxygen isotope equilibrium in sulfate–water systems: a revision of geothermometric applications in low-enthalpy systems. J Geochem Explor 124:92–100

Bowen GJ, Revenaugh J (2003) Interpolating the isotopic composition of modern meteoric precipitation. Water Resour Res 39(10):1299. doi:10.129/2003WR002086

Brown G, Rymer H, Dowden J, Kapadia P, Stevenson D, Barquero J, Morales LD (1989) Energy budget analysis for Poás crater lake: implications for predicting volcanic activity. Nature 339:370–373

Caselli A, Agusto M, Fazio A (2005) Cambios térmicos y geoquímicos del lago cratérico del volcán Copahue (Neuquén): posibles variaciones cíclicas del sistema volcánico. XVI Congreso Geológico Argentino, La Plata, Argentina, pp 751–756

Caselli A, Vélez ML, Agusto M, Forte P, Albite J, Daga R (2013) Erupción del volcán Copahue (Argentina): evolución, productos e impacto social y ambiental. Foro Internacional sobre Peligros Geológicos, Arequipa, Peru, pp 104–109

Christenson BW (2000) Geochemistry of fluids associated with the 1995–1996 eruption of Mt. Ruapehu, New Zealand: signatures and processes in the magmatic hydrothermal system. J Volcanol Geoth Res 97:1–30

Christenson BW, Wood CP (1993) Evolution of a vent-hosted hydrothermal system beneath Ruapehu Crater Lake, New Zealand. Bull Volcanol 55:47–565

Christenson BW, Werner CA, Reyes AG, Sherburn S, Scott BJ, Miller C, Rosenburg MJ, Hurst AW, Britten K (2007) Hazards from hydrothermally sealed volcanic conduits. EOS 88(50):53–55

Christenson BW, Reyes AG, Young R, Moebis A, Sherburn S, Cole-Baker J, Britten K (2010) Cyclic processes and factors leading to phreatic eruption events: Insights from the 25 September 2007 eruption through Ruapehu Crater Lake, New Zealand. J Volcanol Geoth Res 191:15–32

Craig H (1961) Isotopic variations in meteoric waters. Science 133:1702–1703

Craig H, Gordon LI, Horibe Y (1963) Isotopic exchange effects in the evaporation of water. J Geophys Res 68:5079–5087

Cronin SJ, Hodgson KA, Neall VE, Palmer AS, Lecointre JA (1997) 1995 Ruapehu lahars in relation

to the late Holocene lahars of Whangaehu River. New Zealand. NZ J. Geol Geophys 40:507–520

Delmelle P, Bernard A (1994) Geochemistry, mineralogy, and chemical modeling of the acid crater lake of Kawah Ijen Volcano, Indonesia. Geochim Cosmochim Acta 58(11):2445–2460

Delmelle P, Bernard A (2000a) Volcanic lakes. Encyclopedia of Volcanology. Academic Press, pp 877–896

Delmelle P, Bernard A (2000b) Downstream composition changes of acidic volcanic waters discharged into the Banyupahit stream, Ijen caldera, Indonesia. J Volcanol Geoth Res 97:55–75

Delmelle P, Bernard A, Kusakabe M, Fisher TP, Takano B (2000) Geochemistry of the magmatic hydrothermal system of Kawah Ijen volcano, east Java, Indonesia. J Volcanol Geoth Res 97:31–53

Delpino D, Bermudez A (1993) La Actividad del Volcan Copahue durante 1992: Erupcion con emisiones de azufre piroclastico, Provincia del Neuquen, Argentina. XII Congreso Geologico Argentino, Mendoza, Argentina, pp 292–301

Delpino D, Bermúdez A (1995) Eruptions of pyroclastic sulfur at crater lake of Copahue Volcano, Argentina. International Union of Geodesy and Geophysics. XXI General Assembly, Boulder, USA, pp 128

Delpino DH, Bermudez AM (2002) La erupción del volcán Copahue del año 2000. Impacto social y al medio natural. Provincia del Neuquen, Argentina. XV Congresso Geologico Argentina, El Calafate, Argentina

Eggenkamp HG, Middelburg J, Kreulen R (1994) Preferential diffusion of ^{35}Cl relative to ^{37}Cl in sediments of Kau Bay, Halmahera, Indonesia. Chem Geol 116:317–325

Fazio A, Agusto M, Farías S, Caselli A (2008) Evaluación de posibles fases minerales en equilibrio en el sistema volcánico Copahue (Neuquén) y su vinculación con parámetros químicos. XVII Congreso Geológico Argentino. Jujuy. Argentina, pp 1343–1344

Fehn U, Peters E, Tullai-Fitzpatrick S, Kubik P, Sharma P, Teng R, Gove H, Elmore D (1992) 129I and 36Cl concentrations in waters of the eastern Clear Lake area, California: residence times and source ages of hydrothermal fluids. Geochim Cosmochim Acta 56:2069–2079

Fehn U, Snyder G, Varekamp JC (2002) Detection of recycled marine sediment components in crater lake fluids using ^{129}I. J Volcanol Geoth Res 115:451–460

Fournier RO (2006) Hydrothermal systems and volcano geochemistry. In: Dzurisin D (ed) Volcano deformation. Springer, Berlin, pp 153–194

Gammons C, Wood S, Pedrozo F, Varekamp J, Nelson B, Shope C, Baffico G (2005) Hydrogeochemistry and rare earth element behavior in a volcanically acidified watershed in Patagonia, Argentina. Chem Geol 222:249–267

Gat JR (1995) Stable isotopes of fresh and saline lakes. In: Lerman A, Imboden D, Gat J (eds) Physics and chemistry of lakes. Springer, Berlin, pp 139–165

Gat JR, Levy Y (1978) Isotope hydrology of inland sabkhas in the Bardawil area, Sinai. Limnol Oceanogr 23(5):841–850

Gibson JJ, Edwards TW, Prowse TD (1999) Pan-derived isotopic composition of water vapour and its variability in northern Canada. J Hydrol 217:55–74

Giggenbach WF (1974) The chemistry of Crater Lake, Mt. Ruapehu (New Zealand) during and after the 1971 active period. NZ J Sci 17:33–45

Giggenbach WF (1987) Redox processes governing the chemistry of fumarolic gas discharges from White Island, New Zealand. Appl Geochem 2:143–161

Giggenbach WF (1996) Chemical composition of volcanic gases. In: Scarpa WF, Tilling (eds) Monitoring and mitigation of Volcano Hazards. Springer, Berlin, pp 222–256

Giggenbach WF, Glover RB (1975) The use of chemical indicators in the surveillance of volcanic activity affecting the crater lake on Mt. Ruapehu. NZ Bull Volcanol 39:70–81

Giggenbach WF, Corrales Soto R (1992) Isotopic and chemical composition of water and steam discharges from volcanic-magmatic-hydrothermal systems of the Guanacaste geothermal province, Costa Rica. Appl Geochem 7:309–332

GVN (2000a) Frequent Ash explosions and acidic mudflows starting on July 1. Bull Global Volcano Netw 25:6

GVN (2000b) Continued ash explosions and tremor during August–October. Bull of Global Volcano Netw 25:9

Healy J, Lloyd EF, Banwell CJ, Adams RD (1965) Volcanic eruption on Raoul Island, November 1964. Nature 205:743–745

Kading T (2010) Natural pollutant attenuation by schwertmannite at Copahue Volcano, Argentina. M.A. Thesis, Wesleyan University, Middletown, CT, USA, p 247

Kusakabe M, Komoda Y, Takano B, Abiko T (2000) Sulfur isotope effects in the disproportionation reaction of sulfur dioxide in hydrothermal fluids: implications for the δ^{34}S variations of dissolved bisulfate and elemental sulfur from active crater lakes. J Volcanol Geoth Res 97:287–308

Liebscher A, Barnes JD, Sharp ZD (2006) Chlorine isotope vapor–liquid fractionation during experimental fluid-phase separation at 400 C/23 MPa to 450 C/42 MPa. Chem Geol 234:340–345

Martini M (1989) The forecasting significance of chemical indicator in areas of quiescent volcanism: examples from Vulcano and Phlegrean Fields (Italy). In: Latter JH (ed) Volcanic hazard. Springer, Berlin, pp 372–383

Martini M (1993) Gases Volcánicos. In: Martí J, Araña V (eds) La volcanología actual. Nuevas Tendencias. Consejo Superior de Investigaciones Científicas, España, pp 387–444

Martini M, Giannini L, Buccianti A, Prati F, Cellini Legittimo P, Iozzelli P, Capaccioni B (1991) 1980–

1990: ten years of geochemical investigation at Phlegrean Fields (Italy). J Volcanol Geoth Res 48:161–171

Mas L, Mas G, Bengochea L (2000) Heatflow of Copahue geothermal field, its relation with tectonic scheme. In: Proceedings of world geothermal congress, Tohoku, Japan, pp 1419–1424

Mayr C, Lu A, Stichler W, Trimborn P, Ercolano B, Oliva G, Ohlendorf C, Soto J, Fey M, Haberzettl T, Janssen S, Scha F, Schleser GH, Wille M, Zolitschka (2007) Precipitation origin and evaporation of lakes in semi-arid Patagonia (Argentina) inferred from stable isotopes (δ^{18}O, δ^2H). J Hydrol 334:53–63

Morrissey M, Gisler G, Weaver R, Gittings M (2010) Numerical model of crater lake eruptions. Bull Volcanol 72:1169–1178

Naranjo JA, Polanco E (2004) The 2000 AD eruption of Copahue Volcano, Southern Andes. Rev Geol Chile 31(2):279–292

Ohba T, Hirabayashi J, Nogami K (2008) Temporal changes in the chemistry of lake water within Yugama Crater, Kusatsu-Shirane Volcano, Japan: implications for the evolution of the magmatic-hydrothermal system. J Volcanol Geoth Res 178:131–144

Oppenheimer C (1992) Sulphur eruptions at Volcán Poás, Costa Rica. J Volcanol Geoth Res 49:1–21

Ouimette AP (2000) Hydrothermal processes at an active volcano, Copahue, Argentina. M.A. Thesis, Wesleyan University, Middletown, CT, USA, pp 220

Palmer MR, Spivack AJ, Edmond JM (1987) Temperature and pH controls over isotopic fractionation during adsorption of boron on marine clays. Geochim Cosmochim Acta 51:2319–2323

Panarello HO (2002) Características isotópicas y termo-dinámicas de reservorio del campo geotérmico Copahue-Caviahue, provincia del Neuquén. Rev As Geol Arg 57(2):182–194

Parker S, Gammons C, Pedrozo F, Wood S (2008) Diel changes in metal concentrations in a geogenically acidic river: Rio Agrio, Argentina. J Volcanol Geotherm Res 178:213–223

Pasternack G, Varekamp J (1997) Volcanic lake systematics I. Physical constraints. Bull Volcanol 58:528–538

Pedrozo F, Temporetti P, Beamud G, Diaz M (2008) Volcanic nutrient inputs and trophic state of Lake Caviahue, Patagonia, Argentina. J Volcanol Geoth Res 178:205–212

Rapacioli R (1985) Lake Caviahue and its basin. Tech. Report, EPAS Gov. Office, Province of Neuquen, Argentina, pp. 1–72

Rouwet D, Ohba T (2015) Isotope fractionation and HCl partitioning during evaporative degassing from active crater lakes. In: Rouwet D, Christenson BW, Tassi F, Vandemeulebrouck J (eds) Volcanic lakes. Springer, Heidelberg, pp 179–200

Rouwet D, Tassi F (2011) Geochemical monitoring of volcanic lakes. A generalized box model for active crater lake. Ann Geophys 54(2):161–173

Rowe GL Jr, Brantley SL, Fernandez M, Fernandez JF, Borgia A, Barquero J (1992a) Fluid-volcano interaction in an active stratovolcano: the crater lake system of Poás volcano, Costa Rica. J Volcanol Geoth. Res 49:23–51

Rowe GL Jr, Ohsawa S, Takano B, Brantley SL, Fernandez JF, Barquero J (1992b) Using crater lake chemistry to predict volcanic activity at Poás volcano, Costa Rica. Bull Volcanol 54:494–503

Seal RR, Alpers CN, Rye RO (2000) Stable isotope systematics of sulfate minerals. In: Alpers CN, Jambor JL, Nordstrom DK (eds) Sulfate minerals—crystallography: geochemistry and environmental significance, pp 541–602

Sharp ZD, Barnes JD, Brearley AJ, Chaussidon M, Fischer TP, Kamenetsky VS (2007) Chlorine isotope homogeneity of the mantle, crust and carbonaceous chondrites. Nature 446:1062–1065

Stoibert J, Rose W (1970) The geochemistry of Central-American volcanic gas condensates. Geol Soc Amer Bull 81:2891–2912

Symonds RB, Gerlach TM, Reed MH (2001) Magmatic gas scrubbing: implications for volcano monitoring. J Volcanol Geoth Res 108:303–341

Takano B, Watanuki K (1989) Monitoring of volcanic eruptions at Yugama crater lake by aqueous sulfur oxyanions. J Volcanol Geoth Res 40:71–87

Takano B, Ohsawa S, Glover RB (1994a) Surveillance ofRuapehu Crater Lake, New Zealand, by aqueous polythionates. J Volcanol Geoth Res 60:29–57

Takano B, Saitoh H, Takano E (1994b) Geochemical implications of subaqueous molten at Yugama crater lake, Kusatsu-Shirane volcano, Japan. Geochem J 28:199–216

Taran YA, Pokrovsky BG, Dubik YM (1989) Isotopic composition and origin of water from andesitic magmas. Dokl (Trans) Ac Sci USSR 304:440–443

Tassi F, Vaselli O, Capaccioni B, Giolito C, Duarte E, Fernández E, Minissale A, Magro G (2005) The hydrothermal-volcanic system of Rincon de la Vieja volcano (Costa Rica): a combined (inorganic and organic) geochemical approach to understanding the origin of the fluid discharges and its possible application to volcanic surveillance. J Volcanol Geoth Res 148:315–333

Tassi F, Vaselli O, Fernández E, Duarte E, Martínez M, Delgado-Huertas A, Bergamaschi F (2009) Morphological and geochemical features of crater lakes in Costa Rica: an overview. J Limnolo 68(2):193–205

Tonani F (1970) Geochemical methods of exploration for geothermal energy. Geothermics 2:492–515

van Hinsberg V, Berlo K, Sumarti S, van Bergen M, Williams-Jones E (2010) Extreme alteration by hyperacidic brines at Kawah Ijen volcano, East Java, Indonesia: II Metasomatic imprint and element fluxes. J Volcanol Geoth Res 196:169–184

Varekamp J (2003) Lake contamination models: evolution towards steady state in stratified lakes. J Limnol 62 (1):67–72

Varekamp J (2008) The acidification of glacial Lake Caviahue, Province of Neuquen, Argentina. J Volcanol Geoth Res 178:184–196

Varekamp JC, Kreulen R (2000) The stable isotope geochemistry of volcanic lakes: examples from Indonesia. J Volcanol Geoth Res 97:309–327

Varekamp J, Pasternack G, Rowe G (2000) Volcanic lake systematics. II. chemical constraints. J Volcanol Geotherm Res 97:161–179

Varekamp J, Ouimette A, Herman S, Bermudez A, Delpino D (2001) Hydrothermal element fluxes from Copahue, Argentina: a "beehive" volcano in turmoil. Geology 29:1059–1062

Varekamp J, Ouimette A, Kreulen R (2004) The magmato-hydrothermal system of Copahue volcano, Argentina. In: Wanty RB, Seal II RB (eds) Water–rock interaction 11, vol 1. Balkema Publishers, Leiden, pp 215–218

Varekamp J, Maarten de Moor J, Merrill M, Colvin A, Goss A, Vroon P, Hilton D (2006) The geochemistry and isotopic characteristics of the Caviahue Copahue volcanic complex, Province of Neuquen, Argentina. Geol Soc Am 407:317–342

Varekamp J, Ouimette A, Herman S, Flynn K, Bermudez A, Delpino D (2009) Naturally acid waters from Copahue volcano, Argentina. Appl. Geochem 24:208–220

Varekamp J (2015) The chemical composition and evolution of volcanic lakes. In: Rouwet D, Christenson BW, Tassi F, Vandemeulebrouck J (eds) Volcanic lakes. Springer, Heidelberg, pp 93–123

Vaselli O, Tassi F, Duarte E, Fernández E, Poreda R, Delgado-Huertas A (2010) Evolution of fluid geochemistry at the Turrialba volcano (Costa Rica) from 1998 to 2008. Bull Volcanol 72:397–410

Velez ML, Euillades P, Caselli A, Blanco M, Martinez Diaz J (2011) Deformation of Copahue volcano: inversion of InSAR data using a genetic algorithm. J. Volcanol. Geoth. Res 202:117–126

White WM (2013) Geochemistry. Oxford, UK, Blackwell-Wiley, p 672

Risk Assessment and Mitigation at Copahue Volcano

10

A.T. Caselli, C. Liccioli and F. Tassi

Abstract

"Risk assessment" is a relatively new concept in Argentina, since the very first hazard map was only recently constructed on the basis of the 1992 eruption of Copahue volcano (Patagonia). Copahue is considered a very active volcanic system since 13 eruptive events have been recognized over the last 260 years. Most the events are phreatic and phreato-magmatic with VEI ≤ 2; nevertheless such eruptions represent a threat for the communities living in the surrounding areas of the emission centre, not only because of pyroclastic flows and tephra fall (the nearby villages, Caviahue and Copahue, have so far only experienced ash fallout), but also due to the possible formation of mud flows and flank collapse triggered by the volcanic activity. Owing to the frequent eruptions of Copahue, the most recent ones (2000, 2012) showed an increasing explosive character, hazard survey actions, such as thematic maps and contingency plans are constantly, though slowly, modified. The risk assessment described in this chapter calls for the implementation of the monitoring network in the Argentina side of the volcano, since the only currently active seismic stations (OVDAS) are located in the Chilean side of the volcanic edifice, Copahue volcano lying at the border between the two countries. Moreover, the Chilean observatory adopts criteria of alert levels, which

A.T. Caselli (✉)
LESVA, IIPG, Universidad Nacional de Río Negro,
Roca 1242, 8332 General Roca, Argentina
e-mail: atcaselli@unrn.edu.ar

C. Liccioli
GESVA - IDEAN (UBA-CONICET), Dpto. Cs.
Geológicas, FCEN, Universidad de Buenos Aires,
1428 Ciudad Universitaria, Pab.2, Buenos Aires,
Argentina

F. Tassi
Department of Earth Sciences, University of
Florence, (IGG-CNR), Via La Pira, 4, Florence, Italy

are distinctly different with respect to those of Argentina Civil Defense, producing misleading information to the population. The villages of Copahue and Caviahue are regarded as extremely vulnerable to possible future eruptions if larger magnitude events should occur. A review of the presently available potential hazard map, an improvement of people's education about the volcanic risks and a more interactive cooperation between the Chilean and Argentina scientific and administrative institutions are some of the immediate countermeasures to be taken into account before a new explosive phase at Copahue.

10.1 Introduction

Volcanic hazard represents a special case of natural potentially catastrophic events due to the unpredictability of occurrence and duration of volcanic activity. A volcanic eruption can have immediate dramatic consequences on all forms of life under the threat of disaster, besides destroying properties, economic activities, public services, and all goods. Moreover, it may continue to impact on the environment for an indeterminable time span. For example, Arenal, a basaltic andesitic stratovolcano situated in Costa Rica, had a long-lived eruption that began in 1968 with a Pelean eruption after 530 years of dormancy (Alvarado et al. 2006). Since 1974, one of three newly formed craters (crater C) was the only active crater, whose activity lasted until 2011. Arenal has alternated long, predominantly effusive phases with shorter explosive phases (Oramas-Dorta et al. 2012). Damages can directly be related to eruptive activity, such as those caused by the accumulation of ash or indirectly connected. For instance, the phreatomagmatic eruption of the Hudson volcano (southern Chile) in 1991 caused the death of a great part of the sheep flocks in the Province of Santa Cruz, due to the considerable destruction of the vegetal cover. The distribution of the deposits affected a region greater than 300,000 km^2 and a > 1 m thick ash layer accumulated in the areas near the volcano. Bitschene and Menida (1995) evaluated that this eruption implied, in the provinces of Chubut and Santa Cruz, direct losses estimated in about US

$10,000,000 and included cattle death, economic damages, restoration of water supply systems, airports, roads, communication and electric equipment, and so forth.

The active cordilleran magmatic arc, related to the subduction of the Nazca plate under the South American started in early Cretaceous time, has migrated to the west in recent geological times. Active and quiescent volcanoes are mostly located along the Argentina-Chile boundary or few kilometers to the west, in the Chilean territory. The eruptive centers along the arc are mainly Pliocene, Pleistocene, and Holocene huge stratovolcanoes, andesitic-dacitic calderas, and basaltic plateaus (Sruoga et al. 1993), related to the last great uplifting and faulting events in the Andean chain. Some of these volcanoes may be perceived as remote because of limited accessibility, but dispersal of fallout tephra produced by explosive eruptions easily overcomes the distances separating volcanoes from the urban areas, placing them volcanologically in the endangered vicinity (Dzierma et al. 2010). During the twentieth century, several eruptions occurred in this region (Descabezado-Quizapu in 1932; Tupungatito in 1952, 1980, and 1986; Peteroa in 1937 and 1991; Hudson in 1991; Copahue in 1992, 2000; Lascar in 1989 and 1993), all of them accompanied by ash rain, which in some cases extended over wide areas, including western Argentina.

The segment of the Andean chain named the Southern Volcanic Zone where Copahue volcano is located currently presents a big concern, although the volcanoes of this area do not

commonly show explosions of large magnitude (with the exception of Hudson volcano). Large parts of the regions adjacent to this segment of the Andes in both Chile and Argentina are indeed intensely used by the population for living, industrial zones, agricultural production, recreation and tourism (Dzierma and Wehrmann 2012). The increasing urban development implies that even relatively small phreatomagmatic explosions could cause both substantial economic losses and hazard.

Copahue volcano showed an intense activity over the last 260 years, with 13 recognized eruptions (see Caselli et al. this volume), the last of which occurred in December 2012. The eruptive style was mainly phreatic and phreatomagmatic, similar to those occurred in 2000 and 2012. Despite their low explosive character (VEI, Volcanic Explosive Index ≤ 2), the eruptions strongly impacted on the surrounding. The eruptive episodes that occurred in 2000 had negative repercussion on the tourist locality of Caviahue, populated by 800 to 1,500 inhabitants depending on the season.

In this chapter, a critical review of the risk related to Copahue volcano is presented. The description and characterization of the volcanic activity, that is to say the starting points to develop an appropriate risk evaluation, are detailed reported in dedicated chapters of this book. The spatial distribution of products ejected during the past eruptions was considered for the realization of the hazard maps aimed to mitigation strategies from the local authorities and scientist.

10.2 Volcanic Risk Mitigation Measures

Volcanic hazard mitigation is based on three fundamental requisites: (i) construction of an updated volcanic hazard map to determine the best land use to minimize damages in case of eruption, (ii) continuous volcanic monitoring using geophysical, geochemical and geodetic methods, and (iii) a contingency plan involving the whole community, known and practiced by all, in case of volcanic activity.

10.2.1 Hazard Map

Maps of potential volcanic hazards are to identify areas that might be affected by volcanic activity in accordance with the recent history of the volcano. Such maps do not imply analysis of vulnerability and therefore they cannot be considered in a strict sense as maps of risk (Parra and Cepeda 1990). The latter are obtained by combining the hazard maps with socio-vulnerability information. Hazard maps are considered essential tools in the communication of volcanic risk among scientists, local authorities and population (Haynes et al. 2007). Hazard and risk assessment is usually completed for specific authorities, who may have different concerns, i.e. civil defense bodies are mostly interested in evacuation and short term mitigation, while planners are responsible for land use planning (Lirer and Vitelli 1998).

In the last few decades, hazard maps were realized in densely populated areas characterized by active volcanism, often after the occurrence of catastrophic eruptions, as consequence of the low perception of risk due to the long (if considered at human scale) quiescent period between two volcanic events. This factor generates a wait before mitigation measures are taken, as in the case of Nevado del Ruiz volcano (Colombia) that in November 1985, after 140 years from the last explosive activity, produced a relatively small eruption that melted part of the summit glacier. The resulting lahar killed about 25,000 people. It was then decided to give immediate priority to prepare a volcanic hazard map for visual and geochemical surveillance of the volcanic activity and to improve the seismic network (Parra and Cepeda 1990). Merapi volcano (central Java) represents another case study where a detailed hazard map constituted a pivotal element to draft guidelines aimed to reduce risk exposure to persons and property and provide information for the productive use of land and water: here lahar deposition, associated to at least 23 of the 61 reported eruptions since the mid-1500s,

encompassed more than 280 km^2 of the volcano slopes and the surrounding lowlands. Hazard maps (1:10,000 and 1:2,000 for the highly populated areas) allowed the scientists to (i) provide correct values of the previous underscore risk in zone threatened by lahars and (ii) suggest countermeasures such as construction of dam structures to protect and shelter inhabitants and food production areas from disaster caused by lahars (Lavigne et al. 2000). Other noteworthy data emerging from the interpretation of a hazard map were the urgency of a drastic reduction of the density of population both in Pozzuoli town, located in the centre of a caldera, and in the adjacent extension of Naples city (Italy) on the eastern slope of that structure. The emplacement of pyroclastic flows and surges, typically produced during eruptions of this volcanic complex (Di Girolamo et al. 1984), strongly suggests that, even without the knowledge of absolute probability of eruption, the hazard can efficiently be mitigated by redistribution of population of inhabited areas close to volcanic centers based on the hazard map (Lirer and Vitelli 1998).

Volcanic hazard maps usually display the current or potential extent of dangerous volcanic flows (lava, pyroclastic or mud flows) together with the potential distribution of tephra. Topography is a major factor controlling the distribution of many volcanic hazards. Therefore, the presentation of relief, traditionally displayed with contour lines, is a very important component (Haynes et al. 2007).

Copahue volcano, characterized by a hyper-acidic crater lake hosted in the active vent, was the subject of several multidisciplinary investigations, e.g. lithostratigraphic (Pesce 1989; Mazzoni and Licitra 2000; Melnick et al. 2006; Sruoga and Consoli 2011), structural (Folguera and Ramos 2000), petrological (Delpino and Bermudéz 2002), and geochemical (Varekamp et al. 2006; Agusto et al. 2013, Agusto and Varekamp this volume; Tassi et al. this volume). The 1992 eruption (Delpino and Bermúdez 1993) gave a strong pulse for the creation of the Volcano Studies Group (Neuquino Geological Survey) who drew the map of potential hazards for this Argentine sector (Bermúdez and Delpino 1995).

These authors compiled a map indicating the potential geographical limits of: (i) hazardous lava spill, (ii) pyroclastic flows, (iii) pyroclastic fall, (iv) lahars, (v) the areas where volcanic gases emissions were observed and (vi) the zones where earthquakes could possibly generate fractures. The zoning was based on processes occurred during the 1992 eruptions, and geological studies updated to that moment. The phreatomagmatic eruption of July 1992 included three major eruptive phases that produced eruptive columns respectively 0.3, 1.4 and 0.7 km high, corresponding to VEI $\sim$ 2. The columns generated plumes that dispersed ash up to 20 km away and led to the formation of lahars up to 4 km in length (Delpino and Bermúdez 1993). Based on these characteristics, two different potential hazard zones were recognized (Fig. 10.1), both lying inside a radius of 5 km from the crater and corresponding to a higher (dark orange) and a lower (orange color) hazard area, respectively. The innermost zone could potentially be affected by the fall of $\approx$1 m^3 ballistics (Delpino and Bermúdez 1994; Bermúdez and Delpino 1995). In case of eruption, this zone must be evacuated not only because of the likely emission of lava and pyroclastic flows from the active vent, but also to the high probability of lahar formation triggered by the melting of the top glacier. The Travunco and Agrio valleys are the morphological depressions (Fig. 10.1), which are expected to be affected by these events. This simple subdivision, mainly established on qualitative observations, highlights the need of more detailed studies about the eruptive processes of Copahue volcano and the interaction between the crater lake and the magmatic fluids.

In 2000, the "Servicio Nacional de Geología y Minería de Chile" (SERNAGEOMIN), published a new version (after that of Bermúdez and Delpino 1995) hazard map of Copahue at 1:100,000 scale (Fig. 10.2). This map was updated on the basis of more recent stratigraphic studies (Polanco et al. 2000), which suggested the presence of several post-glacial pyroclastic flows outcropping around Copahue volcano. Furthermore, Polanco et al. (2000) recognized three pyroclastic flows interbedded with fluvial conglomerates to form a terrace in the Liay Valley (Chile). These flows were
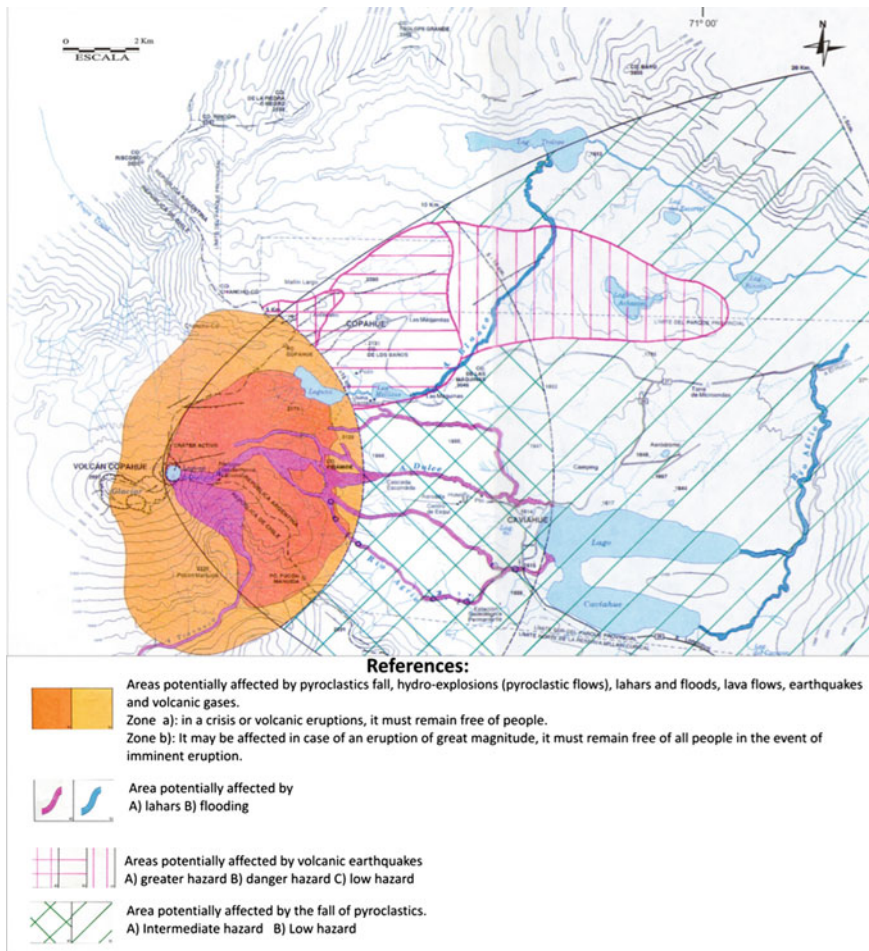
Fig. 10.1 Map of potential hazards of Copahue volcano for the Argentina side. Modified after Delpino and Bermúdez (1993)

probably emitted from the western summit craters. Radiocarbon ages of these flows ranged from $2,280 \pm 50$ to $2,880 \pm 50$ years BP (Cecioni et al. 2000; Polanco et al. 2000). Polanco et al. (2000) also reported two ^{14}C ages from pyroclastic flows of $8,770 \pm 70$ and $5,910 \pm 50$ years BP inside the caldera, probably emitted from the eastern craters. According to the authors, these ages and relations among the postglacial lavas indicate that during the Holocene the summit craters were intermittently active. According to these considerations, the actualized map (Fig. 10.2) shows areas likely affected by (i) lava flows and (ii) lahars (subdivided in low, moderate and high hazard zones), (iii) pyroclastic flows and (iv) pyroclastic falls.

Areas where pyroclastic falls are expected are contoured by lines indicating both the deposit thickness and the tephra diameter (Fig. 10.2). Ash-fall thickness up to 20 cm is located primarily east of the volcano on the Argentina side, reflecting the prevailing orientation of local winds. Directions of gravitational flows as lavas and pyroclastic density currents coincide with the purple arrows, reported only for the Chilean side of the volcano edifice (Fig. 10.2). The spatial limits of the pyroclastic flows refer to both past eruptions and interval of emitted volume between 0.1 and $1\,\mathrm{km}^3$ (dashed violet lines in Fig. 10.2), in order to take into account possible future events.
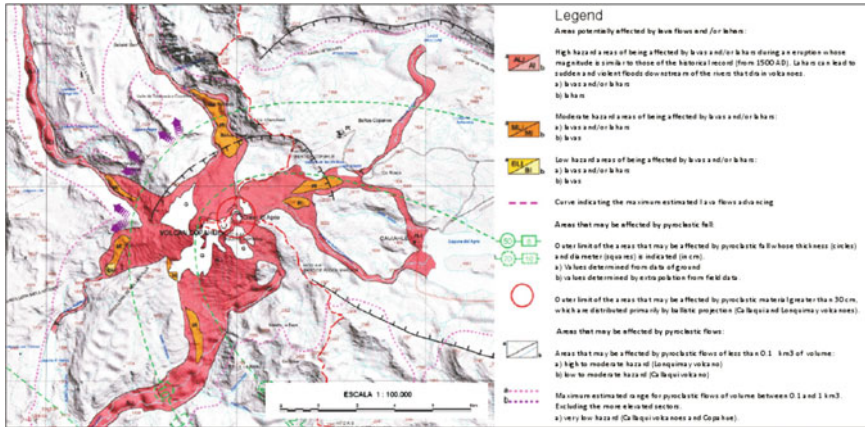
Fig. 10.2 Copahue volcano hazard map made. Modified after Naranjo et al. (2000)

Furthermore, it is observed that the proximal hazard areas (within 15 km) likely to be affected by lava flows and/or lahars do not include populated zones. During larger eruptions (low probability of occurrence), it is suggested that any pyroclastic flows could extend its effects further afield (within 25 km) (SERNAGEOMIN Volcanic Activity report n. 17).

The 2000 eruption was of greater intensity (VEI 2) than the previous ones, being the largest eruptive cycle until 2012, in both magnitude and duration (Naranjo and Polanco 2004). The eruption had different stages, the first and the third ones being the most intense when ash and gas columns reached up to 2–3 km above the crater (Caselli et al. Chap. 3 this book). Phreatic phases frequently occurred during the entire cycle, especially during the first stage that was similar to previous historic eruptions at Copahue volcano (Delpino and Bermúdez 1993, Varekamp et al. 2001). During the eruption, the ejected materials included volcanic dust, sulfur particles, scoria bombs, accessory fragments and most abundantly, juvenile ash and gases. Ash was deposited early in the eruption around the village of Caviahue. The day after the beginning of the eruptive activity, the pyroclastic material was formed by 80 % in volume of fine ash (0.5–1 mm), 15 % of coarse ash (>1 mm) and 5 % of fine to very fine ash (<0.5 mm) (Naranjo and Polanco 2004). Coarse lapilli and bombs ejected during the

eruption were found at distances up to 1 to 1.5 km around the crater. Although very rare, bombs up to 15 cm across were found 8–9 km from the crater. These ballistics did not affect the villages of Copahue and Caviahue although, due to the continuous changes of wind direction, experienced ash-fall that affected the local ski resorts (tephra thickness between 2–5 cm), leading to disadvantageous consequences for the touristic winter season. Inhabitants suffered, for the first time, electric power and water supply cuts (Naranjo and Polanco 2004).

The 2012 eruption occurred on the 22nd of December (VEI 2, Caselli et al. Chap. 4 this book) and can be divided into three phases. The onset of the eruption was characterized by a phreatic activity that after few minutes transitioned to phreatomagmatic (Fig. 10.3), with the ejection of blocks and ash. Hours later, when the interaction with water ceased, a magmatic eruptive style established. Volcanic bombs from the crater and ash-fall dropping from the plume were observed. The ash plume rose about 3,000 m above the summit crater, and the NW prevailing wind blown it over 350 km away. Vesicular scoria were thrown from 0.15 up to 4 km away from the emission centre. Bombs and ballistic ejecta from the crater were launched up to 2 km of distance. No ash-fall was recorded at the villages of Copahue and Caviahue. Apparently, only rural zones (dedicated to the summer

Fig. 10.3   View of the volcano Copahue during the onset of the December 2012 eruption. The Villa Copahue village is located on the Caviahue lakeshore, 9 km from the active crater and at 1,000 m of altitude. Photo by the courtesy of Nicholas Elguero

grazing of transhumance) in the SE surrounding of the volcanic edifice were affected. This caused the evacuation of some Mapuche villages to the upper Río Agrio valley. Less than 1 cm of ash was deposited at Loncopue (54 km E-SE from the volcano crater).

As emerged from the previous description, the eruptive style of the latest (2000 and 2012) eruptions, which culminated with a magmatic phase (Naranjo and Polanco 2004) and ballistic projection of bombs (Caselli et al. Chaps. 3 and 4 this book), looms different from the previous low magnitude (≤VEI 2) historical events. For this reason, together with recent geochemical and stratigraphic findings and relative interpretations (see below), a review of the potential hazard map by Naranjo et al. (2000) is needed, especially regarding the map scale, since the one proposed (1:100,000) does not provide the appropriate detail for a hazard map when referring to a populated zone.

Varekamp et al. (2001) suggested that the crater lake acidity, together with the relatively steep hill-slope, would generate leaching processes able to weaken the eastern slope of the volcano. This might imply a potential flank collapse which, once triggered, may be promoted by the kinematics of the north-east dipping normal faults affecting the eastern side of the volcanic edifice (Rojas Vera et al. 2009).

The possible occurrence of collapse events poses a high risk for the inhabitants of Caviahue at which the water volume of the crater lake (ca. 1.10^6 m^3; Pasternack and Varekamp 1997), the summit glacier and the snow accumulation able to generate lahars that could extend for several kilometers are to be added.

Petrinovic (2008) described diluted pyroclastic flow deposits along Agrio river, likely younger than the absolute ages proposed by Polanco et al. (2000) for those nearby of Caviahue. The proximal facies, 20 m thick, showed impact sags of 0.30 m in diameter at the distance of 1,500 m. Intermediate facies deposits were also recognized and characterized by coarse sand to lapilli grain size, while those of distal facies reached Caviahue with a thickness of 0.50 m with dune facies interbedded with flat layers. These features indicate that the flow did not significantly slow with increasing distance from the eruptive centre, but

rather suggest that it experienced a variable and discontinuous alimentation. The pyroclastic flow reached Agrio lake where by dilution it was able to overcome topographic highs exceeding 10 m in height, spreading beyond the lagoon. The origin of these pyroclastic flows, with the absence of fall deposits, indicates the prompt collapse of a dense, low-rise column eruption, or a "boiling over"-like process generated by repeated phreatic and phreatomagmatic explosions. The spatial limits of these deposits were not either mapped or referred to specific locations, but the information provided by Petrinovic (2008) should be verified since if his interpretation of such recent pyroclastic deposits is correct valid, a revision of the currently estimated volcanic hazard at Copahue has to be reconsidered.

10.2.2 Modeling Support to Hazard Maps

Modeling significantly contributed to the improvement of hazard mapping. In 1988, Wadge and Isaacs proposed a map of hazard from pyroclastic flows at Soufriere Hills Volcano by applying a mathematical model of gravitational flows on the local digital topography, constrained by field evidences related to the deposits of previous eruptions. Advanced modeling techniques are able to reproduce advection-diffusion dispersal of tephra from discrete sources, simulating the particles fallout from multiple plumes generated by dome collapses and vulcanian explosions (Druitt and Kokelaabr 2002). For instance HAZMAP is a suitable 2D physical model that produces two output results: (i) isomass and (ii) probability maps, showing, respectively: (a) the accumulation of mass per unit area for one specific wind profile and (b) the probability distribution of a particular mass loading around the volcano based on the statistical distribution of wind profiles. Fallout after highly violent explosions, such as strombolian events, is better represented by 3D numerical models such as FALL3D, which is also valid within the atmospheric boundary layer.

Inputs for models are: total erupted mass, eruption column height, bulk grain-size, bulk component distribution, and a statistical set of wind profiles (Druitt and Kokelaabr 2002).

The application of these models to Copahue volcano would enable to simulate multiple eruption scenarios and consequent spatial distribution of volcanic products, allowing the proper assessment of volcanic flows and tephra fallout hazard. For this purpose, a first step should be done by accurately completing the input information to produce a reliable output model. For example, Macedonio et al. (2008) used HAZMAP and FALLD3 to compute ground load probability maps for different ash loadings on populated area around Vesuvius (Italy). The various parameters referring to the exhaustively studied deposits of famous historical eruptions, together with a 36-year winds profiles data set, formed a suited input database.

The most comprehensive probabilistic modeling of possible future eruptive scenarios is the so called 'Event Tree' (ET). It was created to summarize in a numerical-graphical form, at different levels of detail, all the relative likelihoods relating to the genesis and style of eruption, development and nature of volcanic hazards, and the probabilities of occurrence of different volcanic risks in the next eruption crisis (Neri et al. 2008). Thus, the hypothetical ET of Copahue would provide, besides the plausible character and evolution of a prospective eruption, a quantitative information about the risk that events related to the volcanic activity, like flank collapse and lahar triggering, are to occur. Furthermore, probability maps obtained for the different scenarios resumed in the ET would support risk mitigation strategies. However, the apparently simple ET structure lies on a complex database that, for Copahue volcano, would require: (i) The compilation of all available historical data, (ii) geological surveys aimed to complete the stratigraphy (included radiometric dating to determine accurate stratigraphic columns) and a common interpretation of geological field data in the light of new fieldwork results (disagreements among authors about the definition

of litostratigraphic units are resumed in Table 1 of Chap. 4 (Caselli et al. this book), (iii) the development of novel numerical modeling codes and of risk assessment techniques.

10.2.3 Volcano Monitoring

Volcanological investigations aimed to the assessment of the hazard of a certain volcanic system are consisting of two steps: (i) description of the eruptive history for understanding the eruptive mechanisms, and (ii) geophysical, geodetic and geochemical monitoring, to follow the evolution of the activity of the volcano.

Geophysical monitoring aimed to identify the seismic precursors of an eruption represents a powerful tool in volcanic hazard investigation. Seismic signals may occur with months or years in advance with respect to any observable external manifestation such as vapor, gas or ash emission, or water lake heating. The rise of volcanic fluids, as well as the generation of fractures or cavities of collapse caused by magma inputs in the area below and within the volcanic edifice, are expected to originate volcanic earthquakes with recognizable seismic signals, whose evolution in time may indicate the prevailing process on a certain time lapse (Zobin et al. 2012). For instance, long-period (LP) events (with dominant periods in the range 0.2–2 Hz) have received particular attention from scientists as they are thought to be associated with moving fluids or resonating fluid-filled conduits (Chouet 1996; Neuberg et al. 2000). Since increases in the occurrence rate of LP events often herald a new episode of unrest, monitoring and investigation of this kind of signals were performed at the active Etna volcano (Bean et al. 2008). The example of Mammoth Mountain (California) underlines the importance of reading the seismic activity as precursor of catastrophic events: in 1989, a seismic swarm was indeed followed by a plume of cold CO_2 that killed *ca* 70 ha of forest. Despite the fact that the emission of CO_2 was waning in a relatively short period of time, it still continues to pose a health hazard to the tourists who visit the area (Lowenstern et al. 2006).

The Southern Andes Volcano Observatory (OVDAS) of Chile, part of the National Network SERNAGEOMIN volcano monitoring, is a scientific-technical unit that performs the (discontinuous or permanent) monitoring of the 43 volcanoes, which are considered the most dangerous in the country due to their type of activity and proximity to populated areas, including Copahue volcano. OVDAS carried out sporadic seismic monitoring in the Trapa Trapa valley, located 13 km to the NW of the crater, and at the village of Copahue, 7.5 km to the NE of the crater, since July–September 2000. From the 22nd of July, 2000, about 2 months of discontinuous seismic activity recording were carried out and associated with strombolian explosions of intermediate energy.

Since May 2012 OVDAS started the permanent monitoring of the seismic activity related to Copahue volcano in real time, web-published in Volcanic Activity Reports (RAV). A pair of broadband seismic stations records such activity that, from the beginning of the monitoring, appeared moderated (with an average of 20 daily seismic events) until the phreatic eruption occurred from July 17–19th 2012, when the number of earthquakes considerably increased. Thereafter, the seismic activity shown a variable trend with peaks of seismic swarms until the eruption occurred on December 22nd 2012 with no precursory signals detected (or recognized) during the time span preceding the explosion.

The National Institute of Seismic Prevention (INPRES, San Juan, Argentina) carried out seismic surveillance recording the seismic activity at Caviahue from August 2000. During the 2012 eruptive period, INPRES provided the daily seismological information to the Civil Defense. In the aftermath of the eruption, the number of daily volcano-tectonic earthquakes increased of one order of magnitude (from ca. 20 to about 200), showing a higher frequency of seismic events with respect to those observed before the explosion. The geophysical investigations carried out from 2004 to 2008 (Ibañez et al. 2008; Caselli et al. 2009) employed a seismic array deployed equidistant from the volcano summit

and the exploited geothermal field close to the village of Caviahue. That survey, being the first systematic study of the seismicity of this volcanic region, helped to determine both the rate and the energy of the seismic activity during a period of quiescence. To date, a real-time monitoring of the Copahue volcano from the Argentine side has started in March 2014, from a collaboration between the UNRN (Universidad Nacional de Rio Negro) and the geophysical group of the Department of Earth Sciences of the University of Florence (Italy) when two seismic stations and an infra-sound array were deployed.

Geodetic methods, focused on the measure of the surface deformation of a volcanic edifice, can also successfully be applied to volcano monitoring. Geodetic data are indeed associated with changes in pressure/volume inside the deep magmatic reservoir (Dzurisin 2006). However, there are many causes that may produce surface deformation in a volcanic environment such as tectonic, magmatic and/or hydrothermal processes. Monitoring adopts in situ sensors, usually tiltmeters and strainmeteres, able to (i) acquire a steady stream of data in real time for analysis and (ii) evaluate even subtle changes in the pattern or rate of deformation (Dzurisin 2006), commonly corroborated by a GPS network positioning system.

Remote sensing, based on the acquisition of images of the surface from satellite-borne sensors, constitutes one of the most recently developed instrumentations (Dzurisin 2006). Although its powerful potential (entire volcanic arcs can be surveyed, and magma movements can be detected even beneath volcanoes with no other sign of activity; Pritchard and Simons 2004 and references therein), this technique is better addressed to characterize the deformation field in space and time rather than to be applied to the survey activity (Dzurisin 2006).

At Copahue volcano, deformation analyses were realized by Velez et al. (2011) using the Differential Synthetic Aperture Radar technique (DInSAR). From Envisat radar images acquired between 2002 and 2007 a negative deformation rate of approximately 2 cm/yr was calculated, located mostly on the NE flank of Copahue

volcano. The source of deformation was related to a depressurization of the system that resulted from the release of magmatic fluids across the boundary between the brittle and plastic domains. These leakages were considered to be responsible for the weak phreatic events registered in between 1992 and 1995 at Copahue volcano. From the end of 2011 the deformation trend changed towards an inflation process (see Velez et al. this volume), showing a positive deformation rate before and after the eruption of December 2012.

In quiescent volcanoes the transition from repose to eruption is accompanied not only by the previously described geophysical variations, but also by the changes of the chemical-physical parameters of fumaroles and ground waters induced by magma upraise. Fluid geochemistry has a relevant potential with respect to eruptions forecast, as the gases released by progressive depressurization of magma during ascent are very mobile and reach the surface well before their parental magma (Carapezza et al. 2004). In high-T crater fumaroles or in volcanic gas plumes the most significant recorded variations are those of the ratios of gas components (such as H_2O/CO_2, SO_2/CO_2, SO_2/HCl) that are differentially released because of their different solubility in the magmatic melts (Carroll and Webster 1994; Dixon and Stolper 1995). Variations of the $^3He/^4He$ isotopic ratio provide clear evidences when new deep magma is entering the shallow volcanic system (Sano et al. 1988) as observed before and during two recent eruptions of Mt. Etna (in 2001 and 2002–2003; Caracausi et al. 2003) that were attributed to degassing of rising magma batches. Geochemical monitoring is usually performed on the hottest gas vents (eruptive gases, plumes, fumaroles) most closely connected to the magmatic volatiles uprising from depth but when the inherent character (high temperature, corrosive nature) or the local topography not allow the permanent access to such fluids, continuous monitoring of low temperature (below the boiling point of water) gases which discharge diffusively through volcanic piles, at a distance from active craters, can corroborate the surveying.

These emanations essentially consist of carbon dioxide, H_2S, N_2, rare gases (He, Ar, Rn), H_2, CH_4, CO and other species at very low concentrations (ppms and ppbs by volume) and their genetic link with crater fumaroles and/or magma degassing at depth can be verified both chemically and isotopically. Furthermore, gas species such as CO_2 represent useful markers of sub-surface thermal anomalies and/or active faults (Baubron et al. 1991), through which volcanoes in a dormant stage, e.g. in Italy, Lesser Antilles, Indonesia (Baubron et al. 1991 and reference therein), are studied by investigating soil diffuse gas emanations.

Changes in chemical and isotopic compositions of discharged fluids, showing a progressive enhancing of the magmatic signature, were detected at Turrialba (Costa Rica) since 2001 (Vaselli et al. 2010), during the reawakening of the system (also supported by geophysical and geodetical evidences) after almost 150 years of quiescence. Fluctuations of the physico-chemical parameters were also observed in hot springs and fumaroles discharges from El Chichòn (Mexico) (Tassi et al. 2003) after the 1982 paroxistic event: the analytical evidence allowed to identify the main processes acting on the magmatic-hydrothermal system, from which two possible future scenarios for the evolution of this volcanic complex were hypothesized.

The current geochemical information relative to the Copahue volcanic system is the result of several investigations carried on during 2004–2012, conducted on the (i) hyper-acidic waters of the crater lake, (ii) hot springs on the volcanic flanks and (iii) the fluid emissions (Fig. 10.4) from the geothermal field (i.e. Varekamp et al. 2001, 2009; Caselli et al. 2005; Agusto et al. 2012, 2013; Agusto and Varekamp this book; Tassi et al. this book). According to the chemical and isotopic features of the different manifestations of the liquid phase collected in the area, different subsystems were defined, based on the volcanic-hydrologic or the melted snow contribution (Agusto and Varekamp this book). Furthermore, a dramatic variation of the solute concentration in the Agrio River upstream and a

sharp temperature decreased were recorded and possibly induced by an obstruction of the fracture system underlying the crater lake, due to an oversaturation and precipitation inside the conducts as a consequence of the arrival of hyper-concentrated deep fluids (Caselli et al. 2005; Agusto et al. 2012, 2013). This mechanism is considered to be possibly responsible of the phreatic events occurred during the 90's (Agusto et al. 2012).

Despite the significant scientific information available, the lack of a proper monitoring network induced the Government of the Neuquén Province (Argentina) in April 2012 to announce the need to establish the Neuquén Volcano Observatory in collaboration with the UNRN. In April 2014 the formal agreement between the two public institutions was signed. The foundation of the Observatory and a partnership with OVDAS is aimed to contribute to favor the construction of integrated modeling of data from different scientific disciplines that can improve the knowledge of the state of the system and its behavior. Firstly, a seismic network, working in real time, will be deployed around the volcano. Secondly, further investigations in the geodetic field (GPS network) will be aimed to detect and measure changes in the surface of the volcano. Researchers from the universities of Rio Negro, Buenos Aires (Argentina) and Florence (Italy) will jointly be carrying out seismic investigation and studies on the geochemical investigation of fluids discharged from the natural emissions located in the surroundings of the volcano and in the summit crater (Tassi et al. this book).

10.3 Contingency Plans

Copahue and Caviahue, as well as the indigenous communities that seasonally live in the valleys near the volcano, are exposed to different types of hazard related to possible rejuvenating activity of Copahue volcano. These two populated centers are located at 9.5 and 7 km east and northeast from the active crater, respectively, with a distance of approximately 19 km between them.

Fig. 10.4 Sampling of fumarolic gases in Copahue thermal manifestation (*top*) and of Agrio River (*bottom*)

Caviahue lies on the shores of the homonymous lake, at 1,647 m. a.s.l., and has a stable population of 600 inhabitants, whereas Copahue is only inhabited in the summer season (December to May). Approximately 80 % of the total population was installed in the area a little more than 15 years ago. Tourism is the main economic activity of the local municipality, with ski fields of excellent quality during the winter and thermal baths throughout the summer (Copahue) (Monasterio et al. this book). The transhumance of livestock, when Mapuche bring their animals to graze in the fields near the volcano, represents another aspect of the summer activities.

The eruptions of 1992, 1995 and especially that of 2000 have significantly affected the perception of the risk posed by the volcano for the local community. The settlement of new residents and the limited information provided by the authorities, in addition to the episodes mentioned, have caused the sensations of doubts and fears that are still unresolved. The inhabitants have had little information about the volcano and the volcanic environment on which their life develops. The most serious consequence of this lack of knowledge is the wrong perception of risk perceived by people. In this sense, Naranjo and Polanco (2004) opined that the inhabitants of these villages perceive that the Copahue volcano

can give only rise to low magnitude eruptions, such as the ones occurred in the sixties, the nineties and even in 2000. However, emergency plans would not be effective to prevent possible effects of major events without implementing an educational program of constant application aimed at the local population.

After the precursory signals observed at the end of 2011, the municipal government of Caviahue-Copahue started to develop a contingency plan that was based on an unpublished report by Caselli et al. (2012) and contemplates the organization of Municipal Emergency Committee (EMCO) and the actions following the warnings. Three levels of alerts, displayed in three colors, were created: green, yellow and red. These levels indicate alert states for the community but they are not referred to the activity state of the volcano. Before a Yellow Alert, the Mayor convenes the EMCO and provides that the radio station keeps the public constantly informed on the status of the volcano. The community is organized in areas (or blocks), each one of these has a public representative, who is in charge of distributing masks, goggles and work in case of evacuation. In the Red Alert state, evacuation is ordered and security forces are dictated to trigger the safety plan. There is a map of the city with escape and alternative routes, depending on the magnitude of the event, the season in which it occurs and the weather conditions. Gas and electricity cuts are planned in the whole town and the representative of each "block" verifies that all the residents have left their habitations. The population is expected to assemble on the shores of lake in vehicles, and together will caravan to Loncopué village, at a distance of 60 km from Caviahue, as occurred during the evacuation of May 2013 (Fig. 10.5). OVDAS uses 8 levels of alert displayed by colors divided into four groups: green (levels 0 to 2), yellow (levels 3), orange (level 4) and red (levels 5 to 8). The yellow alert is reached when there are variations in the levels of monitoring parameters that indicate proximity to instability such as seismic swarms, ash emissions, increased

fumarolic activity, suggesting that the activity can evolve to an eruptive event. As these parameters intensify, the orange alert level is reached. The red alert level corresponds to an eruption in progress of various magnitudes.

Before the eruptive event of December 22nd 2012, Argentina and Chile governments declared yellow alert. The volcano emitted ash to SE, without affecting the villages of Caviahue and Copahue. In the same day, the Chilean OVDAS announced by web the red alert, while in Argentina, since no ash fall-out occurred in the inhabited centers, the Emergency Committee maintained the yellow alert and no evacuation took place. Such a situation of incongruity, with each authority (the Observatory and the Civil Defense) giving its own alert, generated confusion in the media and major concerns in the community.

10.4 Final Recommendations

Although the historical eruptive activity of Copahue volcano has been characterized by activity with low explosivity index, pyroclastic flows and lahars, besides the possibility of flank collapses, are a serious hazard for population living in the surrounding lowlands. This stresses the importance of updating the hazard map for a better land use assessment and for actualizing the contingency plan. These goals require (i) new detailed stratigraphic studies and (ii) a comprehensive knowledge of the magmatic evolution of Copahue to determine the possible existence of eruptive cycles with different magnitudes or VEIs. Single hazard maps integrated with the aid of numerical models under a Geographic Information System, would allow to describe different scenarios as a function of different kinds of volcanic activity and relative magnitudes. To this aim, the application of physical models to simulate both the distribution of gravitational flows (lavas, pyroclastic flows, lahars) and tephra would greatly contribute to the understanding of

Fig. 10.5 Evacuation of the village of Caviahue in May 2012

the risks at which the local population might be affected. The use of advanced probabilistic models (ET) is expected to provide quantitative information about the likelihood of the different (direct and indirect) events associated with the volcanic activity. Although there is a correspondence between the eight levels of alert of the observatory and the succeeding safety procedures (grouped into three hazard classes) pertaining to the civil defense, the creation of a uniform code, aimed to provide a unambiguous public information able to simplify the understanding of the risk by the community, is highly recommended. A common criteria of alert levels are to be adopted by OVDAS and the Argentina Civil Defense, so that in case of an alert situation the population can correctly interpret the information received. This can be achieved by implementing both the monitoring system at Copahue and the collaboration between the two countries, Argentina and Chile, to promote cooperation and exchange of scientific information. Preparedness, mitigation and resilience plans in the case of high magnitude volcanic event should include education programs, periodical meetings with the population, information for tourists and evacuation practices.

References

Agusto M, Caselli A, Tassi F, dos Santos Afonso M, Vaselli O (2012) Caracterización y seguimiento geoquímico de las aguas ácidas del sistema volcán Copahue - río Agrio: posible aplicación para la identificación de precursores eruptivos. Rev Asoc Geol Arg 69(4):481–495

Agusto M, Tassi F, Caselli AT, Vaselli O, Rouwet D, Capaccioni B, Caliro S, Chiodini G, Darrah T (2013) The geochemical and isotopic evolution of the hydrothermal-magmatic system of the Copahue-Caviahue Volcanic Complex (Argentina): evidence for a new unrest phase. J Volcanol Geotherm Res 257:44–56

Alvarado GE, Soto GJ, Schmincke HU, Bolge LL, Sumita M (2006) The 1968 andesitic lateral blast eruption at Arenal Volcano, Costa Rica. J Volcanol Geotherm Res 157:9–33

Bean C, Lokmer I, O'Brien G (2008) Influence of near-surface volcanic structure on long-period seismic signals and on moment tensor inversions: simulated examples from Mount Etna. J Geophys Res 113: B08308. doi:10.1029/2007JB005468

Bermúdez A, Delpino D (1995) Mapa de los Peligros Potenciales en el área del Volcán Copahue Sector Argentino. Serie Mapas de Riesgo Geológico. Servicio Geológico Neuquino. Neuquén

Bitschene PR, Menida J (1995) The august 1991 eruption of the Hudson Volcano (Patagonian Andes): a thousand days after. Cuvillier Verlag, Gottingen, Germany, pp 2–15

Baubron J-C, Allardzy P, Sabroux JC, Tedesco D, Toutal JP (1991) Soil gas emanations as precursory indicators of volcanic eruptions. J Geol Soc London 148:571–576

Caselli AT, Agusto M, Fazio A (2005) Cambios térmicos y geoquímicos del lago cratérico del volcán Copahue (Neuquén): posibles variaciones cíclicas del sistema volcánico. In: XVI Congreso Geológico Argentino, La Plata, Argentina, 751–756

Caselli A, Vélez ML, Agusto MR, Bengoa CL, Euillades PA, Ibáñez JM (2009) Copahue volcano (Argentina): a relationship between ground deformation, seismic activity and geochemical changes. In: Bean CJ, Braiden AK, Lockmer I, Martini F, O'Brien GS (eds) The, vol Project., Volcanoes: Understanding subsurface mass movementJaycee Printing, Dublin, Ireland, pp 309–318

Cecioni A, Alfaro G, Pincheira M, Pineda V, Arce M, Cares R, Reyes M, Valenzuela G, Melnick D (2000) Elaboración de mapas zonificados de peligrosidad volcánica. INGENDESA S.A. (not published), Universidad de Concepción, pp 250

Caracausi A, Favara R, Giammanco S, Italiano F, Nuccio PM, Paonita A, Pecoraino G, Rizzo A (2003) Mount Etna: geochemical signals of magma ascent and unusually extensive plumbing system. Geophys Res Lett 30(2):1057. doi:10.1029/2002GL015463

Carapezza ML, Inguaggiato S, Brusca L, Longo M (2004) Geochemical precursors of the activity of an open-conduit volcano: the Stromboli 2002–2003 eruptive events. Geophys Res Lett v 31:l07620. doi:10.1029/2004gl019614

Carroll MR, Webster JD (1994) Solubilities of sulfur, noble gases, nitrogen, chlorine and fluorine in magmas. In: Carroll MR, Halloway JR (eds) Volatiles in Magmas Rev Mineral vol 30, pp 231–279

Caselli A, Agusto M, Capaccioni B, Tassi F, Chiodini y G, Tardani, D (2012) Aumento térmico y composicional de las aguas cratéricas del Volcán Copahue registradas durante el año 2012 (Neuquen, Argentina). XIII Congreso Geológico Chileno. Antofagasta, 2012. Actas: 441–442

Chouet B (1996) Long-period volcano seismicity: its source and use in eruption forecasting. Nature 380:309–316. doi:10.1038/380309a0

Delpino D, Bermúdez A (1993) La actividad volcánica del volcán Copahue durante 1992. Erupción con emisión de azufre piroclástico. Provincia de Neuquén. In: XII Congreso Geológico Argentino, Menzoda, Argentina, vol 4, pp 292–301

Delpino D, Bermúdez A (1994) Volcanismo post-glacial en el volcan Copahue (37°45'S) sector argentino. Peligros potenciales asociados. In: VII Congreso Geologico Chileno, Puerto Varas, Chile, vol 1, pp 260–264

Delpino DH, Bermúdez AM (2002) La erupción del volcán Copahue del año 2000. Impacto social y al medio natural. Provincia del Neuquén. Argentina. Proceed. XV Congreso Geológico Argentino 3:365–370

Di Girolamo P, Ghiara MR, Lirer L, Munno R, Rolandi G, Stanzione D (1984) Vulcanologia e petrologia dei Campi Flegrei. Boll Soc Geol Ital 103(34):9–413

Druitt TH, Kokelaabr P (eds) (2002) The eruption of SoufriGre hills volcano, Montserrat, from 1995 to 1999. Geol Soc London Mem 21:517–537

Dixon JE, Stolper E (1995) An experimental study of water and carbon dioxide solubilities in mid-ocean ridge basaltic liquids. PART II: applications to degassing. J Petrol 36:1633–1646

Dzierma Y (2010) Wehrmann H (2010) Statistical eruption forecast for the Chilean Southern Volcanic Zone: typical probabilities of volcanic eruptions as baseline for possibly enhanced activity following the large. Concepcion Earthquake Nat Haz Earth Syst Sci 10:2093–2108

Dzierma Y, Wehrmann H (2012) On the likelihood of future eruptions in the Chilean Southern Volcanic Zone: interpreting the past century's eruption record based on statistical analyses. Andean Geol 39(3):380–393

Dzurisin D (2006) Volcano deformation. Springer. http://dx.doi.org/10.1007/978-3-540-49302-0_5

Folguera A, Ramos VA (2000) Control estructural del volcán Copahue (38 ° S–71 ° O): implicancias tectónicas para el arco volcánico cuaternario (36°–39° S). Rev Asoc Geol Arg 55:229–244

Haynes K, Jenni Barclay J, Pidgeon N (2007) Volcanic hazard communication using maps: an evaluation of their effectiveness. Bull Volcanol 70(2):123–138

Ibañez JM, Del Pezzo E, Bengoa CL, Caselli AT, Badi G, Almendros J (2008) Volcanic tremor and local earthquakes at Copahue volcanic complex, southern Andes, Argentina. J Volcanol Geoth Res 174:284–294

Lavigne F, Thouretb B, Voightc H, Suwad A, Sumaryono A (2000) Lahars at Merapi volcano, Central Java: an overview. J Volcanol Geotherm Res 100:423–456

Lirer L, Vitelli L (1998) Volcanic risk assessment and mapping in the Vesuvian area using GIS. Nat Haz 17:1–15

Lowenstern JB, Smith RB, Hill DP (2006) Monitoring super-volcanoes: geophysical and geochemical signals

at Yellowstone and other large caldera systems. Phil Trans R Soc A 364:2055–2072. doi:10.1098/rsta.2006.1813

Mazzoni MM, Licitra D (2000) Significado estratigráfico y volcanológico de ignimbritas neógenas con composición intermedia en la zona del lago Caviahue. Neuquén Rev Asoc Geol Arg 55(3):188–200

Macedonio G, Costa A, Folch A (2008) Ash fallout scenarios at Vesuvius: numerical simulations and implications for hazard assessment. J Volcanol Geotherm Res 178:366–377

Melnick D, Folguera A, Ramos VA (2006) Structural control on arc volcanism: the Copahue-Agrio complex, South-Central Andes (37°50′S). J South Am Earth Sci 22:66–88

Naranjo J, Moreno H, Polanco E, Young S (2000) Mapa de peligros de los volcanes del Alto Biobio. Regiones del BioBio y de la Araucanía. Documento de trabajo N°15. Servicio de Geología y Minería de Chile. ISSN:0717-277X

Naranjo JA, Polanco E (2004) The 2000 AD eruption of Copahue Volcano. Southern Andes. Rev Geol Chile 31(2):279–292

Neri A, Aspinall WP, Cioni R, Bertagnini A, Baxter PJ, Zuccaro G, Andronico D, Barsotti S, Cole PD, Esposti O, Hincks TK, Macedonio G, Papale P, Rosi M, Santacroce R, Woo G (2008) Developing an event tree for probabilistic hazard and risk assessment at Vesuvius. J Volcanol Geotherm Res 178:397–415

Neuberg J, Pointer T (2000) Effects of volcano topography on seismic broadband waveforms. Geophys J Int 143:239–248. doi:10.1046/j.1365-246x.2000.00251.x

Oramas-Dorta D, Cole PD, Wadge G, Alvarado GE, Soto GJ (2012) Pyroclastic flow hazard at Arenal volcano, Costa Rica: scenarios and assessment. J Volcanol Geotherm Res 247–248:74–92

Parra E, Cepeda H (1990) Volcanic hazard maps of the Nevado del Ruiz volcano. Colombia J Volcanol Geotherm Res 42:117–127

Pasternack GB, Varekamp JC (1997) Volcanic lake systematics I. Physical constraints. Bull Volcanol 58:528–538

Pesce A (1989) Evolución volcano-tectónica del complejo efusivo Copahue-Caviahue y su modelo geotérmico preliminar. Rev Asoc Geol Arg 44:307–327

Perucca L, Moreiras S, Bracco A (2009) Determination of seismogenic structures and earthquake magnitud from seismites in Holocene lacustrine deposits. Precordillera Range, Central-Western Argentina. J Iberian Geol:10–20

Petrinovic IA (2008) Variaciones en el régimen de flujo en depósitos de oleadas piroclásticas del volcán Copahue, Neuquén. In: XVII Congreso Geologico Argentino, Jujuy, Argentina, vol 3, 1379–1380

Pritchard ME, Simons M (2004) An InSAR-based survey of volcanic deformation in the southern Andes. Geophys Res Lett 31:L15610. doi:10.1029/2004GL020545

Polanco E, Naranjo JA, Young S, Mareno H (2000) Volcanismo explosivo holoceno en la cuenca del alto biobio, Andes del sur (37°45′38°30′). In: X Congreso Geologico Chileno, Puerto Varas, Chile

Rojas Vera E, Folguera A, Spagnuolo M, Gimenez M, Ruiz F, Martinez P, Ramos V (2009) La neotectonica del arco volcanico a la latitud del volcan Copahue (38° S), andes de Neuquen. Rev Aso Geol Arg 65(1):204–214

Sano Y, Nakamura Y, Notsu K, Wakita H (1988) Influence of volcanic eruptions on helium isotope ratios in hydrothermal systems. Geochim Cosmochim Acta 52:1305–1308

Sruoga P, Guerstein PY, Bermúdez A (1993) Riesgo volcánico. In: Ramos VA (ed) Geología y Recursos Naturales de Mendoza. Parte III: Geología Ambiental y Riesgo Geológico, pp 659–667

Sruoga P, y Consoli VC (2011) Volcán Copahue. In: En Leanza H, Arregui C, Carbone O, Danieli J, y Vallés J (eds) Geología y Recursos Naturales de la provincia del Neuquén. Relatorio del 18° Congreso Geológico. Argentino, Buenos Aires, pp 609–616

Tassi F, Vaselli O, Capaccioni B, Macias JL, Nencetti A, Montegrossi G, Magro G (2003) Chemical composition of fumarolic gases and spring discharges from El Chichon volcano, Mexico: causes and implications of the changes detected over the period 1998–2000. Special Issue of J Volcanol Geoth Res 123:105–121

Vaselli O, Tassi F, Duarte E, Fernández E, Poreda RJ, Delgado Huertas A (2010) Evolution of fluid geochemistry at the Turrialba volcano (Costa Rica) from 1998 to 2008. Bull Volcanol 72(4):397–410

Varekamp CJ, deMoor M, Merrill MD, Colvin AS, Goss AR (2006) Geochemistry and isotopic characteristic of the Caviahue-Copahue volcanic complex, Province of Neuquén, Argentina. In: Kay SM, Ramos VA (eds) Evolution of an Andean margin: a tectonic and magmatic review from the Andes to the Neuquén Basin (35°–39 °S). Geol Soc Am Special Paper 407:317–342

Varekamp J, Ouimette A, Hermán S, Bermúdez A, Delpino D (2001) Hydrothermal element fluxes from Copahue, Argentina: a "beehive" volcano in turmoil. Geology 29(11):1059–1062

Varekamp JC, Ouimette AP, Herman SW, Flynn KS, Bermudez A, Delpino D (2009) Naturally acid waters from Copahue volcano, Argentina. Appl Geochem 24:208–220

Velez ML, Euillades P, Caselli A, Blanco M, y Martínez Díaz J (2011) Deformation of Copahue volcano: Inversion of InSAR data using a genetic algorithm. J Volcanol Geoth Res 202(1–2):117–126

Zobin VM (2012) Introduction to volcanic seismology, 2nd edn. Elsevier, Amsterdam-New York-Tokyo, p 482

Geothermal Energy Development at Copahue Volcano

L.C. Mas and G.R. Mas

Abstract

The Neuquén province (western Argentina) has a significant amount of geothermal resources with a wide range of temperatures in different areas of its territory. Among them, the Copahue Field, located in the southern flank of Copahue volcano, is the most important and the only one with an energy development project since the mid-70s. In 1988 a 0.67 MWe binary-cycle pilot power plant was installed. A technical-economic feasibility study ended in 1992. Since then, the political and economic scenario suffered a profound change in Argentina. As a consequence, radical changes were made to the existing regulations, including privatization of the electrical energy production, transport and distribution sectors throughout the country. In 1996–97 the Neuquén Province launched a heating project for the Copahue village. In the same period, Copahue volcano suffered a series of eruptions, which led to some changes in the hydrothermal system. One of the most significant variations was the development of an active geothermal zone south of the city of Copahue, where several thermal water and gas discharges with temperatures higher than 90 °C and pH <4 appeared, leading to the developing of new mud pools. Interestingly, new mineral species for the Copahue geothermal field were recognized.

L.C. Mas (✉)
EPEN. Área Energías Alternativas, Rioja 385, Neuquén 8300, Argentina
e-mail: lucarmas@yahoo.es

L.C. Mas
Facultad de Ingeniería, UNComa, Buenos Aires 1400, Neuquén 8300, Argentina

G.R. Mas
Departamento de Geología, UNS, San Juan 670, Bahia Blanca 8000, Argentina

G.R. Mas
InGeoSur, CONICET-UNS. Bahía Blanca, San Juan 670, Bahía Blanca 8000, Argentina

11.1 Introduction

Copahue volcano and the related geothermal field are located in the Province of Neuquén, on the western border between Argentina and Chile in the Andes Range (Fig. 11.1), at an altitude ranging from 1,600 to 2,900 m in the Copahue-Caviahue valley and they cover an area of about 15 km NS and 20 km EW. The valley is actually a volcanic caldera formed during the effusive evolution of the Copahue complex, which began at about 4.3 Ma (Linares et al.

1999). The last phase of this evolution, started in the Upper Pleistocene, at about 1 Ma, led to the present-day Copahue volcano (Folguera et al. this book).

The Copahue volcanic complex characterizes and gives its name to a system of volcanic centers locally known as "Zócalo Volcánico Copahue" (Copahue volcanic basement) (Ramos 1978), which covers a surface of about 10,000 km^2 in the central-western part of Neuquén Province. To the east of this area sediments belonging to the Mesozoic Neuquén Basin,
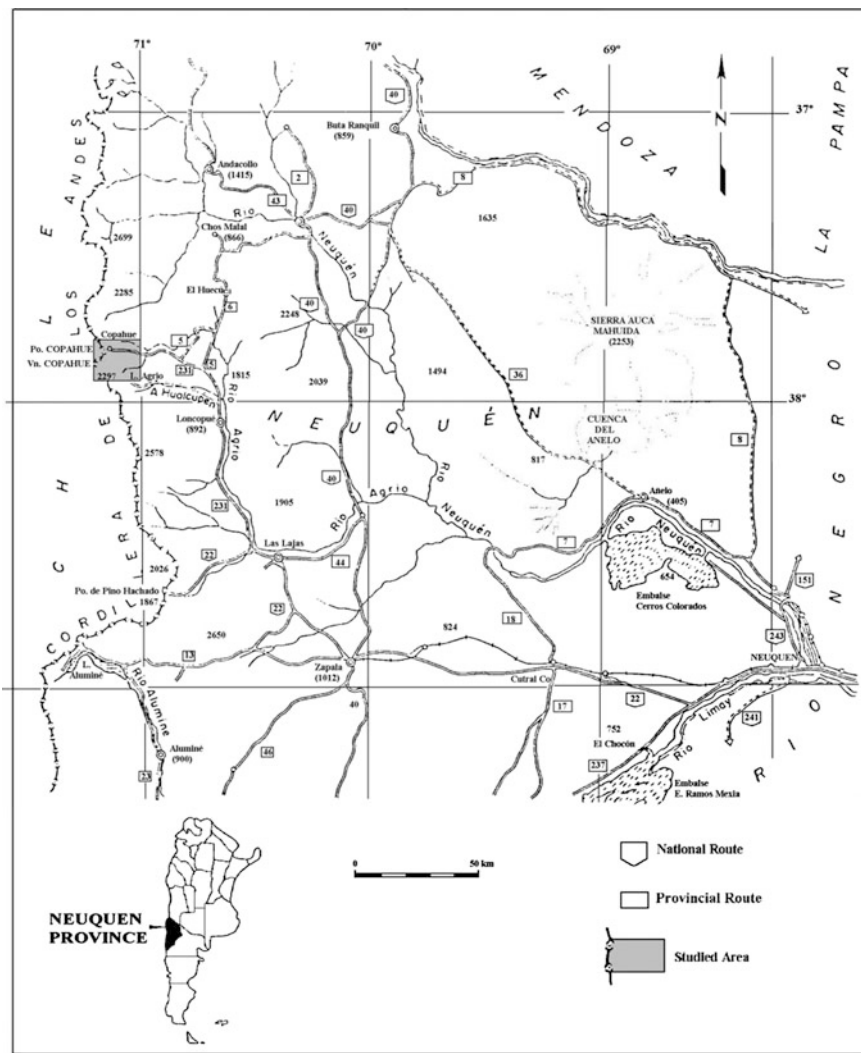

Fig. 11.1 Geographical location of the Copahue volcano in the Neuquén province (western Argentina)

Fig. 11.2   Photo of the Copahue volcano from the east

characterized by hydrocarbon deposits (Giusiano et al. 2011; Vergani et al. 2011) where most of Argentina's oil is produced, largely occur.

The Copahue-Caviahue valley dips ENE, from an altitude of 1,700–1,800 m to W to about 1,500 m to NE. Bordering the valley, at an elevation of over 2,000 m, there is a flat-peak mountain chain in which, in the western part of the valley, Copahue volcano is an exception, with an altitude of 2,977 m (Fig. 11.2).

Copahue volcano has glaciers and snow packs. Glaciers have covered the area and eroded the surface in Pleistocene time. Glacial striation can be found all over the central part of the volcano, in some places on the bottom of the caldera, and in the surrounding valleys. The glacial influence can also be recognized by the U-shape features, which characterize most valleys in the area. Lake Caviahue (Fig. 11.3), the biggest inland water body in the region, was likely formed by glacier melting. There are also many streams and lagoons that have originated from the glaciers, likely due to both the peculiar topographic features of the region and intense precipitations. Annual precipitation in

the area is about 2,000 mm, mostly from snowfalls in winter-time (May to November). Furthermore, the region is well known for the presence of thermal springs, which represent an important source of economic income for the region as spas and wellness and fitness resorts abundantly occur (Monasterio et al. this volume), mainly in the Copahue village (Fig. 11.4).

The main hot springs in the area are, as follows: Termas de Copahue, Las Máquinas, Las Maquinitas, El Anfiteatro, Agrio Spring, the Crater lagoon, Las Mellizas and Chancho Co (Fig. 11.4) (Mas et al. 2011).

- *Termas de Copahue*: the original features of this area, the most important in the region, cannot presently be appreciated because it was deeply modified by buildings, roads, dams and embankments, which have formed small lakes used for balneotherapy purposes. The best-known thermal springs are the Sulfurosa, Verde, Del Chancho and Baño Nº 9.
- *Las Máquinas*: this is the second largest thermal area, a large number of gas and water

Fig. 11.3 Aerial view of Lake Caviahue in winter

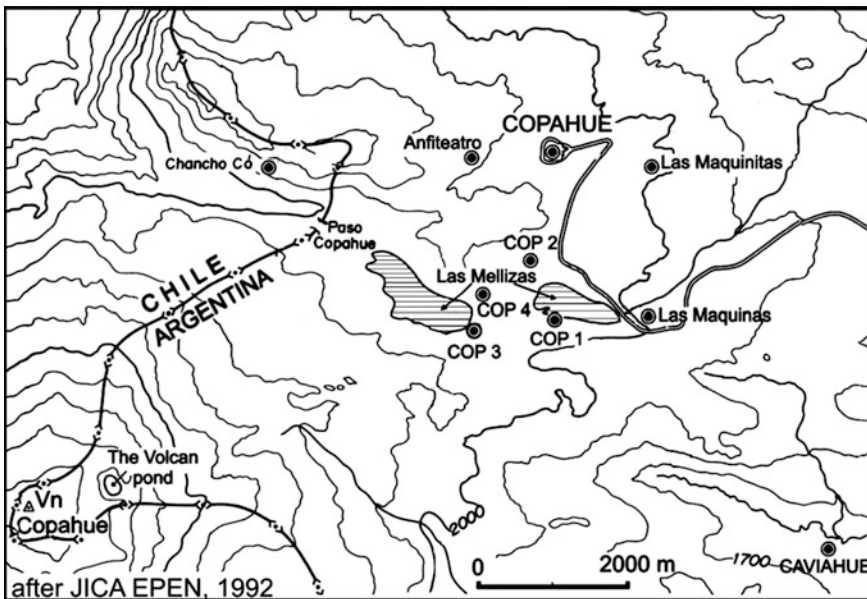**Fig. 11.4** Location map of geothermal wells and hot water and gas and fumarolic discharges

manifestations occur, accompanied by different degree of alteration of the outcropping rocks. Here, an important lagoon formed by damming the hot spring waters is present.

Fumaroles and hot springs surround this lagoon.

- *Las Maquinitas*: it is one of the smaller manifestations. Nevertheless, the highest

fumarolic outlet temperatures (132 °C) are recorded (Latinoconsult and Electroconsult 1981).

- *El Anfiteatro*: it covers a large area with numerous gas and thermal water manifestations whose temperatures are close to that of boiling water. Native sulfur precipitates in pyrite surface forming coatings. The surrounding rocks are deeply altered.
- *Las Mellizas*: few and relatively cold springs occur in this area. The outcropping rocks show a low degree of alteration.
- *Vertiente del Agrio*: this is one of the two vents that seep out directly from the southern flank of Copahue volcano. The low pH (0.75) and the chemical composition likely suggest a direct relationship to the acidic crater lake of Copahue volcano (Agusto et al. this book).
- *Laguna del Cráter*: this site is the center of the latest eruptions of the Copahue volcanic outpourings. The pH, temperature and water level of the fluids change mainly in relation with the activity stage of the volcano (Agusto et al. this book).
- *Chancho Co*: this thermal area extends along a WNW-ESE fault and is the only one in the Chilean territory. Differently from the other thermal discharges in the Argentina side, it is mainly characterized fumarolic activity, whereas hot water is relatively scarce.

These thermal areas were well known for the native people, who had used the hot spring waters for their therapeutic properties. There are records of the utilization of these springs that date back to the beginning of the last century (Groeber 1946). Currently, the geographical characteristics of the region, its landscape, streams and waterfalls, the peculiar araucarias forests (Fig. 11.5), a 6 month skiing season and other available adventure sports, along with the thermal resources, have turned up this region increasingly attractive as a tourist spot over the last years.

Two small tourist centers have developed in the area: (a) Caviahue, which was funded in April 1986 with a population of about 800 habitants throughout the year and (b) Copahue, which is older, but here population has not a permanent character because of the hard weather conditions during winter. The construction and development of hotels and tourist facilities have increased the availability of beds to more than 3,000 in the last few years.

In the present chapter, the most important features of the Copahue Geothermal Field (CGF) were summarized with reference to the history of the field and the new geothermal perspectives in this remote site of the western Argentina.

11.2 Geology Outlines

The CGF is located in a western region of Argentina known as the "Cordillera Neuquina" (Neuquenian range) (Holmberg 1978), to the southwestern of Cordillera Principal (Major Range) (Yrigoyen 1979). From the geological point of view, there is a Tertiary-Quaternary volcanic complex with a huge caldera formed from a large collapsed stratovolcano from the Hualcupén eruptive center. Some effusive centers have developed within this caldera (Pesce 1989). Regional structures of transform-type faults surged in the Quechua orogenic phase, in the Upper Miocene, during which regional N55 W lineaments, developing secondary permeability, were also likely originated (Mas et al. 2000). Other than the N55 W-oriented fault system, secondary N55E, EW and N40 W lineaments affect the volcanic complex.

The outcropping volcanic rocks are predominantly andesitic of calc-alkaline composition, although few trachytic lava flows occur in the periphery of the caldera. Occasionally sedimentary rocks outcrop within the calc-alkaline volcanic products.

Volcanic activity at Copahue was exhaustively described in Chaps. 1, 3 and 4 of this book. Owing to eruptive and tectonic processes, an important zone of geothermal reservoir with a strong structural control has developed, bringing up numerous hot springs at the surface, some of which contributed to the development of

Fig. 11.5 The Araucaria forest and one of the many cascades that characterize Rio Agrio

therapeutic ventures and a high increment of tourism in the central western areas of the Neuquén Province.

Recently, one of the most significant changes observed at surface in the last few years occurred when a new area of active geothermal manifestations south of Copahue formed. Here, thermal springs and gas discharges with temperatures >90 °C and pH <4 seeped out, leading to the developing of new mud pool and an intense alteration of the rocks. In this area, just 5 years before, in 2008, newly formed minerals, mainly sulfates as alunogen, halotrichite, and gypsum (Mas et al. 2010), were recognized.

Geophysical and geochemical surveys suggested the presence of high-temperature geothermal resources below the depths drilled so far. It was assessed a strong structural control of the geothermal reservoir (Mas et al. 2000) by the N55 W and N55 E, EW and N40 W fault systems. According to previous investigation, the geothermal reservoir at Copahue volcano is located primarily in the high permeability zones of the calc-alkaline lavas and pyroclastic rocks of "Las Mellizas" Formation, which gives rise to the known levels of superheated steam.

According to the heat flow distribution map (Mas et al. 2000) in an area of about 100 km^2, which was performed with the data obtained from 12 wells at depths from 50 to 200 m, values up to six times higher than the average heat flux (60 mW.m^{-2}) were measured. The comparative analysis of the heat flow distribution with the tectonic conceptual model of the area shows that there is a correlation between the higher values of heat flow with the main structural lineaments. The distribution map of heat flow shows that there is a zone of potential interest near Caviahue, although these assumptions have all to be confirmed.

11.3 The Copahue Geothermal Project

Although some geological studies were carried out in the Copahue geothermal field since the 50s, it was only in the mid-seventies that systematic exploratory studies began, when the first oil crisis in modern times (in 1974) encouraged the development of renewable energy.

While the geothermal energy was used since prehistoric times as direct use, it was only since 1904 in Italy, that it began to be used for electricity generation. Until 1974, only a few countries, leaded by Italy, applied endogenous vapor for electrical generation. Since then, a significant development of geothermal energy took place. In spite of that, the increase of geothermal energy production in the world did not equalize the magnitude of existing resources. This was largely due to political issues, which exacerbated some negative aspects that this resource has. Among these issues, geothermal fluids have characteristics similar to other "traditional" minerals and energy commodities, like radioactive, water, or oil, with high risk in mining, exploration and development, which generate a degree of uncertainty to their feasibility and implementation. These issues, together with the declining in oil price, brought during the nineties to a relatively poor development of geothermal projects. The rise in the oil price over the first decade of the present century, and a very complex picture of the international energy market, promoted the application of direct use of geothermal heat as an alternative resource to traditional oil or coal, both for space heating and/or industrial applications. These direct uses of geothermal energy are useful not only to cover shortfalls in energy supply or to replace more expensive energy, but also because they imply low environmental impact with very low emission of greenhouse effect gases. While the use of this energy source for power generation is limited to those areas of high temperature fluids, generally associated with volcanic areas, lower temperature resources, which are more globally distributed, can be used in a variety of direct applications. With the tourist development projects under way, the energy requirements in the area have increased accordingly, and in the future it will exceed the capacity of the transmission line connected to the Provincial Interconnected System. The main growth will take place at Caviahue, although there are other projects at Copahue. Estimates of future energy requirements should also take into account the new ski facilities. The growth of energy demand will be affected also by the increased demand for heating, as the region has extremely low temperatures during several months of the winter season. Although the Neuquén Province is well endowed with natural gas, the gas fields are far from Copahue and there are no gas pipelines that reach this zone. Currently, liquid petroleum gas, diesel and oil are used for heating, with a high cost.

11.4 History of the Geothermal Project at Copahue

Exploration in the Copahue geothermal area began in 1974. It has developed in different stages, the first of which comprised geological, geochemical, and gravity surveys, as well as the drilled of gradient wells. The first deep exploration well (COP-1) began to be drilling in 1976. The second stage of the project began in 1980 during which new geological, geochemical and geophysical (with vertical electrical soundings-VES) surveys were carried out. In 1981 COP-1 well was technically modified and completed (1,414 m depth). The characteristics of the well fluid were satisfactory, and the borehole produced superheated steam. A second well, COP-2 (1,240 m depth), also produced superheated steam from 1986. In 1988, a binary-cycle pilot plant, with a capacity of 0.67 MWe, was installed on the COP-1 site (Fig. 11.6). It was the first power plant installed in South America.

In the same year, a technical-economic feasibility study began, with the cooperation of the Japan International Cooperation Agency (JICA-EPEN 1992). This study included the drilling of the well COP-3, to a depth of 1,067 m, which again produced superheated steam. It was estimated that the well would have produced about 60 t/h of steam, and the final report provided encouraging indications for the installation of a 30 MWe geothermal power plant. In Fig. 11.7 the COP-1 to COP-3 well logs are reported.

In 1997–98, the Province of Neuquén launched a district-heating project for the village of Copahue, using the geothermal steam to heat the

**Fig. 11.6** The Power Plant located at the COP-1

streets to prevent winter ice formation on roads, and to supply steam to buildings in the town, with an installed capacity of approximately 18 MW. For this purpose, a new well, the COP-4, was drilled and it produced over than 50 t/h of superheated steam (Fig. 11.8). The heating system consisted in network of pipes embedded in concrete plates. The coils transported the geothermal steam, which condensed on the way transferring heat to the environment (Fig. 11.9). In the tests carried out at that time, it was determined that two test plates maintained a temperature above 5 °C, without any ice formation with environment temperature from 0 to −15 °C and wind of 65 km/h, even in areas where the amount of snow was >4.5 m. The steam feeding the pipe system was maintained constant, with a pressure of about 0.2 Mpa and a temperature of 121 °C. The total length of the heating system is 1,880 m, with plates of 7.5 and 6.5 m of width and a thickness of 0.20 m. The steam consumption rate was about 37 kg/h/plate and the tube heaters made by carbon steel, type ASTM A 106 Gr B (Berwyn 1998).

The system was fed by two wells, COP-2 and COP-4 and the steam was transported via a 2,396 m long pipe.

According to the measurements carried out in the four wells drilled up to now, the following reservoir parameters were obtained (Mas 2005):

- Well COP-1: stabilized temp. = 250 °C; static pressure = 4.0 MPa; flow rate = 12–15 t/h at 1.0–1.4 MPa operation pressure.
- Well COP-2: stabilized temp. = 235 °C; static pressure = 3 MPa; flow rate = 6 t/h (0.6 MPa).
- Well COP-3: stabilized temp. = 240 °C; static pressure = 4.0 MPa; flow-rate: 50–60 t/h (1.0 MPa) (calc.)
- Well COP-4: stabilized temp. = 235 °C; Static pressure = 4.0 MPa; flow rate = 50 t/h (1.0 MPa)

In order to solve the problem of the increasing energy demand of the Copahue-Caviahue area, a number of projects were drawn up in the past, one of which consisted in putting the 0.67 MWe power plant at well COP-1 back into service. At present, this is no possible, for the COP-1 was abandoned because of operative and environmental reasons (Mas 2010). Another project is to put into operation the second phase of the district-heating project at the Copahue village, using directly the geothermal fluid to heat buildings.
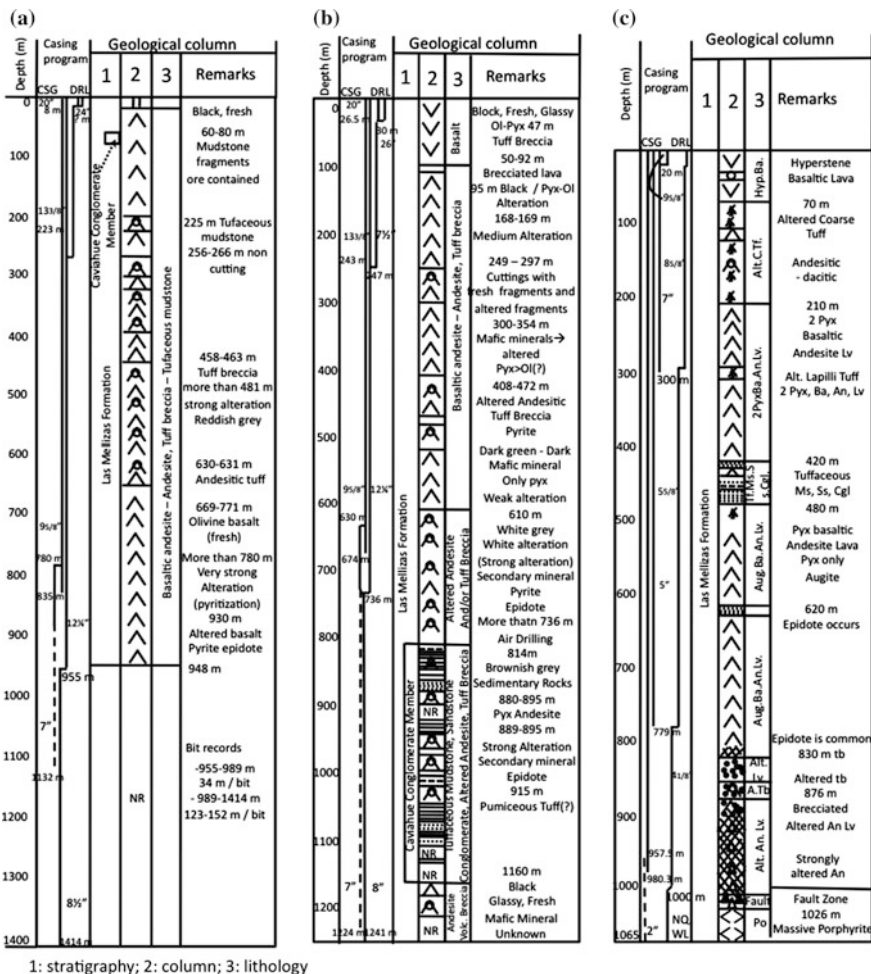
Fig. 11.7 Stratigraphic logs of the COP-1, COP-2 and COP-3 wells (modified after, JICA-EPEN 1992)

11.5 Hydrothermal Alteration and Fluid Inclusions

All the volcanic formations crossed by drillings in the geothermal field have undergone strong hydrothermal alteration. A detailed study of the alteration petrography has evidenced a vertical zoning that results from time-space super-impositions of at least three hydrothermal stages (Mas 2005; Mas et al. 2005). The first stage of hydrothermal alteration affected the totality of the geothermal zone and led to a zoned distribution of mineralogical facies ranging from clay-zeolite to propylitic facies with increasing depth and temperature. Alteration paragenesis suggests that temperatures grades from less than 100 °C at surface to 250/300 °C at 1,200 m depth (chlorite-epidote-prehnite assemblage). This stage represents a thermal event typical of the external part of aureoles during which zoned pervasive alteration developed in response to mainly conductive thermal gradient (Mas et al. 1993).

The second stage of hydrothermal alteration was initiated by a hydraulic fracturing of part of the system (between 800 m and 1,200 m depth). Infiltration of the permeable newly fractured horizons by aqueous fluids of meteoric origin promoted the intense alteration of the wall rocks.

Fig. 11.8 The COP-4 well and the steam pipeline


Fig. 11.9 Ice and snow from the streets of Copahue are removed by a geothermal heating system

Fluid inclusions data indicate boiling during this alteration stage. Quartz, wairakite, prehnite, epidote and even garnet, precipitated mainly in open fractures at temperatures of about 240–280 °C. Clay minerals formed also in open fractures and replaced preexisting igneous and hydrothermal

Fig. 11.10 Scanning electron microscope image of a Wairakite druse
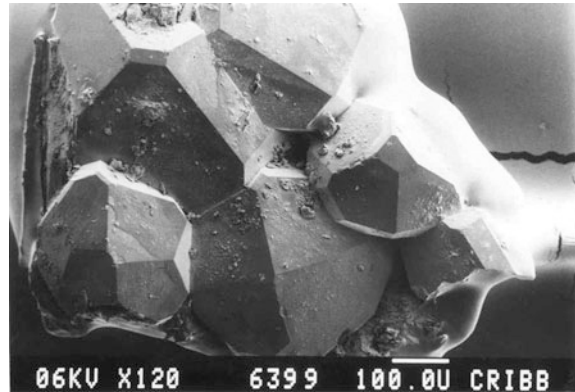
minerals of the early stage in surrounding wall rocks. Clays are essentially non-expandable chlorites or chlorite rich C/S mixed layers. The most common zeolites in Copahue are stilbite, laumontite and wairakite. In addition to these common zeolites, mordenite, clinoptilolite, heulandite and others were also identified. Wairakite is the most abundant zeolitic mineral in the Copahue drill-cores, beginning at depths of 600 m, and extending to the bottom of the holes, although it is more abundant in cracks, fissures and open spaces of the reservoir zones (Fig. 11.10). In the upper levels it appears as a fine filling of pores and amygdales and to a lesser extent replacing plagioclase and fine grain matrix. Calcium silicates of the CaO-MgO-FeO-Al_2O_3-TiO_2-SiO_2-H_2O system constitute an important rock forming mineral group, widespread in well samples of geothermal areas. A given sequence of calcium silicates reflects a progressive dehydration with the increase of the temperature. Taking into account

that the genesis of these calcic minerals depends strongly on the temperature, their identification is a useful guide in the analysis of the temperatures of formation. Among them epidote seems to be one of the most reliably and consistent temperature guide, for its occurrence is common in geothermal fields at temperatures higher than 250 °C, no matter the lithology nature. Another interesting mineral guide is prehnite, although there are discrepancies about the lowest formation temperature (from >220 to >300 °C) probably due to pH differences, calcium content in fluids and the iron rate in solid solution in the mineral. Wairakite, the high temperature calcium zeolite, occurs generally at the same temperatures as prehnite and the calcic garnet, and also indicate temperatures about -or higher- than 270 to 300 °C. The orthorhombic calcium silicate prehnite (Fig. 11.11) is common in cores from approximately 600 m depth and especially in the reservoir zone. It occurs with epidote, wairakite, chlorite, quartz, albite and sporadic actinolite and

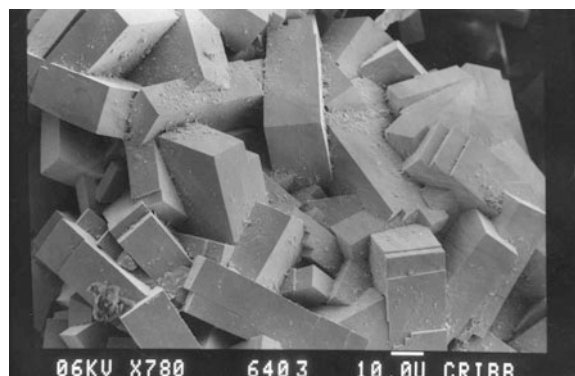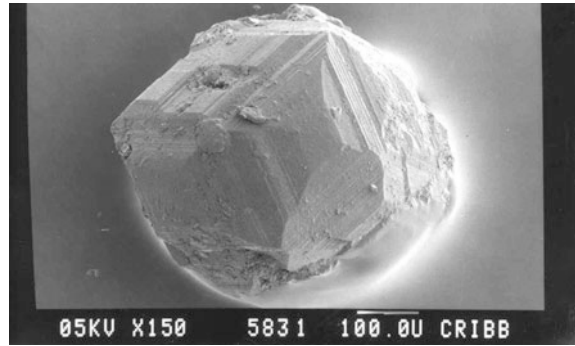**Fig. 11.11** Scanning electron microscope image of a Prehnite druse

**Fig. 11.12** Scanning electron microscope image of a garnet crystal

garnet, as fine grained aggregates after plagioclase, discrete patches in matrix and vesicles, or as veins of variable thickness. Garnet, although not very abundant, is frequent in the samples of the deepest levels. It is frequently associated with prehnite, epidote, quartz and actinolite. Garnet crystals of up to 1 mm of diameter (Fig. 11.12) occur in quartz veinlets of the reservoir level. In spite of the relatively scarcity, its single presence is a fact of interest in the analysis of the temperature formation of a geothermal field, since it implies a temperature over 300 °C.

It is worthy to mention that some changes were observed in the CGF in the last few years. Some of them have been subtle and other rather conspicuous. Between the first it can be mention the deposition of some unusual minerals for a geothermal fields, i.e. the sulfate-carbonates, burkeite (Fig. 11.13): $Na_6(CO_3)(SO_4)_2$ and hanksita: $KNa_{22}(SO_4)_9(CO_3)_2Cl$ deposited around a steam escape from the pipe of COP-2 well (Mas et al. 2007). These minerals usually

appear as efflorescence in saline soils or evaporitic deposits in continental lagoon environments but to the best of our knowledge they were never described associated with geothermal fluids.

At the COP-1 power plant, another new mineral, sassolite (H_3BO_3), was described for the first time in this geothermal field (Mas et al. 2010). The presence of boron, although new in Copahue, is frequent in many geothermal fields of the world, and it is considered an evidence of a magmatic component in the involved fluids. The particular paragenetic characteristics of these minerals allow drawing attention to possible changes in hydrothermal conditions of the geothermal system. Determinations on fluid inclusions were performed on quartz and calcite from different depths. Quartz crystals show primary, secondary and pseudo-secondary inclusions, while calcite crystals show a predominance of pseudo-secondary and secondary inclusions. According to the number and type of phases in the studied inclusions, they can be classified, as follows:

Fig. 11.13 Scanning electron microscope image of burkeite crystals
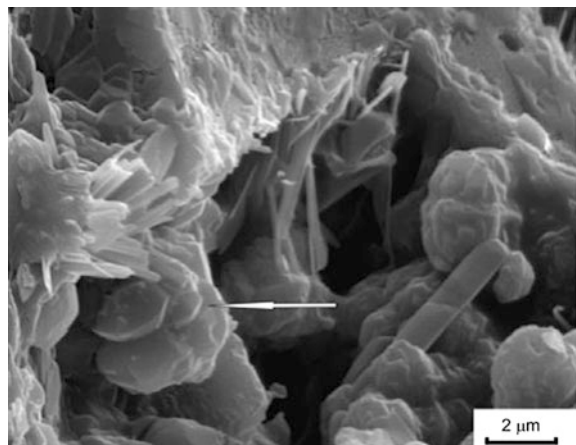
1. aqueous inclusions: two fluid phases, the volume of the liquid phase is greater than the steam one (L > G);
2. gas inclusions: two fluid phases, of which G > L;
3. three-phase inclusions (G-type): with three immiscible fluid phases; constituted by liquid water, steam and a gas phase (H_2S or CO_2).

The homogenization temperatures of the upper zone are very dispersed over a wide range of temperatures that extends towards the highest ones. Besides, all the registered temperatures are higher that the boiling point of the pure water for these depths. This fact suggests that the fluid was not homogeneous at the time of trapping because of the effect of a deeper boiling process, and therefore the inclusions trapped heterogeneous fluids formed by two phases (liquid and steam and/or gas) mixed in different proportions. In the level considered productive, the homogenization temperatures are concentrated in a narrow range, with a much smaller standard deviation, although there are also inclusions that homogenize to liquid and steam in a same sample, because of boiling. The average temperature of these inclusions is very narrow, almost coincident, with the boiling point curve for these depths. This suggests that the boiling produced the net separation of both fluid phases, which were trapped separately. In the deeper zone homogenization temperatures of calcite are similar to that displayed by quartz for this depth. In the upper zone, temperatures are however lower (they are the lowest recorded in whole field) but continue accompanying the trajectory of the curve.

chlorite and tremolite, which form within a temperature range of 200–300 °C (Mas et al. 1995), in rock samples veins from the wells bring up thermometric data with implications for the reservoir. This information is also confirmed by the study of the fluid inclusions (Mas et al. 1993), which found filling temperatures from 240 to 280 °C in quartz coexisting with wairakite.

As previously mentioned, the geothermal reservoir is structurally controlled (Mas et al. 2000) as also confirmed during drillings. Accordingly, geophysical and geochemical data suggest the presence of high-temperature geothermal resources below the depths drilled so far. The research and development projects at the Copahue geothermal field have been under its way for almost 40 years and the obtained results can be considered satisfactory as a superheated steam reservoir, with a temperature over 240 °C and pressure of about 4.0 MPa was identified. This geothermal resource, if exploited, would be able to feed a power plant of 30 MWe. On the other hand, the results also suggest that the reservoir would extend to greater depths and over a wider area than the one covered by previous studies and the parameters of the resources at the deeper levels would likely be higher. Based on the growth in population and in tourist facilities, the demand for energy is going to increase in Caviahue and Copahue and could be satisfied by geothermal resources. It would be profitable also for other villages located in the surrounding areas. Nevertheless, the Copahue Geothermal Project is presently suspended also due to the opposition of an Environmental Defense Group that caused the stop of the developing of a new stage of the project.

11.6 Chemical-Physical Conditions of the Hydrothermal Reservoir

The presence of hydrothermal minerals such as Ca-zeolites, stilbite, laumontite and wairakite, accompanied by epidote, prehnite, garnet,

11.7 Perspectives for Geothermal Exploitation

The existence of a geothermal field with interesting fluid characteristics in a region with an important tourist development would boost the

economic feasibility of tourist projects, and the consequent possibility for economic development of this region. One of the benefits of utilizing the geothermal resource for electricity generation and space heating is the reliability of the energy source since generation takes place in the same place of the utilization. Although the forms of utilization would in the beginning be restricted to electricity generation or space heating, as the project evolves, the resources could be used for balneotherapy, swimming pools, greenhouses and so forth. It should be noted that these activities already exist or are planned to be developed. Another benefit that would derive from a geothermal project in Copahue is that it could be developed in a reasonable time scale, increasing the investment when necessary or as the energy demand increases. The last, but not the least, this project would imply the use of a renewable energy source in the same place in which it is produced, without importing fossil fuel, with the consequent advantage with regard to the environment. Some facts that have taken place in the last years, like the volcanic eruptions of the Copahue, the formation of new large hot springs or the presence of new minerals promote the need to update the knowledge of the Copahue geothermal field. However, the 2012 eruption of has not apparently significantly modified the hydrothermal system that feeds the thermal water and gas discharges in the NE part of the Copahue volcano (Agusto et al. 2013).

References

Agusto M, Tassi F, Caselli AT, Vaselli O, Rouwet D, Capaccioni B, Caliro S, Chiodini G, Darrah T (2013) Gas geochemistry of the magmatic-hydrothermal fluid reservoir in the Copahue-Caviahue Volcanic Complex (Argentina). J Volcanol Geotherm Res 257:44–56

Berwyn A (1998) Copahue streets heating project. In: Productive uses of thermal waters. NRECA national rural electric cooperative association. In: VII Congreso Geológico Argentino. Dept of Energy USA, Neuquén, pp 301–307

Groeber P (1946) Observaciones geológicas a lo largo del meridiano 70°. Rev Asoc Geol Arg 1. Re-printed in 1980, series C

Giusiano A, Mendiberri H, Carbone O (2011) Introducción a los Recursos Hidrocarburíferos. In: XVIII Congreso Geológico Argentino, Neuquén, pp 639–644

Holmberg E (1978) Rasgos Geomorfológicos. In: VII Congreso Geológico Argentino, Neuquén, pp 119–127

JICA-EPEN (1992) Feasibility study on the northern Neuquén geothermal development project. Unpublished final report, Ente Provincial de Energía del Neuquén, Japan international cooperation agency, Japan

Latinoconsult, Electroconsult (1981) Geothermal feasibility study of Copahue. Final report, Secretaría de Estado del COPADE, Neuquen

Linares E, Ostera HA, Mas LC (1999) Cronología Potasio-Argón del complejo efusivo Copahue - Caviahue, Provincia del Neuquén. Rev Asoc Geol Arg 54 (3):240–247

Mas GR, Bengochea AL, Mas LC (2005) Thermometric study of Copahue geothermal field; Argentina. In: Proceedings World geothermal congress, Antalya, Turkey

Mas LC (2005) Present status of the Copahue geothermal project. In: World geothermal congress, Antalya, pp 1–10

Mas LC (2010) Neuquén geothermal project. History and present situation. In: World geothermal congress 2010 Apr 1–17, Bali, pp 25–30

Mas GR, Mas LC, Bengochea L (1993) Inclusiones fluidas en el pozo exploratorio COP-3, campo geotérmico de Copahue, Provincia del Neuquén, Argentina. In: XII Congreso Geológico Argentino, Mendoza, pp 92–98

Mas GR, Mas LC, Bengochea L (1995) Zeolite zoning in drillholes of the Copahue geothermal field, Neuquén. In: World geothermal congress, Florence, pp 1077–1081

Mas LC, Mas GR, Bengochea L (2000) Heat flow of Copahue geothermal field; its relation with tectonic scheme. In: World geothermal congress, Beppu–Morioka, pp 1419–1424

Mas GR, Bengochea L, Mas LC (2007) Burkeite and hanksite at Copahue, Argentina: the first occurrence of sulphate-carbonate minerals in a geothermal field. Miner Mag 71(2):235–240

Mas LC, Bengochea L, Mas GR, López N (2010) Recent changes in the copahue geothermal field, Neuquén Province, Argentina. In: Proceedings World Geothermal Congress, Bali, Indonesia, p 6

Mas LC, Mas GR, Bengochea L (2011) Recursos Geotérmicos. In: XVIII Congreso Geológico Argentino, Neuquén, pp 820–830

Pesce A (1989) Evolución Volcano-Tectónica del Complejo Efusivo Copahue-Caviahue y su Modelo Geotérmico Preliminar. Rev Asoc Geol Arg 44 (1–4):307–327

Ramos V (1978) Estructura. Relatorio VII Congreso Geológico Argentino, Neuquén, pp 99–119

Vergani G, Arregui C, Carbone O (2011) Sistemas Petroleros y Tipos de Entrampamientos en la Cuenca Neuquina, in Geología y Recursos Naturales de la Provincia del Neuquén. In: XVIII Congreso Geológico Argentino, Neuquén, pp 644–656

Yrigoyen MR (1979) Cordillera Principal. Geología Regional Argentina, vol 1. Academia Nacional de Ciencias, Córdoba, pp 651–694

Therapeutic Effects of the Mineral Waters from Copahue Spa

12

A.M. Monasterio, F. Armijo and F. Maraver

Abstract

Nestled in the Andes of Argentina, the Copahue village owes its name to the nearby volcano and boasts an exceptional climate along with several hydrothermal resources. The most outstanding of these resources are its mineral waters (*sulphated*, *sulphurated*, *carbogaseous*, *ferruginous* and *bicarbonated*) and their derived products including sulphurated muds, thermophilic algae and sulphurated gases. All these resources are used as natural remedies to treat rheumatic, skin, respiratory and neurological diseases.

Keywords

Copahue · Hot spring · Balneotherapy · Mineral water · Fangotherapy

12.1 Introduction

Copahue village (37°50′ S–71°00′ W), located 376 km NW of the province capital of Neuquén (Argentina) at 2010 m a.s.l., lies in the immediate surroundings of Copahue volcano, a land characterized for intense hydrothermal activity (Sussini et al. 1938; Pesce 1989; Monasterio 2009, 2010, 2012). The climate at Copahue is dry and cold. During winter, the village is almost completely covered by snow and can only be accessed by caterpillar trucks. Tourists may walk on its rooftops. Its hotels and health resorts are therefore only open in summer (Monasterio 2009, 2012) (Fig. 12.1).

According to the Spanish Law of Mines of 1973, "mineral-medicinal" waters are those of constant composition that feature, naturally or artificially, characteristics or qualities deemed of public utility. To be declared as such, their therapeutic or prevention benefits should be demonstrated (Armijo and San Martin 1994; Maraver and Armijo 2010). The World Health Organisation (WHO) requires that these waters

A.M. Monasterio (✉)
Mapuche S/N Caviahue CP, 8349 Neuquén, Argentina
e-mail: doctoramonasterio@hotmail.com

F. Armijo · F. Maraver
Escuela de Hidrología Médica, Facultad de Medicina, Universidad Complutense, 28040 Madrid, Spain

273

Fig. 12.1 Panoramic view of thermal village Copahue during winter and summer

must be bacteriologically uncontaminated and they should contain a given set of minerals which are proved to induce a beneficial effect on health. Mineral waters discharged from springs may be classified according to temperature as hypothermal, mesothermal or hyperthermal. This temperature refers to that of the water as it emerges from a spring or the temperature at which it is applied to the human body to produce different effects (AETS 2006; Maraver 2008; Maraver and Armijo 2010). The mineral waters used in medical hydrology can also be classified according to their dry residue into waters of high, medium and low mineralisation or weak mineralisation. However, the most useful classification system for health resort medicine is based on their chemical composition and the presence of special elements such as reduced sulphur, iron, free carbonic acid or radon. According to these criteria, mineral waters may be classed as: *chlorated*, *sulphated*, *bicarbonated*, *ferruginous*, *carbogaseous*, *sulphurated* and *radioactive* (Armijo and San Martin 1994; Maraver and Armijo 2010).

In this chapter, the medicinal uses provided by the local mineral resources (mineral waters, algae, gases and peloids) and climatic factors of the Copahue village are described and discussed.

12.2 Types of Thermal Manifestations

Copahue is volcanic system showing a thermal activity related to circulation of hydrothermal-magmatic fluids whose main water source is rainwater heated by heat released from a magma chamber. Thermal springs are rich in chemical elements mainly produced by magmatic degassing and fluid-rock interactions (Dietrich 2011; González Díaz 2005; Agusto et al. 2012, 2013, this book; Tassi et al. this book).

Thermal manifestations in this area mainly consists of: (a) *olletas*, round pools of various diameters containing superheated water; (b) *fumaroles*, pools containing superheated mineral water with a clay bed where mud naturally matures; and (c) *vents*, where vapours rich in gases that are beneficial for health emerge (Groeber and Corti 1920). A clayey muddy area, which is produced by the decomposition of the feldspars comprising surface trachiandesite outcrops (Dietrich 2011), is also present.

As a whole, the Copahue balneology health resort, which occupies 10,500 m^2 and is managed by the Regional Authority, consists of hypothermal, mesothermal and hyperthermal mineral waters of high, medium and low mineralisation including chlorated, sulphated, sodic, calcic, magnesic, and sulphurated, ferruginous and carbogaseous waters, in addition to derived products such as mud, 24 types of thermophilic algae and sulphurated gases (Monasterio 2010). Seven hot springs are currently utilized for medical applications: "Ferruginosa Pileta" (2FP), "Limon" (3L), "Sulfurosa" (4S), "Sulfurosa Pileta Circuito" (5SPC), "Sulfurosa Pileta" (7SP), "Vichy" (9VI) and "Volcán" (10VOL); and the three lagoons "Chancho" (1CHL), "Sulfurosa" (6SL) and "Verde" (8VL) (Figs. 12.1 and 12.2, Tables 12.1 and 12.2). The modern facilities the Copahue thermal centre offer individual,

Fig. 12.2 Location of the main thermal water springs of Copahue Village

Table 12.1 Chemical composition of thermal springs of Copahue village

	SO_4^{2-}	Cl^-	HCO_3^-	F^-	NO_3^-	HS^-	Na^+	Ca^{2+}	Mg^{2+}	K^+	NH_4^+
1CHL—Chancho, L	1438	6.6		0.31			53	77	16	21	135
2FP—Ferruginosa, Pileta	50	5.4	92	0.20	20	1.1	26	20	7.9	14	
3L—Limón	1077	0.80		0.30			25	22	8.6	21	88
4S—Sulfurosa	11	1.2	464	0.20	0.8		51	50	26	27	3.3
5SPC—Sulfurosa, Pileta	115	3.8	24	0.20			23	21	3.7	8.0	6.7
6SL—Sulfurosa, L	586	2.7		0.30			29	45	11	19	55
7SP—Sulfurosa, Pileta	39	3.2	201	0.20	16	1.2	34	30	11	17	
8VL—Verde, L	483	1.9		0.30			15	25	4.8	11	15
9VI—Vichy	11	4.6	311	0.20	14		21	64	10	7.4	0.60
10VOL—Volcán	23207	628		50			1175	752	553	772	

Concentrations are in mg/L

Table 12.2 Chemical-physical features of thermal springs of Copahue village

	T	RS	Fe	CO_2	H_2S	Rn	k	pH	Turbidity	Hardness
1CHL—Chancho, L	35	2067	31			40	3082	2.3	704	256
2FP—Ferruginosa, Pileta	41	242	1.2	50	2.72	13	331	6.0	44	82
3L—Limón	53	2153	8.9			31	4011	3.9	105	90
4S—Sulfurosa	52	442	0.20	2.0	0.10	15	775	7.1		229
5SPC—Sulfurosa, Pileta Circuito	61	226	2.1	440		12	298	6.5	39	68.6
6SL—Sulfurosa, L	54	1075	2.2			11	1210	5.6	118	157
7SP—Sulfurosa, Pileta	42	301	0.70	20	2.3	18	421	6.6		121
8VL—Verde, L	30	1125	2.1			52	857	4.2	37	81
9VI—Vichy	42	331	9.5	45			545	7.4	14	201
10VOL—Volcán	69	36296	82			3	44390	2.8		4156

RS: total solid dried at 110 °C. Fe, dissolved CO_2, H_2S and hardness (as $CaCO_3$) are expressed in mg/L; Rn in Bq/L; turbidity in NTU; conductivity (k at 25 °C) in $\mu S\ cm^{-1}$; temperature in °C

Fig. 12.3 Balneotherapy building, where individual mud and bath therapies are carried out

personalized treatments prescribed by medical staff. The resort receives 30,000 visitors each season and more than 200,000 medical treatments are carried out (Monasterio 2012) (Fig. 12.3).

12.3 Health Therapies

The main medical application of mineral waters, gases and peloids are, as follows: (1) immersion baths, (2) hydromassages, (3) subaquatic massages, (4) water streams at different pressures and temperatures, (5) inhalations, (6) steam baths, (7) local and general applications of peloids, (8) oral treatments and (9) hydrokinesitherapy (Monasterio 2009, 2010, 2012; Armijo et al. 2011).

Mineral waters of Copahue may provide different health benefits, depending on their chemical composition:

Sulphated waters: these springs (Limon, Volcán, lagoons Chancho, Sulfurosa and Verde (Figs. 12.4, 12.5 and 12.6) have a relatively high salinity (>1 g of dry residue per litre) and are characterized by a SO_4-dominated composition. Ingestion of water from the Limon spring has a purgative or laxative effect, and caused increasing intraluminal osmotic pressure and intestinal peristalsis. It is therefore indicated for patients affected by constipation.

The effects of sulphated waters on the liver include enhanced bile production (choleretic effect) and release from the biliary vesicle (cholagoge effect), protecting hepatic cells. It is therefore useful for patients with dyspepsia, favouring liver function (Armijo and San Martin 1994; Maraver and Armijo 2010; Monasterio 2012).

Sulphurated waters: these springs (Sulfurosa Pileta and Ferruginosa Pileta) are characterized by significant SH_2 and/or SH^- concentrations (≥1 mg/L). For dermatological applications, i.e. to eliminate the cells of the outer corneal skin layer, these waters are typically used for baths, hydromassages or subaquatic massages. It is worth to mention that sulphur ions in its reduced forms have a keratoplastic effect on the human skin, whereas sulphate causes a keratolysis. Moreover, sulphur has a significant immunosuppressive effects of the skin, since it inhibits T lymphocyte proliferation, the production of cytokines and Langerhan epidermal cells. This produces an anti-inflammatory effect with benefits for patients affected by psoriasis, eczema or dermatitis. In the deep epidermal layers, reduced sulphur is transformed into pentanoic acid, which has antifungal, bactericidal and anti-pruriginous properties, thus it is often used to treat acne,

Fig. 12.4 "Sulfurosa" Lagoon, where the mud matures and the sulphated water is used in bath therapies programmes

Fig. 12.5 "Chancho" (Pig) Lagoon, where health therapies are carried out

varicose ulcers and tinea versicolor (Matz et al. 2003; Constantino and Lampa 2005; AETS 2006; Kazandjieva et al. 2008; Gisondi et al. 2012; Monasterio 2012). This type of water has also useful application to solve rheumatisms, due to its physical effects (mechanical, thermal) and immunological, anti-inflammatory and chondro-protective actions. The latter are related to modifications in the biochemical and molecular mechanisms responsible for rheumatic symptoms, including a decrease of the levels of tumour necrosis factor alpha (TNF-α), interleukins (IL-1β, IL-1, IL-6), prostaglandins (PGE2) and leukotriene B4 (LTB4). Enhanced synthesis of norepinephrine, cortisol, beta-endorphins and insulin-like growth factor was also documented. In addition, cartilage the induced stimulation of chondrocyte metabolism produces a protective effect on joints, having benefits for patients with osteoarticular diseases, e.g. arthrosis, arthritis, rheumatic diseases and degenerative diseases (Verhagen et al. 2007; Monasterio and

Fig. 12.6 "Verde" Lagoon, mineral waters used in dermatology osteoarticular programs in group or individual sessions

Grenovero 2008; Forestier et al. 2010; Fioravanti et al. 2011, 2012).

At Copahue Spa a particular attention is devoted to medical treatment of respiratory disorders, using vapours produced from sulphurated waters in natural stoves. When inhaled, the effect of these vapours is antiseptic, anti-inflammatory, while defence mechanisms are enhanced as ciliary activity increases. Additional effects include loosening on mucous secretions (mucolytic effect), and increased respiratory mucosa vascularisation and tissue regeneration. Sulphurated vapours are suitable for patients with sinusitis, bronchitis, asthma, or as preventive treatment (Armijo and San Martin 1994; Bellussi et al. 2006; Staffieri et al. 2008; Zingoni 2009; Monasterio et al. 2011; Monasterio 2012).

Ferruginous waters are those showing ≥ 5 mg/L of Fe^{2+}. This category of waters includes the orally used "Vichy" and Limon springs, the Chancho and Verde lagoons, which are used in balneology, and the Volcan spring that is currently in disuse (Varekamp et al. 2009; Augusto et al. 2012). When the former two are ingested, blood iron levels rise due to the intestinal absorption of Fe^{2+}, activating erythropoiesis and oxidizing enzymes. These waters are recommended in patients with anaemia and in

pregnant women (Armijo and San Martin 1994; Monasterio 2012).

Carbogaseous waters are those having ≥ 250 mg/L of CO_2. Sulfurosa Pileta Circuito is the only spring pertaining to this category. However, patients have shown a low tolerance to these waters, thus it is currently in disuse.

Water from the Sulfurosa spring, showing a low salinity with predominance of bicarbonate, calcium, sodium and magnesium ions, has been successfully used for both oral and vapours treatments to nurse dyspepsia and respiratory disorders (Monasterio 2012).

It should be noted that the springs preserve their original nomenclature, although this may not correspond to the chemical composition of their waters.

12.4 Fangotherapy

According to the International Society of Medical Hydrology and Climatology (ISMH) *muds* or *peloids* are "Natural products composed of a mixture of mineral water (sea water and salt lake water included), with organic or inorganic matter, resulting from geologic or biologic processes,

or from both geologic and biologic processes, which are utilized for therapeutic purposes under the form of packs or baths" (Armijo and San Martín 1994). In a recent paper by Gomes et al. (2013), a new definition of peloid was proposed: "A peloid is a maturated mud or muddy dispersion with healing and/or cosmetic properties, composed of a complex mixture of fine-grained natural materials of geologic and/or biologic origin, mineral water or seawater, and common organic compounds from biological metabolic activity".

In their solid phase, the peloids of Copahue contain various mono mineral fragments, rock fragments, clay mineral particles, amorphous silica remains of microorganisms and aggregates of organic substances. This solid phase, together with the microorganisms, algae and the water component, confers to the mixture a liquid consistency (exceeding the Atterberg limit) that is grey coloured, contains particles smaller than 62 μm and has a high moisture content promoting the mud's heat therapy effects (Baschini et al. 2010, 2011). Peloid mineral composition consists of clays (kaolinite and smectite), orthorhombic sulphur, alunite, different forms of silica, pyrites, and iron hydroxide. The main element is sulphur and its major sulphate is alunite in its potassium form (Baschini et al. 2010). Peloids show a medium water content and a high content of materials removable by calcination (organic matter) Armijo et al. (2008). They are of a soft, spongy texture and their non-adhesiveness makes them easy to be removed from the skin.

The peloids from Chancho lagoon have an elevated calorific capacity attributable to their high water content, a low heat conductivity coefficient due to the type of mineralizing components. These features confer the peloids a high heat-retentivity, explaining their cooling curve consisting of a long inertia time and a long relaxation time with the consequence of their slow heat release (Armijo et al. 2008).

Muds or peloids exert their actions on the organism through physical mechanisms mainly linked to heat therapeutic effects and their chemical and biological properties (Hattori 1963).

Thermotherapeutic materials may be classified according to (i) the depth of their heat effects, i.e. superficial or deep acting, and (ii) the main heat-producing mechanism, as conduction, convection or radiation. Fangotherapy is described as a superficial heat therapy mode whereby heat is transferred by conduction (Armijo and San Martin 1994; Mourelle et al. 2008). Notwithstanding, the main effect of peloids on human health is thermotherapeutic, related to its application temperature, generally ranging from 42 to 45 °C. Peloids have also anti-inflammatory, chondroprotective and immunological effects, which may be produced by the absorption through the skin of inorganic and organic substances during their application. Heat therapy using peloids has both local and generalized effects:

Local:

- Increased temperature at the application site perceived by the patient as slight itching and heat.
- Local vasodilation and hyperemia: improved blood supply to the skin and underlying tissues, improved tissue trophism and nutrition. These circulatory effects persist beyond the return to normal temperatures.
- Release of histamine and acetylcholine.
- Modifications in serum levels of amino acids such as triptophan, cysteine and citrulline.

General:

These effects occur via the combined actions of multiple mechanisms and remain detectable after skin temperature normalizes. The most outstanding general effects are:

- A transient increase in the respiratory and heart rate.
- Increased sweating.
- Pleasant feeling of warmth and sleepiness.
- Arterial hypotension.
- Rise in body temperature.
- Hemoconcentration.
- Reduced urine excretion and its increased concentration.

- In response to prolonged applications, increased plasma protein levels.
- Decrease in the alkaline reserve accompanied by an elevated respiratory rate.
- Enhanced immunological response through neuroendocrine and neurovegetative stimulation.
- Activated oxidative function of neutrophils inducing defence mechanisms.
- Chondroprotective effects.
- Analgesic, sedative, reabsorptive and anti-spadmodic effects.

According to Roques (2004), the biological actions of peloids can be summarized as:

- Analgesic action through the self-activation of pain control mechanisms (secretion of endorfins), which translates to the elevation of the pain threshold.
- Anti-inflammatory actions arising from:
  - stimulation of the suprarenal glands
  - inhibition of prostaglandins and leukotrienes
  - improved antioxidative state (superoxide dismutase, glutathione peroxidase, myeloperoxidase, nitric oxide)
  - diminished chondrolytic activity through the inhibition of cytokines and stimulation of immunoglobulins
  - Smooth muscle fibre contraction mediated by adrenergic and dopaminergic mechanisms
- Scarring action through enhanced angiogenesis and hyaluronic acid secretion.

In a recent review of the mechanisms of action of peloids on mediators of the immune response, inflammation and chondrolysis, Fioravanti et al. (2011) reported:

- A reduction in the levels of circulating prostaglandins E2 (PGE-2) and leukotriene B4 (LT-B4) in patients with osteoarthritis or fibromyalgia.
- Reductions in tumour necrosis factor-α (TNF-α), interleukin-6 (IL-6) and circulating levels of interleukin-1β (IL-1β) induced by whole-body hyperthermia.
- A reduction in the release of reactive oxygen species (ROS) and peroxynitrite (RNS) by polymorphonuclear cells (PMN) exposed to n-formyl-methionyl-leucyl-phenylalanine and phorbol-12-miristate-13-acetate.
- Reduced circulating serum nitric oxide (NO) levels in patients with osteoarthritis receiving mud baths.
- Increased circulating immunoglubulin-1 (IGF-1) levels in patients with osteoarthritis administered mud baths.
- Increased circulating transforming growth factor beta (TGF-ß) levels in patients with anchylosing spondylitis following a combined balneotherapy-exercise programme (exercise, hyperthermia and exposure to low doses of radon).

Studies carried out at the Copahue Spa have revealed the bactericidal effects of muds (Schell et al. 2008) and their capability to reduce the presence of interleukin 1 (IL-1), a pro-inflammatory agent with a direct role in the pathogenesis of osteoarthrosis (Monasterio 2010, 2012).

At Copahue Spa, personalized fangotherapy can be prescribed. The grey mud matured in the Sulfurosa and Chancho lagoons is transferred to individual cabins and applied to the body zones and at the temperature prescribed by medical staff. The application time is 15 min followed by a 10 min resting period lying down. Another mud treatment mode is a general application at the Chancho lagoon at a depth of 10–60 cm. The lagoon bed has zones with large amounts of very soft, malleable mud with large quantities of minerals and a high temperature retaining capacity.

12.5 Algae

Algae naturally reproduce in the Verde lagoon and in several springs. They are acidophilic, thermophilic and pertains to different species

(*Phormidium tergestinum*, *Phormidium granulatum Oscillatoria* sp., *Oscillatoria subbrevis*, *Mastigocladus laminosus*, *Oedogonium*, *Scenesdmus ecornis*, *Chorella kessleri*, *Euglena mutabilis*, *Chlamydomonas* sp., *Ulothrix* sp., *Cyanidium caldarium*) (Accorinti et al. 1991, Accorinti and Wenzel 1995; Accorinti 1995). These algae are used to treat skin conditions such as psoriasis, eczema, dermatitis, rosacea, acne, venous ulcers and pressure ulcers (Alvarez 1938; Ubogui and Ficoseco 1990; Ubogui et al. 1991, 1998, 2008; Squadrone 1992; Monasterio 2012).

12.6 Final Considerations

The thermal resources of the Copahue geothermal complex offer the opportunity of treating several health diseases owing to its outstanding hydrothermal resources of excellent quality. This health resort boasts a large array of mineral waters and derived products, such as muds, gases and algae, along with modern installations and exceptional climate conditions. The enhanced activity of Copahue volcano has recent posed severe concerns for the local population. On the other hand, commercial activities related to this natural resource play a key role for the economy of this community, and represent a unique chance for the development of this remote area of the Andes.

References

Accorinti J, Squadrone M, Wenzel M, Perez A (1991) Valoración de las propiedades antimicrobianas del agua de Volcán Copahue (Neuquén Argentina). Arch Arg. Dermat 41:229–237 (in Spanish)

Accorinti J, Wenzel M (1995) Biological essays in Argentine thermal algal. Dominguezia 12:7–15

Accorinti J (1995) Complejo Termal Copahue y Algas del Domuyo. Del Mito al Estudio científico de sus propiedades curativas. 4(3):32–33 (in Spanish)

AETS (2006) Técnicas y Tecnologías en Hidrología Médica e Hidroterapia. ISCIII (in Spanish), Madrid

Alvarez G (1938) Contribución al estudio de las termas de Copahue (Neuquén), en sus aplicaciones dermatológicas. Bol Asoc Med Argent 4:220 (in Spanish)

Armijo F, Ubogui J, Corvillo I, Monasterio AM, Maraver F (2008) Estudios de los peloides de las termas de Copahue (Neuquén, Argentina): Características y propiedades Balnea 4:143–153 (in Spanish)

Armijo F, Monasterio AM, Corvillo I, Aguilera L, Pozo M, Carretero MI, Maraver F (2011) When volcanic waters are beneficial to health. In: Belsino C, Fiore S, Giannossi M (eds) Geological and medical sciences for a safer environment GeoMed Bar Digilabs Pub, 6

Armijo M, San Martín J (1994) Curas balnearias y climáticas. Talasoterapia y helioterapia. Madrid: Ed. Complutense (in Spanish)

Agusto M, Caselli AT, Tassi F, Dos Santos M, Vaselli O (2012) Seguimiento Geoquímico de las aguas ácidas del sistema Volcán Copahue-Río Agrio: Posible aplicación para la identificación de precursores eruptivos. Rev Asoc Geologica Arg 69(4):481–495

Agusto M, Tassi F, Caselli AT, Vaselli O, Rouwet D, Capaccioni B, Caliro S, Chiodini G, Darrah T (2013) Gas geochemistry of the magmatic-hydrothermal fluid reservoir in the Copahue-Caviahue Volcanic Complex (Argentina). J Volcanol Geoth Res 257:44–56

Baschini MT, Pettinari GR, Vallés JM, Aguzzi C, Cerezo P, López-Galindo A, Setti M, Viseras C (2010) Suitability of natural sulphur-rich muds from Copahue (Argentina) for use as semisolid health care products. Appl Clay Sci 49:205–212

Baschini M, Pettinari G, Vallés JM, Monasterio AM, Jimenez J, López-Galindo A, Viseras C, Setti M (2011) Caracterización de fangos en el área geotermal de Copahue-Procesos de maduración natural. Preservación del recurso natural. In: I Congreso Internacional de Termalismo, Neuquén, Argentina, 25–27

Bellussi L, De Benedetto M, Giordano C, Mira E, Paludetti G, Passáli D, Scaglione F (2006) Crenotherapy and upper airways diseases. Consensus Conference. Acta Otorhinolaryngol Ital 26(4 Suppl 83):5–54

Constantino M, Lampa E (2005) Psoriasis and mud therapy: clinical-experimental study. Clin Ter 156 (4):145–149

Dietrich S (2011) Estudio geológico y geoquímica de las aguas termales de la zona aledaña a la localidad de Copahue. Provincia del Neuquén. Ph.D. thesis. Universidad de Buenos Aires (in Spanish)

Fioravanti A, Cantarini L, Guidelli G, Galeazzi M (2011) Mechanisms of action of spa therapies in rheumatic diseases: what scientific evidence is there? Rheumatol Int. 31(1):1–8

Fioravanti A, Giannitti C, Bellisai B, Iacoponi F, Galeazzi M (2012) Efficacy of balneotherapy on pain, function and quality of life in patients with osteoarthritis of the knee. Int J Biometeorol 56(4):583–90

Forestier R, Desfour H, Tessier JM, Françon A, Foote AM, Genty C, Rolland C, Roques CF, Bosson JL (2010) Spa therapy in the treatment of knee osteoarthritis: a large randomised multicentre trial. Ann Rheum Dis 69 (4):660–665

Gisondi P, Farina S, Giordano MV, Zanoni M, Girolomoni G (2012) Attitude to treatment of patients with

psoriasis attending spa center. G Ital Dermatol Venereol 147(5):483–9

Gomes C, Carretero M, Pozo M, Maraver F, Cantista P, Armijo F, Legido J, Teixeira F, Rautureau M, Delgado R (2013) Peloids and pelotherapy: Historical evolution, classification and glossary. Appl Clay Sci 75–76:28–38

González-Díaz E (2005) Geomorfología de la región del volcán Copahue y sus adyacencias (centro- oeste del Neuquén). Rev Asoc Geologica Arg 60(1):72–87

Groeber P, Corti H (1920) Estudio geológico de las Termas de Copahue. Buenos Aires: Dirección General de Minas. Informes Preliminares y Comunicaciones Bol. Nº 3 serie F:1–17 (in Spanish)

Hattori I (1963) Pelotherapy. In: Licht S. (ed) Medical hydrology. Waverly Press, Maryland, pp 273–290

Kazandjieva J, Grozdev I, Darlenski R, Tsankov N (2008) Climatotherapy of psoriasis. Clin Dermatol 26 (5):477–85

Maraver F (2008) Importancia de la medicina termal. Balnea 4:35–50

Maraver F, Armijo F (2010) Vademecun II de aguas mineromedicinales españolas. Complutense, Madrid

Matz H, Orion E, Wolf R (2003) Balneotherapy in dermatology. Dermatol Ther 16(2):132–40

Melnick D, Folguera A, Ramos V (2006) Structural control on arc volcanism: the Copahue-Agrio complex, South-Central Andes (37º50′S). J South Am Earth Sci 22:66–88

Monasterio AM, Grenovero S (2008) Influencia del tratamiento termal en pacientes con diagnóstico de osteoartrosis primaria de rodilla y manos derivados por el plan termalismo al complejo termal de Copahue (Neuquén, Argentina) en la temporada 2006–2007. Balnea 4:133–141 (in Spanish)

Monasterio AM (2009) Termas de Copahue CPH "Lugar de Baños". Impresión Arte, Neuquén

Monasterio AM (2010) Estudio de las aguas minerales de la Provincia de Neuquén. Ph.D. thesis. Universidad Complutense de Madrid, Spain

Monasterio AM, Zingoni E, Merino L, Grenovero S, Maraver F (2011) Comportamiento de la motilidad ciliar en pacientes tratados con aguas minerales de la villa termal de Copahue, Neuquén, Argentina. In: I Congreso Internacional de Termalismo, Neuquén, Argentina, pp 20–23

Monasterio AM (2012) Caminemos por las Termas del Neuquén. Caleuche, Bariloche

Mourelle L, Meijide R, Legido J, Medina C (2008) Curso de Termalismo: Peloides termales. Universidad de Vigo, Vigo, Spain

Mourelle L, Meijide R, Freire A, Maraver F, Carretero MI, (2009) Técnicas hidrotermales y estética del bienestar. 13:125–134

Pesce A (1989) Evaluación Vulcano-Tectónica del Complejo Efusivo Copahue-Caviahue y su Modelo Geotérmico Preliminar. Rev Asoc Geologica Arg 44 (1–4):307–327(in Spanish)

Roques C (2004) Mud therapy and health. In: III Symposium on thermal muds in Europe, Dax, Germany, 75–77

Schell C, Sparo M, De Luca M, Grenovero S, De Michele D, Giacomino M, Monasterio AM, Belderrain A, Basualdo J (2008) Actividad inhibitoria de la fase líquida del fango termal de Copahue (Neuquén, Argentina) sobre cepas de Staphylococcus aureus. An Hidrol Med 3:21–33

Squadrone M (1992) Acción del agua del volcán Copahue (Neuquén, Argentina) sobre las micobacterias. Arch Argent Dermatol 42:97–108 (in Spanish)

Staffieri A, Marino F, Staffieri C, Giacomelli L, D'Alessandro E, Ferraro M, Fedrazzoni U, Marioni G (2008) The effects of sulfurous-arsenical-ferruginous thermal water nasal irrigation in wound healing after functional endoscopic sinus surgery for chronic rhinosinusitis: a prospective randomized study. Am J Otolaryngol 29(4):223–229

Sussini M, Herrero E, Brandam RA, Isnardi H, Galmarini AG, Castillo M, Pastore F (1938) Aguas Minerales de la República Argentina—Vol. XIII Territorio del Neuquen. Buenos Aires: Ministerio del Interior – Comisión Nacional de Climatología y Aguas pp 168 (in Spanish)

Ubogui J, Ficoseco H (1990) Ulceras por decúbito e hidroterapia en las termas de Copahue. Arch Arg Dermatol 40:393–399

Ubogui J, Rodríguez L, Ficoseco H, Sevinsky L, Kien K, Stengel F (1991) Terapéutica no convencional de la Psoriasis en las termas de Copahue (Neuquén Argentina) experiencia preliminar. Arch Arg Dermatol 41:25–39 (in Spanish)

Ubogui J, Stengel FM, Kien K, Sevinsky L, Rodriguez L (1998) Thermalism in Argentina. Alternative or complementary dermatologic therapy. Arc. Dermatol 134(11):1411–1412

Ubogui J, Roma A, Garvier V, García F, Magariños G, Perrotta G, Monasterio AM (2008) Seguimiento clínico de pacientes con psoriasis en las termas de Copahue (Neuquén, Argentina). Balnea 4:123–132

Varekamp J, Ouimette A, Herman S, Flynn K, Bermudez A, Delpino D (2009) Naturally acid waters from Copahue volcano, Argentina. Appl Geochem 24:208–220

Verhagen A, Bierma-Zeinstra S, Boers M, Cardoso J, Lambeck J (2007) Balneotherapy for osteoarthritis. Cochrane Database Syst Rev (4):CD006864

Zingoni E (2009) Crenoterapia respiratoria. Termas de Copahue. Impresión arte patagónicas, Neuquen

Religion, Popular Beliefs and Legends About Copahue Volcano

13

P. Castaño

Abstract

It is not possible to write about Copahue volcano without mentioning the population that, for the last three centuries, has been living in its surroundings: the Mapuche. This chapter accompanies the reader through a fascinating tale, from the settling of the first tribes in the Argentine territory to their nowadays life in the thirty territorial reservations, that host 50–100 families. Their story in the Argentine Andean sector begins with the ethnic replacement of previous inhabitants through a process of adaptation and fusion. The deep contact with nature strongly influenced their beliefs, from the prayers dedicated to productive trees, to the connection they believe exists between the souls of their dead and natural phenomena. Their relationship with the volcano culminates with the narration of a legend that can explain the etymology of the name Copahue.

13.1 Introduction

This chapter was aimed to introduce the reader to the tradition of the Mapuche people, to describe their movements along the times and the origin of their local tribes. A special focus was devoted to the beliefs of Mapuches, including local legend and stories developed by aborigines from the area hosting Copahue volcano. Through these stories, Mapuches merely tried to explain those events they witnessed but they could not control. Through their legends and beliefs, they tried to prevent their people from being harmed.

13.2 The First Humans in Patagonia

The original populations that nowadays are known as Mapuches were the result of a long inhabitation process in the lands of the Neuquen province (Fig. 13.1).

Although the archaeological evidence has recorded the human presence in the Patagonian area as far as 12,000 years ago, towards the Andean Range in the north of Neuquen region,

P. Castaño (✉)
Municipality of Caviahue-Copahue, Calle 8 de Abril
S/N, Caviahue, Argentina
e-mail: patcastano@hotmail.com

Fig. 13.1 The Neuquen Province (to the *left*) located to SW of Argentina in the Patagonia region and the Limay river valley

these records are from about 9,000 years ago mainly due to the fact that the place for settlement and migration of the first human beings were determined by the availability of water. Thus, in the surroundings of the Limay River valley (Fig. 13.1), the historical evidence allows us to know about life of the early hunters that moved around according to the seasons so as to take advantage of the diverse hunting and collecting resources in varied microenvironments, heights and relief. However, when the climate conditions changed after the Ice Age, the hunter-collector population, who had settled in the Limay River

Valley, started to advance over the steppe environment contacting other groups and inter-changing goods and reached the preceding lands of the mountainous areas about 1,300 years ago. Along with a significant geographical advance, in this long journey these people strengthened their subsistence and goods acquisition strategies and the exploitation of different resources. Thus, they developed an economic model which allowed them to adequate to the climatic and environmental diversity of the sites they visited: they made use of the most protected ones in the cold winters (*invernadas: spanish word which refers*
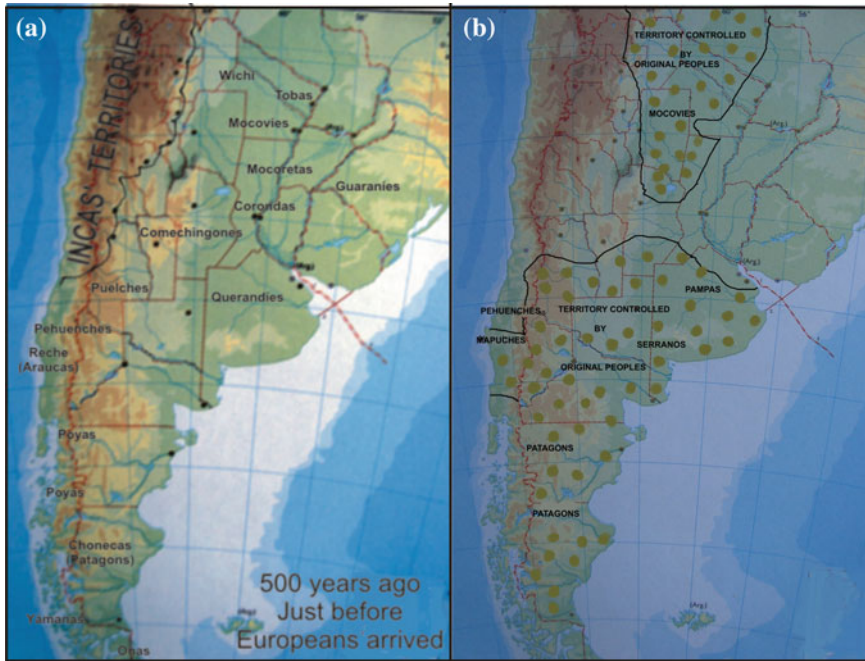
Fig. 13.2 Distribution of the local tribes 500 (**a**) and 250 years ago (**b**)

to the place where Mapuches stay with their animals and family in winter) and visited the intermediate plains and high plateaus during the summer (*veranadas: spanish word which refers to the place where the aborigines move to in summer looking for better grasslands for their cattle*), when the weather conditions were not so hard. As a result, about 800 years ago, human groups had expanded throughout the Patagonian region, significantly increasing both their population and the cultural interchange with other groups. These aspects favored the circulation of knowledge, concepts and common ideas in some way (Mandrini 2008).

13.3   Origin of Mapuches

In 1500 AD and possibly as a result of the very first contacts with the Incas civilization (Fig. 13.2a), the descendants of ancient tribes had incorporated a few elements of Andean origin to their culture. Although they were neither socially

nor politically organized, they spoke a common language and shared basic cultural features.

As far as their survival is concerned, the products from cultivation were only able to partly satisfy their needs. Then, they had other sources of supplies such as fishing and catching bird in lagoons and lakes, hunting and forests, which provided them plenty of fruit and seeds.

13.4   Mapuche People in Argentina

Over three centuries ago the original Mapuche tribes began to infiltrate into Argentina along the Patagonia border. The *Araucas*' or, as they call themselves, 'Mapuches', were the local inhabitants in Chile (Fig. 13.2b) in times of the Spanish conquerors, whose occupation extended over the greatest part of the Chilean land. Owing to strategic reasons, the Spanish pushed the local tribes to concentrate to the south, as it was the furthest place from their incoming point (the north) (Delfino 1968). In the southern Chilean regions

that face Neuquen, Araucas opposed strong resistance to the invaders initiating a period of steady fight, which lasted until the Spanish remained in Chile and long after the Chilean independence. Meanwhile, the local groups, also in the fighting areas, incorporated many Spanish elements, especially those related to horse and war arts (transculturation or acculturation). It was also in those times when, from the south of Chile, a process known as *Argentina araucanization* began (Delfino 1968). What did that process imply? Simply, the strong influence of Araucas on the other tribes' cultures. The first populations who suffered it were those located in the mountains, especially Pehuenches, the inhabitants of a high density of araucaria (pehuen) zone in the northern border with the region occupied by Araucas (Fig. 13.2b). As Mapuches needed horses to continue their war with the Spanish and the Argentine prairies, there was soon an interchange among the tribes on both ranges which were areas densely inhabited by these animals. For example, the Pampas, who were the inhabitants of the prairies, supplied the horses; Araucas, who lived on the other side of the mountains, supplied knitted wooden blankets and other products from their more advanced culture; Pehuenches, who rode their horses on both sides of the mountainous range, were the traders (Erize 1989a, b, c). However, as it usually happens when the relationships between two cultures become too close, there was acculturations and amalgams or fusions that may bring to the disappearance of one of them. This was what happened in this case.

What was this process favored by?

Basically, it was favored by their cultural differences. On one hand, Araucas or Mapuches used to establish their tents permanently in watered areas with alluvial plains, but this did not mean they stopped wandering into distant lands. On the other hand, the people of this race, who were meat eaters, well-built and agile, stronger and smarter than the other tribes, and who had been obliged to be warriors and dynamic because of the small size of their country, easily dominated the idle, lazy, apathetic Pampa rangers. Moreover, as a result of the contact between

Mapuches and Spanish, these people adopted a few elements from the conquerors (such as horses, cows, sheep and steel knifes), which made them superior to the more quiet Tehuelches and Puelches and all the other inhabitants of the vast Pampa (Fig. 13.2b) area. These peculiarities strengthened their rough character, adventurous spirit and the urgent need of food supply by stealing it.

Araucanization or change in population process is not a singular case but something that repeatedly happened in the history of most civilizations. Particularly in this case, due to the nearness in time and the existing data, it is possible for historians to follow it closely, and analyze how through constant filtrations a culture extends to occupy territories that are over a 1000 km away from their primitive habitat. This substitution majorly happened without great violence or displacement of the former population and, when there was an ethnic replacement, it was accompanied by a process of adaptation and fusion. Through this process, people with an Andean culture transformed, under new environmental influences, into a population that supported themselves by cattle rearing, seed collecting and theft (Canals Frau 1953).

13.5 Mapuches and Their Beliefs

According to the researchers, in real Pampas or Mapuches culture there is no God or goodness spirit. All their mythological deities are devils who, depending on the circumstances, are quite good beings. As their supporters, they are nomads as well. In Mapuches beliefs there were gods of the fields or wildness, gods without home who only lived in the volcanoes, in large forests, in swamps, twirling in the air in people's meetings, around their huts or in old trees by a busy road, always expecting to bother or cheat travelers. Then, they assumed it was these spirits action that made them lose or forget things or their horse become tired (Erize 1992).

Another aspect distinguishing the Mapuches belief was that they just saw what happened

around them and tried to explain the phenomena. Thus, for them, a new year began when days became shorter (the winter solstice on 21st June) and it lasted until the longest day of the year. Therefore, Nature immensity was explained by fantastic stories such as the one about the prominent rocks (*Huichralcura*) in the mountains (*chrenchen*) which, they believed, were the petrified bodies of Mapuches that had not saved from the universal diluvia and had then become jealous guardians of their mountains, avoiding strangers to profane the holy majesty of their tops from then on by producing alludes, avalanches, storms and fogs (Erize 1989a, b, c).

Another amazing Mapuche belief explained earthquakes (*Muchrounhueque*) as the movement of shaking the 'vicuña' or 'llama', which is the literal translation of the Mapuche word. The *vicuña* is a typical specimen of the camel family, which is found in the northern Chilean regions

and it may be supposed that they shook this animal when they killed it for its meat, and this shaking or the noise reminded them of earthquakes.

Finally, as these people ignored Nature secrets, they explained through stories events such as the persistent Patagonian winds. Then, they believed that the wind whistling announced that the spirits were angry (Erize 1992).

Nature environment undeniably influenced these cultural beliefs.

On the slopes of the Andean range, in the Neuquen province's Andean forest zone, and distributed in the area located between Copahue and Lanin volcanoes (Fig. 13.1), there is a woody land of pine trees spread in such a way that inspire many abstract thoughts and give a mysterious and prehistoric feature to the region: *pehuen* (*araucaria araucana* or *monkey puzzle tree* in English) woods. (Figure 13.3a). Though a
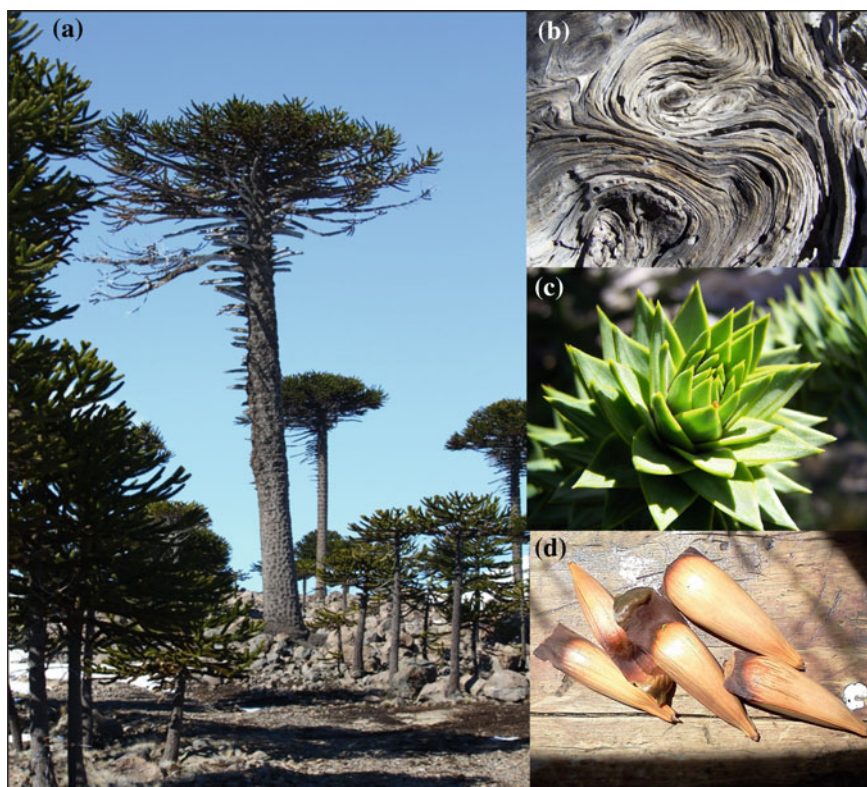

Fig. 13.3 a Whole view of a Pehuen straight trunk. **b** Pehuen bark. **c** Detail of pehuen spiny leaves, helicoidally distributed along the branches. **d** Pehuen kernels ('piñón')

magnificent ancient tree, an araucaria shapes spots in a severe landscape reminding of an old paleontological past when vegetation and fauna were more exuberant. According to some authors (Alvarez 1984; Bisheimer and Fernandez 2009), *pehuen* is the symbol of the Neuquen flora and the most representative tree of the province. It is believed that this pine tree developed gigantically in the Tertiary age and that it may have existed at the same time of the huge antediluvian animals. It has a wide spherical or conical umbrella-like crown (Fig. 13.3a) with cylindrical branches that extend as looking for expansion providing the landscape a severe feature. The trunk, impressively straightened and covered with a thick rough bark, which splits into plates (Fig. 13.3b), is too hard to be axed. The branches disguise seeming to be protective because they are tough and itching with spiny leaves (Fig. 13.3c) distributed in helicoidally way. These trees grow even in the roughest tops where the strongest winds blow but they keep firmly attached to the hard rocks. Sometimes they are aligned on the edge of cliffs elevating their 40 m or more high trunks with their bottom surrounded by hugging *ñires* (Alvarez 1984).

These woods were an important source of supplies for the original people because their fruit, *piñón* (Fig. 13.3d) was a component of their diet. Moreover, the araucaria resins (*üpe, ope*) had medicinal properties exploited from Mapuches. The importance of the *piñon* might have inspired the following praying in the Mapuche culture (Bisheimer and Fernandez 2009):

> When one is about to take piñones, then you have to pray. Pray first and then take the piñones up. You have to say: Our piñon's mother, our piñon's father, wish you gave us plenty of piñones every year Piñon's mother volcano, piñon's father volcano, piñon's girl volcano, piñon's boy volcano. You have given this food in this land. Should they say, supporting those on earth, they do not lack of food, so that they will not feel hunger…
> Ceferino Caitrú 49 years old (Mapuche descendant)

Despite of the reading of this praying made by Bendini (1992), it can be seen that Nature and its forces are related to the aborigines basic supplies as they prayed to the volcano to provide them of the pehuen fruit. In this praying they also refer to four deities (mother, father, girl, boy) related to the volcano.

In the natural environment above described it is magnificently located Copahue volcano (Fig. 13.4). Obviously, trying to explain the volcanic activity with the Mapuche world vision (Erize 1991), it was the origin of numerous beliefs. Then, they gave life to new beings that explained what was happening. Thus, a meteorite or fireball (*cheruve*) was a fabulous being in the Mapuche mythology. Moreover, in some places it was described as a hybrid: a human head and a snake body; in other places it was represented as a giant who lived in the volcanoes. Therefore, when these people watched a meteorite they thought it announced death and miseries to the families that lived in the direction it exploded (Erize 1989a, b, c). Thus, it may be inferred that for these people flames and fire as well as lava or magma from the crater of volcanoes were fabulous events they could simply explain with fantastic stories. Thus, they believed that *cheruve* (Erize 1992), the spirit of fire, lived in the volcanoes and all the mentioned phenomena was related to its burning exhalation. Or, as in some Araucas tales, this spirit was a superman of huge condition and powers. It lived at the top of the volcanoes, ate meat of aboriginal girls, and took revenge by drying rivers or producing earthquakes when the girls' parents did not offer them to him (Erize 1989a, b, c).

Nature magnificence overwhelmed them and the fire of the volcanoes appeared in most of their beliefs. The legend about Copahue, which is a bell-like flower belonging of the flora of the region, is an example of this. It is said that *hueuvü* or evil genius that lived in the high peaks used to rush down to the valleys and get drunk with the *mudai* (alcoholic beverage extracted from the pine kernels) he stole from the aboriginals. On his way back home in order to not get lost, he was used to place to the branches in the forest, thousands of little bells lightened in the fire at the top of the volcanoes. However, as he was too drunk, he left them lighted in the mountains tracks. Once the superior protector spirits defeated him and although he pledged to be allowed to take the lanterns to his exile land,

Fig. 13.4 The Copahue volcano in winter

he was not heard. Thus, today the red Copahue flowers hang like little bells in the forest (Erize 1989a, b, c).

Volcanoes were also present in Mapuche beliefs as related to death. They believed that immediately after a person died an untouchable vaporous being, the *alhue*, only visible at his will, joined the corpse and stayed in the tomb until the body disappeared. In their beliefs the spirit then abandoned the body and occasionally, when leaving, it was caught by the witches (*calcu*), who used it for their curses (*huichan alhue*). Then the aboriginals offered a humble gift in a tree or rock in the mountains to calm down their ire: pebbles, feathers, parts of clothes, leftovers, and so forth (Erize 1992). Father House, a Christian missioner explained in his works that, although the souls for the Araucas were immortal, they had such a materiality that they needed clothes, jugs with "chicha" (alcoholic beverage made from fermentation of apple and cereals), war weapons and working tools in the tombs. For this reason, families often lit fires on the tombs the whole year after a death so that the wandering soul could warm up and get sparks to make a fire in the frozen western lands. Other missioners considered that *alhue* was Satan.

Araucas also believed that the spirit or soul of a dead person (*Pillañ*) accompanied the body and wandered around the tomb as far as their relatives remembered the person and evoked his memory. Then, *Pillañ* became part of the family life being present in his meetings and parties, memories and dreams. As time went by and memories vanished, the dead was no longer present among his descendents and then *Am* turned into *püllü* and left definitely for the spirits' lands or the volcanoes, which was the special destiny for the chiefs' families or important people such as founders (Erize 1992).

Through this spirit, they intended to explain natural forces. Good or bad weather, crops, fertility or infertility of animals depended on Pillañ or Püllu's will. They controlled volcano eruptions and earthquakes as well as thunders, lighting and hails, storms and floods. Once Püllu or Pillañes were in the spirits' land, they continued with their former life. They were corporeal although invisible beings that kept the mentality, tastes and passions, as well as needs, of their previous lives. Then, they took the food, clothes, jewels and utensils piled up on their graves and showed their likes and dislikes by nature forces they could manipulate. Mapuches thought that

they were associated to the founders of tribes to make the good or the evil to their descendents. Some authors say that Araucas believed that Pillañ was originally the name of a remarkable and very old ancestor, who could be located in any volcano (Erize 1992).

Summarizing, "Pilláñ", one of the names given to the volcano, is a word which was also understood in some other ways, such as: referring to the soul of a dead person, to name an important ancestor (with a negative connotation) or a supreme god that shows its ire through the entire phenomenon related to volcanoes. It also seems that *Pilláñ* may be the ancient name of a divinity, apparently later replaced by Nguenechen (Supreme God).

But there were not only Pehuen and volcanoes in the surroundings of the Mapuche land. Some nearby natural pools like lakes and lagoons also inspired their mythological explanations. Maybe they felt fear of the deep waters darkness and through these stories they tried to avoid the disappearance of children in these waters. One of their beliefs was to mention *Chompallhue* (literally curly soul) or Lake Genius like someone who was presented as a mythological being who usually had the shape of a small man, dark complexion and curly hair that lived in the depths of lakes and lagoons.

Another legend related to deep waters tells about the *Fiura* or the woman in the lake. They described her as a fat and back bent being with strong arms and huge feet. Many people thought she was evil because of her repulsive breath and horrible look. However, they believed she was a resented being because no man on Earth desired her and her major wish was to be loved and have children. For this reason, throughout the years she learned to sing with the most beautiful voice and attracted innocent people with it imitating the *coñilauquen* (local bird) hidden behind the waterfalls or in bushy lakes shores to conceal her bad stench. They said she was found trying to kidnap children who were out of their mothers' sight but just because she wanted to look after them as if they were of her own. Mapuches also said Fiura's hands were infected and they produced deformations or malformations when

touching men. For this reason, they tried to keep her away. Maybe they explained in this way what happened with their fingers when they were in water for too long.

13.6 Celebration and Religions

As Mapuches were fatalists from remote times, they always considered their misfortune was the result of hidden forces. As a consequence, and to their own interest, they understood they had to worship such powerful spirits that were so closely related to them. They did not adore them as gods or demons but they tried to have them on their side, making sure by different rituals such as invocations, animals' blood sucking and sacrifices, that pillañes' good will was with them. That was the main reason why they celebrated *Nguillatunes* (annual celebration when Mapuches pledge for a good year) (Erize 1992).

As far as the hierarchy of Mapuche gods is concerned, they believe that Supreme Creator was *Nguenechen*, an all in all creator who dominated the Earth as a king or pastor, gave life and fertility to human beings, animals and plants, controlled nature forces for the joy and misbelieve of men. They called him Father because they believed that they were bred by him. They thought he looked like a human being but maybe of a more subtle spiritual nature, and they had a confusing idea of his nature. They did not know if he was a man or a woman so they believed he was both. That is why they told him '*you have bred us*' treating him as a male being or '*you have given us life*' treating him as a woman. His room is above us maybe at the zenith (father) and in the middle of heavens (mother). In the vast blue regions he deserved the name of Blue father and mother. His house was made of pure gold so maybe it was the sun. He was generous and accessible to the pledge of mortals.

On the other side, Mapuches believe that the Evil genius (or Devil), who controlled miseries and diseases of the Argentine aborigenals, was called *hualichu* or *huecuvü*. Nevertheless, it represented an abstract concept of evilness. He was

invisible, indivisible and was everywhere. He was always thinking about how to cause the others' misfortune. Mapuches made him responsible of unfortunate situations such as unsuccessful raids, the Christians' invasions on their lands, peoples' diseases and death, as well as all the plagues and calamities that worried humanity. *Hualicho* was in everything that was understandable and mysterious. Thus, Mapuches said that people must be in good terms with him because he was over viewing everything and from time to time it was necessary to sacrifice horses, cows and sheep, at least once a year (once each twelve moons for Mapuches) to comfort this evil genius.

Summarizing, for this native people the idea of evil or devil had barely developed in their mind as they had explained it as a spiritual force; nevertheless, they recognized its malicious influence so they feared and hated him. As a way of mitigating the evil's power, they believed that his worst enemy was *machi* (person considered to have medical powers) (Erize 1989a, b, c).

13.7 Copahue Volcano: The Meaning of Its Name

There are many versions about the meaning of this word. The most popular one is that it means sulfur place. In a report about Mapuches sayings by Hassler W., sulfur indicated the *chos lahuén,* which means yellow medicine. The word Copahue referred to a ritual operation that the ancient Mapuches made on their left arm with a piece of burning cane (*quila*). As cold made them suffer so much in this world this ritual aimed to protect them from coldness in their other life. *Copa* would be the name of this operation and *Copahue* would name the instrument used for operating (Erize 1990).

13.8 Copahue Legend

There is a legend that has survived throughout the years and that, for the Indians, thoroughly explains the name of the volcano. This story is told by most ancient Indigenous in the region and has become part of the folk culture of the country. In the Great Chief Pueñ's words:

Copahue was the name of a chief who was very famous not only for his war actions but also for his cruelty to the tribes he submitted. This seems to have happened a century before the Spanish arrived in America. One day, the Cuncos and Promaucaces from Chile organized a violent rebellion and the tyrannical Copahue died.

His elder son, who was also called Copahue, wanted to revenge his father's death. He came from Chile through Chancho Co pathway to the araucarias' woods in Caviahue and The Pines areas to reorganize his father's men that were settled to the east of the Andes Range.

On his foot way to those lands, he saw a young Pehuenche girl from a nearby tribe standing by a pool of green waters. She was collecting medicinal herbs (lahuenes) because she was a machi (pitonese or curator). Her beauty and youth made Copahue fall in love with Pire Rayen (Snow Flower) as soon as he saw her.

All day long, walking down to The Pines first and Trolope later, he could not take the beautiful girl out of his mind or heart. He drove so mad because of her that he lost his will of fighting and consequently his prestige and finally the respect of his warriors (conas) who had in vain constantly reminded him of his past bravery, aggressive spirit and glorious ancestors.

Pire Rayen, who understood the cause of Copahue's illness very well, gave him a bunch of mellico lahuen, which was not only the best medicine for love effects but also the best stimulator for courage and virility. Then she told him: 'You will soon have a victory over your enemies. After that, if you still love me, come to me and then I will love you'.

Being encouraged by hope, the warrior left to the north to ally with Varvarco tribes near Domuyo Mountain. He organized a stronger army and left for Chile to revenge his father's defeat. Then he had an important victory and returned triumphant with treasures to claim for the love of the beautiful mountain Pehuenche girl.

Pire Rayen fulfilled her promise and went away with Copahue, her love, to the place where they had chosen to settle their tent, the Domuyo valleys. They expected their cattle would increase in number in the mallines (green area which works as a water reserve) of Vuta Leuvu.

But, when Copahue arrived, the people were so unsatisfied that the just married couple felt worried. Why did this happen?

On one hand, not all the Indians were satisfied with the treasures he had taken and, on the other hand, the tribes considered that the woman

Copahue had taken with him was a foreigner. As a result, Copahue had no authority over his rigid opponents who accused him of emulating his father in cruelty due to the oppressive attitude he began to have with the peoples. They thought it was a consequence of the magical influence of the machi Pire Rayen. Moreover, they pejoratively nicknamed her as Pire Pillañ which means Snow Demon. They pressed on the Chief by all means so that he could escape from the malicious curse of his beloved woman. But, as they were not successful, they revolted and attacked him one night. A furious fight among partisans and opponents of the young girl held up. Copahue friends won but unfortunately they encouraged themselves and cruelly and blindly prosecuted their opponents who had run away to the Ailinco mallines to recover from the fight and prepare for the revenge.

Not long after they returned and attacked Copahue taking him by surprise. And this time he was defeated. Yet more, the great local chief of the mountainous ranges died in the fight.

In the evening after the riot, Pire Rayen together with Copahue's most loyalist friend searched for his dead body, which they finally found among many of his enemies. After caressing and bathing him with her tears, she asked his friends to take Copahue's body and bury him in his homeland.

But she was followed by the survivors of the battle who were angry because of their defeat and they reproached her for their chief's death. They were sure it had been because of her enchantment and magic that Copahue had abandoned his warriors and left his military practice behind. Then, in their fury, they merciless killed her with their lances and spears.

At the sight of this murder, the women claimed:

'Ay, ay, ay!....tortured youth! Ay, ay, ay!… brutal and unfair execution of the beloved girl!'

In her agony, even though suffering from the pain of her wounds, the unhappy Pire Rayen claimed in a dying breathing for her loved man: 'Copahue! My beloved Copahue!'

But nobody answered….

It was then when the partisans, who were digging the hole to bury their respected chief, suddenly saw a hot boiling water spring appear. It had an odor they had never smelt before. They conferred this prodigious event to the spirit of Copahue that answered to the anguishing call of his woman in this way so they escaped terrified from that place. From then on, they thought that place was cursed.

On their rush, they left both bodies behind, but Nguenechen the Good God of their race did not leave them alone. He made them immortals as a gift for their love. He turned Copahue into the stream that falls in a cascade from the edge of the cliff into the Green Lagoon and Pire Rayen became

the snow pile under which the steam flows to emerge farther down by the hot water bubbles of the lagoon, where the lovers first met (Alvarez 1984).

13.9   Mapuches Nowadays

The most compacted nucleus of the Argentine Mapuche people live in Neuquen Province. Thousands of human beings live among the snowed mountains of the Andes ranges, in the mountains' paths, in the inhospitable stony areas. They are settled in one of the thirty territorial reservations with about 50 and 100 families on each. These reservation inhabitants live very close to the Andes in lands which are apt to rear goats in winter time but its scarce water oblige them by mid November to migrate to higher lands in the mountains to stay for the summer.

These tribes are not completely nomads. The snowfalls begin by April and they have to leave down the highlands for home. This way of living, which is known as transhumance, means that these people spend 7 or 8 months of *invernada* and 4 or 5 months of *veranada*. As a fatal fate, if they could forget that rhythm, the animals would make them remember it because their migratory instinct pushes them to the West when snow recedes in the high mountains and the exuberant mallines appear in their slopes. Then the typical *arreos* (literally this word means herd) are seen in the roads in summer. Thus, a whole family and their kitchenware, blankets and supplies distributed in a few horses move every summer through deserted areas, crossing rivers, riding up mountains slopes, driving a varied number of goats and dogs along with them to reach the green highlands (Erize 1989a, b, c).

Unfortunately, this unnoticeably rhythm will continue until one day this culture will disappear from the timeline.

Religion, popular beliefs and legends have no scientific explanations. Sometimes they record scientific data. Mapuche culture was transmitted orally from generation to generation and it is possible that there were other stories that might

have been of interest for science as records of scientific events in remote times. Unfortunately, the elder representative members of this culture are dying and precious information might go with them.

References

Alvarez G (1984) Leyenda del Copahue "Donde estuvo el paraíso- Del Tronador a Copahue". Siringa Libros (ed) Neuquén, Argentina, pp 262–269

Bendini M (1992) Rogativa del piñon, In: Editorial Fundación Banco Provincia del Neuquén (ed) Testimonios Mapuches en Neuquén. Neuquén, Argentina, pp 146–321

Bisheimer V, Fernández E (2009) The trees of the Andean —Patagonian or subantartic forests. In: 4 colores SA (ed) trees of the southern national parks. Buenos Aires, Argentina, pp 75–84

Canals Frau S (1953) Poblaciones indígenas de la Argentina. Sudamericana (ed) Buenos Aires, Argentina

Delfino A (1968) Miscelánea Sureña Delfino A (ed) Buenos Aires, Argentina

Erize E (1989a) El mapuche en la actualidad "Mapuche 1". Yepun (ed) Buenos Aires, Argentina, p 79

Erize E (1989b) Leyendas y mitos "Mapuche 5". Yepun (ed) Buenos Aires, Argentina, pp 68–169

Erize E (1989c) Pino cordillerano Pehuen, "Mapuche 5". Yepun (ed) Buenos Aires, Argentina. pp 119–120

Erize E (1990) Significado copahue, "Mapuche 4". Yepun (ed) Buenos Aires, Argentina, p 51

Erize E (1992) Espiritu, alma, sombra del muerto, fantasma, espectro, aparicion del otro mundo, "Mapuche 2". Yepun (ed) Buenos Aires, Argentina, pp127–152

Erize E (1991) Cielo, estrellas, "Mapuche 3". Yepun (ed) Buenos Aires, Argentina, pp 126

Mandrini R (2008) La Argentina aborigen De los primeros pobladores a 1910. Biblioteca básica de la historia, Editorial Siglo Veintiuno, Buenos Aires, Argentina